Charakterisierung der Transport- und Oberflächeneigenschaften von Nanopartikeln mittels Fluoreszenz-Korrelations-Spektroskopie

Tobias Preiß

München 2016

Charakterisierung der Transport- und Oberflächeneigenschaften von Nanopartikeln mittels Fluoreszenz-Korrelations-Spektroskopie

Tobias Preiß

Dissertation
an der Fakultät für Physik
der Ludwig–Maximilians–Universität
München

vorgelegt von
Tobias Preiß
aus München

München, den 29.08.2016

Erstgutachter: Prof. Dr. Joachim O. Rädler

Zweitgutachter: Prof. Dr. Ralf Jungmann

Tag der mündlichen Prüfung: 18.10.2016

Inhaltsverzeichnis

Zusammenfassung

In Nanopartikel (NP) werden besonders große Erwartungen und Hoffnungen gesetzt, um Wirkstoffe gezielt in spezifische Zellen transportieren zu können. Mit ihrer Hilfe soll die geringe Löslichkeit, der schnelle Abbau oder die schlechte Zellaufnahme von ansonsten vielversprechenden Wirkstoffen überwunden werden. Damit NP als Transporter Verwendung finden können, müssen sie eine definierte Größe besitzen, an der Oberfläche funktionalisierbar sein und Wirkstoffmoleküle aufnehmen und wieder abgeben können. Eine NP-Klasse, der viele dieser Eigenschaften zugeschrieben werden sind Partikel aus Metall-Organischen Gerüstverbindungen (MOF). MOF sind poröse Materialien, die über kovalente Bindungen zwischen Metall-Ionen bzw. Metall-Sauerstoff-Clustern und organischen Verbindungsmolekülen zu dreidimensionalen, kristallinen Objekten zusammengesetzt sind.
In dieser Arbeit wurde die Größenverteilung von MOF-NP, Bindungseigenschaften von Funktionalisierungsmethoden sowie die Aufnahme und Abgabe von Gastmolekülen untersucht. Als zentrale Messmethode wurde hier Fluoreszenz-Korrelations-Spektroskopie (FCS) verwendet, da sie in der Lage ist, unter Einsatz geringster Probenmengen, die hydrodynamische Größe von fluoreszenzmarkierten Partikeln und deren Änderung in hochverdünnten, wässrigen Proben zu messen. Durch den Vergleich der, mittels FCS bestimmten Größenverteilungen von MOF-NP mit den Ergebnissen aus anderen Messmethoden, ließ sich ein detailliertes Verständnis über die Größe und Morphologie von NP gewinnen.
Im nächsten Schritt wurden die Bindungseigenschaften von drei Funktionalisierungsansätzen für MOF-NP gemessen. So wurde gezeigt, dass MOF-NP mit einer Lipidschicht umhüllt werden können, welche es den Partikeln ermöglicht besser von Zellen aufgenommen zu werden. Mittels FCS konnte eine Kolokalisation der Lipidschicht und der NP nachgewiesen werden. Außerdem wurde die effektive Barrierefunktion der Lipidschicht demonstriert, die das diffusive Entweichen der Gastmoleküle aus den Poren verhindert.

Als zweite Funktionalisierungsmethode wurde eine selektive, postsynthetische, kovalente Anbindung von Polymeren an die externe Oberfläche von MOF-NP untersucht. Die erfolgreiche Polymerfunktionalisierung konnte ebenfalls mittels FCS nachgewiesen werden. Die so modifizierten NP zeigen eine erhöhte kolloidale Stabilität in wässrigen Medien. Das dritte Funktionalisierungskonzept basiert auf einer koordinativen, reversiblen Bindung von Polyhistidinen (His-Tags) an die Metallkomplexe der Oberfläche von MOF-NP. Die Bindung der His-Tags an die MOF-NP und die Reversibilität der Bindung im sauren Milieu wurde mittels FCS bestätigt. Es konnte demonstriert werden, dass sich mehrere verschiedene Funktionseinheiten auf einer NP-Oberfläche anhaften lassen und sich somit ein multifunktioneller Nanotransporter verwirklichen lässt.
Als weiterer Aspekt ist das Verständnis wie MOF-NP Gastmoleküle aufnehmen und wieder abgeben wichtig. Es wurde eine ausgeprägte pH-Abhängigkeit beider Prozesse gefunden. In Wasser wurde eine sehr hohe Beladungsmenge von Fluorescein in den NP-Poren belegt, welche nahe an der geometrisch möglichen Beladung liegt. Es konnte gezeigt werden, dass der Beladungsprozess diffusionslimitiert stattfindet und durch Prozesse innerhalb der NP verlangsamt wird.
Abseits der Festkörper-NP stellt das Einschleusen von Proteinen in Zellen zur Proteintherapie eine große Herausforderung dar. In zwei Studien zur Proteintransduktion konnte die Bindung und Komplexbildung von Proteinen bzw. Einzeldomänenantikörpern mit Oligomeren mittels FCS gezeigt werden. Diese NP aus Protein/Oligomer-Komplexen werden von Zellen besser aufgenommen als einzelne Proteine.
In dieser Arbeit konnte das Bindungsverhalten von Nanotransportern mittels FCS quantitativ verfolgt und deren physikalische Eigenschaften verstanden werden. Die vorgelegten Erkenntnisse werden zum besseren Verständnis von Nanotransportern, insbesondere von MOF-NP, auf dem Weg zum medizinischen Einsatz beitragen.

Summary

To specifically deliver drugs into target cells, high hopes are placed on nanoparticles (NP). They can provide the properties to overcome common issues of other promising drugs such as low solubility, poor stability and uptake deficiencies. In order to be used as a transport vehicle, NP need to possess a defined size, a surface functionalization for targeted uptake and the ability to absorb and release payload molecules. One group of NP that is believed to combine many of these properties are particles featuring a metal-organic framework (MOF). MOFs are porous materials that are composed of metal ions or metal-oxide clusters covalently interlinked with organic molecules to form three-dimensional crystalline objects.

In this thesis, size distribution, binding properties of functionalization methods and guest molecule uptake into and release of MOF NPs was investigated. As a central method, fluorescence correlation spectroscopy (FCS) was chosen due to its ability to measure hydrodynamic size in highly diluted aqueous solutions by fluorescent fluctuations. Comparison of MOF NP size distributions obtained by FCS and other methods provided a deeper understanding of their structure and dimensions.

Additionally, three functionalization concepts of MOF NPs were investigated. It was demonstrated that MOF NPs can be enclosed by a lipid bilayer, improving cellular uptake. FCS measurements displayed co-localization between lipid bilayer and NPs. Moreover, it was shown that fluorescent molecules located inside the NPs pores are actively prevented from being released. As the second functionalization method, selective, post-synthetic covalent attachment of polymers to the outer surface of MOF NPs was studied. The success of the polymeric functionalization was verified by FCS. Polymer functionalized NPs exhibited improved colloidal stability in aqueous media. The third functionalization concept is based on coordinated reversible binding of polyhistidine-tags (His-tag) to the metal complexes on the MOF NP surface. Attachment of His-Tags to MOF NPs and reversibility of binding in acid environment was shown using FCS. The successful

attachment of multiple different functional units to the NP's surface was revealed by FCS measurements, permitting realization of multifunctional nanotransporters.
Investigating the principles of guest particle uptake and release by MOF NPs, a high pH dependency between both processes was found. A high amount of fluoresecin payload in NP pores close to the theoretical maximum was demonstrated. It was shown that the uptake is diffusion-limited and slowed down by processes inside the NPs.
Apart from MOF NPs, the transduction of proteins into cells poses a major challenge in nanomedicine. In two studies of protein transduction, FCS measurements showed, that proteins or single-domain antibodies form complexes. These protein/oligomer nanocomplexes showed enhanced cell uptake as compared to single proteins.
The FCS measurements of this thesis provided a multitude of physical properties of NPs. The findings will contribute to a better understanding of nanotransporters, especially MOF NPs towards future medical applications.

Kapitel 1

Einleitung

In Nanotransporter werden in der Medizin besonders große Erwartungen und Hoffnungen gesetzt, um Wirkstoffe gezielt in bestimmte Gewebegebiete (z.B. Krebstumore) oder spezifische Zellen (z.B. Inselzellen) zu transportieren. Dies ist notwendig, denn viele Krankheitsprozesse sind Folge einer Funktionsstörung in spezifischen Zelltypen auf subzellulärer Ebene. Die immer detailliertere Aufklärung pathobiochemischer Prozesse auf molekularer Ebene führt zu einem zunehmenden Verständnis der Erkrankungsursachen und eröffnet dadurch neue Therapiemöglichkeiten. Heutzutage zielen die meisten etablierten medizinischen Therapien auf makroskopische Methoden ab (Resektion von Tumorgewebe, Gefäßstützen, Strahlentherapie, etc.). Zusätzlich werden Medikamentenwirkstoffe (z.B. Doxorubicin, Cisplatin, Mitotane) appliziert, die sich in der Regel im gesamten Körper ausbreiten und somit auch dort Wirken, wo es therapeutisch nicht notwendig wäre. Diese Unspezifität ist u.a. mit starken Nebenwirkungen verbunden wie zum Teil lebensgefährlichen Blutbildveränderungen, Übelkeit und Haarausfall bei Chemotherapie [1, 2]. Andererseits zeigen viele innovative Wirkstoffe (z.B. Peptide, Proteine, mRNA, siRNA), welche auf direkte intrazelluläre Wirkung abzielen eine sehr geringe Zellaufnahme [3]. Zusammen mit einer raschen Metabolisierung oder Degradation abseits des Wirkungsortes führt dies zu einem hohen Wirkstoffeinsatz und oftmals hohen Kosten bei geringer therapeutischer Wirkung [4]. Vor diesem Hintergrund wird klar, dass ein effizienterer Wirkstofftransport von Nöten ist. Dessen Hauptaufgabe ist es die Wirksubstanz gezielt in spezifische Zellen oder Gewebegebiete zu befördern, um sie erst dort punktuell freizusetzen. Die jüngere Forschung zeigt, dass sich für diesen Zweck sogenannte Nanotransporter (Nanocarrier) eignen [5]. Nanotransporter sind Objekte, welche eine Größe von 1-1000 Nanometern (10^{-9}m) besitzen und dazu ge-

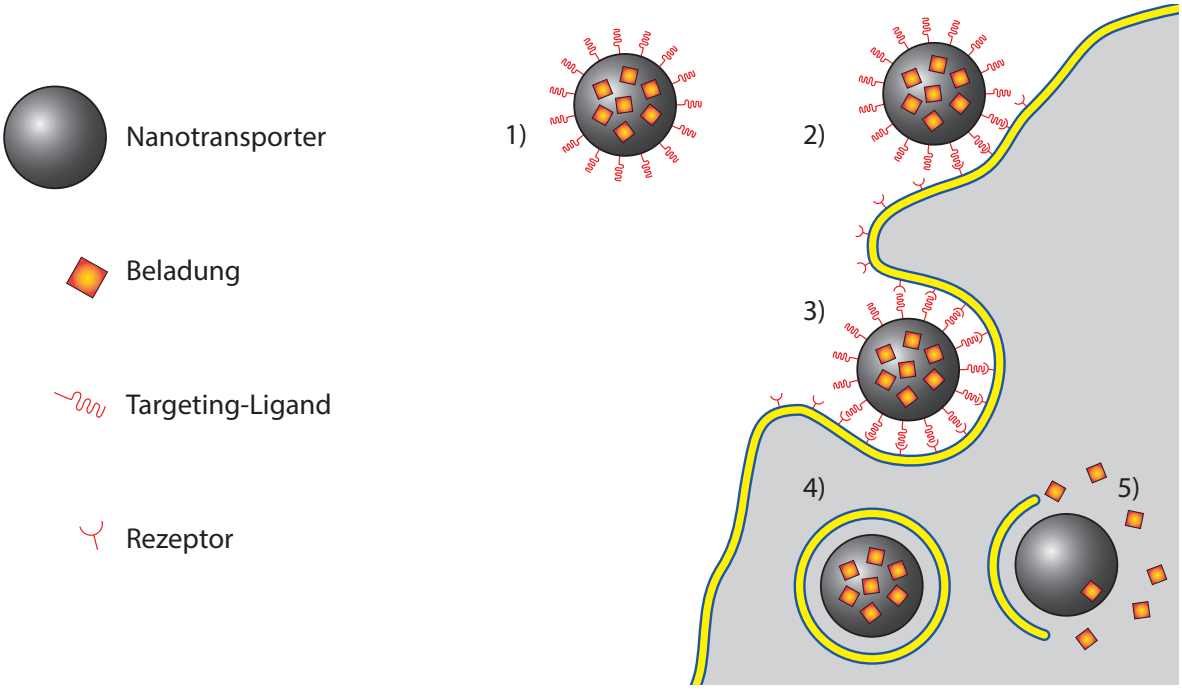

Abbildung 1.1: Idealisiertes Schema zum gezielten Medikamententransport. Ein Nanotransporter wird beladen und mit einem Targeting-Ligand funktionalisiert (1). Durch diese Funktionalisierung wird sichergestellt, dass der Nanotransporter spezifisch an die Rezeptoren der anvisierten Zellen bindet (2). Durch die Ligand-Rezeptor-Interaktion wird die Vesikelbildung eingeleitet (3). Durch die Verschmelzung des Vesikels mit dem Endosom kommt es zu einem Abfall des pH-Werts (4). Dadurch kann es im weiteren Verlauf dazu kommen, dass die Membran platzt und der Inhalt aus dem Endosom entkommt (5).

eignet sind Wirkstoffe in bestimmte Gewebegebiete, Zellen oder Zellbestandteile zu transportieren. So existieren zahlreiche Konzepte des Aufbaus von Nanotransportern wie zum Beispiel Liposome [6–9], Nanoshells [10, 11], Mizellen [7, 12, 13], Dendrimere [14, 15], polymerische Tansporter [1, 5, 16–19] und Festkörper-Nanopartikel (NP) [20, 21]. Letztere sind von besonderem Interesse, da sich eine Vielzahl von Materialklassen zu NP verarbeiten lassen und somit als potentielles Trägersystem zur Verfügung stehen. Als NP bezeichnet man einen Festkörperverbund von typischerweise einigen Tausend Molekülen, dessen Größe im Bereich von zehn bis einigen hundert Nanometern liegt. Von besonderem Interesse in der Nanotransporterforschung sind in jüngster Zeit NP aus Metall-organischen Gerüstverbindungen (engl. Metal-Organic Frameworks, MOF) [20]. MOF stellen eine junge Klasse poröser Materialien dar [22–24], die über kovalente Bindungen zwischen Metall-Ionen bzw. Metall-Sauerstoff-Clustern und organischen Verbindungsmolekülen zu dreidimensionalen kristallinen Objekten zusammengesetzt sind (s. Abb. 2.1). Das große Interesse an dieser Klasse von NP ist eine Folge der Eigenschaften von MOF-Nanopatikeln. Dazu gehören die große Porosität vieler MOF-Strukturen, die eine große Beladungsmenge des Wirkstoffs verspricht, die Kristallinität des Materials, die ein genaues Strukturverständnis erlaubt, und die Möglichkeit eine Vielzahl von potentiellen Bausteinen zum Aufbau der MOF-Struktur zu verwenden was eine optimale Anpassung an die jeweilige Aufgabenstellung verspricht.

Für die Verwendung von MOF-NP für den effizienten Wirkstofftransport müssen mehrere Voraussetzungen erfüllt werden: Ein Wirkstoff muss in die Partikel gefüllt oder an die Partikel gebunden werden können. Durch eine Verkapselung muss der Wirkstoff in bzw. an den Nanotransporter gebunden bleiben solange der Nanotransporter noch nicht an seinem Ziel angekommen ist. Durch geeignete Funktionalisierung der Nanotransporter muss dieses Ziel z.B. durch Targeting-Liganden oder Antikörper adressiert werden können. Die Nanotransporter müssen vom Zeitpunkt ihrer Produktion bis zur Ankunft an ihrem Ziel stabil sein und ihre Eigenschaften nicht verändern. Am Ziel angekommen muss eine kontrollierte Freisetzung des Wirkstoffs möglich sein (s. Abb. 1.1).

Für die Etablierung neuer MOF-NP ist eine detaillierte Charakterisierung hinsichtlich dieser Eigenschaften notwendig. Als zentrale Messmethode wurde in dieser Arbeit Fluoreszenz-Korrelations-Spektroskopie (FCS) verwendet. FCS bietet die Möglichkeit, Diffusion sowie Wechselwirkungen fluoreszenzmarkierter Partikel zu untersuchen [25–28]. Die Fähigkeit zur Bestimmung von Diffusionskoeffizienten und hydrodynamischen

Radii sowie der Nachweis von Bindungen sind maßgeblich für das breite Einsatzgebiet von FCS bei biophysikalischen Fragestellungen [29–31]. Die hohe Sensitivität von FCS erlaubt es in physiologischen Konzentrationen (nanomolare Lösungen) zu messen. Im Gegensatz zu anderen Techniken, welche z.B. auf radioaktive Marker angewiesen sind, basiert FCS auf der Detektion von Fluoreszenz, was dieser Technik zu einem breiten Anwendungsfeld in der Biophysik verholfen hat. Für einige Projekte wurden weitere Techniken genutzt, um die FCS-Ergebnisse zu untermauern oder zu ergänzen. So wurde Elektronenmikroskopie zur Größen- und Morphologiebestimmung eingesetzt. Dynamische Lichtstreuung lieferte hydrodynamische Radii von nicht fluoreszierenden NP. Absorptions- sowie Fluoreszenzspektroskopie ermöglichten die Messung der Aufnahme und Freisetzung von Gastmolekülen in MOF-NP.

Die in dieser Dissertation präsentierte Arbeit ist motiviert von der Vorstellung wohldefinierte, multifunktionelle und gezielt einsetzbare Arzneimitteltransporter zu entwickeln, die ihre Wirkung erst bei Erreichen des Zielgebiets entfalten. In einem ersten Teilprojekt werden MOF-NP hinsichtlich ihrer Größe und Morphologie charakterisiert (Kapitel 4.1). Daraufhin werden verschiedene Funktionalisierungsmethoden für MOF-NP untersucht (Kapitel 4.2). In einer Studie zur postsynthetischen Beladung von MOF-NP werden die Prozesse zur Aufnahme und Freisetzung von Gastmolekülen eingehend ergründet (Kapitel 4.3). Abschließend wird in zwei weiteren Studien eine zweite Klasse von Nanotransportern mittels FCS untersucht. Dabei handelt es sich um NP aus Proteinkomplexen, welche eine effiziente Proteintransduktion ermöglichen (Kapitel 4.4). Zusammengenommen stellt das aus diesen Teilprojekten gewonnene Verständnis einen großen Schritt in Richtung Entwicklung von Arzneimitteltransportern dar, die alle nötigen Voraussetzungen für den medizinischen Einsatz erfüllen.

Kapitel 2

Grundlegende Konzepte von Nanotransportern

2.1 Nanomaterialien

Bei vielen Materialien sind die spezifischen Eigenschaften stark davon abhängig, ob sie als ausgedehnte Körper oder als NP vorliegen. So hat zum Beispiel Gold als ausgedehnter Festkörper einen hohen Schmelzpunkt und keine katalytischen oder ferromagnetischen Eigenschaften. Als NP hingegen weist Gold einen verringerten Schmelzpunkt [32] auf, findet Einsatz als Katalysator [33] und kann ferromagnetisch werden [33–35]. Die Eigenschaften eines Materials lassen sich jedoch nicht nur in makroskopische und nanoskopische Ausdehnung kategorisieren. Viel mehr hängen viele Eigenschaften von NP von ihrer jeweiligen Größe im Submikrometerbereich ab. Durch das hohe Oberfläche-zu-Volumen-Verhältnis dieser Partikel können Oberflächeneffekte die Eigenschaften von NP dominieren. Für eine gezielte Nutzung von NP als Transporter von Arzneistoffen können spezielle größenabhängige Eigenschaften und Oberflächeneffekte von Nanomaterialien genutzt werden. Um Nanotransporter für therapeutische Anwendungen nutzen zu können, ist nicht nur der gezielte Transport des Arzneistoffs erforderlich, sondern auch eine kontrollierbare Freisetzung am Zielort über den gewünschten Zeitraum hinweg. Die Freisetzungskinetik eines Wirkstoffs hängt unter anderem von der Art der Bindung an den NP ab. So können Arzneistoffe an die Oberfläche des NP gebunden oder in poröse NP eingeschlossen werden. Arzneistoffe, die rasch im Körper abgebaut werden, sollten durch eine Verkapselung des Nanotransporters vor der Umgebung geschützt werden, um so die Stabilität des Wirkstoffs zu erhöhen. Für eine zielgerichtete Zell-

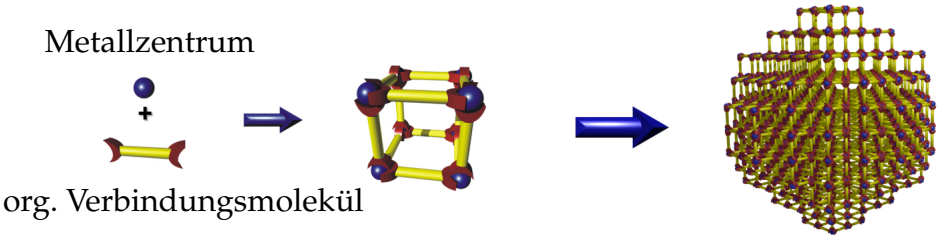

Abbildung 2.1: Vereinfachte Illustration zu Metall-organischen Gerüstverbindungen. Die koordinative Bindung zwischen den Metallzentren und den organischen Verbindungsmolekülen führen zu einer geordneten, kristallinen Struktur. Von links nach rechts: Bausteine, einzelne Pore und ein Nanopartikel.

aufnahme ist eine Funktionalisierung der Oberfläche der Nanotransporter notwendig, sodass die Nanotransporter spezifisch an Rezeptoren der intendierten Zellen binden und wodurch anschließend über die Vesikelbildung die Endozytose eingeleitet wird (s. Abb. 1.1). Durch solch eine geeignete Funktionalisierung soll der Nanotransporter nicht nur in die Zelle gelangen, um dort den Arzneistoff freizugeben, sondern bei Bedarf noch weiter, bis in den Zellkern gelangen können. In den letzten Jahren haben sich NP aus Metall-organischen Gerüstverbindungen als vielversprechende Nanomaterialien für die Anwendung als Nanotransporter erwiesen. Aus diesem Grund werden MOF-NP in dieser Arbeit eingehender auf ihre Einsatzmöglichkeiten in der Nanomedizin untersucht.

2.2 MOF-Nanopartikel

MOF sind kristalline Materialien, die aus metallischen Knotenpunkten und organischen Verbindungsmolekülen poröse Strukturen bilden (s. Abb. 2.1). Über die Länge der gewählten organischen Verbindungsmoleküle kann die Porengröße gesteuert werden. Bislang sind über 20 000 verschiedene MOF-Strukturen bekannt. Besonders die mesoporösen MOF-Strukturen mit Kavitäten größer als 2 nm und damit großen inneren Oberflächen (bis über $4\,500 \mathrm{m}^2\,\mathrm{g}^{-1}$ beim MOF-177) sind von Interesse, da sie viele Anwendungsmöglichkeiten besitzen (z.B. als Katalysator, Gas-Speicher oder Arzneimitteltransporter). [22, 36]

Einige hundert der MOF-Strukturen bieten das Potential Nanokristalle herzustellen. Solche MOF-NP werden als vielversprechende Kandidaten für Nanotransporter im Bereich der Bildgebung [37] oder des Arzneimitteltransport gehandelt [20, 38]. Ein besonderer Vorteil von MOF-NP ist die Möglichkeit eine maßgeschneiderte Struktur für

das jeweilige Gastmolekül zu designen. Außerdem sind einige MOF-NP aus abbaubaren oder im Körper bereits vorhandenen Bausteinen zusammengesetzt, sodass die NP eine geringe Toxizität zeigen. In dieser Arbeit wurden im Wesentlichen drei Sorten von MOF-NP verwendet. Diese sind MIL-100(Fe) [39], MIL-101(Cr) [40] und Zr-*fum* [41]. „MIL" steht hier für „Materials of Institute Lavoisier". Die Partikel wurden von der Arbeitsgruppe von Dr. Stefan Wuttke aus der physikalischen Chemie der LMU hergestellt. Die Synthese der verwendeten MOF-NP wird im Folgenden beschrieben.

MIL-100(Fe)

Die MIL-100(Fe)-NP wurden wie folgt synthetisiert [42, 43]. Trimesinsäure ($C_9H_6O_6$) wurde in eine Lösung aus Eisen(III)-chlorid-Hexahydrat ($FeCl_3 \cdot 6\,H_2O$) und Wasser (MilliQ) gegeben (Verhältnis $FeCl_3$:$C_9H_6O_6$ = 9 : 4). Diese Mischung wurde in einem Teflon-Versuchsautoklaven verschlossen und in einem Mikrowellenofen binnen 30 s auf 130 °C erhitzt. Die Temperatur wurde für 2 min gehalten. Die so entstandene NP-Suspension wurden durch Zentrifugation vom Reaktionsmedium getrennt und in Ethanol resuspensiert.

MIL-101(Cr)

Die MIL-101(Cr)-NP wurden wie folgt synthetisiert [44]. Terephthalsäure ($C_8H_6O_4$) und Chrom(III)-nitrat-Nonahydrat ($Cr(NO_3)_3 \cdot 9\,H_2O$) wurde äquimolar in Wasser (MilliQ) gemischt. Diese Mischung wurde in einem Teflon-Versuchsautoklaven verschlossen und in einem Mikrowellenofen binnen 4 min auf 180 °C erhitzt. Die Temperatur wurde für 2 min gehalten. Die so entstandene NP-Suspension wurde durch Zentrifugation vom Reaktionsmedium getrennt und in Ethanol resuspendiert.

Zirkonium-Fumarat

Die Zr-*fum*-NP wurden wie folgt synthetisiert [41]. Fumarsäure ($C_4H_4O_4$) und Zirconium-(IV)-chlorid ($ZrCl_4$) (Verhältnis $C_4H_4O_4$: $ZrCl_4$ = 3 : 1) wurden in einem Glasreaktor (25 ml) mit einer Lösung von konzentrierter Ameisensäure (CH_2O_2) und Wasser (MilliQ) (Verhältnis Volumina CH_2O_2:H_2O = 39 : 400) vereint. Das Reaktionsgemisch wurde für 24 Stunden in einen auf 120 °C vorgeheizten Ofen gegeben. Die so entstandene NP-Suspension wurde durch Zentrifugation vom Reaktionsmedium getrennt und in Ethanol resuspendiert.

2.3 Liposomen

Der amphiphile Charakter von Lipidmolekülen, mit einem hydrophilen Kopfteil und einem lipophilen Kettenteil, führt dazu, dass sich Lipidmoleküle in dem polaren Lösungsmittel Wasser zu geschlossenen Strukturen anlagern. Eine häufig gefundene Strukturform ist die eines Bläschens, Liposom genannt, bestehend aus einer Doppelschicht aus Lipidmolekülen, welche das Innere vom Äußeren des Liposoms abtrennt. Die Doppelschicht ist aufgrund ihrer hydrophil-hydrophob-hydrophil-Struktur für die meisten Moleküle undurchdringlich. Innerhalb von Zellen dienen Liposomen zum Transport von Proteinen und Zellbestandteilen. Die Lipiddoppelschicht ist ebenfalls die Basis für alle biologischen Membranen, wie z.B. für die Zellmembran oder die Zellkernhülle. So ist es möglich, dass Liposomen mit Membranen der Zelle fusionieren und so der Inhalt der Liposomen die Zellmembran druchdringen kann. Dies wird genutzt, um Wirkstoffe in Zellen zu transportieren. Durch die Umhüllung von NP mit einer Lipiddoppelschicht erscheinen die NP von außen wie Liposomen. Dies eröffnet die Möglichkeit die Zellaufnahme von NP durch eine Lipidumhüllung zu verbessern und die Freisetzung von Molekülen aus den NP zu verhindern, was in Kapitel 4.2.1 gezeigt wird.

Polyhistidin-Tag

Ein Polyhistidin-Tag (kurz His-Tag oder H_6-Tag) ist eine kurze Aminosäuresequenz aus in der Regel sechs Histidinen, die z.B. zur Proteinaufreinigung in der Nickel-Affinitätschromatographie und zum Nachweis markierter Proteine verwendet wird [45]. Als Chelator kann ein His-Tag in einer Lewis-Säure-Base-Reaktion koordinativ an Metallionen binden [46–48]. Dies eröffnet die Möglichkeit His-Tags an die Metallzentren von MOF Strukturen binden zu lassen, was in Kapitel 4.2.3 gezeigt wird.

Kapitel 3

Theorie und Methodik zur Fluoreszenzspektroskopie

3.1 Fluoreszenz

Ein angeregtes physikalisches System (z.B. ein Molekül) kann über verschiedene Wege in seinen Grundzustand zurückkehren. Geschieht die Desaktivierung über einen quantenmechanisch erlaubten Prozess unter Aussendung elektromagnetischer Strahlung, die typischerweise im Bereich des sichtbaren Lichts liegt, so spricht man von Fluoreszenz. Systeme, die diese Eigenschaft zeigen, nennt man Fluorophore oder Fluoreszenzfarbstoffe. Die Anregung eines Fluorophors kann beispielsweise über die Absorption elektromagnetischer Strahlung geeigneter Wellenlänge erfolgen. In der Regel geschieht die Anregung nicht auf das niedrigste angeregte Energieniveau, sondern hin zu einem höheren vibronischen Niveau (s. Abb. 3.1). In kondensierter Materie relaxiert das System strahlungslos und sehr schnell (meist innerhalb von 10^{-12} s) auf das niedrigste angeregte vibronische Energieniveau. Dieser Prozess wird innere Umwandlung genannt. Die Emissionsraten zur Abregung in den Grundzustand sind typischerweise $\approx 10^8\,\mathrm{s}^{-1}$, sodass die typische Lebenszeit des angeregten Zustands, also die Zeit zwischen Aktivierung und Desaktivierung, $\approx 10\,\mathrm{ns}$ andauert. Dies führt dazu, dass die Fluoreszenzemission in der Regel vom niedrigsten angeregten Niveau stattfindet, da die innere Umwandlung nach einer vorangegangenen Anregung bereits abgeschlossen ist. Auch findet die Desaktivierung meist nicht zum niedrigsten Niveau des Grundzustands, sondern hin zu höheren vibronischen Niveaus statt (s. Abb. 3.1). Dies hat zur Folge, dass die Anregungsenergie höher ist als die Energie des Fluoreszenzlichts. Diese sogenannte Stokesverschiebung

erlaubt bei elektromagnetischer Anregung eine Unterscheidung und Trennung von Anregungs- und Fluoreszenzlicht anhand der Wellenlänge des Lichts. Weitere Effekte die zur Stokesverschiebung beitragen können sind z.B. die Lösungsmittelrelaxation oder die Komplexbildung. Die Relaxation des Systems kann durch verschiedene Prozesse erfolgen wie z.B. Schwingungen, Rotationen oder Translationen im System der Fluorophore. [49]

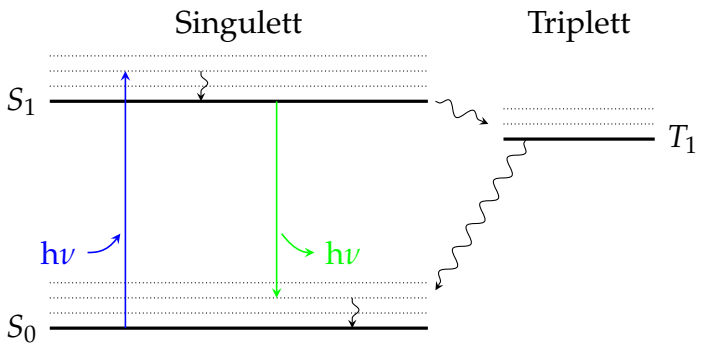

Abbildung 3.1: Jablonskidiagramm eines Fluorophors. Nach Anregung durch Absorption eines Photons (blau) befindet sich das Molekül im elektronisch angeregten Singulett-Zustand. Durch strahlungsfreie innere Umwandlung fällt das System in den niedrigsten angeregten Zustand. Unter Aussendung eines Photons kann das System wieder in den Grundzustand zurück fallen (grün). Alternativ kann das System in den Triplett-Zustand T_1 übergehen. Da der Übergang von T_1 zum Singulett-Grundzustand S_0 quantenmechanisch verboten ist, verharrt das System, im Vergleich zur Verweildauer in S_1, deutlich länger in diesem Zustand (Phosphoreszenz, s. Kap. 3.2.3).

3.2 Fluoreszenz-Korrelations-Spektroskopie

Der Theorie der Fluoreszenz-Korrelations-Spektroskopie liegt die Poisson-Statistik zugrunde [49]. Die Wahrscheinlichkeit $P\,(n,N)$, dass sich n Partikel zu einem Zeitpunkt im Detektionsvolumen aufhalten, ist gegeben durch

$$P\,(n,N) = \frac{N^n}{n!}\mathrm{e}^{-N}, \tag{3.1}$$

wobei N die durchschnittliche Anzahl der Partikel im Detektionsvolumen ist. Die Anzahl n zu einem Zeitpunkt t bestimmt maßgeblich die Fluoreszenzintensität $F\,(t)$. Die Diffusion der Partikel durch das Detektionsvolumen bewirkt Fluktuationen der Fluoreszenzintensität. Ist die Diffusion langsam, so ist $F\,(t)$ vergleichbar mit $F\,(t+\tau)$, für ein

kleines Zeitintervall τ, genannt Korrelationszeit (lag time). Ist die Diffusion schnell, so ändert sich die Fluoreszenzintensität ebenfalls schnell mit der Zeit und $F\left(t\right)$ ist deutlich verschieden von $F\left(t+\tau\right)$.
Die Mittelung über die Zeit

$$\langle F(t)\rangle = \frac{1}{T}\int_0^T F(t)\mathrm{d}t \tag{3.2}$$

wird benutzt, um die Korrelation zu allen gemessenen Zeiten (0 bis T) zu ermitteln:

$$\left\langle F\left(t\right)F\left(t+\tau\right)\right\rangle = \frac{1}{T}\int_0^T F\left(t\right)F\left(t+\tau\right)\mathrm{d}t. \tag{3.3}$$

Damit ist die normierte Korrelationsfunktion $G'(\tau)$ definiert als

$$G'\left(\tau\right) = \frac{\left\langle F\left(t\right)F\left(t+\tau\right)\right\rangle}{\left\langle F\left(t\right)\right\rangle^2} = 1 + \frac{\delta F\left(t\right)\delta F\left(t+\tau\right)}{\left\langle F\left(t\right)\right\rangle^2}, \tag{3.4}$$

mit der Intensitätsfluktuation $\delta F(t)$ gegenüber dem Mittelwert:

$$\delta F(t) = F(t) - \left\langle F(t)\right\rangle. \tag{3.5}$$

Zur Vereinfachung der weiteren Schritte wird das konstante Glied im Folgenden vernachlässigt und man erhält

$$G\left(\tau\right) = \frac{\left\langle \delta F\left(t\right)\delta F\left(t+\tau\right)\right\rangle}{\left\langle F\left(t\right)\right\rangle^2}. \tag{3.6}$$

Mit Hilfe dieser Funktion werden die gemessenen Fluoreszenzintensitäten verrechnet. Das Ergebnis ist eine abfallende Korrelationskurve, welche üblicherweise gegen die Korrelationszeit in logarithmischer Skalierung dargestellt wird. Dies gibt der Kurve eine sigmoide Form (s. Abb. 3.3). $G(\tau)$ ist eine dimensionslose, empirische Funktion, die keine Informationen über die Ursachen der zugrundeliegenden Signalfluktuationen enthält. Aus diesem Grund ist ein theoretisches Modell zur Interpretation der Korrelationskurve nötig.

3.2.1 Theoretisches Modell

Die in dieser Arbeit mit FCS untersuchten Proben waren stets frei diffundierende Partikel (ohne Randbedingungen oder externen Fluss). Somit ist für die vorliegende Arbeit ein Modell zur freien dreidimensionalen Diffusion von punktförmigen Teilchen notwendig. Dieses Modell wird im Folgenden hergeleitet. Unter den genannten Annahmen hängt das Zustandekommen der gemessenen Fluoreszenzintensität $F(t)$ von folgenden Größen ab:

B: die Anzahl der Photonen, die ein Fluorophor pro Zeiteinheit unter den gegebenen Bedingungen abgibt, die sogenannte „Brightness".

$A_{\text{eff}}(\mathbf{r})$: Aufnahmeeffizienz der optischen Anordnung (Mikroskop, Pinhole, etc.) in Abhängigkeit der räumlichen Position im Strahl.

$I(\mathbf{r})$: Räumliche Verteilung der Beleuchtungsintensität - das fokussierte Gaußsche Strahlenbündel in Form eines Doppelkegels.

$C(\mathbf{r},t)$: die räumliche Anordnung der Fluorophore zum Zeitpunkt t.

So ergibt sich die gemessene Fluoreszenzintensität zu

$$F(t) = B \int A_{\text{eff}}(\mathbf{r})\, I\,(\mathbf{r})\; C\,(\mathbf{r},t)\; \mathrm{d}^3\mathbf{r}. \tag{3.7}$$

Als Produkt aus der Quanteneffizienz des Aufnahmegerätes ein Fluoreszenzphoton zu detektieren, dem Absorptionswirkungsquerschnitt des Fluorophors und der Quantenausbeute des Fluorophors ist die „Brightness" B während der Messung konstant.
Fasst man das Anregungsvolumen $I(\mathbf{r})$ und das Beobachtungsvolumen $A_{\text{eff}}(\mathbf{r})$ zusammen zu $p(\mathbf{r}) = A_{\text{eff}}(\mathbf{r})\, I(\mathbf{r})$, kann dieses Detektionsvolumen $p(\mathbf{r})$ unter Annahme einer idealen Gaußförmigen Beleuchtung mit einem dreidimensionalen Gaußprofil angenähert werden:

$$p(\mathbf{r}) = I_0 \exp\left[-\frac{2\left(x^2-y^2\right)}{\omega_0^2}\right] \exp\left[-\frac{2z^2}{z_0^2}\right]. \tag{3.8}$$

Dieses Volumen besitzt keine scharfe Begrenzung (s. Abb. 3.2). Aus diesem Grund bezeichnet man die laterale Distanz zwischen dem Intensitätsmaximum (I_0 bei $\mathbf{r} = 0$) und Punkten, welche eine Intensität von $I_0 \cdot e^{-2} \approx 0{,}135 \cdot I_0$ besitzen und innerhalb der Ebene mit $z = 0$ liegen, als den lateralen Radius ω_0. Entsprechend wird der axiale Radius

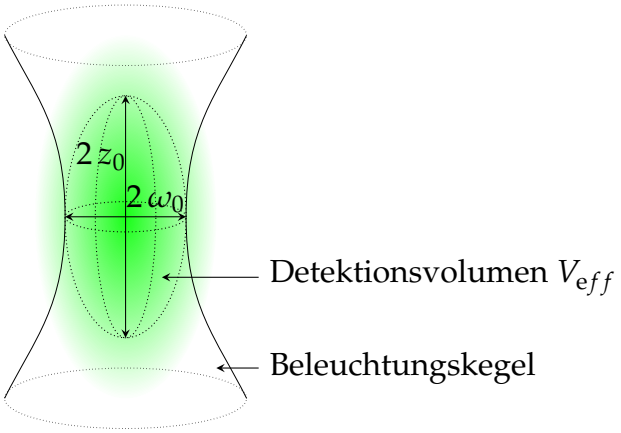

Abbildung 3.2: 3D-Gaußförmiges, konfokales Detektionsvolumen eines beugungsbegrenzten fokussierten Beleuchtungskegels mit ω_0, dem lateralen und z_0 dem axialen Radius.

z_0 auf der z-Achse definiert. Gleichung 3.7 vereinfacht sich so zu

$$F(t) = B \int p\,(\mathbf{r})\; C\,(\mathbf{r},t)\; \mathrm{d}^3\mathbf{r}. \tag{3.9}$$

Wird diese Gleichung in Gleichung 3.6 eingesetzt, so ergibt sich

$$G\,(\tau) = \frac{B^2 \int\int p\,(\mathbf{r})\; p\,(\mathbf{r}')\; \langle \delta C\,(\mathbf{r},t)\; \delta C\,(\mathbf{r}',t+\tau)\rangle\; \mathrm{d}^3\mathbf{r}\; \mathrm{d}^3\mathbf{r}'}{\left[B\,\langle C\rangle \int p\,(\mathbf{r})\; \mathrm{d}^3\mathbf{r}\right]^2}. \tag{3.10}$$

Im hier betrachteten Fall einer einzigen diffundierenden Spezies hängt $G(\tau)$ also nicht von der „Brightness“ B ab. Die eigentliche zeitliche Korrelation steckt im Term der Konzentrationsfluktuationen $\langle \delta C\,(\mathbf{r},t)\; \delta C\,(\mathbf{r}',t+\tau)\rangle$. Bei einer drei-dimensionalen Translations-Diffusion (ohne Rotationsanteile) ergibt sich dafür

$$\left\langle \delta C\,(\mathbf{r},t)\; \delta C\,\left(\mathbf{r}',t+\tau\right)\right\rangle = \langle C\rangle\; (4\,\pi\,D\,\tau)^{3/2} \exp\left[-\frac{|\mathbf{r}-\mathbf{r}'|}{4\,D\,\tau}\right] \tag{3.11}$$

[49, 50]. Setzt man nun die Gleichungen 3.8 und 3.11 in Gleichung 3.10 ein, so erhält man die Beziehung

$$G(\tau) = G(0) \cdot \frac{1}{1+\frac{4\,D\,\tau}{\omega_0^2}} \cdot \frac{1}{\sqrt{1+\frac{4\,D\,\tau}{z_0^2}}}. \tag{3.12}$$

Mit der Diffusionszeit

$$\tau_D = \frac{\omega_0^2}{4\,D}, \tag{3.13}$$

welche die mittlere Verweildauer eines Teilchens im Fokus darstellt, vereinfacht sich Gleichung 3.12 weiter zu

$$G(\tau) = G(0) \cdot \frac{1}{1+\frac{\tau}{\tau_D}} \cdot \frac{1}{\sqrt{1+\frac{\omega_0^2 \tau}{z_0^2 \tau_D}}}. \tag{3.14}$$

Der Wert für $G(0)$ ergibt sich aus der Poisson-Statistik. Demnach ist die relative Abweichung vom Mittelwert gegeben durch

$$\frac{\delta N}{N} = \frac{1}{\sqrt{N}}. \tag{3.15}$$

Die Korrelationsfunktion zur Korrelationszeit $\tau = 0$ stellt das Quadrat dieser Gleichung dar

$$G(0) = \frac{\langle \delta F(t) \delta F(t) \rangle}{\langle F(t) \rangle^2} = \frac{\langle \delta N \delta N \rangle}{\langle N \rangle^2} = \frac{1}{\langle N \rangle}. \tag{3.16}$$

Der Faktor $G(0)$ lässt sich bestimmen, indem $\langle \delta C\,(\mathbf{r},0)\, \delta C\,(\mathbf{r}',0) \rangle$ durch $\langle C \rangle\, \delta(\mathbf{r}-\mathbf{r}')$ ersetzt wird [50], da zu ein und demselben Zeitpunkt nur Positionen mit sich selbst korreliert sein können. Eingesetzt in Gleichung 3.10 ergibt sich für die maximale Amplitude der Korrelationskurve:

$$G(0) = \frac{1}{N}\,, \tag{3.17}$$

mit der mittleren Teilchenanzahl im Detektionsvolumen N. Somit ist die Korrelationsfunktion für die freie Diffusion einer Teilchenspezies gegeben durch

$$G(\tau) = \frac{1}{N} \cdot \frac{1}{1+\frac{\tau}{\tau_D}} \cdot \frac{1}{\sqrt{1+\frac{\tau}{S^2 \tau_D}}}. \tag{3.18}$$

Hierbei wurde der Quotient der Radii des Detektionsvolumen durch den Strukturparameter

$$S = \frac{z_0}{w_0} \tag{3.19}$$

ersetzt.

3.2.2 Auswertung des Messignals

Aus der Korrelationsfunktion lassen sich grundlegende physikalische Eigenschaften der verwendeten Probe ermitteln, wie die Konzentration oder der Diffusionskoeffizient (Diffusionskonstante). Dazu wird die Anpassungsfunktion (Gl. 3.18) an die Korrelationskurve angeglichen (gefittet). Den Diffusionskoeffizienten D erhält man aus der Diffusionszeit τ_D (s. Gl. 3.13) über die Beziehung

$$D = \frac{\omega^2}{4\tau_D}. \tag{3.20}$$

τ_D stellt im im Graphen der Funktion den Punkt dar, bei dem die Korrelationsfunktion auf die Hälfte ihrer maximalen Amplitude $G(0)$ abgefallen ist.

Aus dem Diffusionskoeffizienten lässt sich auch der hydrodynamische Radius R_H der Partikel, mit Hilfe der Stokes-Einstein-Gleichung

$$D = \frac{k_\mathrm{B} T}{6\pi\,\eta\,R_\mathrm{H}} \tag{3.21}$$

berechnen. Hierbei ist k_B der Boltzmann-Konstante, T die Temperatur der Probe und η die Viskosität des Lösungs- bzw. Suspensionsmittels. Unter dem hydrodynamischen Radius (auch Stokesradius genannt) versteht man den Radius einer hypothetischen Kugel, welche dieselben Diffusionseigenschaften besitzt wie das untersuchte Teilchen. Die realen Ausmaße des untersuchten Teilchens können beträchtlich vom hydrodynamischen Radius abweichen. Dies ist naturgemäß besonders bei Teilchen der Fall, deren Morphologie stark von der einer Kugel abweicht (z.B. Polymere). Dennoch gibt der hydrodynamische Radius eine Abschätzung der Größe eines diffundierenden Teilchens und ist gut geeignet, um zwei Proben zu vergleichen, welche im gleichen Medium gelöst sind. Zur Bestimmung der Konzentration einer Probe

$$c = \frac{N}{V_{eff}} \tag{3.22}$$

wird zusätzlich zur Teilchenanzahl $N = \frac{1}{G(0)}$ (s. Gl. 3.16) die Größe des effektiven konfokalen Volumens V_{eff} benötigt. Dieses berechnet sich aus den Radii des Beleuchtungsvolumens ω_0 und z_0 über

$$V_{eff} = \pi^{3/2}\,\omega_0^2\,z_0. \tag{3.23}$$

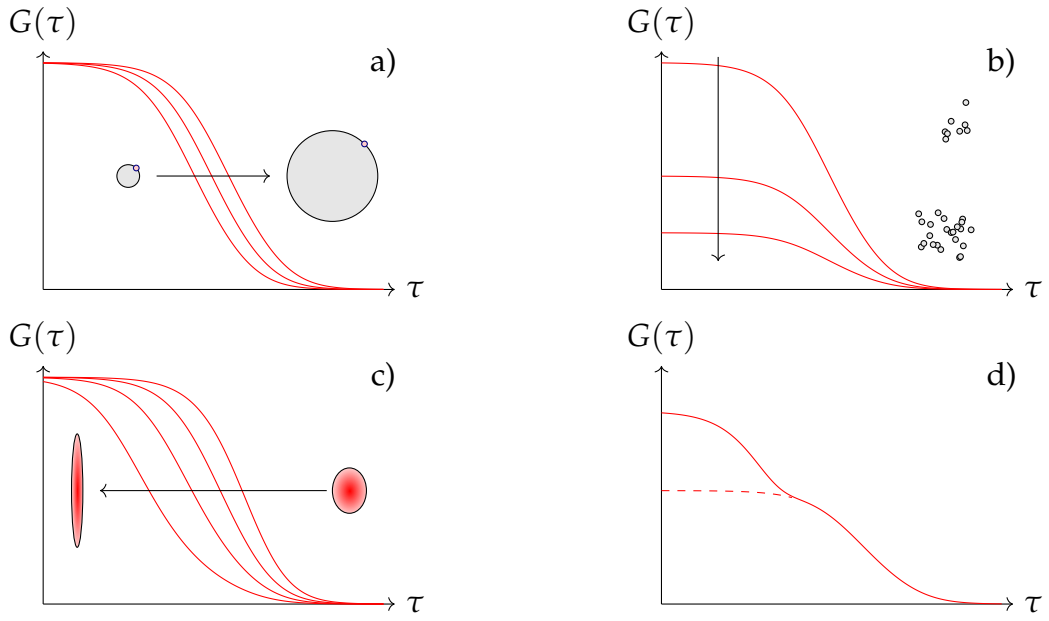

Abbildung 3.3: Veranschaulichung zur Korrelationsfunktion. a) Korrelationsfunktionen von Partikeln mit unterschiedlichen hydrodynamischen Radii. Mit wachsendem Radius der fluoreszenzmarkierten Partikel verlangsamt sich deren Diffusion, wodurch sich die fallende Flanke zu größeren Zeiten τ verschiebt. b) Korrelationsfunktionen von Proben unterschiedlicher Konzentration. Mit wachsender Konzentration verringert sich die maximale Amplitude der Korrelationsfunktion. c) Korrelationsfunktionen mit unterschiedlichem Strukturparameter. Mit wachsender Elliptizität und gleichzeitig festgehaltenem Gesamtvolumen wird der laterale Fokusdurchmesser kleiner und der axiale größer, wodurch sich die fallende Flanke der Korrelationskurve zu kürzeren Zeiten verschiebt. Ein Augenmerk sei hier auf den links-gekrümmten Abschnitt der Kurven gerichtet. Mit wachsendem Strukturparameter verringert sich die Krümmung in diesem Bereich. d) Vergleich der Korrelationsfunktionen mit (durchgezogene Linie) und ohne Triplett-Zustand-Blinken (gestrichelt). Ist die Wahrscheinlichkeit eines Fluoreszenzfarbstoffs in einem Triplett-Zustand zu verweilen hoch, zeigt sich das in der Korrelationsfunktion in einem zusätzlichen Abfall bei kurzen Korrelationszeiten.

Betrachtet man die Korrelationsfunktion und variiert je einen der Parameter der Probe, so zeigen sich folgende Veränderungen im Aussehen der Korrelationskurven (s. Abb. 3.3): Vergrößert sich der hydrodynamische Radius, so erhöht sich auch die Diffusionszeit und die abfallende Flanke der Funktion verschiebt sich zu größeren Korrelationszeiten τ (s. Abb. 3.3 a)). Bei Erhöhung der Konzentration der Probe sind im Mittel mehr Partikel im Fokus enthalten. Dementsprechend verringert sich die maximale Amplitude der Funktion (Abb. 3.3 b)). Wird das Verhältnis S von Höhe zu Breite des effektiven Fokusvolumens vergrößert (Abb. 3.3 c)), ändert sich die Krümmung der Funktion im links-gekrümmten Bereich und somit auch die Lage des Punktes mit der halben Amplitude $G(0)$.

3.2.3 Triplett-Blinken

Fluorophore, die sich im angeregten Zustand S_1 befinden, können, anstatt unter Aussendung eines Photons in den Grundzustand zurückzukehren, in den Triplett-Zustand T_1 übergehen (s. Abb. 3.1). Da der Übergang von T_1 zum Singulett-Zustand S_0 quantenmechanisch verboten ist, verharrt das System im Vergleich zur Verweildauer in S_1 deutlich länger in diesem Zustand T_1 [51]. Das führt dazu, dass das Fluorophor-Molekül für einige Zeit ($< 10\,\mu s$) kein Licht emittiert und somit auch nicht erneut angeregt werden kann. Diese Zeitspanne liegt, im Gegensatz zur kontinuierlichen An- und Abregung unter Aussendung von Fluoreszenzphotonen, im Bereich der zeitlichen Auflösung der verwendeten Photodetektoren. Dadurch wird ein Blinken des Fluorophor-Moleküls, auf dem Weg durch das Fokusvolumen, detektiert. Dies äußert sich in der Korrelationsfunktion in einer zusätzlichen Zerfallszeit (s. Abb. 3.3 d)), die sich durch folgende Ergänzung in der Anpassungsfunktion berücksichtigen lässt:

$$G(\tau) = \frac{1}{N}\left(1 + \frac{T}{1-T}\exp\left(\frac{-\tau}{\tau_T}\right)\right) \cdot \frac{1}{1+\frac{\tau}{\tau_D}} \cdot \frac{1}{\sqrt{1+\frac{\tau}{S^2\tau_D}}}. \tag{3.24}$$

Hierbei ist T der Anteil an Fluorophoren welche sich im Mittel im Triplett-Zustand befinden und τ_T ist die mittlere Verweildauer im Triplett-Zustand.

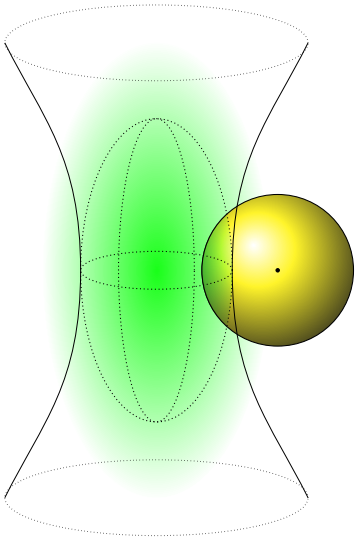

Abbildung 3.4: Illustration zum Partikel-Größen-Effekt: Während sich der Schwerpunkt (schwarzer Punkt) eines fluoreszierenden Teilchens (gelb) mit endlicher Größe noch außerhalb des konfokalen Volumens befindet, ist der Rand des Teilchens schon darin. Somit ist bereits eine Fluoreszenz detektierbar und die scheinbare Diffusionszeit des Teilchens ist länger als sie es für ein punktförmiges Teilchen mit den selben Diffusionseigenschaften wäre.

3.2.4 Partikel-Größen-Effekt

Sind die mittels FCS zu untersuchenden Teilchen nicht wie bislang angenommen nahezu punktförmig, sondern haben einen endlichen Durchmesser, der vergleichbar mit der Größe des Beobachtungsvolumen ($2\omega_0$) ist, so hängt $G(\tau)$ zusätzlich von der Größe und Anordnung der Fluorophore auf dem Partikel ab. Durch die endliche Ausdehnung des Teilchens verlängert sich die Zeit, die ein Teilchen im konfokalen Volumen detektiert wird, mit der Größe des Partikels. Dies lässt sich anhand von Abbildung 3.4 verdeutlichen. Während sich der Schwerpunkt des Teilchens noch außerhalb des Detektionsvolumens befindet, ist der Rand des Teilchens bereits innerhalb des Volumens. Die gemessene, scheinbare Diffusionszeit τ_A verlängert sich im Falle von homogen leuchtenden Kugeln mit Radius R gegenüber der tatsächlichen Diffusionszeit τ_D wie folgt [52]:

$$\tau_A = \tau_D \left(1 + \frac{8}{5}\frac{R^2}{\omega^2}\right). \tag{3.25}$$

Sind die Partikel nur an der Oberfläche fluoreszenzmarkiert so stellen sie für das FCS eine leuchtenden Hohlkugel dar. Für Hohlkugeln verlängert sich die scheinbare Diffusionszeit

gemäß

$$\tau_A = \tau_D \left(1 + \frac{8}{3}\frac{R^2}{\omega^2}\right). \tag{3.26}$$

Diese Beziehungen lassen sich verwenden, um aus der gemessenen, scheinbaren Diffusionszeit einer Probe von Partikeln den tatsächlichen hydrodynamischen Radius über die Strokes-Einstein-Beziehung zu ermitteln. Dies wird in Kapitel 4.1 eingehender erläutert.

3.2.5 Zweikomponenten-Fit

Die Existenz einer zweiten diffundierenden Komponente erweitert die Korrelationsfunktion der Gleichung 3.24 im einfachsten Fall, um einen weiteren Diffusionsterm mit den Diffusionszeiten der beiden Komponenten τ_{D1} und τ_{D2}, die in den Anteilen Y und $(1-Y)$ vorkommen:

$$\begin{aligned} G(\tau) = \frac{1}{N}\left(1 + \frac{T}{1-T}\exp\left(-\frac{\tau}{\tau_T}\right)\right) \cdot \\ \cdot \left(\frac{Y}{1+\frac{\tau}{\tau_{D1}}}\frac{1}{\sqrt{1+\frac{\tau}{S^2\tau_{D1}}}} + \frac{1-Y}{1+\frac{\tau}{\tau_{D2}}}\frac{1}{\sqrt{1+\frac{\tau}{S^2\tau_{D2}}}}\right). \end{aligned} \tag{3.27}$$

Um zwei Spezies mit Hilfe einer FCS Messung voneinander unterscheiden zu können, muss sich deren Diffusionszeit mindestens um den Faktor 1,6 unterscheiden [53]. Dies ist bei den in dieser Arbeit vorgestellten Systemen aus NP und kleinen Molekülen der Fall. N stimmt nur dann mit der tatsächlichen Anzahl der Teilchen überein, wenn beide Spezies dieselbe molekulare Helligkeit besitzen. Unterscheiden sich die zwei diffundierenden Spezies in ihrer Fluoreszenzhelligkeit b, zum Beispiel aufgrund unterschiedlicher Fluoreszenzfarbstoffe oder einer unterschiedlichen Anzahl an Fluorophoren, so beeinflusst dies die Korrelationsfunktion. Das Helligkeitsverhältnis

$$\alpha = \frac{b_{\mathrm{S}pezies1}}{b_{\mathrm{S}pezies2}} \tag{3.28}$$

der beiden Spezies geht quadratisch in die Korrelationfunktion ein:

$$G(\tau) = \frac{1}{N(Y + \alpha(1-Y))^2} \left(1 + \frac{T \cdot \exp\left(-\frac{\tau}{\tau_t}\right)}{1-T}\right) \cdot \cdot \left(\frac{Y}{1+\frac{\tau}{\tau_{D1}}} \frac{1}{\sqrt{1+\frac{\tau}{S^2\tau_{D1}}}} + \alpha^2 \frac{1-Y}{1+\frac{\tau}{\tau_{D2}}} \frac{1}{\sqrt{1+\frac{\tau}{S^2\tau_{D2}}}}\right). \tag{3.29}$$

Solange keine Information über das Helligkeitsverhältnis vorliegt, lassen sich somit aus dem Anteil der beiden Komponenten an der Korrelationskurve keine Erkenntnisse gewinnen. Häufig lassen sich aber Annahmen über das Helligkeitsverhältnis treffen. So ist zum Beispiel die Helligkeit b eines NP, welches an der Oberfläche gleichverteilt Fluorophore trägt, proportional zum Quadrat des Radius r des Partikels und damit zur Diffusionszeit τ_D. Denn die Helligkeit eines Partikels ist direkt proportional zur Anzahl der Fluorophore n. Die Anzahl der Fluorophore skaliert mit der Größe der Oberfläche des Partikels $A = 4\pi r^2$. Und die Diffusionszeit ist direkt proportional zum Radius des Partikels. So lässt sich das Helligkeitsverhältnis α abschätzen:

$$\alpha = \frac{n_2}{n_1} = \frac{r_2^2}{r_1^2} = \frac{\tau_{D1}^2}{\tau_{D2}^2}. \tag{3.30}$$

Mit dieser Abschätzung der Helligkeitsverhältnisse wird Gleichung 3.29 des Zweikomponenten-Fits zu

$$G(\tau) = \frac{1}{N\left(Y + \frac{\tau_{D1}^2}{\tau_{D2}^2}(1-Y)\right)^2} \left(1 + \frac{T \cdot \exp\left(-\frac{\tau}{\tau_t}\right)}{1-T}\right) \cdot \cdot \left(\frac{Y}{1+\frac{\tau}{\tau_{D1}}} \frac{1}{\sqrt{1+\frac{\tau}{S^2\tau_{D1}}}} + \left(\frac{\tau_{D1}}{\tau_{D2}}\right)^4 \frac{1-Y}{1+\frac{\tau}{\tau_{D2}}} \frac{1}{\sqrt{1+\frac{\tau}{S^2\tau_{D2}}}}\right). \tag{3.31}$$

3.2.6 Multikomponenten-Fit

Variiert die Größe der in der zu untersuchenden Probe enthaltenen Partikel, so kann die Korrelationskurve nicht korrekt mit dem einfachen Modell aus Kapitel 3.2.2 angenähert werden. In diesem Fall kann es notwendig sein, eine Größenverteilung der Partikel

in das theoretische Modell einfließen zu lassen [54]. Dies geschieht, indem zu jeder Partikelgröße einer Verteilung die Korrelationskurve berechnet wird und anschließend alle Kurven, gewichtet nach der Häufigkeit der Partikelgrößen, addiert werden:

$$G(\tau) = \sum_{i=1}^{M} c_i \left(1 + \frac{\tau}{\tau_{D,i}}\right)^{-1} \left(1 + \frac{\tau}{S^2\,\tau_{D,i}}\right)^{-1/2} \tag{3.32}$$

mit dem Gewichtungsfaktor c_i und der zugehörigen Diffusionszeit $\tau_{D,i}$. Je nach Anzahl M der unterschiedlichen Partikelgrößen steht einem Regressionsalgorithmus somit eine große Anzahl an freien Parametern $(2 \cdot M)$ zur Verfügung. Dies würde zwar eine sehr genaue Angleichung des Modells an die Messdaten erlauben, gibt aber nicht zwangsläufig die physikalischen Gegebenheiten der Probe wieder. Ein häufig geeigneter Ansatz ist, eine Gaußverteilung der Partikelgrößen anzunehmen. So lässt sich die Anzahl der freien Parameter stark eingrenzen. Wie von Pal *et al.* [28] beschrieben bietet es sich an, die $\tau_{D,i}$ vorzugeben und den Gewichtungsfaktoren c_i eine Gaußverteilung aufzuprägen, die durch drei Parameter beschrieben werden kann: τ_{Peak} die Diffusionszeit der am häufigsten vertretenen Partikelgröße, ω die Breite der Verteilung und A die Amplitude der Verteilung

$$c_i\left(\tau_{Di}\right) = A \cdot \exp\left(-\left(\frac{\tau_{Di} - \tau_{\text{Peak}}}{\omega}\right)^2\right). \tag{3.33}$$

Somit beschränkt sich die Anzahl der freien Parameter für eine Anpassung mit einer Gaußverteilung auf drei. Um eine möglichst fein aufgelöste Verteilung zu erhalten, aber gleichzeitig die Rechenzeit für den Regressionsalgorithmus in einem vertretbaren Rahmen zu halten, bietet sich eine Anzahl von 150 logarithmisch verteilten Werten im für FCS-Messungen relevanten Bereich zwischen 3,2 µs und 1,4 s für die $\tau_{D,i}$ an.

3.2.7 Kreuzkorrelation

Wie in Kapitel 3.2 gezeigt, ist FCS eine Methode, die die Selbstähnlichkeit eines Fluoreszenzsignals zu verschiedenen Zeitpunkten analysiert. Die Fluoreszenz-Kreuzkorrelations-Spektroskopie (FCCS) stellt eine Weiterentwicklung dieser Messtechnik dar. Mit dieser ist es nicht nur möglich ungewollte, durch die Messaparatur verursachte Artefakte wie z.B. das sogenannte Afterpulsing der Photodiode oder Schwankungen der Laserleistung aus dem Messignal zu entfernen, sondern auch die Messgenauigkeit zu steigern. Darüber hinaus sind mit der Kreuzkorrelation Bindungsereignisse detektierbar, deren Nachweis

nicht auf eine Größenänderung zwischen Bindungsedukten und -produkten beruht. Bei der Kreuzkorrelation werden zwei Fluoreszenzsignale von unterschiedlichen Farbstoffen auf ihre Ähnlichkeit hin untersucht [29]. Die Theorie der Kreuzkorrelation stellt eine Erweiterung der FCS-Theorie dar, mit der es möglich wird chemische Reaktionsraten sowie Gleichgewichts- und Bindungskonstanten von Molekülinteraktionen zu erhalten [55]. Wird die Korrelationsfunktion (s. Gl. 3.6) auf zwei verschiedene Fluoreszenzsignale $F_r(t)$ und $F_b(t)$ verallgemeinert, so ergibt sich die Kreuzkorrelationsfunktion zu

$$G_\times(\tau) = \frac{\langle \delta F_r(t)\, \delta F_b(t+\tau)\rangle}{\langle F_r(t)\rangle \langle F_b(t)\rangle}. \tag{3.34}$$

Im Falle ideal separierter Detektionskanäle ergibt sich nur dann eine endliche, positive Amplitude der Kreuzkorrelationskurve, wenn beide Fluorophore im Kollektiv gemeinsam durch das Detektionsvolumen diffundieren. Folglich steigt die Amplitude der Kreuzkorrelationskurve mit wachsendem Anteil kodiffundierender Fluorophore [56]. Jedoch ist die Amplitude der Kreuzkorrelationskurve auch invers proportional zur Gesamtanzahl der kodiffundierenden Fluorophore. Die Anpassungskurve zur Kreuzkorrelation ist gegeben durch

$$G_\times(\tau) = \frac{\langle C_{rb}\rangle M_{rb}(\tau)}{V_{eff}\left(\langle C_r\rangle + \langle C_{rb}\rangle\right)\left(\langle C_b\rangle + \langle C_{rb}\rangle\right)}. \tag{3.35}$$

Hierbei wurde der eigentliche Diffusionsprozess der Spezies in einem Mobilitätsterm $M_\varepsilon(\tau)$ zusammengefasst, mit $\varepsilon = r, b, rb$:

$$M_\varepsilon(\tau) := \left(1 + \frac{\tau}{\tau_{D,\varepsilon}}\right)^{-1}\left(1 + \frac{\tau}{S^2\tau_{D,\varepsilon}}\right)^{-\frac{1}{2}}. \tag{3.36}$$

C_ε ist die Konzentration der jeweiligen Partikel-Spezies. Die Anpassungsfunktion zur Autokorrelationskurve eines Fluoreszenzsignals (hier gezeigt: r) ergibt sich zu:

$$G_r(\tau) = \frac{\left(\langle C_r\rangle M_r(\tau) + \langle C_{rb}\rangle M_{rb}(\tau)\right)}{V_{eff}\left(\langle C_r\rangle + \langle C_{rb}\rangle\right)^2}. \tag{3.37}$$

Mit diesen Beziehungen lässt sich aus den Amplituden der Autokorrelationen ($G_r(0)$ und $G_b(0)$) und der Kreuzkorrelation ($G_\times(0)$) der Anteil σ_{rb} der doppelt markierten im

Vergleich zu den einzel markierten Partikeln bestimmen:

$$\sigma_{rb} = \frac{\langle C_{rb} \rangle}{\langle C_{r,total} \rangle} = \frac{G_{\times}(0)}{G_b(0)}. \tag{3.38}$$

Dabei wurde berücksichtigt, dass die Konzentration der doppelt markierten Partikel durch

$$\langle C_{rb} \rangle = \frac{G_{\times}(0)}{V_{eff}\, G_r(0)\, G_b(0)} \tag{3.39}$$

gegeben ist.
Die große Herausforderung der FCCS-Messungen besteht in der exakten Justierung und Abstimmung zweier Laserstrahlen und Lochblenden im Versuchsaufbau.

3.3 Spektroskopische Methoden

Mittels FCS ist es möglich die Dynamik einzelner Moleküle in Flüssigkeiten zu untersuchen. Für diese Arbeit wurde FCS zur Charakterisierung von NP und deren Interaktion mit biophysikalisch relevanten Molekülen genutzt. Weitere Messmethoden wurden zur Ergänzung der Ergebnisse verwendet.

3.3.1 Fluoreszenz-Korrelations-Spektroskopie

Ein großer Vorteil der Fluoreszenz-Korrelations-Spektroskopie ist das geringe benötigte Probenvolumen (z.B. 20 µl) sowie die Detektierbarkeit sehr geringer Konzentrationen (z.B. 10 nM). Ein weiterer Vorzug von FCS ist, dass das effektive Beobachtungsvolumen lediglich rund $0{,}1 - 0{,}2$ fl beträgt und somit Messungen nicht nur in Lösung sondern auch in lebenden eukaryotischen Zellen oder Bakterien möglich sind. Dies beinhaltet die Beobachtung von biochemischen Reaktionen oder spezifischen Interaktionen zwischen Biomakromolekülen *in vitro*. [53, 57, 58] Ein Typischer FCS-Aufbau ist in Abbildung 3.5 dargestellt.

Die FCS-Messungen wurden hauptsächlich an einem Axiovert 200 Mikroskop mit einer ConfoCor2-Einheit (Carl Zeiss, Jena) durchgeführt. Dabei wurde ein 40x ($NA = 1{,}2$) Apochromat Wasserimmersionsobjektiv verwendet (Carl Zeiss, Jena). Zur Anregung wurden ein Argon-Ionen Laser (488 nm) und ein Helium-Neon Laser (633 nm) eingesetzt. Die Proben wurden in 8-Kammer *LabTek* Probenträgern (Nunc, Rochester, NY) vermessen.

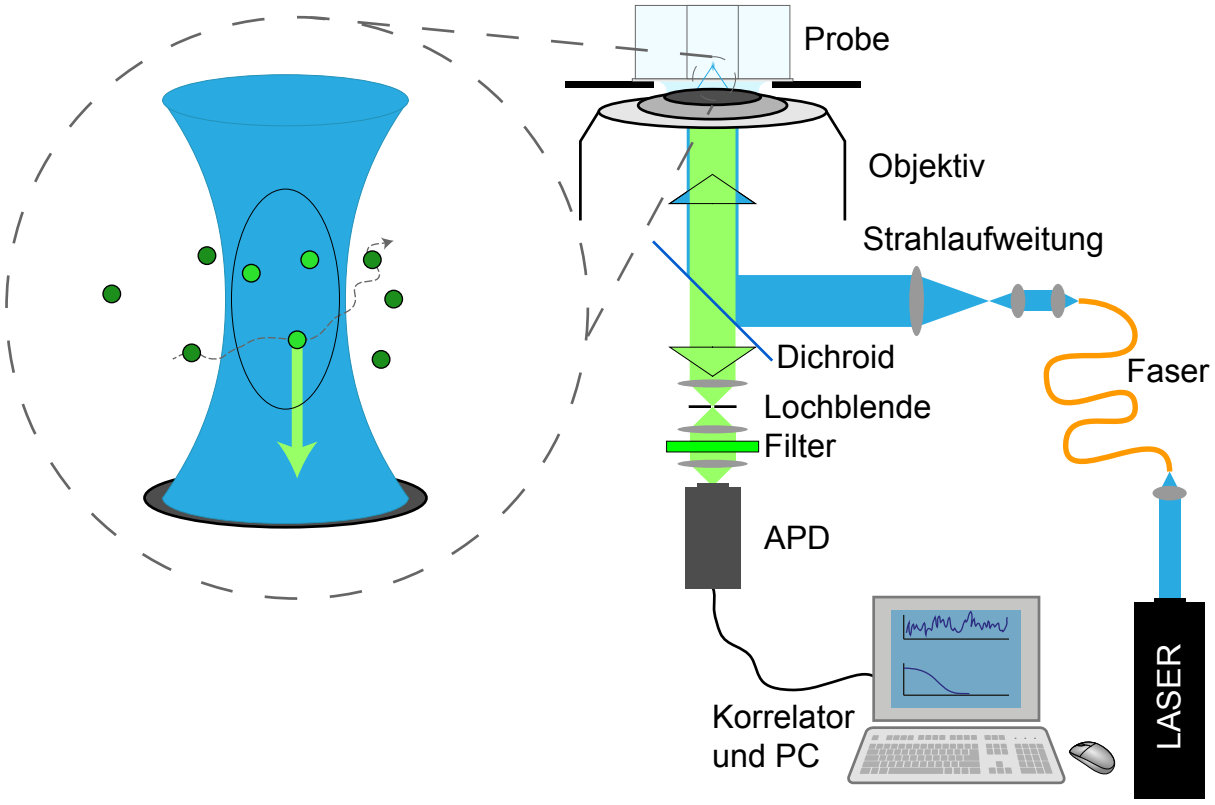

Abbildung 3.5: Schema eines typischen FCS-Aufbaus. Das für die Fluoreszenzanregung genutzte Laserlicht wird mit einem Teleskop aufgeweitet und über einen dichroitischen Spiegel in das Objektiv reflektiert. Das im Fokus des Objektives durch ein- und ausdiffundierende fluoreszierende Partikel erzeugte Fluoreszenzlicht (vergrößerte Darstellung, links) wird vom Objektiv aufgenommen und kollimiert. Danach passiert es den dichroitischen Spiegel. Durch die Fokussierung des Fluoreszenzlichts auf eine Lochblende wird Licht, welches nicht aus dem konfokalen Volumen stammt, blockiert. Eine Avalanche-Fotodiode (APD) detektiert das Fluoreszenzlicht, welches anschließend korreliert und ausgewertet wird.

Die Korrelation wurde mit der ConfoCor 2 Software (Version 3.2, Zeiss, Jena) berechnet. Die Auswertung wurde mit OriginPro 9.1 durchgeführt.

3.3.2 Quantitative Absorptionsspektroskopie

Mit Hilfe des Lambert-Beerschen Gesetz lässt sich die Extinktion $E(\lambda)$, also die Abschwächung der Intensität einer Strahlung mit einer Wellenlänge λ durch eine Substanz in Lösung in Abhängigkeit der Schichtdicke d und der Konzentration c der Substanz beschreiben durch:

$$E(\lambda) = \epsilon(\lambda) \cdot c \cdot d. \tag{3.40}$$

Dabei ist $\epsilon(\lambda)$ der Extinktionskoeffizient der Substanz, welcher als stoffspezifische Größe das Maß der Schwächung des Lichtes angibt. Die Messung der Extinktion bei einer Wellenlänge kann je nach Schichtdicke und Konzentration der untersuchten Substanz stark von temporärem Sensor- oder Lichtquellenrauschen beeinflusst werden und daher sehr unpräzise sein. Um diese Gegebenheit von vornherein auszuschließen, wurde nicht nur die Extinktion bei einer Wellenlänge zur Konzentrationsbestimmung herangezogen sondern die aufsummierte Extinktion über ein Wellenlängenintervall. Im Falle der später gezeigten Fluoresceinkonzentrationsbestimmungen (s. Kap. 4.3) wurde ein Intervall von 400 bis 550 nm gewählt, da Fluorescein in diesem Bereich sein Absorptionsmaximum aufweist (s. Abb. 4.22). Um die aufsummierte Extinktion in Relation zur Konzentration stellen zu können, wurde eine Eichgerade von Lösungen bekannter Konzentration aufgenommen.

Kapitel 4

Ergebnisse und Diskussion

In diesem Kapitel werden die Ergebnisse der Veröffentlichungen P1, P2, P3, P4, P5, P6 und P7 vorgestellt (s. Anhang).

4.1 Charakterisierung von MOF-Nanopartikeln[1]

Größe und Größenverteilung zählen zu den wichtigsten Einflussfaktoren auf die physikalischen und chemischen Eigenschaften von NP. So hängt zum Beispiel die katalytische Wirkung von NP oder die Aufnahme in Zellen stark von der Größe und Form der NP ab [60–68]. Deshalb besteht die Notwendigkeit die Größe und Morphologie der verwendeten NP zu bestimmen [69]. Es existieren verschiedene experimentelle Techniken, um diese Parameter zu ermitteln. Hierfür eignen sich vor allem Fluoreszenz-Korrelations-Spektroskopie (FCS), Dynamische Lichtstreuung (DLS), Kleinwinkel-Röntgenstreuung (SAXS), Rasterkraftmikroskopie (engl. atomic force microscopy AFM), Nanopartikel Verfolgung und Analyse (NTA), Transmissionselektronenmikroskopie (TEM) und Rasterelektronenmikroskopie (REM).

4.1.1 Charakterisierung von Zr-*fum*-Nanopartikeln

Für eine ausführliche Größen-Charakterisierung wurden Zirkonium-Fumarat (Zr-*fum*)-NP gewählt, da diese auch für die spätere Demonstration eines Funktionalisierungskonzepts verwendet wurden (s. Kap. 4.2.3). Diese Charakterisierung entstand in Zusammenarbeit mit der Arbeitsgruppe Wuttke. Alle Methoden zur Charakterisierung

[1] Dieses Kapitel behandelt in Teilen Erkenntnisse, die in [59] publiziert wurden (s. Anhang B.2).

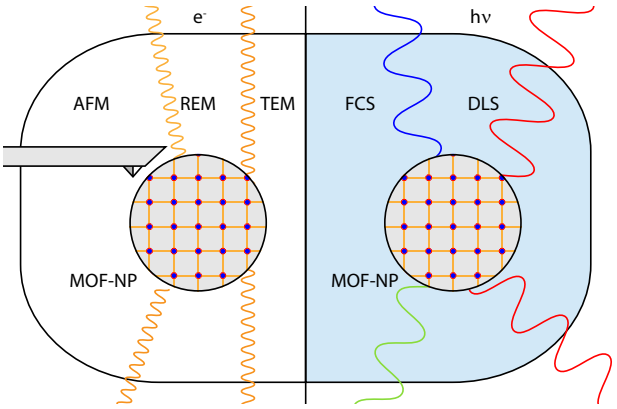

Abbildung 4.1: Charakterisierung von MOF-NP mit fünf der gängigsten Techniken: AFM, REM, TEM, FCS, DLS. Bei der AFM wird die auf einem Substrat ausgetrocknete NP-Probe mit einer Messnadel abgerastert. REM und TEM nutzen die Streuung und Absorption von Elektronenstrahlen an der ausgetrocknete NP-Probe, um ein Bild der NP zu erzeugen. FCS und DLS nutzen die Fluktuationen von gestreutem Laserlicht oder emittiertem Fluoreszenzlicht, um aus dem Diffusionsverhalten der NP deren Größe zu bestimmen.

von NP haben Limitationen, die teilweise erst durch den Vergleich der verschiedenen Messmethoden deutlich werden. Ein ausführlicher Vergleich gängiger Messmethoden zur Charakterisierung von NP fehlte bislang. Aus diesem Grund wurden die NP mit fünf der gängigsten Techniken (s. Abb. 4.1) untersucht, um Unterschiede der erlangten Größen aufzuzeigen und beispielhaft zu demonstrieren wie eine ausführliche Größen- und Morphologie-Analyse durchgeführt werden sollte. Die Zr-*fum*-MOF-NP wurden nach der Beschreibung von Wißmann *et al.* (2012) [41] synthetisiert (s. Kap. 2.2). Die Massenkonzentration der NP-Suspension wurde gravimetrisch durch Austrocknung zu $c = 6\,\mathrm{mg\,ml^{-1}}$ bestimmt.

Fluoreszenz-Korrelations-Spektroskopie zur Messung der Größenverteilung von Nanopartikeln

Drei, voneinander unabhängig, jedoch unter identischen Bedingungen hergestellte Zr-*fum*-NP-Proben, wurden mittels FCS untersucht. Um die nicht-fluoreszierenden Zr-*fum*-NP mit FCS charakterisieren zu können, müssen sie fluoreszenzmarkiert werden. Dies wurde durch die Anbindung von *Alexa Fluor 488* (Molecular Probes, USA) an die NP-Oberfläche erreicht. Zu 10 µl einer 10 nM Lösung aus *Alexa Fluor 488* und Wasser wurden 20 µl der Zr-*fum*-NP-Suspension gegeben. Die Zr-*fum*-NP sind mit einem Po-

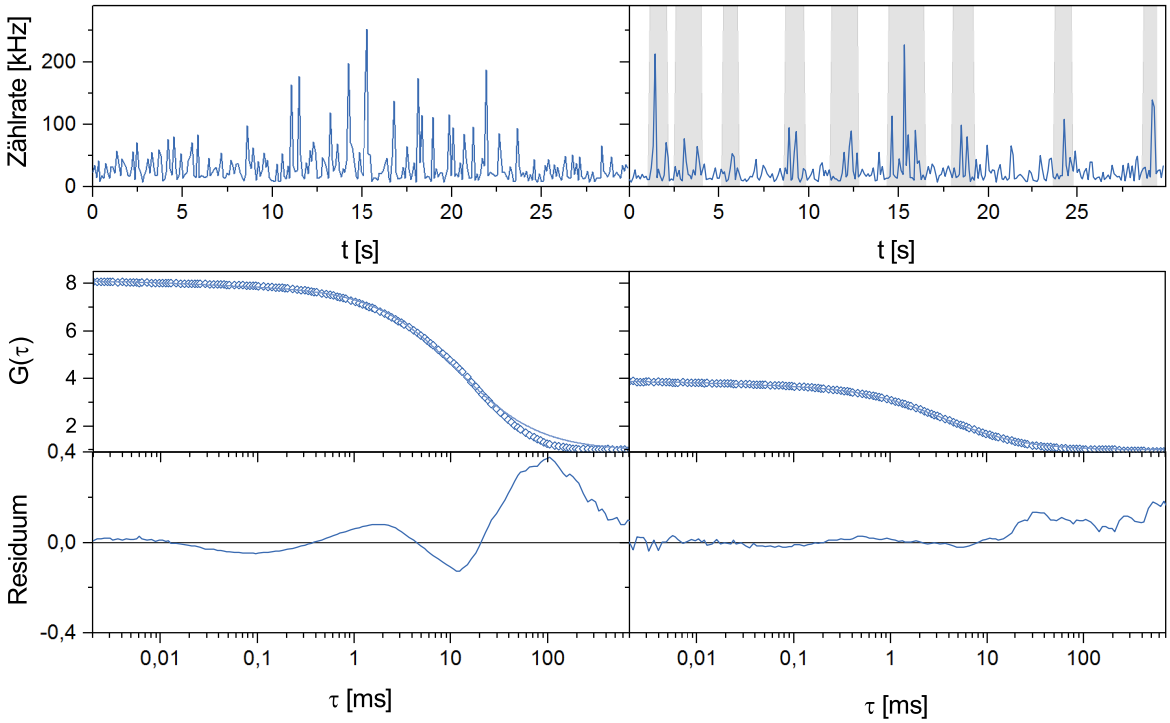

Abbildung 4.2: FCS-Daten der NP ohne (links) und mit (rechts) "Dustfilter"-Funktion. Die Fluoreszenzintensität, dargestellt als Photonenzählrate (oben) zeigt hoch über den Mittelwert hinaus ragende Spitzen. Die "Dustfilter"-Funktion nimmt Zeitbereiche, die solche Spitzen beinhalten aus der Berechnung der Korrelation heraus (grau hinterlegt). Dies wirkt sich auf die Korrelationskurve (mitte) dahingehend aus, dass die Amplitude der Kurve niedriger ist und der Abfall der Kurve bei kürzeren Korrelationszeiten liegt. Die Korrelationskurve mit der "Dustfilter"-Funktion lässt sich besser mit einem Zweikomonenten-Fit anpassen als ohne "Dustfilter", wie aus dem Residuum (unten) ersichtlich wird.

rendurchmesser von $0{,}5 - 0{,}7\,\mathrm{nm}$ mikroporös [70]. Dies hat zur Folge, dass die *Alexa Fluor 488*-Moleküle (hydrodynamischer Durchmesser $\approx 1\,\mathrm{nm}$) nicht in die Poren eindringen und nur an die Oberfläche der NP binden können. Diese Gegebenheit wird später bei der Auswertung berücksichtigt werden. Nach einer Inkubationszeit von fünf Minuten wurde mit der FCS-Messung begonnen. Zur Eichung wurde *Alexa Fluor 488* verwendet. Es ergab sich eine Diffusionszeit von $\tau_D = 21\,\mu\mathrm{s}$ der freien Farbstoffmoleküle. Unter Annahme einer Diffusionskonstanten von $D = 435\,\mu\mathrm{m}^2\,\mathrm{s}^{-1}$ [71] ergibt sich ein lateraler Fokusradius von $\omega_0 = 191\,\mathrm{nm}$. Bei ersten Messungen der NP-Proben stellte sich heraus, dass sich einige große NP-Agglomerate in den NP-Proben befinden.

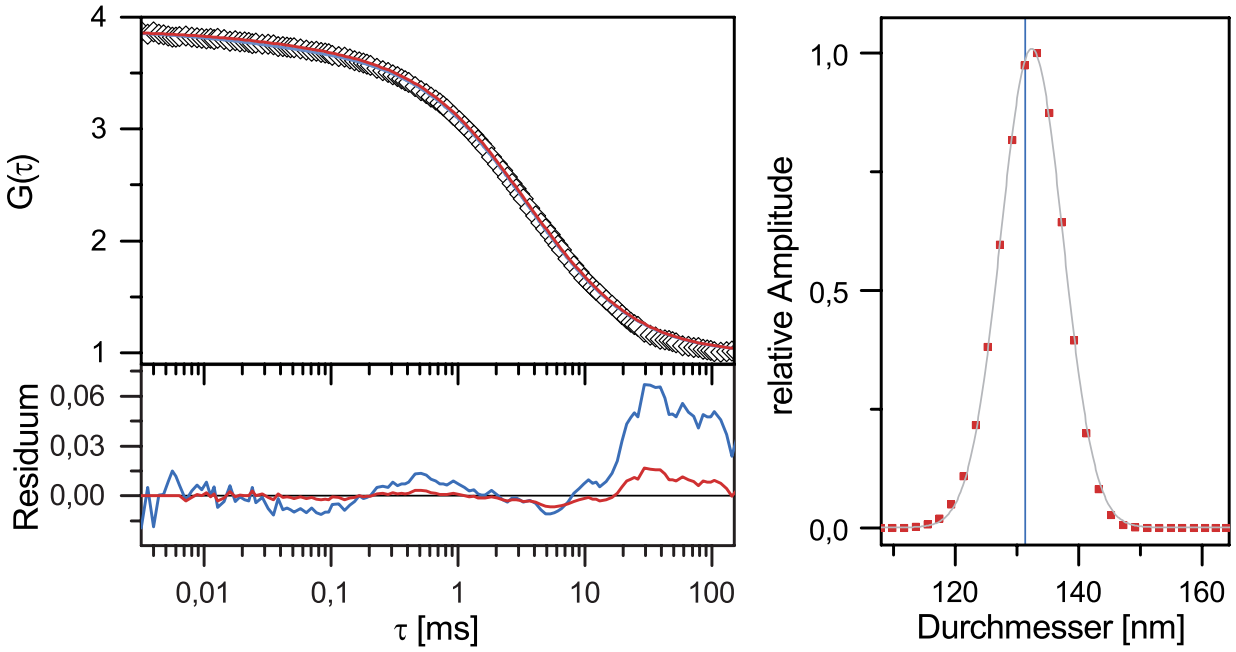

Abbildung 4.3: Der Vergleich von Zweikomponenten-Fit (blau) und GDM-Fit (rot) zeigt kaum Abweichungen der beiden Fits von der Korrelationskurve (links oben). Die Residuen (links unten) verdeutlichen aber, dass der GDM-Fit deutlich näher an den Korrelationsdaten liegt als der Zweikomponenten-Fit. Die sich aus dem GDM-Fit ergebenden Häufigkeiten (rechts) für die festgelegten Diffusionszeiten wurden mit Gleichung 4.3 auf die entsprechenden hydrodynamischen Durchmesser umgerechnet. Der häufigste Durchmesser ist $D_{\mathrm{H}} = 133\,\mathrm{nm}$ bei einer Standardabweichung von $\sigma = 5\,\mathrm{nm}$. Das Ergebnis des Zweikomponenten-Fits (senkrechte blaue Linie) weicht nur wenig vom Mittelwert der Verteilung ab.

Dies führte zu vereinzelten Zählraten-Spitzen in der Fluoreszenzintensität, die deutlich (bis zu zehnfach) über dem Mittelwert lagen. Diese Spitzen führten zu einer Korrelationskurve mit einer erhöhten Amplitude sowie einer Form, die sich nicht adäquat mit einem Zweikomponenten-Fit anpassen ließ (s. Abb. 4.2). Wie in Abbildung 4.6 zu sehen, sind NP-Agglomerate stark polydispers und teilweise größer als der Durchmesser des Fokusvolumens. Durch ihre große Oberfläche tragen sie auch entsprechend viele Farbstoffmoleküle, was eine große Helligkeit eines Agglomerats zur Folge hat. Dadurch tragen Agglomerate überproportional zur Korrelationskurve bei. Um diese Agglomerate aus der Messung auszuschließen, wurde die "Dustfilter" genannte Funktion der Messsoftware (*AIM* Version 3.2 Zeiss) verwendet. Wie bei Persson *et al.* [72] beschrieben, werden durch diese Funktion Teile des Fluoreszenzsignals mit hohen Zählratenspitzen bei der Korrelationsberechnung nicht berücksichtigt und können somit die Korrelations-

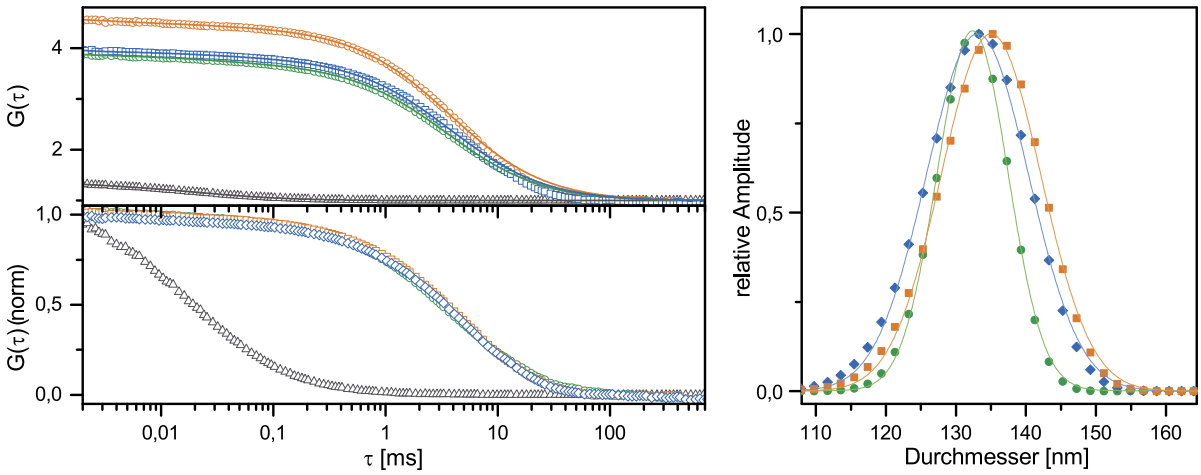

Abbildung 4.4: Der Vergleich der FCS-Messungen der drei NP Proben (blau, grün und orange) zeigt Abweichungen der Amplitude der Korrelationsfunktionen (links oben) und damit der Konzentrationen der Proben. Zum Vergleich zeigt die Korrelationskurve von freien *Alexa Fluor 488*-Molekülen (grau) deutlich schnellere Diffusion. Dies belegt die Bindung der *Alexa Fluor 488*-Moleküle an die NP. In der normierten Darstellung der Korrelationskurven (links unten) sind kaum Abweichungen der drei Partikelproben erkennbar, was auf ein sehr ähnliches Diffusionsverhalten schließen lässt. So zeigt sich dann auch in den Größenverteilungen aus GDM-Fits (rechts) eine geringe Variation in der Lage und Breite der Verteilung: $D_\mathrm{H} = 133\,\mathrm{nm}$ mit $\sigma = 5\,\mathrm{nm}$ (grün), $D_\mathrm{H} = 133\,\mathrm{nm}$ mit $\sigma = 7\,\mathrm{nm}$ (blau), $D_\mathrm{H} = 135\,\mathrm{nm}$ mit $\sigma = 7\,\mathrm{nm}$ (orange).

kurve nicht verfälschen (s. Abb. 4.2). Um eine erste Abschätzung der Diffusionszeit der NP aus der Korrelationskurve zu ermitteln, wurde ein Zweikomponenten-Fit verwendet. Die erste Komponente wurde dabei auf die vorher bestimmte Diffusionszeit von frei diffundierendem *Alexa Fluor 488* festgesetzt. Dies berücksichtigt die Möglichkeit, dass nicht alle Farbstoffmoleküle an die NP gebunden haben. Der Fit weicht deutlich weniger von der Korrelationsfunktion ab als dies bei den Daten ohne „Dustfilter“ der Fall ist (s. Abb. 4.2). Für die Partikel ergab sich eine Diffusionszeit von 3,7 ms. Wie in Abbildung 4.3 erkennbar, gibt es im Bereich von $\tau > 0{,}1\,\mathrm{ms}$ dennoch systematische Abweichungen zwischen Fit und Korrelationsfunktion, die sich bei $\tau > 10\,\mathrm{ms}$ deutlich vergrößern. Dies zeigt, dass ein Zweikomponenten-Fit die Messdaten nicht ausreichend modellieren kann und demnach keine einheitlich großen NP vorliegen, sondern diese eine Polydispersität aufweisen. Um diese Polydispersität eingehender zu untersuchen, wurde ein „Gaußverteilungs-Modell“ (GDM) angewendet. Dieses Modell berücksichtigt die Größenverteilung der NP, indem nicht mehr eine Diffusionszeit für die NP als freier Pa-

rameter angesetzt wird. Stattdessen werden für viele fest vorgegebene Diffusionszeiten, die Anteile an der Korrelationsfunktion ermittelt. Die Anteile werden als Gaußverteilt angenommen, was die Anzahl der freien Parameter für den Fit beschränkt (s. Kap. 3.2.6). Der GDM-Fit liefert als häufigsten Wert eine scheinbare Diffusionszeit von $\tau_A = 3{,}6\,\text{ms}$. Da davon auszugehen ist, dass die NP eine Größe besitzen, die vergleichbar mit dem konfokalen Volumen ist, ist die gemessene Diffusionszeit τ_A gegenüber der tatsächlichen Diffusionszeit τ_D verlängert (s. Kap. 3.2.4). Nachdem die *Alexa Fluor 488*-Moleküle nur auf der Oberfläche der NP binden können, sind die fluoreszenzmarkierten NP, aus Sicht der FCS-Detektion, leuchtende Hohlkugeln. Somit ergibt sich nach Wu *et al.* [52] eine Verlängerung der scheinbaren Diffusionszeit, um den Faktor $\left(1 + \frac{8}{3}\frac{R^2}{\omega^2}\right)$:

$$\tau_A = \tau_D \left(1 + \frac{8}{3}\frac{R^2}{\omega^2}\right). \tag{4.1}$$

Setzt man Gleichung 3.13 $\tau_D = \frac{\omega^2}{4D}$ sowie die Stokes-Einstein-Gleichung 3.21 $D = \frac{k_B T}{6\pi\eta R}$ in Gleichung 4.1 ein, so erhält man

$$\tau_A = \omega^2 \cdot \frac{6\pi\eta}{4k_B T}\left(R + \frac{8}{3\omega^2}R^3\right). \tag{4.2}$$

Die scheinbare Diffusionszeit stellt eine Funktion dritten Grades vom hydrodynamischen Radius dar. Eine Umstellung nach R führt zu drei Lösungen, von denen nur eine nicht-komplex und somit physikalisch relevant ist. Für den späteren Vergleich mit den anderen verwendeten Charakterisierungstechniken wird statt des Radius der Durchmesser D angegeben:

$$D(\tau_A) = 2R(\tau_A) = 2\sqrt[3]{\frac{3a\tau_A}{16} + \sqrt{\frac{9a^2\cdot\tau_A^2}{256} + \frac{\omega^6}{512}}} - \frac{\omega^2}{8}\left(\frac{3a\tau_A}{16} + \sqrt{\frac{9a^2\tau_A}{256} + \frac{\omega^6}{512}}\right)^{-\frac{1}{3}} \tag{4.3}$$

wobei $a := \frac{2k_B T}{3\pi\eta}$ definiert wurde. Mit Hilfe dieser Relation kann aus den Diffusionszeiten direkt die Größenverteilung der NP errechnet werden (s. Abb. 4.3). Der mittlere Durchmesser ergibt sich zu 133 nm mit einer Standardabweichung von $\sigma = 5\,\text{nm}$. Die Verteilung der NP-Größe scheint sehr schmal zu sein. Dies könnte der Tatsache geschuldet sein, dass mit der „Dustfilter"-Funktion nicht-agglomerierte, aber große NP für die Berechnung der Korrelationskurve nicht berücksichtigt wurden. Außerdem wird am Residuum des GDM-Fits deutlich, dass Korrelationszeiten $\tau > 20\,\text{ms}$ vom Fit nicht stark

genug berücksichtigt wurden (s. Abb. 4.3). Trotzdem ist zu erwarten, dass diese Verteilung die reale Größenverteilung der häufig vorkommenden Partikel korrekt wiedergibt und nur seltene, große Partikel und Aggregate vernachlässigt werden. Nach demselben Schema wurden auch die Größenverteilungen der beiden anderen Zr-*fum*-NP-Proben bestimmt. Alle drei Messungen sind zusammengefasst in Abbildung 4.4 zu sehen. Hierbei wird ersichtlich, dass zwischen den verschiedenen Proben geringe Variationen in der mittleren Partikelgröße sowie deren Varianz vorliegen (s. Tab. 4.1). Um die Ursachen

Probennummer	häufigster Durchmesser [nm]	Standardabweichung [nm]
1	133	5
2	133	7
3	135	7

Tabelle 4.1: Zusammenstellung der mittels FCS gemessenen Größenverteilungen von drei Zr-*fum*-NP-Proben.

für die Abweichungen zu ergründen, müssen die gefundenen Ergebnisse mit denen aus anderen Techniken in Relation gestellt werden. Hierzu wurden dieselben NP-Proben mit vier weiteren Methoden zur Bestimmung von Größenverteilungen charakterisiert. Eine detaillierte Beschreibung der jeweiligen Probenpräparation und Messbedingungen ist in der Publikation [59] in Anhang B.2 zu finden.

Dynamische Lichtstreuung zur Messung der Größenverteilung von Nanopartikeln

Eine weitere Methode zur Untersuchung der Größenverteilung der NP ist die Dynamische Lichtstreuung. Ähnlich wie bei FCS wird dabei die Diffusion von Partikeln in einem flüssigen Medium untersucht. Dazu wird das von den NP gestreute Licht eines Laserstrahls unter einem Winkel von 175° detektiert und in derselben Weise wie bei FCS korreliert. Somit ist auch die bei DLS aus einem Fit der Korrelationskurve ermittelte Größe der NP, die einer hydrodynamisch identisch diffundierenden Kugel. Die Polydispersitätsanalyse der genutzten „Zetasizer"-Software liefert eine Verteilung der Durchmesser der Teilchen. Da die Zr-*fum*-NP nach der Synthese in Ethanol aufbewahrt werden, weil sie dort die geringsten Alterungserscheinungen wie Agglomeration oder Sedimentation zeigen, wurde die Größenverteilung der NP zunächst in diesem Medium ermittelt. Um eine Vergleichbarkeit mit der durch FCS bestimmten Größenverteilung herzustellen, wurden die Verteilungen der hydrodynamischen Durchmesser auch in Wasser bestimmt. So ergab sich für die Zr-*fum*-NP in Wasser ein mittlerer Durchmesser

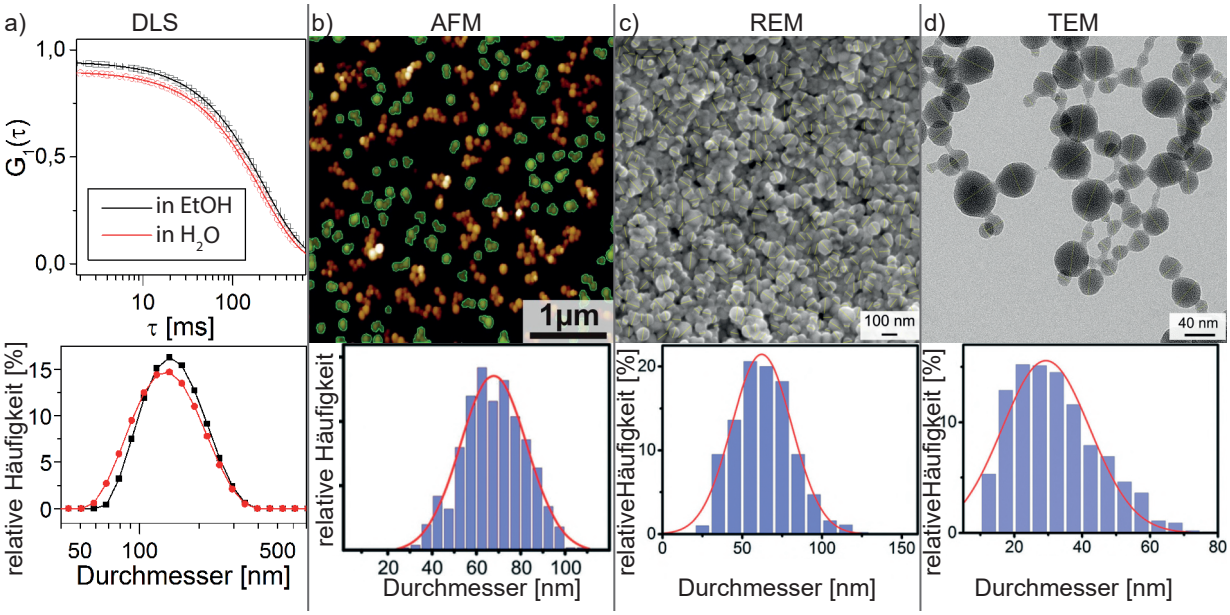

Abbildung 4.5: Vergleich der Ergebnisse der Größenverteilung von Zr-*fum*-NP gemessen mittels a) DLS, b) AFM, c) REM und d) TEM. Die jeweiligen Messdaten (oben) zeigen die Korrelationsfunktion (DLS) und beispielhafte Aufnahmen (bei AFM, REM und TEM). Die grünen Flächen (AFM) und gelben Linien (REM, TEM) zeigen die Vermessung der NP. Die abgeleiteten Größenverteilungen (unten) zeigen die Polydispersität der NP. Die aus den bildgebenden Methoden ermittelten Größen sind deutlich kleiner als die bei DLS gewonnenen (und auch FCS). Abbildung adaptiert von [59].

von $D_{\mathrm{DLS}} = 142\,\mathrm{nm}$ bei einer Standardabweichung von $\sigma = 46\,\mathrm{nm}$ (s. Abb. 4.5 a)). In Ethanol suspendierte NP lieferten einen mittleren Durchmesser von $D_{\mathrm{DLS}} = 130\,\mathrm{nm}$ bei einer Standardabweichung von $\sigma = 48\,\mathrm{nm}$. Somit liegen die mit DLS und FCS ermittelten Größenverteilungen mit einer Abweichung von rund 5% sehr nahe beieinander.

Rasterkraftmikroskopie zur Messung der Größenverteilung von Nanopartikeln

Die Rasterkraftmikroskopie, als äußerst hoch auflösende Technik, bietet sich ebenfalls an, die Größe von NP zu bestimmen. Mit einem Rasterkraftmikroskop (AFM) wurden die auf einem Siliziumdioxyd-Substrat ausgetrockneten NP-Proben mit Hilfe einer Messnadel abgerastert. Dazu wurde der Kantilever, an dem die Messnadel sitzt, in Schwingung versetzt und sehr nahe an die NP herangeführt. Die durch Coulomb- oder Van-der-Waals-Interaktionen zwischen den NP und der Messnadel veränderte Schwingungsamplitude des Kantilevers wurde dazu genutzt, die Messnadel auf konstantem mittlerem Höhenabstand über der Oberfläche zu bewegen. Die so gewonnen topographi-

schen Daten wurden mit der lateralen Position der Messnadel kombiniert und zu Bildern verarbeitet. Auf den Bildern zeigen sich sowohl einzelne, nahezu kugelförmige NP als auch zusammenhängende Agglomerate (s. Abb. 4.5 b)). Ob diese Agglomerate durch die Probenpräparation (Austrocknung der NP-Suspension auf einem Siliziumdioxyd-Substrat) entstanden sind oder schon bei der Synthese zusammengewachsen sind, war nicht feststellbar. Aus den erlangten Bildern wurde die Höhenverteilung (senkrechter Durchmesser) von rund 500 Partikeln in einem Histogramm zusammengestellt. Dem Histogramm der NP-Durchmesser wurde eine Gaußkurve angepasst. So ergab sich ein mittlerer Durchmesser von $D_{\mathrm{AFM}} = 68\,\mathrm{nm}$ bei einer Standardabweichung von $\sigma = 15\,\mathrm{nm}$.

Rasterelektronenmikroskopie zur Messung der Größenverteilung von Nanopartikeln

REM ist eine weitverbreitete Methode zur Charakterisierung von Nanomaterialien. Bei dieser Technik trifft ein fokussierter Elektronenstrahl (im gegebenen Fall 5 keV) auf die Probe und erzeugt dort Sekundärelektronen, welche dann detektiert werden. Durch Abrastern der Probe mit dem Elektronenstrahl entsteht ein Bild der Probe. Eine ethanolische Dispersion von Zr-*fum*-NP wurde ausgetrocknet und anschließend mit Kohlenstoff besputtert. Letzteres ist notwendig, um die nicht-leitenden Zr-*fum*-NP mit einem leitenden Film zu überziehen und dadurch Ladungseffekte zu vermeiden. Es zeigten sich, zu Haufen aneinandergelagerte, nahezu kugelförmige NP. Aus den aufgenommenen Bildern wurde durch manuelle Bildauswertung in *ImageJ* (Version 1.49) die Größe von ca. 1000 NP bestimmt und in einem Histogramm zusammengestellt, welches ebenfalls mit einer Gaußverteilung angenähert wurde (s. Abb. 4.5 c)). So ergab sich ein mittlerer Durchmesser von $D_{\mathrm{REM}} = 62\,\mathrm{nm}$ bei einer Standardabweichung von $\sigma = 19\,\mathrm{nm}$. Da die NP aufeinanderliegend abgebildet werden, ist nicht feststellbar, ob die gefundene Morphologie einzelne Partikel oder zusammengewachsene Agglomerate darstellt. Dennoch ist die Primärgröße der NP gut messbar.

Transmissionselektronenmikroskopie zur Messung der Größenverteilung von Nanopartikeln

In einem Transmissionselektronenmikroskop (TEM) wird ein hochenergetischer Elektronenstrahl (im gegebenen Fall $E_{\mathrm{kin}} = 200\,\mathrm{keV}$) auf die NP fokussiert, welche auf einem Trägernetzchen aufgebracht sind. Der durch die Probe transmittierte Elektronenstrahl,

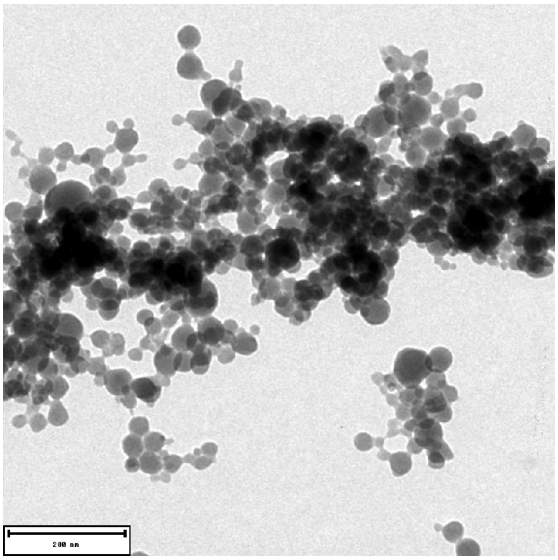

Abbildung 4.6: TEM-Aufnahme einer Zr-*fum*-Probe, die Agglomeration von NP zeigt. Maßstab: 200 nm.

der lokal durch Absorption oder Streuung der Elektronen an den NP verändert wurde, wird auf einen CCD-Chip fokussiert. So kann unmittelbar ein komplettes Bild der 2D-Projektion der NP aufgenommen werden. Es ist kein Abrastern der Probe notwendig. Die hohe Vergrößerung des TEM erlaubt eine detaillierte Betrachtung der NP. So zeigen die NP annähernd eine Kreisform (s. Abb. 4.5 d)). Da es keinen Grund für eine Vorzugsrichtung der NP-Morphologie gibt, kann man aus der Kreisform in der Projektion auf eine annähernd kugelförmige Morphologie der NP schließen. Es scheint, als seien die NP häufig durch Hohlkehlen von geringerer Materialdicke miteinander verbunden. Bislang konnte nicht geklärt werden, ob diese Hohlkehlen durch Trocknungsartefakte bei der Probenpräparation entstehen oder bedeuten, dass die NP schon bei der Synthese zusammengewachsen sind. Deshalb wurde nur die erkennbare Primärgröße der NP durch manuelle Bildauswertung in *ImageJ* bestimmt und eventuelle Zusammenwachsungen (s. Abb. 4.6) nicht berücksichtigt. So ergab sich ein mittlerer Durchmesser von $D_{\mathrm{TEM}} = 29\,\mathrm{nm}$ bei einer Standardabweichung von $\sigma = 13\,\mathrm{nm}$. Das verwendete Elektronenmikroskop erlaubt auch die Aufnahme eines Beugungsbildes des durch die NP-Probe getretenen Elektronenstrahls. Dabei zeigten sich zunächst Beugungsringe (s. Anhang B.2), die die Kristallinität der NP bestätigten. Nach einer Bestrahlungszeit von ca. 30 s verschwanden die Ringe. Das lässt darauf schließen, dass der hochenergetische Elektronenstrahl die NP abträgt und damit auch die Kristallinität zerstört.

Diskussion

Die bestimmten mittleren Größen und deren Standardabweichungen sind in Tabelle 4.2 zusammengestellt. Die Ergebnisse der fünf Techniken zeigen, dass der Begriff der Größe für NP nicht einfach zu definieren ist. Es muss stets das physikalische Prinzip berücksichtigt werden, mit dem diese Größe bestimmt wurde. Auch die mit dem Prinzip verbundene Probenaufbereitung ist nicht vernachlässigbar. Die bildgebenden Verfahren AFM, REM und TEM haben den Vorteil, dass neben der Größe auch eine Form der NP ermittelt werden kann und zeigen eine nahezu kugelförmige Primärstruktur der NP. Wobei anhand der Bilder nicht bestimmt werden kann, ob die sichtbaren Agglomerate tatsächlich zusammengewachsene Partikel sind oder lediglich durch die Austrocknung der NP-Suspension zusammen gelagerte einzelne NP sind. Deshalb wurden bei der Bildauswertung stets solche Partikel ausgewählt, die sich gut von anderen Partikeln abheben. Die ermittelten Größenverteilungen bei AFM und REM stimmen gut überein. Hingegen

	FCS	**DLS**	**AFM**	**REM**	**TEM**
Mittlerer Durchmesser [nm]	135	142	68	62	29
Standardabweichung [nm]	8	46	15	19	13

Tabelle 4.2: Zusammenstellung der gemessenen Größenverteilungen

zeigen die Partikel in den TEM-Bildern einen Durchmesser, der nur etwa halb so groß ist. Dies ist zunächst unerwartet, da alle drei Techniken auf Wechselwirkungen mit den Elektronen der NP beruhen. Bei TEM und REM sind das die Wechselwirkungen des Elektronenstrahls mit den Elektronen der NP. Bei AFM sind es die Wechselwirkungen der Messspitze mit den Elektronen der NP. Bezieht man jedoch die oben beschriebene Beobachtung mit ein, dass ein mittels TEM aufgenommenes Beugungsbild binnen weniger Sekunden verschwindet, wird klar, dass die Zr-*fum*-NP durch den hochenergetischen Elektronenstrahl abgetragen werden. Dies führt dazu, dass die TEM-Bilder zu einer Zeit entstanden sind zu der die Partikel schon stark verkleinert wurden. Dieses Verhalten ist wohl materialspezifisch und könnte durch eine geringere Beschleunigungsspannung des Elektronenstrahls vermindert oder gar vermieden werden. Eine verminderte Beschleunigungsspannung bedeutet gleichzeitig aber ein vermindertes Auflösungsvermögen, sodass in diesem Fall die Bildinformation der Morphologie teilweise verloren gehen könnte. Dennoch bleibt einer der Vorteile von TEM die Geschwindigkeit, mit der Ergebnisse erlangt werden können. Eine Bilderserie mit insgesamt mehreren Tausend abgebildeten NP kann binnen weniger Minuten aufgenommen werden. Hingegen wird die Probe bei

AFM und REM langsam abgerastert und erlaubt damit keine Hochdurchsatz-Messungen. Die beiden Techniken DLS und FCS bestimmen dieselbe physikalische Größe, den hydrodynamischen Durchmesser. Insofern ist es erwartbar, dass die gemessenen Mittelwerte der NP-Größen gut übereinstimmen. Jedoch unterscheiden sich die gemessenen Breiten der Größenverteilung, wobei die mit DLS bestimmte Verteilung knapp fünfmal breiter ist als die mit FCS bestimmte. Dies lässt sich durch die unterschiedlichen Auswertungsarten erklären. Die Breite der mit DLS gemessenen Verteilung wird durch die in der Probe vorhandenen Agglomerate verbreitert. Diese Agglomerate sind während der FCS-Messungen durch die „Dustfilter"-Funktion größtenteils von der Analyse ausgenommen worden, was eine schmalere Größenverteilung zur Folge hat.

Fazit

NP sind als Produkt einer physikalisch-chemischen Synthese eine kolloidale Dispersion von nicht-identischen Partikeln und unterliegen einer polydispersen Größenverteilung. Selbst unter denselben makroskopischen Produktionsbedingungen stellt sich die Reproduzierbarkeit der NP-Synthese als schwierig heraus. Bei der Erforschung und Anwendung von NP ist deren Größe und Größenverteilung aber einer der Schlüsselfaktoren. Aus diesem Grund ist eine sorgfältige und umfassende Charakterisierung der verwendeten NP stets erforderlich. Wird dabei nur eine einzige Methode benutzt so kann dies zu einer verfälschten Charakterisierung der NP führen. Die hier gezeigte Charakterisierung, welche fünf verschiedene Standard-Methoden zur Größenbestimmung kombiniert, empfiehlt sich als neue Standardprozedur der NP-Charakterisierung.

4.1.2 Charakterisierung von MIL-100(Fe)- und MIL-101(Cr)-NP

In den Kapiteln 4.2.1, 4.2.2 und 4.3 werden MIL-100(Fe)- und teilweise auch MIL-101(Cr)-NP verwendet. Dafür ist es notwendig auch von diesen Partikeln eine Größencharakterisierung durchzuführen. Ihre Charakterisierung wurde zunächst mittels TEM-Aufnahmen durchgeführt. Die NP wurden in einer ethanolischen Suspension auf Trägernetzchen (formvar-carbon 300 mesh copper grid von Ted Pella, USA) pipettiert. Der Alkohol wurde anschließend über zwei Stunden durch Verdunstung an der Raumluft entfernt. Die TEM-Aufnahmen sind an einem JEM 1011 (JEOL, Tokyo, Japan) bei einer Beschleunigungsspannung von 80 kV entstanden. Zur Auswertung wurden die TEM-Bilder zunächst in Binärbilder umgewandelt. Der dazu verwendete Schwellwert wurde

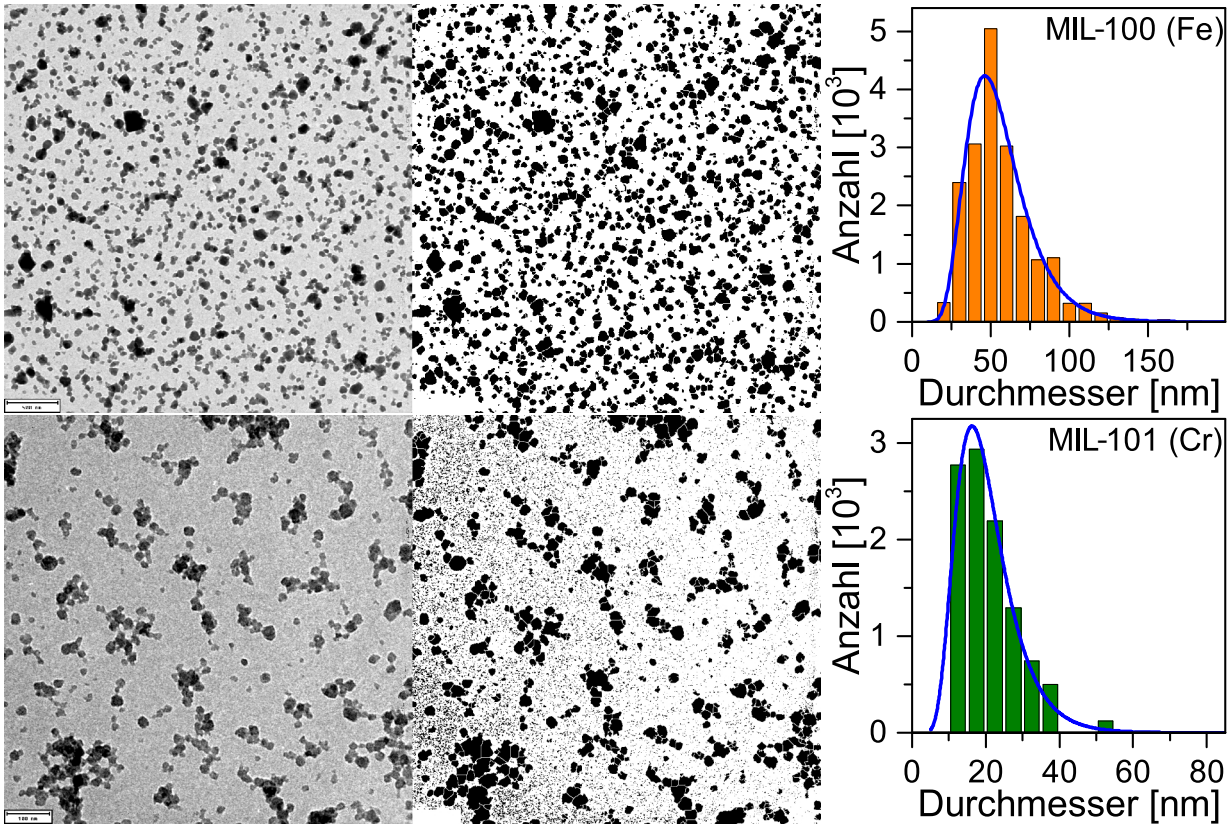

Abbildung 4.7: TEM-Analyse der MIL-100(Fe)- (oben, Maßstab: 500 nm) und MIL-101(Cr)-NP (unten, Maßstab: 100 nm). Auf die TEM-Abbildungen (links) wurden eine Wasserscheidentransformation angewendet, nachdem sie zu Binärbildern umgewandelt wurden (Mitte), um nahe beieinanderliegende NP für die anschließende Analyse zu trennen. Mit Hilfe der „Analyze Particles"-Funktion wurden die Partikel ausgemessen und ihre Durchmesser in einem Histogramm dargestellt (rechts). Zur robusten Bestimmung der häufigsten Partikelgröße wurde eine logarithmische Normalverteilung an die Histogramme angepasst (blaue Linie).

so gewählt, dass die NP in möglichst vollem Umfang in schwarz und der Hintergrund in weiß dargestellt wurde. Der Maßstabsbalken wurde aus den Bildern entfernt damit dieser nicht als Teil der NP interpretiert werden kann. Anschließend wurde eine Wasserscheidentransformation auf den Binärbildern angewendet, welche die zusammengelagerten NP durch eine feine weiße Linie optisch voneinander trennt. Schließlich wurde der Flächeninhalt aller zusammenhängenden schwarzen Flächen, welche nicht am Bildrand lagen, mit Hilfe der „Analyze Particles"-Funktion in *ImageJ* ermittelt. Der niedrige Kontrast der MIL-101(Cr)-Partikel hat zur Folge, dass auch Teile des Hintergrunds durch die

Binärwert-Umwandlung als kleine schwarze Körner dargestellt werden. Dem wurde in der Partikelanalyse Rechnung getragen, indem nur zusammenhängende Flächen größer als $5\,\mathrm{nm}^2$ gezählt wurden. Da der Großteil der Partikel annähernd kreisförmig ist, wurde aus der Fläche der Partikel A_i ein Durchmesser $D_i = 2\sqrt{\frac{A_i}{\pi}}$ errechnet. Die so erlangten Durchmesser wurden in Histogrammen zusammen getragen. Mittels einer logarithmischen Normalverteilung wurde Parameterschätzung an den Histogrammen vorgenommen. Es ergaben sich die mittleren Durchmesser von MIL-100(Fe) zu $D_{\mathrm{MIL100}} = 52{,}4\,\mathrm{nm}$ und von MIL-101(Cr) zu $D_{\mathrm{MIL101}} = 18{,}9\,\mathrm{nm}$. Diese Ergebnisse werden unter anderem für die Berechnungen in Kapitel 4.3 verwendet.

4.2 Funktionalisierung von MOF-Nanopartikeln

Die selektive Funktionalisierung der externen Oberfläche von porösen NP ist von großem Interesse für viele Anwendungsgebiete der Nanotechnologie [73–75]. Als externe Oberfläche der NP wird die Grenzfläche zwischen dem Partikel und dem Umgebungsmedium verstanden [76]. Bei NP ist das Verhältnis aus Oberfläche zu Volumen naturgemäß sehr groß, was Oberflächeneffekte dominant werden lässt. Aus diesem Grund ist es für die Anwendung von NP besonders wichtig, die Oberfläche kontrolliert funktionalisieren zu können [77–79]. Außerdem können NP deren Oberfläche nicht modifiziert sind, schnell vom Immunsystem erkannt werden und können ihre Wirkung nicht mehr entfalten. Im Falle von Nanotransportern kann eine Funktionalisierung auch der Verkapselung des Trägersystems dienen, um eine vorzeitige Freisetzung des Wirkstoffs zu verhindern. Im Folgenden werden mehrere Funktionalisierungskonzepte von NP vorgestellt und charakterisiert.

4.2.1 Lipidbeschichtung von MOF-Nanopartikeln[2]

In diesem Kapitel wird mit der Verkapselung von MOF-NP mittels Lipiden eine neue Klasse von Nanotransportern vorgestellt (s. Abb. 4.8), welche in Zusammenarbeit mit der Arbeitsgruppe Wuttke und der Arbeitsgruppe Vollmar entstand. Diese sollen die Charakteristiken von MOF-NP und Liposomen [1, 81] vereinigen. Ein Vorteil der großen Porosität von MOF-Strukturen ist die Möglichkeit, einen Wirkstoff in die Poren der MOF-NP zu füllen. Allerdings gibt es bei unfunktionalisierten MOF-NP keine Möglichkeit den Wirkstoff an einem frühzeitigen Hinausdiffundieren zu hindern. Aus diesem Grund müssen Verkapselungssysteme entwickelt werden, die den Wirkstoff effektiv innerhalb der NP halten solange der Nanotransporter sein Ziel noch nicht erreicht hat. Es hat sich gezeigt, dass die Zirkulationszeit von Nanotransportern im Blutkreislauf stark von der Größe der Transporter (z.B. Liposomen) abhängt [82]. Unter Liposomen versteht man kleine Bläschen (Vesikel), bei denen eine Lipiddoppelschicht das Innere des Vesikels von der äußeren Umgebung trennt. Liposomen werden bereits zum zielgerichteten und selektiven Transport von Arzneistoffen verwendet und können empfindliche Arzneistoffe vor einer möglichen Metabolisierung schützen oder gesundes Köpergewebe vor den zytotoxischen Eigenschaften der Medikamente bewahren. Jedoch wird bei der liposomalen Formulierung von Arzneistoffen ein großer Teil des eingesetzten Arzneistoffes nicht

[2]Dieses Kapitel behandelt die Erkenntnisse, die in [80] publiziert wurden (s. Anhang B.1).

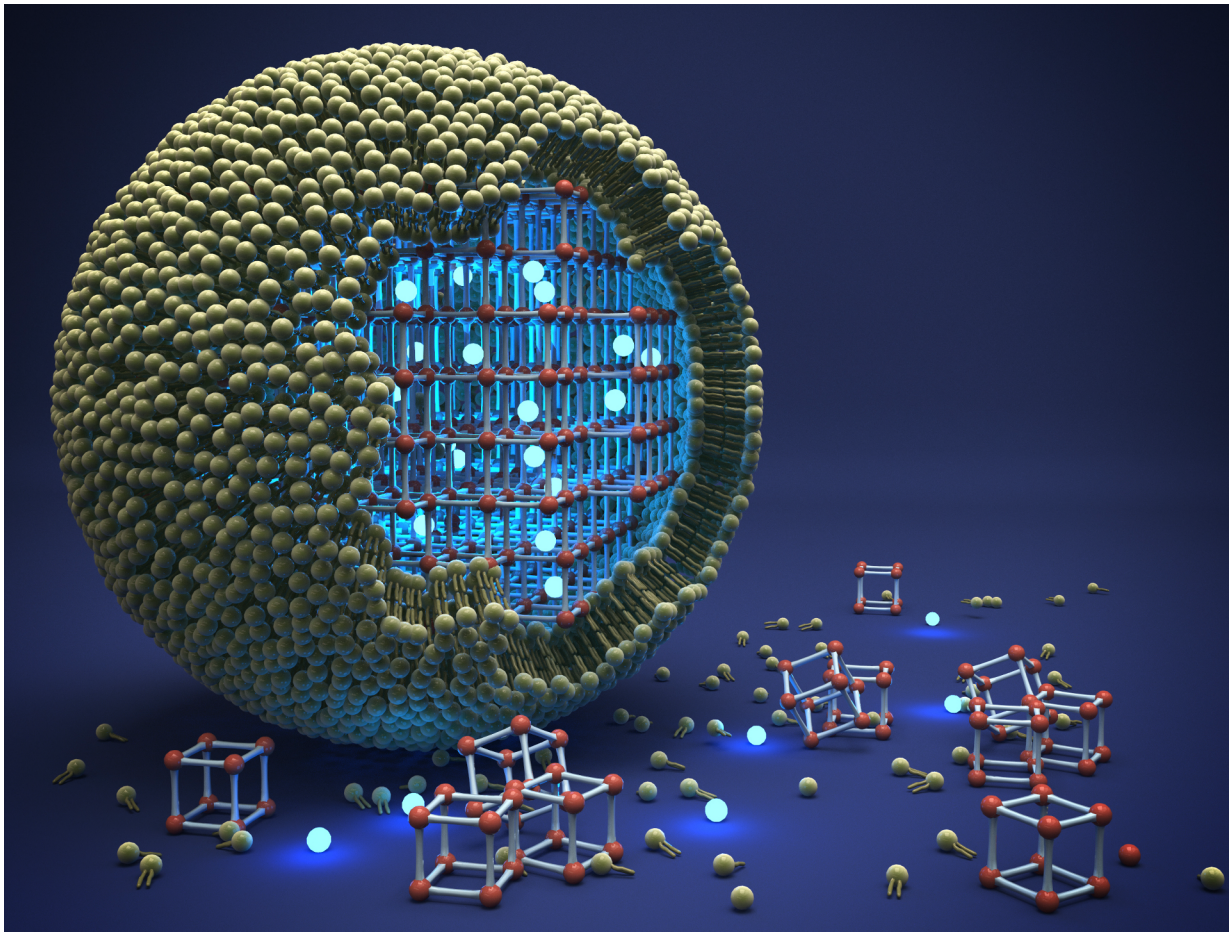

Abbildung 4.8: Illustration eines MOF-Nanopartikels umhüllt von einer Lipidschicht befüllt mit fluoreszierenden Molekülen (mit freundlicher Genehmigung von Christoph Hohmann, Nanosystems Initiative München).

in das Vesikel gebunden und geht so durch die Aufreinigung der Liposomen verloren. Darüber hinaus ist die strukturelle Stabilität schlecht kontrollierbar [21]. Hier können MOF-NP ihre Vorteile einbringen. Zum einen ist es möglich mit einer Funktionalisierung der MOF-Bauteile die Aufnahme und Freigabe der Gastmoleküle zu kontrollieren. Zum anderen kann eine optimierte Beladung der NP entwickelt werden, sodass die Wirkstoffdichte höher ist als die von liposomalen Nanotransportern. Darüber hinaus sind lipidbeschichtete NP stabiler als Liposomen [21]. Aus diesen Gründen erscheint eine Lipidbeschichtung von MOF-NP als ideale Methode, die Vorteile beider Systeme zu vereinigen. Im Folgenden wird untersucht, inwieweit sich eine solche Beschichtung realisieren lässt, sich die geforderte Undurchlässigkeit bestätigt und sich die Beschichtung auf die Zellaufnahme der MOF-NP auswirkt. Für die hier gezeigten Resultate wurden

MIL-101(Cr)-NP [40] verwendet (s. Kap. 2.2). Aufgrund der großen Porenöffnungen der MIL-101(Cr)-Struktur und der schmalen Größenverteilung der NP (s. Kap. 4.1.2) scheint dieser NP-Typ ideale Voraussetzungen für die Modifikation hin zu wohldefinierten, lipidbeschichteten Nanotransportern mit maximaler Beladungskapazität zu besitzen. Die Beschichtung wurde mit dem neutralen Phospholipid DOPC (1,2-dioleoyl-sn- glycero-3-phosphocholine) als Modellsystem realisiert, da sich dieses Lipid bereits bei Beschichtungen von anderen NP-Sorten als geeignet erwiesen hat [83]. Um die NP-Oberfläche mit den Lipidmolekülen zu beschichten, wurde ein Lösemittelübergang verwendet. Dafür wurden die Lipide und MOF-NP in einer Ethanol-Wasser Mischung gelöst. Die Mischung wurde mit 40% Ethanol und 60% Wasser so gewählt, dass die Lipidmoleküle in gelöster Form als Monomere vorliegen und nicht als Mizellen oder Liposomen [84]. Anschließend wurde der Anteil an Wasser in dieser Lösung schnell auf über 90% erhöht. Dadurch können die Lipidmoleküle nicht mehr in Lösung bleiben und formen eine Doppelschicht auf der NP-Oberfläche, um so ihre hydrophoben Ketten vor dem Wasser abzuschirmen [83]. Eine detaillierte Synthesebeschreibung ist in Anhang B.1 zu finden. Um herauszufinden, ob die Formation einer undurchlässigen Lipidbeschichtung auf der NP-Oberfläche erfolgreich war, wurden mehreren Messmethoden herangezogen. DLS-Messungen zeigen, dass die NP durch die Lipidbeschichtung einen Zuwachs des mittleren hydrodynamischen Durchmessers von etwa 10 nm erfahren (siehe *supporting information* in Anhang B.1 [80]). Bei einer erwarteten DOPC-Lipiddoppelschicht-Dicke von 4 nm [85] entspricht dieser Größenzuwachs des Durchmessers von $D_{\text{ohne}} = 69\,\text{nm}$ der unbeschichteten Partikel auf $D_{\text{mit}} = 78\,\text{nm}$ mit Lipidbeschichtung, sehr gut dem erwarteten Größenunterschied. Dabei gilt es zu berücksichtigen, dass die Dicke der Lipiddoppelschicht zweimal zum Durchmesser der lipidbeschichteten NP beiträgt. Dieser Größenzuwachs ist bereits ein starkes Indiz dafür, dass sich eine Lipidschicht auf den NP gebildet hat. Um die Lokalisation der Lipide auf den MOF-NP in Lösung zu bestätigen, wurden die Lipidmembran sowie die NP fluoreszenzmarkiert und die Kodiffusion beider Komponenten mittels FCCS untersucht. Hierzu wurden die MOF-NP vor der Lipidbeschichtung mit dem Fluoreszenzfarbstoff *ATTO 633* (ATTO-TEC, Deutschland) inkubiert, so dass sich die Poren der NP mit dem Farbstoff füllen konnten und die NP fluoreszent wurden. Der DOPC-Lösung wurde ein Anteil von 0,005% des fluoreszenzmarkierten Lipids *BODIPY FL DHPE* (Molecular Probes, USA) beigemengt, um so auch die Lipidmembran fluoreszent zu markieren. Wie in Abbildung 4.9 zu sehen, ist die Amplitude der Kreuzkorrelation deutlich von der Grundlinie (grau)

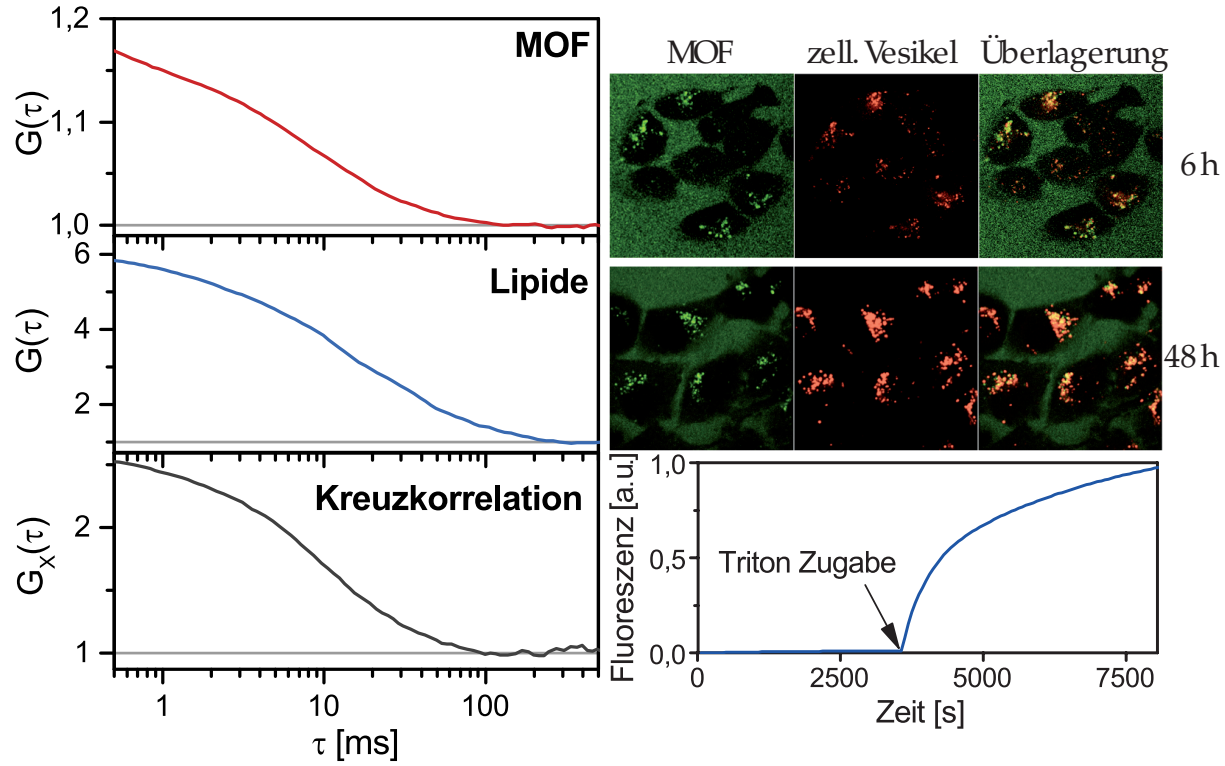

Abbildung 4.9: Links: FCCS-Messungen zum Nachweis der Kodiffusion von Lipiden und MOF-NP zeigen einen hohen Anteil kodiffundierender Lipidmoleküle auf NP. Rechts oben: Konfokalmikroskopieaufnahmen von Blasenkrebszellen (nach 6 und 48 Stunden Inkubation) belegen die Zellaufnahme der lipidbeschichteten MOF-NP. Rechts unten: Fluoreszenz (willkürliche Einheiten) im zeitlichen Verlauf der Uraninfreisetzung der lipidbeschichteten MOF-NP. Nach 60 min ohne nennenswerten Anstieg der Fluoreszenz wurde das Detergenz Triton X-100 zugegeben, um die Lipidmembran aufzulösen und so eine Freisetzung zu bewirken.

verschieden. Dies bestätigt die Kodiffusion von Lipiden und NP und damit die erfolgreiche Beschichtung der Partikel mit Lipiden. Frei diffundierende *ATTO 633* Moleküle in der Probe, die sich nicht durch Zentrifugation der NP entfernen ließen, beeinflussen die Korrelationskurve des roten Kanals (*ATTO 633*). Somit ist eine quantitative Analyse des Anteils der lipidbeschichteten Partikel nicht möglich.

Die Vollständigkeit und Dichtheit der Lipiddoppelschicht um die NP wurde überprüft, indem die Freisetzung von Uranin aus lipidbeschichteten NP untersucht wurde. Dazu wurden die NP vor der Beschichtung mit Lipiden in einer Uranin-Lösung inkubiert. Die so präparierten NP wurden in die Kappe einer Küvette gefüllt. Die Kappe wurde anschließend mit einer Dialysemembran verschlossen und auf eine mit Wasser gefüllte

Küvette gesteckt, so dass die Dialysemembran sowohl mit dem Wasser der Küvette als auch mit der NP-Probe in Kontakt steht. Die Membran wurde so gewählt, dass Uraninmoleküle die Membran passieren können, die NP hingegen zurück gehalten werden. Innerhalb der Küvette wurde nun die Fluoreszenz von Uranin gemessen, welches durch die Dialysemembran in die Küvette diffundiert ist. Durch einen Rührfisch in der Küvette wurde sichergestellt, dass sich innerhalb der Küvette eine homogene Verteilung des durch die Dialysemembran diffundierten Uranins einstellt. Zunächst zeigte sich über 60 Minuten ein sehr geringer Anstieg des Fluoreszenzsignals (s. Abb. 4.9). Daraus wurde geschlossen, dass die Lipidmembran die Uranin-Moleküle effektiv im NP zurückhält. Anschließend wurde das Tensid Octoxinol 9 (Triton X-100) zu den lipidbeschichteten NP gegeben, um die Lipidbeschichtung aufzulösen. Diese Gegenprobe sollte klarstellen, ob grundsätzlich eine Freisetzung von Uranin beobachtbar ist. Es zeigte sich unmittelbar nach Zugabe von Triton eine starke Zunahme der gemessenen Fluoreszenz. Somit ist der vollständige Verschluss der NP durch die Lipidmembran bestätigt. Für zukünftige medizinische Anwendungen der lipidbeschichteten MOF-NP ist es wichtig, das Zellaufnahme-Verhalten dieser Partikel zu untersuchen. Zu diesem Zweck wurden die lipidbeschichteten MOF-NP zu T24-Blasenkrebszellen gegeben. Um den Verlauf der Zellaufnahme mit einem Konfokalmikroskop verfolgen zu können, wurden die NP wie schon für die FCCS-Messungen mit *ATTO 633* befüllt und die Zellmembranen der Blasenkrebszellen mit dem Fluoreszenzfarbstoff PKH26 markiert. Wie in Abbildung 4.9 zu erkennen, kumulieren sich die NP bereits nach 6 Stunden in den intrazellulären Vesikeln und verlassen diese auch nach 48 Stunden nicht.

Zusammenfassend wurde in diesem Kapitel die Entwicklung einer neuartigen MOF-NP-Verkapselung mit Hilfe einer Lipidbeschichtung vorgestellt. Mittels FCCS konnte gezeigt werden, dass die Lipidschicht und die NP kolokalisiert auftreten. Es wurde demonstriert, dass die Lipidschicht Moleküle in den NP-Poren effektiv am Hinausdiffundieren hindern kann. Darüber hinaus konnte eine erhöhte Zellaufnahme der lipidbeschichteten NP gezeigt werden. So hat dieses Modellsystem großes Potential für die Entwicklung von multifunktionellen Wirkstoff-Nanotransportern: einerseits kann der MOF-NP-Kern verschiedene Wirksubstanzen aufnehmen, andererseits bietet die Lipidhülle die Möglichkeit Targeting-Liganden, sowie eine gezielte Auslösung der Wirkstoff-Freisetzung einzubauen.

4.2.2 Polymerbeschichtete MOF-Nanopartikel[3]

In diesem Kapitel wird eine neuartige Funktionalisierungsmethode für MOF-NP vorgestellt und untersucht, welche in Zusammenarbeit mit der Arbeitsgruppe Wuttke und der Arbeitsgruppe Wagner entstand. Für NP im Allgemeinen ist die Oberflächenfunktionalisierung mit Polymeren eine etablierte Methode. So kann mit einer geeigneten Funktionalisierung zum Beispiel die Löslichkeit in Wasser, die Biokompatibilität oder die kolloidale Stabilität verbessert werden [87–89]. Methoden zur selektiven Oberflächenfunktionalisierung von MOF-NP wurden bisher nur wenig untersucht [90–92].

Es stehen zwei grundsätzliche Wege für die Funktionalisierung von MOF-NP zur Verfügung: eine Funktionalisierung schon während der NP-Synthese und eine nachträgliche. Werden die Funktionalisierungseinheiten schon während der MOF-Synthese zugegeben, so ist keine Selektion zwischen externer Oberflächenfunktionalisierung und dem Einbau der Funktionalisierungseinheiten in das MOF-Gitter möglich [93]. Die in diesem Kapitel gezeigte Funktionalisierung von MOF-NP folgt dem postsynthetischen Ansatz [94]. Dadurch bleibt die innere Struktur der MOF-NP unverändert und für andere Zwecke zugänglich (z.B. Befüllung mit Wirkstoffen oder Fluoreszenzmarkern, s. Kap. 4.3). Dies bietet die Möglichkeit Funktionseinheiten kovalent und selektiv an die NP-Oberfläche zu binden. Dieser Umstand ist besonders für die Befüllung mit Wirkstoffen oder Fluoreszenzmarkern von Bedeutung (s. Kap. 4.3). Die kovalente, postsynthetische Anbindung von Polymeren an die externe Oberfläche von MOF-NP wurde zum ersten mal in dem, diesem Kapitel zu Grunde liegenden Artikel gezeigt [86]. Zur Funktionalisierung wurden MIL-100(Fe)-NP gewählt, da diese chemisch stabil in wässriger Umgebung [95, 96] und gleichzeitig biokompatibel sind [97]. Dies kennzeichnet sie als vielversprechende Kandidaten für eine spätere Anwendung als multifunktionelle Nanotransporter. Als Funktionseinheiten wurden zwei verschiedene Polymere als Modellsysteme gewählt. Beide sollten aufgrund ihrer chemischen Eigenschaften geeignet sein, die kolloidale Stabilität der NP zu verbessern: zum einen das häufig zur Stabilisierung genutzte Polyethylenglycol (PEG) - in diesem Fall mit einer Kettenlänge von 5000 Monomeren und einer Aminogruppe zur Anbindung an die MOF-NP - zum anderen das Oligoaminoamid Stp10-C, welches sich als bifunktionales Polymer eignet, um an dessen Thiol-Gruppe z.B. Fluoreszenzmarker anzuhängen.

An der externen Oberfläche der MOF-NP gibt es unter-koordinierte Verbindungsmoleküle (im Falle von MIL-100(Fe) Trimesinsäure) mit freien Carboxygruppen (s. Abb.

[3]Dieses Kapitel behandelt in Teilen Erkenntnisse, die in [86] publiziert wurden (s. Anhang B.4).

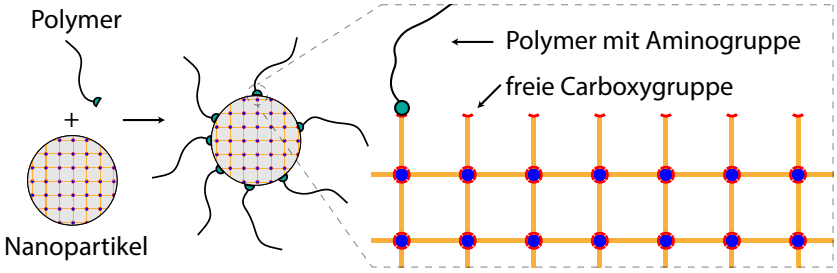

Abbildung 4.10: Illustration der Bindung der Aminogruppe eines Polymermoleküls an eine freie Carboxygruppe des organischen Verbindungmoleküls (Trimesinsäure) an der externen Oberfläche eines MOF-NP (nicht maßstabsgetreu).

4.10). Somit können die Aminogruppen der Polymere eine Peptidbindung mit den freien Carboxygruppen an der MOF-NP-Oberfläche eingehen. Im Inneren der MOF-NP sind die organischen Verbindungsmoleküle vollständig koordiniert und stehen dadurch für Bindungen nicht zur Verfügung. Der genaue Funktionalisierungsprozess ist in Veröffentlichung P4 im Anhang B.4 beschrieben. Da eine kovalente, postsynthetische Funktionalisierung von MOF-NP zuvor noch nicht in der Literatur beschrieben wurde, muss die Bindung zwischen den Polymermolekülen und den NP eingehender untersucht werden. Zum Nachweis der Bindung wurden FCS-Messungen durchgeführt. An die freie Thiol-Gruppe der Stp10-C-Moleküle wurde der Fluoreszenzfarbstoff Cyanin 5 (Cy5) kovalent gebunden, um die Polymermoleküle für das FCS detektierbar zu machen (s. Abb. 4.11). Die PEG5000-Moleküle lassen sich nicht in dieser Form fluoreszenzmarkieren, sodass sich hier auf die Bindung der Stp10-C-Moleküle an die NP beschränkt wird. Da die chemische Bindung zwischen MOF und Polymer jedoch bei beiden Polymeren dieselbe ist (Peptidbindung), sind die Ergebnisse mit Stp10-C auf die Bindung von PEG5000 übertragbar. Der hydrodynamische Radius von frei diffundierenden Stp10-C-Cy5-Molekülen wurde zu $R_H = 1{,}5\,\text{nm}$ bestimmt. Die Korrelationskurve von Stp10-C-Cy5-funktionalisierten MIL-100(Fe)-NP (Stp10-C-Cy5/MIL-100(Fe)) zeigt eine deutlich verlangsamte Diffusionszeit gegenüber freiem Stp10-C-Cy5 (s. Abb. 4.12). Ein Zweikomponenten-Fit ergibt eine Diffusionszeit von $\tau_D = 4{,}8\,\text{ms}$ was einem hydrodynamische Radius von $R_H = 65\,\text{nm}$ entspricht. Der Zweikomponenten-Fit wurde gewählt, da nur eine diffundierende Spezies kein zufriedenstellendes Modell für die gemessene Korrelationskurve darstellte. Die zweite Komponente ist mit einer Diffusionszeit von $\tau_D = 40\,\text{ms}$ deutlich größer und ist durch Aggregation einiger NP zu erklären. Der Anteil dieser Aggregate an der Korrelationskurve erscheint mit 49% zunächst sehr hoch. Es muss jedoch berücksichtigt werden, dass die großen Aggregate auch entsprechend mehr

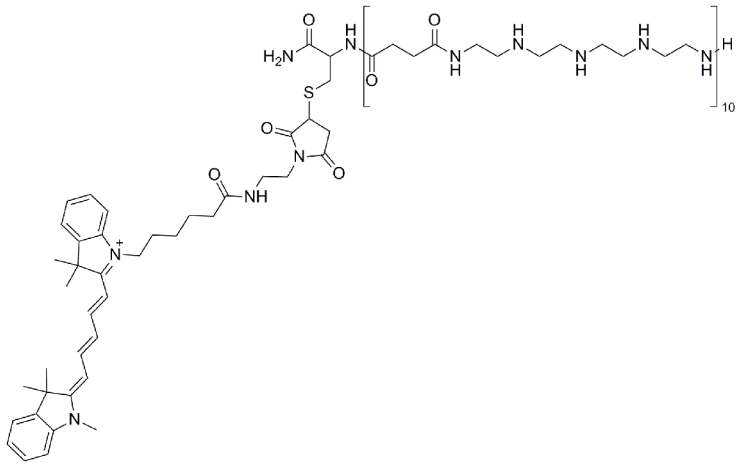

Abbildung 4.11: Strukturformel von C-Stp10-Cy5.

Stp10-C-Cy5 Moleküle tragen und damit deutlich heller sind. Unter Annahme, dass die Helligkeit eines Partikels proportional zum Quadrat des Radius ist (s. Kap. 3.2.5), ergibt sich ein Anteil der Aggregate von weniger als 1%. Neben den gezeigten FCS-Messungen bestätigen auch Ergebnisse von Infrarot-Spektroskopie-Messungen (s. Anhang B.4) die Bindung der Polymere an die NP. Beide Techniken vermögen es aber nicht die Art der Bindung zu bestimmen. Um zu zeigen, dass eine kovalente Bindung zwischen den Polymermolekülen und den NP vorliegt, wurden quantitative Absorptionsspektroskopie- und Kernspinresonanzspektroskopiemessungen durchgeführt (s. B.4). Die Ergebnisse beider Techniken lassen sich nur durch eine kovalente Bindung erklären.

Das Ziel eine kovalent angebundene Funktionalisierung durchzuführen ist somit erreicht. Es ist darüber hinaus wichtig zu zeigen, dass diese Funktionalisierung die NP nicht soweit beeinflusst, sodass ihre Eigenschaften zur Aufnahme von Wirkstoffmolekülen also die Porosität verloren geht. Dies wurde mit Hilfe von Röntgen-Pulverdiffraktogrammen (XRD) und Stickstoffabsorptionsmessungen untersucht (s. Anhang B.4). Die XRD-Messungen zeigen sowohl für funktionalisierte als auch für unmodifizierte NP die typischen Beugungsmuster des MIL-100(Fe)-Kristallgitters. Dies belegt, dass die Funktionalisierung keine grundlegenden Veränderungen an der Struktur der MOF-NP verursacht. Die BET-Analyse der N_2-Absorptionsmessungen von funktionalisierten NP ergibt eine Oberfläche von $S_{\mathrm{BET}}^{\mathrm{PEG}} = 1338\,\mathrm{m^2\,g^{-1}}$ für die mit PEG5000 funktionalisierten Partikel und $S_{\mathrm{BET}}^{\mathrm{Stp10-C}} = 1432\,\mathrm{m^2\,g^{-1}}$ für die mit Stp10-C funktionalisierten Partikel. Gegenüber den unfunktionalisierten MIL-100(Fe)-NP, deren BET-Oberfläche zu $S_{\mathrm{BET}}^{\mathrm{unfunk.}} = 1905\,\mathrm{m^2\,g^{-1}}$ bestimmt wurde, ist dies nur ein geringer Rückgang der zugänglichen Oberfläche. Dies

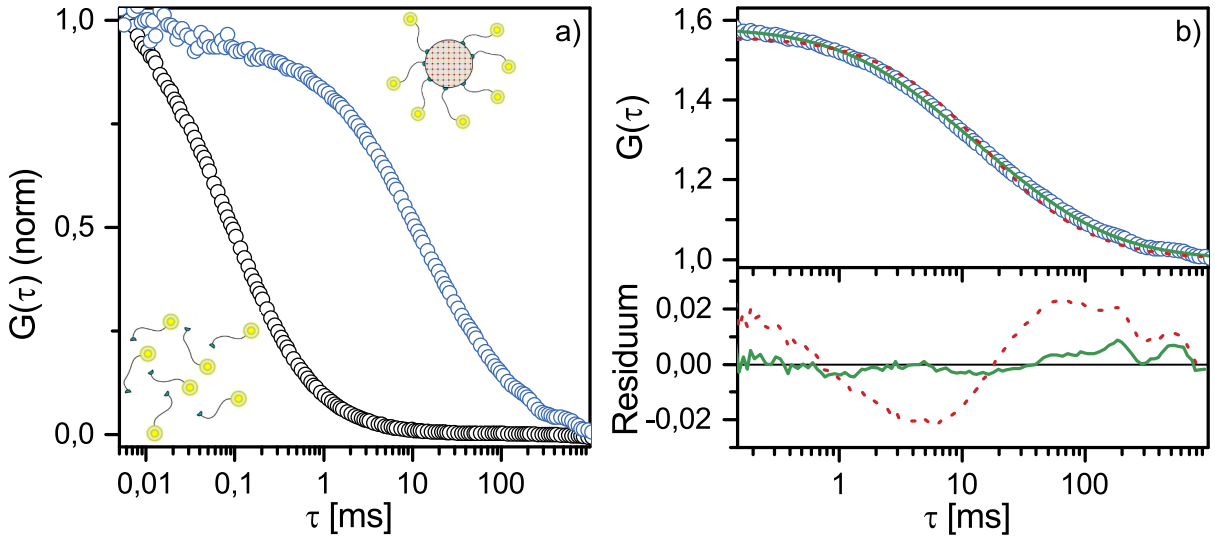

Abbildung 4.12: FCS-Messungen zum Nachweis der Bindung Stp10-C-Cy5 an MIL-100(Fe)-NP. a) Die normierte Korrelationskurve von Stp10-C-Cy5/MIL-100(Fe)-NP (blau) zeigt gegenüber den frei diffundierenden Stp10-C-Cy5 Molekülen (schwarz) eine deutlich verlangsamte Diffusion, was die Bindung bestätigt. Die Illustration von Polymermolekülen und NP ist nicht maßstabsgetreu. b) Die Größenauswertung der Korrelationskurve (oben) von Stp10-C-Cy5/MIL-100(Fe)-NP (blau) mittels Zweikomponenten-Fit (grün) ergibt einen hydrodynamischen Radius von $R_{\mathrm{H}} = 65\,\mathrm{nm}$. Im Vergleich dazu zeigt ein Einkomponenten-Fit (rot) starke Abweichungen von der Korrelationskurve (unten).

lässt darauf schließen, dass die kovalente Anbindung von Polymeren die Beladung der MOF-NP nicht übermäßig beeinträchtigt. Die Differenz der zugänglichen Oberfläche lässt sich einerseits auf die Menge der nicht-porösen angehängten Polymere und andererseits auf den teilweisen Verschluss der Porenöffnungen an der externen NP-Oberfläche durch die Polymermoleküle zurückführen.

Eine weitere wichtige Fragestellung ist, ob die Polymerhülle die intendierte Funktion, die kolloidale Stabilität zu erhöhen, erfüllt. Um diese Frage zu untersuchen, wurden DLS-Messungen der NP durchgeführt. Unmittelbar nach der Suspension frisch synthetisierter NP in Wasser sind sowohl die unmodifizierten als auch die polymerumhüllten MIL-100(Fe)-NP mit mittleren hydrodynamischen Radii im Bereich von $R_{\mathrm{H}} = 75 - 80\,\mathrm{nm}$ kolloidal. Nach einer Inkubationszeit von drei Wochen zeigen die unmodifizierten NP mit $R_{\mathrm{H}} = 107\,\mathrm{nm}$ einen deutlich vergrößerten Radius, was auf Agglomeration hindeutet. Demgegenüber sind die Radii der funktionalisierten NP nahezu unverändert geblieben ($R_{\mathrm{H}} = 73 - 76\,\mathrm{nm}$). Dieser Effekt ist der abschirmenden Wirkung der Polymere zuzuschreiben. Die Polymerhülle erfüllt also ihren Zweck der Stabilisierung der NP-Suspension.

Für eine spätere Anwendung ist es schließlich unerlässlich, dass die funktionalisierten NP von Zellen überhaupt aufgenommen werden. Um dies zu untersuchen, wurden Zellaufnahme- und Zelltoxizitätsstudien (s. Anhang B.4) durchgeführt. Diese Studien zeigen, dass Neuroblasten (N2A) die polymerumhüllten NP vermehrt aufnehmen und keine erhöhte Zellsterblichkeit beobachtbar ist.

Zusammenfassend wurde gezeigt, dass eine selektive, postsynthetische Funktionalisierung der externen Oberfläche von MOF-NP mittels Polymeren möglich ist. Die mögliche kovalente Anbindung von Polymeren wurde untersucht und bestätigt. Die funktionalisierten NP zeigen eine erhöhte kolloidale Stabilität in wässrigen Medien, was für die Anwendung als Nanotransporter essentiell ist. Auch die Zellaufnahme der funktionalisierten NP ist gegenüber den unfunktionalisierten erhöht. All dies zeigt, dass die in diesem Kapitel behandelte Funktionalisierung von MOF-NP ein weiterer Schritt in Richtung multifunktioneller Nanotransporter ist.

4.2.3 pH-reversible Bindung von His-Tags an MOF-Nanopartikel[4]

Das in diesem Kapitel vorgestellte Funktionalisierungskonzept von MOF-NP folgt ebenfalls dem postsynthetischen Ansatz, zielt aber auf andere Einsatzweisen der NP ab. Die hier an die NP gebundenen Funktionseinheiten sollen nicht wie oben beschrieben auf der NP-Oberfläche verbleiben und die Eigenschaften der NP dauerhaft verändern, sondern können sich nachträglich ablösen. Dieses Funktionalisierungskonzept entstand in Zusammenarbeit mit der Arbeitsgruppe Wagner und der Arbeitsgruppe Wuttke und ist im Publikation P6 (s. Anhang B.6) veröffentlicht wurden.

An der Oberfläche von MOF-NP befinden sich unter-koordinierte Metallzentren, an die sich Elektronenpaare anlagern können [99–101]. Mit Hilfe geeigneter Elektronenpaardonatoren lässt sich diese Tatsache nutzen, um ein neues Funktionalisierungskonzept für MOF-NP zu etablieren. Als Elektronenpaardonatoren bieten sich hier His-Tags an, weil sie koordinativ an Metallkomplexe binden (s. Kap. 2.3). Die Vorteile dieses Konzepts

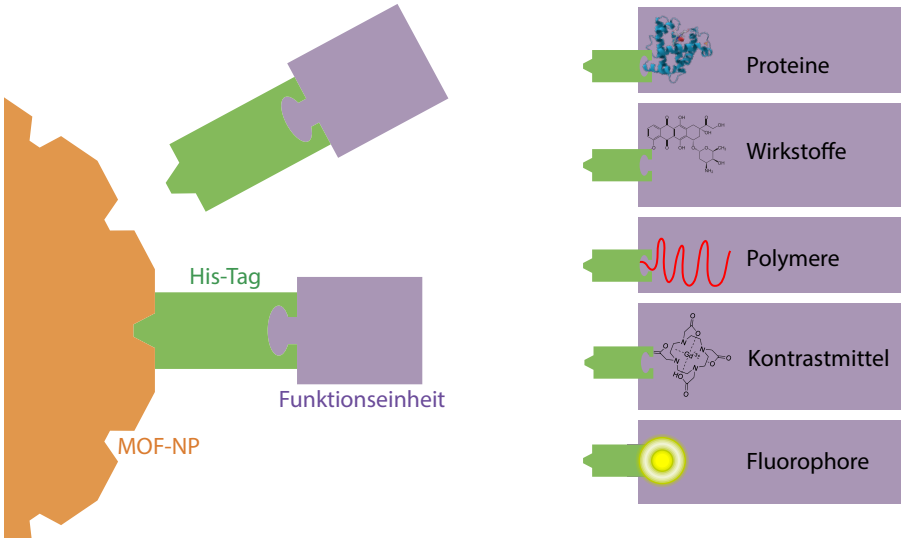

Abbildung 4.13: Schematische Illustration zur Funktionalisierung von MOF-NP. Eine Funktionseinheit (z.B. Wirkstoff, Peptid, Protein, Polymer, etc.) wird mit einem His-Tag kovalent verbunden. Durch einfaches Mischen von MOF-NP und Funktionseinheit in Lösung wird anschließend die Funktionalisierung durchgeführt.

sind unter anderem, dass der Funktionalisierungsschritt bei Raumtemperatur und in wässriger Umgebung stattfinden kann. Es sind keine Katalysatoren oder andere Reaktionspartner notwendig, die eine anschließende Aufreinigung erfordern würden. Die

[4]Dieses Kapitel behandelt in Teilen Erkenntnisse, die in [98] publiziert wurden (s. Anhang B.6).

Interaktion ist reversibel (z.B. durch Protonierung). Ein weiterer wichtiger Vorteil ist, dass die His-Tags an verschiedenste Funktionseinheiten gekoppelt werden können (z.B. Wirkstoffe, Peptide, Proteine, Polymere, etc.). Letzteres bedeutet auch, dass mehrere Funktionen auf einem NP vereint werden können, z.B. ein Wirkstoff und ein Targeting-Ligand. Die Reversibilität der Funktionalisierung durch Protonierung (Verringerung des pH-Wertes) kann zur Freisetzung der angebundenen Funktionseinheiten während der Endozytose genutzt werden. Dies ist ein herausragendes Alleinstellungsmerkmal des Funktionalisierungskonzepts, denn es benötigt keinen extern gesteuerten Auslöser für die Freisetzung.
In diesem Teil der Arbeit wurde die erfolgreiche praktische Umsetzung dieses Funktionalisierungskonzepts gezeigt. Dazu wurde die Bindung His-Tag – MOF-NP eingehend untersucht und charakterisiert. Ergänzend wurde analysiert, ob eine Funktionalisierung mit unterschiedlichen Funktionseinheiten auf der NP-Oberfläche möglich ist. Darüber hinaus wurden Zellexperimente durchgeführt (s. Anhang B.6), die die Zellaufnahme der funktionalisierten NP sowie den intrazellulärer Transport kleiner funktioneller Moleküle nachweisen. In diesem Kapitel sind die Ergebnisse für MOF-NP aus Zr-*fum* vorgestellt. Diese weisen die schmalste Größenverteilung (s. Kap. 4.1.1) und die geringsten Seiteneffekte, wie z.B. Fluoreszenzauslöschung, auf (s. Kap. 4.3) und sind deshalb ein besonders geeignetes Modellsystem.

Charakterisierung der Bindung der His-Tags an MOF-NP in Puffer

Wie schon zuvor (s. Kap. 4.2.2), wurde die Änderung der Diffusionseigenschaften von fluoreszenzmarkierten Molekülen (hier His-Tag) vor und nach Bindung an NP mittels FCS untersucht. Dazu muss sichergestellt werden, dass der einzelne His-Tag eine Diffusionsgeschwindigkeit hat, welche sich deutlich von der der NP-His-Tag Komplexe unterscheidet [53]. Diese Voraussetzung ist hier durch die Größe der NP gegeben, die eine hydrodynamische Größe von rund 140 nm (s. Kap. 4.1.1) haben und durch die Größe der His-Tag-Moleküle welche nur wenige Nanometer groß sind (s. Abb. 4.14 und 4.15).

Einfluss von Ethanol auf His-Tags

Vorversuche haben gezeigt, dass die His-Tag/MOF-NP-Bindung in verschiedenen Lösungsmitteln erfolgen kann (s. Anhang B.6). Zum einen eignet sich hierfür Ethanol, welches als ideales Lagerungsmedium für die MOF-NP relevant ist. Zum anderen kommt auch das Medium HEPES gepufferte Glucose (HBG) bei pH $=$ 7,4 in Frage, welches

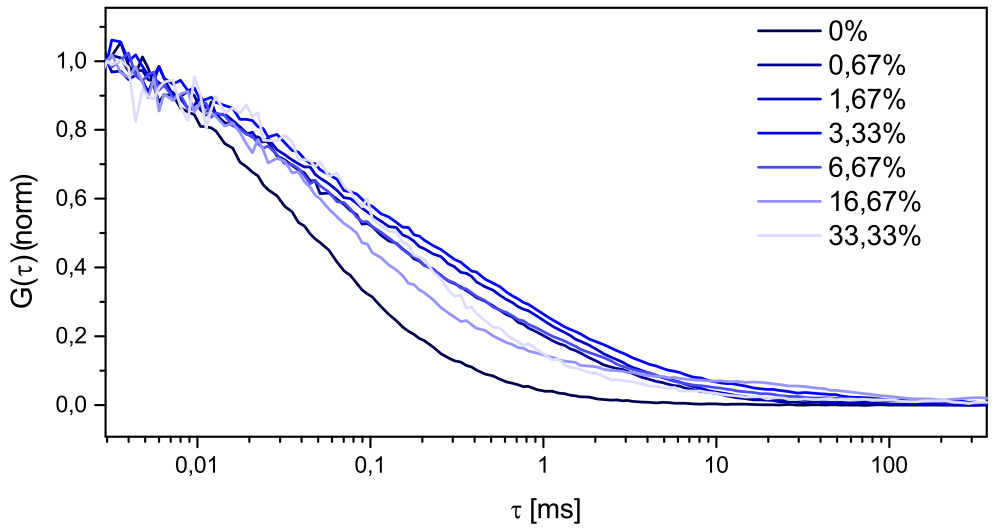

Abbildung 4.14: Normierte Korrelationskurven von H_6-PEG_{12}-CF in HBG, pH = 7,4 mit variierendem Ethanol-Anteil. Ohne Ethanol zeigt sich eine monodisperse Diffusion mit einem hydrodynamischen Radius von R_H = 1,2 nm. Bei einer Beimengung von Ethanol zeigen die Korrelationkurven die Diffusion eines polydispersen Systems, was auf Agglomeration der His-Tag-Moleküle hindeutet.

für die späteren Zellexperimente geeignet ist. Es wurde angenommen, dass eine Kombination aus HBG mit einem geringen Anteil Ethanol ebenfalls geeignet wäre, um die Bindung mittels FCS zu charakterisieren. Zur Überprüfung dieser Hypothese wurden His-Tag-Moleküle, bestehend aus sechs Histidinen (H_6) und einer PEG-Kette (PEG_{12}), welche mit CarboxyFluorescein (CF) fluoreszenzmarkiert wurden, in einer Verdünnung von rund 70 nM in HBG (pH = 7,4) sowie variierendem Anteil an Ethanol mit FCS vermessen (s. Abb. 4.14). Ohne Ethanol-Anteil ergibt sich ein hydrodynamischer Radius

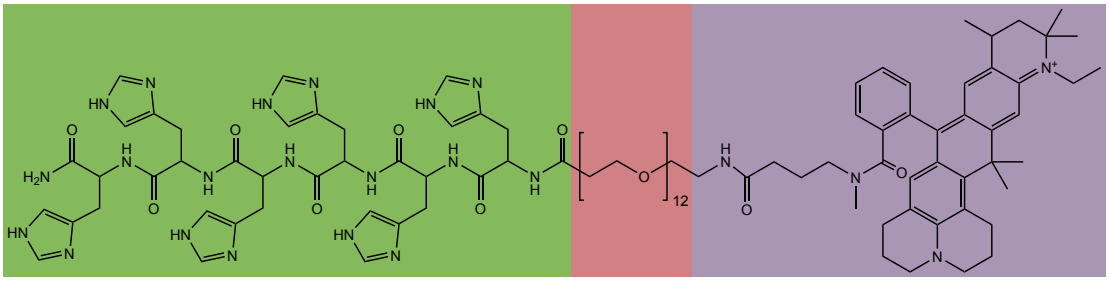

Abbildung 4.15: Chemische Struktur von H_6-PEG_{12}-*ATTO 647 N*. Die sechs Histidine des His-Tag (grün hinterlegt) sind über eine zwölf Monomere lange Polyethylenglycol-Kette (rot hinterlegt) an den Fluoreszenfarbstoff *ATTO 647 N* (violett hinterlegt) gebunden.

von $R_H = 1{,}2\,nm$. Bereits bei einem Anteil von 0,67 Volumenprozent Ethanol bilden sich Agglomerate aus. Zum einen sieht man in der Korrelationskurve eine Verschiebung zu größeren Diffusionszeiten und Auftreten von Agglomerationsartefakten bei Korrelationszeiten $\tau > 1\,ms$. Zum anderen zeigt die Zählrate Spitzen, die sich in ihrer Höhe deutlich von den übrigen Fluktuationen absetzen. Diese Agglomerate treten auch bei höheren Ethanol-Anteilen auf. Um diesen Effekt zu vermeiden wurden die Zr-*fum*-NP für alle weiteren Versuche von Ethanol in HBG überführt. Hierzu wurden die Partikel abzentrifugiert, das überstehende Ethanol entfernt und das verbleibende Pellet im Ultraschallbad mit HGB resuspendiert. Die Überführung hin zu HBG hat den Vorteil, dass die Bindungsstudien somit genauso Ethanol-frei stattfinden wie die späteren Zellexperimente, bei denen ein Ethanol-Anteil zytotoxisch wirken könnte.

Anbindung im Neutralen

Für die folgenden Experimente wurde der Fluoreszenzmarker CF durch *ATTO 647 N* (ATTO-TEC GmbH, Deutschland) ersetzt (s. Abb. 4.15). Ein Grund ist, dass CF wegen seiner fotochemischen Eigenschaften, wie geringe Quantenausbeute oder hohe Anfälligkeit für Bleichen, nicht optimal für FCS geeignet ist. Des Weiteren ist der Spektralbereich von CF (Anregung bei 488 nm, Emission um 510 nm) wegen der Autofluoreszenz von Serum-Bestandteilen ungeeignet für die später gezeigten Messungen in Zellmedium, welches Serum enthält. Zunächst wurden die His-Tags in 200 µl HBG (pH = 7,4) verdünnt und mittels FCS vermessen (s. Abb. 4.16). Es ergab sich ein hydrodynamischer Radius von $R_H = 2\,nm$ für H_6-PEG_{12}-*ATTO 647 N* (His-A647N). Dieser ist im Vergleich zu dem vorher für H_6-PEG_{12}-CF bestimmten etwas größer, was durch den Größenunterschied von *ATTO 647 N* zu CF bedingt ist. Anschließend wurde eine Menge von 30 µg (2 µl bei $15\,mg\,ml^{-1}$) Zr-*fum*-NP zugegeben und gemischt. Die daraufhin gemessene Korrelationsfunktion bestätigt die Anbindung von His-A647N an die NP. Es wurde eine Zweikomponenten-Analyse verwendet, welche berücksichtigt, dass ein Teil der His-Tag-Moleküle ungebunden in Lösung bleibt. Für die NP-His-Tag-Komplexe ergab sich eine scheinbare Diffusionszeit von 3,2 ms, was einem hydrodynamischen Radius von $R_H = 56\,nm$ und einer Diffusionskonstante von $D = 4{,}1\,\mu m^2\,s^{-1}$ entspricht. Hierbei wurde die Korrektur zum Partikel-Größen-Effekt nach Wu *et al.* [52] angewendet (s. Kap. 3.2.4). Es wurde versucht die Kinetik der His-Tag/NP-Bindung zu ermitteln. Es zeigte sich jedoch, dass die Zeit zwischen dem Zugeben und Mischen der NP und dem Beginn der Messung bereits ausreicht, um die Bindung vollständig auszubilden.

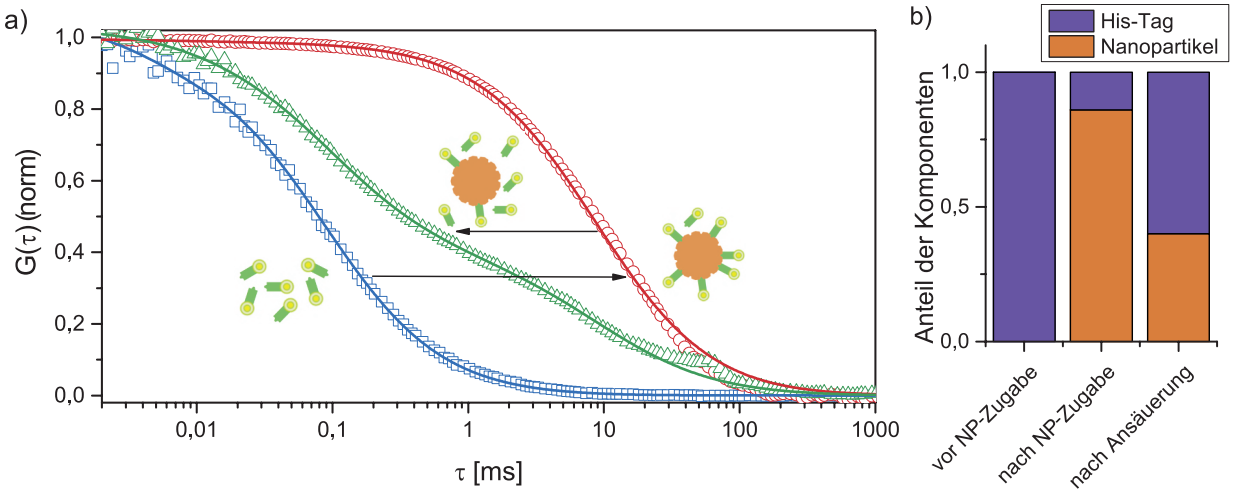

Abbildung 4.16: a) Normierte FCS-Korrelationskurven (Symbole) und Fits (durchgezogene Linien) zeigen die Bindung von His-Tag an Zr-*fum*-NP im Neutralen und die Ablösung im Sauren: His-A647N in HBG bei pH = 7,4 zeigt schnelle Einzel-Molekül-Diffusion (blaue Quadrate). Werden Zr-*fum*-NP dazu gegeben zeigt sich eine deutlich langsamere Diffusion (rote Kreise), welche mit der Anbindung von His-A647N an die NP zu erklären ist. Nach Ansäuerung der Probe zeigt die Korrelationskurve (grüne Dreiecke) sowohl schnelle Einzel-Molekül-Diffusion als auch langsame Partikel-Diffusion. Dies zeigt die (nicht vollständige) Ablösung der His-A647N. b) Der Anteil der beiden Komponenten aus den Fit-Ergebnissen belegt, dass nach der Ansäuerung im Vergleich zum Neutralen ein großer Anteil der His-Tag-Moleküle abgelöst wurden.

Ablösung im Sauren

Während der Endozytose verändert sich der pH-Wert innerhalb des Endosoms vom Neutralen bei pH = 7,0 bis hin zum stark Sauren bei pH = 5,0 [99]. Diese Protonierung kann verwendet werden, um die His-Tag-Moleküle von den Metallionen der MOF-Partikel wieder gezielt abzulösen. Die Ablösung der His-Tags von den Zr-*fum*-NP wurde untersucht, indem eine Probe von His-A647N/Zr-*fum*, die zuvor in HBG bei pH = 7,4 hergestellt wurde, mittels Salzsäure angesäuert wurde. Wie in Abbildung 4.16 zu erkennen, bewirkt die Ansäuerung, dass sich ein großer Teil der His-Tag-Moleküle von der NP-Oberfläche ablöst. Dieser Effekt eignet sich ideal als inhärenter Ablösemechanismus der Funktionseinheiten innerhalb des Endosoms.

Stabilität der Bindung unter Zellkultur-Bedingung

Die Bindung His-Tags/Zr-*fum*-NP muss für Zellexperimente oder eine mögliche Anwendung *in vivo* auch in Anwesenheit von Blutserum stabil sein. Eine vollständige Verdrängung oder Ablösung der His-Tags von der NP-Oberfläche durch Serum-Proteine oder Bestandteile des Serums würde das Funktionalisierungskonzept in seiner Anwendbarkeit stark einschränken. Aus diesem Grund wurden Stabilitätsmessungen durchgeführt. Zum Nachweis der Stabilität der Bindung von His-Tags an MOF-NP unter Zellkultur-Bedingungen, wurden FCS-Messungen in HBG und Dulbecco's Modified Eagle Medium (DMEM) mit jeweils 10 Volumenprozent fötalem Kälberserum (FBS) durchgeführt. In einem ersten Experiment wurden analog zu den bisherigen FCS-Messungen in Puffer, Zr-*fum*-NP zu 200 µl einer Lösung aus 100 nM His-A647N in HBG bei pH = 7,4 gegeben (s. Abb. 4.17). Sowohl vor als auch nach der Zugabe von Serum ist eine langsam diffundierende Spezies nachweisbar. Dies zeigt, dass, nach der Zugabe von FBS, His-Tags-Moleküle in gebundener Form vorliegen und nicht vollständig von der NP-Oberfläche verdrängt werden. Da dieses Vorgehen nicht der Probenpräparation für die Zellexperimente entspricht, wurden in einem zweiten Experiment unverdünnte NP mit His-A647N in HBG funktionalisiert, anschließend in DMEM verdünnt und mittels FCS vermessen (s. Abb. 4.18). Es zeigt sich eine für NP typische, langsame Diffusion.

Um sicher zu stellen, dass die beobachtete langsame Diffusion nicht durch andere Faktoren erklärbar wäre, etwa die hypothetische Agglomeration von His-A647N in Anwesenheit von DMEM, wurde das obige Experiment ohne NP als Negativkontrolle wiederholt. Die Korrelationskurve von His-A647N in DMEM zeigt die, für frei diffundierende Moleküle typische, schnelle Diffusion. Dies schließt andere Faktoren

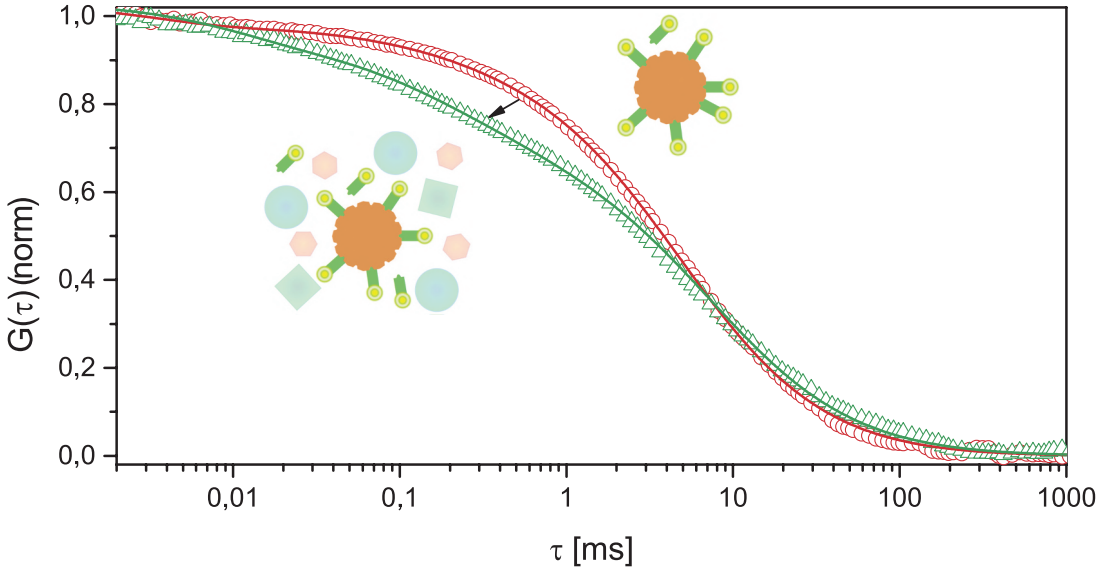

Abbildung 4.17: Normierte Korrelationskurven (Symbole) und Fits (durchgezogene Linien) von H6-A647N/Zr-*fum* in HBG pH = 7,4 vor (rote Kreise) und nach Zugabe von 10 Vol.-% FBS (grüne Dreiecke). Es zeigt sich, dass die Zugabe von FBS dazu führt, dass ein Teil der His-Tag-Moleküle von der NP-Oberfläche verdrängt wird, jedoch weiterhin auch an NP gebundene His-Tags vorhanden sind.

als die Bindung an die NP aus. Somit ist die Stabilität der His-Tag/Zr-*fum*-Bindung in Zellmedium bestätigt.

Nachweis der Multifunktionalität mittels FCCS

Die Bindung von mehr als einem Typ von Funktionseinheiten an einen NP ermöglicht die Gestaltung eines Nanotransporters, der neben dem eigentlichen Wirkstoff (z.B. ein Protein) gleichzeitig noch Targeting-Liganden oder Mittel zur Bildgebung (z.B. grün fluoreszierendes Protein (GFP)) tragen kann. Zum Nachweis der Kolokalisation zweier funktioneller Proteine, die mit His-Tags versehen wurden, wurden FCCS-Messungen durchgeführt. Um die oben erwähnte Autofluoreszenz-Problematik mit Serum im blau-grünen Spektrum zu umgehen, wurden die FCCS-Experimente in HBG-Puffer durchgeführt. Es wurden GFP und fluoreszenzmarkiertes Transferrin (Tf*) als Modellsystem ausgewählt. Aufgrund der nicht-perfekten Überlappung der beiden Laserfoki, ist die Amplitude der Kreuzkorrelationskurve vermindert (s. Kap. 3.2.7). Um festzustellen welche Amplitude der Kreuzkorrelationskurve einer 100%-igen Kodiffusion entspricht, wurde eine Probe eines DNA-Origami FRET-Blocks [102] mittels FCCS vermessen. Da

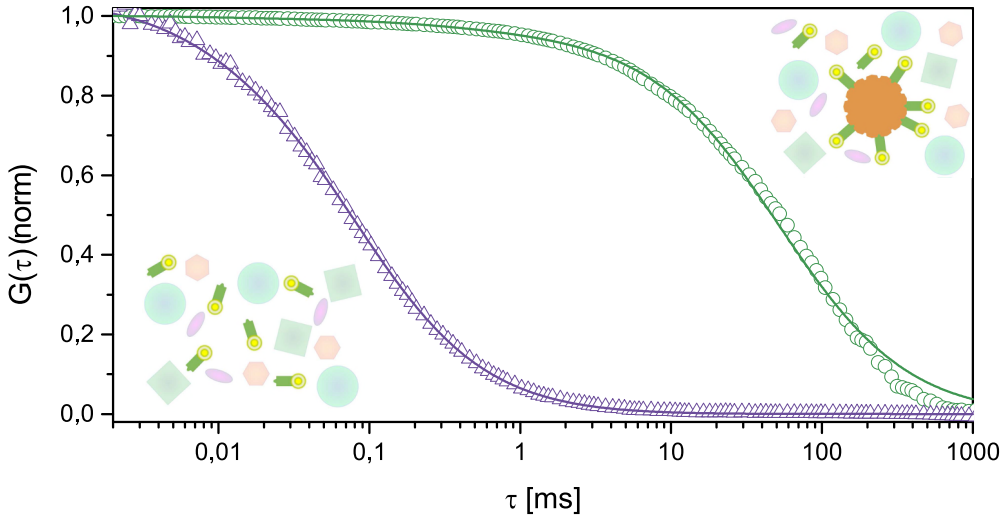

Abbildung 4.18: Die normierte Korrelationskurve von His-A647N in DMEM (violette Dreiecke) zeigt schnelle Einzel-Molekül-Diffusion und stellt sicher, dass His-A647N in Anwesenheit von DMEM nicht verklumpt. Im Vergleich dazu zeigt die Korrelationskurve von zuvor mit His-Tag inkubierten Zr-*fum*-NP eine stark verlangsamte Diffusion (grüne Kreise). Dies bestätigt die Stabilität der His-Tag-Zr-*fum*-Bindung unter Zellkultur-Bedingung.

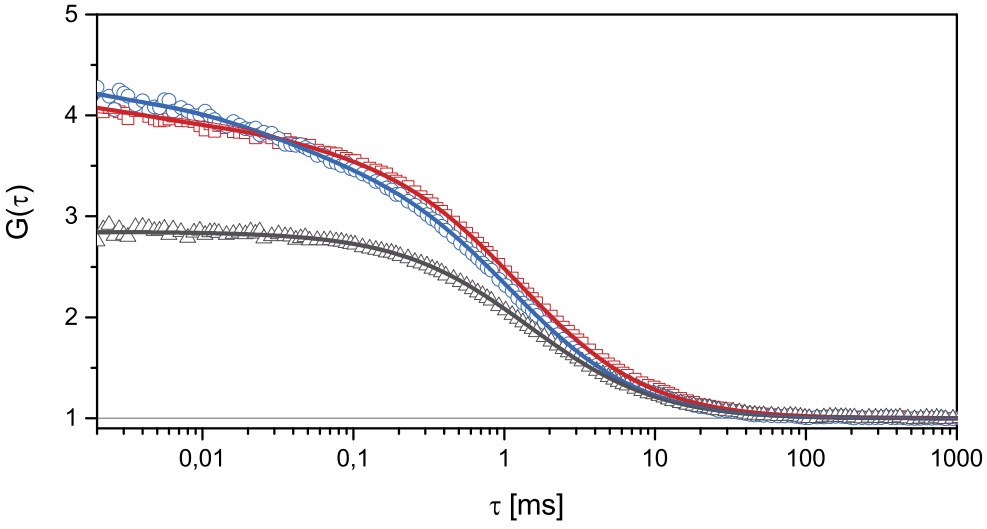

Abbildung 4.19: FCCS-Kalibrierungsmessung mit FRET-Block [102]: Die Amplitude der Kreuzkorrelation beträgt rund 60% der Amplituden der Autokorrelationskurven.

der FRET-Block mit je vier *Alexa Fluor 488*- und *ATTO 647N*-Molekülen fluoreszenzmarkiert ist, kann davon ausgegangen werden, dass jeder FRET-Block in beiden Farbkanälen (blau und rot) kolokalisiert Fluoreszenzlicht emittiert. Die bei dieser FCCS-Messung erlangte relative Kreuzkorrelationsamplitude von 60% der Autokorrelationsamplitude ist das Maximum der erreichbaren Kreuzkorrelation bei vollständiger Kodiffusion. Für den Nachweis der Multifunktionalität wurde zunächst eine Mischung aus beiden

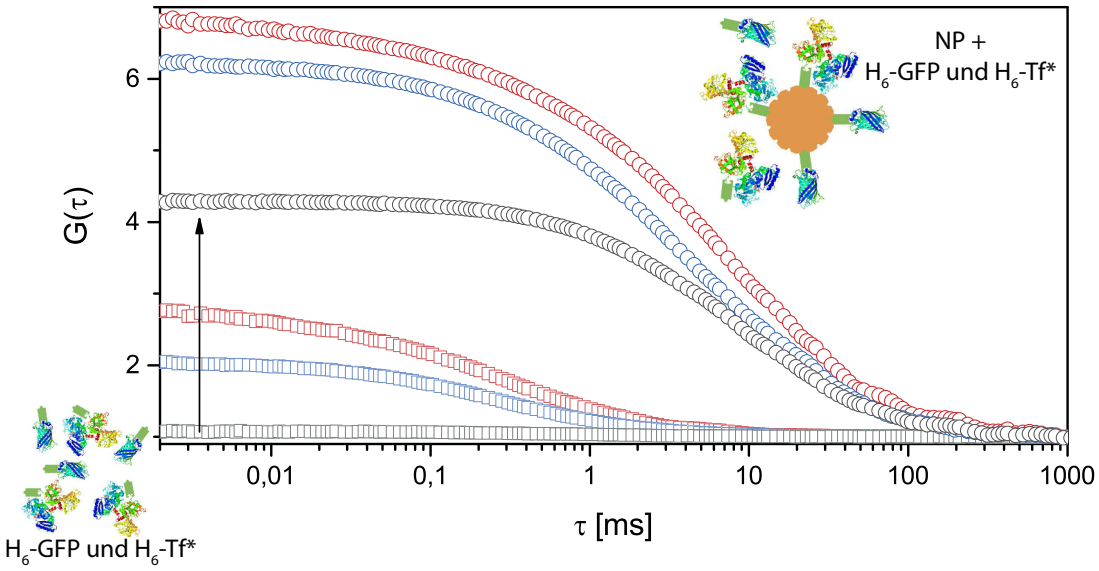

Abbildung 4.20: FCCS-Messungen von H_6-GFP (blau) und H_6-Tf* (rot) in HBG pH = 7,4 vor (Quadrate) und nach Zugabe (Kreise) von NP. Die Kreuzkorrelationskurve (grau) zeigt vor der NP-Zugabe keine Kodiffusion von GFP und Tf. Nach der Zugabe von NP zeigt sich eine hohe Kreuzkorrelation (schwarz), die die simultane Anbindung beider His-Tag-Proteine an die NP nachweist.

His-Tag-Proteinen als Negativkontrolle mittels FCCS vermessen. Anschließend wurden NP hinzugegeben und eine weitere Messung durchgeführt. Abbildung 4.20 zeigt die Autokorrelation sowie die Kreuzkorrelation einer Mischung aus H_6-GFP und H_6-Tf* in HBG (pH = 7,4) vor und nach Zugabe von Zr-*fum*-NP. Die Kreuzkorrelation ohne NP zeigt, wie zu erwarten, eine Amplitude sehr nahe an der Basislinie ($G(\tau) = 1$). Dies bedeutet, dass H_6-GFP und H_6-Tf* keine Bindung untereinander eingehen und somit auch keine Kodiffusion stattfindet. Nach Zugabe von NP zeigt sich eine im Vergleich zu den Amplituden der Autokorrelationen hohe Kreuzkorrelation von etwa 60% der Amplitude der Autokorrelationen. Dies ist eine Folge der Kodiffusion von H_6-GFP und H_6-Tf*, welche auf der Oberfläche der Zr-*fum*-NP angebunden sind und deutet darauf

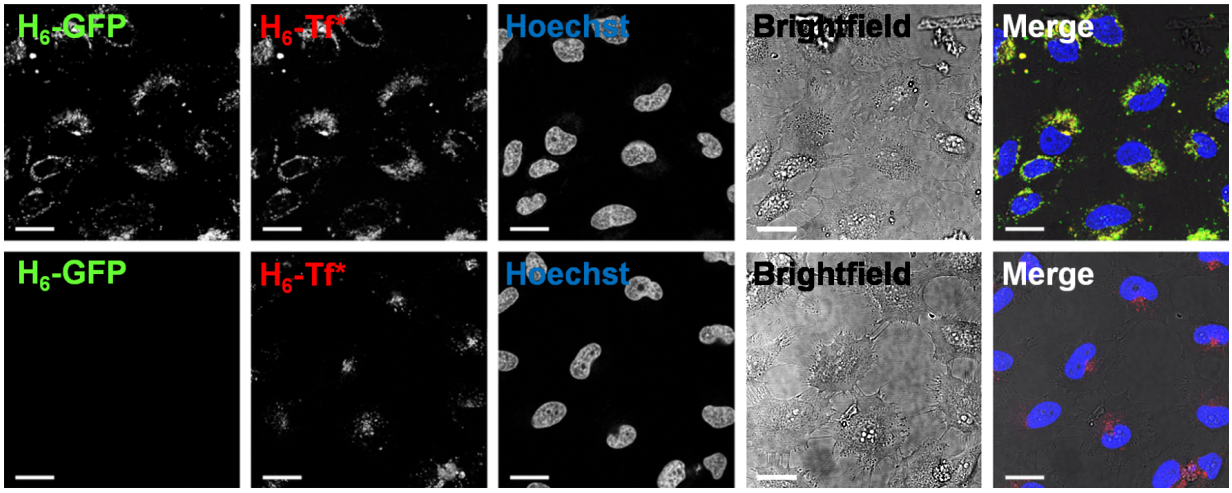

Abbildung 4.21: Konfokalmikroskopie von HeLa-Zellen. Von links nach rechts: Fluoreszenzbild von GFP, von Tf*, des Zellkerns durch Hoechst-Markierung, Hellfeldaufnahme und Überlagerung der vorherigen Bilder. Die Aufnahme der beiden Proteine in HeLa-Zellen ist im Falle der an NP gebundenen Proteine (oben) gegenüber der Negativkontrolle ohne NP (unten) stark erhöht. Die beobachtete Transferrinaufnahme in der Negativkontrolle ist durch das Vorhandensein von Transferrin-Rezeptoren auf den HeLa-Zellen zu erklären. Maßstab: 25 µm.

hin, dass an jeden NP beide Proteine angebunden haben und somit eine erfolgreiche, nahezu 100%-ige Multifunktionalisierung erzielt wurde.

Zellexperimente

Um einen Schritt weiter in Richtung biomedizinischer Anwendung zu gehen, wurde die Aufnahme von funktionalisierten Zr-*fum*-NP in Zellen untersucht. Als Modellsystem wurden HeLa-Zellen gewählt, da sie ein etabliertes System von menschlichen Krebszellen darstellen. Zum Nachweis der Aufnahme der H_6-GFP und H_6-Tf* multifunktionalisierten NP in Zellen wurden Konfokalmikroskopie- und Hellfeldaufnahmen der Zellen angefertigt (s. Abb. 4.21). Die Zellen wurden 24 Stunden inkubiert, anschließend wurden die überständigen NP weggewaschen. Hellfeldaufnahmen zeigen die Begrenzung der Zellen. Die Zellkerne wurden mit Hoechst-Farbstoff angefärbt. Aus der Kombination der Fluoreszenz der Proteine, der Zell- und der Zellkernbegrenzung lässt sich eine detaillierte Lokalisation der NP bzw. der fluoreszierenden Proteine vornehmen. Wie in Abbildung 4.21 erkennbar, ist sowohl die Fluoreszenz von GFP als auch von Tf* innerhalb der Zellen vorhanden. Beide Fluoreszenzen sind räumlich korreliert, was den Schluss zulässt, dass

die NP mitsamt der daran hängenden Proteine aufgenommen werden. Eine Aufnahme in den Zellkern wird nur in geringem Maße beobachtet. Um auszuschließen, dass die beobachtete Aufnahme unspezifisch ist, wurden die Zellen bei einer Negativkontrolle mit H_6-GFP und H_6-Tf* inkubiert. Es zeigte sich, dass das ungebundene H_6-GFP nicht aufgenommen wird. Die beobachtete geringe Aufnahme von freiem H_6-Tf* kann damit erklärt werden, dass HeLa-Zellen Transferrin-Rezeptoren exprimieren [103]. Trotz dieser nicht-NP-induzierten Aufnahme von Transferrin wurde mittels Durchflusszytometrie eine fünffach höhere Inkorporation mit Zr-*fum* nachgewiesen (s. Anhang B.6). Um das Potential von Zr-*fum*-NP als Trägersystem weiter auszuloten, wurde der Transport von vier His-Tag-modifizierten, apoptotischen, aber nicht membrangängigen Peptiden in den Zellkern mit Hilfe eines Zellviabilitätstests (MTT-Tests) untersucht. Es zeigte sich, dass rund 60% der Zellen durch die H_6-Peptid/Zr-*fum*-Kombination sterben. Die Negativkontrolle ohne NP wies dagegen kaum Zellsterblichkeit auf. Die alleinige Zugabe von NP löste ebenfalls keine erhöhte Zellsterblichkeit aus. Diese Ergebnisse belegen, dass einige der apoptotischen Peptide aus den Endosomen entkommen konnten und ihre induzierten biologischen Wirkungen im Zytosol entfalten konnten.

Fazit

Es wurde ein neuartiges Funktionalisierungskonzept für MOF-NP untersucht, das ohne vorhergehende Modifikation der NP auskommt und auf einer einfachen Chemie basiert. Die Funktionalisierung ist im Neutralen stabil ist und lässt sich durch Ansäuerung wieder lösen. Durch diesen Umstand ist dieses neue Funktionalisierungskonzept als Nanotransporter-System prädestiniert für die Zellaufnahme, da sich bei der Endozytose der pH-Wert innerhalb des Endosoms vom ursprünglich Neutralen schnell auf einen pH-Wert von ca. 6,0 absenkt und anschließend bis hin zu $pH = 5{,}0$ fällt. Darüber hinaus hat sich die Bindung auch unter Zellkultur-Bedingungen als stabil erwiesen. Es konnte gezeigt werden, dass sich verschiedene Funktionseinheiten auf einer NP-Oberfläche anheften lassen. Das ermöglicht es das System gleichzeitig mit Wirkstoffen und Targeting-Liganden zu verwenden. Die Zellexperimente zeigten, dass das Transportsystem in die Zellen funktioniert. Auch wenn ein Großteil der Wirkstoffe innerhalb der Endosome eingeschlossen blieb, konnten einige der Funktionsmoleküle bis in den Zellkern gelangen und dort ihre Wirkung entfalten.

4.3 Postsynthetische Beladung von MOF-NP und anschließende Freisetzung [5]

Im folgenden Kapitel, welches auf der Originalpublikation P7 (s. Anhang B.7) basiert, wird die Beladung von MOF-NP mit Fluorescein als Gastmolekül sowie die anschließende Freisetzung der Fluorescein-Moleküle untersucht.

Das Konzept, MOF-NP als Nanotransporter im medizinischen Bereich einzusetzen, ist Gegenstand aktueller Forschung [20]. So wurde die Biokompatibilität einiger MOF-NP gezeigt [105, 106]. MOF-NP haben eine hohe Beladungskapazität [42, 107, 108] und sind funktionalisierbar (s. Kap. 4.2). Die Fähigkeit von mesoporösen MOF-NP Wirkstoffe aufzunehmen und anschließend im Körper wieder gezielt abzugeben ist bislang wenig untersucht. Es ist nachvollziehbar, dass Porengröße und Material die Beladung und Freisetzung von Gastmolekülen mitbestimmen. So ist z.B. die Diffusion in porösem Material stark verlangsamt (Faktor $\approx 10^{-4}$) [109]. Dies beeinflusst die Kinetik der Beladung und Freisetzung der Gastmoleküle. Außerdem spielt die physiochemische Affinität zwischen dem Gastmolekül und dem MOF-Material eine Rolle [110]. Darüber hinaus ist die Affinität in vielen Fällen aufgrund der möglichen elektrischen Ladung der Moleküle und der MOF-Oberfläche vom pH-Wert des umgebenden Mediums beeinflusst.

Um die Prozesse der Aufnahme und der Freisetzung von Gastmolekülen in MOF-NP zu untersuchen wurden MIL-100(Fe)-NP und MIL-101(Cr)-NP gewählt. Sowohl MIL-100(Fe)- als auch MIL-101(Cr)-NP bieten sich durch ihre großen Porendurchmesser ($25-29$ Å und $29-34$ Å) und ihre großen Porenöffnungen ($5-9$ Å und $12-17$ Å) als Modellsysteme zur Untersuchung der Wirkstoffaufnahme und -freisetzung an [39, 40, 42]. Für diese Studie wurde das Natriumsalz des Fluoresceins (Uranin) als Gastmolekül gewählt, da es sich leicht mittels Absorption oder Fluoreszenz nachweisen und quantifizieren lässt. Gleichzeitig ist seine Größe mit der viel genutzter Chemotherapeutika vergleichbar, z.B. Doxorubicin, Mitotane oder Cis-Platin.

Quantitative Gleichgewichtsmessungen der Beladung und Freisetzung von MOF-NP

Zur Bestimmung der Affinität (bzw. deren Kehrwerts, der Dissoziationskonstante) der Sorptionsreaktion von Fluorescein und MOF-NP wurden quantitative UV-Vis-Absorp-

[5] Dieses Kapitel behandelt die Erkenntnisse, die in [104] publiziert wurden (s. Anhang B.7).

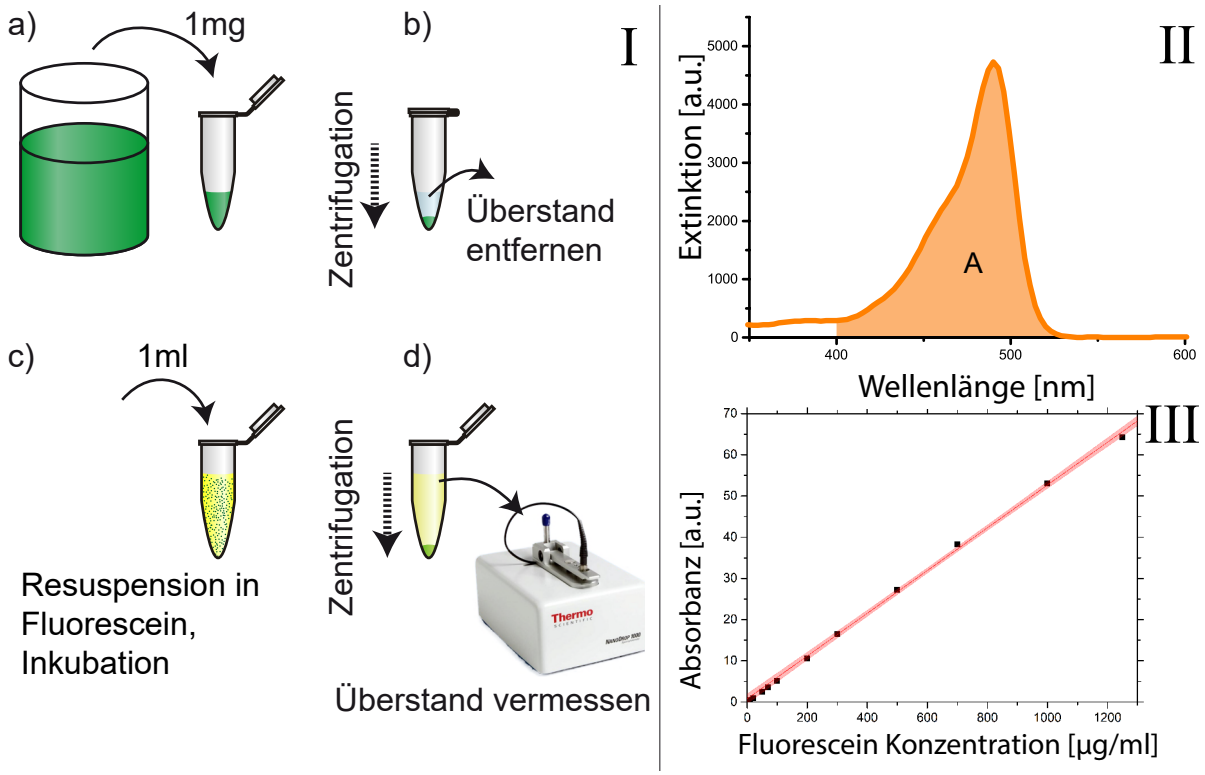

Abbildung 4.22: I) Skizzierung der Messmethode zur Bestimmung der Beladungsmenge: a) Ein Volumen, welches 1 mg NP beinhaltet wird in ein Mikroreaktionsgefäß gefüllt. b) Durch Zentrifugation werden die NP vom Ethanol getrennt, der Überstand wird entfernt.
c) Die NP werden anschließend in einer Fluorescein-Lösung resuspendiert und inkubiert.
d) Nach der Inkubation werden die NP wiederum durch Zentrifugation von der Inkubationslösung getrennt. Die Konzentration des im Überstand befindlichen Fluoresceins wird anschließend mittels Absorptionsspektroskopie (NanoDrop) bestimmt.
II) Zur Bestimmung der Fluorescein-Konzentration wurde die Absorbanz im Bereich von 400 bis 550 nm integriert.
III) Die Absorbanz von Fluorescein bekannter Konzentration in Wasser wurde gemessen, um eine Eichgerade zu erlangen.

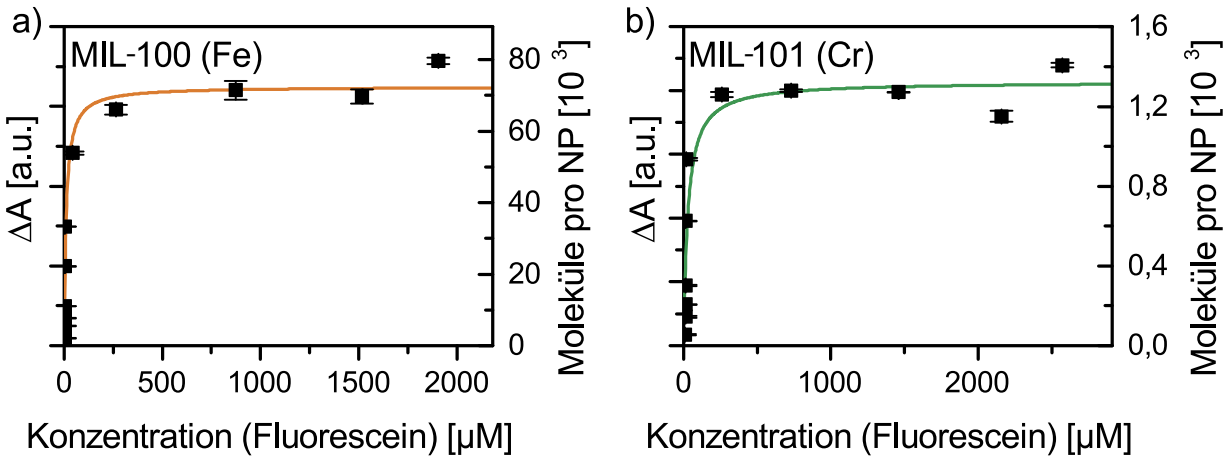

Abbildung 4.23: Die Differenz der Absorbanz zwischen Inkubationslösung und Überstand von MIL-100(Fe)- a) und MIL-101(Cr)-NP b) folgt einer Langmuirschen Bindungskurve (durchgezogene Linie). Diese gibt neben den Dissoziationskonstanten ($K_D^{MIL100} = 11\,\mu M$ und $K_D^{MIL101} = 36\,\mu M$) auch die maximale Beladung der NP mit Fluorescein wieder ($P_{max}^{MIL100} = 0{,}65\,mg$ und $P_{max}^{MIL101} = 0{,}41\,mg$).

tionsmessungen durchgeführt[6] (wie in Kap. 3.3.2 beschrieben). Wie in Abbildung 4.22 dargestellt, wurden hierzu 1 mg NP durch Zentrifugation in einem Mikroreaktionsgefäß (45 min, 20 238 RZB) vom Ethanol, in dem die NP gelagert werden, getrennt. Anschließend wurden die NP in einer Fluorescein-Lösung resuspensiert. Hierzu wurden Fluorescein-Konzentrationen zwischen 20 und 1250 µg/ml verwendet. Die NP wurden über 96 Stunden in der Fluorescein-Lösung inkubiert. Anschließend wurden die NP wieder durch Zentrifugation von der Inkubationslösung getrennt. Die verbleibende Fluorescein-Konzentration im Überstand wurde anschließend mittels UV-Vis Absorption bestimmt. Die Differenz der Absorbanz zwischen der Fluorescein-Lösung vor und nach der Inkubation wurden in Abbildung 4.23 in Abhängigkeit der Fluorescein-Konzentration des Überstands c aufgetragen. Mit Hilfe der Eichgerade (s. Kap. 3.3.2) lässt sich die aufgenommene Menge an Fluorescein pro NP-Menge $P(c)$ über die Differenz der Absorbanz bestimmen. Diese Daten folgen einer Langmuir-Sorptions-Isotherme der Form

$$P(c) = P_{max}\frac{1}{1+\frac{K_D}{c}}, \tag{4.4}$$

[6] Alle in diesem Kapitel gezeigten Absorptions- und Fluoreszenzmessungen wurden dreifach wiederholt.

wobei $P_{\max}$ die Sättigungsmenge an aufgenommenem Fluorescein pro Milligramm NP darstellt und K_{D} als Dissoziationskonstante zu interpretieren ist. Mittels der Regression wurden die Dissoziationskonstanten zu $K_D^{MIL100} = 11\,\mu\mathrm{M}$ im Falle der MIL-100(Fe)-NP und $K_D^{MIL101} = 11\,\mu\mathrm{M}$ für die MIL-101(Cr)-NP bestimmt. Im Vergleich zur Dissoziationskonstante von MIL-100(Fe)-NP mit Doxorubicin als Gastmolekül mit $K_D^{MIL100-DOX} = 91\,\mu\mathrm{M}$ [108] ist die Dissoziationskonstante mit Fluorescein als Gastmolekül rund eine Größenordnung kleiner. Dies deutet auf eine starke Wechselwirkung zwischen Fluorescein und der MIL-100(Fe)-Struktur hin. Die Sättigungsmenge an aufgenommenem Fluorescein pro Milligramm NP-Menge ergab sich zu $P_{\max}^{MIL100} = 0{,}65\,\mathrm{mg}$ im Falle der MIL-100(Fe)-NP und $P_{\max}^{MIL101} = 0{,}41\,\mathrm{mg}$ für die MIL-101(Cr)-NP. Mithilfe der in Kapitel 4.1.2 erlangten mittleren Größen und der Dichte der NP lässt sich die Masse m_{NP} eines NP abschätzen. Damit ist eine grobe Bestimmung der NP-Anzahl N in einer MOF-Probe der Masse $m = 1\,\mathrm{mg}$ möglich, was den Wert der Sättigungsmenge anschaulicher macht:

$$N = \frac{m}{m_{\mathrm{NP}}} \tag{4.5}$$

Die Masse eines in erster Näherung kugelförmigen NP berechnet sich aus dessen Dichte ρ und Kugelvolumen $V = \frac{4}{3}\pi r^3$:

$$m_{\mathrm{NP}} = \rho \cdot \frac{4}{3}\pi r^3 \tag{4.6}$$

Die aus kristallographischen Daten berechnete Massendichte beträgt für MIL-100(Fe) $\rho_{\mathrm{MIL100}} = 0{,}98\,\mathrm{g\,ml^{-1}}$ [39], der mittlere Teilchenradius der NP ist $r_{\mathrm{MIL100}} = 26{,}5\,\mathrm{nm}$. Damit ist die NP-Anzahl in 1 mg MOF-Probe

$$N_{\mathrm{MIL100}}^{\mathrm{in\,1\,mg}} = \frac{3 \cdot m}{4\pi r_{\mathrm{MIL100}}^3 \cdot \rho_{\mathrm{MIL100}}} = \frac{3 \cdot 1\,\mathrm{mg}}{4\pi \cdot (26{,}5\,\mathrm{nm})^3 \cdot 0{,}98\,\mathrm{g\,ml^{-1}}} = 1{,}3 \cdot 10^{13}. \tag{4.7}$$

Selbiges lässt sich auch für MIL-101(Cr) abschätzen

$$N_{\mathrm{MIL101}}^{\mathrm{in\,1\,mg}} = \frac{3 \cdot m}{4\pi r_{\mathrm{MIL101}}^3 \cdot \rho_{\mathrm{MIL101}}} = \frac{3 \cdot 1\,\mathrm{mg}}{4\pi \cdot (9{,}45\,\mathrm{nm})^3 \cdot 0{,}62\,\mathrm{g\,ml^{-1}}} = 5{,}3 \cdot 10^{14}, \tag{4.8}$$

wobei die Dichte $\rho_{\mathrm{MIL101}} = 0{,}62\,\mathrm{g\,ml^{-1}}$ [40] und der mittlere Teilchenradius der NP $r_{\mathrm{MIL101}} = 26{,}5\,\mathrm{nm}$ verwendet wurden. So hat sich für MIL-100(Fe) ein Wert von $P_{\max}^{\mathrm{MIL100}} = 1{,}6\,\mu\mathrm{mol}$ ergeben. Für MIL-101(Cr) wurde $P_{\max}^{\mathrm{MIL101}} = 1{,}0\,\mu\mathrm{mol}$ ermittelt. Dies entspricht

einer relativen Masse von 39% und 29% des Fluoresceins am beladenen NP. Im Vergleich zur Beladungsmenge anderer Gastmoleküle in die MIL-100(Fe)-NP ergibt sich für Fluorescein ein Wert in der gleichen Größenordnung [42, 107, 108, 111]. Bei einer ähnlichen Größe der verwendeten Gastmoleküle lässt das auf den gleichen zugrunde liegenden Sorptionsmechanismus schließen.

N_2-Absorptionsmessungen zur Bestimmung der internen Oberfläche

Um zu ergründen wie dicht sich die Gastmoleküle innerhalb der Poren einlagern, wurde die interne Oberfläche der NP bestimmt. Hierzu wurden Stickstoffgas-Absorptionsmessung an getrockneten MOF-NP durchgeführt. Die anschließende BET-Analyse der Sorptionskurven (s. Abb. 4.24) ergaben eine interne Oberfläche der MIL-100(Fe)-NP von $S^{\mathrm{BET}}_{\mathrm{MIL100}} = 2004\,\mathrm{m^2\,g^{-1}}$ und für die MIL-101(Cr)-NP $S^{\mathrm{BET}}_{\mathrm{MIL101}} = 3205\,\mathrm{m^2\,g^{-1}}$.

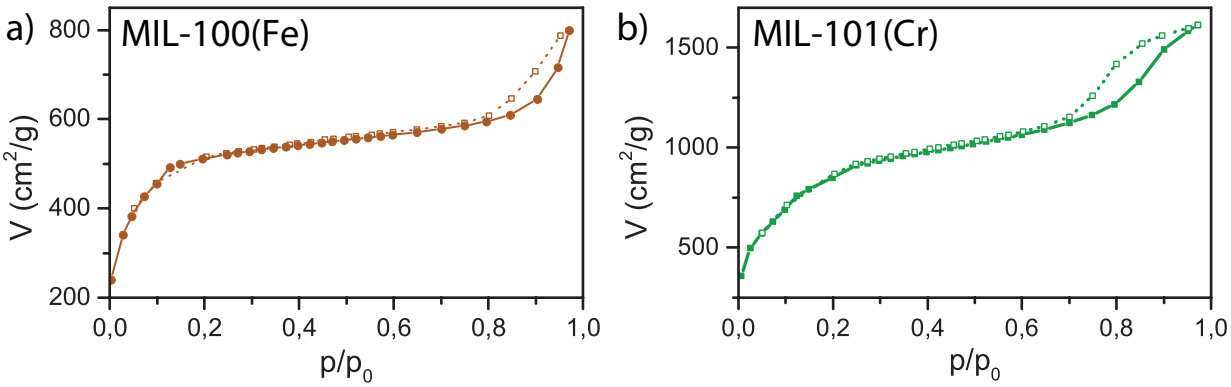

Abbildung 4.24: Stickstoffgas-Absorptions- (gefüllte Symbole) und Desorptionsmessungen (ungefüllte Symbole) von MIL-100(Fe) a) und MIL-101(Cr) b) ergeben eine Oberfläche von $S^{\mathrm{BET}}_{\mathrm{MIL100}} = 2004\,\mathrm{m^2\,g^{-1}}$ für MIL-100(Fe)-NP und $S^{\mathrm{BET}}_{\mathrm{MIL101}} = 3205\,\mathrm{m^2\,g^{-1}}$ für MIL-101(Cr)-NP.

Vergleich der internen Fläche mit der Menge an Beladung

Die interne Fläche A in den NP-Poren, die einem Fluorescein-Molekül zur Verfügung steht lässt sich aus der BET-Gesamtfläche eines Milligramms MOF $S_{\mathrm{BET}} \cdot 1\,\mathrm{mg}$ und der Fluorescein-Sättigungsmenge in einem Milligramm MOF P_{max} abschätzen durch

$$A = \frac{S_{\mathrm{BET}} \cdot 1\,\mathrm{mg}}{P_{\mathrm{max}} \cdot N_A}. \tag{4.9}$$

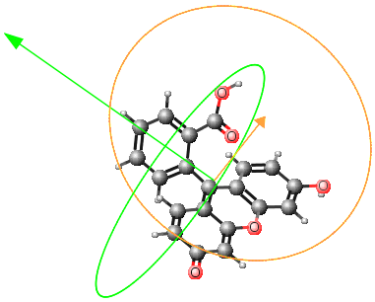

Abbildung 4.25: Chemische Struktur von Fluorescein mit Projektionskreisen (orange und grün) aus MarvinSketch. Die Pfeile zeigen die jeweilige Flächennormale an. Der Projektionsradius ist in beiden Projektonsflächen $r = 0{,}6\,\mathrm{nm}$.

Die Avogradro Zahl N_A wird benötigt, um die molare Angabe der Sättigungsmenge in eine Molekülanzahl umzurechnen. Somit ergibt sich für MIL-100(Fe)

$$A^{\mathrm{MIL100}} = 2004\,\mathrm{m^2\,g^{-1}} \cdot 1\,\mathrm{mg}\left(1{,}6\,\mu\mathrm{mol} \cdot 6{,}022\,14 \times 10^{23}\,\mathrm{mol^{-1}}\right)^{-1} = 2{,}1\,\mathrm{nm^2} \quad (4.10)$$

und für MIL-101(Cr)

$$A^{\mathrm{MIL101}} = 3205\,\mathrm{m^2\,g^{-1}} \cdot 1\,\mathrm{mg}\left(1{,}0\,\mu\mathrm{mol} \cdot 6{,}022\,14 \times 10^{23}\,\mathrm{mol^{-1}}\right)^{-1} = 5{,}3\,\mathrm{nm^2}. \quad (4.11)$$

Der Projektionsradius von Fluorescein, welcher anhand der chemischer Strukturformel bestimmt wurde (s. Abb. 4.25) beträgt $r_{\mathrm{Fluorescein}} = 0{,}6\,\mathrm{nm}$. Der aus FCS-Messungen ermittelte hydrodynamischen Radius von Fluorescein liegt ebenfalls bei $R_{\mathrm{H}} = 0{,}6\,\mathrm{nm}$ (nicht gezeigt). Somit liegt eine Projektionsfläche des Fluoresceins von rund $1\,\mathrm{nm^2}$ vor. Die Fläche, die einem Fluorescein-Molekül innerhalb der MOF-NP zur Verfügung steht, ist damit nicht viel größer als die Fläche, die das Molekül selbst besetzt. Dies lässt darauf schließen, dass die Fluorescein-Moleküle innerhalb der NP dicht gepackt vorliegen und die maximale Beladungsmenge bereits sehr nahe am theoretisch (aus Sicht des zur Verfügung stehenden Platzes) Möglichen ist. Eine ebenso wichtige Frage wie die der Beladungsmenge ist die, ob die Gastmoleküle auch wieder aus den MOF-NP herauskommen. Da die Freisetzung der Gastmoleküle später in der medizinischen Anwendung stets unter physiologischen Bedingungen stattfindet, ist die Untersuchung der Freisetzung auch unter solchen Bedingungen von besonderem Interesse. Aus diesem Grund wurde die Freisetzung des in die MOF-NP geladenen Fluoresceins in Puffer (HBG) als Umgebungsmedium bei den pH-Werten 7,4; 6,2 und 5,1 untersucht. Diese pH-Werte

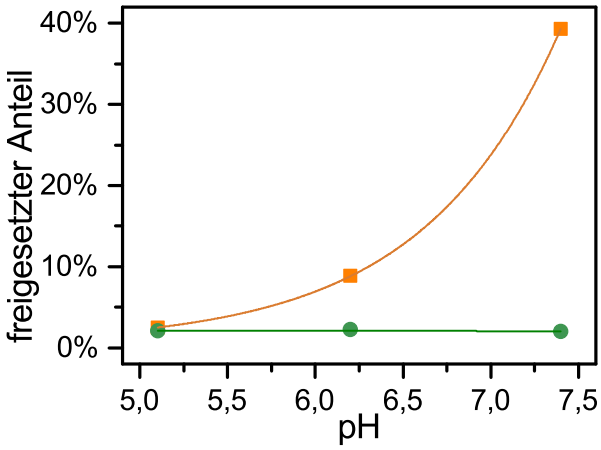

Abbildung 4.26: Anteil der freigesetzten Menge Fluorescein im Vergleich zur Beladungsmenge von MIL-100(Fe)-NP (orange Quadrate) und MIL-101(Cr)-NP (grüne Kreise). Die Schwankungen innerhalb der drei durchgeführten Messwiederholungen sind kleiner als die Symbolgröße. Die Verbindungslinien dienen der optischen Führung.

simulieren die physiologischen Bedingungen in Blut (pH = 7,4), im Endosom kurz nach der Vesikelabschnürung (pH = 6,2) und im Endosom lange nach der Vesikelabschnürung (pH = 5,1). Die, wie oben beschrieben, zuvor beladenen Partikel wurden in Puffer des jeweiligen pH-Wertes resuspendiert. Nach einer Freisetzungszeit von 90 Minuten wurden die NP durch Zentrifugation entfernt. Mittels Extinktionsmessungen wurde anschließend die freigesetzte Fluorescein-Menge bestimmt (wie oben beschrieben) und mit der eingeladenen Fluorescein-Menge ins Verhältnis gesetzt (s. Abb. 4.26). Hierbei wurde durch Eichgeraden in Puffer mit entsprechenden pH-Werten berücksichtigt, dass Fluorescein in den verschieden pH-Werten unterschiedliche Extinktionseigenschaften ausweist. Es zeigt sich, dass die MIL-100(Fe)-NP eine starke pH-Abhängigkeit der Fluorescein-Freisetzung besitzen. So ist der Anteil des freigesetzten Fluoresceins bei pH = 5,0 weniger als 3%. Bei steigendem pH-Wert steigt auch der freigesetzte Anteil des Fluoresceins überproportional (9% bei pH = 6,2 und 39% bei pH = 7,4). Die MIL-101(Cr)-NP hingegen zeigen kaum Freisetzung des Fluoresceins. Der Anteil des freigesetzten Fluoresceins ist bei allen drei pH-Werten unter 3%. Das Freisetzungsverhalten der MIL-100(Fe)-NP weist deutlich auf die Erfordernis hin, die NP vor der Applikation *in vivo* zu verkapseln und so ein vorzeitiges Herausströmen der Gastmoleküle zu verhindern. Eine Verkapselungsstrategie für MOF-NP wurde in Kapitel 4.2.1 vorgestellt. Es wurde vermutet, dass sich diese pH-Abhängigkeit der Fluorescein-Freisetzung aus den MIL-100(Fe)-NP bei *in vitro* Zellexperimenten ebenfalls beobachten lässt. Die Idee

	MIL-100(Fe)	MIL-101(Cr)
K_D [µM]	11	36
P_{max} pro mg NP [mg]	0,65	0,41
N pro mg NP	$1{,}3 \cdot 10^{13}$	$5{,}3 \cdot 10^{14}$
S_{BET} [$m^2\,g^{-1}$]	2004	3205
A pro Fluoresceinmolekül [nm^2]	2,1	5,3

Tabelle 4.3: Zusammenstellung der mittels Extinktionsspektroskopie- und N_2-Absorptionsmessungen ermittelten Parameter von MIL-100(Fe)- und MIL-101(Cr)-NP mit dem Gastmolekül Fluorescein.

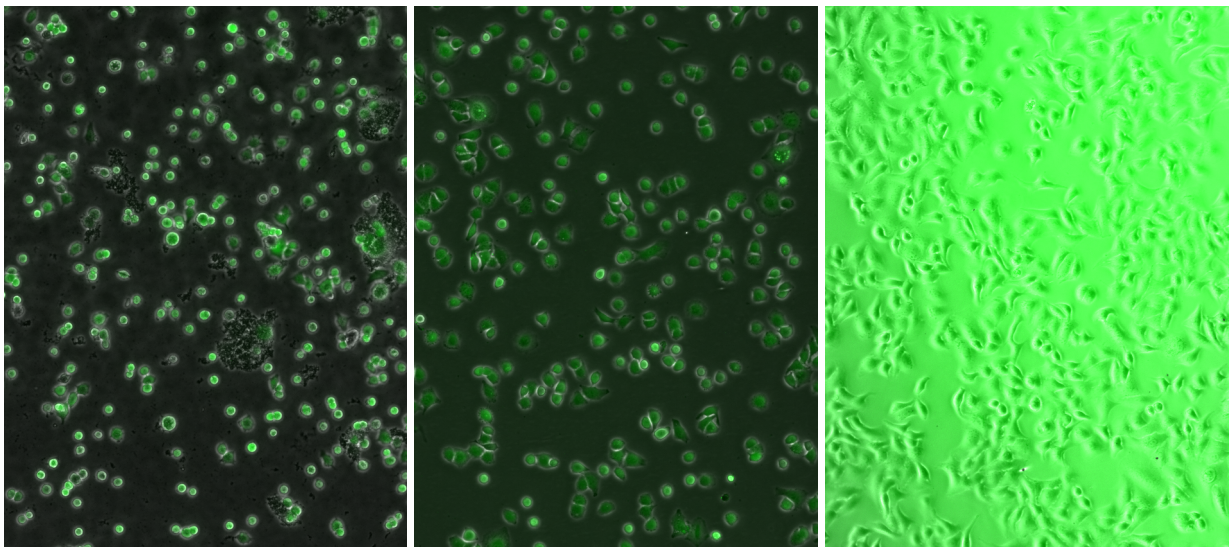

Abbildung 4.27: Überlagerung von Hellfeld- und Fluoreszenzbild von A549-Zellen. Links: Nach Zugabe von mit Fluorescein-befüllten MIL-100(Fe) NP in Puffer bei pH = 5,0. Mitte: Nach Zugabe von Fluorescein-Lösung bei pH = 5,0. Rechts: Nach Zugabe von Fluorescein-Lösung bei pH = 7,4.

bestand darin, dass die MIL-100(Fe)-NP im sauren Millieu auf Zellen gegeben werden, sodass Fluorescein-Freisetzung zunächst behindert wird. Hierbei wurde ausgenutzt, dass MIL-100(Fe) eine ausgeprägte Fluoreszenzlöschung (Quenching) von Fluorophoren in dessen Nähe zeigt und Fluorescein in den NP-Poren nicht fluoresziert. Bei der anschließenden Aufnahme der NP in die Zellen, werden die NP einem ausreichend hohen pH-Wert ausgesetzt, sodass das Fluorescein innerhalb der Zelle freigesetzt wird und anschließend dadurch fluoresziert. Es sollten sich demnach nach kurzer Zeit fluoreszierende Zellen vor einem dunklen Hintergrund nachweisen lassen. Hierzu wurden menschliche Epithel-Krebszellen aus der Lunge (A549 [112]) mit Fluorescein-befüllten NP in 500 µl Puffer bei pH = 5,0 versetzt. Wie in Abbildung 4.27 zu erkennen, war unmittelbar nach der Zugabe Fluoreszenz detektierbar, die mit den im Hellfeldbild aufgenommenen Zellen kolokalisiert war. Dies ließ zunächst den Schluss zu, dass eine Zellaufnahme mit anschließender Freisetzung des Fluoresceins erfolgt ist. Um festzustellen, ob dieser Schluss korrekt ist wurde in einem weiteren Zellexperiment eine Lösung aus Fluorescein in Puffer bei pH = 5,0 auf die Zellen gegeben. Da sich auch in dieser Negativkontrolle eine mit den Zellen kolokalisierte Fluoreszenz zeigte (s. Abb. 4.27), scheint die obige Schlussfolgerung nicht zu zutreffen. In einem dritten Zellexperiment, bei dem eine Lösung aus Fluorescein in Puffer bei pH = 7,4 auf die Zellen gegeben wurde, sollte geprüft werden, ob die zuvor gefundene Kolokalisation der Fluoreszenz mit den Zellen durch eine Aufnahme von Fluorescein-Molekülen in die Zellen zu erklären ist. Eine Aufnahme in die Zellen hätte auch in diesem Experiment eine verstärkte Fluoreszenz am Ort der Zellen zeigen müssen, die sich mit der Zeit verstärkt. Dies wurde nicht beobachtet. Die gleichmäßig über die Probe auftretende Fluoreszenz deutet darauf hin, dass die zuvor beobachteten Ergebnisse lediglich der erwähnten pH-Abhängigkeit der Fluoreszenzeigenschaften von Fluorescein und einer lokalen pH-Änderung an der Oberfläche der Zellen geschuldet sind.

Freisetzungs- und Beladungs-Kinetik von MOF-NP

Die gefundenen Ergebnisse der Freisetzung und Beladung erfordern eine genauere Betrachtung der Kinetik im Bereich der physiologisch relevanten pH-Werte, um zu verstehen welche Prozesse die Freisetzung und Beladung beeinflussen. Zu diesem Zweck wurden zeitaufgelöste Fluoreszenzintensitätsmessungen der Freisetzung sowie der Beladung durchgeführt. Auch hier wurde die ausgeprägte Fluoreszenzlöschung von MIL-100(Fe) ausgenutzt. Da MIL-101(Cr) dieses Quenching nicht so ausgeprägt zeigt,

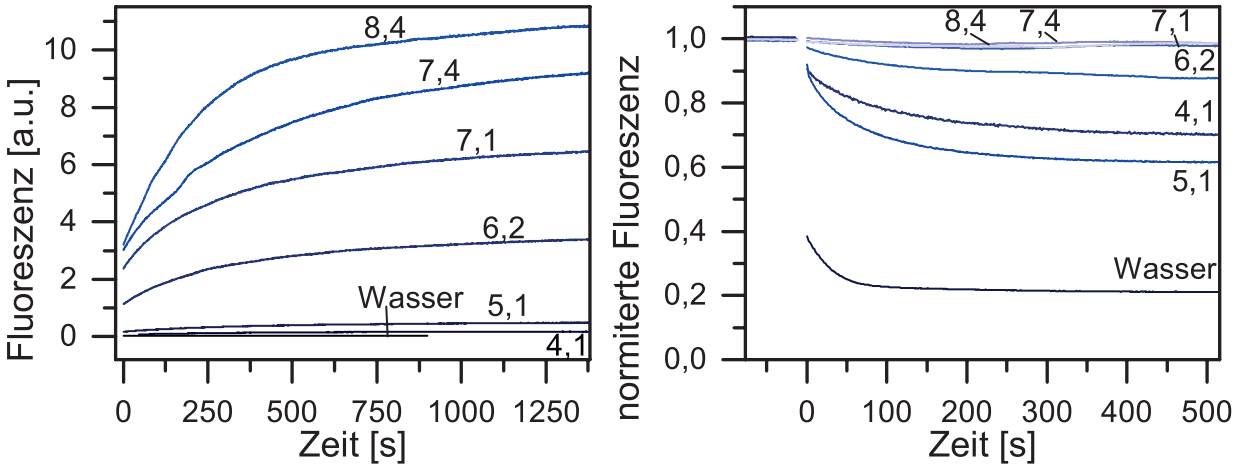

Abbildung 4.28: Fluorescein-Quenching im zeitlichen Verlauf bei der Freisetzung aus MIL-100(Fe)-NP (links) und der Aufnahme von Fluorescein in MIL-100(Fe)-NP (rechts). Die Aufnahmerate sowie die Aufnahmemenge ist in Wasser am größten und in HBG bei pH = 4,1 bis 6,2 etwas geringer (s. Tab. 4.4). Bei pH $\geq$ 7,1 ist keine Aufnahme mehr feststellbar. Bei der Freisetzung ergibt sich ein umgekehrtes Bild: in Wasser ist keine Fluoreszenzzunahme feststellbar, die Fluoreszenzzunahmeraten in HBG steigen mit steigendem pH-Wert.

Lösungsmittel	Rate $[10^{-3}s^{-1}]$
Wasser	13 ± 10
HBG pH = 4,1	10 ± 4
HBG pH = 5,1	10 ± 2
HBG pH = 6,2	6 ± 2

Tabelle 4.4: Raten der Fluorescein-Aufnahme in Wasser und HBG bei verschiedenen pH-Werten.

beschränken sich die Kinetikstudien auf die MIL-100(Fe)-NP. Nicht materialspezifische Prozesse sollten sich jedoch auch auf die MIL-101(Cr)-NP übertragen lassen.

Um die Freisetzungskinetik des Modellsystems aus MOF-NP und Fluorescein zu bestimmen, wurden beladene NP in HBG bei verschiedenen pH-Werten (4,1; 5,1; 6,2; 7,1; 7,4; 8,4) und in Wasser resuspendiert und anschließend das Fluoreszenzsignal des aus den NP freigesetzten Fluoresceins im zeitlichen Verlauf aufgezeichnet. Unmittelbar nach der Resuspension der befüllten NP in HBG ergibt sich ein Anstieg des Fluoreszenzsignals (s. Abb. 4.28). Dieser Anstieg folgt einem exponentiellen Verlauf. Im Falle von Wasser als Suspensionsmedium zeigt sich kein Anstieg der Fluoreszenz was darauf schließen lässt, dass keine Freisetzung stattfindet. Die Beladungskinetik wurde bestimmt, indem der zeit-

liche Verlauf des Fluoreszenzsignals einer Fluorescein-Lösung (0,2 µM, 2 ml) gemessen wurde zu der eine NP-Menge von 10 µg gemischt wurde. Dazu wurden Fluorescein-Lösungen mit Wasser und HBG bei den pH-Werten 4,1; 5,1; 6,2; 7,1; 7,4 und 8,4 als Lösungsmedium verwendet. Zur besseren Vergleichbarkeit wurde das Fluoreszenzsignal normiert, indem die mittlere Fluoreszenz vor der Zugabe der NP als Referenzwert gesetzt wurde. Nach der Zugabe der NP sinkt die gemessene Fluoreszenzintensität (s. Abb. 4.28) über einige hundert Sekunden. Dieser Abfall der Fluoreszenzintensität wird als Abnahme der Konzentration an fluoreszierenden Fluorescein-Molekülen interpretiert (Quenching der Fluorophore innerhalb der NP). Betrachtet man die relative Fluoreszenzabnahme zwischen dem Signal der Fluorescein-Lösung ohne NP ($t < 0\,\mathrm{s}$) und dem Signal lange nach der NP-Zugabe ($t > 400\,\mathrm{s}$) erweist sich, dass der Abfall der Fluoreszenz im Falle von Wasser als Lösungsmedium mit rund 80% am größten ist und im Falle von HBG mit steigendem pH-Wert immer geringer wird. Bei pH-Werten über 7,0 ist kein Abfall mehr feststellbar, was damit erklärt wird, dass bei diesen pH-Werten von den NP kaum mehr Fluorescein-Moleküle aufgenommen werden. Auch die Rate mit der das Fluoreszenzsignal abnimmt (bzw. Fluorescein aufgenommen wird) belegt eine Abhängigkeit vom Lösungsmedium. Um diese Rate zu quantifizieren (s.Tab. 4.4), wurde die Fluoreszenzabnahme mit einer Exponentialfunktion gefittet. In Wasser vollzieht sich der Beladungsprozess am schnellsten und verlangsamt sich mit steigendem pH-Wert in HBG.

Dazu stellt sich die Frage, ob die Beladungskinetik vom Diffusionsprozess außerhalb der Partikel dominiert wird oder von Prozessen innerhalb der NP. Um diese Frage zu ergründen, wurde der zeitliche Fluoreszenzverlauf der Fluorescein-Aufnahme in Abhängigkeit der NP-Konzentration untersucht. Dabei wurde durch gleichzeitige Anpassung der Fluorescein-Konzentration das Verhältnis von Fluorescein- zu NP-Konzentration konstant gehalten. So konnte die mittlere Weglänge, die ein Fluoresceinmolekül durch Diffusion zurücklegen muss um auf ein NP zu treffen, variiert werden. Diese Experimente wurden in HBG bei $\mathrm{pH} = 5{,}1$ durchgeführt, um im Gegensatz zu reinem Wasser, einen definierten pH-Wert vorliegen zu haben. Dieser pH-Wert eignet sich für diese Experimente aufgrund der im Vergleich zu höheren pH-Werten großen Menge an aufgenommenem Fluorescein. Der zeitliche Fluoreszenzverlauf der Fluorescein-Aufnahme ergibt durch die Fluoreszenzlöschung wie zuvor einen exponentiellen Abfall (s. Abb. 4.29). Durch Anpassen einer Regressionskurve wurde die Beladungszeit in Abhängigkeit der NP-Konzentration bestimmt (s. Abb. 4.29).

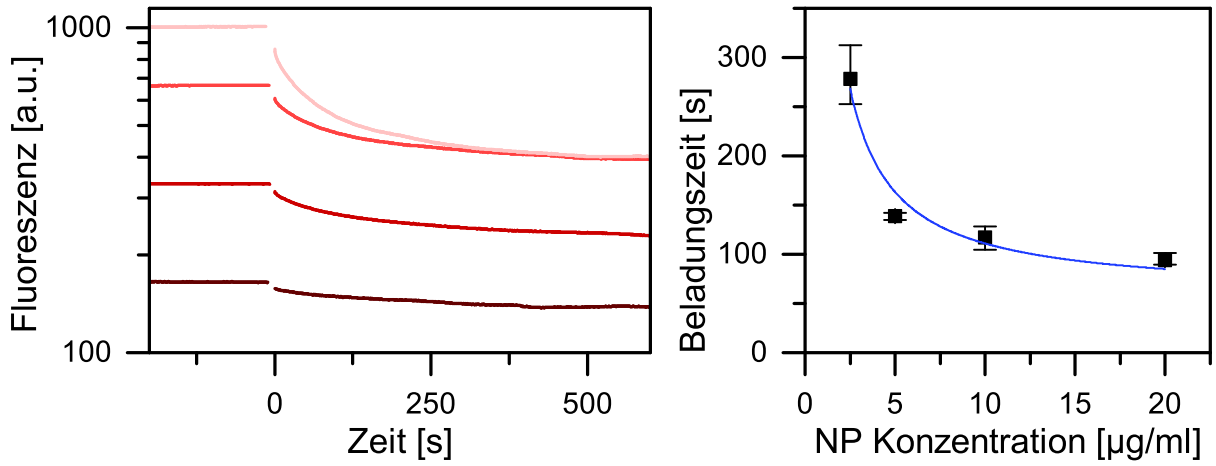

Abbildung 4.29: Fluoreszenz-Quenching im zeitlichen Verlauf der Fluorescein-Aufnahme von MIL-100(Fe)-NP (links) unter Variation der NP-Konzentration (von hell- nach dunkelrot: 20; 10; 5; 2,5 µg ml^{-1}). Die aus dem Fluoreszenzsignalabfall ermittelten Beladungszeiten wurden gegen die entsprechende NP-Konzentration aufgetragen (rechts). Die sich ergebende Konzentrationsabhängigkeit der Beladungszeit (Quadrate, Fehlerbalken aus dreifacher Wiederholung der Experimente) folgt gut dem vorgestellten Modell.

Die Zeit, die ein Fluorescein-Molekül im Mittel benötigt um durch Diffusion auf ein NP zu treffen, lässt sich über die Theorie von Adam und Delbrück [113] abschätzen: In einer homogen mit diffundierenden Molekülen gefüllten Kugel mit Radius R lässt sich die mittlere Zeit, die ein diffundierendes Molekül benötigt um eine kleinere Kugel mit Radius r im Zentrum der großen Kugel zu treffen, durch die Gleichung

$$\tau = \frac{\left(1 - \frac{r}{R}\right)^2}{3rD} \cdot R^3 \tag{4.12}$$

beschreiben, wobei D die Diffusionskonstante der diffundierenden Moleküle ist.

Auf das hiesige Problem bezogen stellt die kleinere Kugel im Inneren einen NP dar. Die diffundierenden Moleküle sind die Fluorescein-Moleküle (mit $D = 390\,\mu m^2$). Der äußeren Kugel entspricht näherungsweise das Volumen v an Fluorescein-Lösung, das im Mittel mit einem NP besetzt ist. Der Radius R lässt sich somit mit dem halben mittleren Abstand der NP abschätzen. Der Abstand lässt sich aus dem Gesamtvolumen der Probe V und der darin enthaltenen NP-Anzahl N ableiten:

$$R = \frac{1}{2}\sqrt[3]{v} = \sqrt[3]{\frac{1}{8}\frac{V}{N}} = \sqrt[3]{\frac{\rho\pi r^3}{6c_{NP}}} \tag{4.13}$$

wobei im letzten Schritt die Gleichungen 4.6 und 4.5 sowie die Massenkonzentration der NP $c_{NP} = \frac{m}{V}$ eingesetzt wurden. Somit resultiert die mittlere Zeit, die ein diffundierendes Fluorescein-Molekül benötigt um ein NP zu treffen, in

$$\tau\left(c_{NP}\right) = \frac{4\pi r^2 \rho}{72 c_{NP} D}\left(1 - \left(\frac{\pi\rho}{6c_{NP}}\right)^{-\frac{1}{3}}\right)^2 \approx \frac{4\pi r^2 \rho}{72D}\frac{1}{c_{NP}}. \tag{4.14}$$

Daraus ergibt sich, dass die äußere Diffusionszeit reziprok zur Partikelkonzentration ist. Wie in Abbildung 4.29 zu erkennen, folgen die experimentellen Daten dieser Beziehung bis auf einen Offset τ_0 von rund einer Minute für die unbeobachteten Prozesse innerhalb der NP. Diese Zeitspanne erscheint zunächst überraschend lang. Denn die freie Diffusion von Fluorescein über eine Fläche mit einem Radius r vergleichbar mit dem der Nanopartikel, abgeschätzt über die mittlere quadratische Verschiebung $\langle r^2 \rangle = 6D\tau$, würde lediglich eine Zeit in der Größenordung von Millisekunden als zusätzliche Zeit rechtfertigen. τ_0 vereint jedoch alle internen Prozesse, welche sich nicht beobachten lassen, wie z.B. zeitweise Sorption mit anschießender Desorption und kurze Zeiten der durch die räumliche Enge behinderte Diffusion.

Fazit

Diese Studie zur Beladung von MOF-NP mit Gastmolekülen und der anschließenden Abgabe der Gastmoleküle gibt einen tieferen Einblick in den Prozess der Aufnahme und Freisetzung. Beide verwendeten NP-Materialien nehmen signifikante Mengen an Fluorescein auf und erfüllen mit dieser hohen Beladungskapazität eine der Hauptanforderungen an Nanotransporter. Die gefundene pH- und Lösemittelabhängigkeit ist für eine spätere Anwendung von großer Bedeutung, um eine optimale Beladung zu erzielen. Der Beladungsprozess wird einerseits von der Diffusion der Gastmoleküle außerhalb der NP und andererseits von internen Prozessen bestimmt. Mögliche wiederkehrende Absorption und Desorption, unterbrochen von kurzen Zeiten der Diffusion in den Poren verlangsamen die Dynamik der Gastmoleküle innerhalb des mesoporösen Geflechts.

4.4 Proteintransduktion durch Komplexierung mit Oligomeren

Eine Klasse von Molekülen, deren gezielter Transport in Zellen von großem Interesse ist, sind Proteine, da sie zu wesentlichen Funktionen der Zellen beitragen. Als Teil einer Proteintherapie wird viel Hoffnung in die Transduktion von Proteinen gesetzt, um die Ursachen und Symptome vieler Krankheiten wie z.B. Diabetis mellitus, Hämophilie oder Morbus Gaucher zu bekämpfen. Proteine haben meist eine höhere Spezifität als viele molekulare Medikamente. Gleichzeitig bietet die Proteintherapie ein potentiell geringeres Risiko für negative genetische Auswirkungen verglichen mit der Gentherapie. Den großen Durchbruch hat die intrazelluläre Proteintherapie jedoch auch deshalb noch nicht erreicht, da die Proteinaufnahme durch Zellen bisher nicht sehr effizient ist. Neben der pharmakologischen Bedeutung bietet eine erfolgreiche Proteintransduktion biotechnologische und biophysikalische Anwendungen. Zum Beispiel lässt sich gezielt ein krankhafter Stoffwechsel von Organismen beeinflussen oder es lassen sich einzelne Zellbestandteile mittels Antikörpern spezifisch markieren. Für eine Beladung in die Poren von NP sind Proteine in der Regel zu groß. Folglich müssen andere Methoden gefunden werden, um Proteine in Zellen zu transportieren. Im Folgenden werden zwei Konzepte zur Protein- und Antikörper-Transduktion untersucht. [114]

4.4.1 pH-reversible Proteinmodifikation zur Proteintransduktion[7]

Durch krankhafte Veränderungen kann es vorkommen, dass Zellen benötigte Proteine nicht mehr korrekt oder überhaupt nicht mehr produzieren können. In diesem Fall kann die Verabreichung der benötigten Proteine von außen ein risikoarmer Weg sein, diesen Mangel auszugleichen. In der Regel besitzen Zellen jedoch keine Aufnahmemechanismen für Proteine, welche sie selbstständig herstellen können sollten. Aus diesem Grund muss ein Weg gefunden werden, die notwendigen Proteine dennoch in die Zellen zu transportieren. Ein Konzept zur pH-reversiblen Komplexbildung mit Hilfe von Oligomeren, welches in Zusammenarbeit mit der Arbeitsgruppe Wagner entstand, wurde untersucht, um so die geringe Transduktion von Proteinen zu überwinden. Die Erkenntnisse dieser Studie sind in Liu et *al.* [115] (s. Anhang B.3) veröffentlicht worden und sollen hier knapp wiedergegeben werden.

[7] Dieses Kapitel behandelt in Teilen Erkenntnisse, die in [115] publiziert wurden (s. Anhang B.3).

In vorhergehenden Studien der Arbeitsgruppe von Prof. Wagner wurde gezeigt, dass Azidomethyl-Methylmaleinsäureanhydrid (AzMMMan) pH-reversibel an Proteine binden kann [116]. Als Weiterentwicklung wurden in diesem Kapitel kationische, dreiarmige Oligoaminoamide verwendet, um Komplexe aus Proteinen, AzMMMan und den Oligomeren herzustellen. Zur Untersuchung der Protein-Komplexierung und Transduktion wurden für dieses Projekt die Proteine GFP und RNase A als Modellsysteme verwendet. Es konnte gezeigt werden, dass die gebildeten Komplexe besser von Zellen aufgenommen werden als die jeweiligen Proteine alleine. Die Komplexe sind bei einem pH-Wert von 7,4 stabil, lösen sich jedoch in einer mild sauren Umgebung (z.B. in Endosomen) auf. FCS-Messungen von unmodifiziertem GFP, AzMMMan modifiziertem GFP sowie Oligomer/GFP-AzMMMan-Komplexen ergaben, dass die Größe von Protein-Oligomer-Komplexen stark vom Konjugationsgrad (Oligomer-zu-GFP Verhältnis = 2, 4, 8, 16) abhängt (siehe Figure 2 in Anhang B.3). Große Komplexe ($> 0{,}1\,\mu m$) wurden nur bei starkem (8- bzw. 16-fachem) Überschuss an Oligomeren gegenüber GFP-AzMMMan beobachtet . Alle mit FCS getesteten Konjugationsgrade zeigen in Zellexperimenten eine effiziente Aufnahme. Darüber hinaus gelangt GFP bei Konjugationsgraden von 4 und 8 sogar bis in den Zellkern.

4.4.2 Einzeldomänenantikörper zur Bildgebung in lebenden Zellen[8]

Im folgenden Kapitel werden Komplexe aus Einzeldomänenantikörpern und Oligomeren untersucht, welche effizient von lebenden Zellen aufgenommen werden, um dort spezifisch Proteine der Zellen zu markieren. Die Erkenntnisse dieser Studie sind in Zusammenarbeit mit der Arbeitsgruppe Wagner entstanden und in Publikation P5 [117] (s. Anhang B.5) detailliert beschrieben, welches bei *Pharmaceutical Research* veröffentlicht wurde.

In der Medizin haben Antikörper ein breites Anwendungsfeld. Beispielsweise werden Antikörper als passiver Impfstoff bei der Behandlung von Autoimmunerkrankungen wie Multipler Sklerose aber auch in der Onkologie zum Auffinden bestimmter Tumorzellen im Körper sowie in der Radioimmuntherapie genutzt. Die komplexe Struktur und der aufwendige Herstellungsprozess von Antikörpern, welche zur Krankheitsbekämpfung entwickelt wurden, machen es notwendig alternative, einfachere Strukturen und Herstellungsprozesse zu entwickeln. Dabei müssen diese neuen Strukturen genauso spezifisch

[8]Dieses Kapitel behandelt die Erkenntnisse, die in Publikation P5 bei *Pharmaceutical Research* veröffentlicht wurden [117]

(Schlüssel-Schloss-Prinzip) und affin an die Zielstrukturen binden. Hierfür bieten sich Einzeldomänenantikörper an. Einzeldomänenantikörper, auch Nanobodies genannt, sind Fragmente von Antikörpern, die aus einer einzelnen, variablen Domäne eines Antikörpers aufgebaut sind. Die Entdeckung der Nanobodies ist eine Folge der Untersuchung des Immunsystems von Dromedaren. Dabei wurde 1993 festgestellt, dass Antikörper von Dromedaren nicht nur aus je zwei schweren und zwei leichten Ketten wie bei anderen Spezies bestehen, sondern auch einfacher gebaute Antikörper vorkommen, die nur aus den schweren Ketten bestehen [118]. Einzeldomänenantikörper gewinnen zunehmende Bedeutung im Bereich der Lebendzell-Bildgebung [119–122] und bei der Bekämpfung einiger Krankheiten wie z.B. der Afrikanischen Schlafkrankheit [123–126]. Zur Krankheitsbekämpfung werden Nanobodies unter anderem benutzt, um Antigene zu verändern und zu blockieren. Bei der Lebendzell-Bildgebung werden Einzeldomänenantikörper verwendet, um Proteine gezielt zu markieren und so zu visualisieren und zu lokalisieren. Die Vorteile dieser Nanobodies sind unter anderem, dass sie vergleichsweise einfach in modifizierten Bakterien, mit hohem Ertrag produzierbar sind und schnell auf ihre Affinität und ihr spezifisches Bindungsverhalten hin untersucht werden können. Darüber hinaus erlaubt ihnen ihre geringe Größe (15 kDa) besser als klassische Antikörper durch Gewebe und Zellkernporen zu diffundieren. Die Zell-Aufnahme von Proteinen im Allgemeinen und Antikörpern im Speziellen ist nicht effizient. Darüber hinaus ist es für Proteine, die mit Hilfe von Transportern über die Endozytose den Weg

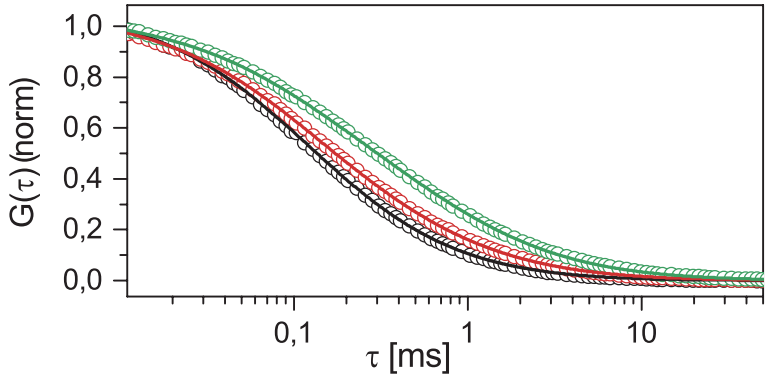

Abbildung 4.30: Normierte Korrelationskurven (Kreise) mit Fits (Linien) von GBP-A647N (schwarz), GBP/735 (rot) und GBP/734 (grün). Während die Nanobody-Moleküle alleine einen hydrodynamischen Radius von $R_H = 2\,\text{nm}$ haben, besitzt GBP/735 Anteile mit $R_H^{\text{GBP}-\text{A647N}/735} = 15\,\text{nm}$ und GBP/734 Anteile mit $R_H^{\text{GBP}-\text{A647N}/734} = 20\,\text{nm}$. Dies zeigt, dass die Nanobodies zusammen mit den Oligomeren Komplexe bilden.

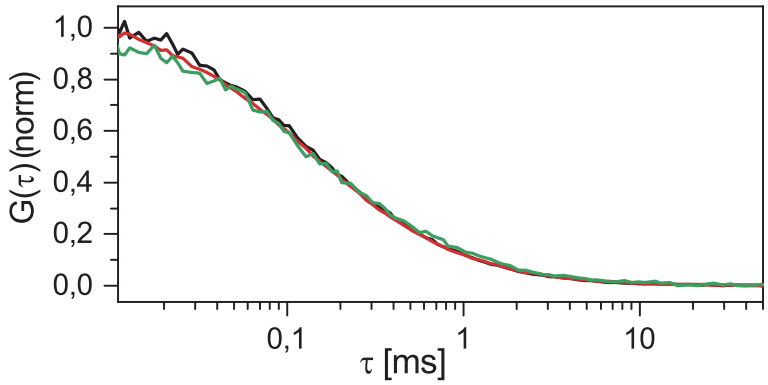

Abbildung 4.31: Normierte Korrelationskurven von GBP-A647N (schwarz), GBP-A647N mit 735-NEM (rot) und GBP-A647N mit 734-NEM (grün). Durch die NEM-Blockade ist die Komplexbildung gehemmt. Dies wird in den FCS-Kurven dadurch deutlich, dass die Proben mit den Oligomeren keine Abweichung der Diffusionszeit zu der GBP-A647N Probe zeigen.

in eine Zelle geschafft haben, schwer aus dem Endosom zu entkommen. Wie in Kapitel 4.4.1 sowie von Maier *et al.* und Zhang *et al.* gezeigt [116, 127, 128], gelingt es Komplexen aus Proteinen und Oligoaminoamiden leichter in die Zelle zu gelangen als Proteinen alleine. Diesen Erkenntnissen folgend wurde versucht die Antikörpertransduktion mittels Komplexbildung zu verbessern. Als Modellsystem wurde zunächst ein an GFP bindender Nanobody (GBP) gewählt. Die verwendeten Oligoaminoamide sind zum einen „735“, welcher Folat enthält, und „734“ welcher kein Folat enthält (Details hierzu in Publikation P5 [117] s. Anhang B.5). Die mit *ATTO 647 N* fluoreszenzmarkierten Nanobodies (GBP-A647N) wurden mit 735 bzw. 734 in einem molaren Verhältnis von 5:1 gemischt und für 4 Stunden bei 37 °C inkubiert. Um die spezifische Komplexierung der Oligomere (734 und 735) mit den fluoreszenzmarkierten Nanobodies nachzuweisen, wurden FCS-Messungen durchgeführt. Dazu wurden zunächst die GBP-Nanobodies in HEPES-Puffer vermessen. Es ergab sich ein hydrodynamischer Radius von $R_H = 2\,\text{nm}$. Dieses Ergebnis ist in guter Übereinstimmung mit der Größe, die Kirchhofer *et al.* für die GFP-bindenden Nanobodies angeben ($2\,\text{nm} \times 4\,\text{nm}$) [121]. Sowohl die Mischung aus GBP-A647N und 735 (GBP/735) als auch die Mischung aus GBP-A647N und 734 (GBP/734) zeigen eine deutlich abweichende Korrelationskurve gegenüber der von unmodifiziertem GBP-A647N (siehe Abb. 4.30). Ein Einkomponenten-Fit führt bei den Mischungen zu keinem zufriedenstellenden Ergebnis, so dass vermutet werden muss, dass zumindest zwei unterschiedliche Spezies in der Probe vorhanden sind. Aufgrund dieser Erkenntnis und der Vermutung, dass nicht alle Nanobodies in Komplexen ge-

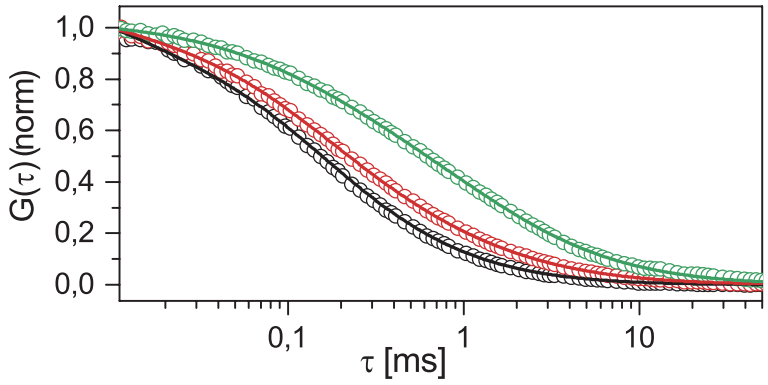

Abbildung 4.32: Normierte Korrelationskurven (Kreise) mit Fits (Linien) von LBP-A647N (schwarz), LBP-A647N/735 (rot) und LBP-A647N/734 (grün). Während die Nanobody-Moleküle alleine einen hydrodynamischen Radius von $R_H = 2\,\mathrm{nm}$ haben, weist LBP-A647N/735 Anteile mit $R_H^{\mathrm{LBP-A647N/735}} = 15\,\mathrm{nm}$ und GBP-A647N/73 Anteile mit $R_H^{\mathrm{LBP-A647N/734}} = 20\,\mathrm{nm}$ auf. Dies zeigt, dass die an Lamin bindenden Nanobodies zusammen mit den Oligomeren Komplexe bilden.

bunden sind, wurde ein Zweikomponenten-Fit verwendet. Für die erste Komponente wurde die Diffusionzeit von unmodifizierten GBP-A647N vorgegeben. Wie in Abbildung 4.30 zu sehen, stimmt das Zweikomponenten-Modell sehr gut mit den Daten überein. Für die zweite, größere Komponente ergab sich so ein hydrodynamischer Radius von $R_H^{\mathrm{GBP/735}} = 15\,\mathrm{nm}$ für GBP/735 und $R_H^{\mathrm{GBP/734}} = 20\,\mathrm{nm}$ für GBP/734. Dies bestätigt die Bindung der Nanobodies mit beiden Oligoaminoamiden, obgleich sich auch ein großer Anteil unmodifizierter Nanobodies in der Probe befindet. Die Spezifität dieser Bindung wurde untersucht, indem selbiges Bindungsexperiment mit den Oligoaminoamiden 734 und 735 durchgeführt wurde, deren terminale Cysteine, welche für die Komplexbildung verantwortlich gemacht werden, mittels N-Etylmaleimid (NEM) blockiert wurden. Wie in Abbildung 4.31 zu erkennen, unterscheiden sich die Korrelationskurven der Mischungen aus GBP-A647N und 735-NEM sowie GBP-A647N und 734-NEM nicht von der Korrelationskurve der GBP-A647N-Probe. Dies zeigt, dass keine Komplexbildung bei blockierten terminalen Cysteinen stattfindet und lässt den Schluss zu, dass diese Cysteine maßgeblich für die Bindung der Oligoaminoamide untereinander verantwortlich sind. Da Nanobodies sich wenig in Größe, Struktur und Oberflächenbeschaffenheit unterscheiden, sollten obige Ergebnisse auch auf Nanobodies übertragbar sein, die mit anderen Proteinen als GFP interagieren. Um dies zu untersuchen wurden an Lamin bindende Nanobodies (LBP) ebenfalls auf ihre Bindung mit den Oligomeren 734 und 735 hin untersucht. Wie in Abbildung 4.32 ersichtlich, zeigen auch die LBP eine Bin-

dung an die Oligoaminoamide. Somit ist auch die Austauschbarkeit der Nanobodies bestätigt. Weitere Experimente (s. Anhang B.5) konnten eine effiziente Zellaufnahme der Komplexe und die Interaktion der Nanobodies mit ihren Zielproteinen (GFP und Lamin) demonstrieren.

Zusammenfassend wurde ein einfacher und effizienter Weg vorgestellt, Nanobodies in Zellen zu transduzieren. Hierzu wurden Komplexe aus Oligoaminoamiden und Nanobodies verwendet, deren Bindung und Spezifität mittels FCS bestätigt wurden. Die beiden verwendeten Oligoaminoamide ermöglichen den Nanobodies das Entkommen aus den Endosomen in das Zytosol, wo diese dann ihre angestrebte Funktion ausführen können.

Kapitel 5

Ausblick

In dieser Arbeit konnten grundlegende Schritte auf dem Entwicklungsweg zu wohldefinierten, multifunktionellen Nanotransportern für den zielgerichteten Arzneimitteltransport gemacht werden. Dazu wurden physikalische Messmethoden, wie FCS, TEM oder Absorptionsspektroskopie, verwendet, um die Transport- und Oberflächeneigenschaften von MOF-Nanotransportern zu charakterisieren und quantifizieren. So konnte die Größenverteilung von MOF-NP unter Anwendung verschiedener Messtechniken detailliert bestimmt werden. Da zukünftige medizinische Anwendungen auf die genaue Kenntnis der Größe und Morphologie der NP angewiesen sind, ist eine ausführliche Charakterisierung für alle NP-Sorten, die für den Einsatz in der Nanomedizin in Frage kommen, von großer Bedeutung. Es ist ebenfalls notwendig die NP zu funktionalisieren, um ihre Oberflächeneigenschaften dahingehend zu beeinflussen, dass sie kolloidal stabil bleiben, zielgerichtet nur in bestimmte Zellen aufgenommen werden und den zu transportierenden Wirkstoff erst im Zielgebiet freigeben. Drei Funktionalisierungsmethoden von MOF-NP konnten etabliert werden. Zum einen wurde eine undurchlässige Lipidbeschichtung von MOF-NP vorgestellt, von der gezeigt werden konnte, dass sie die Zellaufnahme vermittelt. Allerdings besteht für eine medizinische Anwendung die Notwendigkeit, die Lipidhülle gesteuert öffnen zu können, um den Wirkstoff gezielt im krankhaften Gewebe freizusetzen. Eine Möglichkeit das zu erreichen ist, eine Lipid-Mischung zu verwenden, deren Doppelschichten bei einer bestimmten, erhöhten Temperatur durchlässig werden. So könnte durch gezielte Erwärmung des krankhaften Gewebes die Wirkstofffreisetzung lokal ausgelöst werden. Es wird bereits an solchen thermosensitiven Lipid-Mischungen geforscht, welche bei einer wohldefinierten Grenztemperatur für Wirkstoffe durchlässig werden [9]. Eine Kombination aus MOF-NP als

Wirkstoffträger und thermosensitiven Lipidmembranen als Verkapselung hat großes Potential die gezielte Wirkstofffreisetzung umsetzen zu können.

Zum anderen wurde die kovalente Anbindung von Polymermolekülen an die NP-Oberfläche untersucht, welche die kolloidale Suspension stabilisiert und die Zellaufnahme verbessert. Wie von Möller *et al.* [129] gezeigt, können Polymere auf Silika-NP-Oberflächen als Verkapselungssystem eingesetzt werden. Diese Verkapselung lässt sich darüber hinaus gezielt öffnen. Es ist denkbar, dass sich diese Polymere auch an MOF-NP binden lassen und so zusätzlich ein Mechanismus zur gezielten Wirkstofffreisetzung ermöglichen lässt.

Die gezeigte pH-reversible, koordinative Bindung von His-Tag-modifizierten Funktionseinheiten erlaubt die Herstellung von multifunktionellen Partikeln. Es konnte gezeigt werden, dass NP sich mit zwei unterschiedlichen Proteinen funktionalisieren lassen. Daraus ergibt sich die Fragestellung, ob sich noch mehr verschiedene Funktionseinheiten, z.B. mit Targeting-Ligand, Wirkstoff und Kontrastmittel, auf einem NP vereinigen lassen. So kann der Wirkstoff zielgerichtet in einen Zelltyp transportiert und dieser Vorgang gleichzeitig über ein Tomographieverfahren verfolgt werden. Eine Kombination von Targeting-Liganden und dem vielseitig einsetzbaren CRISPR/CAS9-System [130] als Kofunktionalisierung auf der NP-Oberfläche böte sich ebenfalls als möglicher Weg an, das Genom von spezifischen Zellen zu editieren. Weiterhin ist es interessant zu untersuchen, ob sich die gezeigten Ergebnisse auf MOF-NP übertragen lassen, die speziell für die Beladung mit und die anschließende Freigabe von Wirkstoffmolekülen modifiziert wurden.

Die Beladung und Freisetzung von Gastmolekülen in MOF-NP (in der vorliegenden Arbeit von Fluorescein als Modellsystem) sind entscheidende Prozesse. Ihre Kontrollierbarkeit muss für den Einsatz in der Nanomedizin gegeben sein und ist deshalb von großem Interesse. Im untersuchten Modellsystem zeigte sich eine pH- und Lösemittelabhängigkeit von Beladung und Freisetzung sowie eine Diffusionslimitierung des Beladungspozesses, welcher zusätzlich durch Vorgänge innerhalb der NP-Poren verlangsamt ist. Für die künftige Anwendung ist es notwendig die tatsächlichen Wirkstoffmoleküle (z.B. Doxorubicin) auf ihre Beladungs- und Freisetzungseigenschaften zu untersuchen, um auf Unterschiede durch die physiochemischen Eigenschaften der Wirkstoffe bei diesen Prozessen eingehen zu können. Darüber hinaus sollte überprüft werden, welche Veränderungen an den MOF-Bauteilen zu einer höheren Aufnahme oder verbesserten Freisetzungscharakteristik führen. Durch die vielfältige Auswahl der zur

Verfügung stehenden organischen Verbindungsmoleküle ist es denkbar die Porenoberfläche der MOF-Struktur so zu modifizieren, dass eine Freisetzung im Blut bei pH = 7,0 gehemmt wird und erst bei pH = 5,0 im Endosom vermehrt vonstatten geht.

Für Moleküle, die zu groß sind, um sie in die Poren von NP zu füllen, z.B. Proteine oder Antikörper, bieten sich andere Möglichkeiten an, diese in Zellen zu transportieren. Als ein geeignetes Konzept zur Realisierung hat sich die Bildung von Komplexen aus Proteinen oder Nanobodies und Oligomeren erwiesen. In dieser Arbeit konnte die Bindung dieser Komponenten untereinander und die Bildung zu Komplexen nachgewiesen werden. Da Proteine im Allgemeinen oder Antikörper im Speziellen deutlich spezifischer wirken als herkömmliche Medikamente, erschließen sich hier viele erfolgversprechende Möglichkeiten für neuartige, nebenwirkungsarme Therapieansätze.

Ein bislang wenig beachteter Aspekt der Nanomedizin ist der Verbleib der Nanotransporter im Körper. Es bleibt bei allen Konzepten von Nanotransportern zu prüfen, ob von deren Rückständen in Zellen, Blut oder anderen Gewebeteilen Gefahren ausgehen und ob ein Abbau im oder Ausscheiden aus dem Körper stattfinden kann.

Eine Vereinigung der gezeigten Ergebnisse und Methoden zu einem speziell gestalteten multifunktionellen Nanotransporter für die gesteuerte und gezielte Applikation von Wirkstoffen ließe den von Paul Ehrlich ersonnenen weit entfernen Traum von „magischen Kugeln“ in greifbare Nähe rücken. Die große Anzahl an Publikationen im Bereich der Nanotransporter zeigt, dass das große Potential dieses interessanten Forschungsfeldes noch nicht vollends ausgeschöpft ist. Physikalische Herangehensweisen an die Entwicklung und Charakterisierung von wohldefinierten, multifunktionellen Nanotransportern zum zielgerichteten Arzneimitteltransport werden dazu beitragen die Medizin der Zukunft zu gestalten.

Anhang A

Liste der Publikationen

P1 Stefan Wuttke, Simone Braig, **Tobias Preiß**, Andreas Zimpel, Johannes Sicklinger, Claudia Bellomo, Joachim O. Rädler, Angelika M. Vollmar, Thomas Bein. MOF nanoparticles coated by lipid bilayers and their uptake by cancer cells. *Chemical Communications*, 2015, 51, 15752–15755. [80]

P2 Patrick Hirschle, **Tobias Preiß**, Florian Auras, André Pick, Johannes Völkner, Daniel Valdepérez, Gregor Witte, Wolfgang J. Parak, Joachim O. Rädler, Stefan Wuttke. Exploration of MOF nanoparticle sizes using various physical characterization methods – is what you measure what you get? *CrystEngComm*, 2016, 18 (23), 4359–4368. [59]

P3 Xiaowen Liu, Peng Zhang, Dongsheng He, Wolfgang Rödl, **Tobias Preiß**, Joachim O. Rädler, Ernst Wagner, Ulrich Lächelt. pH-Reversible Cationic RNase A Conjugates for Enhanced Cellular Delivery and Tumor Cell Killing. *Biomacromolecules*, 2016, 17 (1), 173–182. [115]

P4 Andreas Zimpel, **Tobias Preiß**, Ruth Röder, Hanna Engelke, Michael Ingrisch, Michael Peller, Joachim Rädler, Ernst Wagner, Thomas Bein, Ulrich Lächelt, Stefan Wuttke. Imparting functionality to MOF nanoparticles by external surface selective covalent attachment of polymers. *Chemistry of Materials*, 2016, 28, 3318-3326. [86]

P5 Ruth Röder, Jonas Helma , **Tobias Preiß**, Joachim O. Rädler, Heinrich Leonhardt, Ernst Wagner. Intracellular Delivery of Nanobodies for Imaging of Target Proteins in Live Cells. *Pharmaceutical Research*, 2017, 34, 161–174. [117]

P6 Ruth Röder, **Tobias Preiß**, Patrick Hirschle, Benjamin Steinborn, Andreas Zimpel, Miriam Hoehn, Joachim O. Rädler, Thomas Bein, Ernst Wagner, Stefan Wuttke, Ulrich Lächelt. Multifunctional nanoparticles by coordinative self-assembly of His-tagged units with metal-organic frameworks.
Journal of the American Chemical Society , 2017, 139 (6), 2359-–2368. [98]

P7 **Tobias Preiß**, Andreas Zimpel, Stefan Wuttke, Joachim O. Rädler. Kinetic Analysis of the Uptake and Release of Fluorescein by Metal-Organic Framework Nanoparticles. *Materials* 2017, 10 (2), 216. [104]

Anhang B

Publikationen

B.1 Originalpublikation P1

Stefan Wuttke, Tobias Preiß, Simone Braig, Andreas Zimpel, Johannes Sicklinger, Claudia Bellomo, Joachim O. Rädler, Angelika M. Vollmar, Thomas Bein.
MOF nanoparticles coated by lipid bilayers and their uptake by cancer cells.
Chemical Communications, 2015, 51, 15752-15755.

Volume 51 | Number 87 | 11 November 2015 | Pages 15741–15868

ChemComm

Chemical Communications
www.rsc.org/chemcomm

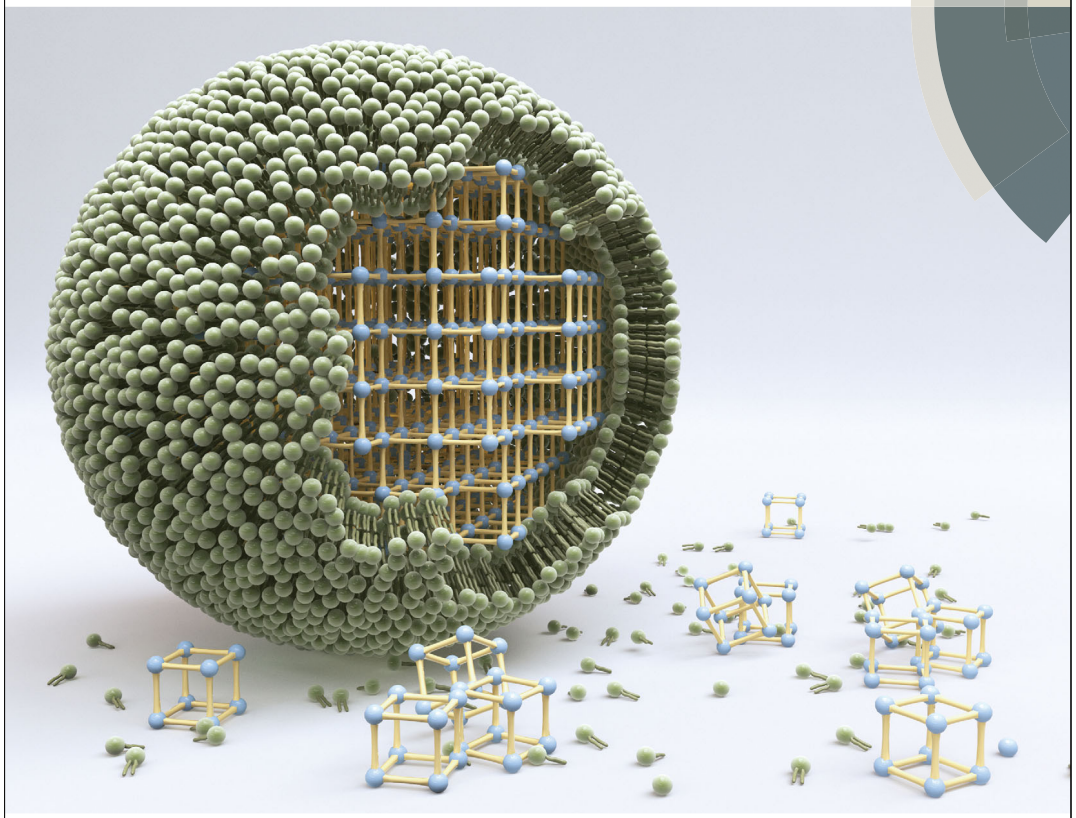

ISSN 1359-7345

ROYAL SOCIETY OF CHEMISTRY

COMMUNICATION
Stefan Wuttke, Thomas Bein *et al.*
MOF nanoparticles coated by lipid bilayers and their uptake by cancer cells

ChemComm

COMMUNICATION

View Article Online
View Journal | View Issue

Cite this: *Chem. Commun.*, 2015, **51**, 15752

Received 12th August 2015,
Accepted 4th September 2015

DOI: 10.1039/c5cc06767g

www.rsc.org/chemcomm

MOF nanoparticles coated by lipid bilayers and their uptake by cancer cells†

Stefan Wuttke,*[a] Simone Braig,‡[b] Tobias Preiß,‡[c] Andreas Zimpel,[a] Johannes Sicklinger,[a] Claudia Bellomo,[a] Joachim O. Rädler,[c] Angelika M. Vollmar[b] and Thomas Bein*[a]

We report the synthesis of MOF@lipid nanoparticles as a versatile and powerful novel class of nanocarriers based on metal–organic frameworks (MOFs). We show that the MOF@lipid system can effectively store dye molecules inside the porous scaffold of the MOF while the lipid bilayer prevents their premature release. Efficient uptake of the MOF@lipid nanoparticles by cancer cells makes these nanocarriers promising for drug delivery and diagnostic purposes.

The chemical synthesis of well-defined functional nano-objects is one of the intriguing challenges of nanoscience. In this context metal–organic frameworks (MOFs) offer the ability to generate crystallographically defined, functionalized, porous nanocrystals. MOFs consist of inorganic clusters acting as nodes connected by organic linker molecules. Together, these building blocks create three-dimensional porous crystalline networks with very high pore volume and surface area. The large range of possible compositions (metals, linkers), the structural diversity (pore size, structure, *etc.*) and the numerous options to functionalize these porous crystalline hybrid inorganic–organic solids make them attractive for different fields of applications such as small molecule storage (H_2, CH_4, CO_2, *etc.*), catalysis, separation, luminescence, magnetism and other applications.[1–4] In addition, MOFs can be scaled down to nanometer size, which makes them potentially useful as nanocarriers in medical applications.[5]

Incorporating drug molecules into nanocarriers offers exciting opportunities to redefine the pharmacokinetic behavior of the drug, improving its therapeutic efficiency and reducing side effects.[6–8] Several types of drug delivery nanocarriers based on organic platforms such as liposomes, polymers, and dendrimers have been used as "smart" systems that can release therapeutic agents under physicological conditions. Recent research has also addressed the potential of inorganic nanoparticles such as gold, iron oxide or mesoporous silica in this context.[9] The high loading capacity of MOFs for bioactive molecules and their applications for drug delivery and imaging purposes have recently been demonstrated.[5] However, the controlled retention of cargo inside the MOF nanoparticles (NPs) and its controlled release is a challenge that still needs to be addressed.[5,10–15]

Here we report on the synthesis of MOF nanoparticle-supported lipid bilayers – MOF@lipid – that synergistically combine properties of liposomes and porous particles. Our aim was to develop a novel route for the flexible, non-covalent encapsulation of biologically active molecules into porous MOF networks that can ultimately serve as functional MOF@lipid nanocarriers for controlled drug delivery or imaging purposes. Conceptually, a MOF@lipid nanoparticle may offer three key advantages in comparison to a liposome. First, surface modifications (*e.g.* modifying the size or the hydrophilic/hydrophobic nature of the pores) of the MOF nanoparticle can control the uptake and release kinetics of the drug.[5,16] In addition, a MOF@lipid nanoparticle is expected to be significantly more stable than a liposome, which has an aqueous core instead of a porous MOF core. Finally, due to their high porosity MOF nanoparticles have been shown to offer exceptionally high loading capacities compared to other nanocarrier systems.[5,11]

To demonstrate our new strategy, we chose the mesoporous iron(III) carboxylate MIL-100(Fe)[17] and the mesoporous chromium(III) carboxylate MIL-101(Cr).[18] MIL-100(Fe) is built up from octahedral trimers connected by trimesate (benzene-1,3,5-tricarboxylate) resulting in a MOF scaffold with large pores (diameter 2.4–2.9 nm) and window sizes (0.6–0.9 nm). MIL-101(Cr) is built up from octahedral trimers connected by terephthalate (benzene-1,4-dicarboxylate), also resulting in a MOF scaffold with large pores (diameter 2.9–3.4 nm) and window sizes (1.2–1.7 nm). Moreover, nanoparticle synthesis is already established for both structures.[11,19]

Both MOF nanoparticles (NPs) were synthesized in a microwave oven from Anton Paar (Synthos 3000). MIL-100(Fe) NPs were obtained by reacting $FeCl_3 \cdot 6H_2O$ and trimesic acid in a

[a] *Department of Chemistry and Center for NanoScience (CeNS), University of Munich (LMU), Butenandtstraße 11 (E), 81377 München, Germany. E-mail: stefan.wuttke@cup.uni-muenchen.de, bein@cup.lmu.de*
[b] *Department of Pharmacy University of Munich (LMU), Butenandtstraße 5, 81377 München, Germany*
[c] *Faculty of Physics and Center for NanoScience (CeNS), University of Munich (LMU), Geschwister Scholl Platz 1, 80539 München, Germany*
† Electronic supplementary information (ESI) available. See DOI: 10.1039/c5cc06767g
‡ These authors contributed equally.

9 : 4 molar ratio in H_2O, using a temperature controlled microwave program (heating to 130 °C in 30 s and holding at that temperature for 2 min). MIL-101(Cr) nanoparticles were synthesized from an equimolar mixture of terephthalic acid and $Cr(NO_3)_3{\cdot}9H_2O$ in H_2O, using a temperature controlled microwave program (heating to 180 °C in 4 min and holding at that temperature for 2 min). The resulting nanoparticles show the characteristic XRD reflections of the MOFs, with line broadening due to the small particle size (Fig. S6 and S7, ESI†).[18,19] The estimated size distribution of MIL-100(Fe) obtained transmission electron microscopy (TEM) is in the range of 54 ± 24 nm (Fig. S11, ESI†). For MIL-101(Cr), it is in the range of 49 ± 20 nm (Fig. S10, ESI†). In addition, TEM images (Fig. S12 and S13, ESI†) confirm the high crystalline quality of the nanocrystals. The calculation of the BET specific surface area based on nitrogen sorption isotherms gave a value of 2004 $m^2\ g^{-1}$ for nanoscale MIL-100(Fe) (Fig. S14, ESI†) and 3205 $m^2\ g^{-1}$ for nanoscale MIL-101(Cr) (Fig. S15, ESI†), which is similar to reported data.[18,19]

In the next step, MIL-100(Fe) and MIL-101(Cr) nanoparticles were coated with a lipid bilayer using the lipid DOPC (1,2-dioleoyl-*sn*-glycero-3-phosphocholine). The principle of the coating procedure is a controlled solvent-exchange deposition of the lipid onto the MOF surface.[20] For this purpose the lipid and the MOF nanoparticles are dispersed in an EtOH/H_2O mixture, where the lipids exist as monomers.[21] When the water concentration is drastically increased, the lipids precipitate on the nanoparticle surface and form a lipid bilayer (Fig. 1). The successful coating of the MOF nanoparticles with lipid was confirmed by different techniques.

The diffraction pattern of the two DOPC-coated nanoparticles shows the same reflections as the uncoated nanoparticles (Fig. S6 and S7, ESI†). Hence, the MOF structures were stable during the procedure of lipid layer coating. Dynamic light scattering (DLS) data of the MIL-101(Cr)@DOPC nanoparticles showed an increased diameter of 78 ± 22 nm (*vs.* 69 ± 19 nm for the pure MIL-101(Cr) nanoparticles, Fig. S16, ESI†). This shift of the hydrodynamic diameter of about 10 nm is close to the expected value.[19] Time series of DLS measurements of MIL-100(Fe) and MIL-100(Fe)@DOPC nanoparticles reveal the colloidal stability of the lipid-coated versions whereas the pure nanoparticles agglomerate in a matter of hours (Fig. S18 and S19, ESI†). Therefore, the supported lipid can serve not only as a cap system to store molecules inside the MOF nanoparticles but also to increase their colloidal stability, which is of great importance for biomedical applications.

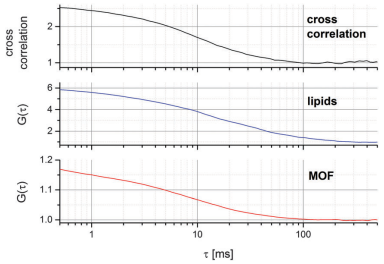

Fig. 2 FCCS of DOPC lipids (BODIPY labeled) on MIL-101(Cr) nanoparticles (Atto633 labeled). The high cross-correlation amplitude indicates the co-localization of lipids and MOF nanoparticles.

In order to confirm the localization of the lipids on the MOF nanoparticles in solution, both components were labelled and fluorescence cross-correlation analysis (FCCS) was performed. FCCS provides evidence for correlated movement of two differently labelled species within the confocal detection volume, by cross-correlating the fluorescence fluctuation signal of both species.[22,23] Fig. 2 shows the auto-correlation curves of the Atto633-labeled MIL-101(Cr) and BODIPY-FL-DHPE-labelled DOPC lipids as well as the cross-correlation. The analysis of the cross-correlation shows a high ratio of co-localization of lipids and MOF particles and hence proves the successful lipid coating of the MOF nanoparticle. For the MIL-100(Fe) we found that the fluorescence of different fluorescence dyes is completely quenched. Therefore, FCCS measurements for the MIL-100(Fe)@DOPC system are not applicable. However, we performed fluorescence correlation spectroscopy (FCS) measurements with BODIPY FL DHPE-labelled DOPC lipids alone and with unlabelled MIL-100(Fe) NPs (Fig. S2, ESI†). Juxtaposition of both sample results shows both a completely different count rate and correlation curve, respectively. This strongly indicates an interaction of MIL-100(Fe) NPs with lipids.

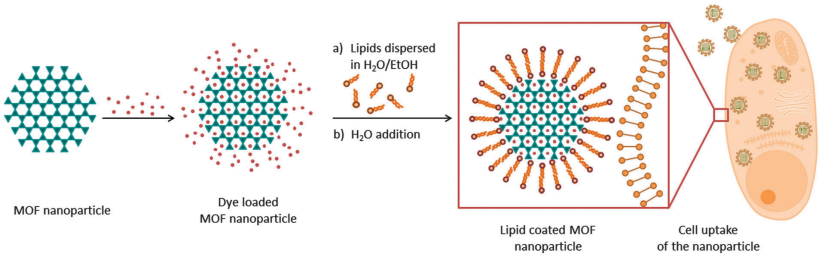

Fig. 1 Schematic description of the synthesis of lipid bilayer-coated MOF nanoparticles loaded with dye molecules and their uptake in cancer cells.

To confirm the successful lipid coating of the porous nanoparticles with another technique, and more importantly, to investigate the sealing properties of the lipid bilayer, we carried out fluorescence release experiments. For this purpose MIL-101(Cr) and MIL-100(Fe) nanoparticles were loaded with fluorescein dye and the dye was encapsulated in the nanoparticles through the formation of the lipid bilayer (Fig. 1). These dye-loaded nanoparticles were transferred into the cap of a fluorescence cuvette that was subsequently sealed with a dialysis membrane. Only free dye molecules, but not nanoparticles, can pass the membrane into the cuvette volume filled with water where the fluorescence measurement is recorded. Consequently, only dye molecules released from the pores of the particles contribute to the fluorescence intensity measured in the cuvette (detailed information is reported in the ESI†).

Fig. 3 shows the result of a typical fluorescence release experiment with MIL-101(Cr); the corresponding experiment with MIL-100(Fe) can be found in the ESI† (Fig. S20). The fluorescence intensity released from DOPC-coated MIL-101(Cr) nanoparticles reached only very low values after 1 h. Hence, we conclude that the dye is retained in the nanoparticles and that the dye molecules do not permeate through the DOPC bilayer. After one hour of monitoring without any significant increase of the fluorescence intensity, the nonionic surfactant triton X-100 was added into the cap. After a short induction period, the fluorescence intensity showed a rapid increase, which subsequently slowed over time. Release kinetics of the dye show a burst release within the first 30 min, which is relatively small in comparison with other nanocarriers,[9,21] and afterwards a release that is mainly governed by diffusion processes combined with dye–host interactions. Such behaviour can be advantageous for later applications as a drug carrier, because the drug release rate can be controlled by tuning the pore size and shape as well as the functionality of the MOF nanocarrier, and at the same time high burst release effects can be avoided, ensuring a fairly constant drug release. Therefore, the structural features of MOFs including crystalline porosity and widely tunable functionality are advantageous for controlling host–guest interactions.

The above results demonstrate the successful creation of a lipid bilayer around MOF nanoparticles that enables encapsulation of a dye or other molecules inside the MOF scaffold.

For future applications of MOF@lipid systems in biomedicine, the cellular uptake of these constructs is of particular interest. Due to the quenching effect of the MIL-100(Fe) nanoparticles, corresponding fluorescence tracking experiments can be only done with the MIL-101(Cr)@DOPC nanoparticles. For this purpose, 20 000 T24 bladder carcinoma cells per well with 250 µl medium were incubated with 20 µl of a suspension of Atto633 labelled MIL-101(Cr)@DOPC NPs (c = 1 mg ml^{-1}). Co-staining with PKH26, a red fluorescent dye that stains cellular membranes incorporating biolipid structures, revealed enrichment of MOF nanoparticles in cellular vesicles over time as demonstrated by confocal laser scanning microscopy. As shown in Fig. 4, strong accumulation of the MOF particles in cellular vesicles is detectable within 6 h and persists for at least 48 h. To investigate whether the MOF@lipid nanoparticles alter the cellular behaviour and/or condition, an impedance-based real time monitoring (xCELLigence System) approach was used. Importantly, xCELLigence analysis showed that both MOF@lipid nanoparticle systems themselves have no cytotoxic or anti-proliferative effect on the cancer cells (Fig. S21 and S22, ESI†).

In summary, we have developed novel metal–organic framework nanoparticles encapsulated by a lipid membrane. We have demonstrated that the MOF@lipid system can effectively store dye molecules inside the porous scaffold of the MOF while the lipid bilayer prevents their premature release. Moreover, for MIL-100(Fe) the lipid bilayer drastically increases the colloidal stability of the nanoparticles. Employing fluorescence microscopy, we were able to demonstrate the high uptake of lipid-coated nanoparticles by cancer cells. Considering the various ways to synthesize different functionalized MOF nanoparticles

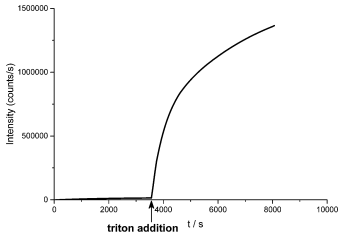

Fig. 3 Fluorescence release experiments of encapsulated fluorescein in MIL-101(Cr)@DOPC nanoparticles (the data points correspond to the intensities at the peak maxima at 512 nm for fluorescein). After 1 hour of measuring time with no significant increase of the fluorescence intensity, triton was added to the cap system. The destabilization of the lipid bilayer can be observed in the release of the fluorescein dye. The measurement took place at 37 °C and was stopped after 2 h of fluorescein dye release due to an oversaturation of the detector (intensity maximum of the detector 2 million counts per second).

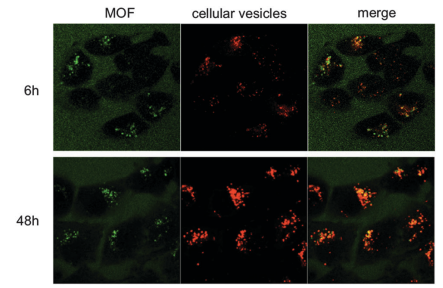

Fig. 4 Cellular uptake of MOF nanoparticles in cancer cells as monitored by confocal laser scanning microscopy. Bladder cancer cells were incubated with fluorescently-labelled MOF particles for 6 h and 48 h and co-stained with the membrane marker PKH26 to confirm enrichment of MOF in cellular vesicles.

as well as the richness of lipids with diverse functions (cap system, triggered release, incorporation of shielding ligand for long circulation times and targeting functions),[24,25] MOF@lipid nanoparticles have great potential as a novel hybrid nanocarrier system. On the one hand, the MOF core could store different active species such as imaging, diagnostic or drug molecules, and on the other hand the lipid shell could be used for the incorporation of targeting or shielding ligands (*e.g.* PEG) as well as for the creation of triggered release mechanisms. Based on the above results with lipid layers serving as model systems, we anticipate further progress in the synthesis of well-defined multifunctional MOF@lipid nanoparticles for drug delivery and diagnostic purposes and the clinical implementation of this nanotechnology.

The authors are grateful for financial support from the Deutsche Forschungsgemeinschaft (DFG) through the SFB 1032 and the DFG-project WU 622/4-1, the Excellence Cluster Nanosystems Initiative Munich (NIM) and the Center for Nano-Science Munich (CeNS).

Notes and references

1 Theme issue: Metal–Organic Frameworks, H.-C. Zhou, J. R. Long and O. M. Yaghi, *Chem. Rev.*, 2012, **112**, 673.
2 Theme issue: Metal–Organic Frameworks, H.-C. J. Zhou and S. Kitagawa, *Chem. Soc. Rev.*, 2014, **43**, 5415.
3 G. Férey, *Chem. Soc. Rev.*, 2008, **37**, 191.
4 H. Furukawa, K. E. Cordova, M. O'Keeffe and O. M. Yaghi, *Science*, 2013, **341**, 974.
5 P. Horcajada, R. Gref, T. Baati, P. K. Allan, G. Maurin, P. Couvreur, G. Férey, R. E. Morris and C. Serre, *Chem. Rev.*, 2012, **112**, 1232.
6 D. Peer, J. M. Karp, S. Hong, O. C. Farokhazad, R. Margalit and R. Langer, *Nat. Nanotechnol.*, 2007, **2**, 751.
7 M. E. Davis, Z. Chen and D. M. Shin, *Nat. Rev. Drug Discovery*, 2008, **7**, 771.
8 K. K. Cati, M. E. Belowich, M. Liong, M. W. Ambrogio, Y. A. Lau, H. A. Khativ, J. I. Zink, N. M. Khashab and J. F. Stoddart, *Nanoscale*, 2009, **1**, 16.
9 Z. Li, J. C. Barnes, A. Bosoy, J. F. Stoddart and J. I. Zink, *Chem. Soc. Rev.*, 2012, **41**, 2590.
10 V. Agostoni, P. Horcajada, M. Noiray, M. Malanga, A. Akykac, L. Jicsinszky, A. Vargas-Berenguel, N. Semiramoth, S. Daoud-Mahammed, V. Nicolas, C. Martineau, F. Taulelle, J. Vigneron, A. Etcheberry, C. Serre and R. Gref, *Sci. Rep.*, 2014, **5**, 7925.
11 P. Horcajada, T. Chalati, C. Serre, B. Gillet, C. Sebrie, T. Baati, J. F. Eubank, D. Heurtaux, P. Clayette, C. Kreuz, J.-S. Chang, Y. K. Hwang, V. Marsaud, P.-N. Bories, L. Cynober, S. Gil, G. Férey, P. Couvreur and R. Gref, *Nat. Mater.*, 2010, **9**, 172.
12 K. Khaletskaya, J. Reboul, M. Meilikhov, M. Nakahama, S. Diring, M. Tsujimoto, S. Isoda, F. Kim, K. Kamei, R. A. Fischer, S. Kitagawa and S. Furukawa, *J. Am. Chem. Soc.*, 2013, **135**, 10998.
13 S. Diring, D. O. Wang, C. Kim, M. Kondo, Y. Chen, S. Kitagawa, K. Kamei and S. Furukawa, *Nat. Commun.*, 2013, **4**, 2684.
14 C. He, K. Lu, D. Liu and W. Lin, *J. Am. Chem. Soc.*, 2014, **136**, 5181.
15 A. C. McKinlay, P. K. Allan, C. L. Renouf, M. J. Duncan, P. S. Wheatley, S. J. Warrender, D. Dawson, S. E. Ashbrook, B. Gil, B. Marszalek, T. Düren, J. J. Williams, C. Charrier, D. K. Mercer, S. J. Teat and R. E. Morris, *APL Mater.*, 2014, **2**, 124108.
16 D. Cunha, M. B. Yahia, S. Hall, S. R. Miller, H. Chevreau, E. Elkaim, G. Maurin, P. Horcajada and C. Serre, *Chem. Mater.*, 2013, **25**, 2767.
17 P. Horcajada, S. Surblé, C. Serre, D.-Y. Hong, Y.-K. Seo, J.-S. Chang, J.-M. Grenèche, I. Margiolaki and G. Férey, *Chem. Commun.*, 2007, 2820.
18 G. Férey, C. Mellot-Draznieks, C. Serre, F. Millange, J. Dutour, S. Surblé and I. Margiolaki, *Science*, 2005, **309**, 2040.
19 A. Demessence, P. Horcajada, C. Serre, C. Boissière, D. Grosso, C. Sanchez and G. Férey, *Chem. Commun.*, 2009, 7149.
20 A. O. Hohner, M. P. David and J. O. Rädler, *Biointerphases*, 2010, **5**, 1.
21 V. Cauda, H. Engelke, A. Sauer, D. Arcizet, C. Bräuchle, J. Rädler and T. Bein, *Nano Lett.*, 2010, **107**, 2484.
22 R. Rigler, *J. Biotechnol.*, 1995, **41**, 177.
23 S. Maiti, U. Haupts and W. W. Webb, *Biophys. J.*, 1997, **72**, 1878.
24 T. M. Allen and P. R. Cullis, *Adv. Drug Delivery Rev.*, 2013, **65**, 36.
25 B. Kneidl, M. Peller, G. Winter, L. H. Lindner and M. Hossann, *Int. J. Nanomed.*, 2014, **4**, 4387.

Supporting Information

MOF nanoparticles coated by lipid bilayers

and their uptake by cancer cells

Stefan Wuttke,*[a] Simone Braig,[‡b] Tobias Preiß,[‡c] Andreas Zimpel [a], Johannes Sicklinger,[a] Claudia Bellomo,[a] Joachim Rädler,[c] Angelika Vollmar,[b] and Thomas Bein*[a]

[a] *Department of Chemistry and Center for NanoScience (CeNS), University of Munich (LMU), Butenandtstraße 11, 81377 München (Germany),*

[b] *Department of Pharmacy, University of Munich (LMU), Butenandtstraße 5, 81377 München (Germany)*

[c] *Department of Physics, University of Munich (LMU), Geschwister Scholl Platz 1, 80539 München (Germany)*

[‡] *Both authors contributed equally to this work.*

E-Mail corresponding authors: stefan.wuttke@cup.uni-muenchen.de and bein@lmu.de.

Methods and Characterization

Powder X-ray diffraction (PXRD) measurements were performed using a Bruker D8 diffractometer (Cu-$K_{\alpha1}$ = 1.5406 Å; Cu-$K_{\alpha2}$ = 1.5444 Å) in *theta-theta* geometry equipped with a Lynx-Eye detector. The powder samples were measured between 2° and 45° *two theta*, with a step-size of 0.05° *two theta*.

Scanning electron microscopy (SEM) images were recorded with a JEOL JSM-6500F microscope equipped with a field emission gun, operated at an acceleration voltage of 5 kV and a working distance of 10 mm. Prior to measurements a thin gold layer (purity: 99.95%) was deposited on the samples using an Oerlikon Leybold Vacuum UNIVEX 350 sputter coater system operated at a base pressure of $1x10^{-6}$ mbar, an Argon pressure of $1x10^{-2}$ mbar, a power of 25 W and a sputtering time of 5 min.

Transmission electron microscopy (TEM). All samples were investigated with a FEI Titan 80-300 operating at 80 kV with a high-angle annular dark field detector. A droplet of the diluted nanoparticle solution in absolute ethanol was dried on a carboncoated copper grid.

Nitrogen sorption measurements were performed on a Quantachrome Instruments Autosorb at 77 K. Sample outgassing was performed for 12 hours at 393 K. Pore size and pore volume were calculated by a NLDFT equilibrium model of N_2 on silica, based on the adsorption branch of the isotherms. BET surface area was calculated over the range of partial pressure between 0.05 – 0.20 p/p_0. The pore volume was calculated based on the uptake (cm^3/g) at a relative pressure of 0.30 p/p_0.

Thermogravimetric (TG) analyses of the bulk samples were performed on a Netzsch STA 440 C TG/DSC with a heating rate of 1 K min^{-1} in a stream of synthetic air at about 25 mL min^{-1}.

Dynamic light scattering (DLS) measurements were performed on a Malvern Zetasizer-Nano instrument equipped with a 4 mW He-Ne laser (633 nm) and an avalanche photodiode. The hydrodynamic radius of the particles was determined by dynamic light scattering in a diluted aqueous suspension.

Fluorescence Correlation Spectroscopy (FCS) is a powerful single-molecule detection technique to characterize interactions and dynamics of fluorescent particles or molecules by correlating their fluorescence fluctuations, in a confocal detection volume ($\sim$1fL $= 10^{-15}$L) in time.[1] Brownian motion or active transport lets particles diffuse though the volume causing spontaneous intensity fluctuations similar to photodynamic processes and chemical reactions. The temporal autocorrelation function is defined by $G(\tau) = \frac{\langle F(t)F(t+\tau)\rangle}{\langle F\rangle^2}$ and provides information about the dynamic properties of the measured sample such as diffusion times and average numbers of particles within the focal volume. From these values the hydrodynamic radius and the particle concentration can be determined.

An extension of FCS is dual-color fluorescence cross-correlation (FCCS), which provides access to binding properties of two differently labeled species of particles in the sample.[2] Lasers with two different wavelengths focused to the same spot excite both of the two fluorophore types with different emission spectra. The two fluorescence signals get separated by a dichroic mirror and are recorded individually. By correlating the fluctuations $F_1(t)$ and $F_2(t)$ not only with themselves (autocorrelation) but also crosswise, the ensuing cross-correlation curve $G(\tau) = \frac{\langle F_1(t)F_2(t+\tau)\rangle}{\langle F_1(t)\rangle\langle F_2(t)\rangle}$ yields the amount of particles that show coincidence of both fluorescence colors. These results are accessible by fitting the correlation curves according to $G(\tau) = G(0)\frac{1}{1+\frac{\tau}{\tau_D}}\frac{1}{\sqrt{1+\frac{\tau}{S^2\tau_D}}}$, where S is the structure parameter, the ratio between the lateral and the axial confocal volume radius while τ_D is the mean time a particle needs to cross the focal volume.[3] The amplitude G(0) contains the mean particle count $N = (G(0))^{-1}$ within the focal volume of the autocorrelations.

The FCCS measurements were conducted with a ConfoCor2 (Zeiss, Jena) setup with a 40x NA1.2 water immersion objective employing a red 633nm HeNe- and a blue 488nm Ar-laser for excitation of the two fluorophores Atto633 (bound to MOF nanoparticles) and BODIPY FL (DHPE-Lipid embedded in the DOPC bilayer)

Due to physical and technical reasons, the alignment of the two exciting laser beams leads to slightly displaced laser foci. In addition to other effects, this causes non-overlapping correlation curves even if a perfect coincidence of both labels is obtained.

In order to subsequently correct these deviations, a DNA double-strand assumed to be perfectly double-labeled with both green and red fluorescent dye (similar to the dyes of the MOF-lipid sample) was measured with the same configuration as the MOF sample.

The data were fitted using OriginPro9 (Fig. S-1). By adjusting the fitted curves of the correlation of the MOF particles (red, ch1) and the cross correlation (black) to the one of the lipids (blue, ch2) we obtained factors to correct the MOF-lipid measurements. The blue-green (ch2) data-set was chosen to overlay the other data-sets because the alignment of the confocal beam path and detection path was optimized to the blue laser (488nm) and therefore the ch2 data provides the most reliable results.

The correction factors obtained are listed in Table 1. To correct the raw data, the formula $G(\tau)_{corrected} = \left((G_{raw}(\tau\cdot\alpha) - 1)\cdot\beta\right) + 1$ was applied. The subtraction and addition of 1 is necessary because the minimum value of the correlation curves is 1.

	α	β
Ch1 (red)	0,3513	0,7298
Cross-correlation (black)	0,2920	3,0922

Table S-1: Correction factors obtained from FCCS Data of a double labeled DNA double strand.

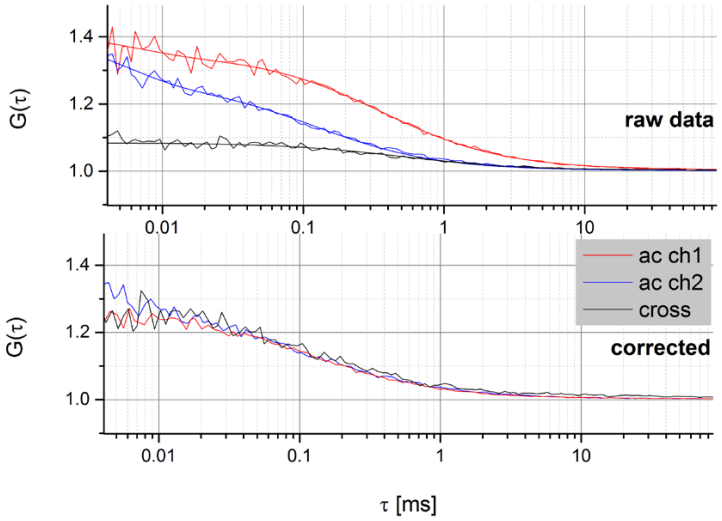

Fig. S-1 FCCS Data of a doubly labeled DNA double strand. The raw data (top) shows that the autocorrelations (red and blue) and cross-correlation (black) are not overlapping due to inevitable minor setup misalignments. To account for this, the fitting results were used to obtain correction factors to align all three curves (bottom). The same procedure was applied to the lipid-MOF results.

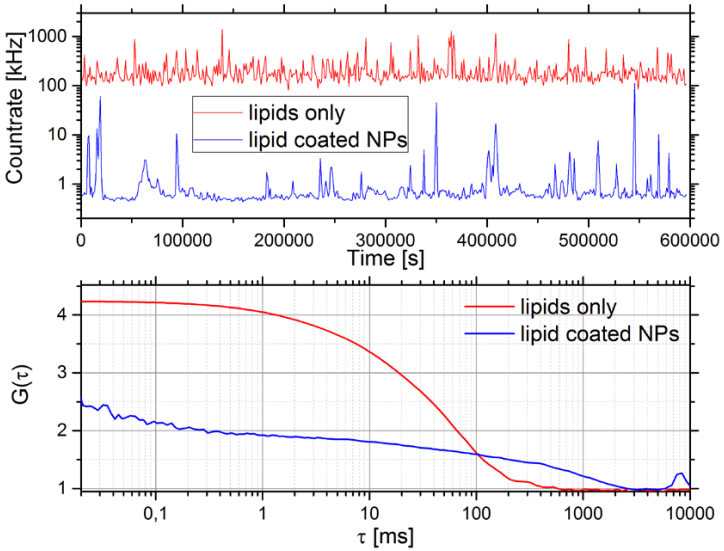

Fig. S-2 FCS Data of labeled lipids with and without MIL-100(Fe) NPs.

For the **fluorescence release experiments** an amount of 200 µL of the aqueous suspension containing MIL-101(Cr)@DOPC or MIL-100(Fe)@DOPC loaded with fluorescein (for preparation see experimental section) was transferred into the cap of a quartz cuvette (Fig. S-2, 1). The cap was sealed with a dialysis membrane (Fig. S-2, 2) and put on top of a cuvette that was filled with 3 ml H_2O. Only dye molecules can pass the membrane, but no nanoparticles. Consequently, dye molecules that were released from the pores of the particles are responsible for the measured fluorescence intensity. During fluorescence measurement, the water inside the cuvette was stirred (Fig. S-2, 3) and was heated to 37 °C. For the fluorescence measurement with a PTI spectrofluorometer (model 810/814, Photon Technology International), the monochromator slit was set to 1.25 mm, all other slits to 1.00 mm. The excitation wavelength of fluorescein (sodium salt) is 490 nm, the emission wavelength 512 nm. The measurement was run for 1 h with 1 point/min. After the addition of 20 µL of absolute Triton X-100 into the cap-system, the lysis of the lipid bilayer on the MOF nanoparticles allows the diffusion of the dye molecules from the pores and their detection in the cuvette (Fig. S-2, 3).

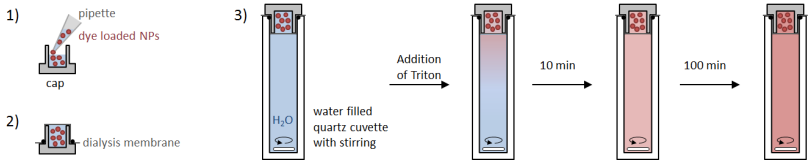

Fig. S-3 Scheme of the fluorescence release experiment. The sample was filled into a cap system that is closed by a dialysis membrane; the volume of the fluorescence cuvette was filled with water.

Confocal laser scanning microscopy and *in vitro* uptake of the nanoparticles. Membranes of bladder carcinoma cells were stained with the red fluorescence dye PKH26 (Sigma-Aldrich, St. Louis, MO, USA) according to manufacturer's instructions. In brief, adhered cells were detached, washed and incubated for 2 min with PKH26 dye solution. After further washing steps, cells were seeded on ibidi µ-slides (Ibidi, Munich, Germany) The next day, cells were treated with 20µl Atto-633 labelled MOF nanoparticles for indicated time points and fluorescence intensities were assessed using a Zeiss LSM 510 Meta microscope.

Impedance-based real-time cell monitoring. Cellular behaviour of MOF treated cells was analysed by utilizing the xCELLigence System (ACEA Biosciences, San Diego, CA, USA), which monitors cellular growth in real-time by measuring the electrical impedance across interdigitated microelectrodes covering the bottom of E-plates. Impedance is displayed as cell index values. T24 bladder carcinoma cells were seeded at a density of 5000 cells per well in E-plates and different charges of MOF nanoparticles (MOF#1 and #2) and amounts (4µl MOF/100µl medium and 8µl MOF/100µl medium) were added directly to the wells after about 18 h. Cell index tracings were normalized shortly after addition of the particles.

Experimental section

Chemicals

Chromium(III) nitrate nonahydrate (99%, *Aldrich*), terephthalic acid (98%, *Aldrich*), ethanol (99%, *Aldrich*) 1,2-dioleoyl-sn-glycero-3-phosphocholine (DOPC, *Avanti Polar Lipids*), fluorescein sodium salt suitable for fluorescence (*Fluka*), triton X-100 (*Aldrich*), N-(4,4-difluoro-5,7-dimethyl-4-bora-3a,4a-diaza-s-indacene-3-propionyl)-1,2-dihexadecanoyl-sn-glycero-3-phosphoethanolamine, triethylammonium salt (BODIPY® FL DHPE, *Invitrogen*).

Synthesis of MIL-101(Cr) nanoparticles

The microwave synthesis of MIL-101(Cr) nanoparticles was based on a modified procedure reported in the literature.[4, 5] An amount of 20 mL (1.11 mol) of H_2O was added to 615 mg (3.70 mmol) terephthalic acid and 1.48 g $Cr(NO_3)_3 \cdot 9\,H_2O$ (3.70 mmol). This mixture was put into a Teflon tube, sealed and placed in the microwave reactor (Microwave, Synthos, *Anton Paar*). Four tubes were filled and inserted into the reactor: one tube contained the reaction mixtures described above; the remaining tubes including the reference tube with the pressure/temperature sensor (PT sensor) were filled with 20 mL H_2O. For the synthesis, a temperature programme was applied with a ramp of 4 min to 180 °C and a holding time of 2 min at 180 °C. After the sample had cooled down to room temperature, it was filtrated and washed with 50 ml EtOH to remove residual e.g. terephthalic acid. For purification, the filtrate was centrifuged and redispersed in 50 ml EtOH three times. The sample was centrifuged at 20000 rpm (47808 rcf) for 60 min. Afterwards the sample was characterized by DLS, XRD, IR, TGA, BET, REM and TEM measurements.

Synthesis of MIL-100(Fe) nanoparticles

For the microwave synthesis of MIL-100 (Fe) nanoparticles, iron(III) chloride hexahydrate (2.43 g, 9.00 mmol) and trimesic acid (0.84 g, 4.00 mmol) in 30 ml H_2O were put into a Teflon tube, sealed and placed in the microwave reactor (Microwave, Synthos, *Anton Paar*).[6] The mixture was heated to 130 °C under solvothermal conditions (p = 2.5 bar) within 30 seconds, kept at 130 °C for 4 minutes and 30 seconds and the tube was cooled down to room temperature. For the purification of the solid, the reaction mixture was centrifuged

(20000 rpm = 47808 rcf, 20 min), the solvent was removed and the pellet was redispersed in 50 ml EtOH. This cycle was repeated two times and the dispersed solid was allowed to sediment overnight. The supernatant of the sedimented suspension was filtrated (filter discs grade: 391, *Sartorius Stedim Biotech*) three times, yielding MIL-100(Fe) nanoparticles. Afterwards the sample was characterized by DLS, XRD, IR, TGA, BET, REM and TEM measurements.

Synthesis of MIL-101(Cr)@DOPC and MIL-100(Fe)@DOPC nanoparticles with encapsulated dyes for fluorescence release and for in vitro experiments

The amount of 1 mg MIL-101(Cr) or MIL-100(Fe) nanoparticles was dispersed in 1 mL of a 1 mM aqueous solution of fluorescein (sodium salt). 24 h later the samples were centrifuged for 5 min at 14000 rpm (16873 rcf). For the application of the lipid layer, the sample was redispersed in 100 µL of a 3.6 mM DOPC (1,2-dioleoyl-sn-glycero-3-phosphocholine) solution in a 60/40 (v/v) H_2O/EtOH mixture. 900 µL H_2O was added and mixed as quickly as possible. By increasing the water concentration, the lipid molecules precipitate and are expected to cover the nanoparticle surface with a lipid layer. For purification, the suspension was centrifuged (5 min, 14000 rpm = 16873 rcf), redispersed in 1 mL H_2O and again centrifuged. Finally the nanoparticles were redispersed in 200 µL H_2O.

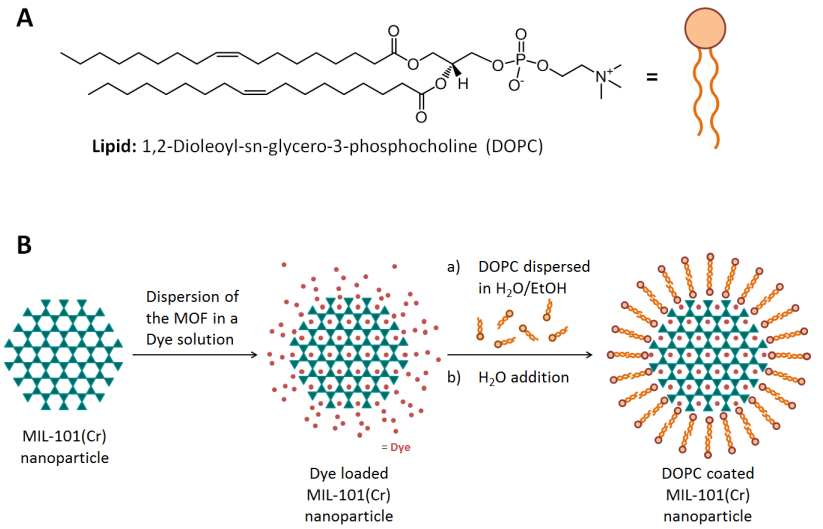

Fig. S-4 (A) Illustration of the lipid DOPC. **(B)** Schematic depiction of MIL-101(Cr) nanoparticles which are loaded with a dye in the first step, and coated with a lipid bilayer on the MOF nanoparticle surface in the second step.

Synthesis of labeled MIL-101(Cr)@DOPC nanoparticles for FCCS measurements

Loading of MOFs with dye. The amount of 1 µL ATTO 633 NHS (ATTOTec) stock solution (c = 1 mg/ml) was mixed with 100 µL MilliQ water (bi-distilled water from a Millipore system (Milli-Q Academic A10)) just before adding 25µL of this solution to 250 µL of a 10 mg/mL aqueous MOF suspension. This labeling solution was then stirred at room temperature for 48 hours. The nanoparticles were separated from free ATTO 633 molecules by centrifugation (19.000rpm = 20138 rcf, 45min) and resuspending with 1mL MilliQ water, and repeating this cycle 5 times.

Lipid preparation. The amount of 2.5 mg DOPC lipid (1,2-dioleoyl-sn-glycero-3-phosphocholine, Avanti Polar Lipids) was mixed with 0.2 µg BODIPY FL DOPE lipid (N-(4,4-difluoro-5,7-dimethyl-4-bora-3a,4a-diaza-s-indacene-3-propionyl)-1,2-dihexadecanoyl-sn-glycero-3-phosphoethanolamine, Invitrogen) in chloroform (99.995 mol% DOPC and 0.005 mol% BODIPY FL DHPE). After evaporating the chloroform with nitrogen gas, the

lipids were further dried in a vacuum overnight. The lipids were then dissolved in 1 mL of a 40 % ethanol/60 % water (v/v) solution to a final concentration of 2.5 mg/mL.

Lipid coating of the MOFs. The amount of 2.5mg labeled MOFs (labeling solution) were centrifuged (19.000 rpm = 20138 rcf, 45min). Afterwards 100 µL of the DOPC/BODIPY FL DHPE lipid in ethanol/water mixture was added. To induce the formation of lipid bilayer on the MOF surface, we quickly added 900 µL of MilliQ water. Afterwards the sample was ready to use for the FCCS measurements.

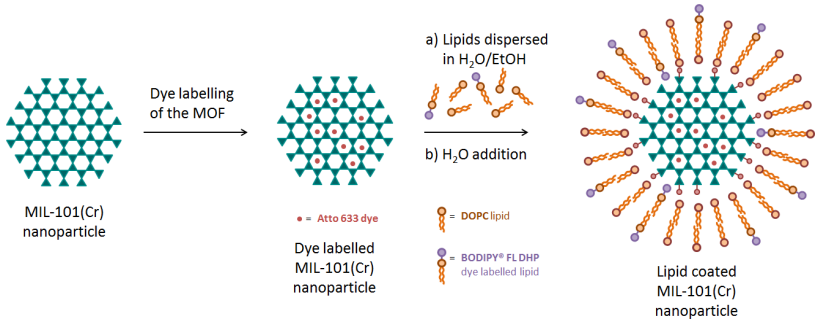

Fig. S-5 Schematic illustration of the dye labelling of MIL-101(Cr) nanoparticles in the first step and the formation of a labeld lipid bilayer on the MOF surface in the second step.

Supplementary Figures

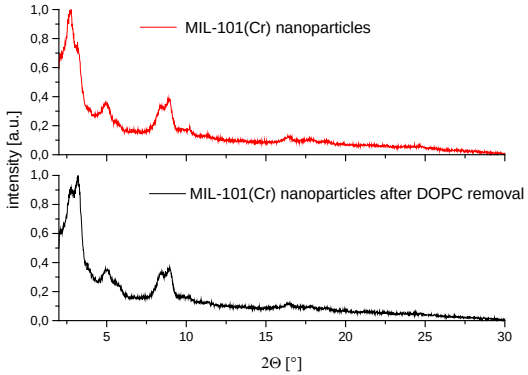

Fig. S-6 X-ray powder diffraction patterns of uncoated MIL-101(Cr) nanoparticles (top) and DOPC coated MIL-101(Cr) nanoparticles after removal of the lipid (bottom).

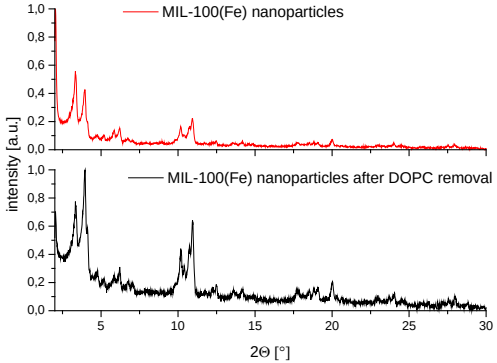

Fig. S-7 X-ray powder diffraction patterns of uncoated MIL-100(Fe) nanoparticles (top) and DOPC coated MIL-100(Fe) nanoparticles after removal of the lipid (bottom).

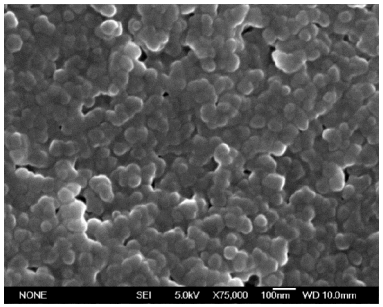

Fig. S-8 Scanning electron micrograph of MIL-101(Cr) nanoparticles.

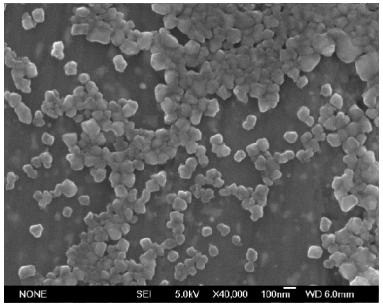

Fig. S-9 Scanning electron micrograph of MIL-100(Fe) nanoparticles.

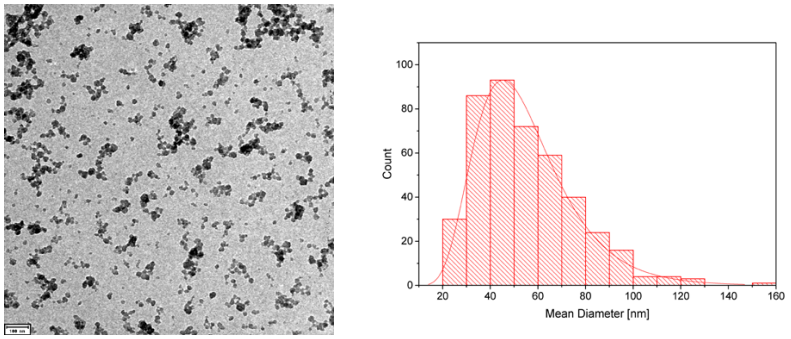

Fig. S-10 Transmission electron micrograph of MIL-101(Cr) nanoparticles (left). Size distribution of MIL-101(Cr) nanoparticles from the TEM picture (right).

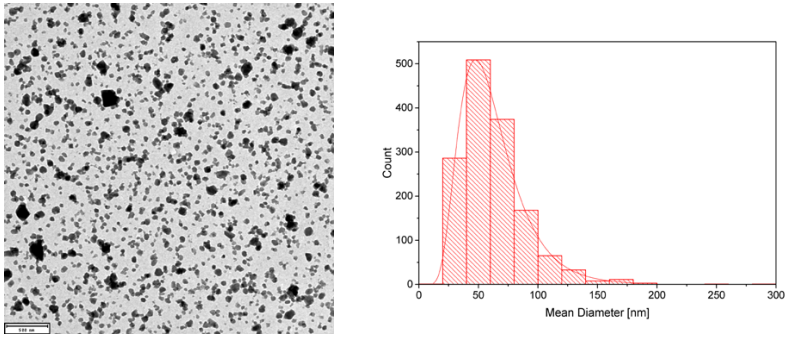

Fig. S-11 Transmission electron micrograph of MIL-100(Fe) nanoparticles (left). Size distribution of MIL-100(Fe) nanoparticles from the TEM picture (right).

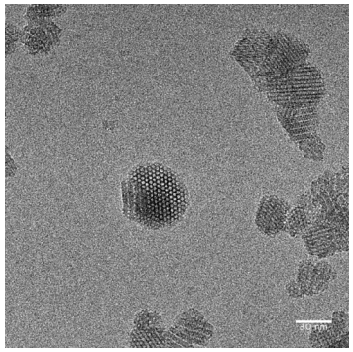

Fig. S-12 Transmission electron micrograph of MIL-101(Cr) nanoparticles – detailed image.

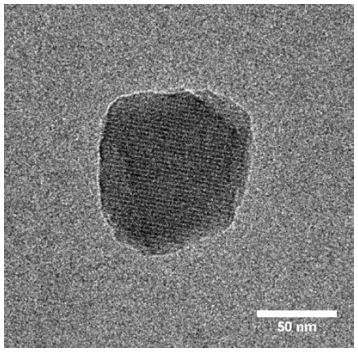

Fig. S-13 Transmission electron micrograph of MIL-100(Fe) nanoparticle – detailed image.

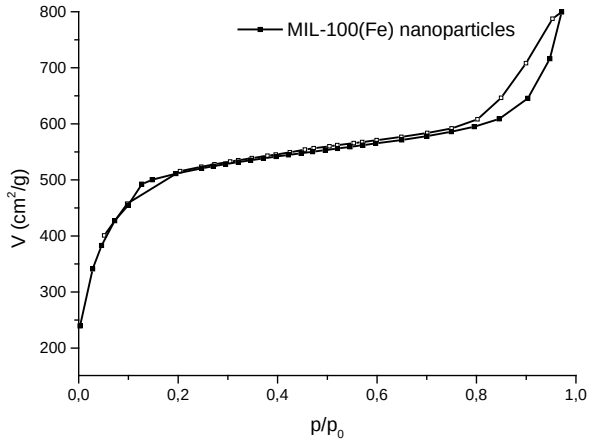

Fig. S-14 Nitrogen sorption isotherm of MIL-100(Fe) nanoparticles. Calculated BET surface: 2004 m^2/g.

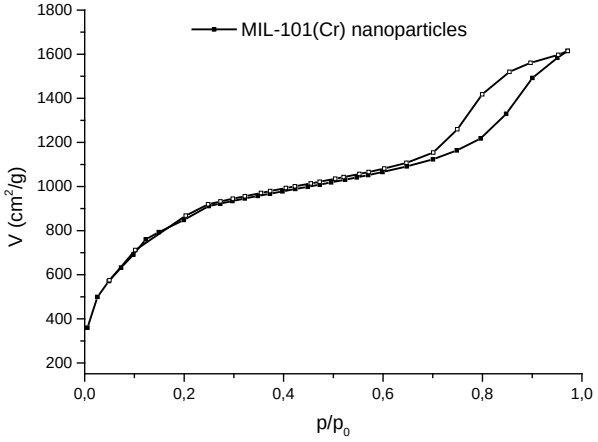

Fig. S-15 Nitrogen sorption isotherm of MIL-101(Cr) nanoparticles. Calculated BET surface: 3205 m^2/g.

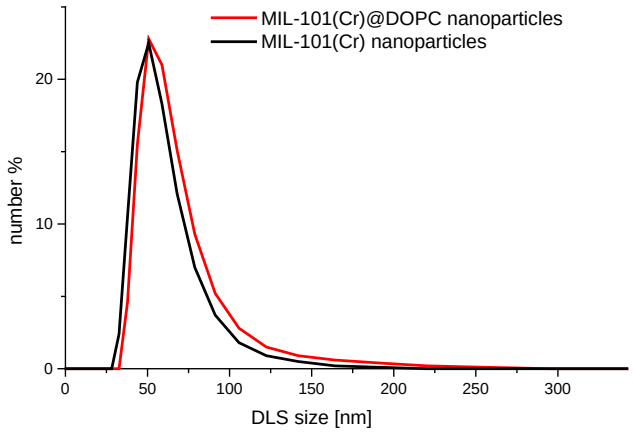

Fig. S-16 DLS size distribution (measured in water) by number comparing uncoated and DOPC-coated MIL-101(Cr) nanoparticles.

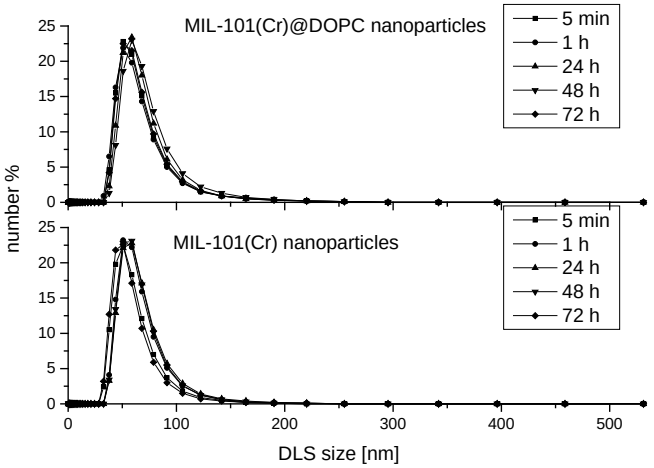

Fig. S-17 DLS size distributions by number comparing uncoated and DOPC-coated MIL-101(Cr) nanoparticles over a time period of 72 h.

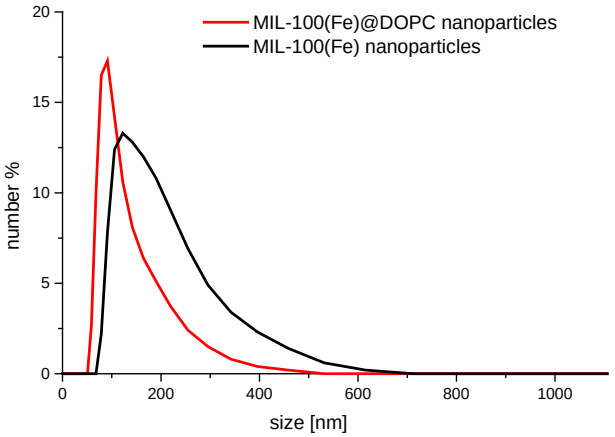

Fig. S-18 DLS size distribution by number (measured in water) comparing uncoated and DOPC-coated MIL-100(Fe) nanoparticles.

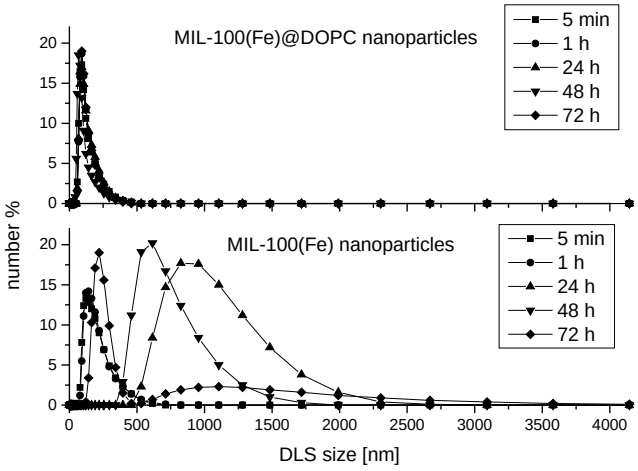

Fig. S-19 DLS size distribution by number, comparing uncoated and DOPC-coated MIL-100(Fe) nanoparticles over a time period of 72 h.

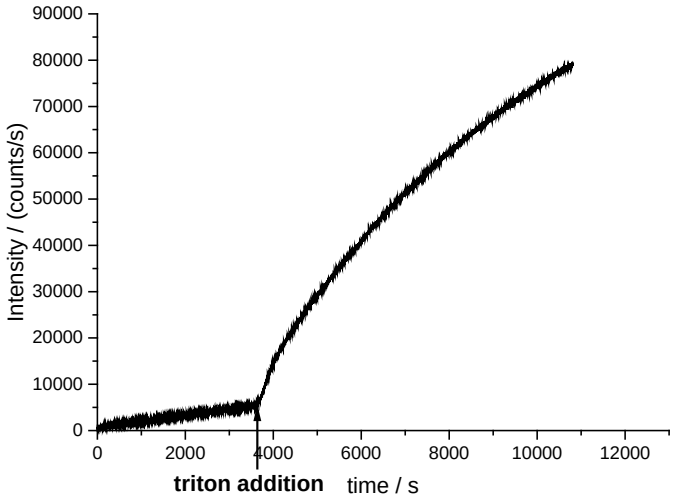

Fig. S-20 Fluorescein release from DOPC-coated MIL-100(Fe) nanoparticles before and after addition of Triton X-100.

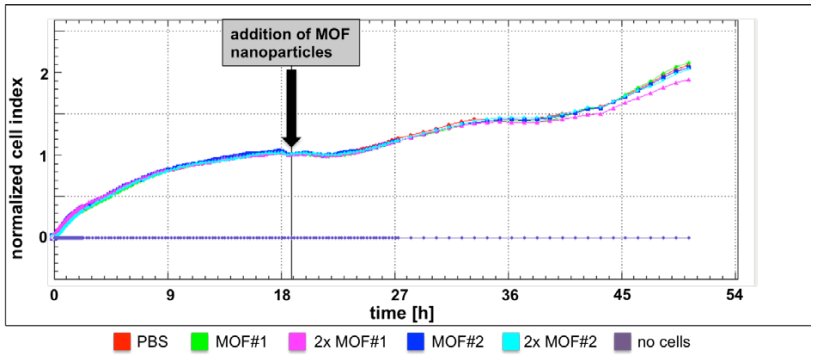

Fig. S-21 Impedance measurements of cell cultures. Bladder carcinoma cells were seeded on xCELLigence E-plates and treated at indicated time points with different charges (MOF#1 and MOF#2) and amounts of 6,4 µl and 12,8 µl of MIL-101(Cr)@DOPC nanoparticles (c = 1 mg/ml) per 200 µl medium. Similar cell index values indicate that cells incubated with MOF nanoparticles show a behaviour very similar to PBS-treated control cells.

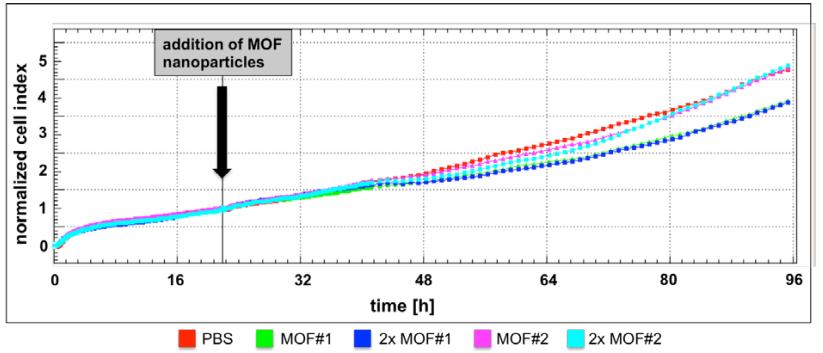

Fig. S-22 Impedance measurements of cell cultures. Bladder carcinoma cells were seeded on xCELLigence E-plates and treated at indicated time points with different charges (MOF#1 and MOF#2) and amounts of 6,4 µl and 12,8 µl of MIL-100(Fe)@DOPC nanoparticles (c = 1 mg/ml) per 200 µl medium. Similar cell index values indicate that cells incubated with MOF nanoparticles show a behaviour similar to PBS-treated control cells.

References

[1] D. Magde, W.W. Webb, E.L. Elson, *Biopolymers*, **1978**, 17, 361.

[2] P. Schwille, F.J. Meyer-Almes, R. Rigler. *Biophysical journal* **1997**, 72, 1878.

[3] P. Schwille, E. Haustein, *Spectroscopy*, 2009, 94, 1.

[4] Demessence, A.; Horcajada, P.; Serre, C.; Boissiere, C.; Grosso, D.; Sanchez, C.; Ferey, G., Chem. Commun. 2009, 46, 7149.

[5] Jiang, D.; Burrows, A. D.; Edler, K. J., CrystEngComm 2011, 13, 23, 6916.

[6] P. Horcajada, T. Chalati, C. Serre, B. Gillet, C. Sebrie, T. Baati, J. F. Eubank, D. Heurtaux, P. Clayette, C. Kreuz, J.-S. Chang, Y. K. Hwang, V. Marsaud, P.-N. Bories, L. Cynober, S. Gil, G. Férey, P. Couvreur, R. Gref, *Nature Mat.*, 2010, **9**, 172.

B.2 Originalpublikation P2

Patrick Hirschle, Tobias Preiß, Florian Auras, André Pick, Johannes Völkner, Daniel Valdepérez, Gregor Witte, Wolfgang J. Parak, Joachim O. Rädler and Stefan Wuttke.
Exploration of MOF nanoparticle sizes using various physical characterization methods – is what you measure what you get?
CrystEngComm, 2016
Reproduced from Ref. [59] with permission from The Royal Society of Chemistry.

CrystEngComm

PAPER

View Article Online
View Journal

Cite this: DOI: 10.1039/c6ce00198j

Exploration of MOF nanoparticle sizes using various physical characterization methods – is what you measure what you get?†

Patrick Hirschle,[a] Tobias Preiß,[b] Florian Auras,[a] André Pick,[c] Johannes Völkner,[c] Daniel Valdepérez,[c] Gregor Witte,[c] Wolfgang J. Parak,[c] Joachim O. Rädler[b] and Stefan Wuttke*[a]

Received 25th January 2016,
Accepted 3rd March 2016

DOI: 10.1039/c6ce00198j

www.rsc.org/crystengcomm

While the size of nanoparticles (NPs) seems to be a concept established in the field of NPs and is commonly used to characterize them, its definition is not that trivial as different "sizes" have to be distinguished depending on the physical characterization technique performed to measure them. Metal–organic frameworks (MOFs) are known for their crystallinity, their large variety of compositions due to a huge number of inorganic building blocks that can be combined with almost endless organic linkers, their tunable pore structure, their ultrahigh porosity, and the different ways their backbones can be functionalised. The combination of these features with the nanoworld offers manifold perspectives for the synthesis of well-defined MOF nanoparticles (NPs), whose size attribute should be accurately determined as it strongly influences their physicochemical properties (at this length scale). In order to elucidate size determination, we synthesised zirconium fumarate metal–organic framework nanoparticles (Zr-fum MOF NPs) and characterized them using various common characterization methods. Herein, we compare the results of different solid-state methods, including powder X-ray diffraction (PXRD), atomic force microscopy (AFM), scanning electron microscopy (SEM) and transmission electron microscopy (TEM) to data obtained from dispersion-based methods, such as fluorescence correlation spectroscopy (FCS) and dynamic light scattering (DLS). In doing so, we illustrate the challenge of finding the appropriate method for obtaining a MOF NP size that is meaningful in the context of the desired application. Moreover, we demonstrate the importance of applying multiple complementary techniques as soon as the MOF NP size is considered. Throughout this paper, we highlight and define some reasonable recommendations of how the MOF NP size should be explored.

Introduction

Metal–organic frameworks (MOFs) are organic–inorganic hybrid crystalline compounds consisting of inorganic metallic clusters, also referred to as nodes, that are connected by organic linker molecules, *i.e.* spacers.[1–3] Owing to the many possible combinations of organic linkers and metal ions, a vast number of MOF structures, now up to more than 20 000, have been reported so far.[3] Over the last few years, MOFs have attracted considerable scientific interest due to their wide structural and chemical tailorability,[4–6] their high surface area,[7–10] as well as the many possible different ways to functionalise their surface.[11–17] These characteristics have allowed for broad applications in various fields such as separation,[18] storage,[19–22] catalysis,[23–28] sensing,[29–31] drug delivery,[32,33] diagnosis[32,33] and ionic conduction.[34] Furthermore, it has been shown that MOF crystal size can be controlled at the nanometre level to build MOF nanoparticles (MOF NPs).[35–45] Owing to the modular synthesis approach, together with spatial control of chemical moieties within the crystalline framework MOF chemistry offers, MOF NPs appear as a promising new class of functional NPs amongst the already existing NP material classes.

Control of MOF crystal size at the nanometre level results in MOF NPs whose properties are no longer determined by their inner surface only, but also by their outer surface properties, due to their high external surface-area-to-volume ratio.[46–50] When bulk materials are reduced to the nanometer size, their properties and their behaviour often become size- and shape-dependent. Examples of downsized MOF NPs and the resulting effects on their crystal structure and sorption behaviour are reported elsewhere.[51–53] Hence, the determination and the knowledge of both the size and shape of NPs are of paramount importance.[54] However, the obvious but important question – *What is the "size" of a NP?* – is not straightforward to answer as the "size" of a NP differs depending on what characterization technique is used and in which state the NP size is measured.[55] Various techniques relying on different physical principles and data processing methods are available to determine particle size and each one has its own advantages and drawbacks. In particular, once dissolved in solution, NPs interact with the solvent, *e.g.* by hydration, ion-adsorption,[56] or agglomeration,[57] and thus their effective size may significantly change.[58]

In this article, the most widespread physical methods in the field of nanomaterial characterization, *i.e.* solid state methods, including X-ray diffraction (XRD), atomic-force microscopy (AFM), scanning electron microscopy (SEM) and transmission electron microscopy (TEM), as well as dispersion-based methods, such as dynamic light scattering (DLS) and fluorescence correlation spectroscopy (FCS), were applied to characterize and determine the size of zirconium-fumarate (Zr-fum) MOF NPs.[59,60] Fig. 1 summarises the characterization techniques that contribute to determine the size of Zr-fum MOF NPs. The Zr-fum MOF NPs were synthesised based on a synthesis route reported by Behrens and co-workers (structural details of the Zr-fum MOF structure can be found in the ESI†).[61] In that report, the authors showed that particle size could be controlled using formic acid as a modulator. The spherical morphology of the Zr-fum MOF NPs and the associated facile definition of the particle size (*i.e.* diameter) make the compound a prime example to showcase the various size determination methods.

In this work, we briefly discuss the physical principle of each size characterization method and show each method's practical advantages and disadvantages in NP size assessment. Then, we compare the various "sizes" obtained for the Zr-fum MOF NPs using the different techniques and finally, we discuss the meaning and appropriateness for MOF NP characterization in general.

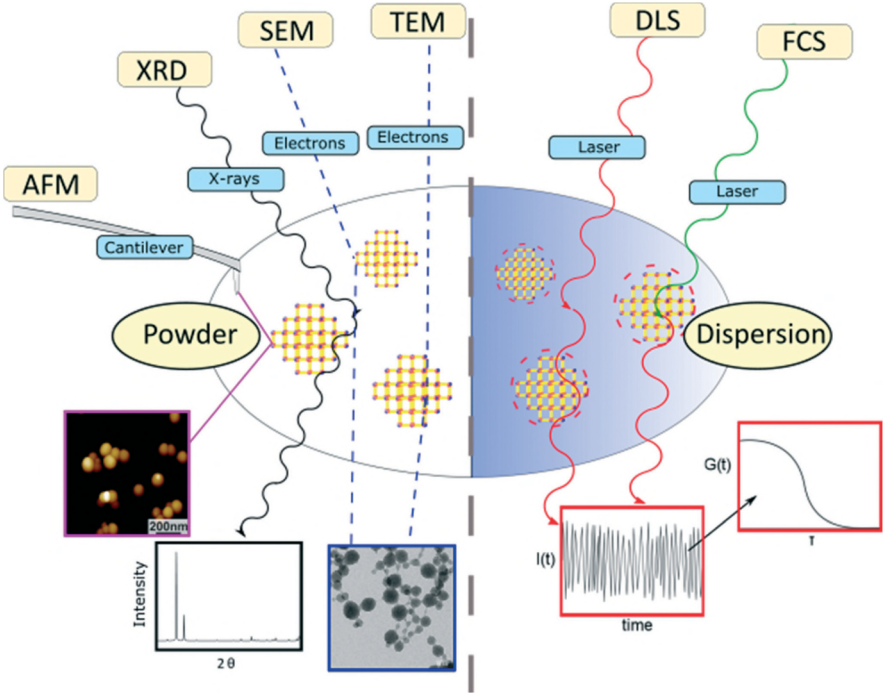

Fig. 1 | Overview of the methods used to determine the size of Zr-fum MOF nanoparticles (atomic-force microscopy (AFM), X-Ray diffraction (XRD), transmission electron microscopy (TEM), scanning electron microscopy (SEM), dynamic light scattering (DLS) and fluorescence correlation spectroscopy (FCS)).

[a] Department of Chemistry and Center for NanoScience (CeNS), University of Munich (LMU), Butenandtstraße 11, 81377 Munich, Germany. E-mail: stefan.wuttke@cup.unimuenchen.de
[b] Faculty of Physics and Center for NanoScience (CeNS), University of Munich (LMU), Geschwister-Scholl-Platz 1, 80539 Munich, Germany
[c] Faculty of Physics, Philipps University Marburg, Renthof 7, 35037 Marburg, Germany
† Electronic supplementary information (ESI) available. See DOI: 10.1039/c6ce00198j

Published on 04 March 2016. Downloaded by Ludwig Maximilians Universitaet Muenchen on 09/05/2016 10:39:35.

Results

The Zr-fum MOF NPs were synthesised using the same approach used by Behrens and co-workers.[61] The synthesis is carried out solvothermally in water using $ZrCl_4$ substrates and fumaric acid (see the ESI† for more details). In the subsequent section, we first display the results of solid-state based methods such as SEM, TEM, AFM and XRD. Even for those methods, the experimental conditions of measurements may be very different. While TEM requires operation in vacuum, for example, AFM could be carried out in a fluid cell on NPs adsorbed on a surface. In addition to determination of particle size, all the techniques offer some different advantages of identifying Zr-fum MOF NPs, such as confirming their crystallinity and determining their 2- or 3-dimensional morphology. Thereafter, the outcomes of dispersion-based methods such as DLS and FCS, which need to be carried out in the liquid phase, are showcased. Those techniques are suitable for studying NP properties such as their aggregation behaviour and their hydrodynamic diameters, which are specific to dispersions.

Scanning electron microscopy (SEM)

Scanning electron microscopy is one of the most widely used techniques to characterise nanomaterials. This method relies on the use of an electron beam, whose energy is around 5 keV, that scans the surface of a solid sample. The electrons of the focused incident beam impinge on the sample surface and generate secondary electrons, which are collected using a detector and used to create the sample image. SEM analyses were performed on a sample that was prepared by drying an ethanol-based dispersion of Zr-fum MOF NPs followed by carbon-sputtering. They reveal the spherical morphology of the NPs, as shown in Fig. 2a. The size distribution of the Zr-fum MOF NPs was determined by measuring the diameter of approximately 1000 NPs (Fig. S4†). The resulting values were plotted in a histogram and fitted with a Gaussian function (Fig. 2b) centred on an average NP diameter of $d^{SEM}_{Zr\text{-}fumNPs}$ = 62.0 ± 18.9 nm. It is worth noting that SEM requires conductive substrates in order to avoid charging effects, and thus a non-conductive Zr-fum MOF NP sample should be sputtered with a conductive film before being analysed.

Transmission electron microscopy (TEM)

In the transmission electron microscopy experiment, a high-energy electron beam (E ~200 keV) is focused on a thin sample (typically less than 200 nm) made of a carbon grid on which a droplet of a NP suspension has been evaporated. The electrons passing through the sample, in other words being transmitted, are scattered at different angles and are then focused with a lens system on a detector to achieve micrographs with a high lateral spatial resolution. TEM offers the important advantages of high magnification, ranging from 50 to 10^6 and the ability to provide both image and diffraction pattern information. The latter one is especially crucial for MOF NPs, as it proves the crystallinity of the structure. A typical TEM micrograph of Zr-fum MOF NPs is depicted in Fig. 2c and proves the spherical shape of the NPs. Moreover, this picture also shows that the NPs are interconnected *via* necks. The histogram shown in Fig. 2e reports the distribution of NP diameter, which was measured on approximately 1000 individual specimens (Fig. S9–S13†). The adjustment of this distribution with a normal law gives rise to an average NP diameter with a standard deviation of $d^{TEM}_{Zr\text{-}fumNPs}$ = 29 ± 12.9 nm.

Fig. 2d shows the electron diffraction pattern of the Zr-fum MOF NP sample. The radial distance of the apparent spots indicates the lattice distance in reciprocal space. A comparison among the tabulated values for the Zr-fum MOF crystal structure shows very good agreement (see Table S4†). Although no crystal fringes are displayed in Fig. 2c, the Debye–Scherrer rings shown in Fig. 2d prove the crystallinity of the sample. Upon prolonged exposure to the high-energy electron beam (200 keV), the Debye–Scherrer rings gradually disappear over an exposure time of around 30 s (Fig. S6–S8†). This indicates that the sample is damaged resulting in loss of the Zr-fum MOF NP crystallinity (Fig. 2c). However, the electron diffraction pattern shown in Fig. 2d was generated from a larger sample area, causing the rate of the impinging electrons to be lower and the sample to be destroyed much slower.

Atomic force microscopy (AFM)

In atomic force microscopy, the sample is analysed by rasterising its surface with a sharp tip attached to a cantilever. In our case, the measurements were performed in a closed loop tapping mode in air, in which the cantilever is excited to vibrate close to its resonance frequency using a piezoelectric device. The interactions between the cantilever-tip and the sample surface, *i.e.* repulsive Coulomb forces and attractive van der Waals forces, change the amplitude of the cantilever oscillation. A feedback loop constantly adjusts the height of the cantilever to maintain a defined oscillation amplitude, whose variations are used to generate a topographic image of the sample. Fig. 2f displays the AFM micrograph of a Zr-fum MOF NP sample prepared by drying an ethanolic NP-dispersion on a SiO_2 slide. Apart from individual NPs, we also observe agglomerated NPs, which can come from the sample preparation. In order to obtain the size of individual particles, the measurements were realised in the outermost periphery of the dried droplet were the density of the particles is minimised. From the AFM images, particle sizes have been determined statistically using the particle and pore analysis tool integrated in the Scanning Probe Image Processing (SPIP) (see the ESI†). The NP height distribution is plotted in Fig. 2g. The Gaussian curve fit is centred on an average NP diameter of $d^{AFM}_{Zr\text{-}fumNPs}$ = 68 nm with a standard deviation equal to 15 nm.

X-Ray diffraction (XRD)

In X-ray diffraction experiments, the elastic diffraction of X-rays on the atoms of a solid sample is used to identify its atomic and molecular structure. The Scherrer equation relates the broadening of a peak in a powder diffraction pattern

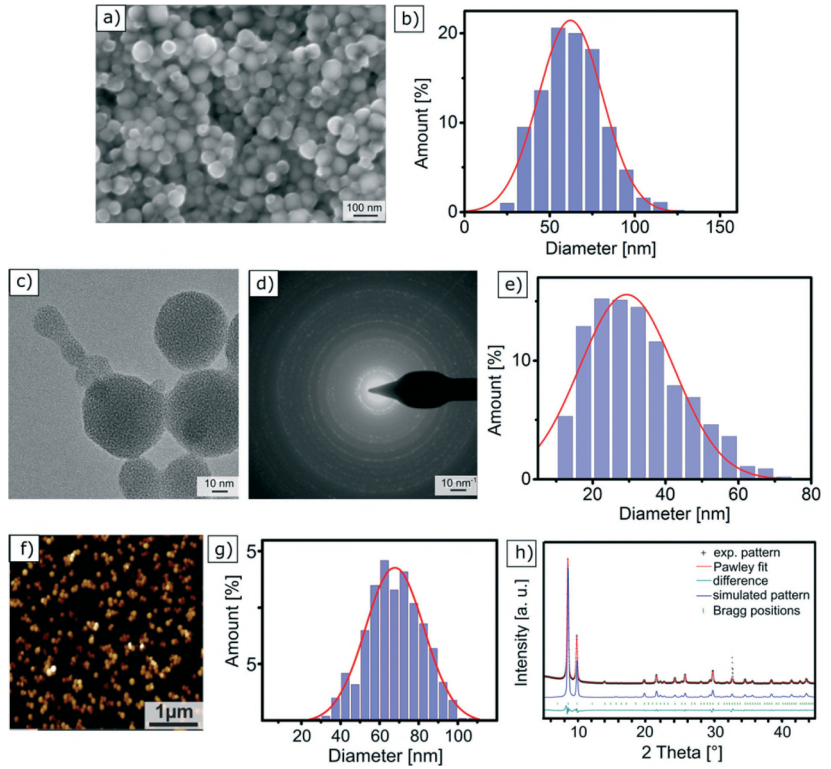

Fig. 2 | Characterisation of Zr-fum MOF NPs with different methods: (a) SEM micrograph; (b) particle size distribution of Zr-fum MOF NPs from SEM images (Fig. S4†); (c) TEM micrograph; (d) electron diffraction pattern of Zr-fum MOF NPs; (e) particle size distribution of Zr-fum MOF NPs from TEM images (Fig. S9–S13†); (f) AFM micrograph; (g) particle size distribution of Zr-fum MOF NPs from AFM images; (h) experimental PXRD pattern of the Zr-fum-3 MOF NPs (black symbols), Pawley fit (red), Bragg positions (green symbols) and the difference between the Pawley fit and the experimental data (dark green). The observed reflection intensities are in very good agreement with the simulated PXRD pattern (blue) based on the *Pn*-3 symmetry of the Zr-fum MOF structure model.[53]

to NP size and is therefore applied to calculate NP diameter (see the ESI†). As MOFs are crystalline materials, the determination of crystallite size and its comparison to particle size is of interest, since it can be used to estimate if single crystals or polycrystals are dominant in a sample.

The powder X-ray diffraction (PXRD) patterns of the Zr-fum MOF NP samples feature well-defined reflections across the entire measurement range, indicating the formation of well-ordered frameworks (Fig. 2h and Fig. S14†). Moreover, the experimental reflection intensities match the simulated pattern based on the reported Zr-fum structure[61] (blue line in Fig. 2h) very well, thus confirming the formation of a cubic Zr-fum MOF.

Analysis of PXRD data is commonly performed *via* Pawley fitting.[62] This method compares a theoretical diffraction pattern derived from a structure model to the corresponding experimental data, and varies unit cell parameters and peak profiles until convergence criteria are reached. Unlike the Rietveld method, Pawley fitting treats peak areas as variables, thus rendering this method also applicable to patterns recorded in reflection geometry, at the cost of not being able to refine atomic positions. We used the Pawley method to extract the lattice parameter *a* from the reflection positions and the average crystal domain size *d* from the peak broadening (see the ESI† for details).

Pawley fitting using the above mentioned structure model led to a lattice parameter *a* ranging from 17.88 ± 0.03 Å to 17.91 ± 0.03 Å for the Zr-fum MOF NP samples (ESI,† Fig. S14), which are very similar to the lattice parameter of 17.91 Å that has been reported for the bulk material.[61] We then extracted the average

crystal domain size d from the peak broadening taking into account the instrument broadening and the line shapes (see Section 2 "X-ray Diffraction" in the ESI† for details). This domain size ranges from $d^{XRD}_{Zr\text{-}fumNPs} = 42 \pm 5$ nm to 60 ± 5 nm.

In contrast to the other methods discussed above, XRD analysis provides the size of crystalline domains rather than the geometrical shape. In the case of defect-free single-crystalline NPs, these two quantities would be identical. In reality, a fraction of NPs will feature grain boundaries or other defects that disrupt the periodicity of the crystal. The average domain size of the NP powder sample will thus be smaller than the average particle size as determined by TEM, for example.

With the presentation of the results stemming from the solid-state based methods being finished, the outcomes of the dispersion-based methods are broached in the following paragraphs. It is worth noting that the results of these methods may strongly depend on the solvent in which the NPs are dispersed.

Dynamic light scattering (DLS)

Dynamic light scattering is probably the most frequently used technique for determining the hydrodynamic diameter of particles, which is defined as the "size" of a hypothetical homogeneous hard sphere that diffuses in the same fashion as that of the particle being measured. The working principle of DLS relies on measuring the intensity fluctuations caused by interference of laser light that is scattered by diffusing particles. Temporal evolution of the fluctuations depends on the particle movement caused by Brownian motion. It is therefore correlated to the diffusion coefficient of NPs, which depends on their size. When tracing this intensity over time, it is possible to plot a second order autocorrelation function. From this autocorrelation function, the diffusion coefficient of a particle can be retrieved using a fitting model. However, caution should be taken as the resultant computed hydrodynamic diameter is dependent on the chosen fit model, which typically is hidden as a black-box in a machine.[63] In our study, the average hydrodynamic diameter of Zr-fum MOF NPs was first determined in water (see Fig. 3b (black)) to have a good comparability with similar FCS measurements (see next section). Subsequently, the particles were examined in ethanol (see Fig. 3b (red)) to show the NPs behaviour in such a typical solvent (see the ESI†). Diluted dispersions of the NPs were analysed, and the resulting autocorrelation function was fitted using the "method of cumulants" (for more details, see the ESI†). In water, this resulted in NPs featuring a hydrodynamic diameter of $d^{DLS}_{Zr\text{-}fumNPs} = 42$ nm with a standard deviation of $\sigma = 46$ nm. In ethanol, their hydrodynamic diameter was equal to $d^{DLS}_{Zr\text{-}fumNPs} = 130$ nm and with a standard deviation of $\sigma = 48$ nm.

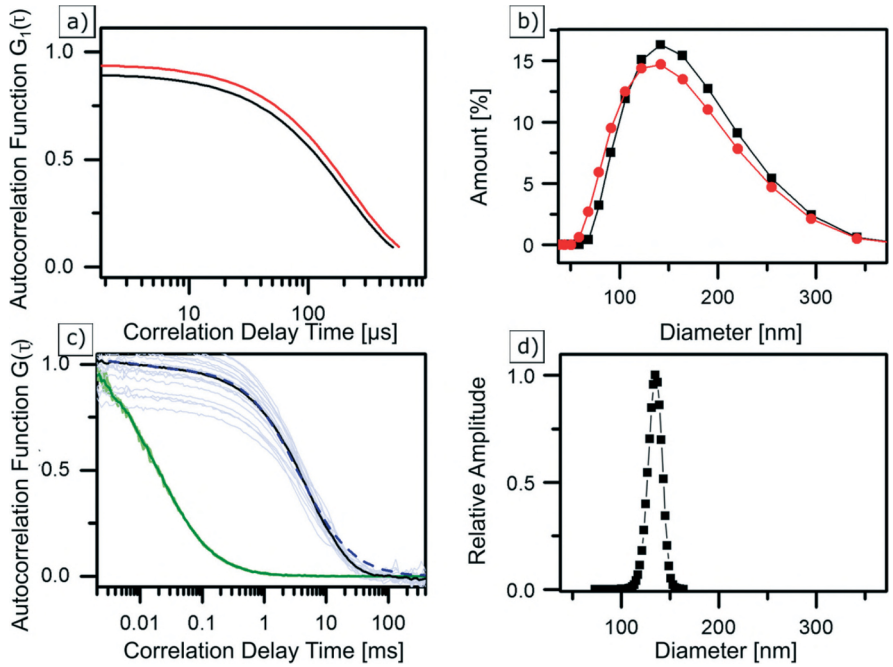

Fig. 3 | DLS correlation data (a) and size distribution (b) of Zr-fum MOF NPs in ethanol (red) and water (black) as well as averaged and normalised FCS autocorrelation curves (c) of Alexa Fluor 488 (green) and labelled Zr-fum MOF NPs in water (black), greyed out curves are underlying single measurements. GDM fit (dashed blue curve) results in a size distribution (d) at a peak diameter of 135 nm, considering finite size correction.[56]

Fluorescence correlation spectroscopy (FCS)

Fluorescence correlation spectroscopy is a fluorescence-based method which is used to determine the hydrodynamic diameter of labelled NPs.[64,65] In this method, a laser is confocally focused into a liquid sample containing fluorescently labelled NPs. Fluorescence intensity fluctuations, resulting from NPs traversing an excitation volume, are recorded using an avalanche photodiode and used to calculate the time autocorrelation function. FCS data analysis yields the diffusion coefficient as well as the concentration of fluorescent particles (see the ESI†). Using the Stokes Einstein relation, the NP hydrodynamic diameter is calculated from the measured diffusion coefficient. Three samples of Zr-fum MOF NPs were labelled with the dye Alexa Fluor 488 (absorption at 488 nm and emission at 519 nm) and were examined with FCS. The normalised autocorrelation functions, shown in Fig. 3c, correspond to one of the labelled Zr-fum MOF NP samples (black). For comparison, the autocorrelation of free Alexa Fluor 488 is shown in green. Normalisation helps to clearly visualise that the autocorrelation function of the dye-labelled NPs is shifted towards higher correlation times with respect to the free Alexa Fluor 488 molecules. This indicates slower diffusion of the particles due to the larger hydrodynamic diameter of the NPs. Using a single component fit model (see the ESI†) results in an apparent diffusion time of 3.68 ms, which corresponds to a hydrodynamic diameter of $d^{FCS}_{Zr\text{-}fumNPs} = 135$ nm after using the finite particle size correction for hollow spheres presented by Wu *et al.*[66] The fit (not shown) is reasonable at lag times $\tau < 10$ ms but deviations from the data show that the model of the monodisperse particles is not satisfactory and indicate that there is a broad distribution of the particle size. Thus, the Gaussian Distribution Model (GDM)[67,68] was used to fit the data. The GDM fit (dashed blue line in Fig. 3c) results (again, after finite size correction) in a peak diameter of $d^{GDMFCS}_{Zr\text{-}fumNPs} = 135$ nm and a FWHM of 17 nm (see Fig. 3d).

Discussion

As stated in the introduction, the concept of the "size" of a NP is intangible since each characterization technique provides its own NP size, which differs from one method to another. This concept becomes clearer when considering on the one hand the different physical principles governing the methods and on the other, the state of the analysed sample.

Herein, the employed characterization techniques were divided into two categories, depending on whether the samples are analysed in the dry state or in a dispersion (Fig. 1). Measuring NPs in the dry state, *i.e.* as a powder, has the crucial disadvantage that it is hard to distinguish between aggregated NPs resulting from the sample preparation itself or agglomerates that were already present before. The agglomeration of NPs is energetically favoured as it minimizes surface areas and can saturate bonds and coordination sites.[69] Therefore, one should exercise caution when determining the NP size distribution from powder based-techniques and assuming the existence of individual NPs. In particular, in the case of promising biomedical applications of MOF NPs as nanocarriers or diagnostic agents or even both, non-agglomerated and colloidally stable MOF NPs are required and thus, their characterization in the liquid state is mandatory to clarify their aggregation state.

SEM, TEM and AFM microscopy techniques provide an image of NPs from which the diameters as well as the shape of NPs are easily extracted. All the microscopy techniques revealed the spherical shape of Zr-fum MOF NPs (Fig. 2). To give a representative insight into the NPs' diameter, a statistical study must be performed on a sufficient number of NPs, independent of the used technique. In this work, the diameter of 1000 NPs for TEM and SEM and of 500 NPs for AFM has been measured on the recorded images (see the ESI† Fig. S4, S9–13). A difficulty encountered in the SEM images is the identification of individual particles (see Fig. S4†). Small particles are easily overlooked, which might shift the resulting NP diameter distribution to higher values. TEM allows the detection of smaller NPs due to its larger spatial enhancement compared to SEM. In the TEM pictures of Zr-fum MOF NPs (Fig S9–13†), it is clearly visible that the NPs are connected together *via* thin necks, which were not taken into account to evaluate the NP diameter. However, one may argue that neck-connected NPs actually originate from agglomeration. Moreover, NPs featuring diameters smaller than the diameter of the thin necks, which connect larger NPs, may be overlooked when two-dimensional TEM images are analysed.

In high quality TEM micrographs of MOF NPs, it is normally possible to detect crystal fringes showcasing the crystallinity of the respective MOF structures.[45] In the case of the Zr-fum MOF NPs, this was not feasible due to beam damage. However, the crystallinity of MOF NPs was unambiguously proven using HRTEM by examining electron diffraction patterns (Fig. S8–S10 and Table S4†). Beam damage of a sample is a known problem in TEM mostly with high-energy electron beams ($E > 100$ keV). Further, it can be stated that the Zr-fum MOF NPs are highly beam sensitive, since the MOF NPs lose their crystallinity over a time frame of 30s (Fig. S8–S10†). Loss of the MOF NP crystallinity goes together with shrinking, which also explains the shift of the particle size distribution to lower values when comparing the TEM and SEM results (Table 1). Therefore, for the Zr-fum MOF NPs, TEM analysis is not suitable for measuring the size distribution, but suitable to confirm the crystallinity of the sample (Table S4†).

The NP diameter distribution obtained using AFM is in good agreement with the one obtained from SEM measurements (Table 1). Contrary to SEM and TEM techniques, the contrast between the Zr-fum MOF NPs and the object slide

Table 1 | Summary of the average diameters of spherical Zr-fum MOF NPs obtained using three different microscopy tools and three different spectroscopic methods. The standard deviation is also reported

	Method	Type of sample	Measured quantity	Average diameter (nm)	Standard deviation (nm)
Microscopy	SEM	Dried on a carbon support	Diameter	62	18.9
	TEM	Dried on a carbon grid	Diameter	29	12.9
	AFM	Dried on a silica slide	Height	68	15.0
Spectroscopy	XRD	Powder	Domain diameter	42–60	—[a]
	DLS	Dispersion (H_2O)	Hydrodynamic diameter	142	46
	FCS	Dispersion (H_2O), labelled	Hydrodynamic diameter	135	17 (FWHM)

[a] This method does not give a particle size distribution but results in a mean size assuming a single species.

(SiO_2) was sufficient to analyse the size of individual particles *via* an imaging software. Another advantage of AFM over SEM and TEM is the gentle nature of this method, which relies on the interaction of a cantilever tip with the particle surface instead of using a high electron energy beam.

Comparing the results of the X-ray diffraction experiments to the AFM and SEM results, similar diameters are measured. In contrast to SEM, TEM and AFM, which all result in NP diameter distributions, X-ray diffraction gives the average size of the sample crystalline domains, which are not necessarily equal to the NP size. Since the resulting value is an average only, no particle size distribution is obtained. The various possible NP species, which may lead to this average value, are not taken into account. In theory, the average crystalline domain size could result from two sample species, each featuring a uniform size. Alternatively, the average crystalline domain size may result from a broad particle size distribution. If all sample particles are not expected to be single crystals due to the presence of an amorphous material, one would expect the crystalline domain size to be shifted towards smaller values in comparison to NP diameter.

Additionally, defects in the crystal structure result in peak broadening. Since the crystalline domain size is calculated from the width of these peaks, this causes the former to shift towards smaller values. The good agreement among AFM, SEM and X-ray diffraction results suggests the presence of highly crystalline Zr-fum MOF NPs, whose crystal domain size is similar to the NP diameter. Finally, the sharp reflections and very small background observed in the X-ray diffraction experiments also prove the high crystallinity of the sample, complementing the results of TEM measurements.

The outcome of DLS and FCS is a distribution of diffusion coefficients D, which is then transformed into a distribution of hydrodynamic diameters, *i.e.* diameters of those spheres that yield the same D-values. Therefore, the hydrodynamic diameter does not describe the morphology of a particle but the chosen fitting model assuming a solid sphere or another ideal geometric shape, which has the same diffusion properties as the measured particle. As the Zr-fum MOF NPs feature a rather good spherical morphology, and as no additional organic surface capping is used, the values obtained from the dispersion-based methods should to some extent be comparable to those obtained from the powder methods. However, the hydrodynamic diameter of the Zr-fum MOF NPs determined using DLS and FCS is significantly larger than the NP diameters determined with the powder-based methods (Table 1).

In the case of DLS measurements, substantial absorption of laser light (λ = 633 nm) by a sample itself, which causes a systematic measurement error, can be ruled out by our white Zr-fum MOF NPs. Hence, the differences in the measured NP size values can be explained by the presence of small aggregates. FCS measurements reveal hydrodynamic diameters close to those obtained using DLS but with a narrower distribution. This can be explained by different fitting models. However, both methods disclose the presence of agglomerates of the Zr-fum MOF NPs in solution as the NP diameter determined by the solid techniques is significantly smaller. Functionalisation of MOF NPs with appropriate organic surface cappings, providing either electrostatic or steric repulsion, could help reduce the amount of aggregates.

Conclusion

One of the key issues in NP research is that the product of a chemical synthesis of NPs is a colloidal dispersion, which exhibits a polydisperse distribution of sizes and shapes, rather than a collection of identical NPs. This is the main reason why the reproducibility of NP synthesis results is so difficult to ensure, even if the same person carries out the synthesis under the same experimental conditions. For this reason, a careful and extensive NP characterization is required. Moreover, future NP database will collect physical dispersion data together with the chemical composition of NPs. Such kind of database is important as it allows researchers to compare different NP data sets and also to put their own results in place. For this reason, recommendations for MOF NP characterization using standard physical characterization tools have been introduced. Zr-fum MOF NPs appeared as ideal candidates to reach this fixed target owing to their perfect spherical shape. In our work, we applied six characterisation methods on Zr-fum MOF NPs and the obtained results were discussed and compared based on the underlying physical process of the characterisation device.

When choosing techniques to characterise a nanomaterial, it is important to bear in mind the later usage of the respective compound. Powder characterisations with SEM, TEM or AFM are essentially sufficient when considering solid based-applications of MOF NPs. However, in solution-based applications such as drug delivery, colloidally stable NP solutions are required, which must thus be characterised in solution with DLS and/or FCS, for instance. Since these methods do not give insight into the morphology of NPs, it is therefore advantageous to complement these techniques by an image-providing technique such as TEM, SEM or AFM.

In the case of MOF NPs, the determination of crystallinity and in particular the quantification of the crystalline domain size is an important parameter. However, the XRD patterns of MOF NPs need to be carefully analysed as high-crystallinity or even the existence of a MOF structure cannot always be stated due to the potential broadening of peaks in an XRD pattern. For example, the crystallinity of MIL-101(Cr) and MIL-100(Fe) NPs is unequivocally proven by TEM analysis only.[48] In comparison to the tested Zr-fum MOF NPs, the respective MOF NPs in those cases were more beam stable. The difficult characterisation of MOF NPs that are sensitive to the electronic beam of TEM could be overcome with the new versions of TEM instruments operating at lower voltage (*e.g.* 60 keV).

TEM analysis usually appears as the most suitable method to determine the size of isolated MOF NPs in the dry state due to its high spatial resolution. However, as shown in the case of the Zr-fum MOF NPs, beam damage can spoil the outcome, making TEM no longer appropriate. SEM represents a good alternative to TEM because it operates at a much lower voltage even if small NPs (<20 nm) of a sample can be hardly detected since they are hidden by bigger ones. TEM and SEM pictures were used to manually determine the Zr-fum MOF NP size distribution. Although this is time consuming, this approach is sufficient when having spherical NPs but cannot be applied to non-spherical NPs.

Many MOF NP applications need dispersions of colloidally stable MOF NPs. Even though most researchers target solution-based NP applications (*e.g.* drug delivery), they often do not furnish evidence on the colloidal properties of MOF NPs. This enigma comes from agglomeration issues often met with nanomaterials. The chemistry of every NP material class, including MOF NP, faces the challenge of synthesising colloidally stable NPs. The saturation of a MOF NP surface immediately after MOF NP nucleation, either by electrostatic repulsion or steric stabilisation, can avoid this agglomeration issue. A stable MOF NP suspension can be easily characterised by DLS analysis, whereby caution should be paid to the automatic evaluation of the size distribution of the instrument. An alternative solution to DLS is FCS, as demonstrated in this article. FCS is based on evaluation of a autocorrelation function to obtain the diffusion coefficient of fluorescence-labelled NPs. Although FCS has the disadvantage of requiring dye labelled NPs, meaning that they are chemically modified, in many applications, such as drug delivery or diagnosis, NPs need to be labelled for the application itself, *e.g.* to carry out cell uptake studies. In these cases, FCS is an excellent characterisation technique due to its high spatial and temporal resolutions and its ability to analyse extremely low NP concentrations (nM to pM concentrations) in a very small volume (~0.1 fL). Consequently, a low amount of sample is needed to precisely determine the hydrodynamic diameter of labelled NPs. Moreover, FCS measurement simultaneously provides information about the concentration (inverse correlation height) of the investigated sample.

In summary, we presented comprehensive physical characterization of the size, shape and bulk properties of Zr-fum MOF NPs. Evidently, the structural properties of MOF NPs provide a large set of parameters allowing for a thorough assessment of MOF NP quality. Future applications that will exploit MOF NPs as hosts, delivery vehicles or catalytic agents rely on the full knowledge of their physical NP properties. The caveats and peculiarities in NP size characterisation discussed here might help for standardisation and better comparability of MOF NP properties.

Acknowledgements

The authors are grateful for financial support from the Deutsche Forschungsgemeinschaft (DFG) through SFB 1032 and DFG-project WU 622/4-1, the Excellence Cluster Nanosystems Initiative Munich (NIM), the Center for NanoScience Munich (CeNS), and the European Commission (project FutureNanoNeeds). Authors AP and JV gratefully acknowledge financial support from the DFG within the RTG 1782 "Functionalization of Semiconductors". Furthermore, we thank Steffen Schmidt and Michael Beetz for TEM measurements, and Beatriz Pelaz, Neus Feliu, and Pablo del Pino for helpful technical discussions. Last but not least, SW thanks Dr. M. Lismont (University of Liège) for valuable discussions and comments.

Notes and references

1 S. Kitagawa, R. Kitaura and S.-I. Noro, *Angew. Chem., Int. Ed.*, 2004, **43**, 2334–2375.
2 G. Férey, *Chem. Soc. Rev.*, 2008, **37**, 191–214.
3 H. Furukuwa, K. E. Cordova, M. O'Keeffe and O. M. Yaghi, *Science*, 2013, **341**, 974–987.
4 W. Lu, Z. Wei, Z.-Y. Gu, T.-F. Liu, J. Park, J. Park, J. Tian, M. Zhang, Q. Zhang, T. Gentle Iii, M. Bosch and H.-C. Zhou, *Chem. Soc. Rev.*, 2014, **43**, 5561–5593.
5 T. R. Cook, Y.-R. Zheng and P. J. Stang, *Chem. Rev.*, 2013, **113**, 734–777.
6 D. J. Tranchemontagne, J. L. Mendoza-Cortés, M. O'Keeffe and O. M. Yaghi, *Chem. Soc. Rev.*, 2009, **38**, 1257.
7 O. M. Yaghi, M. O'Keeffe, N. W. Ockwig, H. K. Chae, M. Eddaoudi and J. Kim, *Nature*, 2003, **423**, 705–714.
8 I. Senkovska and S. Kaskel, *Chem. Commun.*, 2014, **50**, 7089.
9 R. Grünker, V. Bon, P. Müller, U. Stoeck, S. Krause, U. Mueller, I. Senkovska and S. Kaskel, *Chem. Commun.*, 2014, **50**, 3450.
10 O. K. Farha, I. Eryazici, N. C. Jeong, B. G. Hauser, C. E. Wilmer, A. A. Sarjeant, R. Q. Snurr, S. T. Nguyen, A. Ö. Yazaydın and J. T. Hupp, *J. Am. Chem. Soc.*, 2012, **134**, 15016–15021.

11 P. Deria, J. E. Mondloch, O. Karagiaridi, W. Bury, J. T. Hupp and O. K. Farha, *Chem. Soc. Rev.*, 2014, **43**, 5896–5912.
12 J. D. Evans, C. J. Sumby and C. J. Doonan, *Chem. Soc. Rev.*, 2014, **43**, 5933–5951.
13 S. M. Cohen, *Chem. Rev.*, 2012, **112**, 970–1000.
14 H. Furukawa, U. Müller and O. M. Yaghi, *Angew. Chem., Int. Ed.*, 2015, **54**, 3417–3430.
15 H. Hintz and S. Wuttke, *Chem. Mater.*, 2014, **26**, 6722–6728.
16 H. Hintz and S. Wuttke, *Chem. Commun.*, 2014, **50**, 11472–11475.
17 S. Wuttke, C. Dietl, F. M. Hinterholzinger, H. Hintz, H. Langhals and T. Bein, *Chem. Commun.*, 2014, **50**, 3599.
18 B. Van de Voorde, B. Bueken, J. Denayer and D. De Vos, *Chem. Soc. Rev.*, 2014, **43**, 5766–5788.
19 S. Van der Perre, B. Bozbiyik, J. Lannoeye, D. E. De Vos, G. V. Baron and J. F. M. Denayer, *J. Phys. Chem. C*, 2015, **119**, 1832–1839.
20 S. Van der Perre, T. Van Assche, B. Bozbiyik, J. Lannoeye, D. E. De Vos, G. V. Baron and J. F. M. Denayer, *Langmuir*, 2014, **30**, 8416–8424.
21 Y. He, W. Zhou, G. Qian and B. Chen, *Chem. Soc. Rev.*, 2014, **43**, 5657–5678.
22 J. Canivet, A. Fateeva, Y. Guo, B. Coasne and D. Farrusseng, *Chem. Soc. Rev.*, 2014, **43**, 5594–5617.
23 J. Lee, O. K. Farha, J. Roberts, K. A. Scheidt, S. T. Nguyen and J. T. Hupp, *Chem. Soc. Rev.*, 2009, **38**, 1450.
24 K. Na, K. M. Choi, O. M. Yaghi and G. A. Somorjai, *Nano Lett.*, 2014, **14**, 5979–5983.
25 C.-H. Kuo, Y. Tang, L.-Y. Chou, B. T. Sneed, C. N. Brodsky, Z. Zhao and C.-K. Tsung, *J. Am. Chem. Soc.*, 2012, **134**, 14345–14348.
26 S. Saha, G. Das, J. Thote and R. Banerjee, *J. Am. Chem. Soc.*, 2014, **136**, 14845–14851.
27 H.-Q. Xu, J. Hu, D. Wang, Z. Li, Q. Zhang, Y. Luo, S.-H. Yu and H.-L. Jiang, *J. Am. Chem. Soc.*, 2015, **137**, 13440–13443.
28 Y. Li, H. Xu, S. Ouyang and J. Ye, *Phys. Chem. Chem. Phys.*, 2016, **18**, 7563–7572.
29 L. E. Kreno, K. Leong, O. K. Farha, M. Allendorf, R. P. Van Duyne and J. T. Hupp, *Chem. Rev.*, 2012, **112**, 1105–1125.
30 F. M. Hinterholzinger, B. Rühle, S. Wuttke, K. Karaghiosoff and T. Bein, *Sci. Rep.*, 2013, **3**, 2562.
31 G. Nickerl, I. Senkovska and S. Kaskel, *Chem. Commun.*, 2015, **51**, 2280–2282.
32 P. Horcajada, R. Gref, T. Baati, P. K. Allan, G. Maurin, P. Couvreur, G. Férey, R. E. Morris and C. Serre, *Chem. Rev.*, 2012, **112**, 1232–1268.
33 C. He, D. Liu and W. Lin, *Chem. Rev.*, 2015, **115**, 11079–11108.
34 S. Horike, D. Umeyama and S. Kitagawa, *Acc. Chem. Res.*, 2013, **46**, 2376–2384.
35 H. Chevreau, A. Permyakova, F. Nouar, P. Fabry, C. Livage, F. Ragon, A. Garcia-Marquez, T. Devic, N. Steunou, C. Serre and P. Horcajada, *CrystEngComm*, 2016, DOI: 10.1039/c5ce01864a.
36 A. Carné-Sánchez, I. Imaz, M. Cano-Sarabia and D. Maspoch, *Nat. Chem.*, 2013, **5**, 203–211.
37 A. Schaate, P. Roy, A. Godt, J. Lippke, F. Waltz, M. Wiebcke and P. Behrens, *Chem. – Eur. J.*, 2011, **17**, 6643–6651.
38 T. Tsuruoka, S. Furukawa, Y. Takashima, K. Yoshida, S. Isoda and S. Kitagawa, *Angew. Chem., Int. Ed.*, 2009, **48**, 4739–4743.
39 K. Liang, R. Ricco, C. M. Doherty, M. J. Styles, S. Bell, N. Kirby, S. Mudie, D. Haylock, A. J. Hill, C. J. Doonan and P. Falcaro, *Nat. Commun.*, 2015, **6**, 7240.
40 S. Furukawa, J. Reboul, S. Diring, K. Sumida and S. Kitagawa, *Chem. Soc. Rev.*, 2014, **43**, 5700–5734.
41 P. Falcaro, R. Ricco, C. M. Doherty, K. Liang, A. J. Hill and M. J. Styles, *Chem. Soc. Rev.*, 2014, **43**, 5513–5560.
42 R. Ameloot, E. Gobechiya, H. Uji-i, J. A. Martens, J. Hofkens, L. Alaerts, B. F. Sels and D. E. De Vos, *Adv. Mater.*, 2010, **22**, 2685–2688.
43 G. Lu, S. Li, Z. Guo, O. K. Farha, B. G. Hauser, X. Qi, Y. Wang, X. Wang, S. Han, X. Liu, J. S. DuChene, H. Zhang, Q. Zhang, X. Chen, J. Ma, S. C. J. Loo, W. D. Wei, Y. Yang, J. T. Hupp and F. Huo, *Nat. Chem.*, 2012, **4**, 310–316.
44 P. Falcaro, A. J. Hill, K. M. Nairn, J. Jasieniak, J. I. Mardel, T. J. Bastow, S. C. Mayo, M. Gimona, D. Gomez, H. J. Whitfield, R. Riccò, A. Patelli, B. Marmiroli, H. Amenitsch, T. Colson, L. Villanova and D. Buso, *Nat. Commun.*, 2011, **2**, 237.
45 R. Ameloot, F. Vermoortele, W. Vanhove, M. B. J. Roeffaers, B. F. Sels and D. E. De Vos, *Nat. Chem.*, 2011, **3**, 382–387.
46 A. Carné, C. Carbonell, I. Imaz and D. Maspoch, *Chem. Soc. Rev.*, 2011, **40**, 291–305.
47 P. Li, R. C. Klet, S.-Y. Moon, T. C. Wang, P. Deria, A. W. Peters, B. M. Klahr, H.-J. Park, S. S. Al-Juaid, J. T. Hupp and O. K. Farha, *Chem. Commun.*, 2015, **51**, 10925–10928.
48 S. Wuttke, S. Braig, T. Preiß, A. Zimpel, J. Sicklinger, C. Bellomo, J. O. Rädler, A. M. Vollmar and T. Bein, *Chem. Commun.*, 2015, **51**, 15752–15755.
49 G. Xu, K. Otsubo, T. Yamada, S. Sakaida and H. Kitagawa, *J. Am. Chem. Soc.*, 2013, **135**, 7438–7441.
50 C. V. McGuire and R. S. Forgan, *Chem. Commun.*, 2015, **51**, 5199–5217.
51 Y. Sakata, S. Furukawa, M. Kondo, K. Hirai, N. Horike, Y. Takashima, H. Uehara, N. Louvain, M. Meilikhov, T. Tsuruoka, S. Isoda, W. Kosaka, O. Sakata and S. Kitagawa, *Science*, 2013, **339**, 193–196.
52 Y. Hijikata, S. Horike, D. Tanaka, J. Groll, M. Mizuno, J. Kim, M. Takata and S. Kitagawa, *Chem. Commun.*, 2011, **47**, 7632.
53 D. Tanaka, A. Henke, K. Albrecht, M. Moeller, K. Nakagawa, S. Kitagawa and J. Groll, *Nat. Chem.*, 2010, **2**, 410–416.
54 J. Jiang, G. Oberdörster and P. Biswas, *J. Nanopart. Res.*, 2009, **11**, 77–89.
55 R. A. Sperling, T. Liedl, S. Duhr, S. Kudera, M. Zanella, C.-A. J. Lin, W. Chang, D. Braun and W. J. Parak, *J. Phys. Chem. C*, 2007, **111**, 11552–11559.
56 F. Zhang, Z. A, F. Amin, A. Feltz, M. Oheim and W. J. Parak, *ChemPhysChem*, 2010, **11**, 730–735.
57 E. Caballero-Díaz, C. P., L. Kastl, P. Rivera-Gil, B. Simonet, M. Valcárel, J. Jiménez-Lamana, F. Laborda and W. J. Parak, *Part. Part. Syst. Charact.*, 2013, **30**, 1079–1085.

Published on 04 March 2016. Downloaded by Ludwig Maximilians Universitaet Muenchen on 09/05/2016 10:39:35.

58 P. Rivera-Gil, D. J. De Aberasturi, V. Wulf, B. Pelaz, P. del Pino, Y. Zhao, J. M. de la Fuente, I. Ruiz de Larramendi, T. Rojo, X.-J. Liang and W. J. Parak, *Acc. Chem. Res.*, 2013, **46**, 743–749.
59 G. Zahn, H. A. Schulze, J. Lippke, S. König, U. Sazama, M. Fröba and P. Behrens, *Microporous Mesoporous Mater.*, 2015, **203**, 186–194.
60 G. Zahn, P. Zerner, J. Lippke, F. L. Kempf, S. Lilienthal, C. A. Schröder, A. M. Schneider and P. Behrens, *CrystEngComm*, 2014, **16**, 9198–9207.
61 G. Wißmann, A. Schaate, S. Lilienthal, I. Bremer, A. M. Schneider and P. Behrens, *Microporous Mesoporous Mater.*, 2012, **152**, 64–70.
62 G. S. Pawley, *J. Appl. Crystallogr.*, 1981, **14**, 357–361.
63 C. Y. Tay, M. I. Setyawati, J. Xie, W. J. Parak and D. T. Leong, *Adv. Funct. Mater.*, 2014, **24**, 5936–5955.
64 T. Pellegrino, L. Manna, S. Kudera, T. Liedl, D. Koktysh, A. L. Rogach, S. Keller, J. Rädler, G. Natile and W. J. Parak, *Nano Lett.*, 2004, **4**, 703–707.
65 T. Liedl, S. Keller, F. C. Simmel, J. O. Rädler and W. J. Parak, *Small*, 2005, **1**, 997–1003.
66 B. Wu, C. Yan and J. D. Müller, *Biophys. J.*, 2008, **7**, 2800–2808.
67 J. J. Mittag, S. Milani, D. M. Walsh, J. O. Rädler and J. J. McManus, *Biochem. Biophys. Res. Commun.*, 2014, **448**, 195–199.
68 N. Pal, S. D. Verma, M. K. Singh and S. Sen, *Anal. Chem.*, 2011, **83**, 7736–7744.
69 H. Goesmann and C. Feldmann, *Angew. Chem., Int. Ed.*, 2010, **49**, 1362–1395.

Electronic Supplementary Material (ESI) for CrystEngComm.

Supporting Information

Exploration of MOF nanoparticles sizes using various physical characterisation methods - Is what you measure what you get?

Patrick Hirschle,[a] Tobias Preiß,[b] Florian Auras,[a] André Pick,[c] Johannes Völkner,[c] Daniel Valdepérez,[c] Gregor Witte,[c] Wolfgang J. Parak,[c] Joachim O. Rädler,[b] and Stefan Wuttke[a]*

[a] *Department of Chemistry and Center for NanoScience (CeNS), University of Munich (LMU), Butenandtstraße 11, 81377 Munich*

[b] *Department of Physics and Center for NanoScience (CeNS), University of Munich (LMU), Geschwister-Scholl-Platz 1, 80539 Munich*

[c] *Faculty of Physics, Philipps University Marburg, Renthof 7, 35037 Marburg*

Correspondence to:

stefan.wuttke@cup.uni-muenchen.de

Table of Contents

1 Methods and Characterisation

Thermogravimetry (TG): A dried sample of Zr-*fum* (6.3 mg) was examined on a *TASC 414/4* (*Netzsch*). The thermogravimetric experiment was performed with a heating rate of 10 °C/min up to 900 °C. The results were evaluated using the included software Proteus v4.3.

Nitrogen Sorption: Dried powder of Zr-fum (6.3 mg) was degassed for 12 h at 120 °C in high vacuum. Subsequently, nitrogen sorption was performed on the sample using an Autosorb-1 (Quantachrome). The results were evaluated using the software ASiQwin v3.0. Brunauer-Emmett-Teller (BET) surface areas[1] were calculated by using the linearised form of the BET equation. A correlation coefficient of r = 0.999755 was achieved. The pore size distribution of the sample was determined by using the software`s non-local density functional theory (NLDFT) equilibrium model based on slit and cylindrical pores.

Scanning Electron Microscopy (SEM): The experiments, which are presented here, were performed on a *Jeol JSM-6500F* with EDX-Detektor and *Inca*-software (*Oxford Instruments*). For sample preparation, an ethanolic dispersion of the Zr-*fum* nanoparticles was dried and subsequently sputtered with carbon. The resulting micrographs were evaluated manually using the software *ImageJ v1.49*.

Transmission Electron Microscopy (TEM): All of the experiments were performed on a *Tecnai G2* (*Fei*) with an acceleration voltage of 200 kV. For sample preparation, a dispersion of the Zr-*fum* nanoparticles in ethanol was dried on a carbon-coated copper grid. The resulting micrographs were evaluated manually by using the software *ImageJ v1.49*. The micrographs shown in Figure S5 and Figure S9-Figure S13 have been measured in imaging mode. The electron diffraction patterns shown in Figure S6-Figure S8 have separately been recorded in separately diffraction mode.

Atomic Force Microscopy (AFM): Epi-ready silicon wafers coated with a native oxide (Siegert Wafer GmbH) were used as ultraflat supporting substrates. Initially, all supports were cleaned in an ultrasonic bath in ethanol and subsequently blown dry in a nitrogen stream. 2 µL of the nanoparticle solution were pipetted onto a substrate. Slow evaporation of the solvent at room

temperature led to a concentric density gradient of the nanoparticles deposited on the surface. The morphology of nanoparticles was characterised by means of atomic force microscopy using a SPM5500-AFM instrument (Agilent) operated in closed loop tapping mode at ambient conditions, and using HQ:NSC15/AlBS cantilevers (MikroMasch; resonance frequency, 325 kHz). The z-range of the scanner had been carefully calibrated using a standard silicon grating with a step height of 84.3 nm and an accuracy of 1.5 nm.

X-Ray Diffraction (XRD): Powder X-ray diffraction (PXRD) measurements were performed using a Bruker D8 Discover with Ni-filtered Cu K_α radiation and a LynxEye position-sensitive detector. In order to reduce the peak broadening caused by the instrument to a minimum, 0.05 mm and 3 mm slits were installed at the X-ray tube assembly and the detector, respectively. In conjunction with a detector opening of 0.8 °, the instrument broadening was thus reduced to 0.05 ° 2ϑ (calibrated against LaB_6). The Pawley fitting[2] of the resulting data treats peak areas as variables. Hence, they were not being used for atom-position refinement. Only the unit cell size *a* and the crystallite size *d* were refined. The reflections were assumed to feature a Pseudo-Voigt profile and peak asymmetry was corrected using the Berar-Baldinozzi function.

Dynamic Light Scattering (DLS): During the experiments, all DLS measurements were performed on a *Zetasizer Nano Series* (Nano-ZS, *Malvern*). The employed laser operated at a wavelength λ = 633 nm. The measurement of Zr-*fum* was conducted directly after washing the freshly synthesised nanoparticles. For the respective measurement, the sample dispersion in ethanol was diluted in ethanol (1:200) or water (1:200).

Fluorescence Correlation Spectroscopy: All experiments were conducted on an Axiovert 200M equipped with a ConfoCor2 unit (Carl Zeiss), using a 40x NA1.2 water immersion objective and an argon ion laser at 488 nm wavelength. Emitted light was separated from excitation light with a dichroic mirror and a bandpass emission filter (505 – 550 nm). Samples were prepared and measured in Nunc 8 well plates (Thermo Scientific). The focal width w = 0.2 µm was determined by a calibration measurement using Alexa Fluor 488 with a known diffusion coefficient of D = 435 µm²/s. [3] Samples of three individually produced batches of Zr-*fum* were investigated with FCS. For this purpose Zr-*fum* nanoparticles were fluorescently labeled by adding 20µL of

Zr-*fum* dispersed in ethanol suspension to 200 µL of an Alexa Fluor 488 solution. After 10 minutes of incubation FCS measurements were performed. To avoid singe particle aggregates, which would distort the correlation curves, the so called dust filter of the instrument's software (70%) was used. By this the fluorescence fluctuations are analysed prior to correlation and spikes caused by agglomerated particles having a deviation of more than 70% from the average count rate within a binned count rate time are cut out and not used for the correlation analysis similar to the method described by Persson *et al.* (2009).[4]

2 Experimental Section

2.1 Chemicals

The chemicals Zr(IV) chloride (≥ 95 %, Aldrich), formic acid (> 85 %, Aldrich), fumaric acid (≥ 99.5 %, Fluka) and ethanol (99.9 %, VWR) were all used without further purification.

2.2 Synthesis of Zr-*fum* samples

$ZrCl_4$ and Fumaric acid (see Table S1) were put into a glass reactor (25 mL). A mixture of water (10 mL) and formic acid (975 µL) was added to the educts. The reactor was then sealed and placed in an oven at 120 °C for 24 h.

After cooling down, the resulting white precipitate was washed. The dispersion was divided into 8 vials (1.5 mL), and then centrifuged (14000 rpm, 5 min). After discarding the supernatants, the precipitates were redispersed in water (1.25 mL per precipitate) via sonication. The dispersions were centrifuged (14000 rpm, 5 min) and the supernatants removed. The precipitates were redispersed in ethanol (1.25 mL per precipitate). After repeating this last washing cycle for an additional washing cycle the ethanol-based dispersions were unified.

Table S1 | Weight-ins of the respective Zr-*fum* batches.

Sample	m($ZrCl_4$) [mg]	m(fumaric acid) [mg]
Zrfum-1	120.9	180.4
Zrfum-2	120.4	180.2
Zrfum-3	120.6	180.4
Zrfum-4	120.5	180.3

2.3 Characterisation of Zr-*fum*

Structure of Zr-*fum*

As reported by Wißman *et al.*[5] the microporous, cubic structure of Zr-*fum* featuring the formula $Zr_6O_4(OH)_4(O_2C\text{-}(CH)_2\text{-}CO_2)_6$ displays the space group $Pn\bar{3}$. The X-ray diffraction experiments conducted in this work (see Figure S14) have resulted in a lattice parameter of a = (17.91 ± 0.03) nm to (17.88 ± 0.03) nm.

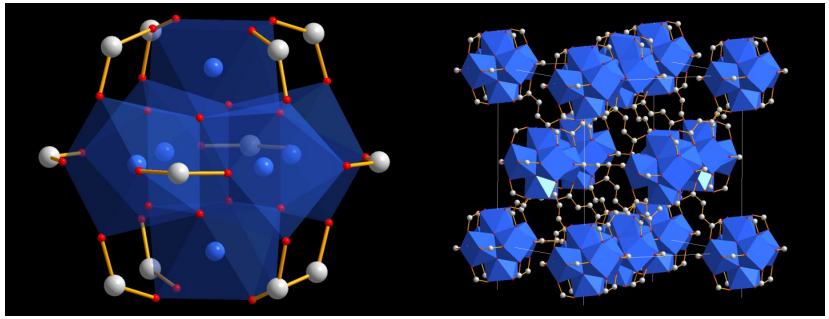

Figure S1 | Secondary building unit (left) and architecture (right) of Zr-*fum*; Zr (*blue*), O (*red*), C (*grey*).

Figure S1 shows the composition of the structure and the position of the secondary building units (SBUs) on the vertices and faces of a cubic cell. Each SBU comprises of 6 Zr-atoms (*blue*) that are octahedrally aligned and coordinated by 8 oxygen-atoms (*red*). The carbon atoms (*grey*) are the first segment of the emerging fumaric acid linker chains, which are arranged cuboctahedrally and thereby connecting each SBU to 12 neighboring clusters.

Nitrogen sorption

The Zr-*fum* nanoparticles displayed a specific BET surface area of 408 $m^2 \cdot g^{-1}$. The pore size distribution (see Figure S2) was determined to feature a maximum at the pore with d = 0.57 nm. The corresponding nitrogen sorption graph (see Figure S2) can be identified as an IUPAC Type I microporous adsorption isotherm.[6]

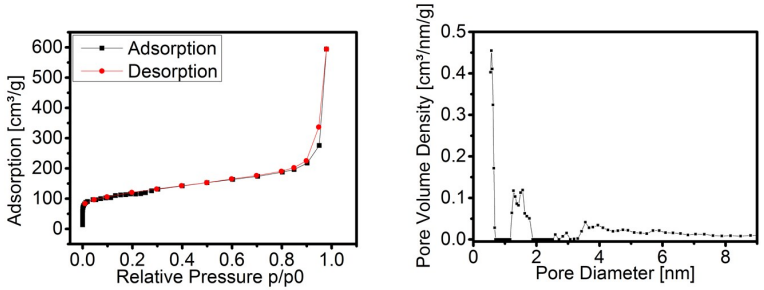

Figure S2 | Nitrogen sorption isotherm showing the adsorption of nitrogen in dependency of its relative pressure (left) and the differential pore size distribution in dependency of the pore-diameter (right).

Thermogravimetry

From 48 °C to 250 °C a mass loss occurred which was probably caused by desorption of water from the framework. At 260 °C the decomposition of the organic linker began, similar to the decomposition of pure fumaric acid at 200 °C as reported by Wißman *et al.*[5] This decomposition-step was finished at 480 °C. Subsequently at around 600 °C a final mass loss occurred, which was finished at around 750 °C. Comparing the TG measurement with the data published by Wißman *et al.*, similarities can be seen: they report a similar decomposition range for the linker starting at 250 °C and ending at 400 °C. Wißman *et al.* also provide an explanation for the final mass loss: CO_2 is released from the decomposition of carboxylate groups. Overall, this mass loss caused by the sample during the decomposition of the linker and release of CO_2 is at 47.5 %, which is in a good agreement with the calculated results at 45.8 %.[5] The corresponding graph is shown in Figure S3.

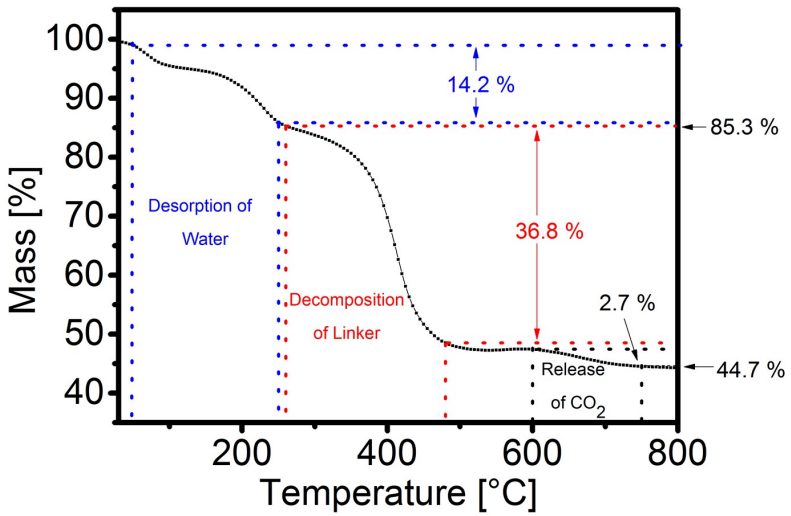

Figure S3 | Thermogravimetric evaluation of Zr-*fum*.

Scanning Electron Microscopy

The image, which is used to obtain the SEM size distribution, is shown in Figure S4.

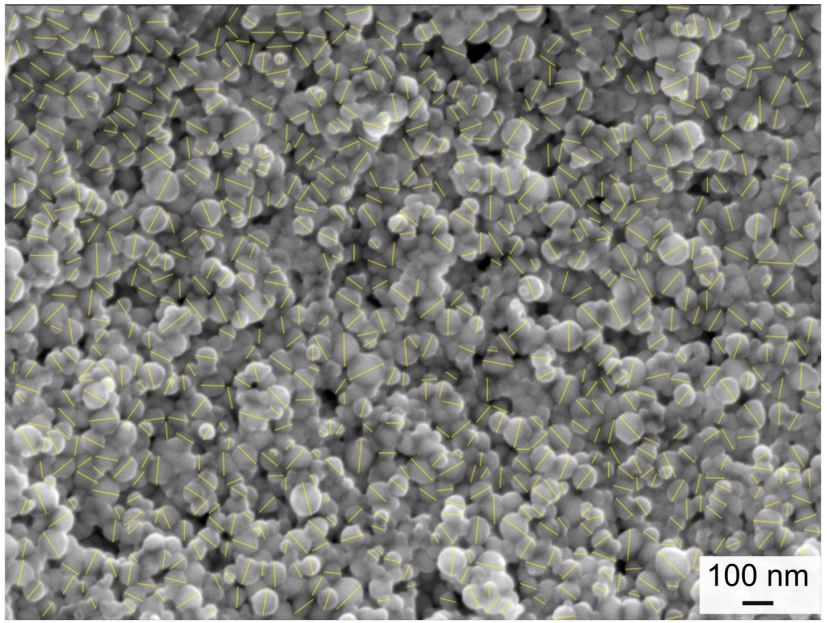

Figure S4 | Zr-*fum* particles measured for SEM size determination.

Transmission Electron Microscopy

An overview picture of dried Zr-*fum* nanoparticles is shown in Figure S5.

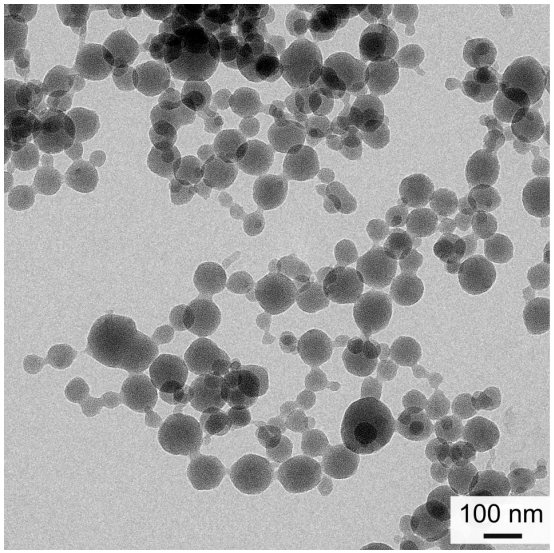

Figure S5 | Overview picture of Zr-*fum.*

Figure S6, Figure S7, and Figure S8 show Zr-fumarate when exposed to an electron beam (200 keV) for a prolonged period of time. The Debye-Scherrer rings, which are initially still recognisable after an exposure time of 6.5 s, gradually disappear indicating the damage the sample is taking from the electron beam.

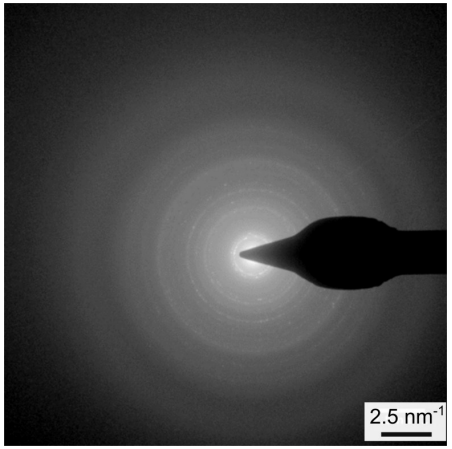

Figure S6 | Electron diffraction pattern of sample Zr-*fum* after 6.5 seconds in a 200 kV electron beam.

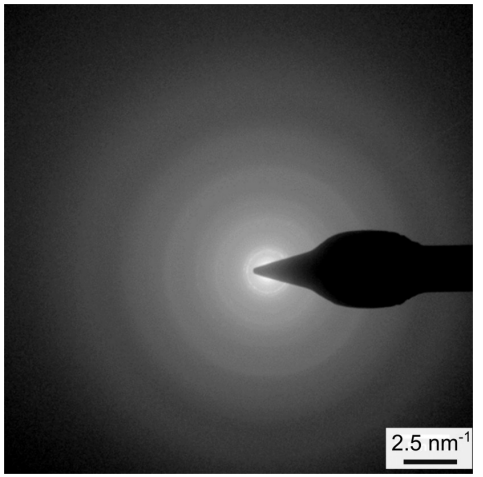

Figure S7 | Electron diffraction pattern of sample Zr-*fum* after 13 seconds in a 200 kV electron beam.

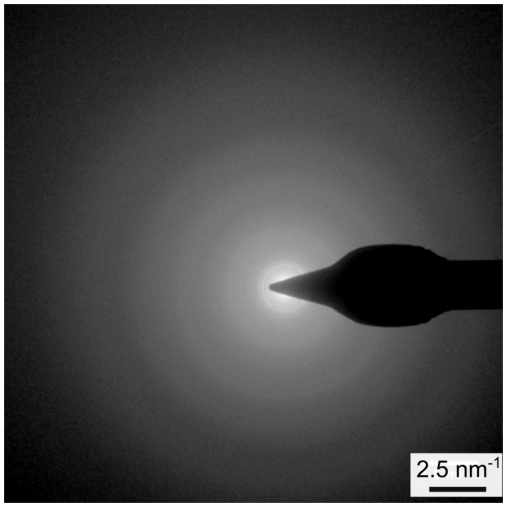

Figure S8 | Electron diffraction pattern of sample Zr-*fum* after 26 seconds in a 200 kV electron beam.

In Table S2 the Debye-Scherrer rings of Zr-*fum* shown in Figure S6 are shown along with their corresponding HKL indices and interplanar spacings *d*. They are in good agreement with the crystallographic data published by Wißmann *et al.*[5], which verifies the successful synthesis of Zr-fumarate MOF nanoparticles.

Table S2 | Diffraction rings of Zr-*fum* with their indices and interplanar spacing.

Diffraction Ring	*d (experiment)* [Å]	HKL	d (literature)[4] [Å]	deviation [%]
1	10.1365	(111)	10.3591	2.1
2	8.7538	(200)	8.9545	2.2
3	4.3961	(400)	4.4776	1.8
4	4.0201	(331)	4.1084	2.1
5	3.5727	(422)	3.6554	2.3
6	3.3966	(333)	3.4466	1.5
7	2.9373	(600)	2.9847	1.6
8	2.6755	(533)	2.7312	2.0
9	2.5374	(444)	2.5850	1.8
10	2.4732	(551)	2.5081	1.4
11	2.2804	(553)	2.3315	2.2

The particles that were measured to determine the TEM size distribution are shown in Figure S9, Figure S10, Figure S11, Figure S12, and Figure S13.

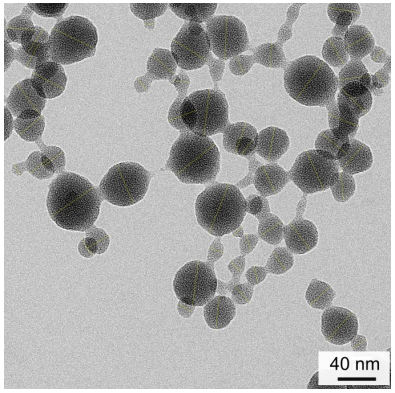

Figure S9 | Zr-*fum* particles measured for TEM size determination.

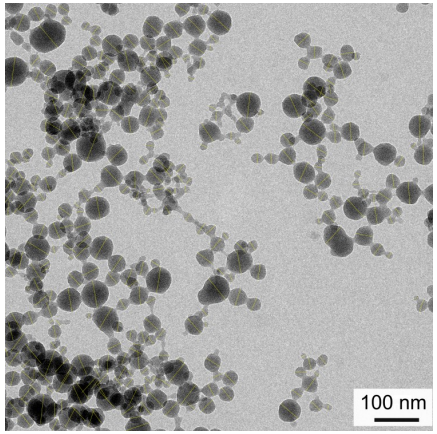

Figure S10 | Zr-*fum* particles measured for TEM size determination.

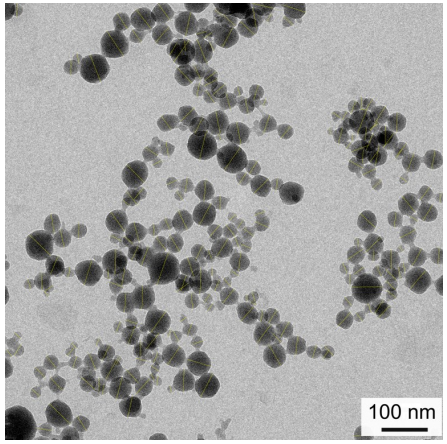

Figure S11 | Zr-*fum* particles measured for TEM size determination.

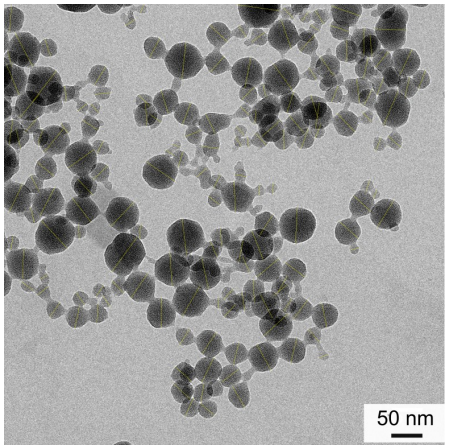

Figure S12 | Zr-*fum* particles measured for TEM size determination.

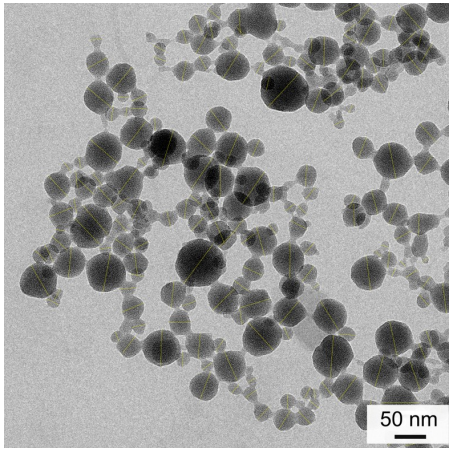

Figure S13 | Zr-*fum* particles measured for TEM size determination.

X-Ray Diffraction

The theoretical PXRD pattern of the Zr-*fum* MOF was simulated using the structure model and atomic coordinates reported by Wißmann *et al.*[5] and assuming a domain size of 50 nm.

The results of the X-ray diffraction experiments for samples Zrfum-1, Zrfum-2, Zrfum-3 and Zrfum-4 are shown in Figure S14. The corresponding average size of the crystalline domains is shown in Table S2. Besides slightly smaller crystalline domains for sample Zrfum-3, the crystalline domains of the sample generally feature a similar size, which confirms the good reproducibility of the aqueous synthesis.

Pawley fitting of the experimental PXRD data was carried out using in the Reflex module of the Accelrys Materials Studio software and refining the unit cell parameter *a* and the domain size *d*. We used Pseudo-Voigt peak shape functions with fixed profile parameters (determined from measurements of a LaB_6 micropowder sample). Peak asymmetry was corrected using the Berar-Baldinozzi function. Overlay of the observed and refined profiles shows very good correlation with small deviations at low angles, where the peak asymmetry is more pronounced.

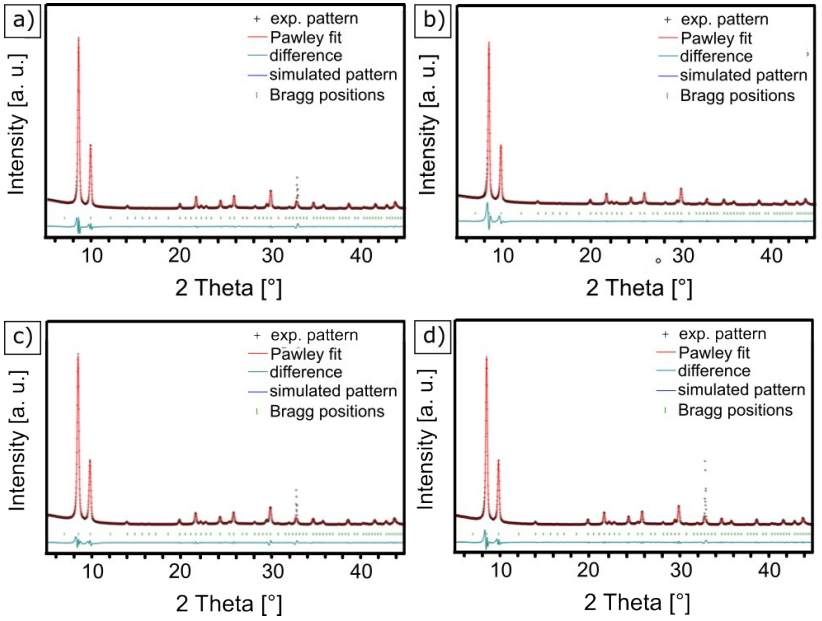

Figure S14 | PXRD patterns of the Zrfum-1 (a), Zrfum-2 (b), Zrfum-3 (c), and Zrfum-4 (d). The experimental data are shown in black, corresponding Pawley fits in red, Bragg positions as green symbols, and the difference between the experimental pattern and the fits as dark green lines. All four experimental patterns were found to feature an additional peak at 31.5 ° of variable intensity, which could not be attributed to any of the starting materials or the MOF. This reflection was masked during the Pawley fitting.

Table S3 | Results of the Pawley fitting of the Zrfum-1-4 samples

Sample	Zrfum-1	Zrfum-2	Zrfum-3	Zrfum-4
Space Group	$Pn\bar{3}$	$Pn\bar{3}$	$Pn\bar{3}$	$Pn\bar{3}$
R_p [%]	10.00	14.11	9.45	10.61
R_{wp} [%]	6.79	13.22	4.92	7.79
Lattice parameter *a* [Å]	17.91 ± 0.03	17.89 ± 0.03	17.89 ± 0.03	17.88 ± 0.03
Average domain size *d* [nm]	60 ± 5	55 ± 5	42 ± 5	54 ± 5

Atomic Force Microscopy

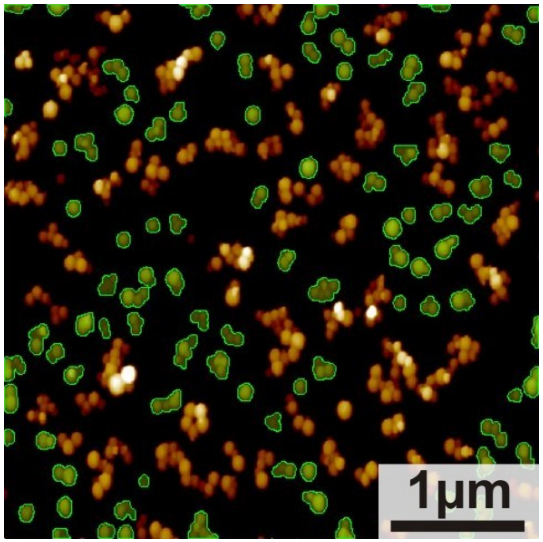

Figure S15 | AFM image of MOFs after performing particle and pore analysis in Scanning Probe Image Processing (SPIP). The maximum height of green coloured areas was determined with respect to the surrounding substrate (black). Among chosen particles agglomeration in image plane is clearly observable. However, data indicated no stacking in evaluated z-direction.

In Figure S16 a zoom-in is shown (a), together with an exemplary topographical cross-section of a single particle (b). For a quantitative particle size analysis, only the height was used, since the lateral extension is mainly given by the apex of the AFM tip and thus appears larger than the height (cf. Figure S16 b).

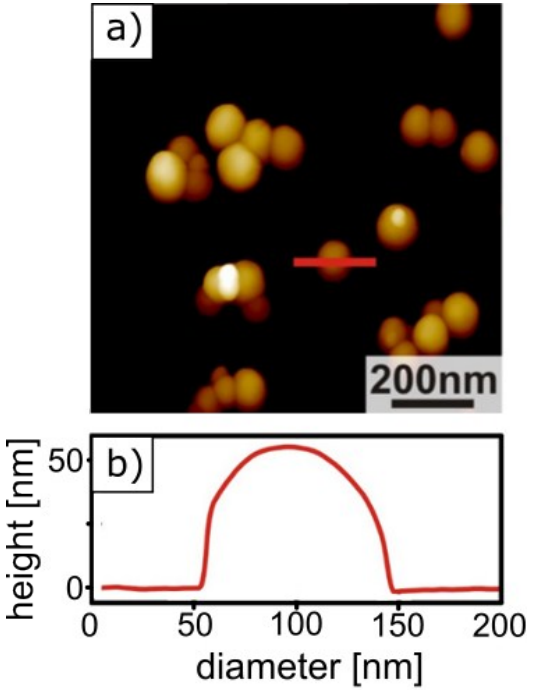

Figure S16 | Zoomed-in AFM micrograph (a) with corresponding cross section of one single particle (b).

2.4 Ensuring Reproducibility

To ensure reproducibility in the synthesis of the Zr-*fum* nanoparticles, multiple batches (Zrfum-1 to Zrfum-4) were synthesised and examined for their size attributes. This was done with X-ray diffraction, additionally with dynamic light scattering in ethanol.

Dynamic Light Scattering

The particle size distribution of samples Zrfum-1, Zrfum-2, Zrfum-3, and Zrfum-4 were determined *via* dynamic light scattering in ethanol. The results are shown in Table S4. Each sample was measured two consecutive times after finishing the washing steps of the synthesis. The similarities in the resulting diameters ranging from 129 nm to 136 nm show the good reproducibility of the synthesis of the particles. However, there are fluctuations regarding the polydispersity index (PDI), even for two consecutive measurements of the same sample, which shows, that the PDI can only be used as a rough estimation for the polydispersity of the sample.

Table S4 | Results (intensity distribution) of the DLS measurements of samples Zrfum-1 to Zrfum-4 in ethanol.

Sample	Measurement	Diameter(Cumulants) [nm]	PDI
Zrfum-1	1	130	0.135
	2	129	0.168
Zrfum-2	1	135	0.094
	2	132	0.136
Zrfum-3	1	135	0.098
	2	135	0.111
Zrfum-4	1	136	0.117
	2	134	0.086

Fluorescence Correlation Spectroscopy

The particle size and size distribution of samples Zrfum-1, Zrfum-2, Zrfum-3 were determined with FCS. The results are shown in Table S5. The similarities in the resulting diameters show the good reproducibility of the synthesis of the particles.

Table S5 | Results of the FCS measurements of samples Zrfum-1 to Zrfum-3 labeled with Alexa Fluor 488 in water. FWHM = full width at half maximum

Sample	Diameter (single component Fit) [nm]	Diameter & FWHM (GDM Fit, see calculations) [nm]
Zrfum-1	127	133, 12
Zrfum-2	136	133, 18
Zrfum-3	136	135, 17

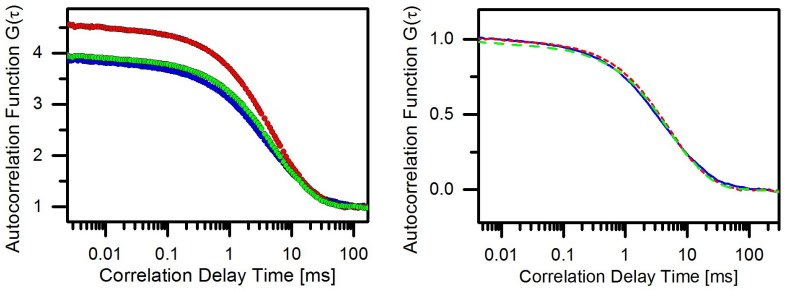

Figure S17 | FCS Autocorrelation functions of labelled Zr-fum particles sample 1(blue), 2(red) and 3(green). Original correlation curves (left) show slightly different correlation heights implying slightly different concentrations of the three nanoparticle samples. The same data after normalisation (b) shows small variation in the diffusion times of the Zr-fum samples denoting small batch to batch variations in the hydrodynamic diameter which was also confirmed by single component and GDM fit.

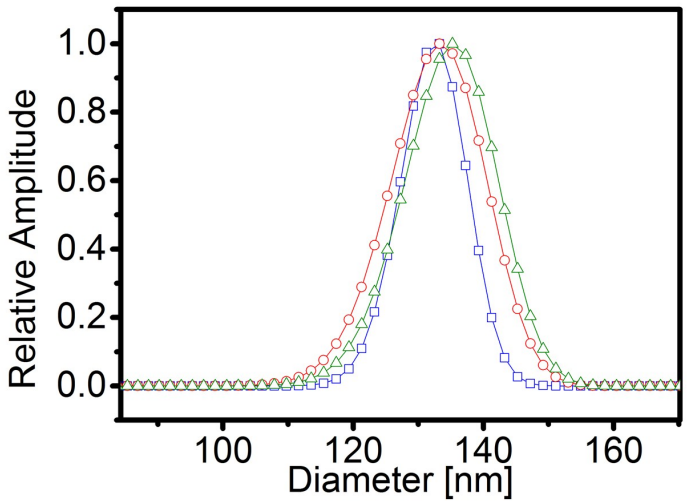

Figure S18| FCS size distribution of three measured nanoparticle batches 1(blue), 2(red) and 3(green) obtained from GDM Fit. The similarities in the resulting diameters show the great reproducibility of the synthesis of the particles.

3 Calculations

3.1 Dynamic Light Scattering

The data received during the DLS measurements was evaluated using the "method of cumulants"[7], which is shortly described in the following section. It introduces a polydispersity index (PDI, see equation (6)) as an indicator of the size distribution of the particles. Generally, DLS uses the time-dependent intensity fluctuations of a sample-scattered laser. These intensity fluctuations can be described with a second order intensity-autocorrelation function as shown in equation (1):

$$G^{(2)}(\tau) = \frac{\langle I(t)I(t+\tau)\rangle}{\langle I(t)\rangle^2} \quad (1)$$

The intensity-autocorrelation function is linked by the Siegert relation[8] to a field-correlation function as presented in equation (2), using the baseline *B* and a geometry factor β.

$$G^{(2)}(\tau) = B + \beta[g^{(1)}(\tau)]^2 \quad (2)$$

This field-correlation function of monodisperse particles can be described with equation (3) featuring the decay rate Γ and the passed time τ:

$$G^{(1)}(\tau) = \exp(-\Gamma\tau) \quad (3)$$

The decay rate $\Gamma = Dq^2$ includes the diffusion coefficient *D* and the magnitude of the scattering vector *q*, which is given by equation (4):

$$q = \frac{4\pi n}{\lambda_0} sin\left(\frac{\theta}{2}\right) \quad (4)$$

Here, *n* is the refractive index of the solvents, θ is the angle at which the scattered intensity was measured (θ = 173 °), and λ_0 is the wavelength of the laser in vacuum (λ_0 = 633 nm).

For polydisperse samples, the "method of cumulants" can be used. Here, the intensity-autocorrelation function is described by equation (5):

$$G^{(2)} = B + \beta\, exp(-2\Gamma\tau)\left(1 + \frac{\mu_2}{2!}\tau - \frac{\mu_3}{3!}\tau^2 \ldots\right)^2 \quad (5)$$

With this method, the correlation function was fitted up to the point, where the amplitudes are 10% of the initial amplitude. The term $\left(1 + \frac{\mu_2}{2!}\tau - \frac{\mu_3}{3!}\tau^2 \ldots\right)$ was cut off at its second segment. Using this method of cumulants, it is possible to take into account multiple species in dispersion. It introduces a polydispersity index (PDI, see equation (6)) as an indicator of the size distribution of the particles.

$$PDI = \frac{\mu_2}{\Gamma^2} \quad (6)$$

This polydispersity index was used to determine the standard deviation *σ* of the particle size distribution using equation (7) with the average hydrodynamic particle diameter *d.*

$$PDI = \left(\frac{\sigma}{d}\right)^2 \quad (7)$$

3.2 Fluorescence Correlation Spectroscopy

Fluorescence correlation spectroscopy (FCS) is a versatile technique that makes use of fluorescence intensity fluctuations to characterise the dynamics of a low number of particles (e.g. single molecules or nanoparticles) diffusing through a very small confocal detection volume. It has been used in plentiful biophysical studies and many applications in analytical chemistry and Biochemistry were found.[9-12] FCS is ideal for measuring molecular diffusion and, thus, the molecular size in highly dilute solutions without any need to perturb the system.[13, 14]

Since Magde *et al.* demonstrated the principles of FCS in 1972 and improvements of Rigler *et al.* using confocal microscopy, FCS evolved immensely in terms of its applicability, sensitivity and versatility.[15, 16]

In FCS, information is extracted by determination of the autocorrelation function (equation (8))

$$G(\tau) = \frac{\langle F(t)F(t+\tau)\rangle}{\langle F\rangle^2} \quad (8)$$

of the fluctuating fluorescence signal F(t) and fitting an physical model to the resulting correlation curve. In the case of free diffusion the correlation is given by equation (9),

$$G(\tau) = 1 + G(0)\frac{1}{1+\frac{\tau}{\tau_D}}\frac{1}{\sqrt{1+\frac{\tau}{S^2\tau_D}}}, \quad (9)$$

where $G(0)$ is the correlation's amplitude, S is the ratio between the lateral and the axial confocal volume radius, while τ_D is the mean time a particle needs to diffuse across the focal volume[17]. Knowing the width ω of the confocal volume, the hydrodynamic radius is given by equation (10)

$$R_H = \frac{2k_B T\tau_D}{3\pi\eta\omega^2} \quad (10)$$

using the Boltzmann constant k_B as well as the temperature $T = 295\,\mathrm{K}$ and viscosity $\eta = 0.958\,\mathrm{mPas}$ of the measured aqueous suspension.

In order to obtain a size distribution from FCS fits a Gaussian Distribution Model (GDM) fit[12] was also applied. The underlying concept of GDM is that the sample is not monodisperse with a single value for the diffusion time, τ_D, but a Gaussian distribution on a fixed logarithmic diffusion time-scale with a peak diffusion time τ_P. The fit to the autocorrelation function is described by equation (11)

$$G(\tau) = 1 + \sum_{i=1}^{n} a_i(\tau_{Di})\frac{1}{1+\frac{\tau}{\tau_{Di}}}\frac{1}{\sqrt{1+\frac{\tau}{S^2\tau_{Di}}}}, \quad (11)$$

where $a_i(\tau_{Di}) = \mathrm{A}\exp\left[-\left(\frac{\ln\left(\frac{\tau_{Di}}{\tau_P}\right)}{b}\right)^2\right]$ with relative amplitude *A* and a distribution width of *b*.

Taking into account that Zr-fum nanoparticles have radii comparable to the beam waist ω, the measured diffusion time has a larger value than it would have if point particles with the same diffusive behavior were observed. Due to the fact that Alexa Fluor 488 labeling was applied at the outer surface of the nanoparticles they are fluorescing hollow spheres from the FCS view. The equation $\tau_{measured} = \tau_{D_{pointparticle}} \cdot (1 + \frac{8R^2}{3\omega^2})$, taken from Wu et al. [18] was used to correct this finite particle size effect of hollow spheres.

4 References

1. S. Brunauer, P. H. Emmet and E. Teller, *J. Am. Chem. Soc.*, 1938, **60**, 309-319.
2. G. S. Pawley, *J. Appl. Cryst.*, 1981, **14**, 357-361.
3. Z. Petrásek and P. Schwille, *Biophys J.*, 2008, **94**, 1437-1448.
4. G. Persson, P. Thyberg, T. Sandén and J. Widengren, *J. Phys. Chem. B*, 2009, **113**, 8752-8757.
5. G. Wißmann, A. Schaate, S. Lilienthal, I. Bremer, S. A. M and B. P, *Microporous Mesoporous Mater.*, 2012, 64-70.
6. K. S. W. Sing, D. H. Everett, R. A. W. Haul, L. Moscou, R. A. Pierotti, J. Rouquérol, T. Siemieniewska, *Pure & Appl. Chem.*, 1985, **57**, 603-619.
7. B. J. Frisken, *Appl. Opt.*, 2001, **40**, 4087-4091.
8. K. Schätzel, *"Single-photon correlation techniques" in Dynamic Light Scattering, W. Brown*, Oxford University, 1993.
9. M. A. Digman and E. Gratton, *Annu. Rev. Phys. Chem.,* 2011, **62**, 645-668.
10. E. Haustein and P. Schwille, *Annu. Rev. Biophys. Biomol. Struct.,* 2007, **26**, 151-169.
11. J. J. Mittag, S. Milani, D. M. Walsh, J. O. Rädler and J. J. McManus, *Biochem. Biophys. Res. Commun.*, 2014, **448**, 195-199.
12. S. Lippok, T. Obser, J. P. Müller, V. K. Stierle, M. Benoit, U. Budde, R. Schneppenheim and J. O. Rädler, *Biophys. J.*, 2013, **105**, 1208-1216.
13. C. L. Kuyper, K. L. Budzinski, R. M. Lorenz, Chiu and D. T., *J. Am. Chem. Soc.*, 2006, **128**, 730-731.
14. N. Pal, S. D. Verma, M. K. Singh and S. Sen, *Anal. Chem.*, 2011, **83**, 7736-7744.
15. D. Madge, E. Elson and W. W. Webb, *Phys. Rev. Lett.*, 1972, **29**, 705-708.
16. R. Rigler, Ü. Mets, J. Widengren and P. Kask, *Eur. Biophys. J.*, 1993, **22**, 169-175.
17. P. Schwille and E. Hausstein, *Anal. Chem.*, 2009, **94**, 1-33.
18. B. C. Wu, Yan, Müller, Joachim D., *Biophys. J.*, 2008, **7**, 2800-2808.

B.3 Originalpublikation P3

Xiaowen Liu, Peng Zhang, Dongsheng He, Wolfgang Rödl, Tobias Preiß, Joachim O. Rädler, Ernst Wagner, Ulrich Lächelt.

pH-Reversible Cationic RNase A Conjugates for Enhanced Cellular Delivery and Tumor Cell Killing

Biomacromolecules, 2016, 17 (1), 173-182.

Article

pubs.acs.org/Biomac

pH-Reversible Cationic RNase A Conjugates for Enhanced Cellular Delivery and Tumor Cell Killing

Xiaowen Liu,[†] Peng Zhang,[†] Dongsheng He,[†,§] Wolfgang Rödl,[†] Tobias Preiß,[‡] Joachim O. Rädler,[‡,§] Ernst Wagner,[†,§] and Ulrich Lächelt*[,†]

[†]Pharmaceutical Biotechnology, Center for System-based Drug Research, Ludwig-Maximilians University Munich, Butenandstrasse 5-13, D-81377 Munich, Germany

[‡]Faculty of Physics and Center for NanoScience (CeNS), Ludwig-Maximilians University Munich, Geschwister-Scholl-Platz 1, 80539 Munich, Germany

[§]Nanosystems Initiative Munich, Schellingstrasse 4, D-80799 Munich, Germany

Supporting Information

ABSTRACT: Intracellularly-acting therapeutic proteins are considered promising alternatives for the treatment of various diseases. Major limitations of their application are low efficiency of intracellular delivery and possible reduction of protein activity during derivatization. Herein, we report pH-sensitive covalent modification of proteins with a histidine-rich cationic oligomer (689) for efficient intracellular transduction and traceless release of functional proteins. Enhanced Green fluorescent protein (EGFP), as model for the visualization of protein transduction, and RNase A, as therapeutic protein with antitumoral effect, were modified with the pH-sensitive bifunctional AzMMMan linker and varying amounts of cationic oligomer. The modification degree showed impact on the internalization and cellular distribution of EGFP as well as the biological effect of RNase A conjugates, which mediated considerable toxicity against cancer cells at optimal ratio. The presented conjugates demonstrate their qualification to achieve efficient intracellular delivery and controlled release without protein inactivation and potential prospective applications in protein-based therapies.

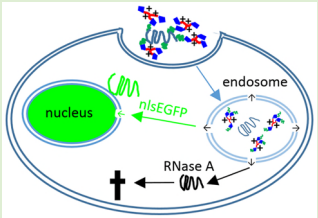

INTRODUCTION

Proteins represent biomolecules with most functional and diverse character within living organisms: shaping cells, transporting essential nutrients, catalyzing biochemical reactions, or transmitting signals.[1,2] The biotechnological production of proteins facilitated the rapid evolvement of a new pharmaceutical field since the first recombinant protein therapeutic, human insulin, received approval by the US Food and Drug Administration (FDA) in 1982.[1] Since then, more than 130 proteins or peptides have been approved by FDA for clinical applications, such as cancer therapy, diabetes mellitus, hemophilia, and AIDS, and many more are in development.[1] Protein therapy represents an innovative approach with higher specificity than many simple small molecular drugs and lower risk for potential genetic adverse effects comparing to gene therapy. In addition to pharmaceuticals, direct protein delivery into the intracellular space provides a wide range of biological applications including specific interaction with metabolic processes or signaling pathways.[3−5] A major bottleneck to expand protein therapy is their efficient delivery to the target sites without affecting their natural function. Hence, many strategies have been followed to enable controlled delivery of therapeutic proteins, such as thermal,[6,7] light[8−10] redox, and magnetic stimuli-triggered functional units combined with a number of synthetic materials, including liposomes[11,12] and polymers.[13,14] Intracellular transduction of proteins can be achieved by attachment of cell-penetrating peptides (CPPs) and protein-transduction domains (PTDs)[15,16] or genetic engineering of supercharged proteins.[17,18] However, protein activity and function can be affected by irreversible protein modification. Thus, the realization of a stable interaction between the native protein and the carrier system, which is reversible after intracellular delivery, is desirable.

Previous studies from our laboratory demonstrated that small molecular azidomethyl-methylmaleic anhydride (AzMMMan) can be used as a pH-labile bifunctional linker that connects the amino groups of proteins by acyl substitution with oligocations by azide alkyne cycloaddition based click chemistry.[19] The resulting conjugates are stable at physiological pH but are disassembled in the mild acidic environment of endosomes. This kind of conjugate shows high efficiency and achieves traceless delivery of the native protein to the target site of cells. In the current work, we carry out systematic studies to investigate the conjugation degree of the proteins with two defined three-arm oligoamino amides (386 and its histidine-containing analog 689) and the effect on intracellular delivery and activity. A series of conjugates with different molar ratios of oligocation to enhanced green fluorescent protein (EGFP) were synthesized and investigated; the applied EGFP contained a nuclear localization signal (NLS) for nuclear delivery of nlsEGFP. The established method was then used to modify RNase A, an endoribonuclease that specifically degrades single-stranded RNA and exhibits tumoricidal activity.[20] The RNase A conjugates showed very high uptake by cells, which resulted in significant toxicity for cancer cells.

Received: September 24, 2015
Revised: December 9, 2015
Published: December 11, 2015

DOI: 10.1021/acs.biomac.5b01289
Biomacromolecules 2016, 17, 173−182

MATERIALS AND METHODS

Materials. Dimethylmaleic anhydride, N-bromosuccinimide, benzoyl peroxide, sodium azide, and RNase A (from bovine pancreas) were purchased from Sigma-Aldrich (Munich, Germany). Dibenzylcyclooctyne-PEG$_4$-maleimide (DBCO-PEG$_4$-maleimide) was purchased from Jena Bioscience (Jena, Germany). Cyanine5 dye NHS ester (Cy5-NHS) was obtained from Lumiprobe (Hannover, Germany). Sephadex G25 material and HisTrap HP 5 mL column were supplied by GE Healthcare (Freiburg, Germany). Isopropyl-β-D-thiogalactopyranoside (IPTG) was purchased from Biomol (Hamburg, Germany). RNA (M, 5000−8000, Torula utilis) was purchased from Sigma-Aldrich (Munich, Germany). Cell culture media, antibiotics, and fetal bovine serum (FBS) were purchased from Invitrogen (Karlsruhe, Germany).

Synthesis of 3-(Bromomethyl)-4-methyl-2,5-furandione (BrMMMan). The compound was synthesized following a previous protocol with slight modifications.[19,21] Briefly, dimethylmaleic anhydride (5.04 g, 40 mmol), N-bromosuccinimide (14.24 g, 80 mmol), and benzoyl peroxide (200 mg, 0.83 mmol) were dissolved in carbon tetrachloride (CCl_4, 300 mL) in a 500 mL round-bottom flask. The mixture was gently refluxed for 5 h. Then the reaction mixture was allowed to cool to room temperature, and afterward a second portion of benzoyl peroxide (200 mg, 0.83 mmol) was added. The mixture was refluxed for another 5 h and then left overnight at room temperature. The solids were removed by filtration and washed two times with CCl_4 (25 mL). The combined organic solutions were washed two times with water (100 mL) and one time with brine (100 mL), then dried over Na_2SO_4 and concentrated in vacuo to result in thick yellow oil. The oil was first purified by chromatography on a silica gel column (elution with petroleum ether/ethyl acetate 8:2) to obtain a crude product and then further purified by distilling twice using a miniature high vacuum distillation system. Three fractions were observed, and the second fraction was collected (purity, about 90%) and distilled again. A yield of the product (BrMMMan) of 1.30 g (purity, about 97%) was obtained. ^{1}H NMR (500 MHz, $CDCl_3$) δ(ppm) = 2.17 (s, 3H, -C$\underline{H}_3$), 4.17 (s, 2H, -C$\underline{H}_2$-Br), 7.25 ($CHCl_3$) (cf. Figure S2).

Synthesis of 3-(Azidomethyl)-4-methyl-2, 5-furandione (AzMMMan). Synthesis was performed analogously as described by Maier et al. with minor modifications.[19] 3-(Bromomethyl)-4-methyl-2,5-furandione (BrMMMan, 310.5 mg, 1.5 mmol) was dissolved in dry acetone (10 mL); afterward, sodium azide (105.6 mg, 1.6 mmol) was added in one portion. The mixture was stirred overnight at room temperature. After filtering, the solvent was evaporated, and the crude product was purified by silica gel column using hexane/ethyl acetate (7:3) as mobile phase. After the solvent was evaporated, the product (83.6 mg, yield 33.4%) was obtained. ^{1}H NMR (500 MHz, $CDCl_3$) δ(ppm) = 2.22 (s, 3H, -C$\underline{H}_3$), 4.27 (s, 2H, -C$\underline{H}_2$-N$_3$), 7.25 ($CHCl_3$) (cf. Figure S3).

Expression and Purification of nlsEGFP. Recombinant nlsEGFP was produced as previously reported.[19] Briefly, *E. coli* bacterial strain BL21(DE3)pLysS, transformed with a pET23a(+) plasmid containing the nlsEGFP gene construct, was grown to an optical density of 0.75 (600 nm) under constant shaking in TB medium (37 °C). Protein expression was induced by addition of IPTG to a final concentration of 1 mM, and incubation was continued for 16 h at 32 °C. The cells were harvested by centrifugation at 4000 rpm. After ultrasonic cell lysis, the EGFP containing a polyhistidine tag was purified by nickel chromatography using a HisTrap HP column and a gradient from binding buffer (50 mM sodium hydrogen phosphate, 300 mM sodium chloride, 20 mM imidazole) to elution buffer (50 mM sodium hydrogen phosphate, 500 mM sodium chloride, 250 mM imidazole). The protein was dialyzed (MWCO 14000) overnight at 4 °C against phosphate buffered saline (PBS) buffer (pH 7.3).

Synthesis of EGFP-AzMMMan. The modification of nlsEGFP with AzMMMan was carried out as reported before.[19] Briefly, nlsEGFP (5 mg, 0.16 μmol) was dissolved in Hepps buffer (950 μL, 0.5 M, pH = 9.0). Afterward, AzMMMan (5 mg, 30 μmol) was diluted in acetonitrile (50 μL) and dropped slowly to the protein solution. Subsequently, the mixture was incubated for 2 h under constant stirring (800 rpm) at 20 °C and then purified by size exclusion chromatography (SEC) using Sephadex G25 material, PBS 8.0 as mobile phase. The concentration of EGFP-AzMMMan was quantified photometrically (extinction coefficient of 55 000 M^{-1} cm^{-1} at 488 nm). AzMMMan-modified EGFP was snap frozen by liquid nitrogen and stored in the freezer (−80 °C).

DBCO Functionalization of Cationic Oligomers. Oligomers 689 and 386 were synthesized following our previous protocol.[22,23] Oligomer 689 (HCl salt, MW = 6038.4 g/mol, 3 mg, 0.5 μmol) was dissolved in 0.9 mL of Hepps (pH = 8.5); afterward, DBCO-PEG$_4$-Mal (1 mg, 1.5 μmol) dissolved in 100 μL of DMSO was slowly added, and the mixture was reacted for 1 h under constant shaking (800 rpm) at 20 °C. Then this solution was directly used for conjugation with EGFP-AzMMMan or RNase A-AzMMMan (see below). The 386-AzMMMan was synthesized in an analog way using 2 mg of 386 (HCl salt, MW = 3955.2 g/mol, 0.5 μmol) and 1 mg of DBCO-PEG4-Mal (1.5 μmol).

Synthesis of EGFP-AzMMMan-DBCO-PEG4-Mal-689 and -386. Protein conjugates were synthesized by copper free click chemistry. Briefly, four parts of EGFP-AzMMMan (0.25 mg, 7.90 × 10^{-3} μmol) were separately diluted in Hepps (0.5 M, pH = 8.5) and subsequently reacted with the cationic oligomer (DBCO-PEG$_4$-Mal-689) at four different molar ratios (689: EGFP = 2, 4, 8, 16) for 4 h under constant shaking (800 rpm, 20 °C). Free oligomer was removed by dialysis (dialysis membrane MWCO 14000) against 5 L of PBS (pH = 8.0) overnight at 4 °C. The purified solution was collected, and the concentration of EGFP-AzMMMan-DBCO-PEG$_4$-Mal-689 was quantified photometrically (extinction coefficient of 55 000 M^{-1} cm^{-1} at 488 nm). The solution was snap frozen by liquid nitrogen and stored in the freezer (−80 °C). Protein conjugates with DBCO-PEG$_4$-Mal-386 were synthesized analogously.

Synthesis of RNase A-Cy5. RNase A (5 mg, 0.37 μmol) was dissolved in 900 μL of PBS (pH = 8.5), and then NHS-Cy5 (0.225 mg, 0.37 μmol) was dissolved in 100 μL of DMSO and added to the protein solution. The mixture reacted for 2 h under constant shaking at 20 °C. Then SEC using Sephadex G25 material and PBS 8.0 as mobile phase was carried out to remove free dye. The purified RNase A-Cy5 was used to react with AzMMMan and DBCO-PEG4-Mal-689 as described below.

Synthesis of RNase A-AzMMMan. RNase A-AzMMMan conjugate was prepared similarly to the EGFP-AzMMMan conjugate. Briefly, RNase A or RNase A-Cy5 (5 mg, 0.37 μmol) was dissolved in 950 μL of Hepps (0.5 M, pH = 9.0) buffer; AzMMMan (5 mg, 30 μmol) dissolved in acetonitrile (50 μL) was added to the protein solution followed by 2 h of incubation under constant shaking at 20 °C. The mixture was purified by SEC (Sephadex G25 material, PBS 8.0 as mobile phase). RNase A-AzMMMan was collected and quantified by BCA assay. Then the solution was snap frozen by liquid nitrogen and stored in the freezer (−80 °C).

Synthesis of RNase A-AzMMMan-DBCO-PEG4-Mal-689. Four batches of RNase A-AzMMMan (0.25 mg, 1.83 × 10^{-2} μmol) were diluted in 900 μL of Hepps (0.5 M, pH = 8.5); afterward, different amounts of DBCO-PEG$_4$-Mal-689 (molar ratios of 689: RNase A = 6, 3, 1.5, 0.75) were added to the separate batches of AzMMMan modified protein. The mixtures reacted for 4 h under constant shaking

DOI: 10.1021/acs.biomac.5b01289
Biomacromolecules 2016, 17, 173−182

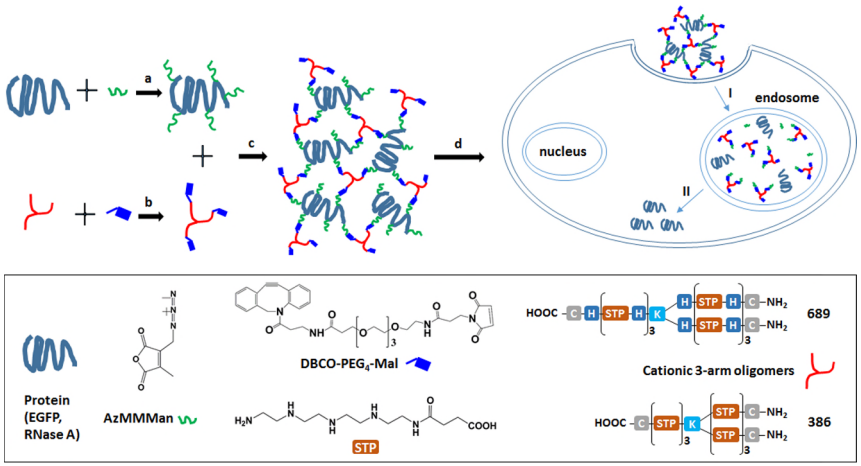

Figure 1. Schematic illustration of the preparation of pH-sensitive protein conjugates. (a) Amino functions of the protein (EGFP, RNase A) react with the amine-reactive AzMMMan linker; (b) cysteine containing cationic three-arm oligomers react with DBCO-PEG_4-Mal via thiol-maleimide reaction; (c) linker-modified proteins couple with three-arm oligomers via strain-promoted azide−alkyne cycloaddition; (d) native proteins are delivered to the cytosol via cellular uptake (I) and endosomal release (II) facilitated by the conjugated cationic oligomers, which get cleaved off in the acidic environment of the endosomes. C, H, and K represent the corresponding α-amino acids in one-letter-code; STP stands for the used oligoamino acid succinoyl tetraethylene pentamine.[28]

(800 rpm) at 20 °C. RNase A conjugates were snap frozen by liquid nitrogen and stored in the freezer (−80 °C). RNase A-AzMMMan-DBCO-PEG_4-Mal-386 conjugates were synthesized analogously.

SDS-PAGE of EGFP and RNase A Conjugates. Protein samples were loaded on a 12.5% SDS-PAGE gel. The gel ran for 2 h at 125 V. After electrophoresis, the gel was stained with coomassie solution (acetic acid/ethanol/water, 1:3:6, v/v/v and 0.3% coomassie brilliant blue G250, w/v). Then the gel was destained by washing with a solution of acetic acid/ethanol/H_2O (1:3:6, v/v/v).

Fluorescence Correlation Spectroscopy (FCS). The measurements were conducted on a home-built setup using a 63× NA1.2 water immersion objective (Zeiss Germany) that focuses the exciting laser light (470 nm) into the sample. A 525/50 bandpass filter (AHF Germany) only lets emission light of EGFP through to the detector (CountBlue LaserComponents Germany). A 15 μm pinhole constricts the effective detection volume to sub femtoliter size at a focal width of ω = 210 nm (determined by calibration using Alexa Fluor 488). An ALV-7004 hardware correlator (ALV Germany) processed the detected fluorescence fluctuations $F(t)$ into a correlation curve with the correlation function $G(\tau) = (\langle F(t)F(t+\tau)\rangle)/\langle F\rangle^2) - 1$. To derive the hydrodynamic radius of 689-EGFP conjugates, correlation curves were fitted using

$$G(\tau) = G(0)\frac{1}{1+\frac{\tau}{\tau_D}}\frac{1}{\sqrt{1+\frac{\tau}{S^2\tau_D}}}$$

where τ_D is the mean time a particle needs to diffuse across the focal volume, S is the ratio between the lateral and the axial confocal volume radius, while $G(0)$ is the correlation's amplitude.[24] The hydrodynamic radius is given by

$$R_H = \frac{2k_BT\tau_D}{3\pi\eta\omega^2}$$

where ω is the width of the confocal volume, k_B is the Boltzmann constant, and T = 295 K and η = 0.958 mPas, the temperature and the viscosity of the measured aqueous suspension.

Solutions containing 5 μg/mL of EGFP, EGFP-AzMMMan, or 689-EGFP conjugates (molar ratios of 689: EGFP = 2, 4, 8, and 16) were measured.

Release of RNase A from Conjugates Detected by SDS-PAGE. The 689 and 386 modified RNase A (ratio 6) were incubated in acidic buffer (pH = 5, disodium hydrogen phosphate-citric acid buffer) and PBS (pH 7.4) for 24 h at 37 °C. Then the treated samples were loaded on a 12.5% SDS-PAGE gel. The gel ran for 2 h at 125 V. After electrophoresis, the gel was stained with coomassie solution (acetic acid/ethanol/water, 1:3:6, v/v/v and 0.3% coomassie brilliant blue G250, w/v). Then the gel was destained by washing with a solution of acetic acid/ethanol/H_2O (1:3:6, v/v/v).

Ethidium Bromide Assay for Determination of Enzymatic RNase A Activity. One microliter of EtBr (0.5 μg/mL) was added into 997 μL of PBS buffer (pH = 7.4) as blank control; then 2 μL of RNA (10 mg/mL) was added, the solution was stirred, and fluorescence intensity was monitored during 5 min equilibration. After addition of RNase A samples (1 μg of RNase A), the solutions were incubated under stirring for additional 5 min. The EtBr fluorescence was measured at the excitation wavelength λ_{ex} = 510 nm and emission wavelength λ_{em} = 590 nm using a Cary Eclipse spectrophotometer (Varian, Germany).

Cell Culture. HeLa (human cervical adenocarcinoma cells) and Neuro 2A (mouse neuroblastoma cells) cells were grown in Dulbecco's modified Eagle's medium (DMEM), supplemented with 10% fetal bovine serum (FBS), 4 mM stable glutamine, 100 U/mL of penicillin, and 100 μg/mL of streptomycin. All cells were cultured in an incubator at 37 °C with 5% CO_2 and humidified atmosphere.

Flow Cytometric Measurement of EGFP or RNase A-Cy5 Uptake. HeLa cells were seeded into 24-well plates at a density of 50 000 cells per well. After 24 h, the medium was replaced with fresh medium. Subsequently, the EGFP conjugates (final concentration 1 μM) or the RNase A-Cy5 conjugates (final concentration 4 μM) were added into each well and incubated at 37 °C for 2 h. Then the cells were washed with 500 μL of PBS containing 1000 IU heparin per mL. After additional wash with PBS only, the cells were detached with trypsin/EDTA, diluted with PBS containing 10% FBS, harvested by centrifugation, and taken up in PBS containing 10% FBS. The cellular fluorescence was assayed by excitation of EGFP at 488 nm and detection of emission at 510 nm with a Cyan ADP flow cytometer (Dako, Hamburg, Germany). For RNase A-Cy5 conjugates, the cellular fluorescence was assayed by excitation of Cy5 at 635 nm and detection of emission at 665 nm. Cells were appropriately gated by forward/sideward scatter and pulse width for exclusion of doublets, and counterstained with DAPI (4′,6-diamidino-2-phenylindole) to discriminate between viable and dead cells. Minimum ten thousand gated cells per sample were collected. Data were recorded with Summit software (Summit, Jamesville, NY). Analysis was done by FlowJo 7.6.5 flow cytometric analysis software. All experiments were performed in triplicates.

DOI: 10.1021/acs.biomac.5b01289
Biomacromolecules 2016, 17, 173−182

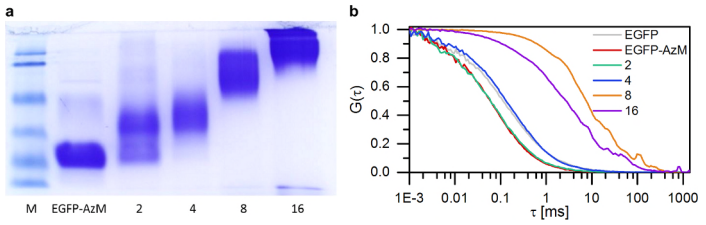

Figure 2. Effect of the functionalization and cross-linking degree of 689-EGFP conjugates on electrophoretic mobility and particle size determined by (a) SDS-PAGE and (b) FCS measurments. Numbers indicate the molar ratio of 689 to EGFP. (a) Equal amounts (10 μg) of EGFP protein were loaded in each lane. M, molecular weight marker. (b) Normalized average correlation curves show clustered (R_H > 0.1 μm) 689-EGFP conjugates at high 689 to EGFP ratios (8, 16), whereas particle size at low ratios (2, 4) remain in the range of EGFP and EGFP-AzM (R_H = 2−4 nm).

Fluorescence Microscopy of EGFP. HeLa cells were seeded into eight-well Nunc chamber slides (Thermo Scientific, Braunschweig, Germany) at a density of 10 000 cells per well. After 24 h, the medium was replaced with fresh medium. Subsequently, the EGFP conjugates were added into each well (final concentration 1 μM) and incubated at 37 °C for 24 h. Then the cells were washed with 300 μL of PBS containing 1000 IU heparin per mL. After additional wash with PBS only, the cells were fixed with 4% paraformaldehyde. Nuclei were stained with DAPI (1 μg/mL). The cells were observed on a Zeiss Axiovert 200 fluorescence microscope (Jena, Germany). A 20× objective or a 40× objective and appropriate filter sets for analysis of EGFP and DAPI were used. Data were analyzed and processed by AxioVision Rel. 4.8 software (Zeiss, Jena, Germany).

MTT Assay. HeLa cells or Neuro 2A cells were seeded into 96-well plates at a density of 10 000 cells per well. After 24 h, the medium was replaced with 80 μL of fresh medium. Subsequently, the RNase A conjugates (final concentration 0.5; 1.0; 2.0; 4.0 μM), RNase A-AzMMMan (final concentration 0.5; 1.0; 2.0; 4.0 μM), oligomers (final concentration 3.0; 6.0; 12.0; 24.0 μM), and mixture of RNase A-AzMMMan (final concentration 0.5; 1.0; 2.0; 4.0 μM) and oligomers (final concentration 3.0; 6.0; 12.0; 24.0 μM) were diluted into 20 μL with PBS, added to each well, and incubated at 37 °C for 48 h. Afterward, MTT solution (10 μL per well, 5.0 mg/mL) was added. After incubation for 2 h, the medium was removed, and the 96-well plates were stored at −80 °C for at least 1 h. One-hundred microliters of DMSO per well was added to dissolve the purple formazan product. The optical absorbance was measured at 590 nm, with a reference wavelength of 630 nm, by a microplate reader (Tecan Spectrafluor Plus, Tecan, Switzerland). The relative cell viability (%) related to control wells treated only with 20 μL of PBS was calculated as ([A] test/[A] control) × 100. All experiments were performed in triplicates.

RESULTS AND DISCUSSION

Protein Carrier Design. Lysine residues are convenient anchor points in proteins for synthetic modification by acylation. However, irreversible modification can affect the activity of proteins. Our work is based on the formation of covalent amide bonds between the lysines of proteins (Enhanced Green Fluorescent Protein, EGFP; Ribonuclease A, RNase A) and the pH-sensitive bifunctional (amine-reactive anhydride and alkyne-reactive azide function) linker AzMM-Man (Figure 1, Figure S1). The pH in the endo- and lysosomes (early endosomes 6.0−6.5, late endo- and lysosomes 4.5−5.5) is lower than in any other part of the cell.[25−27] This unique feature can be utilized as a specific trigger for a dynamic response to the environment within the acidic vesicles. By using the AzMMMan linker for conjugation, a protein vector can be designed, which is stably associated with the protein in the extracellular space and releases the cargo in a traceless fashion at the low endosomal pH after cellular uptake. The AzMMMan linker modified proteins (EGFP, RNase A; Figure 1a) were conjugated with sequence defined cationic oligomers DBCO-PEG_4-Mal-689 and -386 by copper free click chemistry for mediation of cellular uptake and endosomal escape. Both compounds, 689 and 386, represent cationic three-arm oligomers comprising the artificial oligoamino acid succinoyl tetraethylene pentamine (STP) and terminal cysteines for reaction with DBCO-PEG_4-Mal (Figure 1b) and subsequent cross-linking of AzMMMan modified proteins (Figure 1c). Since huge proteins generally contain multiple reactive lysine groups and the extent of surface modification and cross-linking can impact the properties of nanostructures, special focus has been put on the optimization of the modification and coating degree of EGFP as a model protein with regards to cellular uptake and intracellular localization. RNase A conjugates were assembled as potential tumoricidal protein therapeutics. Here, the pH-responsive release and biological activity of RNase A was investigated.

The lysines of the proteins (EGFP, RNase A) were first reacted with an excess amount of AzMMMan linker in Hepps (0.5 M, pH 9.0) for 2 h followed by size exclusion chromatography to remove noncoupled linker. Successful AzMMMan modification of EGFP could be confirmed by UV spectroscopy since AzMMMan and EGFP-AzMMMan have an intensive absorbance around 240 nm compared to nonmodified EGFP (Figure S4). The sequence-defined oligoamino amides 689 and 386 were synthesized by solid phase synthesis,[22,23] and

DOI: 10.1021/acs.biomac.5b01289
Biomacromolecules 2016, 17, 173−182

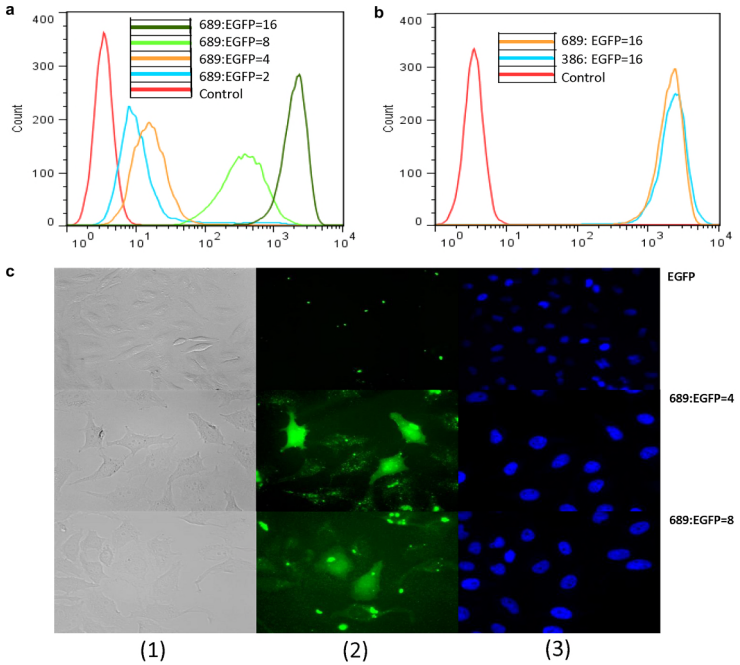

Figure 3. (a) Cellular uptake of conjugates with different 689 to EGFP molar conjugation ratios determined by flow cytometry. Untreated control cells (red), 689: EGFP = 2 (blue), 689: EGFP = 4 (orange), 689: EGFP = 8 (light green), 689: EGFP = 16 (dark green). (b) Flow cytometry of cells incubated with 689 (orange) or 386 (blue) modified EGFP with the same molar ratio (16). HeLa cells were incubated with samples (1 μM EGFP) at 37 °C for 2 h before flow cytometry. (c) Microscopy images of cells treated with different EGFP samples. First row: unmodified EGFP control; second row 689: EGFP = 4; third row 689: EGFP = 8; (1) bright field images; (2) EGFP fluorescence; (3) DAPI fluorescence (nuclear staining). HeLa cells were incubated with samples (1 μM EGFP) for 24 h at 37 °C. A 40× objective was used for image acquisition with EGFP conjugates; 20× objective was used for free EGFP control.

the three contained cysteines were modified with DBCO-PEG$_4$-maleimide.

The reaction of the AzMMMan functionalized proteins with the trifunctional cationic cross-linkers DBCO-PEG$_4$-maleimide-689 and -386 followed. The AzMMMan modified proteins bring in azide groups, which can be used for biorthogonal reaction with dibenzylcyclooctyne (DBCO) by strain promoted azide alkyne cycloaddition that enables the conjugation of two components via a stable triazole structure.[29] By this means, linker-modified proteins were incubated with various molar ratios of DBCO-PEG$_4$-Mal-689 (molar ratios of 689: EGFP = 2, 4, 8, 16; 689: RNase A = 0.75, 1.5, 3, 6), initiating the click reaction between the DBCO group of the cationic conjugate and the azide group of AzMMMan modified proteins (Figure 1c). Since the used SV40nls-EGFP contains 26 and RNase A only 11 primary amines, approx. 2.7-fold higher molar ratios were used during synthesis of the EGFP conjugates to compensate the multiplicity.

The conjugates were analyzed by SDS polyacrylamide gel electrophoresis (PAGE) to confirm successful assembly (Figure 2a and S6). The SDS-PAGE gel reveals a gradual shift of the protein band toward lower migration distance with increasing 689 to protein ratio as a result of the increasing size and modified charge of cross-linked protein conjugates. The protein conjugates with highest modification ratio (689: EGFP = 16 and 689: RNase A = 6) exhibited the shortest migration, which can be explained by more extensive DBCO-PEG$_4$-Mal-689 attachment and cross-linking. To show the cross-linking of 689-EGFP conjugates more detailed, fluorescence correlation spectroscopy (FCS) measurements of EGFP were performed (Figure 2b). FCS is a highly sensitive single-molecule technique for measuring hydrodynamic radii of fluorescent molecules or particles in highly diluted solutions in the nanomolar concentration range.[30] EGFP and EGFP-AzMMMan, as well as the conjugates with 689 to EGFP ratios of 2 and 4, were shown to have hydrodynamic radii of 2−4 nm. In contrast, the samples with 689 to EGFP ratios of 8 and 16 showed clusters

DOI: 10.1021/acs.biomac.5b01289
Biomacromolecules 2016, 17, 173−182

with a hydrodynamic radius above 0.1 μm. This indicates that large EGFP complexes are formed depending on the molar ratio of cross-linking three-arm oligomer. However, it has to be noted that also at the high ratios small particles were detected, which suggests that the conjugation approach results in rather heterogeneous mixtures of variably cross-linked proteins.

Flow Cytometry of EGFP Conjugates. EGFP was equipped with positive charge by modification with the cationic oligomer 689. The sequence-defined oligomer 689 contains nine repeats of the artificial amino acid STP,[28] which exhibits positive charge at neutral pH but also a buffer capacity in the endolysosomal pH range, which was intended to enable transport of the protein into cells and escape from endosomes by the proton-sponge effect.[26,31,32] We hypothesized that different ratios of oligomer on the protein surface could influence the amount of intracellular protein transduction. To investigate this, the internalization of different EGFP conjugates with varied modification ratios into HeLa cells was investigated by flow cytometry. The results demonstrated that the sequence defined three-arm cationic oligomer could deliver the protein into cells. As expected, increasing oligomer conjugation promoted the intracellular protein delivery indicated by a shift toward higher cellular fluorescence intensity in Figure 3, panel a. This illustrates the importance of an optimization of cross-linking degree even when the protein is modified by the same carrier. Having successfully demonstrated efficient cellular uptake of 689 modified EGFP, a comparison study between the two similar cationic oligomers 386 and 689 has been carried out. Oligomer 386 is also a three-arm cationic STP-based oligomer, having been successfully used for siRNA, DNA, and protein delivery before,[23,33,34] but 689 additionally contains histidines after each STP unit to enhance endosomal buffering.

The flow cytometry results show 386 and 689 oligomer modified EGFP being internalized into cells to comparable extent (Figure 3b). In the extracellular environment, the pH is about 7.4, and the additional histidines in 689 are not protonated. Therefore, these two oligomers mediate similar uptake of modified EGFP.

Intracellular Distribution of EGFP. The cellular uptake and intracellular distribution of the EGFP conjugates with varied modification degree were further investigated by fluorescence microscopy (Figure 3c). In case of all four protein conjugates, significant intracellular EGFP fluorescence could be observed (Figure S5); even the protein conjugates with low conjugation ratio (689: EGFP = 2 and 689: EGFP = 4) were efficiently internalized. This accounts for the high potency of the used sequence-defined cationic oligomer to mediate transport of EGFP into cells. Since the used recombinant EGFP contains a NLS, we investigated nuclear delivery after protein conjugate internalization. The protein conjugates (689: EGFP = 4 and 689: EGFP = 8) show successful nuclear entry, whereas the protein conjugates (689: EGFP = 2 and 689: EGFP = 16) did not seem to mediate high nuclear EGFP accumulation (data not shown). We hypothesize that since ratio 2 (689: EGFP) also mediates lower cellular uptake (cf. Figure 3a), the amount of accumulated conjugates with proton-sponge activity is not enough to break through the endosome. On the other hand, since the SV40 large T antigen NLS contains multiple lysines, the extensive modification in case of ratio 16 might affect intracellular trafficking. We conclude that the four EGFP conjugates have high intracellular uptake efficiency, and two optimized conjugates show successful nuclear delivery.

pH-Responsive Release of RNase A Conjugates. RNase A was utilized to demonstrate the feasibility of covalent modification by the established method with a biologically active protein. RNase A, an endoribonuclease, catalyzes the cleavage of the phosphodiester bond between the 5′-ribose of a nucleotide and the phosphate group attached to the 3′-ribose of an adjacent pyrimidine nucleotide. The enzyme has been used as an alternative chemotherapy drug for clinical cancer treatment since it can degrade intracellular RNA inducing apoptosis of tumor cells.[35] Wang recently used cationic lipid-like nanoparticles to coat negatively charged RNase A through electrostatic interaction, which showed an intracellular delivery and cancer killing result.[11] Herein, we used the cationic vector to attach with pH-sensitive AzMMMan modified RNase A. The resulting protein conjugate was expected to form a more stable delivery system than the often used electrostatic noncovalent complexes. A series of 689 or 386 oligocation modified RNase A conjugates was synthesized. To investigate the pH-responsive cleavage, RNase A-AzMMMan-DBCO-PEG$_4$-Mal-689/386 were incubated (molar conjugation ratio of 689 or 386 to RNase A = 6) at neutral or acidic pH, and the release of free RNase A was monitored by SDS-PAGE (Figure 4). The gel

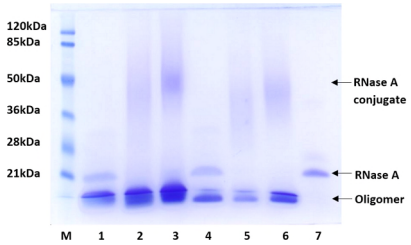

Figure 4. pH dependent traceless release of RNase A from protein conjugates (molar conjugation ratio 6). M, molecular weight marker; (1) 689 modified RNase A incubated in citrate-phosphate buffer (pH = 5) for 24 h at 37 °C; (2) 689 modified RNase A incubated in PBS (pH = 7.4) for 24 h at 37 °C ; (3) 689 modified RNase A without any treatment; (4) 386 modified RNase A incubated in citrate-phosphate buffer (pH = 5) for 24 h at 37 °C; (5) 386 modified RNase A incubated in PBS (pH = 7.4) for 24 h at 37 °C; (6) 386 modified RNase A without any treatment; (7) free RNase A control. Equal amounts (3 μg) of RNase A were loaded in each lane.

demonstrated that incubation for 24 h at pH 5 resulted in significant protein release, in contrast to incubation in PBS buffer at pH 7.4 where almost no cleavage of RNase A could be observed.

Moreover, for detecting the enzymatic activity of RNase A and its conjugates, we developed an ethidium bromide (EtBr) fluorescence assay (Figure 5). The fluorescence intensity of a solution containing 0.5 ng EtBr and 20 μg RNA in 1 mL of PBS (pH = 7.4) was monitored during an equilibration time of 5 min. After addition of RNase A samples, the decrease of fluorescence intensity based on the enzymatic RNA degradation was monitored over 5 min.

While unmodified RNase A solutions that were incubated for 24 h at pH 7.4, pH 5, or freshly prepared did not exhibit remarkable differences (Figure 5, left), the enzymatic activity of RNase A-AzMMMan conjugates was strongly dependent on

DOI: 10.1021/acs.biomac.5b01289
Biomacromolecules 2016, 17, 173−182

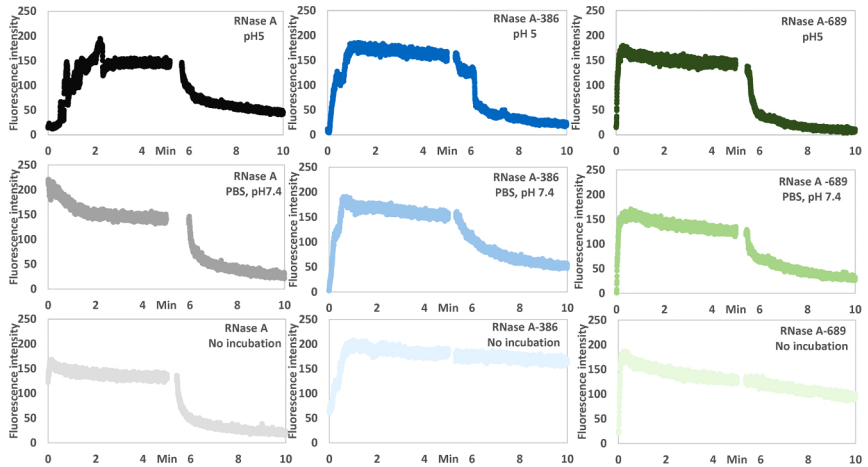

Figure 5. Enzymatic activity of RNase A measured by an ethidium bromide assay. Unmodified RNase A (left), RNase A-AzMMMan-DBCO-PEG_4-Mal-386 (molar ratio 6, middle), and RNase A-AzMMMan-DBCO-PEG_4-Mal-689 (molar ratio 6, right) after different treatments. First row, incubated in citrate-phosphate buffer (pH = 5) for 24 h at 37 °C; second row, incubated in PBS (pH = 7.4) for 24 h at 37 °C; third row, fresh solutions of unmodified RNase A (left), 386 (middle), and 689 conjugates (right) without incubation. Each reaction contained 20 μg RNA and 0.5 ng EtBr; RNase A samples (1 μg protein) were added after 5 min.

the pH during the preincubation phase. RNase A-AzMMMan-386 (Figure 5, middle), -689 (Figure 5, right), and RNase A-AzMMMan (Figure S7, left) revealed extremely low activity after a 24 h incubation phase at pH 8.5, whereas activity was restored after incubation at pH 5, indicating the pH-responsive release of unmodified RNase A. After 24 h incubation at pH 7.4, an intermediate activity was observed, which obviously is caused by partial AzMMMan cleavage. In contrast, stable amidation of RNase A by bifunctional SMCC linker reduced the enzymatic activity in an irreversible, pH-independent fashion (Figure S7, right).

Cytotoxic Potency of RNase A Conjugates. To verify that the covalently modified therapeutic protein can be successfully delivered into the cytoplasm, cell viability assays (MTT) were performed with the two series of oligomer (689 and 386) modified RNase A to investigate the biological activity and effect on tumor cell viability after 48 h treatment. As shown in Figure 6, panel a, all RNase A conjugates revealed some cytotoxicity, while the control RNase-AzMMMan did not induce any obvious inhibition of metabolic activity. For the same series of oligomer (689 or 386) modified RNase A, the toxicity increased with the degree of conjugation. In direct comparison of conjugates with same molar ratio (0.75, 1.5, 3, 6) and at the same concentration, 689 modified RNase A showed higher toxicity than the 386 based analog. Flow cytometry experiments with the most toxic protein conjugates (molar ratio 689: RNase A = 6, 386: RNase A = 6) have been carried out to verify their internalization. The results shown in Figure 6, panel b confirm again that 689 and 386 show similar uptake ability, consistent with Figure 3, panel b and our former study. Considering the cellular uptake results, the differential acitivity possibly can be explained by an enhanced endosomal escape due to the increased buffer capacity of the histidine-rich oligomer 689, which could promote an improved proton sponge effect resulting in higher toxicity of 689 modified RNase A.[22,36]

Finally, to demonstrate that the process of cell killing is dependent on the protein concentration, various amounts of 386 and 689 modified RNase A conjugates (0.5 μM, 1 μM, 2 μM, 4 μM) as well as control groups (free oligomers 386, 689, RNase A-AzMMMan, RNase A-AzMMMan + free 689) were incubated with HeLa cells for 48 h. Figure 6, panel c reveals that cells treated with RNase A-AzMMMan-DBCO-PEG_4-Mal-689 show significantly decreased cell viability. Cells have only 19% survival rate when treated with 4.0 μM RNase A conjugate, while cells treated with 0.5 μM do not seem to be affected. This accounts for the dose−response correlation between cytotoxicity and added concentration of the RNase A conjugate. Cells treated only with RNase A-AzMMMan, 386, or 689 oligomer alone do not show remarkable reduction of cell viability. Likewise, the mixture of RNase A-AzMMMan and oligomer 689 did not decrease cell viability below 80% but showed slightly higher cytotoxicity than RNase A-AzMMMan alone. This could be explained by electrostatic binding between negatively charged RNase A-AzMMMan and positively charged 689, which may result in delivery of a small amount of RNase A-AzMMMan into the cytoplasm, inducing slightly toxic effects. Interestingly, when cells were treated with the same concentration of 386- and 689- modified RNase A, 689-modified RNase A always showed higher cytotoxicity than 386-modified RNase A (viability 40% compared to 78% at 2 μM, 19% compared to 49% at 4 μM. We hypothesize that both protein conjugates have the same intracellular delivery ability as a result of same protonation degree at extracellular pH, which is

DOI: 10.1021/acs.biomac.5b01289
Biomacromolecules 2016, 17, 173−182

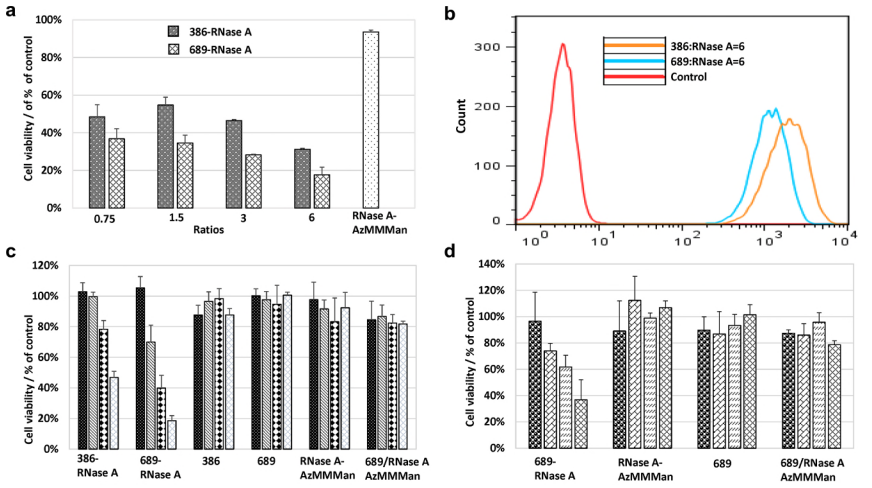

Figure 6. Cellular uptake and cytotoxic potency of RNase A conjugates. (a) Viability of HeLa cells (MTT) after treatment with 4 μM of 386-RNase A conjugates (left bars) or 689-RNase A conjugates (right bars) with different oligomer to RNase A molar ratios (0.75, 1.5, 3, 6). (b) Cellular uptake of 4 μM 386- or 689-modified RNase A-Cy5 (oligomer: RNase A molar ratio 6). (c) Viability of HeLa cells (MTT) after treatment with 386-RNase A, 689-RNase A conjugates (molar ratio 6) and control groups (free 386, free 689, RNase A-AzMMMan, mixture of free 689 and RNase A-AzMMMan) at various concentrations. Concentrations of RNase A in conjugates, RNase A-AzMMMan, and oligomer/RNase A control mixtures (from left to right): 0.5 μM, 1.0 μM, 2 μM, 4 μM. Concentrations of bare oligomers 386 and 689 in control groups: 3.0 μM, 6.0 μM, 12 μM, 24 μM. (d) Viability of Neuro 2A cells (MTT) after treatment with 689 modified RNase A conjugates (molar ratio 6) under the same conditions as described in panel c.

supported by the Figure 3, panel b and Figure 6, panel b. However, after cellular uptake and entering endosomes, as the pH drops from 7.4 to 6.0, the histidines of 689 could promote the proton sponge effect and endosomal escape resulting in more efficient protein delivery into the cytoplasm. We further demonstrated that the potency of the 689 modified RNase A to kill cancer cells is not restricted to HeLa. MTT assays of murine neuroblastoma Neuro 2A cells incubated with the most potent RNase A conjugate also showed dose dependent tumor cell killing (Figure 6d).

CONCLUSION

In summary, we have reported covalent protein conjugates equipped with pH sensitivity as intracellular delivery platform. We synthesized a library of cationic three-arm oligoamino amide oligomers (386 and its histidinylated analog 689) conjugated with proteins (EGFP or RNase A) at different molar ratios using the pH-labile AzMMMan linker and copper-free click chemistry. Fluorescence correlation spectroscopy measurements of unmodified EGFP, EGFP-AzMMMan and 689-EGFP conjugates revealed that the formation of cross-linked protein clusters strongly depends on the conjugation degree. Only at high molar ratios of 689: EGFP = 8 and 16, large complexes with hydrodynamic radii above 0.1 μm could be detected. We then investigated the relationship between the conjugation degree of EGFP and cell internalization efficiency. The conjugation degree had effects both on the amount of protein conjugate taken up by cells and the extent of nuclear delivery after endosomal escape. All four kinds of cationic oligomer modified EGFP (689: EGFP = 2, 4, 8, 16) have efficient internalization capability, but only EGFP conjugates (689: EGFP = 4, 8) showed nuclear delivery. Furthermore, we also used the therapeutic protein RNase A as an agent for killing cancer cells.[11,12] The cationic oligomer 689 modified RNase A showed pH dependent bioactive release in in vitro experiments and, after cellular uptake, high ability to kill cancer cells. Consistent with the known higher endosomal escape efficacy due to histidinylation,[22,36−39] conjugates of 689 demonstrated higher delivery efficacy than 386 conjugates. Taking together, this study suggests that fine-tuning of pH-reversible conjugation of therapeutic proteins with potent intracellular transfection oligomers opens a new window for future medical applications.

ASSOCIATED CONTENT

Supporting Information

The Supporting Information is available free of charge on the ACS Publications website at DOI: 10.1021/acs.biomac.5b01289.

^{1}H NMR spectra, UV−vis spectra, fluorescence microscopy images, SDS-PAGE gels, RNase A activity assay data (PDF)

DOI: 10.1021/acs.biomac.5b01289
Biomacromolecules 2016, 17, 173−182

AUTHOR INFORMATION

Corresponding Author

*E-mail: ulrich.laechelt@cup.uni-muenchen.de. Phone: +49 89 218077842.

Notes

The authors declare no competing financial interest.

ACKNOWLEDGMENTS

X.L., P.Z., and D.H. appreciate China Scholarship Council fellowships as support of their Ph.D. studies at the Ludwig-Maximilians University Munich, Germany. We also acknowledge the financial support by the DFG Excellence Cluster Nanosystems Initiative Munich (NIM) and the Munich Center for Nanoscience (CeNS).

REFERENCES

(1) Leader, B.; Baca, Q. J.; Golan, D. E. Protein therapeutics: a summary and pharmacological classification. *Nat. Rev. Drug Discovery* **2008**, *7* (1), 21−39.

(2) Lu, Y.; Sun, W.; Gu, Z. Stimuli-responsive nanomaterials for therapeutic protein delivery. *J. Controlled Release* **2014**, *194* (0), 1−19.

(3) Hoffman, R. M. Application of GFP imaging in cancer. *Lab. Invest.* **2015**, *95* (4), 432−452.

(4) Filonov, G. S.; Piatkevich, K. D.; Ting, L.-M.; Zhang, J.; Kim, K.; Verkhusha, V. V. Bright and stable near-infrared fluorescent protein for in vivo imaging. *Nat. Biotechnol.* **2011**, *29* (8), 757−761.

(5) Hanson, M. R.; Köhler, R. H. GFP imaging: methodology and application to investigate cellular compartmentation in plants. *J. Exp. Bot.* **2001**, *52* (356), 529−539.

(6) Mayol, L.; Biondi, M.; Quaglia, F.; Fusco, S.; Borzacchiello, A.; Ambrosio, L.; La Rotonda, M. I. Injectable Thermally Responsive Mucoadhesive Gel for Sustained Protein Delivery. *Biomacromolecules* **2011**, *12* (1), 28−33.

(7) Zentner, G. M.; Rathi, R.; Shih, C.; McRea, J. C.; Seo, M.-H.; Oh, H.; Rhee, B. G.; Mestecky, J.; Moldoveanu, Z.; Morgan, M.; Weitman, S. Biodegradable block copolymers for delivery of proteins and water-insoluble drugs. *J. Controlled Release* **2001**, *72* (1−3), 203−215.

(8) Azagarsamy, M. A.; Anseth, K. S. Wavelength-Controlled Photocleavage for the Orthogonal and Sequential Release of Multiple Proteins. *Angew. Chem., Int. Ed.* **2013**, *52* (51), 13803−13807.

(9) Petersen, S.; Alonso, J. M.; Specht, A.; Duodu, P.; Goeldner, M.; del Campo, A. Phototriggering of Cell Adhesion by Caged Cyclic RGD Peptides. *Angew. Chem.* **2008**, *120* (17), 3236−3239.

(10) Brieke, C.; Rohrbach, F.; Gottschalk, A.; Mayer, G.; Heckel, A. Light-Controlled Tools. *Angew. Chem., Int. Ed.* **2012**, *51* (34), 8446−8476.

(11) Wang, M.; Alberti, K.; Sun, S.; Arellano, C. L.; Xu, Q. Combinatorially Designed Lipid-like Nanoparticles for Intracellular Delivery of Cytotoxic Protein for Cancer Therapy. *Angew. Chem.* **2014**, *126* (11), 2937−2942.

(12) Wang, M.; Sun, S.; Neufeld, C. I.; Perez-Ramirez, B.; Xu, Q. Reactive Oxygen Species-Responsive Protein Modification and Its Intracellular Delivery for Targeted Cancer Therapy. *Angew. Chem.* **2014**, *126* (49), 13662−13666.

(13) Lee, J. S.; Feijen, J. Polymersomes for drug delivery: Design, formation and characterization. *J. Controlled Release* **2012**, *161* (2), 473−483.

(14) Lu, L.; Zou, Y.; Yang, W.; Meng, F.; Deng, C.; Cheng, R.; Zhong, Z. Anisamide-Decorated pH-Sensitive Degradable Chimaeric Polymersomes Mediate Potent and Targeted Protein Delivery to Lung Cancer Cells. *Biomacromolecules* **2015**, *16* (6), 1726−1735.

(15) Schwarze, S. R.; Ho, A.; Vocero-Akbani, A.; Dowdy, S. F. In Vivo Protein Transduction: Delivery of a Biologically Active Protein into the Mouse. *Science* **1999**, *285* (5433), 1569−1572.

(16) Nischan, N.; Herce, H. D.; Natale, F.; Bohlke, N.; Budisa, N.; Cardoso, M. C.; Hackenberger, C. P. Covalent attachment of cyclic TAT peptides to GFP results in protein delivery into live cells with immediate bioavailability. *Angew. Chem., Int. Ed.* **2015**, *54* (6), 1950−3.

(17) Thompson, D. B.; Villaseñor, R.; Dorr, B. M.; Zerial, M.; Liu, D. R. Cellular Uptake Mechanisms and Endosomal Trafficking of Supercharged Proteins. *Chem. Biol. (Oxford, U. K.)* **2012**, *19* (7), 831−843.

(18) Pesce, D.; Wu, Y.; Kolbe, A.; Weil, T.; Herrmann, A. Enhancing cellular uptake of GFP via unfolded supercharged protein tags. *Biomaterials* **2013**, *34* (17), 4360−4367.

(19) Maier, K.; Wagner, E. Acid-Labile Traceless Click Linker for Protein Transduction. *J. Am. Chem. Soc.* **2012**, *134* (24), 10169−10173.

(20) Leland, P. A.; Raines, R. T. Cancer chemotherapy − ribonucleases to the rescue. *Chem. Biol. (Oxford, U. K.)* **2001**, *8* (5), 405−413.

(21) Deshpande, A. M.; Natu, A. A.; Argade, N. P. Chemoselective Carbon−Carbon Coupling of Organocuprates with (Bromomethyl)-methylmaleic Anhydride: Synthesis of Chaetomellic Acid A. *J. Org. Chem.* **1998**, *63* (25), 9557−9558.

(22) Kos, P.; Lächelt, U.; Herrmann, A.; Mickler, F. M.; Döblinger, M.; He, D.; Krhac Levacic, A.; Morys, S.; Bräuchle, C.; Wagner, E. Histidine-rich stabilized polyplexes for cMet-directed tumor-targeted gene transfer. *Nanoscale* **2015**, *7* (12), 5350−5362.

(23) Schaffert, D.; Troiber, C.; Salcher, E. E.; Fröhlich, T.; Martin, I.; Badgujar, N.; Dohmen, C.; Edinger, D.; Kläger, R.; Maiwald, G.; Farkasova, K.; Seeber, S.; Jahn-Hofmann, K.; Hadwiger, P.; Wagner, E. Solid-Phase Synthesis of Sequence-Defined T-, i-, and U-Shape Polymers for pDNA and siRNA Delivery. *Angew. Chem., Int. Ed.* **2011**, *50* (38), 8986−8989.

(24) Haustein, E.; Schwille, P. Fluorescence correlation spectroscopy: novel variations of an established technique. *Annu. Rev. Biophys. Biomol. Struct.* **2007**, *36*, 151−69.

(25) Geisow, M. J.; Evans, W. H. pH in the endosome: Measurements during pinocytosis and receptor-mediated endocytosis. *Exp. Cell Res.* **1984**, *150* (1), 36−46.

(26) Varkouhi, A. K.; Scholte, M.; Storm, G.; Haisma, H. J. Endosomal escape pathways for delivery of biologicals. *J. Controlled Release* **2011**, *151* (3), 220−228.

(27) Tjelle, T. E.; Brech, A.; Juvet, L. K.; Griffiths, G.; Berg, T. Isolation and characterization of early endosomes, late endosomes and terminal lysosomes: their role in protein degradation. *J. Cell Sci.* **1996**, *109* (12), 2905−2914.

(28) Schaffert, D.; Badgujar, N.; Wagner, E. Novel Fmoc-Polyamino Acids for Solid-Phase Synthesis of Defined Polyamidoamines. *Org. Lett.* **2011**, *13* (7), 1586−1589.

(29) Ning, X.; Guo, J.; Wolfert, M. A.; Boons, G.-J. Visualizing Metabolically Labeled Glycoconjugates of Living Cells by Copper-Free and Fast Huisgen Cycloadditions. *Angew. Chem.* **2008**, *120* (12), 2285−2287.

(30) Magde, D.; Elson, E.; Webb, W. W. Thermodynamic Fluctuations in a Reacting System—Measurement by Fluorescence Correlation Spectroscopy. *Phys. Rev. Lett.* **1972**, *29* (11), 705−708.

(31) Khalil, I. A.; Kogure, K.; Akita, H.; Harashima, H. Uptake Pathways and Subsequent Intracellular Trafficking in Nonviral Gene Delivery. *Pharmacol. Rev.* **2006**, *58* (1), 32−45.

(32) Behr, J.-P. The Proton Sponge: a Trick to Enter Cells the Viruses Did Not Exploit. *Chimia* **1997**, *51* (1−2), 34−36.

(33) Maier, K.; Martin, I.; Wagner, E. Sequence Defined Disulfide-Linked Shuttle for Strongly Enhanced Intracellular Protein Delivery. *Mol. Pharmaceutics* **2012**, *9* (12), 3560−3568.

(34) Wagner, E. Polymers for siRNA Delivery: Inspired by Viruses to be Targeted, Dynamic, and Precise. *Acc. Chem. Res.* **2012**, *45* (7), 1005−1013.

(35) Raines, R. T.; Ribonuclease, A. *Chem. Rev. (Washington, DC, U. S.)* **1998**, *98* (3), 1045−1066.

(36) Lächelt, U.; Kos, P.; Mickler, F. M.; Herrmann, A.; Salcher, E. E.; Rödl, W.; Badgujar, N.; Bräuchle, C.; Wagner, E. Fine-tuning of proton sponges by precise diaminoethanes and histidines in pDNA polyplexes. *Nanomedicine (N. Y., NY, U. S.)* **2014**, *10* (1), 35−44.

DOI: 10.1021/acs.biomac.5b01289
Biomacromolecules 2016, 17, 173−182

(37) Midoux, P.; Monsigny, M. Efficient Gene Transfer by Histidylated Polylysine/pDNA Complexes. *Bioconjugate Chem.* **1999**, *10* (3), 406−411.

(38) Leng, Q.; Mixson, A. J. Modified branched peptides with a histidine-rich tail enhance in vitro gene transfection. *Nucleic Acids Res.* **2005**, *33* (4), e40.

(39) Shi, J.; Schellinger, J. G.; Johnson, R. N.; Choi, J. L.; Chou, B.; Anghel, E. L.; Pun, S. H. Influence of Histidine Incorporation on Buffer Capacity and Gene Transfection Efficiency of HPMA-co-oligolysine Brush Polymers. *Biomacromolecules* **2013**, *14* (6), 1961−1970.

DOI: 10.1021/acs.biomac.5b01289
Biomacromolecules 2016, 17, 173−182

B.4 Originalpublikation P4

Andreas Zimpel, Tobias Preiß, Ruth Röder, Hanna Engelke, Michael Ingrisch, Michael Peller, Joachim O. Rädler, Ernst Wagner, Thomas Bein, Ulrich Lächelt, Stefan Wuttke.
Imparting functionality to MOF nanoparticles by external surface selective covalent attachment of polymers.
Chemistry of Materials, 2016, 28, 3318-3326.

CHEMISTRY OF MATERIALS

Article

pubs.acs.org/cm

Imparting Functionality to MOF Nanoparticles by External Surface Selective Covalent Attachment of Polymers

Andreas Zimpel,[†] Tobias Preiß,[‡] Ruth Röder,[§] Hanna Engelke,[†] Michael Ingrisch,[∥] Michael Peller,[∥] Joachim O. Rädler,[‡] Ernst Wagner,[§] Thomas Bein,[†] Ulrich Lächelt,*[,§] and Stefan Wuttke*[,†]

[†]Department of Chemistry and Center for NanoScience (CeNS), LMU Munich, Butenandtstraße 11, 81377 Munich, Germany
[‡]Department of Physics and Center for NanoScience (CeNS), LMU Munich, Geschwister-Scholl-Platz 1, 80539 Munich, Germany
[§]Department of Pharmacy and Center for NanoScience (CeNS), LMU Munich, Butenandtstraße 5, 81377 Munich, Germany
[∥]Josef Lissner Laboratory for Biomedical Imaging, Institute for Clinical Radiology, University Hospital, LMU Munich, Marchioninistraße 15, 81377 Munich, Germany

Supporting Information

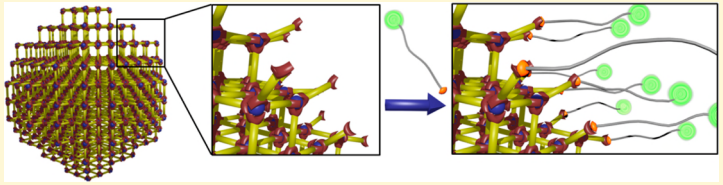

ABSTRACT: Selective functionalization of the external surface of porous nanoparticles is of great interest for numerous potential applications in the field of nanotechnology. Regarding metal−organic frameworks (MOFs), few methods for such modifications have been reported in the literature. Herein, we focus on the covalent attachment of functional polymers on the external surface of MIL-100(Fe) nanoparticles in order to implement properties such as increased chemical and colloidal stability or dye-labeling for the investigation of the particles by fluorescence based techniques. We prove covalent nanoparticles-polymer bond formation by liquid NMR after dissolution of the functionalized MOF under mild conditions and estimate the amount of covalently attached polymer by UV−vis spectroscopy. The functionalization of the MOF nanoparticles with fluorescently labeled polymers enables the investigation of nanoparticle uptake into tumor cells by fluorescence microscopy. Furthermore, the influence of the polymer shell on the magnetic resonance imaging activity of MIL-100(Fe) is investigated in detail. The functionalization approach presented here is expected to enable the fabrication of hybrid nanomaterials, extending the enormous chemical space of MOFs into polymer materials.

INTRODUCTION

Manipulating the surface of nanoparticles (NPs) has been a prominent research topic in recent years.[1−3] The nanoparticle surface is defined as the interface between the nanoparticle and its surroundings and determines the interactions with the environment.[4] In addition, particle surface properties become dominant in the nanometer range due to the high surface-to-volume ratio. Therefore, the controlled surface functionalization is of great importance for nanoparticle applications in fields like sensing, imaging, or drug delivery.[5−7]

Surface functionalization has been adapted to many different nanoparticles such as gold, metal oxides, carbon, polymers, or mesoporous silica.[8,9] Metal−organic framework nanoparticles (MOF NPs), consisting of metal clusters and organic linker molecules, are a relatively new class of nanomaterials.[10−12] Besides their unique properties such as structural diversity, crystalline structure, tunable porosity, and high surface area, they further provide great potential for functionalization on their internal as well as on their external surface.[13−17] In particular, the use of MOF nanoparticles in biomedical applications requires that the external surface functionalization fulfills different tasks varying from inhibiting agglomeration within the bloodstream to the specific recognition of cancer cells.[18] Attachment of biocompatible polymeric structures or proteins is a common method to achieve those functionalities.[19]

Two different general strategies have been proposed so far, regarding the attachment of molecules onto the external surface of MOFs: "functionalization during synthesis", also known as coordination modulation approach, and "postsynthetic modification" (PSM).[20] According to the literature, PSM is the most common way to achieve core−shell MOF nanoparticles. With this approach, four different ways of external surface functionalization of MOFs have been already mentioned and discussed.

Received: January 14, 2016
Revised: April 28, 2016
Published: April 28, 2016

DOI: 10.1021/acs.chemmater.6b00180
Chem. Mater. 2016, 28, 3318−3326

First, one possibility consists of grafting, through coordinative bonds, polymeric structures on the coordinatively unsaturated metal sites (CUS) present on the external surface of MOF particles (Figure 1a). This was reported for the first time by Rowe et al.[21] and was adopted by other groups to create core−shell functionalized MOF nanoparticles in recent years.[22,23] However, due to the potential presence of CUS on the MOF particle internal surface, the latter can also be potentially functionalized, especially if the functional unit is smaller than the pore aperture. Consequently, this undesired inner functionalization, added to the weak interaction between the functional unit and CUS,[24] restricts the implementation of this approach.

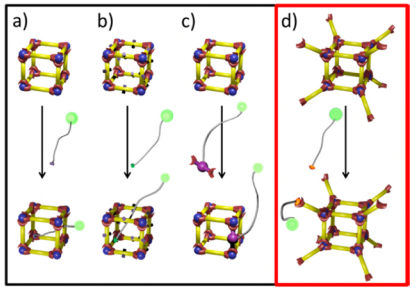

Figure 1. Schematic illustration of the different postsynthetic functionalization possibilities for MOFs: coordinative binding on CUS (a), covalent binding to prefunctionalized linkers (b), ligand exchange (c), and covalent binding to the linking group (d, red box), which was applied in this work.

Second, covalent postsynthetic modification of MOFs, a well-known method, using linker molecules with functional groups to functionalize the internal surface of MOF bulk material, can also be implemented to functionalize the MOF NP's external surface (Figure 1b). Once more, the selectivity of this functionalization toward the MOF NP's external surface is only achieved as long as functional units are large enough not to access the internal surface of the framework. To overcome this limitation, an improved method was developed by Fischer, Wöll, and co-workers.[25] Their approach consisted of the selective anchoring of functional groups on the external surface of the metal−organic framework only (surface-attached metal−organic framework multilayers, SURMOFs).[26] These groups were subsequently functionalized with a fluorescent dye, which was detected via fluorescence microscopy. Recently, a similar approach was reported for the preparation of MOF core−shell bulk structures, as demonstrated by Matzger et al.[27]

Third, the group of Kitagawa demonstrated that postsynthetic ligand exchange with functional linker molecules only occurs on the first external monolayer of MOF microcrystals (Figure 1c). The authors pointed out that the key point for this functionalization strategy was the dynamic nature of the underlying MOF scaffold along with the chemical properties of the functional ligand, which somehow limits the broad applicability of this strategy to MOF NP surface functionalization.[28]

Finally, unsaturated functional groups of the organic linker can be used for covalent attachment of functional molecules. This approach allows for the selective functionalization of the MOF NP external surface without further restrictions, since the functional groups are used within the framework for coordinative bonding to metal ions and are not addressable for covalent bonding (Figure 1d, Figure 2). It was first presented by Jung et al., who anticipated the presence of externally exposed carboxyl groups of the linker and addressed them by attachment of enhanced green fluorescent protein (eGFP) on bulk MOF material.[29] In a water-based carbodiimide-mediated amidation, they successfully functionalized aliphatic carboxylates but faced issues with aromatic

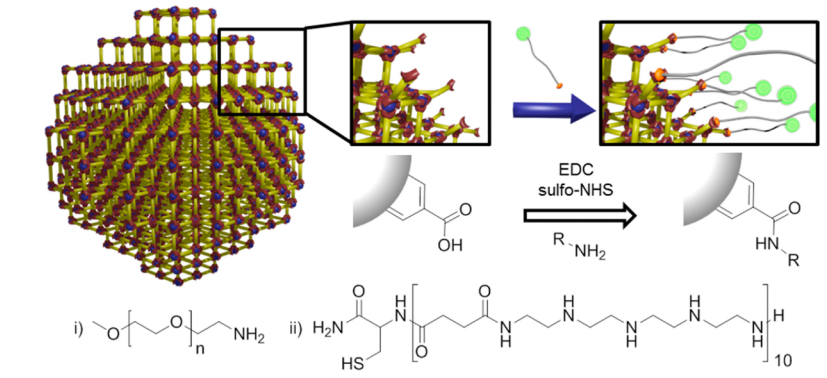

Figure 2. Schematic illustration of the polymer coating and reaction scheme of the amidation by EDC hydrochloride and sulfo-NHS mediation. Chemical structures of the polymers used this work: (i) PEG and (ii) Stp10-C.

DOI: 10.1021/acs.chemmater.6b00180
Chem. Mater. 2016, 28, 3318−3326

carboxylic linkers because of their reduced reactivity. They were able to overcome this only by changing the reaction medium to an organic solvent (dichloromethane). Shih et al. used a similar way to immobilize trypsin on the external surface and transferred this functionalization approach to the field of nanoparticles.[30] To the best of our knowledge, no further work was published on this interesting concept of MOF NPs external surface functionalization, and hence it has not yet been investigated in greater detail.

In our work, we explicitly focus on the latter functionalization approach, which provides the advantage of covalent bonding in combination with a high selectivity for the external surface of the MOF nanoparticle. This allows precise control over the external nanoparticle interface while retaining the porous MOF scaffold. We show successful covalent surface coating of MOF nanoparticles containing aromatic linkers by a water-based "green" carbodiimide mediated reaction (Figure 2). We chose MIL-100(Fe) nanoparticles (MIL: Materials of Institute Lavoisier) as the MOF platform because of their biocompatibility[31] and chemical stability in aqueous environments,[32,33] which is required for the chosen reaction conditions. Further, MIL-100(Fe) NPs already showed high potential for applications in biomedicine.[34−37] The framework consists of iron clusters acting as nodes and trimesic acid serving as linker molecules, which are expected to provide free aromatic carboxylic acid groups at the particle external surface.[38] We show the covalent nature of the bonding to polymers and estimate the achievable amount of functionalization. For surface modification we chose two different kinds of polymer (shown in Figure 2): (i) commercially available amino-polyethylene glycol (PEG5000), a hydrophilic polymer, frequently used to increase colloidal stability and to mediate surface shielding of nanoparticles[39−41] and (ii) Stp10-C, a solid-phase synthesis-derived oligoamino amide serving as a bifunctional linking polymer, providing a primary amine for conjugation with the nanoparticle surface groups and a thiol for fluorescent labeling or additional functionalization. The two terminal groups of Stp10-C are connected via a repetitive diaminoethane motif with proton-sponge characteristics, which can be utilized for electrostatic binding of nucleic acids, enhancement of cellular uptake, and improvement of endosomal escape.[42−44] By means of a covalent Stp10-C attachment, we combine the high precision of crystalline MOF nanoparticles with the sequence-definition of solid-phase derived polymers and thus generate a controlled interface toward solution. In addition, the two polymers, PEG and Stp10-C, were chosen as representative compounds because of the potential prospective use of the resulting MOF@Polymer core−shell nanoparticles in biomedical applications and for multi-imaging purposes.[45] We demonstrate the first promising results of that kind of hybrid nanoparticles by fluorescence microscopy and magnetic resonance imaging (MRI).

EXPERIMENTAL SECTION

Details for all synthesis procedures, sample preparations, and characterization techniques are described in the Supporting Information. Here we focus on the MOF NP synthesis, the functionalization approach, and the dissolution of the functionalized nanoparticles as well as on MRI and fluorescence microscopy measurements.

MIL-100(Fe) NPs. Iron(III) chloride hexahydrate (2.43 g, 9.00 mmol) and trimesic acid (0.84 g, 4.00 mmol) in 30 mL of H_2O were put into a Teflon tube, sealed, and placed in the microwave reactor. The mixture was heated to 130 °C under solvothermal conditions (p = 2.5 bar) within 30 s and kept at 130 °C for 4 min and 30 s. The resulting MIL-100(Fe) NPs were washed three times in EtOH using a centrifuge (47808 rcf for 20 min) and sonication.

MIL-100(Fe)@Polymer NPs. MIL-100(Fe) nanoparticles (1.0 mg) were dispersed in ethanol (100 μL). EDC hydrochloride (approximately 1 mg) and a catalytic amount of sulfo-NHS were added to the suspension. The polymer (20.0 nmol) was dissolved in bidistilled H_2O (100 μL), and the solution was poured into the MOF dispersion. The mixture was stirred for 30 min at ambient temperature. The functionalized nanoparticles were washed three times in bidistilled H_2O using a centrifuge (16873 rcf for 10 min) and sonication.

Dissolution of MIL-100(Fe)@Polymer NPs and Extraction of Functionalized Linker. MIL-100(Fe)@Polymer NPs were dispersed in an EDTA solution (0.1 mM). The dispersion was stirred overnight, and the resulting solution was extracted three times with dichloromethane (20 mL). The organic phases were combined and dried over sodium sulfate for 1 h under vigorous stirring. After removal of the organic solvent, the product was dried under high vacuum.

Magnetic Resonance Imaging (MRI). Imaging was performed with a 1.5 T clinical MRI system (Magnetom Aera, Siemens Health Care, Germany). Samples were filled into 2 mL Eppendorf tubes that were imaged in parallel rows of 5 samples. A PMMA sample holder fixed the tubes submersed in a basin filled with 650 mL of water and 0.4 mL of Gd-DTPA (0.5 mmol/mL) at 24 °C. As a reference sample tubes with Gd-DTPA-BMA (Omniscan, GE Healthcare) diluted in water (0−2.5 mM) have been examined. This setup was placed in a standard MRI head coil for imaging. After using standard MRI pulse sequences for orientation, a gradient echo sequence with a nonselective saturation recovery (SR) preparation pulse was applied for calculation of T1 parameter maps varying the saturation recovery time from 130−3000 ms in 17 steps. T2-weighted multicontrast 2D spin echo sequences (SE MC) were repeated varying the echo time 16 times in steps of 15 ms starting with 15 ms and ending with 240 ms for T2 parameter map calculation. Other imaging parameters for SR were as follows: echo time = 1.71 ms; repetition time = 747 ms; matrix = 128 × 128; in plane resolution = 1 mm; slice thickness = 6 mm; α = 15°; parallel imaging acceleration factor = 2. Slice thickness, FOV, and the parallel imaging acceleration factor were the same for SE MC. However, here the repetition time was 3 s; the in plane resolution was 0.5 mm; the echo train length was 16; and the matrix was 256 × 256. All data were transferred in DICOM format and processed off-line using the software PMI 0.3, written in-house using IDL 6.4 (ITT Visual Information Systems, Boulder, CO). Calculations were done using mean signal intensity values that were determined in region of interests (ROI). ROIs were placed in the center of each sample tube as displayed in Figure S-1. Least-squares fitting was done using the Levenberg−Marquardt algorithm.

Fluorescence Microscopy. Murine neuroblastoma (N2A) cells were seeded in Nunc chamber slides (Thermo Scientific, Germany) at a density of 30.000 cells/well 24 h prior to incubation with different particle concentrations. Before incubation with the particles, medium was replaced with 80 μL of fresh medium containing 10% fetal bovine serum (FBS). Particles diluted in 60 μL of HEPES-buffered glucose (HBG) were added to each well and incubated for 7 and 24 h at 37 °C and 5% CO_2. Cell membranes were stained with wheat germ agglutinin Alexa Fluor 488 conjugate (Life Technologies) at a final concentration of 5 μg/mL prior to imaging. Live cells were imaged using spinning disc microscopy (Zeiss Cell Observer SD utilizing a Yokogawa spinning disk unit CSU-X1). The objective was a 1.40 NA 63x Plan apochromat oil immersion objective (Zeiss). Cy5 was imaged with 639 nm and WGA 488 with 488 nm laser excitation, respectively. For two color detection a dichroic mirror (560 nm, Semrock) and band-pass filters 525/50 and 690/60 (both Semrock) were used in the detection path. Separate images for each fluorescence channel were acquired using two separate electron multiplier charge coupled device (EMCCD) cameras (PhotometricsEvolve).

DOI: 10.1021/acs.chemmater.6b00180
Chem. Mater. 2016, 28, 3318−3326

RESULTS AND DISCUSSION

Synthesis, Functionalization, and Characterization of MOF@Polymer Nanoparticles. The nanoparticles were synthesized following a slightly modified procedure developed by Agostoni et al.[46] Iron(III) chloride hexahydrate was dissolved in bidistilled water, and trimesic acid was added to the solution. The mixture was sealed in a Teflon autoclave and heated to 130 °C by microwave irradiation, yielding a homogeneous dispersion of MIL-100(Fe) nanoparticles. The particles were filtered and washed with ethanol. For the functionalization process, the nanoparticles were dispersed in ethanol, and 1-ethyl-3-(3-(dimethylamino)propyl) carbodiimide (EDC) hydrochloride was added. PEG5000 or Stp10-C was dissolved in water, hydroxy-2,5-dioxopyrrolidine-3-sulfonic acid sodium salt (sulfo-NHS) was added, and the solution was pipetted to the MOF suspension. After a reaction time of 30 min, the functionalized nanoparticles were washed with water or ethanol, respectively (for further details see the Supporting Information).

Functionalized as well as unfunctionalized MIL-100(Fe) nanoparticles showed characteristic X-ray diffraction (XRD) reflections, which indicate retained crystallinity after functionalization (see SI, Figure S-2). This was further confirmed by transmission electron microscopy (TEM), where the crystalline arrangement of the MOF could be visualized (see SI, Figures S-3, S-4, and S-5). Particle sizes measured by dynamic light scattering (DLS) in colloidal ethanolic dispersion revealed a hydrodynamic diameter of 130 ± 45 nm (see SI, Figure S-6). DLS measurements in aqueous nanoparticle dispersions showed an increased colloidal stability of the functionalized particles in comparison to unfunctionalized ones. After 3 weeks in water, pure MIL-100(Fe) nanoparticles tend to form agglomerates, while polymer-shielded particles retained their colloidal stability (see SI, Table S-1, Figure S-7). Furthermore, functionalized particles provided increased stability in 10% fetal bovine serum (Figure 3, Table S-2). While unfunctionalized particles formed large agglomerates within minutes after dispersion, the functionalized ones stayed in dispersion over a time period of at least 72 h. This behavior can be explained by the shielding ability of the polymers and demonstrates the change in the physicochemical behavior of the MOF NPs by external surface modification. These results are promising with regard to later applications, e.g. in drug delivery, where colloidal stability in aqueous media is mandatory. The change of the external surface of the MOF NP can also be observed with zeta-potential measurements, revealing an increased pH value of the isoelectric point for functionalized particles (see SI, Figure S-8). We attribute this shift (pH 4.1 for unfunctionalized particles to pH 5.6 for PEG, and to pH 5.8 for Stp10-C) to the changes on the particle surface resulting from polymer attachment. The acidic carboxy-groups were chemically changed and covered by the polymer, resulting in reduced influence of the negative charges of these groups and, therefore, leading to an increased zeta-potential of the particles. Moreover, both polymers additionally impact zeta-potential by shielding the surface charge or even introducing positive charges in case of the amine-rich Stp10-C. The calculations of the BET specific surface area based on nitrogen sorption measurements gave a value of 1905 m^2/g for unfunctionalized MIL-100(Fe) nanoparticles. For functionalized particles, the surface areas decreased moderately to 1338 m^2/g or 1432 m^2/g, for the PEG and Stp10-C treated nanoparticles, respectively (see SI, Figure S-9). This can be attributed to the attached amount of nonporous organic material on the external surface as well as to partial pore blocking under the dry and cold measurement conditions, where the polymer chains collapse and freeze on the external surface of the nanoparticles. An increase of the organic fraction after functionalization could be detected by thermogravimetric analysis (TGA). Heating the samples stepwise to 900 °C in synthetic air, a lower percentage of inorganic mass (iron oxides) remained for functionalized compared to unfunctionalized particles after combustion of the material (see SI, Figure S-10).

A further confirmation of successful functionalization was given by IR spectroscopy, which revealed the appearance of bands of the C−O or C−N stretching vibrations of the polymeric backbone for MIL-100(Fe)@PEG5000 and MIL-100(Fe)@Stp10-C, respectively (Figure 4).

We further performed fluorescence correlation spectroscopy (FCS), a single molecule technique, which is able to measure the diffusion coefficient and the concentration of fluorescently labeled particles.[48−50] In order to probe the binding of the functional polymer to MOF nanoparticles, Cy5 was attached on

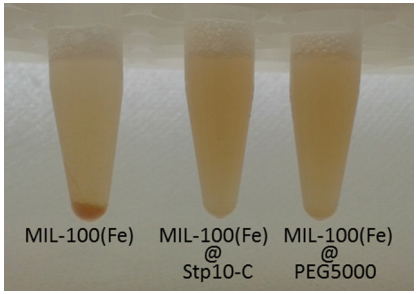

Figure 3. Particles dispersion of functionalized and unfunctionalized MIL-100(Fe) nanoparticles after 3 h in 10% FBS in water. Unfunctionalized particles start to agglomerate immediately, while polymer-functionalized particles retain their colloidal stability.

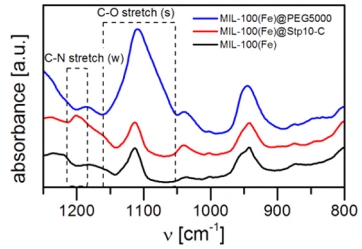

Figure 4. IR spectra of functionalized and unfunctionalized MIL-100(Fe) nanoparticles (offset to show differences): dashed lines frame the specific vibrations resulting from attached polymer, increased C−O stretching vibration for PEG5000 (blue line) or increased C−N stretching vibration for Stp10-C (red line)[47] (full IR spectra are provided in the Supporting Information; Figure S-11).

DOI: 10.1021/acs.chemmater.6b00180
Chem. Mater. 2016, 28, 3318−3326

the free thiol group of the Stp10-C polymer tail by a maleimide−thiol coupling reaction. A sample of Stp10-C*Cy5 as well as a suspension of MIL-100(Fe)@Stp10-C*Cy5 nanoparticles (50% labeled, 50% unlabeled Stp10-C) in water was measured. The normalized autocorrelation curve of Stp10-C*Cy5 exhibited diffusion corresponding to an effective hydrodynamic radius of 1.1 nm (Figure 5).

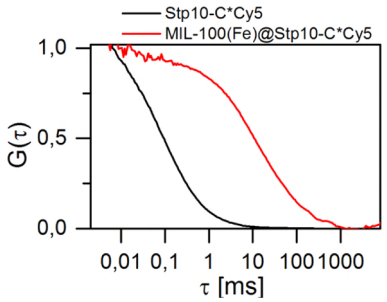

Figure 5. Normalized autocorrelation curves of Stp10-C*Cy5 (black) and MIL-100(Fe)@Stp10-C*Cy5 nanoparticles (red). The shift to higher lag-times τ of nanoparticles' correlation curve confirms the successful attachment of polymer molecules to nanoparticles.

In contrast, the FCS signal of the nanoparticle samples showed a distinct increase in the diffusion time (t = 4.8 ms), which corresponds to a hydrodynamic radius of 56 nm. As the measured hydrodynamic radius agrees well to the size of the particles determined by DLS (see Supporting Information), we conclude that labeled polymer molecules are attached to the nonfluorescing nanoparticles. This indicates a successful polymer coating of MIL-100(Fe) particles. A variation of the amount of labeled Stp10-C in the nanoparticle coating process showed no difference in the normalized autocorrelation curves (see SI, Figure S-12), indicating that the fluorescent label Cy5 has no effect on the functionalization process with Stp10-C.

Examination of the Covalent Bonding and Estimation of Polymer Amount. The above results confirm the formation of MOF@Polymer core−shell nanoparticles but do not reveal the nature of the connection. Using UV−vis spectroscopy, we gained first indications concerning the expected covalent bonding. After the conventional functionalization reaction, the supernatant after centrifugation of the nanoparticles was analyzed and revealed no residue of dye-labeled polymer, which indicated a successful attachment to the MOF. When omitting sulfo-NHS in the reaction mixture, which is essential for the activation of the carboxylic group in aqueous media, almost all initial dye-labeled polymer was still detected in the supernatant (see SI, Figure S-13). This led to the conclusion that the MOF-polymer bonding is of covalent nature, as sulfo-NHS is required for the attachment. Furthermore, for postsynthetic modification of the internal surface, liquid NMR analysis after digestion of the functionalized MOF but without destroying the newly formed bonds is a common method to verify the covalent attachment of molecules.[51]

Therefore, we dissolved the functionalized nanoparticles in a gentle way by adding ethylenediaminetetraacetic acid (EDTA).[52] Due to its chelate effect, EDTA is able to strongly bind the iron(III) ions. When performing the dissolution of the MOF NPs, we found an increased stability for the PEG-functionalized particles compared to unfunctionalized ones. This was reflected by a prolonged dissolution time and prevention of crystallinity (see SI, Figure S-14). After digestion of the MOF, the aqueous solution was extracted with dichloromethane (DCM) for separation of the functionalized trimesic acid from the pure organic linker. ^{1}H NMR spectroscopy exhibited peaks in the aliphatic region for the polymeric part as well as an aromatic signal resulting from the trimesic acid (Figure 6). Splitting of the aromatic peak indicates

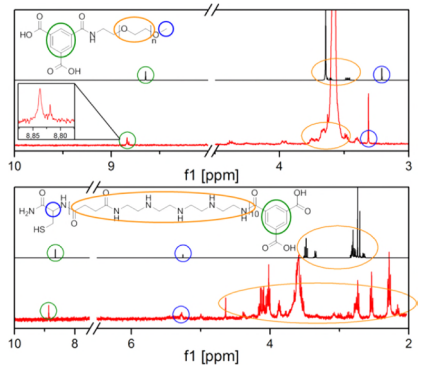

Figure 6. NMR spectra of functionalized trimesic acid after dissolution of the MIL-100(Fe) nanoparticles and extraction in DCM in comparison to calculated spectra:[53] TrimesicAcid@PEG (top) and TrimesicAcid@Stp10-C (bottom). Colored lines encircle the aliphatic proton signals of the polymeric backbone (orange), the aromatic proton signals of the trimesic acid (green), and the tertiary proton of the cysteine or the methyl protons for Stp10-C or PEG5000, respectively (blue).

the covalent nature of the bonding, since the aromatic protons lose their chemical equivalence after functionalization of one carboxylic group (inset in Figure 6). After having shown the covalent nature of the bonding, we further estimated the amount of anchored polymer on the NPs surface. This was again determined by UV−vis measurements of unbound Stp10-C*Cy5 left in the supernatant after EDC-reaction and centrifugation.

Assuming that all polymer molecules that are covalently bound to the MOF nanoparticles can be removed from the supernatant, we estimated the attached amount of Stp10-C to approximately 10−20 nmol per milligram MIL-100(Fe) nanoparticles (see SI, Figure S-15). This amount corresponds to approximately 460−920 polymer molecules per MIL-100(Fe) nanoparticle or an external surface coverage of 9−17 pmol/cm^2. These values were calculated from geometry and mass density of the NPs (ρ = 0.98 g/mL;[38] r = 26.5 nm; for further details see the Supporting Information). Furthermore, the results are in good agreement with TGA data, which

DOI: 10.1021/acs.chemmater.6b00180
Chem. Mater. 2016, 28, 3318−3326

provided an increased mass loss of 2.7% for PEG5000 and 1% for Stp10-C functionalized nanoparticles, respectively (see SI, Figure S-10). Regarding the rather low functionalization degree, which is at the border of the brush regime,[54] the amount of free carboxylic acid functions on the nanoparticles external surface is considered to be the major limiting factor.

Toward Application in Theranostics. As we had altered the external surface of the MOF nanoparticles and functionalized them with fluorescent moieties, we were interested in the cellular uptake and toxicity of these particles. Cellular biocompatibility and the interactions between nanoparticles and cells were studied since they are fundamental prerequisites for biomedical applications. The particles were incubated with murine neuroblastoma N2A cells. Cell membranes were stained with WGA 488, and all nonabsorbed particles were removed from cells by washing with buffer solution. Fluorescence microscopy revealed successful uptake of particles after 7 h, which can be seen in Figure 7a.

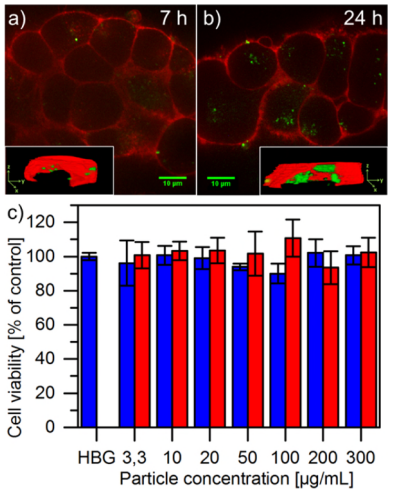

Figure 7. Fluorescence microscope images of N2A cells after 7 h (a) and 24 h (b) incubation with MIL-100(Fe)@Stp10-C nanoparticles under standard cell culture conditions in serum-containing medium (insets: 3D images of single cells calculated from stacked confocal fluorescence microscope images[55]); MTT-plot of N2A cells after 24 h incubation of MIL-100(Fe)@Stp10-C (red) and MIL-100(Fe) (blue) nanoparticles (c).

After 24 h of incubation (Figure 7b), cell images showed a significantly increased uptake of the functionalized nanoparticles, while further incubation showed no additional effect. Hence, this time period was chosen for the investigation of the influence of nanoparticle exposure and uptake on cell viability. MTT-assays with N2A cells were carried out after 24 h incubation with unmodified MIL-100(Fe) and MIL-100(Fe)@Stp10-C*Cy5 in a dosing range between 3.3 and 300 μg/mL (Figure 7c). In all investigated concentrations no significant effect on the metabolic activity of N2A cells could be observed, indicating the good cellular tolerance toward the bare as well as the functionalized MOF nanoparticles. In addition, the influence of the polymer shell on the MRI activity of MIL-100(Fe) was investigated. As MIL-100(Fe) is known to be MR active,[34] we studied the change of the MRI signal in order to ensure that magnetic resonance imaging is still possible with polymer attached at the external surface. Magnetic resonance imaging is a particularly attractive modality for clinical and preclinical imaging, e.g. in cancer research. As MIL-100(Fe) may serve either as drug carrier or as potentially highly selective contrast agent, we studied the visualization of both uncoated and coated nanoparticles and the effect of surface functionalization on longitudinal and transversal relaxivities of MIL-100(Fe).

Here, the relaxivity is the property of a substance to alter the relaxation rate of the water protons in the aquaeous solution, in which the substance is dissolved. Two independent sets of samples (MIL-100(Fe), MIL-100(Fe)@PEG5000, and MIL-100(Fe)@Stp10-C) were prepared in concentrations up to 10 mg/mL in water and underwent imaging at a clinical 1.5 T MRI system (Magnetom Aera, Siemens Healthcare) using T1-weighted saturation recovery sequences and T2-weighted multiecho sequences. Longitudinal (T1) and transverse (T2) relaxation times and relaxation rates (R1 and R2) were calculated in region of interests (ROI) in each sample as described. Longitudinal and transversal relaxivities of each sample were estimated assuming a linear relation between concentration and relaxation time, as shown in Figure 8. Relaxivities were calculated for mmol of entire nanoparticles as well as for mmol Fe^{3+} ions, to ensure comparability to existing contrast agents in clinical use (Table 1).

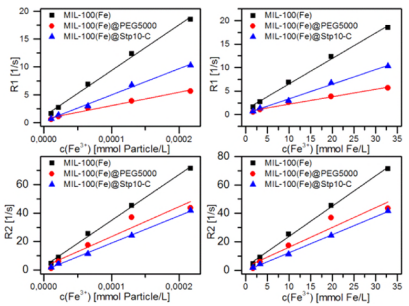

Figure 8. Plots of longitudinal and transverse relaxation rates R1 (top) and R2 (bottom) of coated and uncoated MOF particles for "per particle" (left) and "per Fe3+" (right).

All samples could be visualized in a clinical MRI setting (see Figure 9). Longitudinal and transversal relaxation rates showed a linear dependence on the MOF NP concentration (see Figure 8). T1 relaxivity, i.e. the slope of the relaxation rate, was highest for uncoated MIL-100(Fe) and somewhat reduced for coated NPs (top of Figure 8). In T2 (bottom of Figure 8), this difference was less obvious, but a difference still remains between coated and uncoated MIL-100(Fe). As a reference, samples with clinically used Gd-DTPA-BMA (0−2.5 mM; Omniscan, GE) diluted in water have been examined. r_1

DOI: 10.1021/acs.chemmater.6b00180
Chem. Mater. 2016, 28, 3318−3326

Table 1. Relaxivities (L s^{-1} $mmol^{-1}$) Calculated from the Linear Slopes of Figure 8

	calculations per mmol particles		calculations per mmol Fe^{3+}	
	relaxivity r_1	relaxivity r_2	relaxivity r_1	relaxivity r_2
MIL-100(Fe)	8.21×10^4	3.22×10^5	0.54	2.12
MIL-100(Fe)@Stp10-C	4.72×10^4	1.92×10^5	0.31	1.27
MIL-100(Fe)@PEG5000	2.40×10^4	2.10×10^5	0.16	1.36

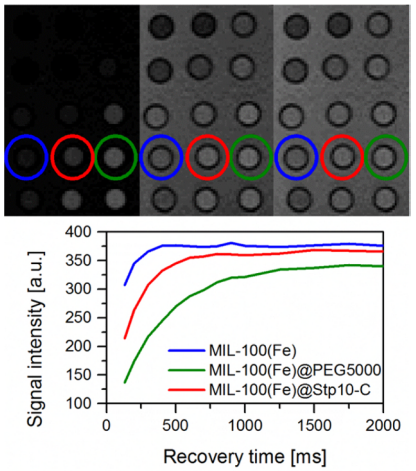

Figure 9. Top: MR images of MIL-100(Fe) samples (left column), MIL-100(Fe)@Stp10-C samples (center column), and MIL-100(Fe) @PEG5000 samples (right column), at concentrations of 0.5, 1, 3, 6, and 10 mg/mL from top to bottom. Images are shown with recovery times of 130 ms (left), 800 ms (center), and 1250 ms (right). Bottom: Signal intensity curves of the three indicated samples with a concentration of 6 mg/mL. Uncoated MOF NP show the fastest T1 relaxation (blue); the T1 relaxation of both coated MOFs (red and green) is slower.

relaxivity of 3.33 s^{-1} mM^{-1} at 35.7 °C or for r_2 3.55 s^{-1} mM^{-1} at 35 °C which is according to the literature.[56] Based on these results and using the same methods, the observed relaxivities of MOF preparations were considered valid.

Overall, the r_2 relaxivity of the MIL-100(Fe) samples is higher than the r_1 relaxivity, showing that the T2 relaxation process is more effective. Calculated per mmol Fe^{3+} ions, both relaxivities were lower than for commercially available superparamagnetic iron-based contrast agents (e.g., Feridex, r_1 = 4.7 L s^{-1} $mmol^{-1}$, r_2 = 41 L s^{-1} $mmol^{-1}$).[56] We assume that the coating of the MOF NPs reduces water exchange between the NP pores and its surroundings as seen before using thermosensitive liposomes.[57] Since T1 relaxation is a short-range effect, this would account for the reduced relaxivity of coated MOF NPs. T2 relaxation, on the other hand, is a long-range effect, which is less affected by reduced water exchange between pores and the surroundings.

Contrary to our results, previous reports about gadolinium based MOF nanoparticles have shown that surface modification can even enhance MRI properties.[58] We point out that the iron-based MOF nanoparticles used in our study exhibit different MRI properties which can be attributed to differences in size, shape, and composition.[59] Further, the polymer nature as well as the way of functionalization were different from previous publications. Despite the reduced MR-activity of coated MOF NPs, relaxivities were still high enough to allow visualization by means of MR imaging. This highlights the potential of such core−shell particles as a smart theranostic system with a wide range of possible functionalities and applications.

CONCLUSION

In summary, we successfully report the selective covalent external surface functionalization of MIL-100(Fe) nanoparticles with two different polymeric structures. Using the mild reaction conditions of peptide coupling chemistry to attach the polymer at the MOF NP surface revealed unchanged crystallinity of the MOF scaffold, proven by XRD and TEM. The attachment of polymer and covalent nature of the bonding was investigated and proven by several techniques, e.g. IR, zeta-potential measurements, and liquid NMR. Further, the amount of polymer attachable to the external surface was estimated by UV−vis spectroscopy. The functionalized MOF nanoparticles showed increased colloidal stability in aqueous media and in initial cell studies, and they revealed potential for biomedical applications, displaying good uptake by cells but no cytotoxic effects up to rather high nanoparticle concentrations over 24 h. Furthermore, the influence of the surface coating on MIL-100(Fe) nanoparticles regarding their magnetic resonance imaging properties was investigated and evaluated in detail. Although the coating affected the MRI signal, visualization of functionalized particles was still possible. This allows for the modification of the coating according to the scientific and clinical needs and, at the same time, *in vivo* investigation of MOF nanoparticle distributions such as accumulation in a tumor. The work presented here opens the door for the precise functionalization of the external surface of MOF NPs and, hence, defined control over the nanoparticle/environment interface. Furthermore, this functionalization approach provides the potential to be extended to a large variety of MOF-polymer combinations and thus is a versatile tool for the design of multifunctional nanoparticle systems.

ASSOCIATED CONTENT

Supporting Information

The Supporting Information is available free of charge on the ACS Publications website at DOI: 10.1021/acs.chemmater.6b00180.

Detailed preparation procedures, measurement techniques and characterization by XRD, DLS, zeta-potential measurements, UV−vis spectroscopy, TEM, TGA, nitrogen sorption measurements and BET calculations, FCS, MRI, MALDI-MS, ^{1}H NMR spectroscopy as well as calculations on the amount of attachable polymer (PDF)

DOI: 10.1021/acs.chemmater.6b00180
Chem. Mater. 2016, 28, 3318−3326

AUTHOR INFORMATION

Corresponding Authors

*E-mail: stefan.wuttke@cup.uni-muenchen.de.
*E-mail: ulrich.laechelt@cup.uni-muenchen.de.

Author Contributions

A.Z. and T.P. contributed equally. The manuscript was written through contributions of all authors. All authors have given approval to the final version of the manuscript.

Notes

The authors declare no competing financial interest.

ACKNOWLEDGMENTS

The authors are grateful for financial support from the Deutsche Forschungsgemeinschaft (DFG) through SFB 1032, DFG-project WU 622/4-1 and PE 925/3-1, the Excellence Cluster Nanosystems Initiative Munich (NIM), and the Center for NanoScience Munich (CeNS). Furthermore, we thank Markus Döblinger for TEM measurements and Constantin Schirnding for 3D visualization of the cells.

REFERENCES

(1) Zhang, F.; Lees, E.; Amin, F.; Rivera Gil, P.; Yang, F.; Mulvaney, P.; Parak, W. J. Polymer-Coated Nanoparticles: A Universal Tool for Biolabelling Experiments. *Small* **2011**, *7*, 3113−3127.
(2) Goesmann, H.; Feldmann, C. Nanoparticulate Functional Materials. *Angew. Chem., Int. Ed.* **2010**, *49*, 1362−1395.
(3) Choi, K. M.; Jeong, H. M.; Park, J. H.; Zhang, Y.-B.; Kang, J. K.; Yaghi, O. M. Supercapacitors of Nanocrystalline Metal−Organic Frameworks. *ACS Nano* **2014**, *8*, 7451−7457.
(4) Tay, C. Y.; Setyawati, M. I.; Xie, J.; Parak, W. J.; Leong, D. T. Back to Basics: Exploiting the Innate Physico-chemical Characteristics of Nanomaterials for Biomedical Applications. *Adv. Funct. Mater.* **2014**, *24*, 5936−5955.
(5) Nel, A. E.; Madler, L.; Velegol, D.; Xia, T.; Hoek, E. M. V.; Somasundaran, P.; Klaessig, F.; Castranova, V.; Thompson, M. Understanding biophysicochemical interactions at the nano-bio interface. *Nat. Mater.* **2009**, *8*, 543−557.
(6) Bogart, L. K.; Pourroy, G.; Murphy, C. J.; Puntes, V.; Pellegrino, T.; Rosenblum, D.; Peer, D.; Lévy, R. Nanoparticles for Imaging, Sensing, and Therapeutic Intervention. *ACS Nano* **2014**, *8*, 3107−3122.
(7) Falcaro, P.; Ricco, R.; Doherty, C. M.; Liang, K.; Hill, A. J.; Styles, M. J. MOF positioning technology and device fabrication. *Chem. Soc. Rev.* **2014**, *43*, 5513−5560.
(8) Biju, V. Chemical modifications and bioconjugate reactions of nanomaterials for sensing, imaging, drug delivery and therapy. *Chem. Soc. Rev.* **2014**, *43*, 744−764.
(9) Li, Z.; Barnes, J. C.; Bosoy, A.; Stoddart, J. F.; Zink, J. I. Mesoporous silica nanoparticles in biomedical applications. *Chem. Soc. Rev.* **2012**, *41*, 2590−2605.
(10) Cohen, S. M. Modifying MOFs: new chemistry, new materials. *Chem. Sci.* **2010**, *1*, 32−36.
(11) Horcajada, P.; Gref, R.; Baati, T.; Allan, P. K.; Maurin, G.; Couvreur, P.; Férey, G.; Morris, R. E.; Serre, C. Metal−Organic Frameworks in Biomedicine. *Chem. Rev.* **2012**, *112*, 1232−1268.
(12) Hirschle, P.; Preiß; Auras, F.; Pick, A.; Volkner, J.; Valdeperez, D.; Witte, G.; Parak, W. J.; Radler, J. O.; Wuttke, S. Exploration of MOF nanoparticle sizes using various physical characterization methods - is what you measure what you get? *CrystEngComm* **2016**, DOI: 10.1039/C6CE00198J.
(13) Cohen, S. M. Postsynthetic Methods for the Functionalization of Metal−Organic Frameworks. *Chem. Rev.* **2012**, *112*, 970−1000.
(14) Furukawa, H.; Cordova, K. E.; O'Keeffe, M.; Yaghi, O. M. The Chemistry and Applications of Metal-Organic Frameworks. *Science* **2013**, *341*, 974−986.
(15) Furukawa, H.; Müller, U.; Yaghi, O. M. Heterogeneity within Order" in Metal−Organic Frameworks. *Angew. Chem., Int. Ed.* **2015**, *54*, 3417−3430.
(16) Guillerm, V.; Kim, D.; Eubank, J. F.; Luebke, R.; Liu, X.; Adil, K.; Lah, M. S.; Eddaoudi, M. A supermolecular building approach for the design and construction of metal-organic frameworks. *Chem. Soc. Rev.* **2014**, *43*, 6141−6172.
(17) Doherty, C. M.; Grenci, G.; Riccò, R.; Mardel, J. I.; Reboul, J.; Furukawa, S.; Kitagawa, S.; Hill, A. J.; Falcaro, P. Combining UV Lithography and an Imprinting Technique for Patterning Metal-Organic Frameworks. *Adv. Mater.* **2013**, *25*, 4701−4705.
(18) Alexis, F.; Pridgen, E.; Molnar, L. K.; Farokhzad, O. C. Factors Affecting the Clearance and Biodistribution of Polymeric Nanoparticles. *Mol. Pharmaceutics* **2008**, *5*, 505−515.
(19) Monopoli, M. P.; Aberg, C.; Salvati, A.; Dawson, K. A. Biomolecular coronas provide the biological identity of nanosized materials. *Nat. Nanotechnol.* **2012**, *7*, 779−786.
(20) McGuire, C. V.; Forgan, R. S. The Surface Chemistry of Metal-Organic Frameworks. *Chem. Commun.* **2015**, *51*, 5199−5217.
(21) Rowe, M. D.; Thamm, D. H.; Kraft, S. L.; Boyes, S. G. Polymer-Modified Gadolinium Metal-Organic Framework Nanoparticles Used as Multifunctional Nanomedicines for the Targeted Imaging and Treatment of Cancer. *Biomacromolecules* **2009**, *10*, 983−993.
(22) Bellido, E.; Hidalgo, T.; Lozano, M. V.; Guillevic, M.; Simón-Vázquez, R.; Santander-Ortega, M. J.; González-Fernández, Á.; Serre, C.; Alonso, M. J.; Horcajada, P. Heparin-Engineered Mesoporous Iron Metal-Organic Framework Nanoparticles: Toward Stealth Drug Nanocarriers. *Adv. Healthcare Mater.* **2015**, *4*, 1246−1257.
(23) Wang, S.; Morris, W.; Liu, Y.; McGuirk, C. M.; Zhou, Y.; Hupp, J. T.; Farha, O. K.; Mirkin, C. A. Surface-Specific Functionalization of Nanoscale Metal−Organic Frameworks. *Angew. Chem., Int. Ed.* **2015**, *54*, 14738−14742.
(24) Wuttke, S.; Dietl, C.; Hinterholzinger, F. M.; Hintz, H.; Langhals, H.; Bein, T. Turn-on fluorescence triggered by selective internal dye replacement in MOFs. *Chem. Commun.* **2014**, *50*, 3599−3601.
(25) Liu, B.; Ma, M.; Zacher, D.; Bétard, A.; Yusenko, K.; Metzler-Nolte, N.; Wöll, C.; Fischer, R. A. Chemistry of SURMOFs: Layer-Selective Installation of Functional Groups and Post-synthetic Covalent Modification Probed by Fluorescence Microscopy. *J. Am. Chem. Soc.* **2011**, *133*, 1734−1737.
(26) Liu, B.; Fischer, R. Liquid-phase epitaxy of metal organic framework thin films. *Sci. China: Chem.* **2011**, *54*, 1851−1866.
(27) McDonald, K. A.; Feldblyum, J.; Koh, K.; Wong-Foy, A.; Matzger, A. J. Polymer@MOF@MOF: "Grafting From" Atom Transfer Radical Polymerization for the Synthesis of Hybrid Porous Solids. *Chem. Commun.* **2015**, *51*, 11994−11996.
(28) Kondo, M.; Furukawa, S.; Hirai, K.; Kitagawa, S. Coordinatively Immobilized Monolayers on Porous Coordination Polymer Crystals. *Angew. Chem., Int. Ed.* **2010**, *49*, 5327−5330.
(29) Jung, S.; Kim, Y.; Kim, S.-J.; Kwon, T.-H.; Huh, S.; Park, S. Bio-functionalization of metal-organic frameworks by covalent protein conjugation. *Chem. Commun.* **2011**, *47*, 2904−2906.
(30) Shih, Y.-H.; Lo, S.-H.; Yang, N.-S.; Singco, B.; Cheng, Y.-J.; Wu, C.-Y.; Chang, I. H.; Huang, H.-Y.; Lin, C.-H. Trypsin-Immobilized Metal−Organic Framework as a Biocatalyst In Proteomics Analysis. *ChemPlusChem* **2012**, *77*, 982−986.
(31) Baati, T.; Njim, L.; Neffati, F.; Kerkeni, A.; Bouttemi, M.; Gref, R.; Najjar, M. F.; Zakhama, A.; Couvreur, P.; Serre, C.; Horcajada, P. In depth analysis of the in vivo toxicity of nanoparticles of porous iron(iii) metal-organic frameworks. *Chem. Sci.* **2013**, *4*, 1597−1607.
(32) Bezverkhyy, I.; Weber, G.; Bellat, J.-P. Degradation of fluoride-free MIL-100(Fe) and MIL-53(Fe) in water: Effect of temperature and pH. *Microporous Mesoporous Mater.* **2016**, *219*, 117−124.
(33) Bellido, E.; Guillevic, M.; Hidalgo, T.; Santander-Ortega, M. J.; Serre, C.; Horcajada, P. Understanding the Colloidal Stability of the Mesoporous MIL-100(Fe) Nanoparticles in Physiological Media. *Langmuir* **2014**, *30*, 5911−5920.

DOI: 10.1021/acs.chemmater.6b00180
Chem. Mater. 2016, 28, 3318−3326

(34) Horcajada, P.; Chalati, T.; Serre, C.; Gillet, B.; Sebrie, C.; Baati, T.; Eubank, J. F.; Heurtaux, D.; Clayette, P.; Kreuz, C.; Chang, J.-S.; Hwang, Y. K.; Marsaud, V.; Bories, P.-N.; Cynober, L.; Gil, S.; Ferey, G.; Couvreur, P.; Gref, R. Porous metal-organic-framework nanoscale carriers as a potential platform for drug delivery and imaging. *Nat. Mater.* **2010**, *9*, 172−178.
(35) Wuttke, S.; Braig, S.; Preiß, T.; Zimpel, A.; Sicklinger, J.; Bellomo, C.; Radler, J. O.; Vollmar, A. M.; Bein, T. MOF nanoparticles coated by lipid bilayers and their uptake by cancer cells. *Chem. Commun.* **2015**, *51*, 15752−15755.
(36) He, C.; Liu, D.; Lin, W. Self-Assembled Core−Shell Nanoparticles for Combined Chemotherapy and Photodynamic Therapy of Resistant Head and Neck Cancers. *ACS Nano* **2015**, *9*, 991−1003.
(37) Huxford-Phillips, R. C.; Russell, S. R.; Liu, D.; Lin, W. Lipid-coated nanoscale coordination polymers for targeted cisplatin delivery. *RSC Adv.* **2013**, *3*, 14438−14443.
(38) Horcajada, P.; Surble, S.; Serre, C.; Hong, D.-Y.; Seo, Y.-K.; Chang, J.-S.; Greneche, J.-M.; Margiolaki, I.; Ferey, G. Synthesis and catalytic properties of MIL-100(Fe), an iron(iii) carboxylate with large pores. *Chem. Commun.* **2007**, 2820−2822.
(39) Cauda, V.; Argyo, C.; Bein, T. Impact of different PEGylation patterns on the long-term bio-stability of colloidal mesoporous silica nanoparticles. *J. Mater. Chem.* **2010**, *20*, 8693−8699.
(40) Gref, R.; Domb, A.; Quellec, P.; Blunk, T.; Müller, R. H.; Verbavatz, J. M.; Langer, R. The controlled intravenous delivery of drugs using PEG-coated sterically stabilized nanospheres. *Adv. Drug Delivery Rev.* **1995**, *16*, 215−233.
(41) Mori, Y.; Nagaoka, S.; Takiuchi, H.; Kikuchi, T.; Noguchi, N.; Tanzawa, H.; Noishiki, Y. A New Antitrhombogenic Material with long Polyethyleneoxide Chains. *ASAIO J.* **1982**, *28*, 459−463.
(42) Schaffert, D.; Troiber, C.; Salcher, E. E.; Fröhlich, T.; Martin, I.; Badgujar, N.; Dohmen, C.; Edinger, D.; Kläger, R.; Maiwald, G.; Farkasova, K.; Seeber, S.; Jahn-Hofmann, K.; Hadwiger, P.; Wagner, E. Solid-Phase Synthesis of Sequence-Defined T-, i-, and U-Shape Polymers for pDNA and siRNA Delivery. *Angew. Chem., Int. Ed.* **2011**, *50*, 8986−8989.
(43) Lächelt, U.; Kos, P.; Mickler, F. M.; Herrmann, A.; Salcher, E. E.; Rödl, W.; Badgujar, N.; Bräuchle, C.; Wagner, E. Fine-tuning of proton sponges by precise diaminoethanes and histidines in pDNA polyplexes. *Nanomedicine* **2014**, *10*, 35−44.
(44) Scholz, C.; Kos, P.; Leclercq, L.; Jin, X.; Cottet, H.; Wagner, E. Correlation of Length of Linear Oligo(ethanamino) Amides with Gene Transfer and Cytotoxicity. *ChemMedChem* **2014**, *9*, 2104−2110.
(45) Ali, Z.; Abbasi, A. Z.; Zhang, F.; Arosio, P.; Lascialfari, A.; Casula, M. F.; Wenk, A.; Kreyling, W.; Plapper, R.; Seidel, M.; Niessner, R.; Knöll, J.; Seubert, A.; Parak, W. J. Multifunctional Nanoparticles for Dual Imaging. *Anal. Chem.* **2011**, *83*, 2877−2882.
(46) Agostoni, V.; Horcajada, P.; Noiray, M.; Malanga, M.; Aykaç, A.; Jicsinszky, L.; Vargas-Berenguel, A.; Semiramoth, N.; Daoud-Mahammed, S.; Nicolas, V.; Martineau, C.; Taulelle, F.; Vigneron, J.; Etcheberry, A.; Serre, C.; Gref, R. A "green" strategy to construct non-covalent, stable and bioactive coatings on porous MOF nanoparticles. *Sci. Rep.* **2015**, *5*, 7925.
(47) Socrates, G. *Infrared and Raman Characteristic Group Frequencies: Tables and Charts*, 3rd ed.; John Wiley and Sons, Ltd.: Chichester, 2001.
(48) Rusu, L.; Gambhir, A.; McLaughlin, S.; Rädler, J. Fluorescence Correlation Spectroscopy Studies of Peptide and Protein Binding to Phospholipid Vesicles. *Biophys. J.* **2004**, *87*, 1044−1053.
(49) Rigler, R.; Mets, Ü.; Widengren, J.; Kask, P. Fluorescence correlation spectroscopy with high count rate and low background: analysis of translational diffusion. *Eur. Biophys. J.* **1993**, *22*, 169−175.
(50) Elson, E. L.; Magde, D. Fluorescence correlation spectroscopy. I. Conceptual basis and theory. *Biopolymers* **1974**, *13*, 1−27.
(51) Wang, Z.; Tanabe, K. K.; Cohen, S. M. Accessing Postsynthetic Modification in a Series of Metal-Organic Frameworks and the Influence of Framework Topology on Reactivity. *Inorg. Chem.* **2009**, *48*, 296−306.
(52) Ikezoe, Y.; Washino, G.; Uemura, T.; Kitagawa, S.; Matsui, H. New Autonomous Motors of Metal-Organic Framework (MOF) Powered by Reorganization of Self-Assembled Peptides at interfaces. *Nat. Mater.* **2012**, *11*, 1081−1085.
(53) Banfi, D.; Patiny, L. Resurrecting and Processing NMR Spectra On-line. *Chimia* **2008**, *62*, 280−281.
(54) Brittain, W. J.; Minko, S. A structural definition of polymer brushes. *J. Polym. Sci., Part A: Polym. Chem.* **2007**, *45*, 3505−3512.
(55) Torrano, A. A.; Blechinger, J.; Osseforth, C.; Argyo, C.; Reller, A.; Bein, T.; Michaelis, J.; Brauchle, C. A fast analysis method to quantify nanoparticle uptake on a single cell level. *Nanomedicine (London, U. K.)* **2013**, *8*, 1815−28.
(56) Rohrer, M.; Bauer, H.; Mintorovitch, J.; Requardt, M.; Weinmann, H. J. Comparison of magnetic properties of MRI contrast media solutions at different magnetic field strengths. *Invest. Radiol.* **2005**, *40*, 715−24.
(57) Hossann, M.; Wang, T.; Syunyaeva, Z.; Wiggenhorn, M.; Zengerle, A.; Issels, R. D.; Reiser, M.; Lindner, L. H.; Peller, M. Non-ionic Gd-based MRI contrast agents are optimal for encapsulation into phosphatidyldiglycerol-based thermosensitive liposomes. *J. Controlled Release* **2013**, *166*, 22−29.
(58) Rowe, M. D.; Chang, C.-C.; Thamm, D. H.; Kraft, S. L.; Harmon, J. F.; Vogt, A. P.; Sumerlin, B. S.; Boyes, S. G. Tuning the Magnetic Resonance Imaging Properties of Positive Contrast Agent Nanoparticles by Surface Modification with RAFT Polymers. *Langmuir* **2009**, *25*, 9487−9499.
(59) Hatakeyama, W.; Sanchez, T. J.; Rowe, M. D.; Serkova, N. J.; Liberatore, M. W.; Boyes, S. G. Synthesis of Gadolinium Nanoscale Metal−Organic Framework with Hydrotropes: Manipulation of Particle Size and Magnetic Resonance Imaging Capability. *ACS Appl. Mater. Interfaces* **2011**, *3*, 1502−1510.

DOI: 10.1021/acs.chemmater.6b00180
Chem. Mater. 2016, 28, 3318−3326

Supporting Information

Imparting functionality to MOF nanoparticles by external surface selective covalent attachment of polymers

Andreas Zimpel,‡[a] Tobias Preiß,‡[b] Ruth Röder,[c] Hanna Engelke,[a] Michael Ingrisch,[d] Michael Peller,[d] Joachim O. Rädler,[b] Ernst Wagner,[c] Thomas Bein,[a] Ulrich Lächelt[c], and Stefan Wuttke*[a]*

[a] *Department of Chemistry and Center for NanoScience (CeNS), LMU Munich, Butenandtstraße 11, 81377 Munich (Germany)*

[b] *Department of Physics and Center for NanoScience (CeNS), LMU Munich, Geschwister-Scholl-Platz 1, 80539 Munich (Germany)*

[c] *Department of Pharmacy and Center for NanoScience (CeNS), LMU Munich, Butenandtstraße 5, 81377 Munich (Germany)*

[d] *Josef Lissner Laboratory for Biomedical Imaging, Institute for Clinical Radiology, University Hospital, LMU Munich, Marchioninistraße 15, 81377 Munich (Germany)*

‡ *Both authors contributed equally to this work.*

E-Mail corresponding authors: stefan.wuttke@cup.uni-muenchen.de and ulrich.laechelt@cup.uni-muenchen.de

Table of Contents

1. Methods and Characterization

X-ray diffraction (XRD): X-ray diffraction was measured with the STOE transmission diffractometer system Stadi MP with Cu $K\alpha_1$ radiation (λ = 1.54060 Å) and Ge(111) single crystal monochromator. Diffraction patterns were recorded with a DECTRIS solid state strip detector MYTHEN 1K in an omega-2-theta scan mode using a step size of 4.71° and a counting time of 80 s per step.

Dynamic light scattering (DLS) and zeta-potential measurements: DLS and zeta-potential measurements were carried out using a Malvern Zetasizer (Nano Series, Nano-ZS). For pH dependent zeta-potential measurements the zetasizer was equipped with a Malvern Multi Purpose Titrator (MPT-2). 10 mL of an aqueous solution of nanoparticles (0.1 mg/mL) was set to pH 4 with HCl (0.1 M) and titrated stepwise (steps of 0.5) to pH 8 with NaOH (0.01 or 0.1 M, respectively).

Thermogravimetric analysis (TGA): Thermogravimetric analysis was performed with a thermo-microbalance (Netzsch, STA 449 C Jupiter) with a heating rate of 10 °C/min up to 900°C. Approximately 10 mg of the material were heated under synthetic air conditions with a flow rate of 25 mL/min.

Sorption measurements: Nitrogen sorption isotherms were measured at 77 K with a Quantachrome NOVA 4000e. Approximately 20 mg of nanoparticles was degassed at 150 °C in high vacuum for at least 12 h prior to measurement. Evaluation of the sorption data was carried out using the ASiQwin^{TM} software (Version 2.0, Quantachrome Instruments). BET surface areas were calculated employing the linearized form of the BET equation. For all samples the correlation coefficient was higher than 0.999. Adsorption isotherms were used to calculate the pore size distribution by employing quenched solid density functional theory (QSDFT, N_2 at 77 K on carbon, cylindrical/spherical pores adsorption branch).

Infrared (IR) spectroscopy: IR spectroscopy was performed on an FT-IR spectrometer (Thermo Scientific, NICOLET 6700) in transmission mode. Transparent potassium bromide pellets (150 mg) served as matrix for 1 mg MOF nanoparticles.

UV-Vis spectroscopy: UV-Vis measurements were carried out using a Perkin Elmer Lambda 1050 UV-Vis-NIR spectrometer equipped with a 150 mm InGaAs integrating sphere. For the measurements, all samples were diluted with water at a 1 to 4 ratio and precision cells (Hellma, SUPRASIL®, light path: 5 mm) were filled with 0.75 mL of these solutions.

Transmission electron microscopy (TEM): All samples were investigated with an FEI Titan Themis equipped with an extreme field emission gun (X-FEG). A 4k × 4k Ceta 16M™ camera detected bright field and high-resolution TEM images. The samples were prepared by adding a droplet of the diluted ethanolic nanoparticle suspension on a carbon-coated copper grid followed by drying for a few minutes.

TEM image analysis

Transmission electron micrographs of MIL-100(Fe) were analyzed with ImageJ 1.48v. After converting to binary pictures (pixels are either black or white) with a threshold which is set such that most of the background is set to white, the image is processed with a "watershed" that separates particles that are lying close to each other with a line of white pixels. With this step it is possible that particle clusters are separated by mistake. This error is taken into account during the next step using the "analyze particles" function. By excluding non-circular particles (separated clusters), particles smaller than 20 nm² (background grain) and particles at the edges of the field of view, only single MIL-100(Fe) NPs are analyzed in their area. The area of the analyzed particles was then converted into a diameter by assuming circular shape of the particles.

Nuclear magnetic resonance (NMR): ^{1}H-NMR spectroscopy was performed on a Bruker 400 or a Bruker 400 TR NMR spectrometer, respectively. The samples were prepared by dissolving a few milligram of the material in 700 µL $CDCl_3$ in NMR tubes (Hilgenberg, standard 5 mm).

Fluorescence Correlation Spectroscopy (FCS): FCS is a confocal fluorescence technique for measuring concentrations and diffusion constants of fluorescently labeled molecules in highly diluted solutions. Its principles were already described by Magde et al. in 1972.[1] The fluctuating fluorescence signal F(t) is used to determine the autocorrelation function $G(\tau) = \frac{\langle F(t)F(t+\tau)\rangle}{\langle F\rangle^2}$. From the correlation curve it is possible to derive the hydrodynamic radius and the particle concentration of a freely diffusing particle in solution. In this case the correlation

of one species is given by $G(\tau) = G(0)\frac{1}{1+\frac{\tau}{\tau_D}}\frac{1}{\sqrt{1+\frac{\tau}{S^2\tau_D}}}$, where $G(0)$ is the correlation's amplitude, S is the ratio between the lateral and the axial confocal volume radius, while τ_D is the mean time a particle needs to diffuse across the focal volume.[2] Knowing the width ω of the confocal volume, the hydrodynamic radius is given by $R_H = \frac{2k_BT\tau_D}{3\pi\eta\omega^2}$ (using the Boltzmann constant k_B as well as the temperature $T = 295\text{K}$ and viscosity $\eta = 0.958\text{mPas}$ of the measured aqueous suspension). The FCS measurements were carried out on a ConfoCor2 (Zeiss, Jena) setup with a 40x NA1.2 water immersion objective employing a red 633 nm HeNe-Laser for excitation of Cy5 fluorophore. 200 µl of a diluted aqueous suspension of Stp10-C*Cy5 was measured with FCS as well as 200 µl suspension of MIL-100(Fe)@Stp10-C*Cy5. The focal width $\omega = 0{,}28$ µm was determined by calibration using Alexa Fluor 633. The hydrodynamic radius of Stp10-C*Cy5 was found to be 1.1 nm. As MIL-100(Fe)@Stp10-C*Cy5 particles showed to form some agglomerates a two component fitting routine was used taking into account that brighter particles are overestimated in correlation curve[3] and the supposition that the number of dye molecules at NPs surface scales with its radius squared. Thereby a dominant (>99%) species of MIL-100(Fe)@Stp10-C*Cy5 particles with a hydrodynamic radius of 56nm was found.

2. Experimental section

2.1. Chemicals

Iron (III) chloride hexahydrate (Grüssing GmbH), trimesic acid (BTC, Aldrich), 1-ethyl-3-(3-dimethylaminopropyl)carbodiimide (EDC hydrochloride, Aldrich, crystalline), hydroxy-2,5-dioxopyrrolidine-3-sulfonic acid sodium salt (sulfo-NHS, Aldrich) sodium sulfate (Grüssing GmbH, water-free), 2-[4-(2-hydroxyethyl)piperazine-1-yl]ethanesulfonic acid (HEPES, Biomol GmbH), Glucose (Applichem), α-methoxy-ω-amino poly(ethylene glycol) (PEG5000 amine, Rapp Polymere, PEG-MW: 5000 g/mol), Tentagel S RAM resin (Rapp Polymere), Nα-Fmoc-S-trityl-L-cysteine (Fmoc-Cys(Trt)-OH, Iris Biotech), N-methyl-2-pyrrolidone (NMP, Iris Biotech), 1-hydroxybenzotriazole (HOBt, Aldrich), 2-(1H-benzotriazol-1-yl)-1,1,3,3-tetramethyluronium hexafluorophosphate (HBTU, Multisyntech), N,N-diisopropylethylamine (DIPEA, Iris Biotech), piperidine (Iris Biotech), trifluoroacetic acid (TFA, Iris Biotech), triisopropylsilane (TIS, Aldrich), acetonitrile (HPLC grade, VWR), tris(2-carboxyethyl)phosphine hydrochloride solution (TCEP, 0.5 M, pH 7.0, Aldrich), Cyanine5 maleimide (Lumiprobe) were used as received. The solvents ethanol (EtOH, Aldrich, absolute), N-N,-dimethylformamide (DMF, Iris Biotech) and deuterated trichloromethane ($CDCl_3$, Euriso-top, 99.8 % D) were used without further purification. Dichloromethane (DCM) and methyl-tert-butyl ether (MTBE, Brenntag) were distilled before use. Cell culture media, antibiotics and fetal bovine serum (FBS) were purchased from Life Technologies or Sigma-Aldrich, respectively. As a reference in MRI Gd-DTPA-BMA (Omniscan, GE Healthcare) diluted in water (0-2.5 mM) have been examined.

2.2. Synthesis of MIL-100(Fe) nanoparticles

MIL-100(Fe) nanoparticles were prepared in a procedure similar to a literature method.[4] For the microwave synthesis of MIL-100 (Fe) nanoparticles, iron(III) chloride hexahydrate (2.43 g, 9.00 mmol) and trimesic acid (0.84 g, 4.00 mmol) in 30 ml H_2O was put into a Teflon tube, sealed and placed in the microwave reactor (Microwave: Synthos3000, *Anton Paar*). The mixture was heated to 130 °C under solvothermal conditions (p = 2.5 bar) within 30 seconds, kept at 130 °C for 4 minutes and 30 seconds, and the resulting solid was cooled down to room temperature. For the purification of the solid, the reaction mixture was centrifuged (Sorvall Evolution RC, *Thermo Scientific* , 47808 rcf / 20000 rpm, 20 min), the solvent was removed and the pellet was redispersed in EtOH. This cycle was repeated two times and the dispersed solid was allowed to sediment overnight. The supernatant was

filtrated three times (filter discs grade: 391; Sartorius Stedim Biotech), yielding MIL-100(Fe) nanoparticles, which are left in the filtrate. Afterwards the material was characterized by DLS, XRD, IR, TGA, TEM, N_2 sorption and zeta-potential measurements.

2.3. External surface coating of MIL-100(Fe) nanoparticles with PEG5000

In a standard reaction, MIL-100(Fe) nanoparticles (1.0 mg) were dispersed in ethanol (100 µL). EDC hydrochloride (approx. 1 mg) and a catalytic amount of sulfo-NHS were added to the suspension and stirred for a few minutes. Afterwards, PEG5000amine (100 µg, 20.0 nmol) dissolved in bi-distilled H_2O (100 µL) was poured into the MOF dispersion and the mixture was stirred for 30 min. The functionalized nanoparticles were centrifuged (Eppendorf 5418/5418R, 16873 rcf / 14000 rpm; 10 min), the supernatant was removed and the pellet was washed three times with water by the centrifugation and redispersion technique.

2.4. Synthesis of Stp10-C

The oligoamino amide Stp10-C was synthesized on solid-phase using the artificial oligoamino acid Fmoc-Stp(Boc_3)-OH[5] and conventional Fmoc solid-phase peptide synthesis conditions. 416.6 mg Tentagel S RAM resin (0.24 mmol/g loading; 100 µmol scale size) were weighed into a 10 mL syringe microrector with PTFE frit (Mutltisyntech). The syringe was put on a vacuum manifold (Promega) and 5 mL DCM were added for resin swelling. After 30 min the DCM was discarded. The resin was washe0d once with 5 mL DMF and the reactor was put in the microwave reactor block of a Biotage Syro Wave automated peptide synthesizer. Fmoc deprotection was carried out by 5-fold incubation with 3 mL 20 % piperidine in DMF for 10 min under shaking. The resin was washed 5 times with 3.2 mL DMF after Fmoc deprotection. Coupling of the C-terminal cysteine was initiated by addition of 1.2 mL of a solution containing 0.33 M Fmoc-Cys(Trt)-OH and HOBt in NMP (400 µmol, 4 eq), 1.26 mL of 0.32 M HBTU in DMF (400 µmol, 4 eq) and 0.6 mL of 1.33 M DIPEA in NMP (800 µmol, 8 eq). The mixture was incubated for 60 min at room temperature under shaking. Subsequently, the solution was removed and the resin was washed twice with 3.2 mL DMF. The coupling step was repeated followed by 5-fold resin washing with 3.2 mL DMF. Fmoc deprotection was carried out as described above followed by 5-fold resin wash with 3.2 mL DMF. The subsequent Stp units were coupled using the same stoichiometry under microwave irradiation. For this, the resin was incubated with 1.2 mL of a solution containing 0.33 M Fmoc-Stp(Boc_3)-OH and HOBt in NMP (400 µmol, 4 eq), 1.26 mL of 0.32 M HBTU in DMF (400 µmol, 4 eq) and 0.6 mL of 1.33 M DIPEA in NMP (800 µmol, 8 eq) at 60 °C for 10 min.

After removal of the coupling solution and twofold resin wash with 3.2 mL DMF, the coupling step was repeated. The solution was removed and the resin was washed 5-fold with 3.2 mL DMF. The following Fmoc deprotection, washing and coupling steps were carried out and repeated as described above to assemble the final sequence H_2NCO-C(Trt)-[Stp(Boc_3)]$_{10}$-NH_2. The resin was washed once with 5 mL DCM and dried in vacuo. Cleavage was carried by incubation with 5 mL TFA/TIS/H_2O (95/2.5/2.5, v/v/v) for 90 min at room temperature. The mixture was collected and the resin was washed twice with 2 mL of TFA. The combined solutions were concentrated under reduced pressure and the product was precipitated in 50 mL of cold MTBE/n-Hexan (25/25, v/v). The supernatant was discarded, the pellet was dried under a nitrogen stream. The compound was purified by size exclusion chromatography using the ÄKTApurifier 10 system (GE Healthcare). Sephadex G-10 (GE Healthcare) was used as gel filtration medium and 10 mM hydrochloric acid solution/acetonitrile (7/3, v/v) as eluent. The absorption at 214, 260 and 280 nm was monitored and the fractions corresponding to the high-molecular weight oligomer were pooled, snap-frozen and freeze-dried. As a result of the eluent used, the HCl salt of the multiple amino groups was formed after purification. Stp10-C was analyzed by ^{1}H-NMR (Fig. S-17), MALDI-MS (Fig. S-18) and RP-HPLC.

*2.5. Synthesis of Stp10-C*Cy5*

24.1 mg of Stp10-C (6.1 µmol) were dissolved in 1000 µL HEPES buffer (10 mM, pH 7.4). 122 µL of 0.5 M TCEP solution (61 µmol, 10 eq) were added and the solution was incubated for 30 min under shaking. 5.85 mg of Cyanine5 maleimide (9.1 µmol, 1.5 eq) were dissolved in 200 µL DMF and added to the Stp10-C solution. The reaction tube was flushed with nitrogen and incubated for 4 hours at room temperature under shaking in the dark. The compound was purified by size exclusion chromatography as described above using the ÄKTA purifier 10 system (GE Healthcare), Sephadex G-10 (GE Healthcare) as gel filtration medium and 10 mM hydrochloric acid solution/acetonitrile (7/3, v/v) as eluent. The absorption at 214, 280 and 646 nm was monitored, and the fractions corresponding to the high-molecular weight oligomer were pooled, snap-frozen and freeze-dried.

2.6. External surface coating of MIL-100(Fe) nanoparticles with Stp10-C

In a standard reaction, MIL-100(Fe) nanoparticles (1.0 mg) were dispersed in ethanol (100 µL). EDC hydrochloride (approx. 1 mg) and a catalytic amount of sulfo-NHS were added to the suspension and stirred for a few minutes. Afterwards, Stp10-C (79.3 µg, 20.0 nmol) dissolved in bi-distilled H_2O (100 µL) was poured into the MOF dispersion and the

mixture was stirred for 30 min. The functionalized nanoparticles were centrifuged (14000 rpm; 10 min), the supernatant was removed and the pellet was washed three times with water by the centrifugation and redispersion technique.

2.7. Dissolution of MOF particles in EDTA solution and extraction of functionalized linker

Functionalized MIL-100(Fe) particles were dispersed in an EDTA solution (0.1 mM) to result in a 2 mg/mL concentration. The dispersion was stirred for approx. 24 h until complete dissolution had occurred. Afterwards, the aqueous phase was extracted three times with equal amounts of DCM (20 mL). The organic phases were combined and dried over sodium sulfate for 1 h. After removal of the solvent, the product was dried under high vacuum. NMR spectroscopy was performed in $CDCl_3$.

2.8. Cell Culture

Murine neuroblastoma (N2A) were cultured in Dulbecco's modified Eagle's medium (DMEM), supplemented with 1 g/L glucose, 10% FBS, 100 U/mL penicillin, 100 µg/mL streptomycin and 4 mM stable glutamine.

2.9. Preparation of HEPES-buffered glucose (HBG)

In an aqueous solution of HEPES (20 mM), 5% glucose was added and the pH was adjusted to 7.4 by addition of hydrochloric acid.

*2.10. Metabolic activity assay of MIL-100(Fe) and MIL-100(Fe)@Stp10-C*Cy5 (MTT assay)*

Murine neuroblastoma (N2A) cells were seeded in 96-well plates at a density of 10.000 cells/ well 24 h prior to incubation with the different particle concentrations. Before incubation with the particles, medium was replaced with 80 µL fresh medium containing 10% FBS. Particles diluted in 20 µL HBG were added to each well and incubated on cells for 24 h at 37°C and 5% CO_2. 10 µL of MTT (3-(4,5-dimethylthia-zol-2-yl)-2,5-diphenyltetrazolium bromide) (5 mg/mL) were added to each well reaching a final concentration of 0.5 mg/mL. After an incubation time of 2 h, unreacted dye and medium were removed and the 96-well plates were frozen at −80°C for at least one hour. The purple formazan product was then dissolved in 100 µL DMSO (dimethyl sulfoxide) per well and quantified measuring absorbance using microplate reader (TecanSpectrafluor Plus, Tecan, Switzerland) at 590 nm with background correction at 630 nm. All studies were performed in quintuplicate. The relative cell

viability (%) related to control wells treated only with 20 µL HBG was calculated as ([A] test/[A] control) × 100%.

3. *Supplementary Figures*

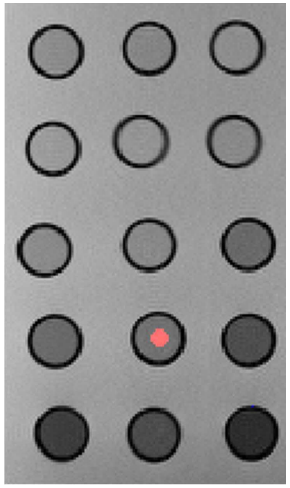

Figure S-1: Image of axial cross section of sample tubes acquired with SE MC (TE = 15 ms). ROI (red region of interest) used for calculation of T2 using mean signal intensities determined in these ROIs. As the samples comprise a wide range of T2 times it was not possible to set the window in such a way that all samples appear differently.

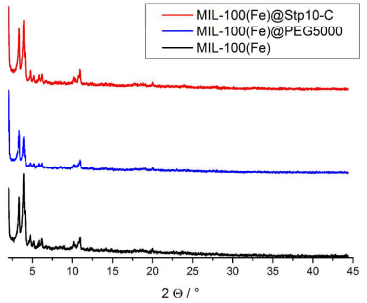

Figure S-2: XRD pattern of functionalized and unfunctionalized MIL-100(Fe) nanoparticles.

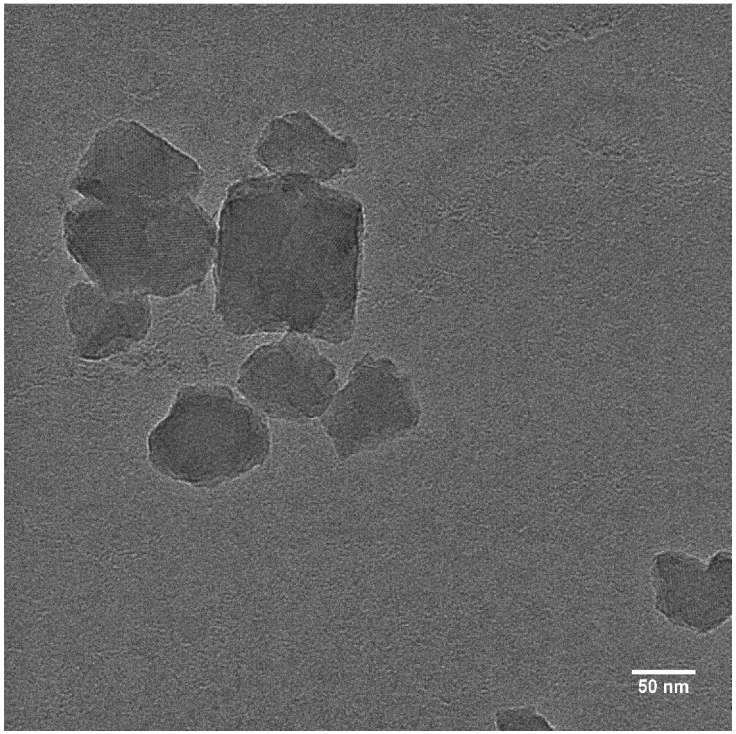

Figure S-3: TEM image of unfunctionalized MIL-100(Fe) nanoparticles.

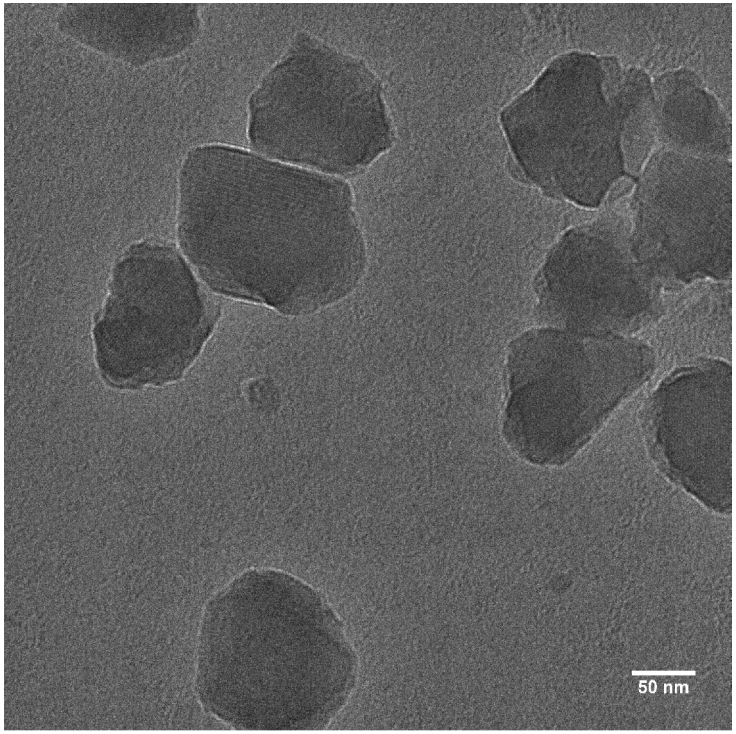

Figure S-4: TEM image of MIL-100(Fe)@Stp10-C nanoparticles.

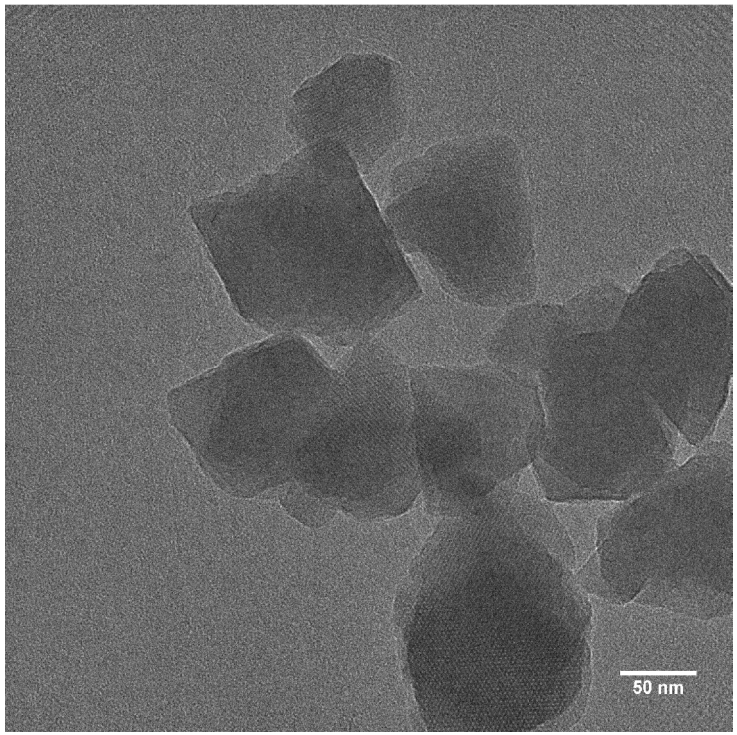

Figure S-5: TEM image of MIL-100(Fe)@PEG5000 nanoparticles.

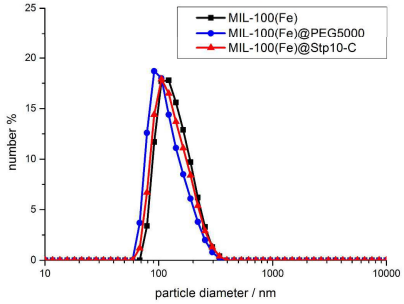

Figure S-6: DLS measurements of functionalized and unfunctionalized MIL-100(Fe) nanoparticles in EtOH.

Table S-1: DLS (Z-Average) data of functionalized and unfunctionlized MIL-100(Fe) nanoparticles dispersed in bi-distilled water . After 3 weeks, MIL-100(Fe) particles start to agglomerate, while the functionalized particles retain their colloidal stability.

Sample	MIL-100(Fe)	MIL-100(Fe)@Stp10-C	MIL-100(Fe)@PEG5000
after dispersion	159 nm	156 nm	154 nm
after 3h	153 nm	156 nm	150 nm
after 24h	157 nm	156 nm	150 nm
after 72h	156 nm	154 nm	147 nm
after 1 week	158 nm	155 nm	148 nm
after 3 weeks	**213 nm**	152 nm	146 nm

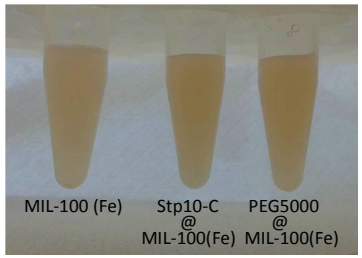

Figure S-7: Particles dispersion of functionalized and unfunctionalized MIL-100(Fe) nanoparticles after 3h in H_2O

Table S-2: DLS (Z-Average) data of functionalized and unfunctionlized MIL-100(Fe) nanoparticles dispersed in 10% fetal bovine serum (FBS) within 3 weeks. Unfunctionalized particles start to agglomerate immediately, while polymer-functionalized particles retain their colloidal stability for 72 h.

Sample	MIL-100(Fe)	MIL-100(Fe)@Stp10-C	MIL-100(Fe)@PEG5000
after dispersion	> 1000 nm	376 nm	600 nm
after 3h	> 1000 nm	429 nm	669 nm
after 24h	> 1000 nm	432 nm	695 nm
after 72h	> 1000 nm	489 nm	715 nm
after 1 week	> 1000 nm	721 nm	> 1000 nm
after 3 weeks	> 1000 nm	879 nm	958 nm

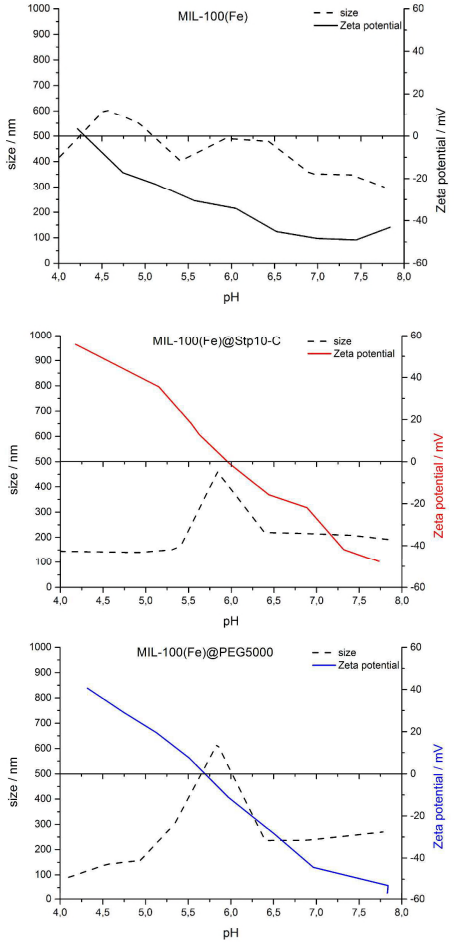

Figure S-8: Zeta-potential compared to particle size in the pH range from 4 to 8 for functionalized and unfunctionalized MIL-100(Fe) nanoparticles.

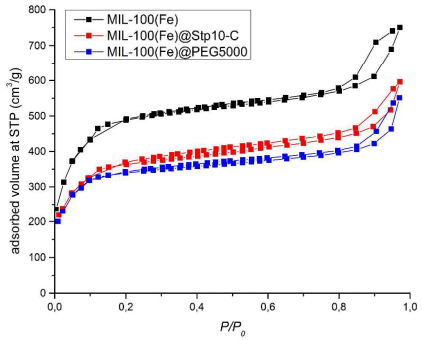

Figure S-9: Nitrogen sorption isotherms of functionalized and unfunctionalized MIL-100(Fe) nanoparticles.

Table S-3: Pore volume and BET surface areas of MIL-100(Fe) and functionalized MIL-100(Fe) nanoparticles calculated from N2 sorption isothermes of Figure S-9

MOF	pore volume (cm^3/g)	BET surface area (m^2/g)
MIL-100(Fe)	1.057	1905
MIL-100(Fe)@PEG5000	0.750	1338
MIL-100(Fe)@Stp10-C	0.823	1432

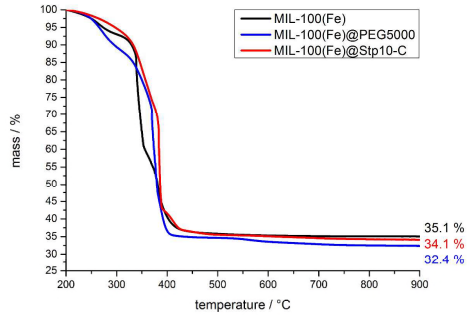

Figure S-10: TGA of functionalized and unfunctionalized MIL-100(Fe) nanoparticles.

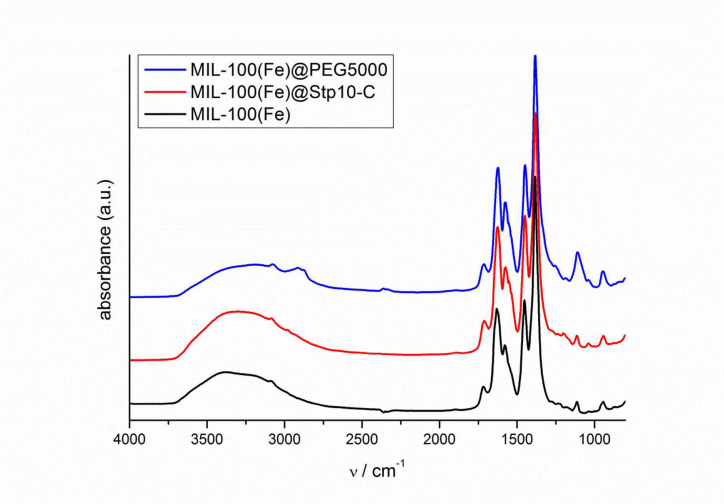

Figure S-11: IR spectra of functionalized and unfunctionalized MIL-100(Fe) nanoparticles.

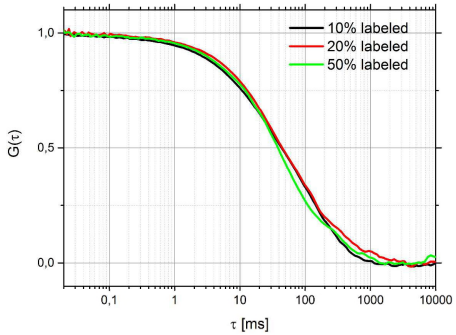

Figure S-12: Normalized FCS curves of MIL-100(Fe)@Stp10-C*Cy5 nanoparticles with varied amount of labelled Stp10-C. As the curves show no significant deviation we conclude that the fluorescent label has no effect on the function of Stp10-C.

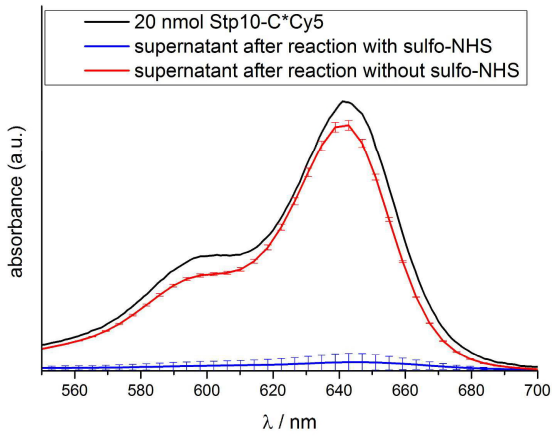

Figure S-13: UV-Vis spectra of supernatant with and without addition of sulfo-NHS to the reaction mixture.

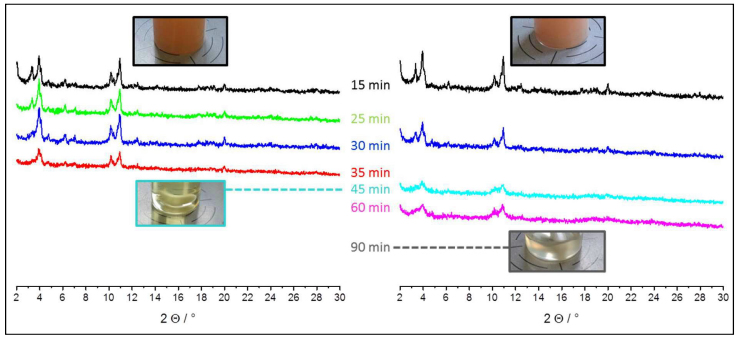

Figure S-14: XRD spectra of PEG-functionalized (right) and unfunctionalized (left) MOF nanoparticles in comparison; time-based dissolution behaviour in EDTA-solution (0.1 mM; 2.0 mg (MOF)/mL). After 45 minutes, the unfunctionalized particles are completely dissolved. PEG-functionalized nanoparticles are stable up to 90 minutes.

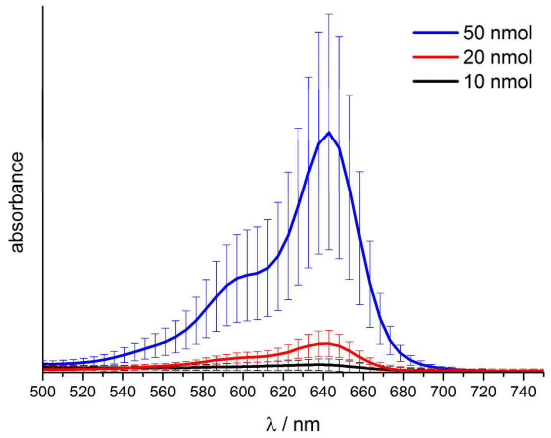

Figure S-15: Averaged UV-Vis data with standard deviations (error bars indicate the deviation of three individual measurements) of supernatant after coating reactions of Stp10-C; for 10 nmol polymer, the whole amount of polymer was attached to the MOF while there is some residue for 20 nmol. Therefore the covalent attachable amount was estimated to be between 10 and 20 nmol.

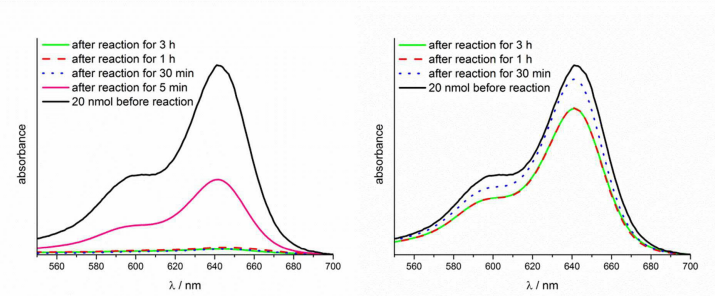

Figure S-16: Time-dependent amount of polymer left in the supernatant after reaction with (left) and without sulfo-NHS added to the reaction mixture. After 30 minutes with sulfo-NHS the reaction is already completed. During the same period of time almost no dye was adsorbed unspecifically to the particles, as there is no decrease of polymer visible after 30 minutes reaction without sulfo-NHS.

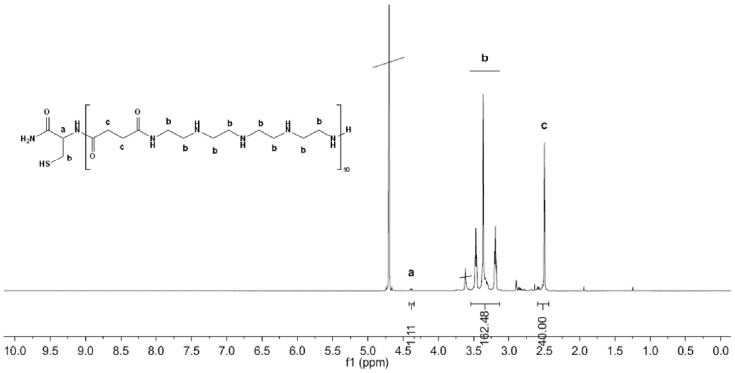

Figure S-17: ^{1}H-NMR (400 MHz, deuterium oxide) δ = 4.39 (t, 1H), 3.55 – 3.12 (m, 162H), 2.50 (s, 40H).

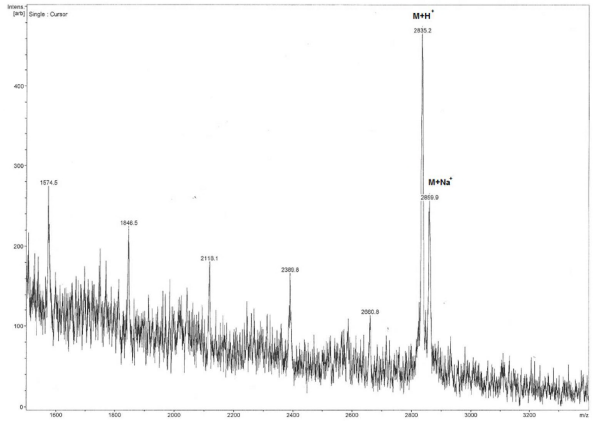

Figure S-18: MALDI-MS spectrum of C-Stp10. Mass calculated for $[M+H]^+$ 2833.1, mass found 2835.2; mass calculated for $[M+Na]^+$ 2855.0, mass found 2859.9.

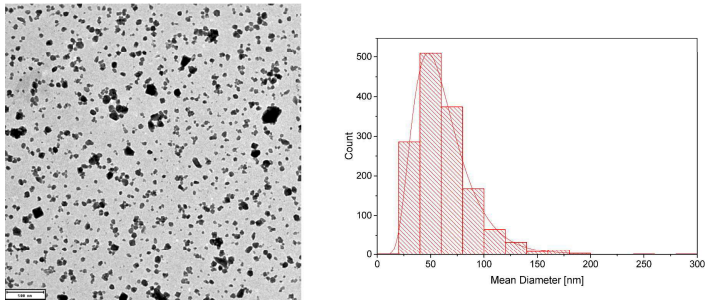

Figure S-19: Representative transmission electron micrograph of MIL-100(Fe) nanoparticles (left). Size distribution of more than 1500 analyzed MIL-100(Fe) nanoparticles acquired from TEM pictures via image analysis (right). The mean radius was determined to be 26.5 nm.

4. Calculations on the amount of attachable polymer

The mass density of MIL-100(Fe), determined by structure refinement of XRD pattern, is $\rho = 0.98 \frac{g}{mL}$.[6] Using a mass of $m = 1\,mg$, and a mean radius for the nanoparticles of $r = 26.5\,nm$ taken from TEM-analysis (see Figure S-19), one derives a **number of particles per mg** of

$$\boldsymbol{N = \frac{V_{overall}}{V_{NP}} = 1.309 \cdot 10^{13}}$$

with

$$V_{overall} = m/\rho = 1.020\,\mu L = 1.020\,mm^3$$

as the volume taken up by one mg of material, and

$$V_{NP} = \frac{4}{3}\pi r^3 = \frac{4}{3}\pi\,(26.5\,nm)^3 = 77951.8\,nm^3 = 7.795 \cdot 10^{-14}\,mm^3,$$

the volume of a sphere with the size of one nanoparticle.

The amount of polymer used per mg nanoparticles was 10 nmol and 20 nmol. With the Avogadro constant the respective number of polymer molecules is

$$10\,nmol = 6.022 \cdot 10^{15} \text{ and } 20\,nmol = 1.204 \cdot 10^{16}.$$

Assuming a full uptake of polymer, the **number of polymer molecules per particle** is

$$\frac{10\,nmol}{N} = \frac{6.022 \cdot 10^{15}}{1.309 \cdot 10^{13}} = 460 \text{ in the case of 10 nmol}$$

and

$$\frac{20\,nmol}{N} = \frac{6.022 \cdot 10^{15}}{1.204 \cdot 10^{16}} = 920 \text{ in the case of 20 nmol.}$$

To estimate the mean area one polymer molecule could occupy on the nanoparticle surface we evaluate the **surface area** of a sphere with the size **of a nanoparticle** to

$$S = 4\,\pi\,r^2 = 8.825 \cdot 10^3\,nm^2.$$

By dividing this number with the number of polymer molecules per nanoparticle we get the **surface space per polymer molecule**:

$$\frac{8.825 \cdot 10^3\,nm^2}{460} = 19.2\,nm^2 \text{ in the case of 10 nmol}$$

and

$$\frac{8.825 \cdot 10^3\,nm^2}{920} = 9.59\,nm^2 \text{ in the case of 20 nmol.}$$

This corresponds to a surface coverage of:

$$8.65\,pmol/cm^2 \text{ in the case of 10 nmol}$$

and

$$17.3\,pmol/cm^2 \text{ in the case of 20 nmol}$$

Compared to the size of the polymer molecules (hydrodynamic radius determined by FCS: 1.1 nm) the surface of one nanoparticle is loosely occupied by polymer molecules.

Mass % of polymer per MOF nanoparticles was calculated to allow comparison to TGA (see Fig. S-10).
Using a molecular mass of 5000 g/mol for PEG5000 and assuming 20 -10 nmol of PEG5000 attached to 1 mg MOF, the mass % is

$$\frac{20\,nmol \cdot 5000\frac{g}{mol}}{20\,nmol \cdot 5000\frac{g}{mol} + 1\,mg} = 9.1\,\% \text{ in the case of 20 nmol}$$

and

$$\frac{10\,nmol \cdot 5000\frac{g}{mol}}{10\,nmol \cdot 5000\frac{g}{mol} + 1\,mg} = 4.8\,\% \text{ in the case of 10 nmol}$$

Using a molecular mass of 2800 g/mol for Stp10-C (free base) and assuming 20 -10 nmol of Stp10-C attached to 1 mg MOF, the mass % is

$$\frac{20\ nmol \cdot 2800\frac{g}{mol}}{20\ nmol \cdot 2800\frac{g}{mol} + 1\ mg} = 5.3\ \%$$ in the case of 20 nmol

and

$$\frac{10\ nmol \cdot 2800\frac{g}{mol}}{10\ nmol \cdot 2800\frac{g}{mol} + 1\ mg} = 2.7\ \%$$ in the case of 10 nmol

This is in good agreement with TGA data (2,7% and 1%, respectively; see Fig. S-1), considering the accuracy of TGA.

5. References

1. Magde, D., Thermodynamic Fluctuations in a Reacting System - Measurement by Fluorescence Correlation Spectroscopy. *Phys. Rev. Lett.* **1972**, 705–708.
2. Schwille, P.; Haustein, E., Fluorescence Correlation Spectroscopy: An Introduction to its Concepts and Applications. *Spectroscopy* **2009,** 94, 1.
3. Thompson, N. L., Fluorescence Correlation Spectroscopy. In *Topics in Fluorescence Spectroscopy*, Lakowicz, J., Ed. Springer US: 1999; Vol. 1, pp 337-378.
4. García Márquez, A.; Demessence, A.; Platero-Prats, A. E.; Heurtaux, D.; Horcajada, P.; Serre, C.; Chang, J.-S.; Férey, G.; de la Peña-O'Shea, V. A.; Boissière, C.; Grosso, D.; Sanchez, C., Green Microwave Synthesis of MIL-100(Al, Cr, Fe) Nanoparticles for Thin-Film Elaboration. *Eur. J. Inorg. Chem.* **2012,** 2012, 5165-5174.
5. Schaffert, D.; Badgujar, N.; Wagner, E., Novel Fmoc-Polyamino Acids for Solid-Phase Synthesis of Defined Polyamidoamines. *Org. Lett.* **2011,** 13, 1586-1589.
6. Horcajada, P.; Surble, S.; Serre, C.; Hong, D.-Y.; Seo, Y.-K.; Chang, J.-S.; Greneche, J.-M.; Margiolaki, I.; Ferey, G., Synthesis and catalytic properties of MIL-100(Fe), an iron(iii) carboxylate with large pores. *Chem. Commun.* **2007**, 2820-2822.

B.5 Originalpublikation P5

Ruth Röder, Jonas Helma , Tobias Preiß, Joachim O. Rädler, Heinrich Leonhardt, Ernst Wagner.

Intracellular Delivery of Nanobodies for Imaging of Target Proteins in Live Cells.

Pharmaceutical Research, 2017, 34, 161–174.

Pharm Res (2017) 34:161–174
DOI 10.1007/s11095-016-2052-8

RESEARCH PAPER

Intracellular Delivery of Nanobodies for Imaging of Target Proteins in Live Cells

Ruth Röder[1] • Jonas Helma[2] • Tobias Preiß[3] • Joachim O. Rädler[3] • Heinrich Leonhardt[2] • Ernst Wagner[1]

Received: 1 August 2016 / Accepted: 10 October 2016 / Published online: 31 October 2016

ABSTRACT

Purpose Cytosolic delivery of nanobodies for molecular target binding and fluorescent labeling in living cells.

Methods Fluorescently labeled nanobodies were formulated with sixteen different sequence-defined oligoaminoamides. The delivery of formulated anti-GFP nanobodies into different target protein-containing HeLa cell lines was investigated by flow cytometry and fluorescence microscopy. Nanoparticle formation was analyzed by fluorescence correlation spectroscopy.

Results The initial oligomer screen identified two cationizable four-arm structured oligomers (***734, 735***) which mediate intracellular nanobody delivery in a receptor-independent (***734***) or folate receptor facilitated (***735***) process. The presence of disulfide-forming cysteines in the oligomers was found critical for the formation of stable protein nanoparticles of around 20 nm diameter. Delivery of labeled GFP nanobodies or lamin nanobodies to their cellular targets was demonstrated by fluorescence microscopy including time lapse studies.

Conclusion Two sequence-defined oligoaminoamides with or without folate for receptor targeting were identified as effective carriers for intracellular nanobody delivery, as exemplified by GFP or lamin binding in living cells. Due to the conserved nanobody core structure, the methods should be applicable for a broad range of nanobodies directed to different intracellular targets.

KEY WORDS folate · nanobody · oligoaminoamides · protein delivery · receptor targeting

Electronic supplementary material The online version of this article (doi:10.1007/s11095-016-2052-8) contains supplementary material, which is available to authorized users.

✉ Ernst Wagner
ernst.wagner@cup.uni-muenchen.de

[1] Pharmaceutical Biotechnology, Center for System-Based Drug Research, and Center for Nanoscience (CeNS), Ludwig-Maximilians-Universität München, Butenandtstraße 5, 81377 Munich, Germany

[2] Department of Biology II, Center for Integrated Protein Science Munich, Ludwig-Maximilians-Universität München, Munich, Germany

[3] Faculty of Physics and Center for NanoScience, Ludwig-Maximilians-Universität München, Geschwister-Scholl-Platz 1, D-80539 Munich, Germany

ABBREVIATIONS

FCS	Fluorescence correlation spectroscopy
FolA	Folic acid
HcAb	Heavy-chain only camelid antibody
Nb	Nanobody
PEG	Polyethyleneglycol
Stp	Succinoyl tetraethylene pentamine

INTRODUCTION

Nanobodies are single domain- antibody fragments (VHH) derived from heavy-chain only camelid antibodies (HcAb) (1). Especially with regard to their possible use as biopharmaceuticals (2,3) or imaging tools (4–6), nanobodies have significant advantages compared to standard antibodies. They can be easily screened for affinity and specificity; due to their compact, single domain structure, they stay chemically active in the reducing environment of the cell; they can be produced in prokaryotic systems in high yield and be easily chemically and genetically modified (7–9). Additionally, due to their small size (15 kDa), nanobodies can better diffuse through tissues or also intracellularly across nuclear pores, and also bind and inhibit targets such as enzymes which are addressed by standard antibodies to a far lesser extend (10,11).

Potential intracellular molecular targets can be accessed in fixed and permeabilized cells only. Intracellular protein delivery, also called "protein transduction" (12) may expand possible

applications of nanobodies for the treatment of live cells for bioimaging and functional biological or therapeutic purposes. Besides, labeling of proteins, prior to their delivery is possible, broadening the scope of dyes which can be used from intracellular expressed fluorescent proteins to any desired marker.

In general, low cellular uptake and endolysosomal entrapment hamper efficient protein transduction. Furthermore, there is no universal carrier for proteins, as they differ largely in size and surface charge. Many strategies such as virus like particles (13), silica nanoparticles (14–16), nanocapsules (17), charge-conversional polyion complex micelles (18–20), liposomal carriers (21), or cell penetrating peptides (22–24) have been applied to deliver therapeutic proteins. In recent work from our lab (25–28), we have reported the effective intracellular delivery of functional proteins such as RNase, green fluorescent protein (GFP), or β-galactosidase covalently coupled to sequence defined oligoaminoamide carriers.

For nanobody delivery, our investigations aimed at non-covalent interactions with oligomers for the following reasons. Due to the small nanobody size, covalent modification with dye and additional linkers appears to be problematic.

Nanobodies have a conserved core sequence, providing the beta-sheet based barrel-like domain structure. Variation occurs mostly in their complementarity determining regions (CDRs), which are responsible for specific antigen recognition (29). This results in very similar structures with only slightly modified properties from adapting to target other proteins or molecules of interest. Taking advantage of these quite conserved structural characteristics, we conducted a screen based on a small oligomer library, previously developed for nucleic acid delivery, and found two related precise sequence-defined oligoaminoamide carriers which are suitable to efficiently deliver different labeled nanobodies into cells.

These two PEGylated oligomers ***735*** (containing folate for receptor targeting) and ***734*** (analogous structure without folate) (30) lead to efficient transduction of a GFP binding nanobody, demonstrated by intracellular binding to its various recombinant target proteins (PCNA-GFP, Actin-GFP, Tubulin-GFP) in different recombinant HeLa cell lines. Comparison of uptake efficiencies of ***735*** and ***734*** showed enhanced binding for nanobody/folate-oligomer ***735***, which was confirmed by folic acid competition experiments. The formulation approach could successfully be extended to a lamin binding nanobody, visualizing the endogenous nuclear lamina, paving the way for numerous other nanobody applications.

MATERIAL AND METHODS

Materials

Atto-647 N (NHS ester) was purchased from Atto-Tec GmbH (Siegen, Germany), 2-(4-(2-hydroxyethyl)-1-piperazinyl)-ethansulfonic acid (HEPES) from Biomol (Hamburg, Germany), collagen A from Merck KGaA (Grafing Germany), DMSO from Bernd Kraft GmbH (Duisburg, Germany) and Blue Prestained Protein Standard, Broad Range from NEB (Frankfurt am Main). All other chemicals were purchased from Sigma-Aldrich (Germany). Antibiotics, fetal bovine serum (FBS) and cell culture medium were bought from Life Technologies (Carlsbad, USA). PBS adjusted to pH 7.4, was prepared in house. Sequence-defined oligomers ***734***, K-(PEG_{24}-E)-K-[K-(Stp_4-C)$_2$]$_2$ (52 protonable amines, molecular weight of HCl salt, 8437,9 g/mol), and ***735***, K-(PEG_{24}-FolA)-K-[K-(Stp_4-C)$_2$]$_2$ (52 protonable amines, molecular weight of HCl salt, 8732,1 g/mol), were synthesized by solid-phase assisted synthesis as described in (30–32). Oligomer ID numbers represent the identification numbers of the oligomers within the local data base at LMU Pharmaceutical Biotechnology. Oligomers were numbered in the order of first synthesis. Purification of the GFP binding nanobody (GBP; in the following termed α-GFP-Nb) and the lamin binding nanobody (α-lamin-Nb) was carried out as has been described previously (5,6).

Cell Culture

KB cells (ATCC CCL-17) (KB_*wt*) present an established subline of the human epithelial cervical adenocarcinoma cell line HeLa (ATCC CCL-2). The generation of the HeLa_PCNA-GFP cell line has been described in Rothbauer *et al.* (6). HeLa_Actin-GFP and HeLa_Tubulin-GFP cells were generated by Dr. K. von Gersdorff according to the procedure for the generation of HUH7_Actin-GFP and HUH7_Tubulin-GFP cell lines which has been described elsewhere (PhD thesis LMU, 2006).

All cell lines were grown in folic acid free RPMI-1640 medium supplemented with 10% FBS, 100 U ml^{-1} penicillin, 100 µg ml^{-1} Streptomycin and 4 mM stable glutamine. All cells were cultured at 37°C and 5% CO_2 in a humified incubator.

Modification of Nanobodies with Atto647N

α-GFP-Nb or α-lamin-Nb were diluted in PBS (pH 8.0) to a concentration of 1 mg/ml (0.08 µmol ml^{-1}). Atto647N was solubilized in DMSO (10 mM) and 0.2 molar equivalents were added to the protein solution. The mixture was incubated under constant stirring for 3 h at 37°C. Uncoupled dye was removed by size exclusion chromatography (Äkta purifier system GE Healthcare Bio-Sciences AB, Uppsala, Sweden) via a Sephadex G25 column using PBS (pH 8.0) as a mobile phase. The purified protein-dye conjugate was concentrated using Amicon Ultra centrifugal filter units (Millipore; MWCO 10 kDa). Protein concentration was determined spectrophotometrically (NanoDrop 2000 Spectrophotometer, Thermo

Scientific) using an extinction coefficient of 27.000 M^{-1} cm^{-1}. The purity of the protein- dye conjugate was confirmed on SDS-PAGE (Fig. S1).

Modification of Nanobodies with Fluorescein Isothiocyanate

α-GFP-Nb or α-lamin-Nb were diluted in PBS to a concentration of 2 mg/ml (0.16 µmol ml^{-1}). Fluorescein isothiocyanate (FITC) was solubilized in DMSO (13 mM) and 0.2 molar equivalents were added to the protein solution. The mixture was incubated under constant stirring for 4 h at 37°C. Uncoupled dye was removed by size exclusion chromatography (Äkta purifier system GE Healthcare Bio-Sciences AB, Uppsala, Sweden) via a Sephadex G25 column using PBS (pH 7.4) as a mobile phase. The purified protein-dye conjugate was concentrated using Amicon Ultra centrifugal filter units (Millipore; MWCO 10 kDa). Protein concentration was determined spectrophotometrically (NanoDrop 2000 Spectrophotometer, Thermo Scientific) using an extinction coefficient of 27.000 M^{-1} cm^{-1}.

Preparation of Nanobody/Oligomer Formulations

Nanobodies were formulated with oligomers (see Supporting Information Table SI) at a molar ratio of 1:5, which equals a weight/weight ratio of 0.32 for nanobody/***735*** or 0.33 for nanobody/***734*** formulations. Different oligomer amounts were diluted in HEPES buffer (pH 8.0) and the pH was adjusted with NaOH (1 M) to pH 8.0, to ensure efficient disulfide crosslinkage by the terminal cysteines of the different oligomers. Afterwards the dye modified nanobody was added to a final concentration of 0.5 mg ml^{-1} (0.04 µmol ml^{-1}). The mixture was incubated for 4 h with shaking at 37°C and used for further experiments.

Zeta Potential Measurements

Zeta potentials of nanobody/oligomer formulations were measured by dynamic laser-light scattering using a Zetasizer Nano ZS (Malvern Instruments, Worcestershire, UK). 30 µg of oligomer formulated nanobody were measured in HEPES buffer (pH 7.4), at a final volume of 800 µl.

Fluorescence Correlation Spectroscopy (FCS)

To permit measurements at the same nanobody/oligomer concentrations which were used for cell experiments, non-modified nanobody was spiked with 1% A647N-labeled nanobody. Afterwards nanobody/oligomer formulations were prepared as described above and diluted 1:1 to the same concentration as subsequently was put on cultured cells. Nanobody or nanobody/oligomer formulations (at a molar ratio of 1:5) were measured at a final nanobody concentration of 0.25 mg ml^{-1} (0.02 µmol ml^{-1}) in HEPES buffer.

The measurements were conducted on a ConfoCor2 setup (Zeiss Germany) using a 40× NA1.2 water immersion objective (Zeiss Germany) that focuses the exciting laser light (633 nm) into the sample. Fluorescence fluctuations of labeled molecules diffusing through the focal spot were recorded by an avalanche photodiode and correlated with the correlation function $G(\tau) = (\, F(t)F(t+\tau)\,) / \, F^2) - 1$. To derive the hydrodynamic radius of nanobody/oligomer formulations, correlation curves were fitted using a two component fit were the first component was fixed to the diffusion time of freely diffusing nanobodies. For further explanation of FCS see Supporting information.

Inhibition of Disulfide Formation via NEM Blocking

The oligomer solution was diluted in HEPES to a final concentration of 2 mg/ml, adjusted to a pH of 7.0 with NaOH (1 M) and reacted with a tenfold molar excess of N-ethylmaleimid (NEM), calculated on the amount of cysteines, for 2 h. Subsequently free NEM was reacted with a 20-fold molar excess of N-Acetylcysteine for 2 h. The oligomer solutions were purified by size exclusion chromatography (Äkta purifier system GE Healthcare Bio-Sciences AB, Uppsala, Sweden) via a Sephadex G10 column using acetonitrile/H_2O (7/3) (10 mM HCl) as a mobile phase.

Flow Cytometry

Cells were seeded in 24-well plates at a density of 30.000 cells/well. In case of KB_*wt* cells, wells were coated with collagen A prior to seeding. After 24 h medium was replaced with 400 µl fresh, serum-containing medium. For folic-acid competition experiments, medium was changed to medium containing 100 µM folic acid, 30 min prior to the addition of the samples. The various samples were prepared as described above, diluted in HEPES (pH 8.0) and 100 µl of the sample were added into each well at a final nanobody concentration of 3.6 µM and incubated for 1 h at 37°C.

Cells were put on ice, washed with PBS, detached with trypsin/EDTA and diluted in cold PBS containing 10% FBS. Cells were centrifuged and resuspended in PBS (10% FBS, pH 4.0) to extinguish the outside fluorescence. The cellular fluorescence was assayed by excitation of fluorescein at 488 nm and detection of emission at 510 nm.

For long-time uptake experiments, medium was changed after 1 h incubation at 37°C and cells were incubated for 18 h in fresh serum containing folate free RPMI medium. Cells were washed with PBS, detached with trypsin/EDTA and diluted with fresh medium. After centrifugation the cells were taken up in PBS (10% FBS, pH 7.4). The cellular fluorescence

was assayed by excitation of Atto647N at 635 nm and detection of emission at 665 nm.

Cells were appropriately gated by forward/sideward scatter and pulse width for exclusion of doublets. DAPI (4′,6-diamidino-2-phenylindole) was used to discriminate between viable and dead cells. Data were recorded by Cyan™ ADP flow cytometer (Dako, Hamburg, Germany) using Summit™ acquisition software (Summit, Jamesville, NY) and evaluated by FlowJo 7.6.5 flow cytometric analysis software.

Fluorescence Microscopy

Cells were seeded in 96-well plates (Greiner bio-one) at a density of 4000 cells/well. In case of KB_*wt* cells, wells were coated with collagen A prior to seeding. After 24 h medium was replaced with 80 µl fresh, serum-containing folate free RPMI medium. Then the various Atto647N labeled samples were prepared as described above, added into each well and incubated in case of targeted oligomers for 1 h at 37°C. Medium was removed and cells were incubated for 18 h in fresh serum containing folate free RPMI medium. Mixtures containing non-targeted oligomers were incubated for 15 h on the cells followed by 4 h incubation in fresh medium. Medium was replaced with PBS and cells were imaged using PerkinElmer Operetta® High Content Imaging System (Germany). For time series experiments, medium was replaced with DMEM without phenol red. Imaging was started either 1.5 h or 19 h after transduction. Cells were imaged for 2 h every 5 min followed by imaging every 15 min for 22 h.

Determination of Efficiencies of Co-localization of Nanobody and Target Protein

To evaluate efficiencies of nanobody delivery leading to specific co-localization of nanobody and target protein, experiments were carried out as has been described above for the screening experiments. To determine efficiencies, at least 500 cells were imaged using PerkinElmer Operetta® High Content Imaging System (Germany). Cells in which specific co-localization of nanobody and target protein was visible were counted. The percentage of cells in which co-localization of nanobody and target protein occurred was calculated as follows: (number of cells with co-localization of nanobody and target protein/total number of cells) ×100%.

Confocal Laser Scanning Microscopy

Cells were seeded in 8-well Nunc chamber slights (Thermo Scientific, Germany) at a density of 12.000 cells/well. In case of KB_*wt* cells, wells were coated with collagen A prior to seeding. After 24 h medium was replaced with 240 µl fresh, serum-containing folic acid free RPMI medium. Then the various samples were prepared as described above, added into each well and incubated for 1 h at 37°C. Medium was removed and cells were incubated for 18 h in fresh serum containing folate free RPMI medium. Medium was replaced by PBS and cells were imaged using a Leica TCS SP8 confocal microscope with an 63× DIC oil immersion objective (Plan-Apochromat).

RESULTS

Nanobody Formulation Strategy

Nanobodies are derived from heavy-chain only camelid antibodies (HcAb) which comprise a single antigen binding domain the V_{HH} and are devoid of the light chain and the C_{H1} domain (Fig. 1a). When designing nanobody carriers directed towards target cells, various extra- and intracellular barriers have to be overcome. To ensure efficient nanobody delivery, our approach in the current work was to form stable nanoparticles by mixing nanobody with cationizable carrier oligomers. We have analyzed 16 different sequence-defined cationic oligoaminoamides (Table SI) (30,33–35) from a library of more than 1000 oligomers for their potential to deliver nanobodies effectively into cells. We have investigated PEGylated as well as non-PEGylated carriers exhibiting different topologies. Carrier subunits comprise the diaminoethane building blocks Stp (succinoyl tetraethylene pentamine) or Sph (succinoyl pentaethylene hexamine), and α, ε-amidated lysines as branching points. Optionally histidines as protonable buffering units or oleic acids to enhance endosomal escape, as well as cysteines which are supposed to serve for bioreversible crosslinkage of nanobody-bound oligomers, thus expected to stabilize the nanobody-oligomer network (36). Ligand-PEG was included as functional shielding and cell targeting domain and glutamic acid as non-functional subunits.

The schematic formulation strategy as it is used in the present work is shown in Fig. 1c, d. In order to visualize its cellular uptake and localization as well as its interaction with a target protein the nanobody was first labeled with a dye (I) followed by mixing and incubating with an oligomer (II) to form stable nanoparticles (Fig. 1c). Thereafter the nanobody/oligomer complexes were incubated with the cells (Fig. 1d), resulting in both receptor dependent and - independent cellular uptake (III). After successful endosomal escape (IV) the nanobody diffuses to its target protein (V) which can be visualized upon binding of the labeled nanobody (VI).

Evaluation of Nanobodies and their Molecular Targets

For first general screening experiments, GFP was selected as a target protein. Delivery and binding of a GFP-binding nanobody (α-GFP-Nb) fused to a fluorescent protein - so

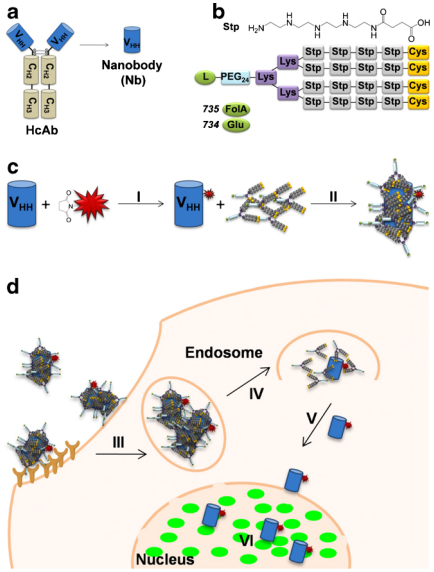

Figure 1 (**a**) Camelide heavy chain Antibody (HcAb), which compared to a normal antibody lacks the light chain and the C_{H1} domain and comprises a single antigen binding domain the V_{HH} domain. A Nanobody (Nb) is derived from HcAb and consists of one V_{HH} domain only. (**b**) Structure of the 4-arm oligomers which showed the best delivery efficiency: ***735*** containing folic acid (FolA) as targeting ligand and ***734*** comprising glutamic acid instead of a targeting ligand; Stp, succinoyl tetraethylene pentamine; Lys, Cys, amino acids L-lysine, L-cysteine. (**c**) After fluorescent labeling of the nanobody (I), the nanobody is mixed with a carrier oligomer leading to non-covalent interactions (II). (**d**) The nanobody/oligomer nanoparticles are incubated with the cells leading to either receptor specific or non-specific cellular uptake (III). After endosomal escape and freeing from the oligomer (IV) the native nanobody can diffuse within the cell (V). In this scheme, diffusion into the nucleus and binding to focal PCNA-GFP as target structures in the nucleus is depicted (VI).

called chromobodies (6) - to its target protein has recently been shown by Chiu *et al.* (16). Furthermore, there are plenty of existing cell lines, where GFP has been fused to a variety of proteins with well-characterized subcellular localization, providing "visible" antigens to directly test the delivery of α-GFP-Nb in different subcellular compartments (5,37,38). Secondly, lamin was selected as an endogenous target protein. It is localized at the nuclear membrane. Therefore, binding of the labeled lamin binding nanobody (α-lamin-Nb) results in the visualization of the typical round nuclear rim structure. Interaction of intracellular expressed lamin-chromobody with lamin had already been shown in *Drosophila melanogaster* S2 and HeLa cells (6).

α-GFP-Nbs and α-lamin-Nbs were purified as has been described previously (5,6). Both nanobodies were fluorescently labeled with NHS-Atto647N by coupling to primary amines, i.e. lysine residues and N-terminal amino acids, and purified (Fig. S1). To investigate if the binding affinity of nanobodies was not affected by dye coupling, staining of fixated cells was performed with both labeled nanobodies and four different folate receptor expressing cell lines, HeLa_PCNA-GFP, HeLa_Actin-GFP, HeLa_Tubulin-GFP, and KB_*wt* cells (Fig. S2), which were later on used for the protein delivery experiments. Using labeled α-GFP-Nb, specific staining could be shown for all three different GFP-tagged proteins (Figs. 4a and 5). Staining of KB_*wt* cells with labeled α-lamin-Nb lead to specific staining of endogenous lamin (Fig. 6a), confirming that nanobody activity was not affected by dye coupling.

Screening of Different Oligomers for Nanobody Delivery

Dye modified nanobody on its own does not diffuse into live cells, as is shown in Fig. S3. For effective delivery of α-GFP-Nb into living cells, cationizable oligomers from an existing library of cationic oligoaminoamides were screened (Table SI). All oligomers had been synthesized by solid-phase supported synthesis to gain well defined chemical structures and topologies. For the library screen, labeled α-GFP-Nb was mixed with different oligomers and incubated at 37°C for 4 h to form

non-covalent nanobody/oligomer formulations as explained above.

HeLa_PCNA-GFP cells (6,39) exhibiting a nucleoplasmic epitope were used to investigate protein delivery efficiency. Cells were incubated with two different amounts of labeled α-GFP-Nb/oligomer mixtures (final concentration of 1.5 μM and 3.6 μM nanobody). The formulations were prepared in HEPES buffer (pH 8.0) and incubated on cells in folate-free, but serum containing medium. Folate-free medium was used to ensure that folate receptors can be accessed by the folate targeted oligomers without folate competition. All nanobody/oligomer formulations were tested at molar ratios of 1:1, 1:5 and 1:10. As the molar ratios of 1:1 and 1:10 did not lead to an as efficient cellular uptake, just the results of the 1:5 ratio are presented in this work.

An overview of cellular uptake and effective delivery leading to specific binding of intracellular PCNA-GFP is given in Table SI. Transductions using 3.6 μM labeled α-GFP-Nb formulated with ***735*** at a molar ratio of 1:5 resulted in the highest efficiency in specific binding of PCNA-GFP in the nucleus (binding of nuclear PCNA-GFP in 40% of the cells, Table I). 3.6 μM of the α-GFP-Nb formulation with ***734***, the non-targeted counterpart of ***735***, also lead to intracellular binding of PCNA-GFP, but with a slightly lower efficiency of 30% (Table I). The structures of these two oligomers are depicted in Fig. 1b.

Investigation of Nanobody/Oligomer Nanoparticles Using FCS

The interaction of nanobody and the two most effective oligomers was investigated using fluorescence correlation spectroscopy (FCS). FCS is a highly sensitive single-molecule technique for measuring hydrodynamic radii of fluorescent molecules or particles in highly diluted solutions in the nanomolar

Table I Efficiencies of Co-Localization of Nanobody and Target Protein

HeLa_PCNA-GFP		HeLa_Actin-GFP		HeLa_Tubulin-GFP		KB_*wt*	
α-GFP-Nb		α-GFP-Nb		α-GFP-Nb		α-lamin-Nb	
735	**734**	**735**	**734**	**735**	**734**	**735**	**734**
50%	30%	60%	30%	50%	35%	70%	40%
40%	20%	40%	35%	60%	50%	60%	40%
35%	20%	60%	40%	70%	50%	50%	30%
Average							
40%	30%	50%	35%	60%	45%	60%	40%

Evaluation of at least 500 cells per value. Cells in which specific co-localization of nanobody and target protein was visible were counted. The percentage of cells in which co-localization of nanobody and target protein occurred was calculated as follows: (number of cells with co-localization of nanobody and target protein/total number of cells) ×100%

concentration range (40). The normalized results are shown in Fig. 2a. The GFP-binding nanobody possesses a hydrodynamic radius (R_H) of 2 nm which fits well with its published size of 2 × 4 nm (5). The formulation of α-GFP-Nb/***735*** at a molar ratio of 1:5 resulted in a homogenous solution containing two particle fractions; one with a R_H of 15 nm consisting of complexes of multiple Nbs with ***735***, and one fraction with a R_H of 2 nm presenting just slightly or not modified monomeric nanobody. In case of the α-GFP-Nb/***734*** mixtures a slightly different R_H of 20 nm for the nanoparticles (Fig. 2a) was found.

Terminal Cysteines are Important for Nanoparticle Formation

Additionally, the importance of incorporated terminal cysteines within the oligomeric structure was evaluated by comparing samples of α-GFP-Nb/***735*** or /***734*** mixtures with free cysteines to samples where the terminal cysteines were blocked by N-ethylmaleimide (NEM) (Fig. S4) using FCS. After modification of the terminal cysteines, only particles of the size of monomeric nanobodies were found. Thus no stable binding of nanobody with oligomer could be observed. To confirm these findings, microscopy was performed using NEM modified oligomers ***735*** and ***734*** (data not shown). Consistent with FCS measurements, no cellular uptake or binding to intracellular PCNA-GFP was found, leading to the assumption that cysteines are absolutely essential for nanoparticle stabilization.

To further investigate the mechanism of nanoparticle formation, the oxidation of free cysteines of oligomer ***735*** and ***734*** was followed during the 4 h incubation time (Fig. S5). A continuous oxidation could be observed resulting in a final oxidation of 90% of the thiols.

Targeting Efficiency of Oligomer *735*

To evaluate the folate receptor specific uptake of the nanobody/***735*** formulations, cellular internalization experiments on KB_*wt* cells were carried out. The α-GFP-Nb was labeled with fluorescein (α-GFP-Nb-CF). Fluorescein loses its fluorescence at acidic pH (41). Thus the selection of this dye allows quenching of the fluorescence of extracellular bound nanobody by performing the measurement in acidic buffer. Cells were incubated with 3.6 μM α-GFP-Nb-CF formulated with oligomers ***735*** or ***734*** at a molar ratio of 1:5 for 45 min and uptake efficiency was determined by flow cytometry (Fig. 3). The targeting ligand containing nanobody/***735*** nanoparticles showed enhanced cellular uptake compared to the folate-free nanobody/***734*** formulations (Fig. 3a). To verify if nanoparticles are specifically taken up via the folate receptor, folate competition experiments were carried out. Cells were pre-incubated with saturating 100 μM folic-

acid before the uptake experiments. As it is depicted in Fig. 3b, short-time uptake of α-GFP-Nb-CF/***735*** could be inhibited by the addition of folic acid. Both experiments were also carried out for CF-labeled α-lamin-Nb, resulting in comparable folate receptor specific uptake of the ***735*** nanobody formulation.

Although comparison of cellular internalization experiments using oligomers ***735*** and ***734*** after 45 min showed higher uptake efficiency using the folic acid modified oligomer ***735***, flow cytometry analysis (Fig. S6) and microscopic examination (Fig. S7) of the cells after 19 h, also resulted in a quite high uptake of non-targeted nanobody/***734*** nanoparticles.

Evaluation of the zeta potential measurements of all nanobody/oligomer formulations showed a positive zeta potential of ~ +15 mV.

Evaluation of Specific Binding of GFP Binding Nanobody to Target Proteins

Images of different cell lines after the delivery of Atto647N-labeled α-GFP-Nb using oligomer ***735*** are shown in Figs. 4b and 5. Figure 4b depicts the transduction into HeLa_PCNA-GFP cells. The first picture shows the specific punctuated pattern of concentrated PCNA-GFP at replication foci (thick arrows) as it is visible in S-phase and the diffuse pattern (white stars) indicating the G1- and G2-phase. The second picture depicts the co-localization of the specific pattern of PCNA-GFP and α-GFP-Nb at the replication foci (thick arrows), but also co-localization of α-GFP-Nb and PCNA-GFP in G1 and G2 (white stars), indicating binding of the nanobody to its GFP-tagged target protein through the whole cell cycle. Enlarged pictures can be found in Fig. 4b (bottom row).

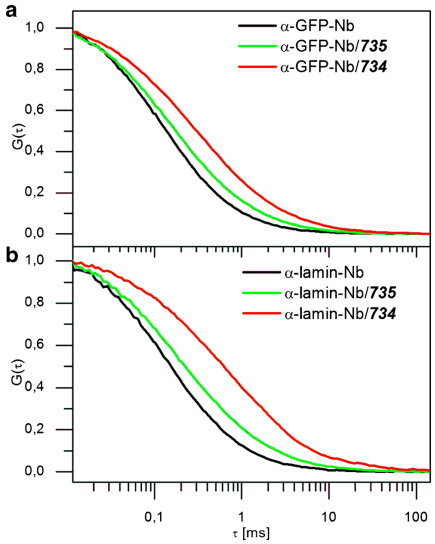

Figure 2 Non-labeled nanobodies spiked with 1% Atto647N-labeled nanobodies were mixed with ***735*** or ***734*** at a molar ratio of 1:5 and incubated for 4 h at 37°C. Normalized average correlation curves (**a**), anti-GFP nanobody (α-GFP-Nb); (**b**), anti-lamin nanobody (α-lamin-Nb)) show R_H of 2 nm for non-formulated nanobody (*black*), R_H of 15 nm – 20 nm for nanobody/***735*** nanoparticles (*green*) or nanobody/***734*** nanoparticles (*red*).

We furthermore investigated the delivery efficiency of the selected α-GFP-Nb/oligomer nanoparticles on HeLa_Actin-GFP and HeLa_Tubulin-GFP cells, exhibiting two different targets at the cytoskeleton. Transduction experiments were carried out with 3.6 µM Atto647N-labeled Nb formulated with ***735*** at a molar ratio of 1:5, as has been described above for HeLa_PCNA-GFP cells. Figure 5a displays the delivery into HeLa_Actin-GFP and Fig. 5b into HeLa_Tubulin-GFP cells. In both cell lines specific co-localization of α-GFP-Nb (second row) with GFP tagged proteins (first row) can be seen. This demonstrates the versatility of the delivery approach. Images applying oligomer ***734*** as delivery agent are depicted in Fig. S7. The efficiency of specific binding to target protein was determined by microscopic evaluation resulting in specific co-localization of nanobody and GFP-tagged proteins in 60% of HeLa_Tubulin-GFP and 50% in HeLa-Actin-GFP cells (Table I).

Apart from specific binding of the α-GFP-Nb to target proteins, Figs. 4 and 5 (second and fourth column) display small intense dots (dashed arrows). These dots are oligomer/protein nanoparticles still being entrapped in cellular vesicles, indicating the escape from these endolysosomal vesicles as the main bottleneck. Additionally metabolic activity was determined for all different cell lines used in this manuscript by a dimethylthiazolyldiphenyltetrazolium bromide (MTT) assay, showing absence of significant toxicity for the used nanobodies and the oligomer/nanobody formulation under the applied conditions (Fig. S8).

Application of the Delivery Strategy to a Lamin Binding Nanobody

Taking advantage of the fact that nanobodies exhibit low variations in terms of size, structure and surface properties, the delivery strategy outlined above should be easily transferable to various other nanobodies. To investigate this, we evaluated the delivery of a lamin binding nanobody (α-lamin-Nb) into KB_*wt* cells. First, the association of Atto647N-labeled α-lamin-Nb with either oligomer ***735*** or ***734*** in HEPES buffer (pH 8.0) after incubation for 4 h at 37°C was investigated by FCS, giving similar results as for α-GFP-Nb (Fig. 2b). The labeled α-lamin-Nb was found to have a R_H of 2 nm, α-lamin-Nb/oligomer mixtures resulted in two fractions with R_H of 2 nm for non-bound or modified monomeric α-lamin-Nb, and R_H of 20 nm for formulated α-lamin-Nb/oligomer.

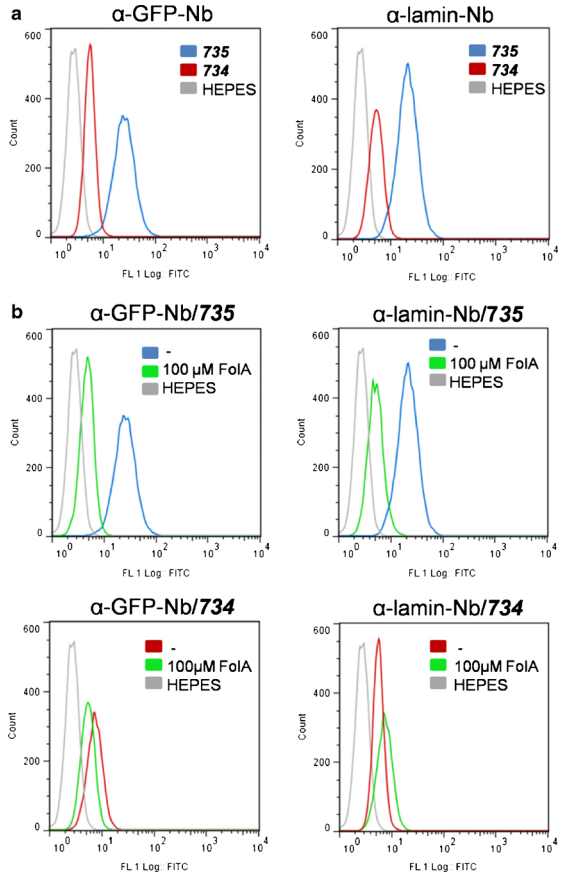

Figure 3 Cellular internalization of carboxyfluorescein (CF) modified GFP- or lamin nanobodies (α-GFP-Nb or α-lamin-Nb). CF-nanobodies were mixed with ***735*** or ***734*** at a molar ratio of 1:5 and incubated for 4 h at 37°C. (**a**) KB_*wt* cells were transduced with 3.6 µM nanobody/***735*** (*blue*) or /***734*** (*red*). After 1 h incubation at 37°C cellular internalization was determined by flow cytometry. (**b**) Free folic acid competition experiments: KB_*wt* cells were pre-incubated for 30 min with 100 µM free folic acid. Afterwards cells were transduced with 3.6 µM α-GFP- or α-lamin-Nb/***735*** (*upper histograms*) or 3.6 µM α-GFP- or α-lamin-Nb/***734*** (*lower histograms*). After 45 min incubation at 37°C, cellular internalization was determined by flow cytometry. Green, with 100 µM folic acid inhibition; blue or red, without folic acid inhibition; grey, control incubation of cells with HEPES.

Figure 6b depicts the delivery of Atto647N-labeled α-lamin-Nb/***735*** nanoparticles into KB_*wt* cells leading to co-localization of delivered nanobody with endogenous lamina lining the nucleus. The delivery of α-lamin-Nb/***734*** is shown in Fig. S9. As for the α-GFP-Nb, some nanobody was still being entrapped in intracellular vesicles showing no co-localization with nuclear lamin (dashed arrow shows exemplary vesicles).

For transduction experiments, Atto647N-labeled α-lamin-Nb/oligomer formulations were incubated for 1 h on the cells at a final concentration of 3.6 µM nanobody in serum containing folate-free RPMI medium, followed by 18 h incubation in fresh medium. Microscopic evaluation showed specific binding of Atto647N-labeled nanobody to lamin in 60% of KB_*wt* cells for the folat receptor-targeted ***735*** formulation, and 40% for the non-targeted ***734*** formulation (Table I). Cellular internalization experiments resulted in folate receptor specific uptake of CF-labeled α-lamin-Nb/***735*** after 45 min incubation (Fig. 3).

Live Cell Imaging of Intracellular Delivered Lamin Nanobody

To further evaluate the uptake and delivery process, real-time imaging of the delivery of Atto647N-labeled α-lamin-Nb/***735***

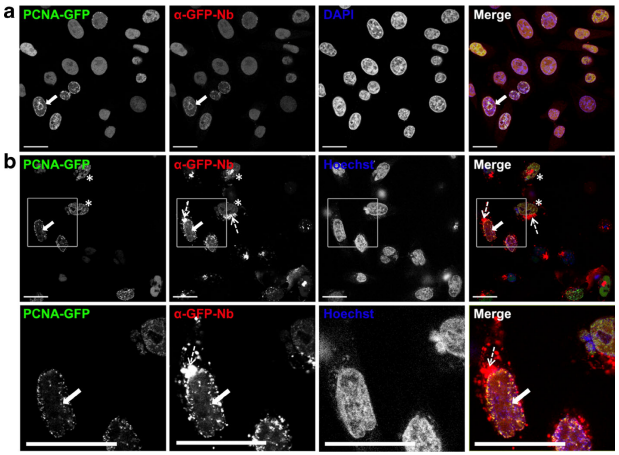

Figure 4 Confocal laser scanning microscopy of fixated (a) or live (b) HeLa_PCNA-GFP cells. First column, GFP fluorescence of GFP tagged proteins; second column, Atto647N fluorescence of α-GFP-Nb; third column, nuclear staining with DAPI or Hoechst dye; fourth column, merge of all three channels. Thick arrows indicate cells in S-phase where the typical punctuated pattern of PCNA-GFP at the replication foci is visible. Stars indicating cells in G1 and G2-phase. Dashed arrows (second and fourth column) exemplary indicating nanoparticles being trapped in cellular vesicles. Scale bar: 25 μm. (**a**) Staining of paraformaldehyde fixated HeLa_PCNA-GFP cells with 0.5 μM Atto647N-labeled α-GFP-Nb, to demonstrate that the modification of primary amines i.e. lysine residues and N-terminal amino acids of nanobodies with NHS-Atto647N does not affect specific binding to their target proteins. (**b**) Confocal laser scanning microscopy of live cells after transduction with 3.6 μM Atto647N-labeled α-GFP-Nb formulated with ***735*** at a molar ratio of 1:5. Cells were incubated for 1 h with the nanobody/oligomer mixture, followed by 18 h incubation in fresh media. The second row depicts enlarged pictures of a cell in S-phase, where co-localization of α-GFP-Nb and PCNA-GFP is visible.

nanoparticles into KB_*wt* cells was performed. For this purpose, the transduction was carried out as described above. Time series were either taken 1.5 h (Supplementary Video 1) or 19 h (Supplementary Video 2) after transduction. Selected frames of these time series are shown in Fig. 7. Figure 7a depicts images following the escape of cellular vesicles right after cellular uptake of α-lamin-Nb/***735*** nanoparticles (Supplementary Video 1). For this time series pictures were taken every 5 min for 2 h. For cell 1 and 2, the first picture (0 min) shows nanoparticles suggested to be entrapped in cellular vesicles. In the second picture (70 min) the even distribution of α-lamin-Nb through the cell can be seen. Additionally concentrated dots are visible resulting from nanobody suggested to be entrapped in cellular vesicles (dashed arrows show exemplary vesicles). After 120 min highlighting of the nuclear rim structure that is characteristic of the nuclear lamina is visible (red circle), caused by specific binding of the labeled α-lamin-Nb to nuclear lamin. Concentrated dots (dashed arrows show exemplary vesicles) are a result of nanoparticles suggested to be entrapped in cellular vesicles. In cell 3 no release from cellular vesicles is visible.

Selected frames from Supplementary Video 2 are shown in Fig. 7b. Pictures were taken every 5 min for 2 h and afterwards every 15 min for additional 22 h. From the beginning of the imaging (0 min), specific co-localization of α-lamin-Nb and endogenous lamin lining the nucleus could be observed (thick arrow). At that time this cell was probably in G2-phase. Concentrated dots (dashed arrows show exemplary vesicles) are again resulting from nanoparticles being entrapped in cellular vesicles. From 275 to 350 min the cell could be followed through cell division. Specific binding of α-lamin-Nb to the nuclear lamina could still be found at 515 min and 815 min in the two freshly divided cells. In sum, functional nanobodies were delivered into live cells leading after escape from cellular vesicles to specific binding of an endogenous target, and the target was visualized throughout the cell cycle.

DISCUSSION

The intracellular delivery of nanobodies is of high research interest in the field of live cell imaging as well as for therapeutic approaches, but so far there is no effective delivery system available. In this work, a library of sequence defined oligoaminoamides was evaluated for their ability to efficiently transduce a GFP binding nanobody in different folic acid receptor expressing recombinant HeLa

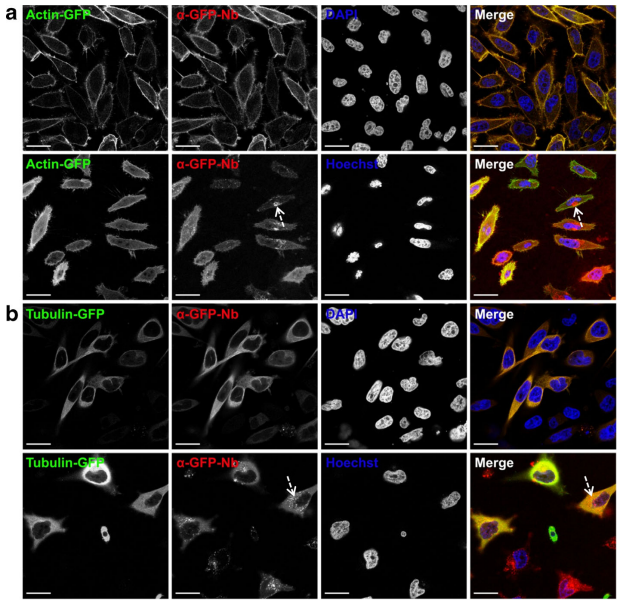

Figure 5 Confocal laser scanning microscopy of fixated (first and third row) or live (second and fourth row) HeLa_Actin-GFP (**a**) or HeLa_Tubulin-GFP (**b**) cells. First column, GFP fluorescence of GFP tagged proteins; second column, Atto647N fluorescence of α-GFP-Nb; third column, nuclear staining with DAPI or Hoechst dye; fourth column, merge of all three channels. Dashed arrows (second and fourth column) exemplary indicating nanoparticles being trapped in cellular vesicles. Paraformaldehyde fixated cells were stained with 0.5 μM Atto647N-labeled α-GFP-Nb, to demonstrate that the modification of primary amines i.e. lysine residues and N-terminal amino acids of nanobodies with NHS-Atto647N does not affect specific binding to their target proteins. Second and fourth row show images of live cells after transduction with 3.6 μM Atto647N-labeled α-GFP-Nb formulated with ***735*** at a molar ratio of 1:5. Cells were incubated for 1 h with the nanobody/oligomer mixture, followed by 18 h incubation in fresh media. Scale bar: 25 μm.

cell lines. Previous protein delivery experiments from our lab were based on the bioreversible covalent modification of proteins with oligomers (26–28). The current work aimed at non-covalent formulation, where nanoparticles are formed through mixing nanobody and oligomers. An initial oligomer library screen identified two oligomers (***735*** and ***734***) which upon incubation with a GFP binding nanobody lead to stable nanoparticle formation, resulting in efficient intracellular delivery and specific co-localization of labeled nanobody with GFP-tagged target proteins. These two oligomers differ only by the presence (***735***) or absence (***734***) of folate as possible targeting ligand. They were initially described by He *et al.* (30) for testing receptor-mediated delivery of pDNA and siRNA, contain a PEG molecule for nanoparticle shielding and prevention of unspecific aggregations, optionally linked with folic acid as receptor-targeting ligand, attached to a four-arm core oligoaminoamide structure comprising a repeating sequence pattern of four cationizable Stp units (assumed to facilitate endosomal escape) and one terminal cysteine per arm (for disulfide formation between neighboring oligomers). According to our initial screening experiments, comparing these two oligomers ***735*** or ***734*** with the others, the relatively larger size and topology seems to be critical for effective nanobody/oligomer nanoparticle formation. In this setup especially the inclusion of cysteines within the oligomeric structure was proven as absolutely necessary for the generation of stable nanoparticles by disulfide crosslinkage upon cysteine oxidation during the 4 h incubation after nanobody/oligomer mixing. Blocking of the terminal cysteine mercapto groups by maleimide prevented stable particle formation. Oligomer disulfide formation before nanobody complexation was also unsuccessful (data not shown). This is consistent with previous work which demonstrated favorable effects of disulfide crosslinkage on siRNA polyplex formation (32,36,42,43). As the R_H of the nanobodies used in this study is comparable to the R_H of siRNA of

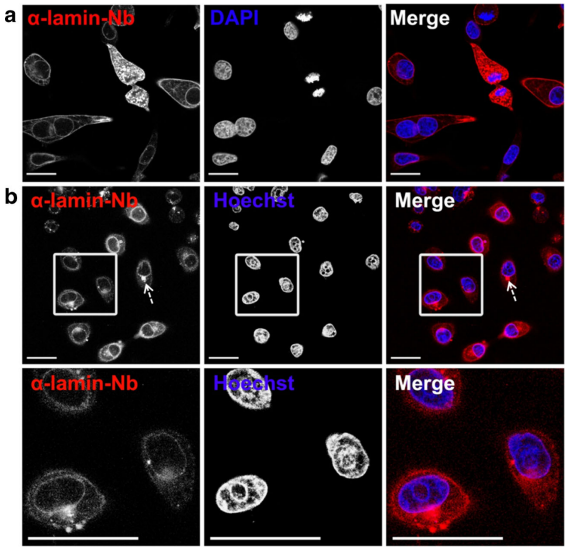

Figure 6 Confocal laser scanning microscopy of fixated (**a**) or live (**b**) KB_*wt* cells. First column, Atto647N fluorescence of α-lamin-Nb; second column, nuclear staining with DAPI or Hoechst dye; third column, merge of both channels. Dashed arrows (first and third column) exemplary indicating nanoparticles being trapped in cellular vesicles. Scale bar: 25 μm. (**a**) Staining of paraformaldehyde fixated KB_*wt* cells with 0.5 μM Atto647N-labeled α-lamin-Nb, to demonstrate that the modification of primary amines i.e. lysine residues and N-terminal amino acids of nanobodies with NHS-Atto647N does not affect specific binding to their target proteins. (**b**) Confocal laser scanning microscopy of live cells after transduction with 3.6 μM Atto647N-labeled α-lamin-Nb formulated with ***735*** at a molar ratio of 1:5. Cells were incubated for 1 h with the nanobody/oligomer mixture, followed by 18 h incubation in fresh media.

2.2 nm (44,45) but with a far lower negative charge density the requirement of cysteines for stable nanoparticle formation fits well with the aforesaid findings. Altogether the findings suggest that the oligomers are first non-covalently bound to the surface of nanobodies where disulfide formation between oligomers triggers the formation of stable nanoparticles.

Oligomer ***735*** contains folic acid as targeting ligand. We could show that upon short-time incubation nanoparticles containing oligomer ***735*** exhibit higher cellular uptake compared to particles formed with the non-targeted oligomer ***734***. Cellular internalization was shown to be blocked upon pre-incubation of the cells with free folic acid, suggesting receptor-dependent cellular uptake. Nanoparticles containing oligomer ***734*** however also lead to quite high uptake efficiency when cellular uptake was investigated after 24 h. There are two possible explanations for this; one is the positive charge of the protein/oligomer complexes. In contrast to almost neutral polyplexes formed with highly negatively charged nucleic acids, nanobodies do not effectively neutralize the cationic charges of the oligomer, exhibiting a zeta potential of ~ +15 mV for all nanobody/oligomer formulations. Therefore positively charged nanobody/oligomer nanoparticles may interact with cells either via the folate receptor or directly with negative charged cell membranes, leading to receptor independent cellular uptake. Moreover, FCS data indicate formation of slightly more nanobody nanoparticles for ***734*** than for ***735***, leading to more nanobody cargo being available for non-specific cellular uptake.

The escape from endolysosomal cellular vesicles is suggested to be the major bottleneck for cytosolic delivery of macromolecules. Therefore it is not surprising to observe a significant fraction of internalized labeled nanobody remaining localized in intracellular vesicles. The four arm oligomer ***735*** contains a significant number of sixteen cationizable Stp (31) units (sixty-four aminoethylene units) per oligomer which by endosomal acidification should be sufficient to trigger endosomal escape analogously to the 'proton sponge effect' as observed for polyethylenimine (46,47). It has to be noted that according to the oligomer screen by *He et al.* (30) as well as related work on pDNA delivery (34,48), ***735*** and analogous oligomers did not possess optimized proton sponge activity and require the presence of the endolysomotropic agent chloroquine for effective endosomal escape. In this respect the successful protein delivery at slightly higher doses of incorporated ***735*** carrier is encouraging, but the persistent endosomal bottleneck for this oligomer also suggests an important direction for further optimization of oligomers.

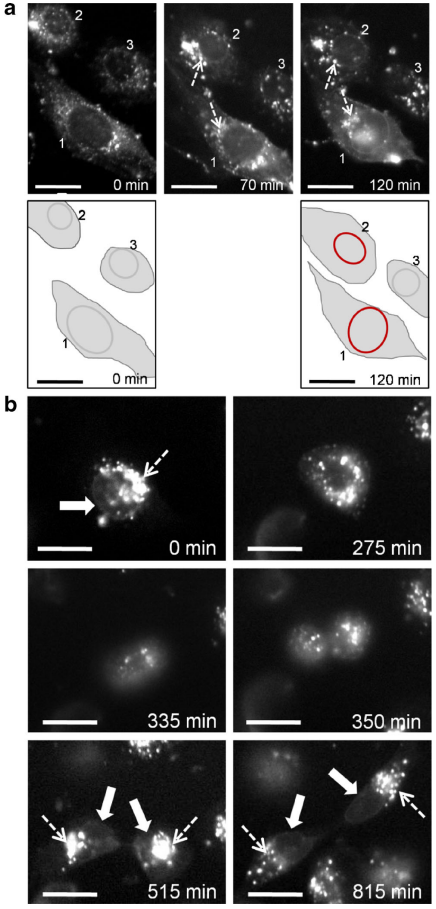

◀ **Figure 7** KB_*wt* cells were incubated with 3.6 μM Atto647N-labeled α-lamin-Nb, formulated with ***735*** at a molar ratio of 1:5 for 1 h, followed by incubation in fresh media. Time series were taken by wide field fluorescence microscopy. Selected frames from these time series are shown. Scale bar: 25 μm. (**a**) Time series was started 1.5 h after transduction of the cells. Cell 1 and 2, 0 min, nanobody is trapped in cellular vesicles; 70 min, even distribution of nanobody throughout the cell, some nanobody is still being trapped in cellular vesicles (*dashed arrows*); 120 min, Specific co-localization of labeled nanobody with the lamina lining the nucleus can be seen. Concentrated dots (*dashed arrows*) are resulting from nanoparticles still being trapped in cellular vesicles. Cell 3, nanoparticles are trapped in cellular vesicles for the length of the time series. Schemes depicting cells without specific binding of α-lamin-Nb (0 min) and after specific binding of nanobody to nuclear lamin (120 min) indicated by red coloring of the nuclear membrane in cell 1 and 2. (**b**) Imaging was started 19 h after transduction of the cells. At that time this cell was probably in G2-phase (0 min). Specific binding of α-lamin-Nb to the lamina lining the nucleus (*thick arrows*) can be seen. Concentrated dots (*dashed arrows*) are resulting from nanoparticles being trapped in cellular vesicles. The cell could be followed through mitosis (275–350 min). Scale bar: 25 μm.

To broaden our delivery technology towards a universal nanobody transduction system, we also applied it for a lamin binding nanobody. After successful delivery of α-lamin-Nb, we were able to visualize nuclear lamin, an endogenous target, and to follow it through the whole cell cycle in living cells. As nanobodies have a quite conserved structure and differ mostly in their complementarity determining regions, their properties in terms of oligomer binding ought to be quite similar. Thus this system should be transferable to many kinds of nanobodies- being able to target a huge variety of intracellular molecular targets.

CONCLUSION

In this work we presented an easy and efficient transduction system to deliver nanobodies into live cells. Mixing of nanobodies with optimal candidates of sequence-defined oligoaminoamides and incubation for air-oxidation of cysteines lead to nanoparticles with a small size around 20 nm. This represents an advancement over covalent modification of a protein with a carrier, as it has been done in previous work from our lab (25–28). Two oligomers, with and without folic acid as receptor targeting ligand, were identified as potent carriers leading to intracellular delivery, as evidenced by interaction of nanobodies with their target proteins. The two oligomers additionally comprise sixteen Stp units to interact with the nanobody and enhance endosomal escape, cysteines to enhance oligomer crosslinking leading to the formation of stable nanoparticles and PEG as hydrophilic shielding agent. Tracing PCNA-GFP as well as Tubulin-GFP and Actin-GFP through the cell cycle, we showed that the transduction of a GFP binding nanobody works in different reporter cell lines. Furthermore, this approach was extended to a lamin binding nanobody, broadening the scope to direct imaging of an endogenous target. This demonstrates that due to the conserved structure and size of nanobodies, the evaluated sequence-defined oligomers can be used to deliver nanobodies with diverse intracellular targets. Thus, the technology may enable facile labeling and visualization of various epitopes in live cells over an extended period of time and also may pave the way for their possible use as therapeutic agents.

ACKNOWLEDGMENTS AND DISCLOSURES

We thank Dr. Dongsheng He, Dr. Edith Salcher, Dr. Claudia Scholz and Philipp Klein for the synthesis of the different oligomers. We also thank Dr. Katharina von Gersdorff for

the generation of the HeLa_Actin-GFP and HeLa_Tubulin-GFP cell lines. The German Research Foundation is gratefully acknowledged for financial support of related research by the authors within the Cluster of Excellence Nanosystems Initiative Munich (NIM). Prof. Dr. Heinrich Leonhardt also acknowledges the support by additional grants from the German Research Foundation (SPP1623; LE 721/13-1).

REFERENCES

1. Muyldermans S, Atarhouch T, Saldanha J, Barbosa JA, Hamers R. Sequence and structure of VH domain from naturally occurring camel heavy chain immunoglobulins lacking light chains. Protein Eng. 1994;7(9):1129–35.
2. Broisat A, Hernot S, Toczek J, De Vos J, Riou LM, Martin S, *et al.* Nanobodies targeting mouse/human VCAM1 for the nuclear imaging of atherosclerotic lesions. Circ Res. 2012;110(7):927–37.
3. Bleck M, Itano MS, Johnson DS, Thomas VK, North AJ, Bieniasz PD, *et al.* Temporal and spatial organization of ESCRT protein recruitment during HIV-1 budding. Proc Natl Acad Sci U S A. 2014;111(33):12211–6.
4. Rajan M, Mortusewicz O, Rothbauer U, Hastert FD, Schmidthals K, Rapp A, *et al.* Generation of an alpaca-derived nanobody recognizing gamma-H2AX. FEBS Open Bio. 2015;5:779–88.
5. Kirchhofer A, Helma J, Schmidthals K, Frauer C, Cui S, Karcher A, *et al.* Modulation of protein properties in living cells using nanobodies. Nat Struct Mol Biol. 2010;17(1):133–8.
6. Rothbauer U, Zolghadr K, Tillib S, Nowak D, Schermelleh L, Gahl A, *et al.* Targeting and tracing antigens in live cells with fluorescent nanobodies. Nat Methods. 2006;3(11):887–9.
7. Helma J, Cardoso MC, Muyldermans S, Leonhardt H. Nanobodies and recombinant binders in cell biology. J Cell Biol. 2015;209(5):633–44.
8. Dmitriev OY, Lutsenko S, Muyldermans S. Nanobodies as probes for protein dynamics *in vitro* and in cells. J Biol Chem. 2016;291(8):3767–75.
9. Arbabi-Ghahroudi M, Tanha J, MacKenzie R. Prokaryotic expression of antibodies. Cancer Metastasis Rev. 2005;24(4):501–19.
10. Lauwereys M, Arbabi Ghahroudi M, Desmyter A, Kinne J, Holzer W, De Genst E, *et al.* Potent enzyme inhibitors derived from dromedary heavy-chain antibodies. EMBO J. 1998;17(13):3512–20.
11. Lisy MR, Goermar A, Thomas C, Pauli J, Resch-Genger U, Kaiser WA, *et al. In vivo* near-infrared fluorescence imaging of carcinoembryonic antigen-expressing tumor cells in mice. Radiology. 2008;247(3):779–87.
12. Sawant R, Torchilin V. Intracellular transduction using cell-penetrating peptides. Mol BioSyst. 2010;6(4):628–40.
13. Kaczmarczyk SJ, Sitaraman K, Young HA, Hughes SH, Chatterjee DK. Protein delivery using engineered virus-like particles. Proc Natl Acad Sci U S A. 2011;108(41):16998–7003.
14. Mendez J, Morales Cruz M, Delgado Y, Figueroa CM, Orellano EA, Morales M, *et al.* Delivery of chemically glycosylated cytochrome c immobilized in mesoporous silica nanoparticles induces apoptosis in HeLa cancer cells. Mol Pharm. 2014;11(1):102–11.
15. Schlossbauer A, Sauer AM, Cauda V, Schmidt A, Engelke H, Rothbauer U, *et al.* Cascaded photoinduced drug delivery to cells from multifunctional core-shell mesoporous silica. Adv Healthc Mater. 2012;1(3):316–20.
16. Chiu HY, Deng W, Engelke H, Helma J, Leonhardt H, Bein T. Intracellular chromobody delivery by mesoporous silica nanoparticles for antigen targeting and visualization in real time. Sci Rep. 2016;6:25019.
17. Ray M, Tang R, Jiang Z, Rotello VM. Quantitative tracking of protein trafficking to the nucleus using cytosolic protein delivery by nanoparticle-stabilized nanocapsules. Bioconjug Chem. 2015;26(6):1004–7.
18. Lee Y, Ishii T, Kim HJ, Nishiyama N, Hayakawa Y, Itaka K, *et al.* Efficient delivery of bioactive antibodies into the cytoplasm of living cells by charge-conversional polyion complex micelles. Angew Chem Int Ed Engl. 2010;49(14):2552–5.
19. Lee Y, Ishii T, Cabral H, Kim HJ, Seo JH, Nishiyama N, *et al.* Charge-conversional polyionic complex micelles-efficient nanocarriers for protein delivery into cytoplasm. Angew Chem Int Ed Engl. 2009;48(29):5309–12.
20. Kim A, Miura Y, Ishii T, Mutaf OF, Nishiyama N, Cabral H, *et al.* Intracellular delivery of charge-converted monoclonal antibodies by combinatorial design of block/homo polyion complex micelles. Biomacromolecules. 2016;17(2):446–53.
21. Sarker SR, Hokama R, Takeoka S. Intracellular delivery of universal proteins using a lysine headgroup containing cationic liposomes: deciphering the uptake mechanism. Mol Pharm. 2014;11(1):164–74.
22. Saalik P, Elmquist A, Hansen M, Padari K, Saar K, Viht K, *et al.* Protein cargo delivery properties of cell-penetrating peptides. A comparative study. Bioconjug Chem. 2004;15(6):1246–53.
23. Nischan N, Herce HD, Natale F, Bohlke N, Budisa N, Cardoso MC, *et al.* Covalent attachment of cyclic TAT peptides to GFP results in protein delivery into live cells with immediate bioavailability. Angew Chem Int Ed Engl. 2015;54(6):1950–3.
24. Erazo-Oliveras A, Najjar K, Dayani L, Wang TY, Johnson GA, Pellois JP. Protein delivery into live cells by incubation with an endosomolytic agent. Nat Methods. 2014;11(8):861–7.
25. Liu X, Zhang P, He D, Rodl W, Preiss T, Radler JO, *et al.* pH-reversible cationic RNase a conjugates for enhanced cellular delivery and tumor cell killing. Biomacromolecules. 2016;17(1):173–82.
26. Maier K, Wagner E. Acid-labile traceless click linker for protein transduction. J Am Chem Soc. 2012;134(24):10169–73.
27. Maier K, Martin I, Wagner E. Sequence defined disulfide-linked shuttle for strongly enhanced intracellular protein delivery. Mol Pharm. 2012;9(12):3560–8.
28. Zhang P, He D, Klein PM, Liu X, Röder R, Döblinger M, *et al.* Enhanced intracellular protein transduction by sequence defined tetra-oleoyl oligoaminoamides targeted for cancer therapy. Adv Funct Mater. 2015;25(42):6627–36.
29. Vincke C, Muyldermans S. Introduction to heavy chain antibodies and derived Nanobodies. Methods Mol Biol. 2012;911:15–26.
30. He D, Muller K, Krhac Levacic A, Kos P, Lachelt U, Wagner E. Combinatorial optimization of sequence-defined oligo(ethanamino)amides for folate receptor-targeted pDNA and siRNA delivery. Bioconjug Chem. 2016;27(3):647–59.
31. Schaffert D, Badgujar N, Wagner E. Novel Fmoc-polyamino acids for solid-phase synthesis of defined polyamidoamines. Org Lett. 2011;13(7):1586–9.
32. Schaffert D, Troiber C, Salcher EE, Frohlich T, Martin I, Badgujar N, *et al.* Solid-phase synthesis of sequence-defined T-, i-, and U-shape polymers for pDNA and siRNA delivery. Angew Chem Int Ed Engl. 2011;50(38):8986–9.
33. Scholz C, Kos P, Wagner E. Comb-like oligoaminoethane carriers: change in topology improves pDNA delivery. Bioconjug Chem. 2014;25(2):251–61.
34. Lachelt U, Kos P, Mickler FM, Herrmann A, Salcher EE, Rodl W, *et al.* Fine-tuning of proton sponges by precise diaminoethanes and histidines in pDNA polyplexes. Nanomedicine. 2014;10(1):35–44.
35. Salcher EE, Kos P, Frohlich T, Badgujar N, Scheible M, Wagner E. Sequence-defined four-arm oligo(ethanamino)amides for pDNA and siRNA delivery: Impact of building blocks on efficacy. J Control Release. 2012;164(3):380–6.

36. Frohlich T, Edinger D, Klager R, Troiber C, Salcher E, Badgujar N, *et al.* Structure-activity relationships of siRNA carriers based on sequence-defined oligo (ethane amino) amides. J Control Release. 2012;160(3):532–41.
37. Rothbauer U, Zolghadr K, Muyldermans S, Schepers A, Cardoso MC, Leonhardt H. A versatile nanotrap for biochemical and functional studies with fluorescent fusion proteins. Mol Cell Proteomics. 2008;7(2):282–9.
38. Ekstrand MI, Nectow AR, Knight ZA, Latcha KN, Pomeranz LE, Friedman JM. Molecular profiling of neurons based on connectivity. Cell. 2014;157(5):1230–42.
39. Leonhardt H, Rahn HP, Weinzierl P, Sporbert A, Cremer T, Zink D, *et al.* Dynamics of DNA replication factories in living cells. J Cell Biol. 2000;149(2):271–80.
40. Magde D, Elson E, Webb WW. Thermodynamic fluctuations in a reacting system—measurement by fluorescence correlation spectroscopy. Phys Rev Lett. 1972;29(11):705.
41. Zhu H, Derksen RC, Krause CR, Fox RD, Brazee RD, Ozkan HE. Fluorescent intensity of dye solutions under different pH conditions. J ASTM Int. 2005;2(6):1–7.
42. Frohlich T, Edinger D, Russ V, Wagner E. Stabilization of polyplexes via polymer crosslinking for efficient siRNA delivery. Eur J Pharm Sci. 2012;47(5):914–20.
43. Taratula O, Garbuzenko OB, Kirkpatrick P, Pandya I, Savla R, Pozharov VP, *et al.* Surface-engineered targeted PPI dendrimer for efficient intracellular and intratumoral siRNA delivery. J Control Release. 2009;140(3):284–93.
44. Dohmen C, Edinger D, Frohlich T, Schreiner L, Lachelt U, Troiber C, *et al.* Nanosized multifunctional polyplexes for receptor-mediated siRNA delivery. ACS Nano. 2012;6(6):5198–208.
45. Troiber C, Kasper JC, Milani S, Scheible M, Martin I, Schaubhut F, *et al.* Comparison of four different particle sizing methods for siRNA polyplex characterization. Eur J Pharm Biopharm. 2013;84(2):255–64.
46. Behr JP. The proton sponge: a trick to enter cells the viruses did not exploit. Chimia. 1997;51(1–2):34–6.
47. Lachelt U, Wagner E. Nucleic acid therapeutics using polyplexes: a journey of 50 years (and beyond). Chem Rev. 2015;115(19):11043–78.
48. Martin I, Dohmen C, Mas-Moruno C, Troiber C, Kos P, Schaffert D, *et al.* Solid-phase-assisted synthesis of targeting peptide-PEG-oligo(ethane amino)amides for receptor-mediated gene delivery. Org Biomol Chem. 2012;10(16):3258–68.

Supporting Information

Intracellular Delivery of Nanobodies for Imaging of Target Proteins in Live Cells

Ruth Röder[1], Jonas Helma[2], Tobias Preiß[3], Joachim Rädler[3], Heinrich Leonhardt[2], Ernst Wagner[1]

[1] Pharmaceutical Biotechnology, Center for System-Based Drug Research, and Center for Nanoscience (CeNS), Ludwig-Maximilians-Universität München, Germany

[2] Department of Biology II, Center for Integrated Protein Science Munich, Ludwig-Maximilians-Universität München, Germany

[3] Faculty of Physics, and Center for NanoScience (CeNS), Ludwig-Maximilians-Universität München, Germany

Supplementary Material and Methods

Material

Atto-647N (NHS-Ester) was purchased from Atto-Tec GmbH (Siegen, Germany), HEPES from Biomol (Hamburg, Germany), collagen A from Merck KGaA (Grafing Germany) and Blue Prestained Protein Standard, Broad Range from NEB (Frankfurt am Main). All other chemicals were purchased from Sigma-Aldrich (Germany). Antibiotics, fetal bovine serum (FBS) and cell culture medium were bought from Life Technologies (Carlsbad, USA).

PBS adjusted to pH 7.4, was prepared in house.

Purification of the GFP binding protein (α-GFP-Nb) and the lamin binding protein (α-lamin-Nb) was carried out as has been described previously (1, 2).

Cell Fixation and Staining

Cells were seeded in 8-well Nunc chamber slights (Thermo Scientific, Germany) at a density of 12.000 cells/well. In case of KB_*wt* cells, wells were coated with collagen A prior to seeding. After 24 h incubation at 37 °C and 5% CO_2 in a humified incubator, medium was removed and cells were washed with PBS (pH 7.4). 4% (w/v) cold paraformaldehyde solution was added and cells were incubated for 10 min at room temperature with shaking. Cells were washed three times with PBS containing 0.1% Tween 20 (PBST). Afterwards cells were permeabilized for 5 min by adding PBS containing 0.5% Triton X-100. Cells were washed twice with PBST and incubated for 10 min in blocking solution (PBST containing 4% (w/v) bovine serum albumin). Atto647N labeled α-GFP-Nb or α-lamin-Nb were diluted in blocking solution (7 µg ml^{-1}) and incubated on the cells for 45 min at room temperature. Cells were washed three times for five minutes with PBST and stored at 4 °C.

Screening of Different Oligomers for Nanobody Delivery

Nanobody was always formulated with oligomer at a molar ratio of 1:5. Different oligomer amounts were diluted in HEPES buffer (pH 8.0) and the pH was adjusted with NaOH (1 M) to pH 8.0. Afterwards the dye modified nanobody was added to a final concentration of 0.5 mg ml^{-1} (0.04 µmol ml^{-1}). The mixture was incubated for 4 h with shaking at 37 °C. For the screening experiment, cells were seeded in 96-well plates (Greiner bio-one) at a density of 4.000 cells/well. In case of KB_*wt* cells, wells were coated with collagen A prior to seeding. After 24 h medium was replaced with 80 µl fresh, serum-containing folate free RPMI medium. The various samples were added into each well at a final concentration of nanobody of 1.5 µM or 3.6 µM and incubated in case of targeted oligomers for 1 h at 37°C. Medium

was removed and cells were incubated for 18 h in fresh serum containing folate free RPMI medium. Mixtures containing non-targeted oligomers were incubated for 15 h on the cells followed by 4 h incubation in fresh medium. Medium was replaced with PBS and cells were imaged using PerkinElmer Operetta® High Content Imaging System (Germany).

Cell Viability Assay (MTT)

Cells were seeded in 96-well plates at a density of 6.000 cells/well. In case of KB_*wt* cells, wells were coated with collagen A prior to seeding. Samples were prepared as described above. After 24 h medium was replaced with 80 µl of fresh medium containing 10% FBS. Samples were diluted 1:1 with HEPES (pH 8.0) (0.02 µmol ml^{-1}), 20µl of each sample were added to each well (final protein concentration 3.6 µM) and incubated on the cells for 1 h at 37 °C and 5% CO_2. Afterwards medium was replaced with fresh serum containing folate free RPMI medium and cells were incubated for 18 h. 10 µl of MTT (3-(4,5-dimethylthia-zol-2-yl)-2,5-diphenyltetrazolium bromide) (5 mg/ml) were added to each well reaching a final concentration of 0.5 mg/ml. After an incubation time of 2 h, unreacted dye and medium were removed and the 96-well plates were frozen at −80 °C for at least 30 min. The purple formazan product was then dissolved in 100 µl DMSO per well and quantified measuring absorbance using a microplate reader (TecanSpectrafluor Plus, Tecan, Switzerland) at 590 nm with background correction at 630 nm. All studies were performed in quintuplicates. The relative cell viability (%) related to control wells treated only with 20 µl HEPES (pH 8.0) was calculated as ([A] test/[A] control) × 100%.

Fluorescence Correlation Spectroscopy (FCS)

FCS is a fluorescence technique that is able to determine concentrations and diffusion coefficients of fluorescently labeled molecules or particles in nanomolar concentrated solutions. Magde *et al.* (3) described its principles in 1972 and Rigler *et al.* (4) improved its signal to noise by including a confocal design. The fluctuating fluorescence signal F(t) of fluorophores diffusing though the 3D Gaussian detection volume is used to calculate the autocorrelation function $G(\tau) = \frac{\langle F(t)F(t+\tau)\rangle}{\langle F\rangle^2}$. In case of one species that is diffusing in the sample (e.g. unmodified nanobody molecules), it is possible to derive the hydrodynamic radius and the particle concentration from the correlation curve by a physical model that is represented by $G(\tau) = G(0)\frac{1}{1+\frac{\tau}{\tau_D}}\frac{1}{\sqrt{1+\frac{\tau}{S^2\tau_D}}}$, where $G(0)$ is the correlations' amplitude and is the reciprocal of the mean number of fluorescent particles in the detection volume. S is the ratio

between the lateral and the axial confocal volume radius, while τ_D is the diffusion time, the mean time a particle needs to diffuse across the focal volume (5). By calibration measurement with a sample of known diffusion coefficient, the width ω of the confocal volume could be determined. With that, the Boltzmann constant k_B, temperature $T = 295$ K and viscosity $\eta = 0.96$ mPas of the measured aqueous suspension, the hydrodynamic radius is given by $R_H = \frac{2k_BT\tau_D}{3\pi\eta\,\omega^2}$ (5).

In case of two diffusing species (e.g. nanobody complexes and unmodified nanobodies) the correlation function is a superposition of two single component models: $G(\tau) = G(0)\left(\frac{Y}{1+\frac{\tau}{\tau_{D1}}}\frac{1}{\sqrt{1+\frac{\tau}{S^2\tau_{D1}}}} + \frac{1-Y}{1+\frac{\tau}{\tau_{D2}}}\frac{1}{\sqrt{1+\frac{\tau}{S^2\tau_{D2}}}}\right)$ with the diffusion times of both components τ_{D1} and τ_{D2} and their relative contribution to the correlations amplitude Y and $(1-Y)$. Normalization of the correlation curves helps to visualize the shift in diffusion times.

Ellman's Assay

As a stock solution, 0.4 mg Ellman's reagent, 5,5'- dithiobis(2-nitrobenzoicacid), DTNB, was dissolve in 1 ml of Ellman's buffer (0.2 M Na_2HPO_4 with 1 mM EDTA, pH 8.0). Standard cysteine solution and samples were serially diluted in Ellman's buffer and 10% (v/v) of the stock solution and incubated for 15 min at 37 °C. The solutions were measured at 412 nm with Ellman's stock solution diluted 1:10 in Ellman's buffer, as a blank. Concentration of the free thiol group was calculated via the calibration curve.

Determination of Folate Receptor Levels by Flow Cytometry

Different cell lines were washed with PBS, detached with trypsin/EDTA and diluted with fresh medium. Cells were centrifuged and resuspended in 100 µl PBS (10 % FBS). Allophycocyanin (APC)-conjugated anti folic acid receptor 1 IgG1 antibody (10 µl; R&D Systems, USA) or IgG1 (Dako) (1:100 dilution) as isotype control were added. Cells were incubated for 1 h on ice, washed twice with PBS (10% FBS) and resuspended in 500 µl PBS (10% FBS). The amount of folic acid positive cells was analyzed through excitation of APC at 635 nm and detection of emission at 665 nm. Cells were appropriately gated by forward/ sideward scatter and pulse width for exclusion of doublets. DAPI (4′,6-diamidino-2-phenylindole) was used to discriminate between viable and dead cells. Data were recorded by Cyan™ ADP flow cytometer (Dako, Hamburg, Germany) using Summit™ acquisition

software (Summit, Jamesville, NY). Analysis was done by FlowJo 7.6.5 flow cytometric analysis software.

Confocal Laser Scanning Microscopy

Cells were seeded in 8-well Nunc chamber slights (Thermo Scientific, Germany) at a density of 12.000 cells/well. In case of KB_*wt* cells, wells were coated with collagen A prior to seeding. After 24 h medium was replaced with 240 µl fresh, serum-containing folic acid free RPMI medium. Then the various samples were prepared as described above, added into each well at a final nanobody concentration of 3.6 µM and incubated for 1 h at 37 °C. Medium was removed and cells were incubated for 18 h in fresh serum containing folate free RPMI medium. Medium was replaced by PBS and cells were imaged using a Leica TCS SP8 confocal microscope with an 63x DIC oil immersion objective (Plan-Apochromat).

Supplementary Tables and Figures

Screening Experiment

For a first screening experiment, the delivery of an Atto647N-labeled GFP binding nanobody (α-GFP-Nb) into HeLa_PCNA-GFP cells was evaluated. Cellular uptake was considered to be positive if α-GFP-Nb was visualized inside cellular vesicles. It is marked with "+" in Table SI "Cellular uptake". Co-localization of α-GFP-Nb and PCNA-GFP in the nucleus was regarded as specific binding to target protein and is marked with "+" in Table SI "Specific binding to target protein". "+-" describes the fact that delivery experiments using α-GFP-Nb formulated with ***730*** or ***731*** at a molar ratio of five, lead to co-localization with PCNA-GFP, but the signal was far less intense than if oligomer ***734*** or ***735*** were used. The delivery of α-GFP-Nb at a final concentration of 1.5 µM did not result in any significant cellular uptake and therefore just the results for a final concentration of 3.6 µM are depicted in Table SI. A more detailed description of these two structures can be found in (10).

Table SI. Summary of oligoaminoamide oligomers used for nanobody delivery.

ID	Topology	Sequence (C-to N terminal)	Cellular uptake	Specific binding to target protein	Ref
392		A-K-(K-(Stp$_3$-C)$_2$)$_2$	-	-	(7)
402		A-K-(K-(Stp$_4$-C) $_2$)$_2$	-	-	(7)
606		A-K-[H-K-(H-Sph-Sph-H-Sph-H-C)$_2$]$_2$	+	-	(8)
730		K-(PEG$_{24}$-E)-K-(K-OleA$_2$)-K(Stp$_4$-C)$_2$	+	+-	(9)
731	4-arm	K-(PEG$_{24}$-FolA)-K-(K-OleA$_2$)-K(Stp$_4$-C)$_2$	+	+-	(9)
732		K-(PEG$_{24}$-E)-K-[K-(Stp$_3$-C)$_2$]$_2$	+-	-	(10)
733		K-(PEG$_{24}$-FolA)-K-[K-(Stp$_3$-C)$_2$]$_2$	+-	-	(10)
734		K-(PEG$_{24}$-E)-K-[K-(Stp$_4$-C)$_2$]$_2$	+	+	(10)
735		K-(PEG$_{24}$-FolA)-K-[K-(Stp$_4$-C)$_2$]$_2$	+	+	(10)
728		K-(PEG$_{24}$-E)-K-(Stp4-C-K-OleA$_2$)$_2$	+	-	(11)
729		K-(PEG$_{24}$-FolA)-K-(Stp$_4$-C-K-OleA$_2$)$_2$	+	-	(11)
737	2-arm	K-(PEG$_{24}$-FolA)-K-(Stp$_4$-C)$_2$	-	-	(11)
788		K-(PEG$_{24}$-E)-K-[(H-Stp)$_3$-H-C]$_2$	-	-	(10)
789		K-(PEG$_{24}$-FolA)-K-[(H-Stp)$_3$-H-C]$_2$	-	-	(10)
488	U-shape	K-(Stp$_4$-K-(K-OleA$_2$)-C)$_2$	-	-	(12)
622	comb structure	C-[K(Stp)]$_8$-C	+	-	(13)

ID: identification number of oligomers, PEG$_{24}$: polyethylene glycol containing 24 ethylene oxide monomer units, FolA: folic acid, OleA: oleic acid, Stp: succinoyl tetraethylene pentamine, Sph: succinoyl pentaethylene hexamine, A, C, E, H, K: amino acids, +: positive effect, -: negative effect, + -: indicating a slight effect

As a result of our analysis, larger oligomers (4-arm structures) lead to better cellular uptake than smaller oligomers (2-arm, U-shape or comb structures). Oligomers comprising histidines or Sph did not improve cellular uptake or release of cellular vesicles. In the end, transductions using oligomer ***735*** and ***734*** resulted in the highest efficiency in specific binding of PCNA-GFP in the nucleus.

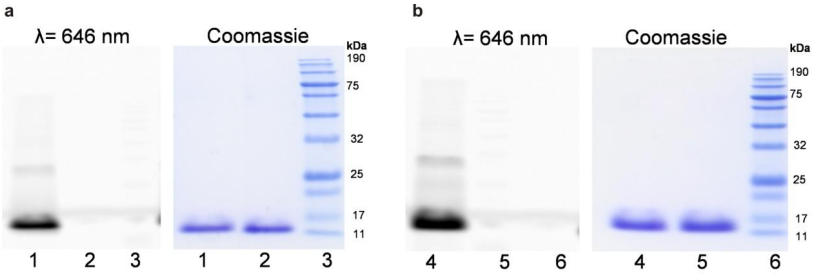

Fig. S1 SDS-PAGE analysis of the modification of α-GFP-Nb (a) and α-lamin-Nb (b) with NHS-Atto647N dye (for the modification protocol, see methods part in the manuscript. Grey pictures, imaging of gels at a wavelenght of 646 nm using Typhoon (GE Healthcare). Blue pictures, imaging of Coomassie staining. a) 1: Atto647N-labeled α-GFP-Nb, 2: α-GFP-Nb without modification, 3: Protein Standard Broad Range (NEB); b) 4: Atto647N-labeled α-lamin-Nb 5, α-lamin-Nb without modification, 6: Protein Standard Broad Range (NEB).

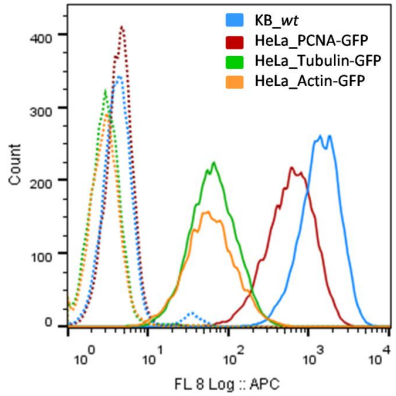

Fig. S2 Determination of the surface expression level of the folic acid receptor in different cell lines by flow cytometry. Control cells (dotted lines) were treated with isotype control, mouse IgG1. Allophycocyanin (APC)-conjugated anti folic acid receptor 1 IgG1 antibody was used for the detection of the folic acid receptor (solid lines). Blue, KB_*wt*; red, HeLa_PCNA-GFP; green, HeLa_Tubulin-GFP; orange, HeLa_Actin-GFP.

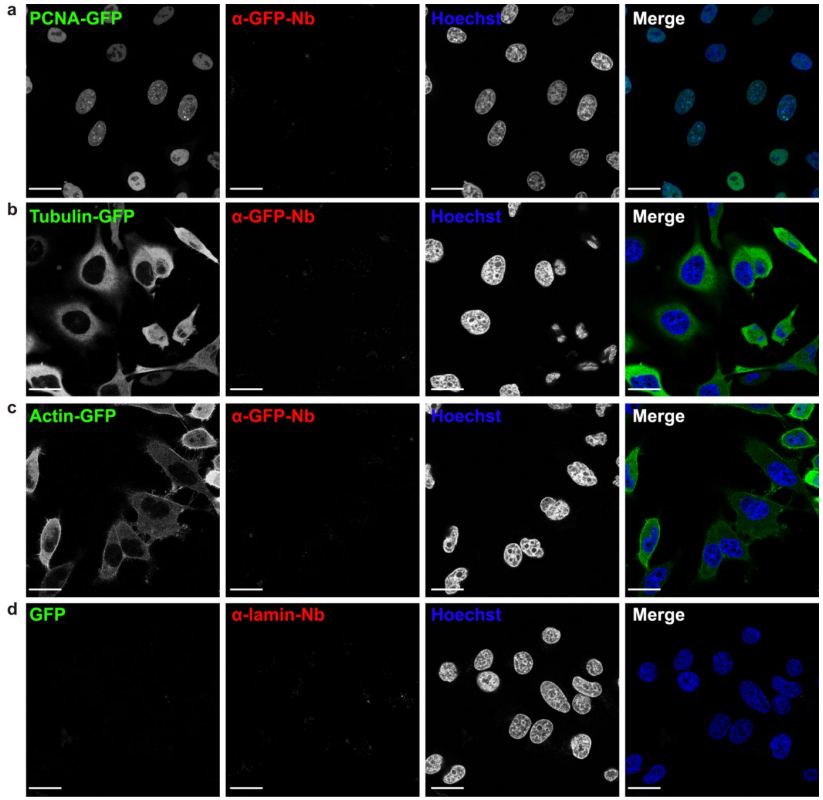

Fig. S3 Confocal laser scanning microscopy of live cells incubated with 3.6 µM Atto647N-labeled α-GFP-Nb (a-c) or α-lamin-Nb (d) for 18 h, followed by 4 h incubation in fresh media. First column, GFP fluorescence of GFP tagged proteins; second column, Atto647N fluorescence of α-GFP-Nb or α-lamin-Nb; third column, nuclear staining with Hoechst dye; fourth column, merge of all three channels. Scale bar: 25 µm. a) HeLa_PCNA-GFP cells; b) HeLa_Tubulin-GFP cells; c) HeLa_Actin-GFP cells; d) KB_*wt* cells.

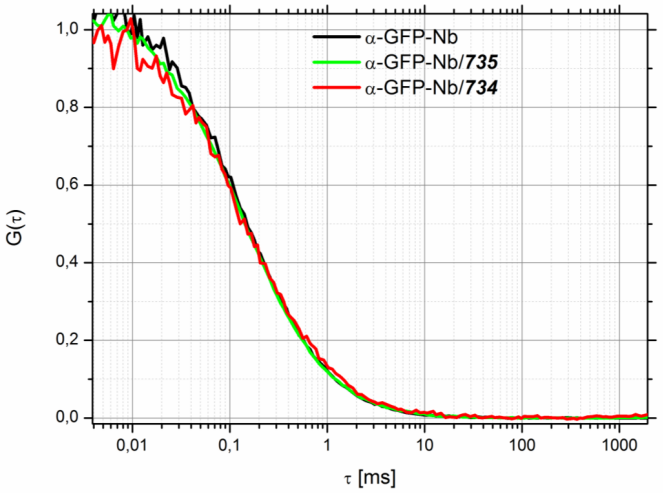

Fig. S4 α-GFP-Nb spiked with 1% Atto647N-labeled α-GFP-Nb was mixed with ***735*** or ***734*** with NEM blockade at a molar ratio of 1:5 and incubated for 4 h at 37°C. Fluorescent correlation spectroscopy measurements were carried out at a final concentration of α-GFP-Nb of 0.5 mg/ml in HEPES buffer. Normalized average correlation curves show R_H of 2 nm for α-GFP-Nb (black) and no change in correlation curves upon incubation with ***735*** (green) or ***734*** (red) indicating that free terminal cysteines are absolutely essential for the formation of α-GFP-Nb/oligomer nanoparticles.

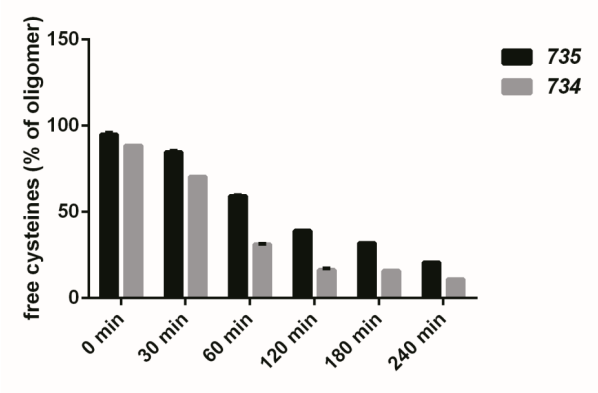

Fig. S5 The oxidation of free thiols during the formation of nanobody/oligomer nanoparticles was investigated over a period of 4 h. α-GFP-Nb was mixed with ***735*** or ***734*** at a molar ratio of 1:5 and incubated for 4 h at 37°C. At the indicated times points, samples were drawn and the amount of free thiols was determined by Ellman's-Assay. The percentage of free cysteines left in the reaction was calculated ± SD (*n*=3). Black bars, nanobody/***735***; grey bars, nanobody/***734***.

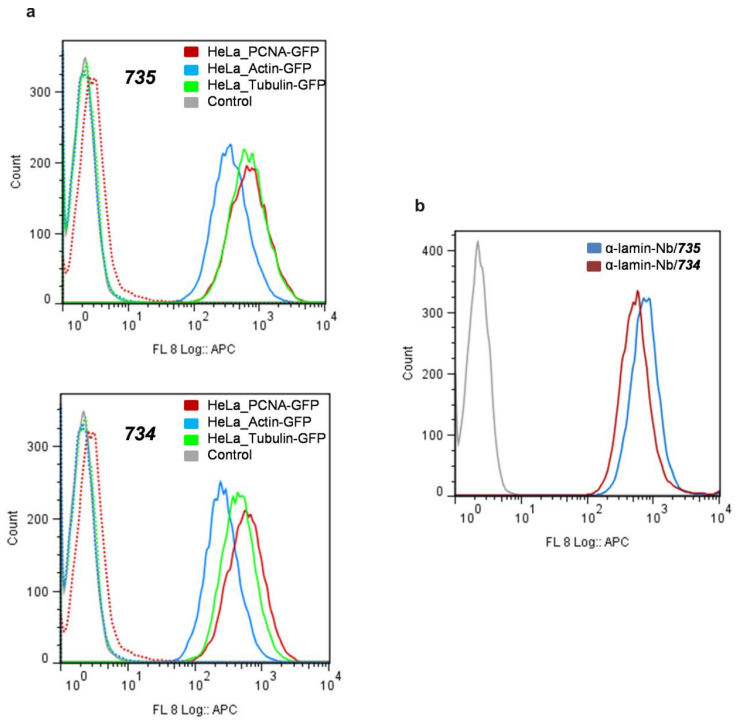

Fig. S6 Atto647N-labeled α-GFP-Nb or α-lamin-Nb were mixed with ***735*** or ***734*** at a molar ratio of 1:5 and incubated for 4 h at 37 °C. Afterwards cells were incubated for 1 h with 3.6 µM labeled nanobody formulated with oligomer ***735*** ((a) upper histograms solid lines, (b) blue) or oligomer ***734*** ((a) lower histograms solid lines, (b) red) or pure nanobody (dotted lines), followed by 18 h incubation in fresh media. a) Cellular uptake of α-GFP-Nb into different recombinant HeLa cell lines. Red, HeLa_PCNA-GFP cells; blue, HeLa_Actin-GFP cells; green, HeLa_Tubulin-GFP cells; grey, exemplary HEPES control in HeLa_PCNA-GFP cells. b) Cellular uptake of α-lamin-Nb into KB_*wt* cells; blue, α-lamin-Nb/***735***; red, α-lamin-Nb/***734***; grey, HEPES control.

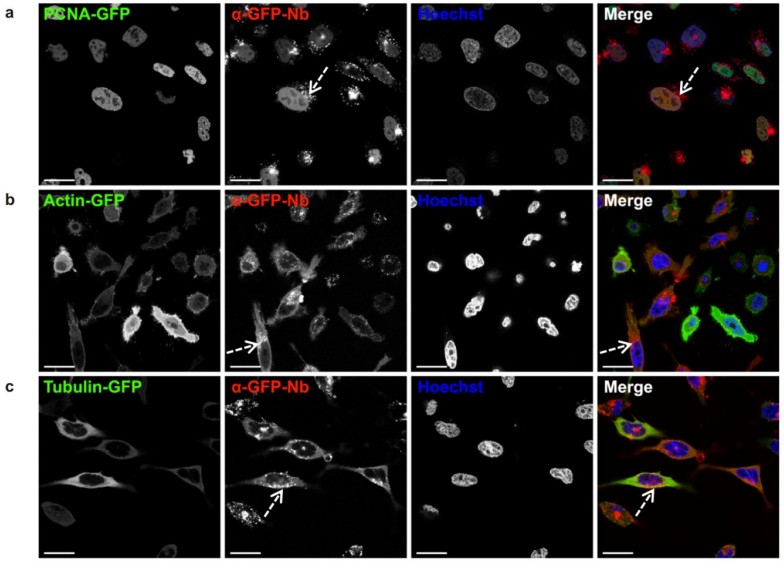

Fig. S7 Confocal laser scanning microscopy of live cells after transduction with 3.6 µM Atto647N labeled α-GFP-Nb formulated with ***734*** at a molar ratio of 1:5. Different recombinant HeLa cell lines were incubated for 1 h with the protein/oligomer mixture, followed by 18 h incubation in fresh media. First column, GFP fluorescence of GFP tagged proteins; second column, Atto647N fluorescence of α-GFP-Nb; third column, nuclear staining with Hoechst dye; fourth column, merge of all three channels. Dashed arrows indicate exemplary nanoparticles being trapped in cellular vesicles. Scale bar: 25 µm. a) HeLa_PCNA-GFP cells; b) HeLa_Actin-GFP cells; c) HeLa_Tubulin-GFP cells.

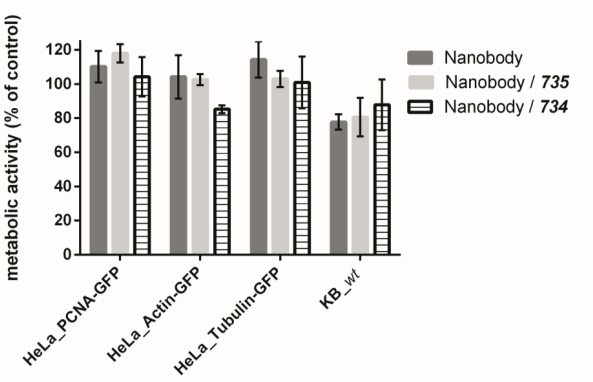

Fig. S8 Evaluation of cytotoxicity of nanobody formulated with oligomer ***735*** or ***734*** at a molar ratio of 1:5 on different cells lines. Data are presented as % metabolic activity of control cells ± SD (*n*=5). Cells were incubated for 1 h with the protein/oligomer mixture at a final nanobody concentration of 3.6 µM, followed by 18 h incubation in fresh media. Dark grey, free nanobody; light grey, transduction of cells with nanobody/***735***; patterned, transduction of cells with nanobody/***734***. Atto647N-labeled α-GFP-Nb was used for all recombinant HeLa cell lines and Atto647N-labeled α-lamin-Nb for KB_*wt* cells.

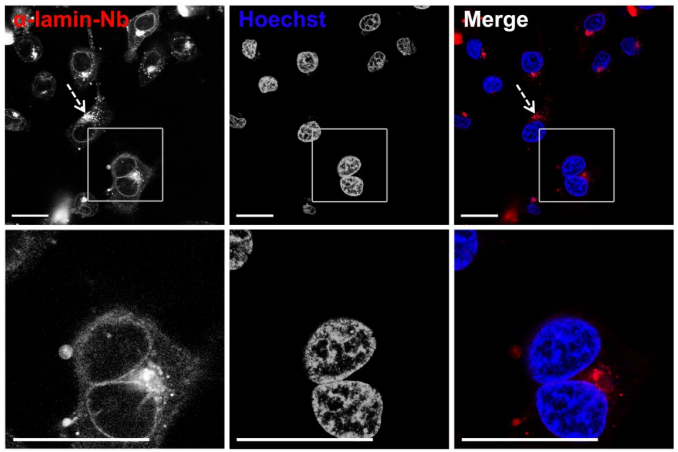

Fig. S9 Confocal laser scanning microscopy of live cells after transduction with 3.6 µM Atto647N-labeled α-lamin-Nb formulated with ***734*** at a molar ratio of 1:5. KB_*wt* cells were incubated for 1 h with the protein mixture, followed by 18 h incubation in fresh media. First column, Atto647N fluorescence of α-lamin-Nb; α-lamin-Nb binds to endogenous lamina lining the nucleus, visualizing the typical nuclear rim structure; second column, nuclear staining with Hoechst dye; third column, merge of both channels. Dashed arrows indicate exemplary nanoparticles being trapped in cellular vesicles. Scale bar: 25 µm.

Supporting Information References

1. Kirchhofer A, Helma J, Schmidthals K, Frauer C, Cui S, Karcher A, *et al*. Modulation of protein properties in living cells using nanobodies. Nat Struct Mol Biol. 2010;17(1):133-8.
2. Rothbauer U, Zolghadr K, Tillib S, Nowak D, Schermelleh L, Gahl A, *et al*. Targeting and tracing antigens in live cells with fluorescent nanobodies. Nat Methods. 2006;3(11):887-889.
3. Magde D, Elson E, Webb WW. Thermodynamic Fluctuations in a Reacting System—Measurement by Fluorescence Correlation Spectroscopy. Phys Rev Lett. 1972;29(11).
4. Rigler R, Mets Ü, Widengren J, Kask P. Fluorescence Correlation Spectroscopy with High Count Rate and Low Background: Analysis of Translational Diffusion. Eur Biophys J. 1993;22:169-75.
5. Haustein E, Schwille P. Fluorescence correlation spectroscopy: novel variations of an established technique. Annu Rev Biophys Biomol Struct. 2007;36:151-69.
6. Schaffert D, Troiber C, Salcher EE, Frohlich T, Martin I, Badgujar N, *et al*. Solid-phase synthesis of sequence-defined T-, i-, and U-shape polymers for pDNA and siRNA delivery. Angew Chem Int Ed Engl. 2011;50(38):8986-9.
7. Salcher EE, Kos P, Frohlich T, Badgujar N, Scheible M, Wagner E. Sequence-defined four-arm oligo(ethanamino)amides for pDNA and siRNA delivery: Impact of building blocks on efficacy. J Control Release. 2012;164(3):380-6.
8. Lachelt U, Kos P, Mickler FM, Herrmann A, Salcher EE, Rodl W, *et al*. Fine-tuning of proton sponges by precise diaminoethanes and histidines in pDNA polyplexes. Nanomedicine. 2014;10(1):35-44.
9. He D. Combinatorial optimization of nucleic acid carriers for folate-targeted delivery: LMU München; 2016.
10. He D, Muller K, Krhac Levacic A, Kos P, Lachelt U, Wagner E. Combinatorial optimization of sequence-defined oligo(ethanamino)amides for folate receptor-targeted pDNA and siRNA delivery. Bioconjug Chem. 2016;27(3)647-59.
11. Zhang P, He D, Klein PM, Liu X, Röder R, Döblinger M, *et al*. Enhanced Intracellular Protein Transduction by Sequence Defined Tetra-Oleoyl Oligoaminoamides Targeted for Cancer Therapy. Adv Funct Mater. 2015;25(42):6627-36.
12. Frohlich T, Edinger D, Klager R, Troiber C, Salcher E, Badgujar N, *et al*. Structure-activity relationships of siRNA carriers based on sequence-defined oligo (ethane amino) amides. J Control Release. 2012;160(3):532-41.
13. Scholz C, Kos P, Wagner E. Comb-like oligoaminoethane carriers: change in topology improves pDNA delivery. Bioconjug Chem. 2014;25(2):251-61.

B.6 Originalpublikation P6

Ruth Röder, Tobias Preiß, Patrick Hirschle, Benjamin Steinborn, Andreas Zimpel, Miriam Hoehn, Joachim O. Rädler, Thomas Bein, Ernst Wagner, Stefan Wuttke, Ulrich Lächelt.
Multifunctional nanoparticles by coordinative self-assembly of His-tagged units with metal-organic frameworks.

Journal of the American Chemical Society , 2017, 139 (6), 2359-–2368

JACS
JOURNAL OF THE AMERICAN CHEMICAL SOCIETY

Article

pubs.acs.org/JACS

Multifunctional Nanoparticles by Coordinative Self-Assembly of His-Tagged Units with Metal–Organic Frameworks

Ruth Röder,[†] Tobias Preiß,[‡] Patrick Hirschle,[§] Benjamin Steinborn,[†] Andreas Zimpel,[§] Miriam Höhn,[†] Joachim O. Rädler,[‡] Thomas Bein,[§] Ernst Wagner,[†] Stefan Wuttke,*[,§] and Ulrich Lächelt*[,†]

[†]Pharmaceutical Biotechnology, Department of Pharmacy and Center for NanoScience (CeNS), LMU Munich, 81377 Munich, Germany

[‡]Department of Physics and Center for NanoScience (CeNS), LMU Munich, 80539 Munich, Germany

[§]Department of Chemistry and Center for NanoScience (CeNS), LMU Munich, 81377 Munich, Germany

Supporting Information

ABSTRACT: Self-assembly of individual units into multicomponent complexes is a powerful approach for the generation of functional superstructures. We present the coordinative interaction of oligohistidine-tags (His-tags) with metal–organic framework nanoparticles (MOF NPs). By this novel concept, different molecular units can be anchored on the outer surface of MOF NPs in a self-assembly process generating multifunctional nanosystems. The article focuses on two main objectives: first, the detailed investigation of the assembly process and fundamental establishment of the novel functionalization concept; and second, its subsequent use for the development of biomacromolecule (e.g., peptides and proteins) delivery vehicles. Three exemplary MOF structures, MIL-88A, HKUST-1, and Zr-*fum*, based on different metal components, were selected for the external binding of various His-tagged synthetic peptides and recombinant or chemically H_6-modified proteins. Evidence for simultaneous assembly of different functional units with Zr-*fum* MOF NPs as well as their successful transport into living cells illustrate the promising potential of the self-assembly approach for the generation of multifunctional NPs and future biological applications. Taking the high number of possible MOF NPs and different functional units into account, the reported functionalization approach opens great flexibility for the targeted synthesis of multifunctional NPs for specific purposes.

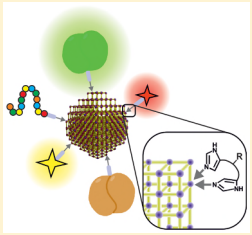

INTRODUCTION

Nanoparticles (NPs) that combine different functional domains are of high interest for various scientific disciplines requiring multifunctionality at the nanoscale. The controlled manipulation of the external surface of NPs is of paramount importance as it defines the interface between the NP and its surroundings and strongly determines the overall performance of the NP especially in biological environments.[1,2] Researchers have shown that surface functionalization is a powerful tool for the creation of programmable NP interfaces. In this respect, the self-assembly of the functional units onto the NPs surface appears as a powerful approach because it would ensure a defined arrangement of these units without any guidance from an external source. Examples of self-assembly processes used for the generation of multifunctional colloidal NPs are micelle, liposome, or polymerosome formation of amphiphilic compounds[3−6] and cyclodextrin-adamantane host–guest interactions.[7,8] Especially for biomedical applications, multifunctional NPs that interact with biological systems at the molecular level and perform tasks within cellular systems are in great demand.[9,10] The intracellular delivery of biomacromolecules, such as peptides and proteins, represents a particularly challenging task. Several different barriers have to be overcome, including cellular uptake, endosomal escape, intracellular trafficking and cargo release.[11,12] The heterogeneity of this compound class (hydrophilicity, charge, functional groups) hampers the development of universal delivery platforms. For this reason, nanocarriers with a functionalization mode, which is independent from the individual properties of the functional units, would be advantageous.

Here, we present the coordinative interaction of oligohistidine-tags with metal–organic frameworks (MOFs) as a novel external functionalization concept for MOF NPs based on a self-assembly process. MOFs are a class of materials synthesized of inorganic building units, metal ions, or metal oxide clusters, which are coordinatively connected by organic linkers to create porous three-dimensional frameworks (Figure 1a).[13] Their crystallinity, chemically functionalizable pores, and potential systematic structural variation are some factors among others that allow one to precisely design these materials for particular purposes.[14,15] Regarding biomedical applications, the hybrid MOF nature provides the advantageous potential of degradability and disintegration into the low molecular weight

Received: November 18, 2016
Published: January 11, 2017

DOI: 10.1021/jacs.6b11934
J. Am. Chem. Soc. 2017, 139, 2359−2368

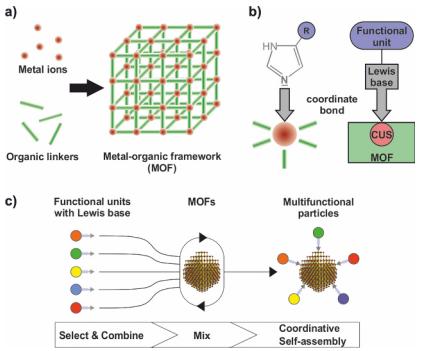

Figure 1. Illustration of coordinative self-assembly of His-tagged molecules with MOF NPs: (a) molecular composition of MOFs; (b) coordinative bond between the imidazole group of histidines acting as Lewis base and coordinatively unsaturated metal sites (CUS) acting as Lewis acid; (c) multifunctional MOF NPs generated by coordinative attachment of different functional units via self-assembly.

components which can be eliminated from the body.[16−19] Different research groups have already reported pioneering examples of MOF NPs as transport vehicles for the delivery of biologically active molecules.[16,20−27] Here the combination of the high MOF surface area for high drug loading and the possibility to engineer the internal surface to control MOF scaffold-guest interaction was used to optimize the nanocarrier performance.[28] Even biomacromolecules such as proteins, DNA or enzymes could be encapsulated into MOFs recently,[29,30] or the MOF scaffold itself could be used as a part of the therapeutic principle.[31−34] Therefore, combining the rich and versatile bulk chemistry of MOF materials with controlled and programmable NP interfaces may lead to novel multifunctional nanosystems.[35−40] Our concept uses the interaction between Lewis bases, such as the imidazole function of histidine and coordinatively unsaturated metal sites (CUS) present on the external surface of MOF NPs (Figure 1b) to self-assemble different functional units (Figure 1c).

The exemplary set of (oligohistidine-tag) functional units used in this study is summarized in Table 1. Since His-tags can be readily integrated into peptides or proteins by synthetic, recombinant or bioconjugation techniques, they appear to be ideal connectors to create a versatile inorganic/bioorganic interface at the MOF NPs' surface. The same interaction (Figure 1b) is routinely used for the purification of recombinant proteins by immobilized metal ion chromatography.[41,42] Applicability of the coordinative His-tag interactions for intracellular delivery of proteins has been demonstrated before by using conjugates of nitrilotriacetic acid derivatives and cell-penetrating peptides,[43,44] polymers[45] or silica NPs.[46] In these approaches, the delivery platforms and vehicles were synthetically modified with separate metal-chelators. Since the metal-sites already are an integral part of the coordinative MOF structure, the external secondary modification via coordinate bonds in the presented approach of 'self-assembling multifunctional coordination particles' (SAMCOPs) is considered a powerful tool for the combinatorial and stoichiometric generation of functional MOFs.

RESULTS AND DISCUSSION

Selection and Characterization of MOF NPs. A set of three exemplary MOF structures, MIL-88A (Fe^{3+}/fumaric acid),[16] HKUST-1 (Cu^{2+}/trimesic acid)[47] and Zr-*fum* (Zr^{4+}/fumaric acid)[48,49] was selected for testing the assembly strategy. HKUST-1 was chosen based on the high His-tag affinity toward chelated Cu^{2+}, which even exceeds affinity toward Ni^{2+} and Co^{2+}.[50,51] MIL-88A and Zr-*fum* represent well established MOFs with potential for biomedical applications.[16,18] Although Ni^{2+}, Co^{2+}, and Zn^{2+} are known to have high affinity to His-tags,[50,51] they were not included in the study due to the expected cytotoxicity of Ni^{2+} and Co^{2+} MOFs and the low stability of Zn-based MOFs in aqueous media. Together, the set covers a range of well-established MOF species with individual material characteristics and each based on a different di-, tri-, or tetravalent metal component with expected different His-tag binding capacities.

The quality of the MOF NPs used in this study was ensured by applying multiple complementary characterization techniques: scanning electron microscopy (SEM, Figures S10–S15), dynamic light scattering (DLS, Figures S1 and S2, Table S2), X-ray diffraction (XRD, Figures S3–S5), thermogravimetric analysis (TGA, Figures S6–S8), and nitrogen sorption measurements providing the surface area (Figure S9, Table S3). Powder XRD patterns were determined for all MOF NP species (Figures S3–S5). The diffractograms were used to verify the successful synthesis of the MOF species as well as to show the high crystallinity of the Zr-*fum* and HKUST-1 NPs. It

Table 1. His-tagged functional units used for the assembly with MOF NPs

code	sequence[a]/description	function
H_6–Acr	acridine-PEG_{28}-H_6-NH_2	photometric detection
$H_{0/3/6}$-Acr	acridine-STOTDA-$H_{0/3/6}$	
$H_{0/3/6}$-FITC	FITC-STOTDA-H_6	fluorescence detection
H_6-A647N	ATTO647N-PEG_{12}-H_6-NH_2	
H_6-CF	carboxyfluorescein-PEG_{12}-H_6-NH_2	
H_6-GFP	recombinant eGFP (H_6–tag)	model proteins
H_6-Tf*	transferrin conjugated with H_6–PEG_{36} and ATTO 647N	
H_6-Bak	H_6-GGQVGRQLAIIGDDINR-NH_2	pro-apoptotic peptides
H_6-Bad	H_6-GNLWAAQRYGRELRRMSDEFVD-NH_2	
H_6-KLK	H_6-GGKLAKLAKKLAKLAK-NH_2	
H_6-CytC	cytochrome *c* conjugated with H_6	pro-apoptotic protein

[a]Peptide sequences are indicated from N- to C-terminus using the one-letter code for α-amino acids (H_n, *n* = number of histidines).

DOI: 10.1021/jacs.6b11934
J. Am. Chem. Soc. 2017, 139, 2359−2368

should be noted that the poor crystallinity of the MIL-88A NPs are expected and have been frequently reported and discussed in the literature.[16,52−55] At the same time, XRD was used to prove the stability of the three MOFs under the later used conditions (Figures S3−S5). For additional bulk characterization, all NP species were examined with both nitrogen sorption experiments (Figure S9, Table S3) and TGA (Figures S6−S8). The microporosity of all three NP species ranging from 0.6 up to 1.5 nm was confirmed and the BET surface area yielded typical results.[16,47−49] Thus, we have successfully synthesized the MIL-88A, HKUST-1, and Zr-*fum* MOF structures with their expected bulk properties.

In order to characterize their corresponding NP properties a combination of two techniques was used: particle size distributions were determined via scanning electron microscopy (SEM, Figures S10−S15) for the dried species and, more importantly, for the dispersed species via dynamic light scattering (DLS, Figures S1 and S2, Table S2). For Zr-*fum*, SEM measurements resulted in a diameter of (84 ± 7) nm for the dried particles. The corresponding *z*-average diameter measured via DLS in water was determined at (182 ± 4) nm with a polydispersity index (PDI) of 0.205. This deviation toward larger diameters is to some extent expected, since DLS provides the hydrodynamic diameter of the particles and is influenced among others by particle−solvent interactions and aggregation.[56,57] The other MOFs behave similarly: DLS experiments resulted in an average intensity based diameter of (191 ± 1) nm (PDI = 0.130) for MIL-88A and (530 ± 27) nm (PDI = 0.290) for HKUST-1 with the corresponding dried particle size distributions of (61 ± 7) nm for MIL-88A and for HKUST-1 (177 ± 39) nm. We suppose that the main reason for the larger NP diameters determined using DLS is due to the fact that the MOF samples reveal agglomeration behavior in solution.[56]

Photometrical Analysis of His-Tag Binding to MOF NPs. The binding of different His-tag model peptides (e.g., H_n-Acr, H_n-FITC, H_6-A647N) to MIL-88A, HKUST-1 and Zr-*fum* in HEPES buffered glucose (HBG) at pH 7.4 was determined by the detection of residual free peptide in the supernatant after incubation and centrifugation of the MOF suspensions (Figures 2a,b,d, 3, S17, and S19, Scheme S1). An exemplary movie demonstrating the binding of H_6-A647N to HKUST-1 MOF NPs visualized by decoloration of the supernatant after centrifugation is provided in the Supporting Information. The exclusive reduction of H_6-Acr (in contrast to A_6-Acr) in the supernatant, illustrated by the discrete diminution of the H_6-Acr peak in the RP-HPLC chromatograms, represents qualitative evidence for the histidine-dependent interaction with all three investigated MOF species (Figure 2b). The peptide-specific binding was also verified by zeta potential measurements (Figure 2c) showing a significant shift toward neutrality caused by the His-tag containing derivatives only. Quantitative determination of binding as a function of histidine residues, i.e., number of Lewis base units (H_0, H_3, H_6) was carried out by photometric quantification of residual free peptide using a UV-photometer (Figure 2d). The amount of bound H_3- and H_6-peptides increased with increasing amounts of MOFs, but binding of the H_0 derivative, corresponding to no histidine residue, was generally negligible. Notably, in case of all three MOFs significantly higher peptide binding was observed with higher number of histidines (H_0 vs H_3 and H_3 vs H_6).

This correlation was additionally confirmed for Zr-*fum* via fluorescence spectroscopy by using FITC labeled peptides

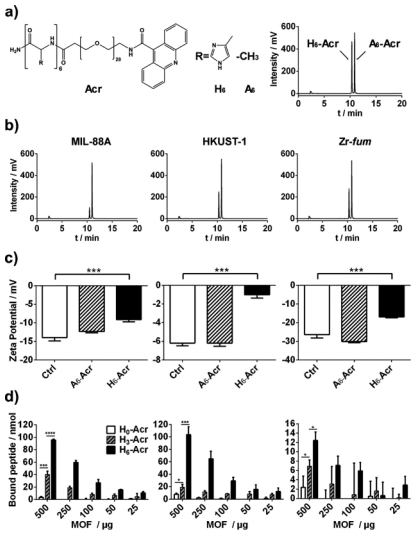

Figure 2. Acridine (Acr) peptide binding to MIL-88A (left), HKUST-1 (middle), and Zr-*fum* (right) particles in HEPES buffered glucose (HBG) at pH 7.4. (a) Chemical structure and control chromatogram of model compounds H_6-Acr, A_6-Acr. (b) Peptide binding (H_6 vs A_6) by detection of reduced free peptides in the supernatant (RP-HPLC, λ = 360 nm). (c) Effect of peptide binding on zeta potential. (d) Quantitative determination of bound peptides H_0 (white), H_3 (pattern), and H_6 (black) as difference to photometrically quantified free peptides in the supernatant (λ = 360 nm) using a UV-photometer. Please note that the scaling of *y*-axes is adjusted to the different binding capacities: 0−120 nmol peptide in case of MIL-88A and HKUST-1, 0−16 nmol peptide in case of Zr-*fum*.

($H_{0/3/6}$-FITC) (Figure S19). Excessive addition of imidazole decreased binding of H_6−FITC to levels of H_0-FITC, suggesting competition of histidine and free imidazole for coordinative interaction with the MOF surface, similar to the elution of His-tagged proteins from a nickel-column in immobilized-metal ion chromatography purifications. Comparing H_6-tag binding to 500 μg MOF NPs, HKUST-1 achieved the highest binding (104 nmol), followed by MIL-88A (96 nmol) and Zr-*fum* (12 nmol) which is consistent with reported relative metal ion affinities (Cu^{2+} > Fe^{3+}, Zr^{4+}) for His-tags.[41] A time course experiment (Figure 3b) revealed stable association of Zr-*fum*/H_6-A647N for 24 h at pH 7.4 and rapid partial (pH 5) or complete (pH 3) release upon acidification. This is consistent with the hypothesis of unprotonated histidines acting as Lewis base and being responsible for binding (Figure 3a). We suggest that the incomplete detachment at pH 5 is caused by a lowered pK_a of the imidazole group due to metal ion binding[58] and an equilibrium between protons and metal ions competing for histidine interactions.

Fluorescence Correlation Spectroscopy (FCS). Using FCS the binding of fluorescently labeled H_6-tags to MOF particles was measured at low concentrations with single-

DOI: 10.1021/jacs.6b11934
J. Am. Chem. Soc. 2017, 139, 2359−2368

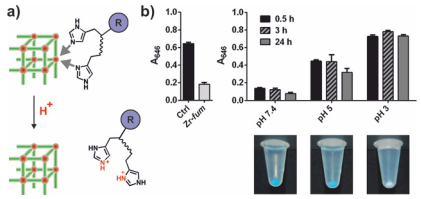

Figure 3. pH dependent stability of H_6-tag binding to Zr-*fum* NPs. (a) Schematic illustration of acidic detachment due to histidine protonation. (b) Experimental data obtained by photometric determination (λ = 646 nm) of free H_6-A647N in the supernatant after centrifugation. Left: Zr-*fum* NPs were loaded with H_6-A647N at pH 7.4 for 15 min, centrifuged and the supernatant was analyzed; Ctrl illustrates absorbance of free peptide in a sample without MOF NPs. Right: MOF NP suspensions were acidified to a defined pH and incubated for indicated times before centrifugation and analysis of the supernatant. Reaction tubes below show the MOF pellets of the same samples after 24 h at pH 7.4 (left), pH 5 (middle), and pH 3 (right) and centrifugation; decoloration of the pellet due to acidic H_6-A647N detachment at pH 3 can be observed.

molecule sensitivity (Figures 4 and S18). Figure 4 (upper left) and Figure S18 show a significant increase in the

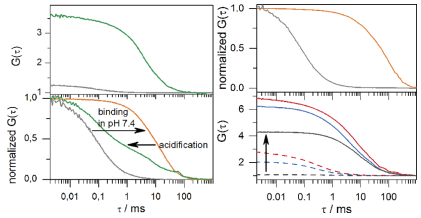

Figure 4. Investigation of Zr-*fum*/H_6-A647N interaction by fluorescence correlation spectroscopy (FCS). Upper left: FCS time correlation functions of H_6-A647N before (gray) and after Zr-*fum* NP addition (green). Lower left: Normalized time correlation functions showing binding of H_6-A647N at pH 7.4 (orange) and release upon acidification (green); free H_6-A647N (gray). Upper right: Normalized time correlation functions of measurements in DMEM (10% FBS) of free H_6-A647N (gray) and Zr-*fum*/H_6-A647N (orange). Lower right: fluorescence cross correlation spectroscopy (FCCS) measurements of H_6-GFP (blue) and H_6-Tf* (red) in HBG pH 7.4 before (dotted) and after (solid) Zr-*fum* addition. Cross correlation before (dotted gray) and after (solid gray) Zr-*fum* addition.

autocorrelation amplitude after addition of all three MOF species, indicating a reduction of the H_6-tag number concentration most likely due to multiple binding to MOF NPs. In case of MIL-88A and HKUST-1 (Figure S18), however, no change in the characteristic correlation decay time could be detected. We attribute this to the known phenomenon of MOF induced fluorescence quenching[59,60] as well as rather large effective particle sizes, in particular of HKUST-1, resulting from aggregation, which both can cause a decline of detectable tags after binding. For Zr-*fum* NPs several key observations could be made (Figure 4). Free H_6-tags (gray) showed fast single molecule diffusion prior to NP addition (Figure 4, lower left). After addition of Zr-*fum* NPs at pH 7.4 (orange) the collective diffusion was shifted toward higher diffusion times revealing H_6-tag binding to Zr-*fum* NPs. Following acidification (green) the diffusion rate increased relative to the pH 7.4 measurement indicating partial detachment of His-tags from the MOF NP surface, due to the protonation of histidines.

Importantly, H_6-tag association with Zr-*fum* NPs remained stable after dilution in DMEM medium containing 10% fetal bovine serum (FBS), confirming the suitability for use under cell culture conditions (Figure 4, upper right). Finally, two His-tagged proteins with distinct fluorescence spectra (recombinant eGFP with genetically encoded His-tag: H_6-GFP, and human transferrin chemically conjugated with a H_6-tag and ATTO 647N label: H_6-Tf*) were used for fluorescence cross correlation spectroscopy (FCCS) measurements to investigate simultaneous binding of both entities to single particles (Figure 4, lower right). In a solution containing equimolar amounts of both proteins the cross correlation showed high coincidence of H_6-GFP and H_6-Tf* after addition of Zr-*fum* NPs (solid gray), which demonstrated binding of different His-tagged proteins to the same Zr-*fum* particles. Importantly, both FCS and FCCS experiments revealed the colloidal stability of the MOF NPs. Additionally, the framework stability of the particles prior to and after functionalization under aqueous conditions was investigated by XRD measurements (Figures S3−S5). The experiments showed the nearly unchanged crystallinity of all samples under each tested condition. In the case of Zr-*fum* MOF NPs, this was also confirmed by SEM and DLS measurements, exhibiting no observable change in morphology of dried particles and moderate effect on hydrodynamic size of dispersed particles upon modification with H_6-Acr in HBG pH 7.4 (Figures S2 and S16).

Cellular Uptake of Model Peptides and Proteins with MOF NPs. To assess the potential of MOF NPs to mediate cellular internalization of biomacromolecules, H_6-carboxyfluorescein (H_6-CF), recombinant eGFP with genetically encoded His-tag (H_6-GFP) and chemically His-tagged and ATTO 647N labeled human transferrin (H_6-Tf*) were used as fluorescent model compounds. Based on the photometrical analysis of His-tag binding to the three MOF species (Figure 2d), the His-tagged functional units were used at a ratio of 10 nmol of H_6-tag per 1 mg of MOF which is considerably below the determined binding capacities of 192 nmol/mg MIL88A, 208 nmol/mg HKUST-1 and 24 nmol/mg Zr-*fum*. First, cell viability of HeLa cells after incubation with different amounts of all three MOF NPs and different His-tags for 48 h was evaluated by MTT-assay (Figure S20). MIL-88A, Zr-*fum*, and the tested His-tags H_6-CF, H_6-GFP, and H_6-Tf, were very well tolerated. HKUST-1 exhibited considerable cytotoxicity, which could be avoided by shortening the incubation time with cells to 2 h followed by medium exchange, which deleted observable effects on metabolic activity at the end point evaluation after 48 h (Figure S20b). Next, cellular uptake of the different MOF NPs after functionalization with the H_6-tagged fluorescent dye H_6-CF or H_6-GFP was investigated. For prefunctionalization by coordinative self-assembly, His-tags and MOF NPs were mixed at a final concentration of 10 μM H_6-tag and 1 mg/mL MOF in HBG buffer (ratio of 10 nmol H_6-tag per 1 mg MOF) and incubated for 15 min at room temperature. Cells were then incubated with the different functionalized MOF NPs for 24 h in medium at a concentration of 0.1 mg/mL MOF corresponding to 1 μM His-tag, followed by flow cytometry

DOI: 10.1021/jacs.6b11934
J. Am. Chem. Soc. 2017, 139, 2359−2368

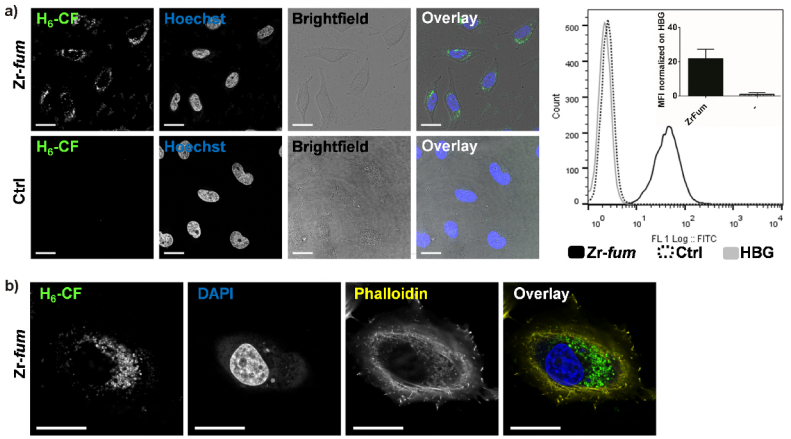

Figure 5. Cellular uptake of fluorescent peptide H_6-CF mediated by Zr-*fum* NPs. H_6-CF was incubated with Zr-*fum* MOF NPs for 15 min at room temperature in HBG for prefunctionalization by coordinative self-assembly. The functionalized particles were incubated with HeLa cells for 24 h at a concentration of 0.1 mg/mL Zr-*fum* corresponding to 1 μM H_6-CF. Solutions containing H_6-CF at same concentration but no Zr-*fum* NPs served as control (Ctrl). (a) Confocal laser scanning microscopy (CLSM, left) and flow cytometry (right) after incubation of HeLa cells with functional NPs Zr-*fum*/H_6-CF (Zr-*fum*, CLSM upper row, flow cytometry solid black), H_6-CF control without Zr-*fum* NPs (Ctrl, CLSM lower row, flow cytometry dotted black) or HBG (flow cytometry gray). Mean fluorescence intensity (MFI) was normalized to HBG and is depicted in the inset. CLSM left to right: green fluorescence of H_6−CF, nuclear staining with Hoechst dye, brightfield image, overlay of all three channels. (b) Enlarged CLSM image of a fixated HeLa cell after incubation with Zr-*fum*/H_6-CF. Left to right: green fluorescence of H_6-CF, nuclear staining with DAPI dye, actin staining with rhodamine-phalloidin, overlay of all three channels. Scale bar: 25 μm. Additional images can be found in Supporting Information Figures S23 and S24.

and confocal laser scanning microscopy (CLSM) (Figures 5, S21, S22a, and S23−S26). MIL-88A and HKUST-1 MOF NPs showed low levels of detectable cellular uptake (Figure S21) presumably due to the presence of huge particles with a tendency to aggregate (Figures S1 and S10−S13) and fluorescence quenching effects (Figure S18). Compared to MIL-88A and HKUST-1, Zr-*fum* MOF NPs exhibit several favorable characteristics such as very narrow particle size distribution, uniform sphere morphology, low aggregation behavior, negligible fluorescence quenching and also good cellular tolerance. Thus, despite their comparatively low His-tag binding capacity, they were selected to be used for further experiments. Zr-*fum*/H_6-CF showed cellular uptake in CLSM (Figure 5a, left) and flow cytometry (Figure 5a, right). Additional z-stacks of CLSM images can be found in Figures S23 and S24. The mean fluorescence intensity (MFI, inset) of cells treated with Zr-*fum*/H_6-CF increased 20-fold compared to free H_6-CF. The cellular uptake of Zr-*fum*/H_6-GFP alone is depicted in Figures S22a, S25, and S26 showing 30-fold higher MFI values compared to free H_6-GFP. A 3D reconstruction movie of a cell treated with Zr-*fum*/H_6-GFP is provided in the Supporting Information.

A distinct advantage of the self-assembly concept demonstrated here is the possible one-step multifunctionalization of MOF NPs by simultaneously mixing of different H_6-tagged functional units with bare MOF NPs (Figure 1c). This procedure facilitates the creation of multifunctional MOF NPs with various stoichiometric ratios as required for optimization of spatiotemporal co-delivery into cells. As the simultaneous assembly of H_6-GFP and H_6-Tf* with Zr-*fum* MOF NPs had been confirmed by FCCS measurements (Figure 4, lower right), HeLa cells were subjected to these double-functionalized particles (Zr-*fum*/H_6-GFP + H_6-Tf*) for 24 h at a concentration of 0.1 mg/mL MOF corresponding to 0.5 μM H_6-GFP and H_6-Tf*, followed by investigation of the internalization (Figures 6 and S22b). Considerable colocalization of H_6-GFP and H_6-Tf* could be observed (Figure 6a, upper row and 6b). In contrast to free H_6-GFP, free H_6-Tf* was also taken up by the cells without the addition of Zr-*fum* MOF NPs to a certain extent (Figure 6a, lower row). This can be explained by the fact that HeLa cells express the transferrin receptor (Figure S29), thus enabling receptor-mediated uptake of free H_6-Tf*. However, despite the MOF-independent uptake route of H_6-Tf*, association with Zr-*fum* resulted in 5-fold higher internalization, confirming an additional boost due to NP mediated uptake. Additional z-stacks of CLSM images can be found in Figures S27 and S28. Looking at the intracellular distribution of fluorescent peptides and proteins internalized via Zr-*fum* MOF NPs in detail, the spotty arrangement indicates high vesicular entrapment and suggests endosomal escape being a hurdle for cytosolic delivery.

Endocytosis Mechanism. The cellular uptake pathway of Zr-*fum*/H_6-GFP NPs was investigated in an uptake experiment (Figure 7). HeLa cells were preincubated for 30 min at 4 °C, to reduce cellular metabolism and block energy dependent processes, or with various concentrations of the individual endocytosis inhibitors chlorpromazine (clathrin-mediated endocytosis), amiloride (macropinocytosis) and genistein

DOI: 10.1021/jacs.6b11934
J. Am. Chem. Soc. 2017, 139, 2359−2368

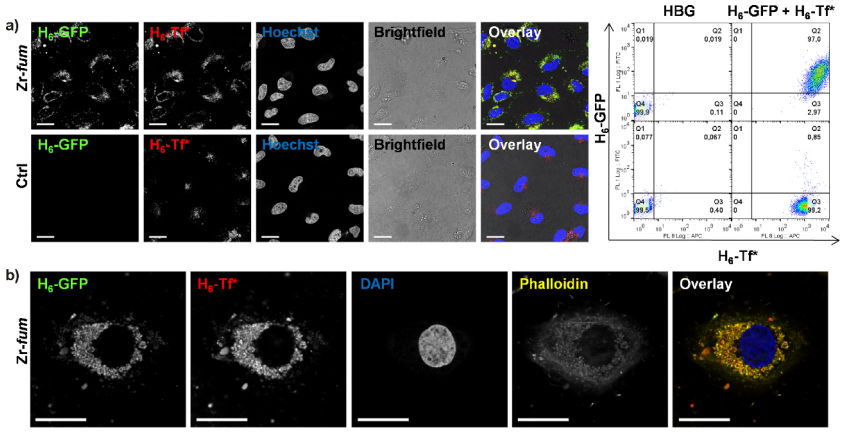

Figure 6. Simultaneous cellular uptake of fluorescent proteins H_6-GFP and H_6-Tf* mediated by Zr-*fum* NPs. An equimolar mixture of H_6-GFP and H_6-Tf* was incubated with Zr-*fum* MOF NPs for 15 min at room temperature in HBG for prefunctionalization by coordinative self-assembly. The double functionalized particles were incubated with HeLa cells for 24 h at a concentration of 0.1 mg/mL Zr-*fum* corresponding to 0.5 μM H_6-GFP and H_6-Tf*. Solutions containing H_6-GFP and H_6-Tf* at same concentration but no Zr-*fum* NPs served as control (Ctrl). (a) Cellular uptake of Zr-*fum*/H_6-GFP+H_6-Tf* (upper row) or control without MOF NPs (lower row). CLSM left to right: green fluorescence of H_6-GFP, red fluorescence of H_6-Tf*, nuclear staining with Hoechst dye, brightfield picture, overlay of all four channels, yellow color indicates colocalization of H_6-GFP and H_6-Tf*. Flow cytometry analysis: HBG (left) or H_6-GFP + H_6-Tf* (right) with Zr-*fum* MOF NPs (upper row) or Ctrl without MOF NPs (lower row). (b) Enlarged CLSM image of a fixated HeLa cell after incubation with Zr-*fum*/H_6-GFP + H_6-Tf*. Left to right: green fluorescence of H_6-GFP, red fluorescence of H_6-Tf*, nuclear staining with DAPI dye, actin staining with rhodamine-phalloidin, and overlay of all four channels. Scale bar: 25 μm. Additional images can be found in Figures S27 and S28, and a 3D reconstruction movie of a cell treated with Zr-*fum*/H_6-GFP is provided in the Supporting Information.

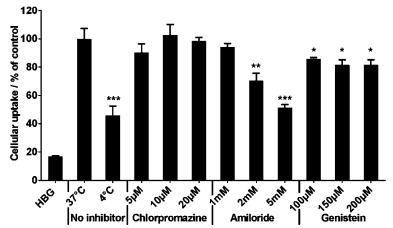

Figure 7. Evaluation of endocytosis inhibition of Zr-*fum*/H_6-GFP nanoparticles. Pre-Incubation of HeLa cells with different inhibitors or at 4 °C for 30 min, followed by incubation with Zr-*fum*/H_6-GFP for 2 h at 37 °C or 4 °C. Flow cytometric analysis was carried out in PBS (pH 4.0) to quench the extracellular fluorescence. Cellular uptake was determined as MFI. Data are presented as % cellular uptake normalized to uptake of Zr-*fum*/H_6-GFP NPs at 37 °C ± SD (n = 3).

(caveolae-mediated endocytosis) to discriminate the particular endocytotic routes. Afterward the cells were subjected to Zr-*fum*/H_6-GFP NPs at a concentration of 0.1 mg/mL MOF NPs corresponding to 1 μM H_6-GFP for 2 h, followed by flow cytometric analysis in acidified PBS (pH 4, 10% FBS) to quench the extracellular fluorescence. The results clearly show, that the NPs are internalized via an energy dependent process. Preincubation with amiloride showed the greatest inhibitory effect which suggests macropinocytosis is having major contribution to the uptake of Zr-*fum*/H_6-GFP nanoparticles. Since some effect of genistein was observed, caveolae mediated uptake might also be involved to a minor extent. A recent study investigated the endocytosis mechanisms of UiO-66 (Zr^{4+}/terephthalate) MOF NPs.[61] Consistently, the cellular uptake of UiO-66 was also identified to be an energy dependent process with distinct involvement of macropinocytosis; however, also a major contribution of clathrin-mediated endocytosis was found.

Transduction of Biologically Active Peptides and Proteins. To further evaluate the potential of Zr-*fum* MOF NPs as carrier system for cytosolic cargo release, transduction of membrane impermeable bioactive pro-apoptopic peptides (Bak, Bad, KLK) and mitochondrial cytochrome *c* (CytC) protein was investigated and cell killing was used as reporter of successful cytosolic delivery. H_6-tags were chemically conjugated to CytC or integrated at the N-terminus of the peptide sequences derived from the BH3 domain of Bak and Bad proteins[62] or the antibacterial and mitochondrial membrane-disruptive artificial peptide KLK.[63,64] Endogenous cellular CytC represents an essential part of the electron transfer chain in mitochondria but also a crucial player in the intrinsic mitochondrial apoptosis pathway after release into the cytosol.[65] Several approaches for the intracellular delivery of exogenous CytC, induction of apoptosis and cell killing have been reported before.[66−69] Notably, for the purification of H_6-CytC (and H_6-Tf*) carrying a H_6-tag after chemical conjugation, immobilized metal-ion chromatography was used, which is based on the same principle as the binding to

DOI: 10.1021/jacs.6b11934
J. Am. Chem. Soc. 2017, 139, 2359−2368

MOFs. The utilization of the same interaction for isolation and subsequent attachment to the carrier system is considered a very convenient and robust manufacturing process. Binding of the pro-apoptotic factors to Zr-*fum* NPs was confirmed by measuring the change of zeta potential upon addition of the MOFs (Figure S30a). For biological evaluation, HeLa cells were treated with Zr-*fum*/H_6-Bak, /H_6-Bad, /H_6-KLK, or /H_6-CytC (0.2 mg/mL Zr-*fum* and 10 μM peptide or protein) for 48 h. Cell viability was assessed by MTT assay and approximately 60% cell killing could be detected in case of all functionalized Zr-*fum* NPs (Figure 8).

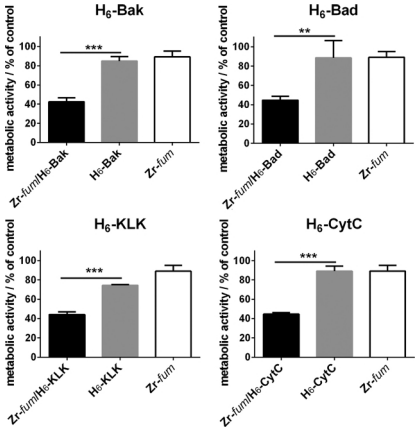

Figure 8. Intracellular transport of pro-apoptotic factors by Zr-*fum* MOF NPs and induction of HeLa cell killing upon incubation for 48 h. Final concentration of H_6-Bak, H_6-Bad, H_6-KLK, and H_6-CytC was 10 μM (0.2 mg Zr-*fum*/10 nmol His-tag per mL medium). Data are presented as percent of metabolic activity of control cells ± SD (n = 3) (MTT assay).

Without the addition of MOF NPs all pro-apoptotic factors did not exhibit any detectable toxicity up to a concentration of 20 μM (Figure S30b). These findings indicate that, despite the bottleneck of vesicular entrapment, significant fractions of cargo molecules were able to escape and induce biological effects in the cytosol.

CONCLUSION

In summary, the proposed coordinative interaction of functionalized His-tags with MOF NPs was successfully established, exhibiting His-tag length and MOF species dependent binding. The fact that all investigated MOF structures showed considerable H_6-tag binding, despite their different metal components, provided flexibility for consideration of additional parameters and material characteristics (e.g., particle size distribution, aggregation behavior, fluorescence quenching and cytotoxicity) relevant for the intended purpose. The inherent properties of the individual compounds (His-tag containing functional units, MOF NPs) and the reversible nature of interaction account for the strength of the approach. Numerous available recombinant proteins already contain His-tags or they can readily be integrated in peptidic structures by conjugation. For biomedical applications, MOF NPs are promising materials due to their precise assembly of an enormous number of inorganic and organic molecular building blocks resulting in a highly variable chemical composition, porosity and degradability into their small building units. The MOF structural designability at the molecular level chemistry together with an extension of the functional unit library opens the perspective to generate a variety of "self-assembling multifunctional coordination particles" (SAMCOPs) by simple combinatorial and stoichiometric mixing. In this respect, this work presents a versatile functionalization concept of MOF NPs with great potential for co-delivery of proteins, drugs, or other pharmacologically active agents, including those that can be adsorbed within the pore systems.

METHODS

Synthesis of MIL-88A. MIL-88A was synthesized using an approach based on the results of Chalati et al.[52] $FeCl_3{\cdot}6H_2O$ (1.084 g, 4.01 mmol) and fumaric acid (485 mg, 4.18 mmol) were given into water (20 mL). After $FeCl_3{\cdot}6H_2O$ was completely dissolved, the reaction vessel was placed in a microwave reactor (Synthos 3000, Anton Paar). In addition to the reaction vessel, a reference vessel containing an aqueous solution of $FeCl_3{\cdot}6H_2O$ (1.080 g, 20 mL) and two vessels containing water (20 mL) were placed in the microwave reactor. The sample was heated in 30 s to 80 °C, stayed at 80 °C for 5 min and cooled down to room temperature in 1 h.

Synthesis of HKUST-1. The synthesis of HKUST-1 was conducted following a method shown by Huo et al.[47] $Cu(NO_3)_2{\cdot}2.5H_2O$ (70 mg, 0.30 mmol) was dissolved in water (6 mL). Trimesic acid (126 mg, 0.60 mmol) was added to this solution under stirring. The reaction mixture was left stirring for 60 min. Subsequently, the resulting product was washed via centrifugation (15 min, 8750 rpm). The supernatant was removed and the precipitated nanoparticles were dispersed in ethanol (6 mL). This washing cycle was repeated three times to yield the final product.

Synthesis of Zr-*fum*. Zr-*fum* were synthesized using an approach based on the results of Wißmann et al.[48] $ZrCl_4$ (120.4 mg, 0.52 mmol) and fumaric acid (180.1 mg, 1.54 mmol) were given into a glass vessel (25 mL). A mixture of water (10 mL) and formic acid (975 μL) was added to the glass reactor. After sealing the reactor the dispersion was placed in an oven (120 °C) for 24 h. Subsequently, the reaction mixture was cooled down to room temperature followed by separation into eight equal portions. The nanoparticle dispersions were washed in a first step via centrifugation (4 min, 14 000 rpm) and subsequent redispersion in water (8 × 1.5 mL) under sonication. The samples were further washed in three additional washing cycles comprising centrifugation (4 min, 14 000 rpm), removal of the supernatant, and redispersion of the remaining nanoparticles in ethanol (8 × 1.5 mL). Afterward, the eight dispersions were reunified.

Preparation of MOF Suspension in HBG. MOF suspensions in HBG were always freshly prepared prior to performing the experiment. The necessary amount of MOF material in ethanol was centrifuged (10 min, 10 000 rpm), and the supernatant was removed. The MOF pellet was resuspended in HBG (pH 7.4) at a final concentration of 5 or 10 mg/mL by continuous pipetting, followed by 10 min sonication.

Investigation of Peptide Binding (A_6, H_6) by RP-HPLC. Three μL of a solution containing equimolar amounts of H_6–Acr and A_6-Acr (5 mM) in HBG (pH 7.4) were added to 47 μL HBG in a 1.5 mL reaction tube. 100 μL of MOF suspension (5 mg/mL in HBG, pH 7.4) were added and vortexed briefly. As control, 100 μL HBG without MOF particles were added to an analogous sample. The mixtures were incubated at room temperature for 15 min under shaking and centrifuged for 10 min at 13 400 rpm. Subsequently, the supernatant (120 μL) was transferred into HPLC sample vials. RP-HPLC analysis was carried out using a YMC Pack Pro C18 RS column (250 × 4.6 mm) connected to a VWR Hitachi Chromaster HPLC system (5160 pump module, 5260 auto sampler, 5310 column oven, 5430 diode array detector). A volume of 10 μL of the samples was injected, and a gradient from 5% acetonitrile (0.1% TFA) to 100% acetonitrile (0.1% TFA) over 15 min was used for the analysis. Acridine containing compounds were detected photometrically at 360 nm.

Zeta Potential Measurements of MOF Nanoparticle Functionalization. H_6-Acr or A_6-Acr (3 nmol) was diluted in HBG (pH 7.4) buffer. In case of pro-apoptotic peptides and CytC, an amount of 5 nmol was used. Next, the amount of 100 μg of MOF NPs (5 mg/mL, HBG pH 7.4) was added (final volume 30 μL) and samples were incubated at room temperature for 15 min with shaking. Shortly before the measurement in a folded capillary cell (DTS1070), samples were diluted to a final MOF concentration of 0.1 mg/mL. Zeta potential was measured by electrophoretic laser-light scattering using a Zetasizer Nano ZS (Malvern Instruments, Worcestershire, U.K.). Zeta potentials were calculated by using the Smoluchowski equation, and each sample was measured three times with 10 to 30 subruns at 25 °C.

Quantitative Determination of H_0-, H_3-, and H_6-Acr Binding to MOF NPs. A solution containing a total amount of 130 nmol oligopeptide-based structure to be examined was prepared in HBG. The required amount of 10 mg/mL MOF nanoparticles dispersed in HBG was added featuring a total volume of 1 mL. Right after the addition of the MOF nanoparticles, samples were briefly vortexed. After subsequent incubation (15 min, 25 °C, 600 rpm) and centrifugation (5 min, 14 000 rpm), the supernatant (100 μL) was collected and photometrically measured at 360 nm against HBG as a blank. For each examined oligopeptide-based structure, a control of 130 nmol peptide without MOF in a total volume of 1 mL was also prepared and measured (n = 3). To obtain the amount of bound peptide, the absorption of the supernatant, representing the amount of peptide that remained in solution and thereby unbound by the MOF, was subtracted from the average absorption of the MOF free control: A(bound) = A(control) − A(supernatant). Final binding values were calculated as follows, %(bound) = A(bound)/A(control) × 100. The average of percent bound determined in three independent measurements ± SD was plotted.

Investigation of Binding Stability of H_6-tags to Zr-*fum* and pH Dependent Release. In order to evaluate the stable binding and extent of acidic release of His-tags and Zr-*fum* MOF NPs over a longer period, Zr-*fum* NPs in HBG were loaded with H_6-A647N. 50 μL of the freshly prepared Zr-*fum* NPs were diluted in ∼500 μL of HBG pH 7.4 (depending on the amount of HCl added to the sample in the next step), followed by addition of 4 μL of 1 mM H_6-A647N. The HBG volume therefore slightly varied in order to always allow for equal final sample volumes of 500 μL. Samples were briefly vortexed and incubated under agitation for 15 min (25 °C, 600 rpm, light protection). Afterward, samples were acidified to pH 3, pH 5, and pH 7.4 by addition of 9.2, 4.5, or 0 μL of 1 M HCl, respectively. After 0.5, 3, and 24 h, the respective samples were centrifuged (5 min, 14 000 rpm). The presence of free dye in the supernatant was determined photometrically at 646 nm (n = 3). Independent samples were used for each time point.

Fluorescence Correlation Spectroscopy (FCS). The non-fluorescent MOF nanoparticles are not detectable by the FCS unless fluorescently labeled His-tags are attached to the NPs. Thus, a shift to higher diffusion times of the correlation curve after addition of NPs to fluorescently labeled His-tags certifies the binding of His-tags to the NPs surface. Normalization of autocorrelation curves helps to clearly visualize that the autocorrelation function of the MOF/His-tag is shifted toward higher correlation times with respect to the free His-tag molecules. Dual-color fluorescence cross-correlation spectroscopy (FCCS) allows for a comparison between spectrally separated channels to extract codiffusion events that reflect interactions between differently labeled molecules.[70,71] For FCS and FCCS measurements, an Axiovert 200 microscope with a ConfoCor 2unit (Carl Zeiss, Jena, Germany) equipped with a 40× (NA 1.2) water immersion apochromat objective (Carl Zeiss) was used. A helium neon laser (633 nm) and for FCCS additionally an argon laser (488 nm) was used for illumination. Samples were measured in eight-well LabTekchamber slides (Nunc, Rochester, NY). If nothing else mentioned, measurements were performed in HBG pH 7.4 at a temperature of 22.5 °C. Correlation was performed using ConfoCor 2 software. A detailed description of the various experimental setups of FCS and FCCS measurements and the theory of FCS can be found in the Supporting Information.

Cell Culture. HeLa cells were grown in Dulbecco's Modified Eagle's Medium (DMEM) (1000 mg/mL glucose, L-glutamine and sodium bicarbonate) supplemented with 10% FBS, 100 U/mL penicillin, 100 μg/mL streptomycin at 37 °C and 5% CO_2 in a humidified incubator.

Cellular Uptake Experiments Using Flow Cytometric Analysis. Cells were seeded in 24-well plates (Corning Costar, Sigma-Aldrich, Germany) at a density of 20 000 cells/well. After 24 h, medium was replaced with 400 μL of fresh medium. H_6-CF or H_6-GFP (0.5 nmol) was diluted in HBG (pH 7.4), 50 μg of MOF NPs (5 mg/mL in HBG, pH 7.4) were added (final volume 50 μL), and the solution was strongly mixed. For the co-delivery of H_6-GFP and H_6-Tf*, 0.25 nmol of H_6-GFP and 0.25 nmol of H_6-Tf* were premixed in HBG (pH 7.4) before the amount of 50 μg of Zr-*fum* MOF NPs (5 mg/mL in HBG, pH 7.4) was added (final volume 50 μL). The mixtures were incubated for 15 min at room temperature, diluted 1:2 with HBG (pH 7.4, final volume 100 μL), and added to the cells (100 μL MOF/His-tag solution per well). Controls were performed without the addition of MOF NPs. Cells were incubated for 24 h at 37 °C and 5% CO_2 in a humidified incubator. In the case of HKUST-1 MOF NPs, medium was changed after 2 h and cells were incubated for further 22 h in fresh medium. Cells were washed with PBS (pH 7.4), detached with trypsin/EDTA and diluted with fresh medium. Cells were centrifuged and resuspended in 500 μL PBS containing 10% FBS at pH 4 to quench extracellular fluorescence. DAPI (4′,6-diamidino-2-phenylindole) was added to a final concentration of 1 ng/μL shortly before the measurement. The cellular fluorescence was assayed by excitation of DAPI at 405 nm and detection of emission at 450 nm, fluorescein at 488 nm and detection of emission at 510 nm. For the co-delivery of H_6-GFP and H_6-Tf*, the cellular fluorescence was also assayed by excitation of A647N at 635 nm and detection of emission at 665 nm. Cells were appropriately gated by forward/sideward scatter and pulse width for exclusion of doublets. DAPI was used to discriminate between viable and dead cells. Data were recorded by Cyan ADP flow cytometer (Dako, Hamburg, Germany) using Summit acquisition software (Summit, Jamesville, NY). Ten thousand gated cells per sample were collected. Analysis was done by FlowJo 7.6.5 flow cytometric analysis software. All experiments were performed in triplicate. MFI was calculated by FlowJo 7.6.5 flow cytometric analysis software and is depicted as normalization to HBG ± SD (n = 3).

Confocal Laser Scanning Microscopy. Cells were seeded in 8-well Nunc chamber slights (Thermo Scientific, Germany) at a density of 12 000 cells/well. Wells were coated with collagen A prior to seeding. After 24 h, medium was replaced with 240 μL of fresh medium. The various samples were prepared in the same way as has been described above but in a final volume of 60 μL of HBG. MOF NPs (30 μg) were functionalized with 0.3 nmol of H_6-CF or H_6-GFP in 30 μL of HBG (pH 7.4). In the case of the co-delivery experiment, the amount of 0.15 nmol of H_6-GFP was mixed with 0.15 nmol of H_6-Tf* before the addition of 30 μg of Zr-fum MOF NPs. After incubation of the mixtures for 15 min at room temperature, they were diluted 1:2 in HBG (pH 7.4, final volume 60 μL). The mixtures were added to the cells (60 μL MOF/His-tag solution per well) and incubated for 24 h. Controls were performed without the addition of MOF NPs. In the case of HKUST-1 MOF NPs, the medium was changed after 2 h and cells were incubated for further 22 h in fresh medium. Prior to imaging, nuclei were stained with Hoechst dye (1 ng/μL). Medium was replaced by DMEM without phenol red supplemented with 10% FBS, 100 U/mL penicillin, and 100 μg/mL streptomycin, and cells were imaged using a Leica TCS SP8 confocal microscope with an 63× DIC oil immersion objective (Plan-APOCHROMAT). For imaging of z-stacks, cells were fixated for 30 min, using 4% (w/v) paraformaldehyde solution followed by three washes with PBS (pH 7.4). The nucleus was stained with DAPI (1 ng/μL) and actin with rhoadmine-phalloidin (2 μL/mL) for 15 min at room temperature. Staining solution was replaced with PBS (pH 7.4),

DOI: 10.1021/jacs.6b11934
J. Am. Chem. Soc. 2017, 139, 2359−2368

DOI: 10.1021/jacs.6b11934
J. Am. Chem. Soc. 2017, 139, 2359−2368

and cells were stored at 4 °C. Images were recorded with a *z*-distance of 0.3 μm from basolateral (top) to apical (bottom) pole of a representative cell. Pictures were taken at 405 nm (Hoechst dye or DAPI), 488 nm (H_6-GFP or H_6-CF), 514 nm (rhodamine-phalloidine), and 633 nm (ATTO 647N).

Endocytosis Inhibitory Assay. HeLa cells were seeded in 24-well plates (Corning Costar, Sigma-Aldrich, Germany) at a density of 50 000 cells/well. After 24 h, medium was replaced with 400 μL fresh medium containing the different endocytosis inhibitors, chlorpromazine (final concentration 5, 10, and 20 μM), amiloride (final concentration 1, 2, and 5 mM), and genistein (final concentration 100, 150, and 200 μM). Cells were preincubated with the different inhibitors or at 4 °C for 30 min before addition of the H_6-GFP/Zr-*fum* MOF NPs. 0.5 nmol H_6-GFP were diluted in HBG (pH 7.4), 50 μg Zr-*fum* MOF NPs (5 mg/mL in HBG, pH 7.4) were added (final volume 50 μL) and the solution was strongly mixed. The mixture was incubated for 15 min at room temperature, diluted 1:2 with HBG (pH 7.4, final volume 100 μL) and added to the cells (100 μL Zr-*fum*/H_6-GFP solution per well). Cells were incubated for 2 h at 37 °C and 5% CO_2 or at 4 °C. Cells were washed with PBS (pH 7.4), detached with trypsin/EDTA, and diluted with fresh medium. Cells were centrifuged and resuspended in 500 μL of PBS containing 10% FBS at pH 4 to quench extracellular fluorescence. DAPI (1 ng/μL) was added shortly before the measurement. The cellular fluorescence was assayed by excitation of DAPI at 405 nm and detection of emission at 450 nm, and fluorescein at 488 nm and detection of emission at 510 nm. Cells were appropriately gated by forward/sideward scatter and pulse width for exclusion of doublets. DAPI was used to discriminate between viable and dead cells. Data were recorded by Cyan ADP flow cytometer (Dako, Hamburg, Germany) using Summit acquisition software (Summit, Jamesville, NY). Five thousand gated cells per sample were collected. Analysis was done by using FlowJo 7.6.5 flow cytometric analysis software. Data is presented as percentage of cellular uptake of Zr-*fum*/H_6-GFP NPs at 37 °C ± SD (n = 3).

Delivery of Pro-apoptopic Peptides and CytC. Cells were seeded in 96-Well plates (Corning Costar, Sigma-Aldrich, Germany) at a density of 4000 cells/well. After 24 h, medium was replaced with 80 μL fresh medium. Then 1 nmol of H_6-Bak, H_6-Bad, H_6-KLK, or H_6-CytC was diluted in HBG (pH 7.4), and the amount of 20 μg of Zr-*fum* MOF NPs (5 mg/mL in HBG pH 7.4) was added followed by strongly mixing of the samples (final volume 10 μL). Controls were performed without the addition of Zr-*fum* MOF NPs. The mixtures were incubated for 15 min at room temperature, diluted 1:2 with HBG (pH 7.4, final volume 20 μL), added to the cells (20 μL Zr-*fum*/His-tag solution per well), and incubated for 48 h. Analysis of cytotoxicity was carried out by MTT assay, as is described in the following.

Cell Viability Assay. Cells were seeded in 96-well plates (Corning Costar, Sigma-Aldrich, Germany) at a density of 4000 cells/well. After 24 h, medium was replaced with 80 μL of fresh medium. The appropriate amount of compound to be tested was diluted in HBG (pH 7.4), and a sample volume of 20 μL was added per well. Cells were incubated for 48 h at 37 °C and 5% CO_2 in a humified incubator. Then a solution of MTT (3-(4,5-dimethylthiazol-2-yl)-2,5-diphenyltetrazolium bromide) (10 μL, 5 mg/mL) was added to each well, reaching a final concentration of 0.5 mg/mL. After an incubation time of 2 h, unreacted dye and medium were removed and the 96-well plates were frozen at −80 °C for at least 30 min. To dissolve the purple formazan product, DMSO (100 μL/well) was added and the plate was incubated for 30 min at 37 °C with shaking. The wells were quantified by measuring absorbance at 590 nm with background correction at 630 nm using a microplate reader (TecanSpectrafluor Plus, Tecan, Switzerland). All studies were performed in triplicate. The relative cell viability (%) related to control wells treated only with 20 μL of HBG (pH 7.4) was calculated as ([A] test/[A] control) × 100%.

Statistical Analysis. The statistical significance of experiments was analyzed using the t test; ****$p \leq 0.0001$, ***$p \leq 0.001$, **$p \leq 0.01$, and *$p \leq 0.05$.

■ ASSOCIATED CONTENT

Supporting Information

The Supporting Information is available free of charge on the ACS Publications website at DOI: 10.1021/jacs.6b11934.

Additional materials and methods, synthesis and analysis of peptides and His-tagged functional units, characterization of MOF NPs (PDF)

Movie demonstrating the binding of H_6-A647N to HKUST-1 MOF NPs visualized by decoloration of the supernatant after centrifugation (AVI)

Three-dimensional reconstruction movie of a HeLa cell treated with Zr-*fum*/H_6-GFP (AVI)

■ AUTHOR INFORMATION

Corresponding Authors

*ulrich.laechelt@cup.uni-muenchen.de

*stefan.wuttke@cup.lmu.de

ORCID

Ernst Wagner: 0000-0001-8413-0934

Ulrich Lächelt: 0000-0002-4996-7592

Notes

The authors declare no competing financial interest.

■ ACKNOWLEDGMENTS

We are grateful for financial support from the Excellence Cluster Nanosystems Initiative Munich (NIM) and the Center for NanoScience Munich (CeNS). Funding through the DFG SFB 1032 and DFG project WU 622/4-1 is greatly appreciated. We thank Olga Brück and Wofgang Rödl for technical assistance and appreciate the help of cameraman Michael Beetz.

■ REFERENCES

(1) Goesmann, H.; Feldmann, C. *Angew. Chem., Int. Ed.* **2010**, *49*, 1362.

(2) Tibbitt, M. W.; Dahlman, J. E.; Langer, R. *J. Am. Chem. Soc.* **2016**, *138*, 704.

(3) Calandra, P.; Caschera, D.; Turco Liveri, V.; Lombardo, D. *Colloids Surf., A* **2015**, *484*, 164.

(4) Torchilin, V. P. *Pharm. Res.* **2007**, *24*, 1.

(5) Nishiyama, N.; Matsumura, Y.; Kataoka, K. *Cancer Sci.* **2016**, *107*, 867.

(6) Discher, B. M.; Won, Y. Y.; Ege, D. S.; Lee, J. C.; Bates, F. S.; Discher, D. E.; Hammer, D. A. *Science* **1999**, *284*, 1143.

(7) Davis, M. E. *Mol. Pharmaceutics* **2009**, *6*, 659.

(8) Park, I. K.; von Recum, H. A.; Jiang, S.; Pun, S. H. *Langmuir* **2006**, *22*, 8478.

(9) Sanvicens, N.; Marco, M. P. *Trends Biotechnol.* **2008**, *26*, 425.

(10) Jia, F.; Liu, X.; Li, L.; Mallapragada, S.; Narasimhan, B.; Wang, Q. *J. Controlled Release* **2013**, *172*, 1020.

(11) Torchilin, V. P. *Annu. Rev. Biomed. Eng.* **2006**, *8*, 343.

(12) Fu, A.; Tang, R.; Hardie, J.; Farkas, M. E.; Rotello, V. M. *Bioconjugate Chem.* **2014**, *25*, 1602.

(13) Furukawa, H.; Cordova, K. E.; O'Keeffe, M.; Yaghi, O. M. *Science* **2013**, *341*, 1230444.

(14) Zhou, H. C.; Long, J. R.; Yaghi, O. M. *Chem. Rev.* **2012**, *112*, 673.

(15) Zhou, H. C.; Kitagawa, S. *Chem. Soc. Rev.* **2014**, *43*, 5415.

(16) Horcajada, P.; Chalati, T.; Serre, C.; Gillet, B.; Sebrie, C.; Baati, T.; Eubank, J. F.; Heurtaux, D.; Clayette, P.; Kreuz, C.; Chang, J. S.; Hwang, Y. K.; Marsaud, V.; Bories, P. N.; Cynober, L.; Gil, S.; Ferey, G.; Couvreur, P.; Gref, R. *Nat. Mater.* **2010**, *9*, 172.

(17) Baati, T.; Horcajada, P.; Gref, R.; Couvreur, P.; Serre, C. *J. Pharm. Biomed. Anal.* **2011**, *56*, 758.

(18) Wuttke, S.; Zimpel, A.; Bein, T.; Braig, S.; Stoiber, K.; Vollmar, A.; Muller, D.; Haastert-Talini, K.; Schaeske, J.; Stiesch, M.; Zahn, G.; Mohmeyer, A.; Behrens, P.; Eickelberg, O.; Bolukbas, D. A.; Meiners, S. *Adv. Healthcare Mater.* **2017**, *6*, 1600818.

(19) Taylor-Pashow, K. M.; Della Rocca, J.; Xie, Z.; Tran, S.; Lin, W. *J. Am. Chem. Soc.* **2009**, *131*, 14261.

(20) Zheng, H.; Zhang, Y.; Liu, L.; Wan, W.; Guo, P.; Nystrom, A. M.; Zou, X. *J. Am. Chem. Soc.* **2016**, *138*, 962.

(21) Yang, Y.; Hu, Q.; Zhang, Q.; Jiang, K.; Lin, W.; Yang, Y.; Cui, Y.; Qian, G. *Mol. Pharmaceutics* **2016**, *13*, 2782.

(22) Wuttke, S.; Braig, S.; Preiss, T.; Zimpel, A.; Sicklinger, J.; Bellomo, C.; Radler, J. O.; Vollmar, A. M.; Bein, T. *Chem. Commun. (Cambridge, U. K.)* **2015**, *51*, 15752.

(23) He, C.; Lu, K.; Liu, D.; Lin, W. *J. Am. Chem. Soc.* **2014**, *136*, 5181.

(24) Tan, L.-L.; Li, H.; Qiu, Y.-C.; Chen, D.-X.; Wang, X.; Pan, R.-Y.; Wang, Y.; Zhang, S. X.-A.; Wang, B.; Yang, Y.-W. *Chem. Sci.* **2015**, *6*, 1640.

(25) Wang, X. G.; Dong, Z. Y.; Cheng, H.; Wan, S. S.; Chen, W. H.; Zou, M. Z.; Huo, J. W.; Deng, H. X.; Zhang, X. Z. *Nanoscale* **2015**, *7*, 16061.

(26) Levine, D. J.; Runcevski, T.; Kapelewski, M. T.; Keitz, B. K.; Oktawiec, J.; Reed, D. A.; Mason, J. A.; Jiang, H. Z.; Colwell, K. A.; Legendre, C. M.; FitzGerald, S. A.; Long, J. R. *J. Am. Chem. Soc.* **2016**, *138*, 10143.

(27) Zhuang, J.; Kuo, C. H.; Chou, L. Y.; Liu, D. Y.; Weerapana, E.; Tsung, C. K. *ACS Nano* **2014**, *8*, 2812.

(28) Wuttke, S.; Lismont, M.; Escudero, A.; Rungtaweevoranit, B.; Parak, W. J. *Biomaterials* **2017**, DOI: 10.1016/j.biomaterials.2017.01.025.

(29) Liang, K.; Ricco, R.; Doherty, C. M.; Styles, M. J.; Bell, S.; Kirby, N.; Mudie, S.; Haylock, D.; Hill, A. J.; Doonan, C. J.; Falcaro, P. *Nat. Commun.* **2015**, *6*, 7240.

(30) Liang, K.; Coghlan, C. J.; Bell, S. G.; Doonan, C.; Falcaro, P. *Chem. Commun. (Cambridge, U. K.)* **2016**, *52*, 473.

(31) Lu, K.; He, C.; Lin, W. *J. Am. Chem. Soc.* **2015**, *137*, 7600.

(32) Park, J.; Feng, D.; Yuan, S.; Zhou, H. C. *Angew. Chem., Int. Ed.* **2015**, *54*, 430.

(33) Liu, J.; Yang, Y.; Zhu, W.; Yi, X.; Dong, Z.; Xu, X.; Chen, M.; Yang, K.; Lu, G.; Jiang, L.; Liu, Z. *Biomaterials* **2016**, *97*, 1.

(34) Lismont, M.; Dreesen, L.; Wuttke, S. *Adv. Funct Mater.* **2017**, DOI: 10.1002/adfm.201606314.

(35) Horcajada, P.; Gref, R.; Baati, T.; Allan, P. K.; Maurin, G.; Couvreur, P.; Ferey, G.; Morris, R. E.; Serre, C. *Chem. Rev.* **2012**, *112*, 1232.

(36) Rungtaweevoranit, B.; Zhao, Y.; Min Choi, K.; Yaghi, O. M. *Nano Res.* **2016**, *9*, 47.

(37) Furukawa, S.; Reboul, J.; Diring, S.; Sumida, K.; Kitagawa, S. *Chem. Soc. Rev.* **2014**, *43*, 5700.

(38) He, C.; Liu, D.; Lin, W. *Chem. Rev.* **2015**, *115*, 11079.

(39) Zimpel, A.; Preiß, T.; Röder, R.; Engelke, H.; Ingrisch, M.; Peller, M.; Rädler, J. O.; Wagner, E.; Bein, T.; Lächelt, U.; Wuttke, S. *Chem. Mater.* **2016**, *28*, 3318.

(40) McGuire, C. V.; Forgan, R. S. *Chem. Commun.* **2015**, *51*, 5199.

(41) Block, H.; Maertens, B.; Spriestersbach, A.; Brinker, N.; Kubicek, J.; Fabis, R.; Labahn, J.; Schafer, F. *Methods Enzymol.* **2009**, *463*, 439.

(42) Hochuli, E.; Bannwarth, W.; Döbeli, H.; Gentz, R.; Stuber, D. *Bio/Technology* **1988**, *6*, 1321.

(43) June, R. K.; Gogoi, K.; Eguchi, A.; Cui, X. S.; Dowdy, S. F. *J. Am. Chem. Soc.* **2010**, *132*, 10680.

(44) Wieneke, R.; Laboria, N.; Rajan, M.; Kollmannsperger, A.; Natale, F.; Cardoso, M. C.; Tampe, R. *J. Am. Chem. Soc.* **2014**, *136*, 13975.

(45) Postupalenko, V.; Desplancq, D.; Orlov, I.; Arntz, Y.; Spehner, D.; Mely, Y.; Klaholz, B. P.; Schultz, P.; Weiss, E.; Zuber, G. *Angew. Chem., Int. Ed.* **2015**, *54*, 10583.

(46) Chiu, H. Y.; Deng, W.; Engelke, H.; Helma, J.; Leonhardt, H.; Bein, T. *Sci. Rep.* **2016**, *6*, 25019.

(47) Huo, J.; Brightwell, M.; El Hankari, S.; Garai, A.; Bradshaw, D. *J. Mater. Chem. A* **2013**, *1*, 15220.

(48) Wißmann, G.; Schaate, A.; Lilienthal, S.; Bremer, I.; Schneider, A. M.; Behrens, P. *Microporous Mesoporous Mater.* **2012**, *152*, 64.

(49) Zahn, G.; Schulze, H. A.; Lippke, J.; König, S.; Sazama, U.; Fröba, M.; Behrens, P. *Microporous Mesoporous Mater.* **2015**, *203*, 186.

(50) Ueda, E. K.; Gout, P. W.; Morganti, L. *Journal of chromatography. A* **2003**, *988*, 1.

(51) Gaberc-Porekar, V.; Menart, V. *J. Biochem. Biophys. Methods* **2001**, *49*, 335.

(52) Chalati, T.; Horcajada, P.; Gref, R.; Couvreur, P.; Serre, C. *J. Mater. Chem.* **2011**, *21*, 2220.

(53) Baati, T.; Njim, L.; Neffati, F.; Kerkeni, A.; Bouttemi, M.; Gref, R.; Najjar, M.; Zakhama, A.; Couvreur, P.; Serre, C.; Horcajada, P. *Chem. Sci.* **2013**, *4*, 1597.

(54) Lin, K.-Y. A.; Chang, H.-A.; Hsu, C.-J. *RSC Adv.* **2015**, *5*, 32520.

(55) McKinlay, A. C.; Eubank, J. F.; Wuttke, S.; Xiao, B.; Wheatley, P. S.; Bazin, P.; Lavalley, J.-C.; Daturi, M.; Vimont, A.; De Weireld, G.; Horcajada, P.; Serre, C.; Morris, R. E. *Chem. Mater.* **2013**, *25*, 1592.

(56) Hirschle, P.; Preiß; Auras, F.; Pick, A.; Volkner, J.; Valdeperez, D.; Witte, G.; Parak, W. J.; Radler, J. O.; Wuttke, S. *CrystEngComm* **2016**, *18*, 4359.

(57) Tay, C. Y.; Setyawati, M. I.; Xie, J.; Parak, W. J.; Leong, D. T. *Adv. Funct. Mater.* **2014**, *24*, 5936.

(58) Martin, R.; Edsall, J. *J. Am. Chem. Soc.* **1960**, *82*, 1107.

(59) Dietl, C.; Hintz, H.; Ruhle, B.; Schmedt Auf der Gunne, J.; Langhals, H.; Wuttke, S. *Chem. - Eur. J.* **2015**, *21*, 10714.

(60) Wuttke, S.; Dietl, C.; Hinterholzinger, F. M.; Hintz, H.; Langhals, H.; Bein, T. *Chem. Commun. (Cambridge, U. K.)* **2014**, *50*, 3599.

(61) Orellana-Tavra, C.; Mercado, S. A.; Fairen-Jimenez, D. *Adv. Healthcare Mater.* **2016**, *5*, 2261.

(62) Li, R.; Boehm, A. L.; Miranda, M. B.; Shangary, S.; Grandis, J. R.; Johnson, D. E. *Neoplasia* **2007**, *9*, 801.

(63) Javadpour, M. M.; Juban, M. M.; Lo, W. C.; Bishop, S. M.; Alberty, J. B.; Cowell, S. M.; Becker, C. L.; McLaughlin, M. L. *J. Med. Chem.* **1996**, *39*, 3107.

(64) Ellerby, H. M.; Arap, W.; Ellerby, L. M.; Kain, R.; Andrusiak, R.; Rio, G. D.; Krajewski, S.; Lombardo, C. R.; Rao, R.; Ruoslahti, E.; Bredesen, D. E.; Pasqualini, R. *Nat. Med.* **1999**, *5*, 1032.

(65) Bratton, S. B.; Salvesen, G. S. *J. Cell Sci.* **2010**, *123*, 3209.

(66) Kim, S. K.; Foote, M. B.; Huang, L. *Biomaterials* **2012**, *33*, 3959.

(67) Zhang, J.; Wu, L.; Meng, F.; Wang, Z.; Deng, C.; Liu, H.; Zhong, Z. *Langmuir* **2012**, *28*, 2056.

(68) Ng, D. Y.; Fahrer, J.; Wu, Y.; Eisele, K.; Kuan, S. L.; Barth, H.; Weil, T. *Adv. Healthcare Mater.* **2013**, *2*, 1620.

(69) Mendez, J.; Morales Cruz, M.; Delgado, Y.; Figueroa, C. M.; Orellano, E. A.; Morales, M.; Monteagudo, A.; Griebenow, K. *Mol. Pharmaceutics* **2014**, *11*, 102.

(70) Schwille, P.; Meyer-Almes, F. J.; Rigler, R. *Biophys. J.* **1997**, *72*, 1878.

(71) Rigler, R.; Földes-Papp, Z.; Meyer-Almes, F. J.; Sammet, C.; Volcker, M.; Schnetz, A. *J. Biotechnol.* **1998**, *63*, 97.

Supporting Information

Multifunctional nanoparticles by coordinative self-assembly of His-tagged units with metal-organic frameworks

Ruth Röder, Tobias Preiß, Patrick Hirschle, Benjamin Steinborn, Andreas Zimpel, Miriam Höhn, Joachim O. Rädler, Thomas Bein, Ernst Wagner, Stefan Wuttke, and Ulrich Lächelt**

Pharmaceutical Biotechnology, Department of Pharmacy and Center for NanoScience (CeNS), LMU Munich, Butenandtstraße 5-13, 81377 Munich (Germany)

Department of Physics and Center for NanoScience (CeNS), LMU Munich, Geschwister-Scholl-Platz 1, 80539 Munich (Germany)

Department of Chemistry and Center for NanoScience (CeNS), LMU Munich, Butenandtstraße 11, 81377 Munich (Germany)

**E-Mail corresponding authors: ulrich.laechelt@cup.uni-muenchen.de*
stefan.wuttke@cup.uni-muenchen.de

Table of Contents

1 MOF Synthesis and Characterization

1.1 Synthesis of MIL-88A

MIL-88A were synthesized using an approach based on the results of Chalati *et al.*[1]: $FeCl_3 \cdot 6\ H_2O$ (1.084 g, 4.01 mmol) and fumaric acid (485 mg, 4.18 mmol) were given into water (20 mL). After $FeCl_3 \cdot 6\ H_2O$ was completely dissolved, the reaction vessel was placed in a microwave reactor (Synthos3000, Anton Paar). In addition to the reaction vessel, a reference vessel containing an aqueous solution of $FeCl_3 \cdot 6\ H_2O$ (1.080 g, 20 mL) and 2 vessels containing water (20 mL) were placed in the microwave reactor. The sample was heated with the following temperature program:

Table S1. Temperature program applied during the synthesis of MIL-88A

Heating to 80 °C	Staying at 80 °C	Cooling down to RT
30 s	5 min	1 h

After cooling down, the product was washed via centrifugation (20000 rpm, 45 min), removal of the supernatant and redispersion of the pellet in ethanol (30 mL). This step was repeated 3 times. To separate nanoparticles from bulk material the sample was centrifuged (3000 rpm, 3 min) followed by discarding of the pellet.

1.2 Synthesis of HKUST-1

The synthesis of HKUST-1 was conducted following a method shown by Huo *et al.*[2]: $Cu(NO_3)_2$ x 2.5 H_2O (70 mg, 0.30 mmol) was dissolved in water (6 mL). Trimesic acid (126 mg, 0.60 mmol) was added to this solution under stirring. The reaction mixture was left stirring for 60 min. Subsequently, the resulting product was washed via centrifugation (15 min, 8750 rpm). The supernatant was removed and the precipitated nanoparticles were dispersed in ethanol (6 mL). This washing cycle was repeated three additional times to yield the final product.

1.3 Synthesis of Zr-*fum*

Zr-*fum* MOF nanoparticles were synthesized using an approach based on the results of Wißmann *et al.*[3]: $ZrCl_4$ (120.4 mg, 0.52 mmol) and fumaric acid (180.1 mg, 1.54 mmol) were given into a glass vessel (25 mL). A mixture of water (10 mL) and formic acid (975 µL) was

added to the glass reactor. After sealing the reactor the dispersion was placed in an oven (120 °C) for 24 h. Subsequently, the reaction mixture was cooled down to room temperature (RT) followed by separation into 8 equal portions. The nanoparticle dispersions were washed in a first step via centrifuging (4 min, 14000 rpm) and subsequent redispersion in water (8 x 1.5 mL) under sonication. The samples were further washed in 3 additional washing cycles comprising centrifugation (4 min, 14000 rpm), removal of the supernatant, and redispersion of the remaining nanoparticles in ethanol (8 x 1.5 mL). Afterwards, the 8 dispersions were reunified.

1.4 Dynamic Light Scattering

Dynamic light scattering (DLS) experiments were performed on a *Zetasizer Nano Series* (Nano-ZS, *Malvern*) with the employed laser operating at the wavelength λ = 633 nm. The measurements were conducted in ethanol immediately after synthesizing and washing of the particles and additionally in water. For the measurement of the MOF suspension in water, the MOFs were centrifuged (10 min, 10000 rpm), EtOH was removed and the pellet was resuspended in H_2O at a final concentration of 5 mg/mL followed by 10 min sonication.

The intensity based particle size distributions of each of the examined nanoparticle batches are shown in Figure S1. The corresponding intensity based particle diameters are given in Table S2 along with their polydispersity index.

In case of Zr-*fum* MOF NPs the initial Zr-*fum* nanoparticles and H_6-tagged Zr-*fum* nanoparticles in HBG buffer at pH 7.4 were compared both in DLS (Figure S2) and Scanning electron microscopy (Figure S16).

For the diameters in EtOH the average of two independent measurements was calculated. For the diameter in H_2O and HBG, the average of three independent measurements was calculated.

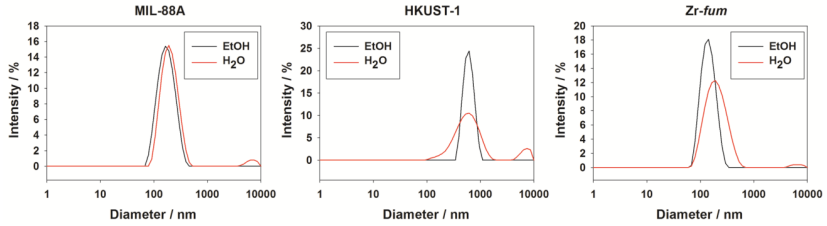

Figure S1. **Intensity based particle size distribution of MIL-88A (left), HKUST-1 (middle) and Zr-*fum* (right) measured in ethanol (black) and water (red).**

Table S2. **Intensity based particle diameters (z-Average) and polydispersity indices (PDI) of the respective MOF species in ethanol and water**

	EtOH		H_2O	
MOF	**Diameter [nm]**	**PDI**	**Diameter [nm]**	**PDI**
Zr-*fum*	132	0.091	182	0,205
MIL-88A	172	0.122	191	0,130
HKUST-1	600	0.166	530	0,290

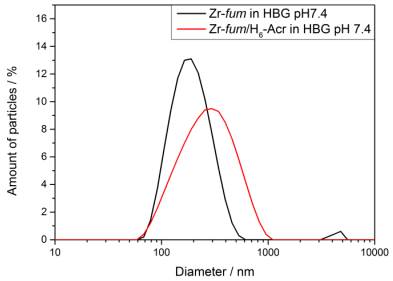

Figure S2. **Intensity based particle size distribution of Zr-*fum* prior (black) and after functionalization with H_6-Acr (red) measured in HBG pH 7.4.**

Zr-*fum* MOF NPs have a diameter of 177 nm. After functionalization with H_6-Acr the diameter increases slightly to 230 nm.

1.5 X-Ray Diffraction (XRD)

X-ray diffraction experiments were performed to confirm the successful synthesis of the respective MOF nanoparticles as well as to test their stability towards the media to which the nanoparticles were exposed to. For MIL-88A, X-ray diffraction experiments were conducted on a *D8 Discover* (*Bruker*), which was used to measure the samples in Bragg-Brentano geometry. The diffractometer was controlled with the included program *DIFFRAC plus XRD Commander v2.6.1*. In order to evaluate the data, the software *FileExchange v1.2.26* was utilized. In case of HKUST-1 and Zr-*fum,* these experiments were performed on a *STOE Transmissions-Diffraktometer System STADI P* that is measuring samples in transmission setup, a variant based on Debye-Scherrer geometry. Cu$K_{\alpha1}$-radiation was used in all experiments. For data analysis and simulation of diffraction patterns the built-in software *STOE WINXPOW v3.05*

including the software package *WinXPOW RawDat v3.0.2.5*, *WinXPOW PowDat_n v3.0.2.7* and WinXPOW the o v3.0.2.1 was utilized. The results are shown in Figure S3-S5.

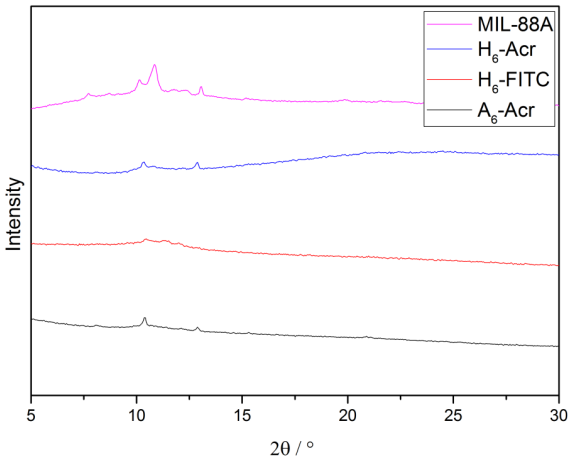

Figure S3. **XRD patterns of MIL-88A under different conditions.** Diffraction patterns of MIL-88A nanoparticles (pink) in comparison to acquired diffraction patterns of MIL-88A nanoparticles loaded with H_6-Acr (blue), loaded with H_6-FITC (red) and loaded with A_6-Acr (black). The initial MIL-88A nanoparticles show amorphous nature, which was expected taking into account the synthesis method and particle size [1].

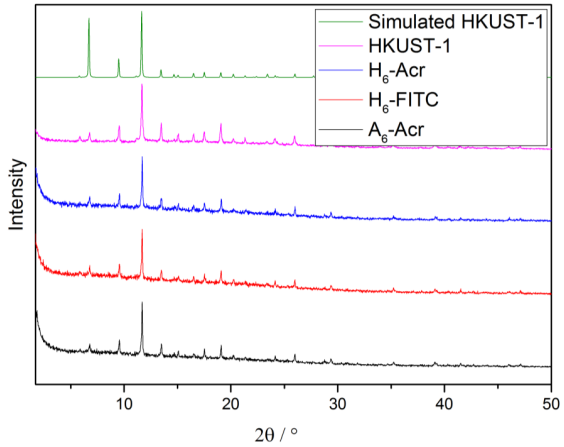

Figure S4. **XRD patterns of HKUST-1 under different conditions.** Diffraction patterns of HKUST-1 bulk material simulated from crystallographic data [4] (green) in comparison to acquired diffraction patterns of HKUST-1 nanoparticles (pink) and HKUST-1 nanoparticles loaded with H_6-Acr (blue), loaded with H_6-FITC (red) and loaded with A_6-Acr (black). The crystallinity and structure of all samples could be confirmed before and after loading.

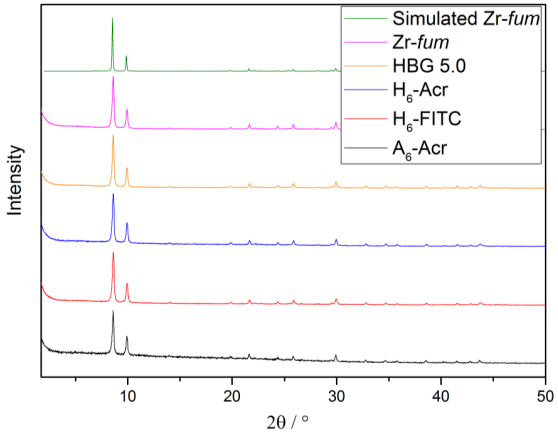

Figure S5. **XRD patterns of Zr-*fum* under different conditions.** Diffraction patterns of Zr-*fum* nanoparticles simulated from crystallographic data[3] (green) in comparison to acquired diffraction patterns of Zr-*fum* nanoparticles (*pink*), Zr-*fum* nanoparticles exposed to aqueous HBG buffer at pH 5.0 for two days (orange), Zr-*fum* nanoparticles loaded with H_6-Acr (blue), loaded with H_6-FITC (red) and loaded with A_6-Acr (black). The crystallinity and structure of all samples could be confirmed before and after loading.

1.6 Thermogravimetry

Thermogravimetric experiments were performed on all three MOF types on a *TASC 414/4 (Netzsch)* by heating the dried samples from room temperature to 900 °C employing a heating rate of 10 °C/min under synthetic air. The results were analyzed using the software Proteus v4.3.

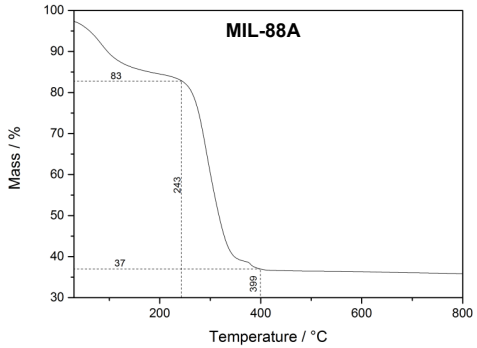

Figure S6. **Thermogravimetric Analysis of MIL-88A.**

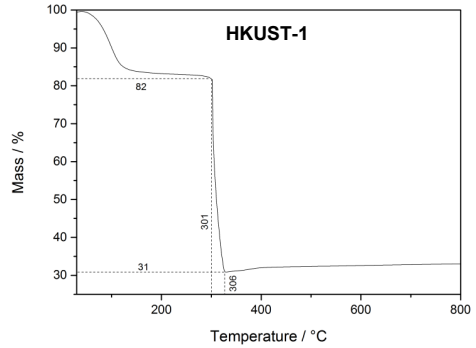

Figure S7. **Thermogravimetric Analysis of HKUST-1**

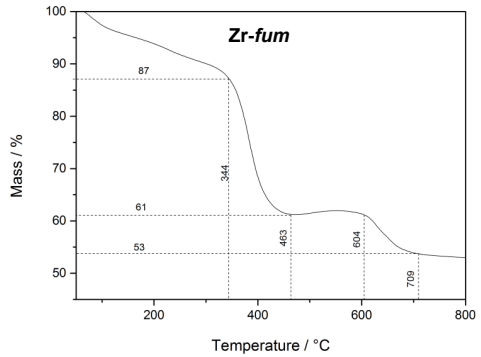

Figure S8. **Thermogravimetric Analysis of Zr-*fum*.**

1.7 Nitrogen sorption

All nitrogen sorption experiments were performed on an *Autosorb-1 (Quantachrome)*. Prior to the measurements, the samples were outgassed at 120 °C for 12 h. The measurement data was evaluated for their pore size distribution and BET surface area utilizing the corresponding software ASiQwin v3.0. Applying the linearized form of the BET equation Brunauer-Emmett-Teller (BET) surface areas of all samples were determined. The pore size distribution of all three samples was calculated using either a Non-local (NLDFT) or a quench solid density functional theory based method (QSDFT).

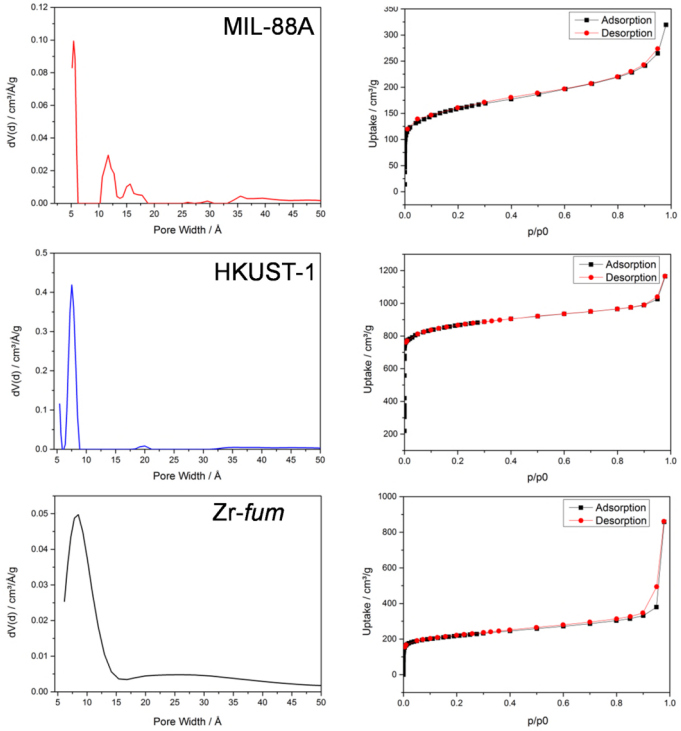

Figure S9. **Pore size distribution (left) and Sorption Isotherm (right) of MIL-88A (top), HKUST-1 (middle) and Zr-*fum* (bottom).**

Table S3. **BET surface areas and pore sizes of Zr-*fum*, MIL-88A and HKUST-1 as well as analysis details.**

Sample	Zr-*fum*	MIL-88A	HKUST-1
BET-surface area [m²/g]	797	576	3354
Relative pressure range	0.01404 – 0.08940	0.019230-0.132023	$1.06724*10^{-6}$ – 0.0406237
Correlation coefficient	0.999996	0.999996	0.99994
C-constant	Positive	Positive	Positive
Calculation-model	N_2 at 77K on carbon (slit/cylinder. pore, QSDFT equilibrium model)	N_2 at 77K on carbon (slit/cylinder. pore, NLDFT equilibrium model)	N_2 at 77K on carbon (slit/cylinder. pore, QSDFT equilibrium model)
Main Pore Size [Å]	8.520	5.450	7.530
Fitting Error [%]	1.504	0.582	1.021

1.8 Scanning electron microscopy

All three MOF species were measured on a *Helios NanoLab G3UC* (*FEI*) operating with 3 eV. Sample preparation was performed via drying the particles from ethanolic solutions followed by sputtering the respective MOFs with carbon. The resulting micrographs (Figure S10, S12, S14) were evaluated manually using the software ImageJ v1.49 for their particle diameter. The corresponding histograms are shown in Figure S11, S13 and Figure S15 in combination with the respective average particle size of the species as determined via the software Origin v9.0.0.

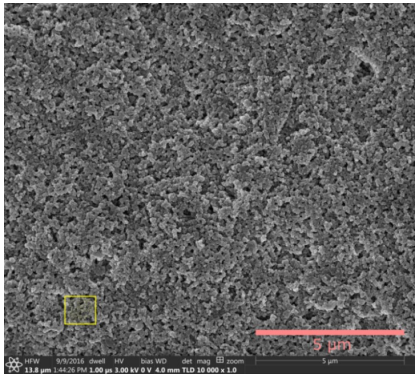

Figure S10. **SEM micrograph of MIL-88A MOF.** The particles measured for the corresponding particle size distribution shown in Figure S11 are marked with a yellow box. Scale bar: 5 µm.

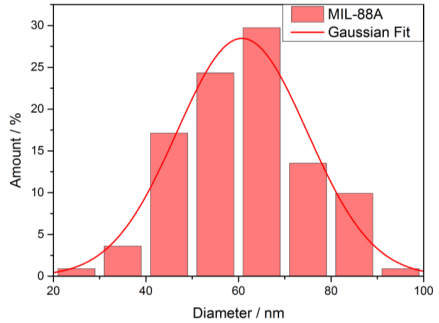

Figure S11. **Particle size distribution of MIL-88A.** The particle size was determined from the particles in the yellow box marked in Figure S10. The average particle size was determined to be 60 nm with a standard deviation of σ = 14 nm.

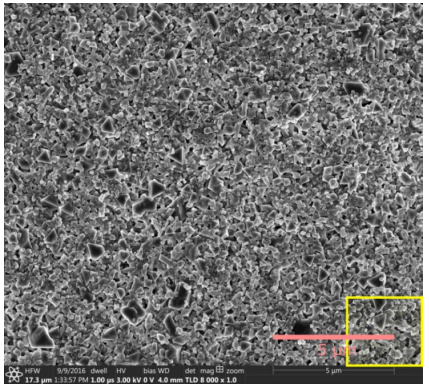

Figure S12. **SEM micrograph of HKUST-1 MOF.** The particles measured for the corresponding particle size distribution shown in Figure S13 are marked with a yellow box.

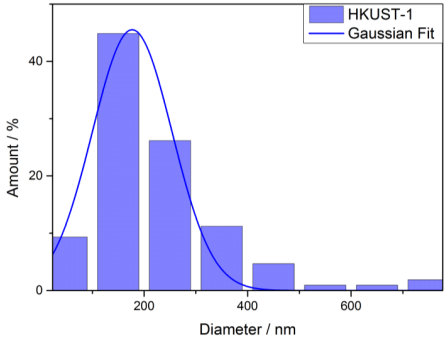

Figure S13. **Particle size distribution of HKUST-1.** The particle size was determined from the particles in the yellow box marked in Figure S12. The average particle size was determined to be 177 nm with a standard deviation of σ = 77 nm.

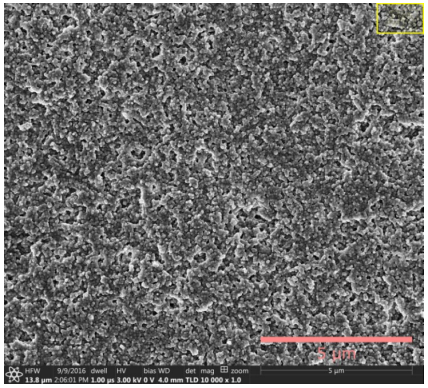

Figure S14. **SEM micrograph of Zr-*fum* MOF.** The particles measured for the corresponding particle size distribution shown in Figure S15 are marked with a yellow box.

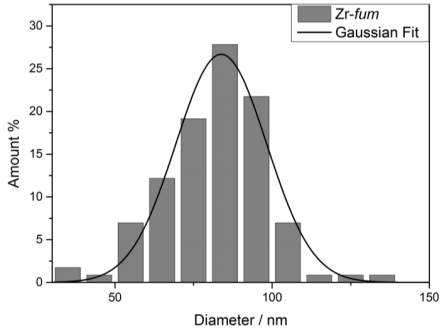

Figure S15. **Particle size distribution of Zr-*fum*.** The particle size was determined from the particles in the yellow box marked in Figure S14. The average particle size was determined to be 83 nm with a standard deviation of σ = 14 nm.

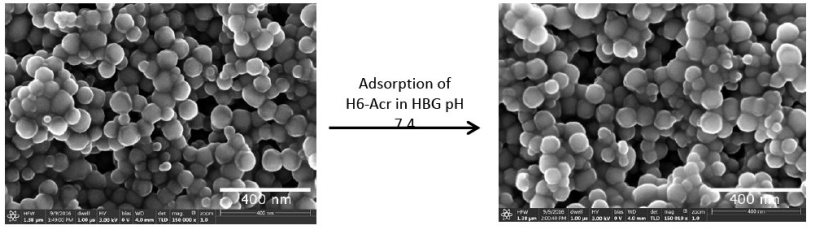

Figure S16. **SEM micrographs of Zr-*fum* MOF NP prior and after adsorption of H_6-Acr in HBG pH 7.4**

2 Materials and Methods

2.1 Material

HEPES was purchased from Biomol, collagen A from Merck KGaA (Darmstadt, Germany), DBCO-PEG_4-NHS ester from Jena Biosciences (Jena, Germany), TentaGel S RAM resin was obtained from Rapp Polymere GmbH (Tübingen, Germany). 2-Chlorotrityl chloride resin, all Fmoc or Boc protected α-amino acids, peptide grade dimethylformamide (DMF), N,N-diisopropylethylamine (DIPEA), piperidine, and trifluoroacetic acid (TFA) were purchased from Iris Biotech (Marktredwitz, Germany). Benzotriazol-1-yl-oxy-tris-pyrrolidi-no-phosphonium hexafluorophosphate (Pybop), N,N,N′,N′-tetramethyl-O-(1H-benzotriazol-1-yl)uroniumhexafluorophosphate (HBTU) and syringe microreactors were obtained from Multisyntech GmbH (Witten, Germany). Fmoc-N-amido-$dPEG_{12}$-acid and Fmoc-N-amido-$dPEG_{36}$-acid from Quanta Biodesign (Powell, USA), Fmoc-NH-(PEG)27-COOH (PEG_{28}) from Polypure (Oslo, Norway). HPLC grade acetonitrile was purchased from VWR (Darmstadt, Germany). Copper(II) nitrate hemipentahydrate (analytical grade) was purchased from Riedel-de Haën (Seelze, Germany). Ethanol (99.9 %) was bought from VWR (Darmstadt, Germany). Fumaric acid (≥ 99.5 %) was obtained from Fluka (Buchs, Switzerland). Iron(III) chloride hexahydrate (99 %) was purchased from Grüssing GmbH (Filsum, Germany). ATTO 647N NHS ester was obtained from ATTO-TEC GmbH (Siegen, Germany), 5(6)-carboxyfluorescein NHS ester from Sigma-Aldrich (Germany). 1-Hydroxy-benzotriazole (HOBt), N-Fmoc-N″-succinyl-4,7,10-trioxa-1,13-tridecanediamine (STOTDA), Fmoc-5-azido-L-norvaline (5ANV), triisopropylsilane (TIS), trimesic acid (95 %), zirconium(IV)chloride (≥ 95 %), dimethyl sulfoxide (DMSO), cytochrome C (equine heart), and all chemicals which are not listed were purchased from Sigma-Aldrich (Germany). Rhodamine phalloidine, antibiotics, fetal bovine serum (FBS) and cell culture medium were bought from Life Technologies (USA) or Sigma-Aldrich (Germany). HBG buffer containing 20 mM HEPES, 5 % glucose (w/v), adjusted to pH 7.4 and PBS adjusted to pH 7.4 or 4.0, were prepared in house. Water used during the nanoparticle synthesis was purified using a Mili-Q Academic A-10 system from Millipore (Billerica, USA).

Recombinant H_6-GFP was expressed and purified as has been reported previously[5].

Table S4. **Overview of synthesized peptides.**

Name	Sequence (N ->C)	Function
H_6-Acr	Acridine-PEG_{28}-H_6-NH_2	Photometric detection
A_6-Acr	Acridine-PEG_{28}-A_6-NH_2	Photometric detection
H_0-Acr	Acridine-STOTDA	Photometric detection
H_3-Acr	Acridine-STOTDA-H_3	Photometric detection
H_6-Acr	Acridine-STOTDA-H_6	Photometric detection
H_6-PEG_{12}	PEG_{12}-H_6-NH_2	Fluorescent labeling
H_6-PEG_{36}-5ANV	5-Azidonorvaline-PEG_{36}-H_6-NH_2	Azide-alkyne cycloaddition
H_6-Azide	6-AzidohexanoicAcid-H_6-NH_2	Azide-alkyne cycloaddition
H_6-Bak	H_6-GGQVGRQLAIIGDDINR-NH_2	Induction of cell death
H_6-Bad	H_6-GNLWAAQRYGRELRRMSDEFVD-NH_2	Induction of cell death
H_6-KLK	H_6-GGKLAKLAKKLAKLAK-NH_2	Induction of cell death

Name: notation as it appears in the text; sequence, from N- to C-terminus; function, utilization of peptide in the present work. α-amino acids are abbreviated in one-letter code; PEG_n: subscript n indicates number of repeating ethylene oxide units; STOTDA, N-succinyl-4,7,10-trioxa-1,13-tridecanediamine; 5ANV, 5-azidonorvaline.

Table S5. **Overview of synthesized peptide and protein conjugates.**

Name	Description	Conjugation units
H_6-A647N	ATTO647N-PEG_{12}-H_6-NH_2	ATTO 647N-NHS, H_6-PEG_{12}
H_6-CF	Carboxyfluorescein-PEG_{12}-H_6-NH_2	Carboxyfluorescein-NHS, H_6-PEG_{12}
H_6-Tf*	human serum transferrin conjugated with H_6-PEG_{36} and ATTO647N	Tf, DBCO-PEG_4-NHS, H_6-PEG_{36}-5ANV, ATTO647N-NHS
H_6-CytC	Equine heart cytochrome C, chemically conjugated with H_6	CytC, DBCO-PEG_4-NHS, H_6-Azide

Name, notation as it appears in the text; description of sequence (N- to C-terminus) or composition of conjugate; conjugation units, overview on conjugation partners during synthesis. α-amino acids are abbreviated in one-letter code; PEG_n, subscript n indicates number of repeating ethylene oxide units; A647N, ATTO 647N; CF, carboxyfluorescein; Tf, transferrin; CytC, cytochrome C; DBCO, dibenzocyclooctyne;5ANV, 5-azidonorvaline.

2.2 Peptide Synthesis

All peptides were synthesized on TentaGel S RAM (C-terminal amide) or 2-chlorotrityl chloride resin (C-terminal carboxylic acid) using an automated Syro Wave or semi-automated Initiator + SP Wave Peptide Synthesizer (Biotage, Uppsala, Sweden). The peptides were sequentially assembled from C- to N-terminus under standard Fmoc solid phase peptide synthesis conditions. Automated synthesis using the Syro Wave was carried out with HBTU as activating reagent and double-coupling steps. Semi-automated synthesis with the Initiator+ SP Wave and manual coupling steps were carried out with Pybop as activating reagent. Coupling steps were

carried out using 4 eq Fmoc L-amino acid (relative to free resin-bound amines), 4 eq HOBt, 4 eq activating reagent and 8 eq DIPEA in NMP–DMF 6 : 4 (7 mL per g resin) and 10 min incubation at 60 °C (60 min at room temperature during synthesis of pro-apoptotic peptides H_6-Bak, H_6-Bad, H_6-KLK and coupling of azide containing building blocks 5ANV or 6-azido-hexanoic acid). Fmoc deprotection was accomplished by 4 × 10 min incubation with 20 % piperidine in DMF (10 mL per g resin) at room temperature. After each coupling and deprotection step a washing procedure comprising 5 × 1 min DMF incubation (10 mL per g resin) was carried out. Finally, all peptides were cleaved off the resin by incubation with TFA–TIS–H_2O 95 : 2.5 : 2.5 (10 mL per g resin) for 90 min at room temperature. In case of intense yellow color of collected cleavage solution, TIS was added in small portions until decolorization occurred.

The cleavage solution was concentrated by evaporation under nitrogen stream and peptides were precipitated in 50 mL pre-cooled MTBE (2-Methoxy-2-methylpropane) – n-hexane 1 : 1. All peptides were purified by size exclusion chromatography using an Äkta purifier system (GE Healthcare Bio-Sciences AB, Sweden) based on a P-900 solvent pump module, a UV-900 spectrophotometrical detector, a pH/C-900 conductivity module, a Frac-950 automated fractionator, a Sephadex G-10 column and 10 mM hydrochloric acid solution – acetonitrile 7 : 3 as solvent. All peptides were lyophilized after SEC resulting in hydrochloride salts of the peptides. The compounds were analyzed by matrix-assisted laser desorption/ionization mass spectrometry (MALDI-MS) using 2,5-Dihydroxybenzoic acid an Autoflex II mass spectrometer (Bruker Daltonics, Bremen, Germany). The peptides were used without further purification.

2.3 Peptide Analytics

H_6-Acr

Sequence: Acridine-PEG_{28}-H_6-NH_2

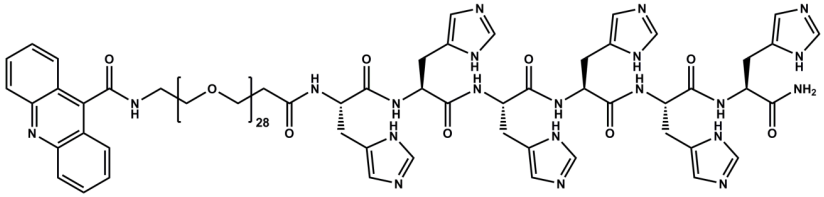

Chemical Formula: $C_{109}H_{169}N_{21}O_{36}$
Exact Mass: 2348,2039

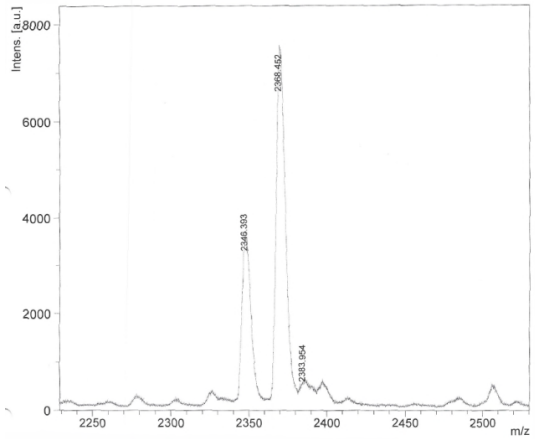

Mass found: 2346.393 $[M+H]^+$, 2368.452 $[M+Na]^+$, 2383.954 $[M+K]^+$

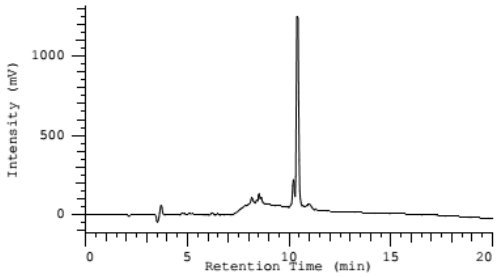

RP-HPLC chromatogram. (YMC Pack Pro C18 RS column, 5-100 % acetonitrile containing 0.1 % TFA in 15 min, detection at 214 nm).

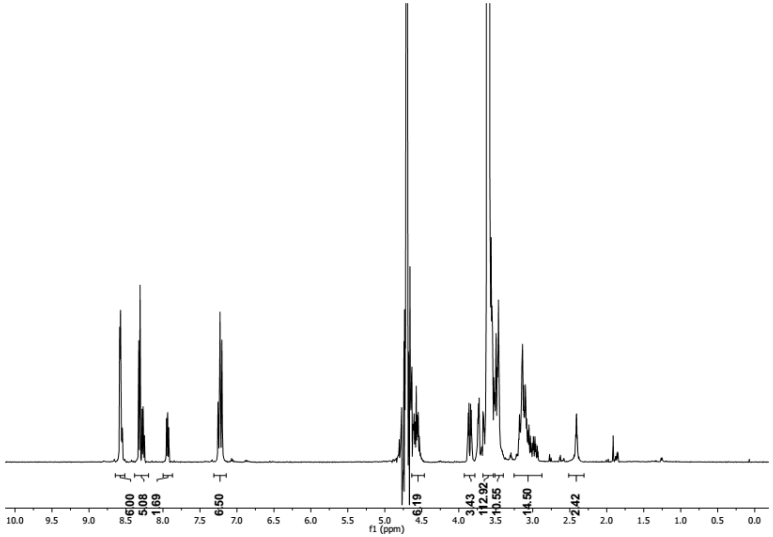

^{1}H-NMR (500 MHz, deuterium oxide) δ = 8.64 – 8.51 (m, 6H, Ar-H histidine), 8.38 – 8.20 (m, 6H, Ar-H acridine), 8.0-7.84 (m, 2H, Ar-H acridine),7.23 (m, 6H, Ar-H histidine), 4.64 – 4.47 (m, 6H, αH histidine), 3.67 – 3.53 (m, 114H, CH_2-O- dPEG$_{28}$, -CH_2-N- dPEG$_{28}$), 3.25 – 2.88 (m, 12H, βH histidine), 2.50-2.31 (m, 2H, -CH_2-COO- dPEG$_{28}$).

A_6-Acr

Sequence: Acridine-PEG$_{28}$-A_6-NH_2

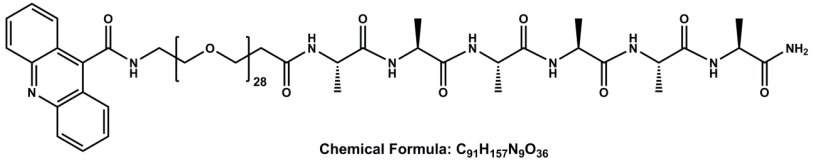

Chemical Formula: $C_{91}H_{157}N_9O_{36}$
Exact Mass: 1952,0731

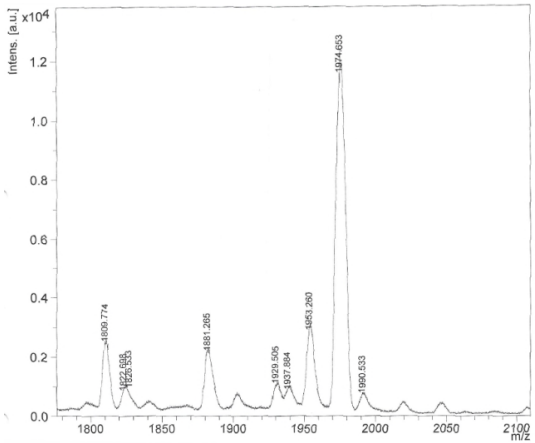

Mass found: 1953.260 $[M+H]^+$, 1974.653 $[M+Na]^+$, 1990.533 $[M+K]^+$

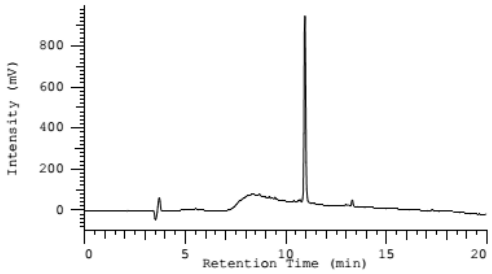

RP-HPLC chromatogram. (YMC Pack Pro C18 RS column, 5-100 % acetonitrile containing 0.1 % TFA in 15 min, detection at 214 nm).

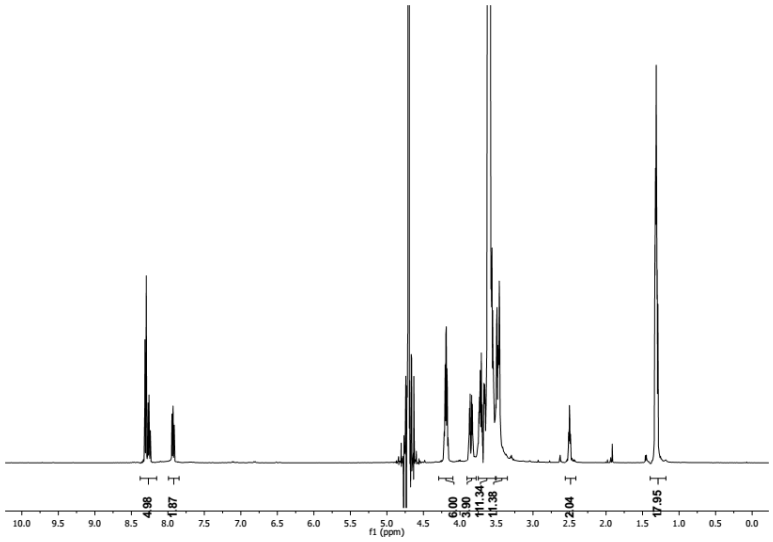

^{1}H-NMR (500 MHz, deuterium oxide) δ = 8.31 (m, 6H, Ar-H acridine), 7.91 (m, 2H, Ar-H acridine), 4.19 (q, 6H, αH alanine), 3.75 – 3.51 (m, 114H, CH_2-O- $dPEG_{28}$, -CH_2-N- $dPEG_{28}$), 2.50 (m, 2H, -CH_2-COO- $dPEG_{28}$), 1.31 (d, 18H, -CH_3 alanine).

H_0-Acr

Sequence: Acridine-STOTDA

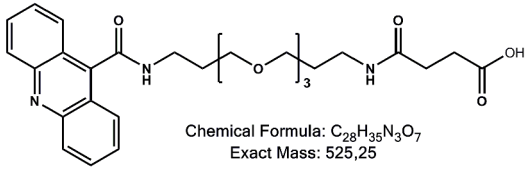

Chemical Formula: $C_{28}H_{35}N_3O_7$
Exact Mass: 525,25

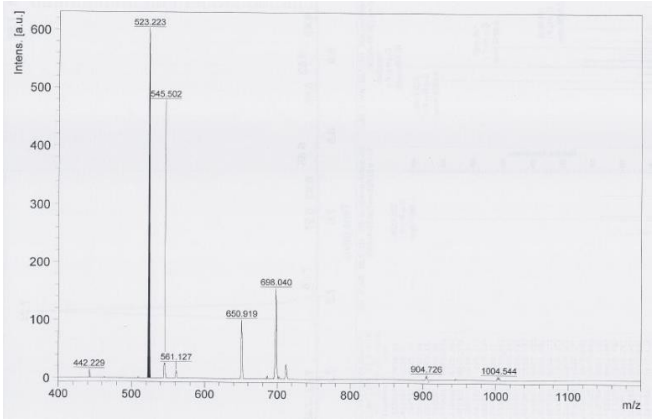

Mass found: 523.223 $[M+H]^+$, 545.502 $[M+Na]^+$, 561.127 $[M+K]^+$

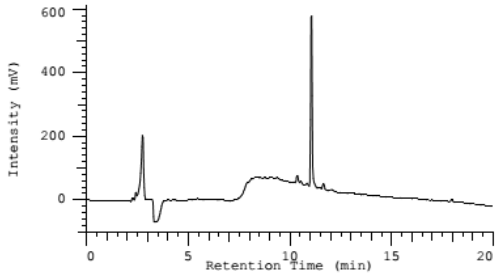

RP-HPLC chromatogram. (YMC Pack Pro C18 RS column, 5-100 % acetonitrile containing 0.1 % TFA in 15 min, detection at 214 nm).

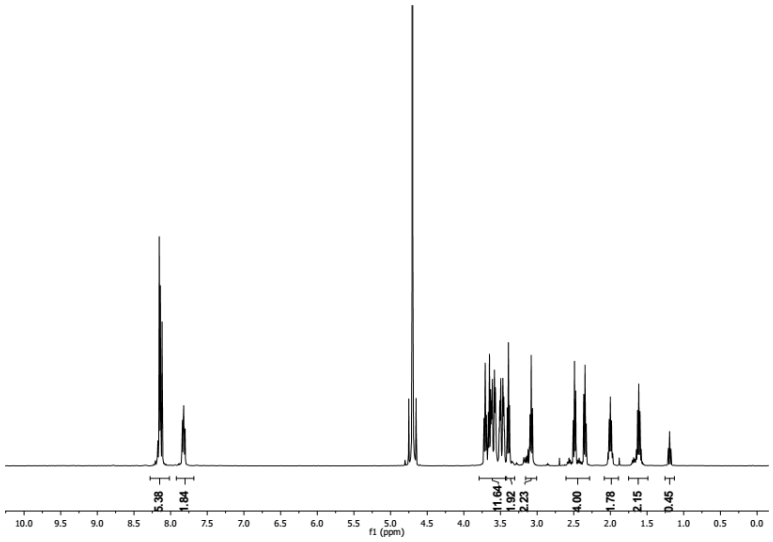

^{1}H-NMR (400 MHz, deuterium oxide) δ = 8.28 – 8.02 (m, 6H, Ar-H acridine), 7.82 (m, 2H, Ar-H acridine), 3.79 – 3.43 (m, 12H, -O-CH_2-CH_2-O- STOTDA, -C-C-CH_2-O- STOTDA), 3.39 (t, 2H, -CH_2-N-CO- STOTDA), 3.08 (t, 2H, -CH_2-N-CO- STOTDA), 2.42 (m, 4H, -CO-CH_2-CH_2-CO- STOTDA), 2.00 (m, 2H, -C-CH_2-C- STOTDA), 1.61 (m, 2H, -C-CH_2-C- STOTDA).

H_3-Acr

Sequence: Acridine-STOTDA-H_3

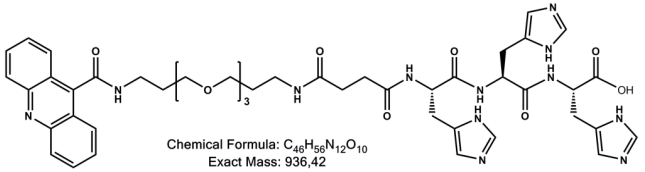

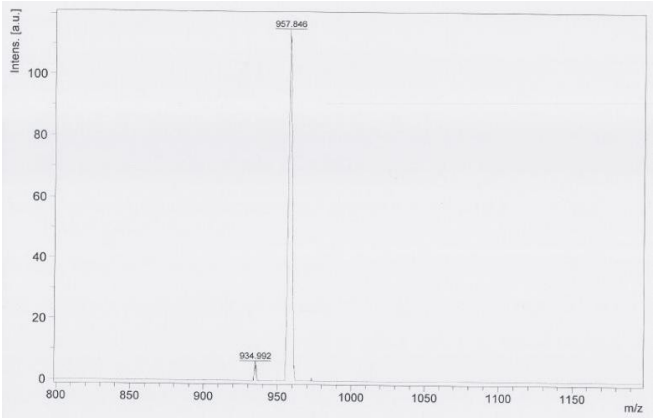

Mass found: 934.992 $[M+H]^+$, 957.846 $[M+Na]^+$

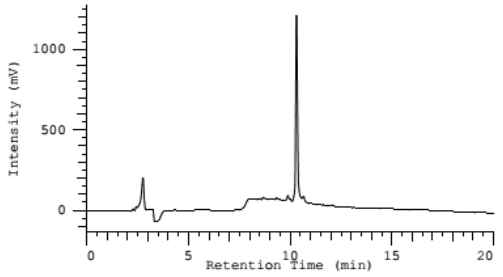

RP-HPLC chromatogram. (YMC Pack Pro C18 RS column, 5-100 % acetonitrile containing 0.1 % TFA in 15 min, detection at 214 nm).

H_6-Acr

Sequence: Acridine-STOTDA-H_6

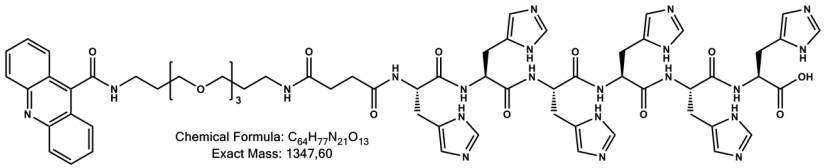

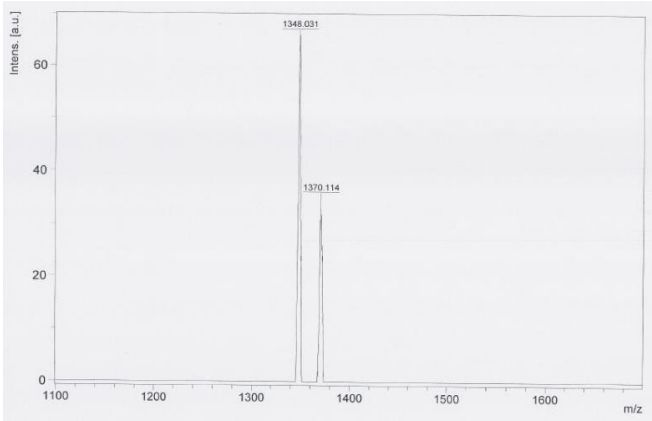

Mass found: 1348.031 $[M+H]^+$, 1370.114 $[M+Na]^+$

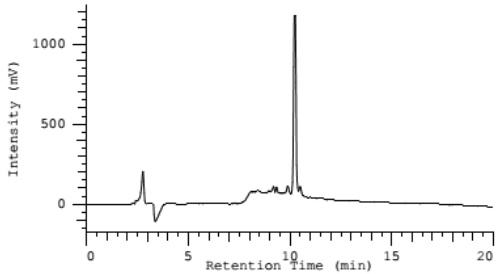

RP-HPLC chromatogram. (YMC Pack Pro C18 RS column, 5-100 % acetonitrile containing 0.1 % TFA in 15 min, detection at 214 nm).

H_0-FITC

Sequence: FITC-STOTDA

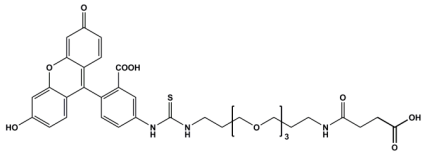

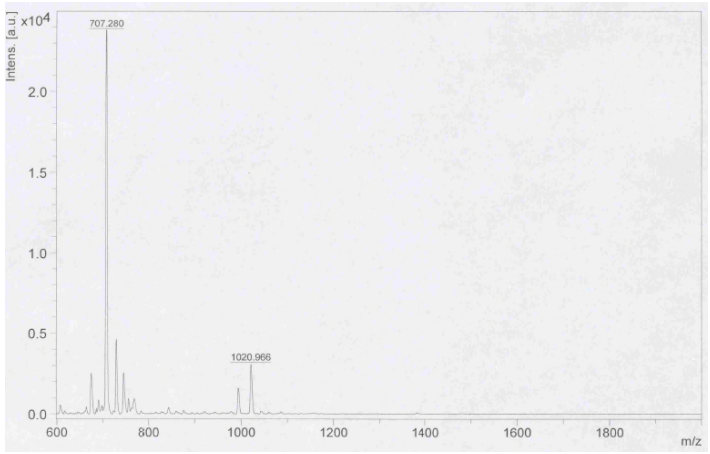

Mass found: 707.280 $[M+H]^+$

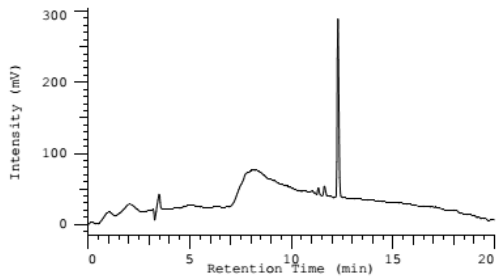

RP-HPLC chromatogram. (YMC Pack Pro C18 RS column, 5-100 % acetonitrile containing 0.1 % TFA in 15 min, detection at 214 nm).

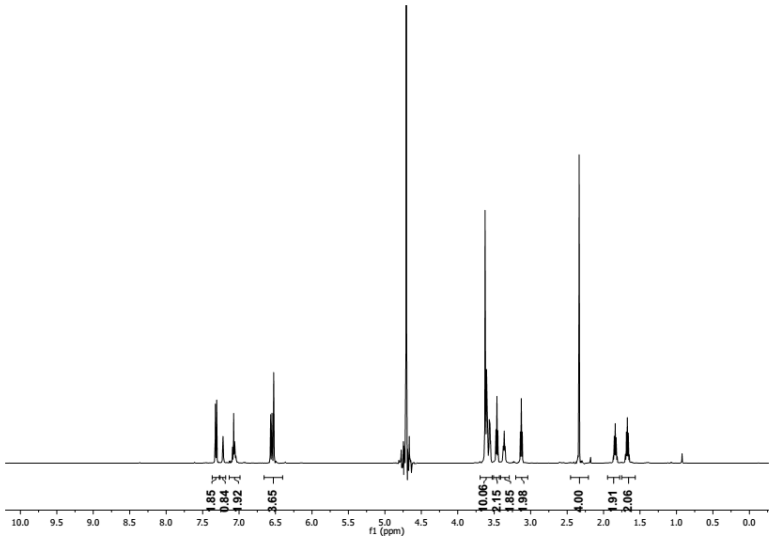

^{1}H-NMR (500 MHz, deuterium oxide) δ = 7.32 (d, 2H, Ar-H FITC), 7.22 (s, 1H, Ar-H FITC), 7.07 (m, 2H, Ar-H FITC), 6.66 – 6.40 (m, 4H, Ar-H FITC), 3.69 – 3.53 (m, 10H, -O-CH_2-CH_2-O- STOTDA, -CH_2-N-CS- STOTDA), 3.46 (t, 2H, -C-C-CH_2-O- STOTDA), 3.36 (t, 2H, -C-C-CH_2-O), 3.13 (t, 2H, -CH_2-N-CO- STOTDA), 2.34 (s, 4H, -CO-CH_2-CH_2-CO- STOTDA), 1.84 (t, 2H, -C-CH_2-C- STOTDA), 1.67 (t, 2H, -C-CH_2-C- STOTDA).

H_3-FITC

Sequence: FITC-STOTDA-H_3

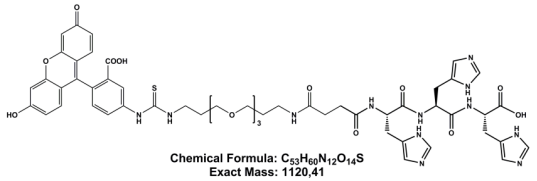

Chemical Formula: $C_{83}H_{60}N_{12}O_{14}S$
Exact Mass: 1120,41

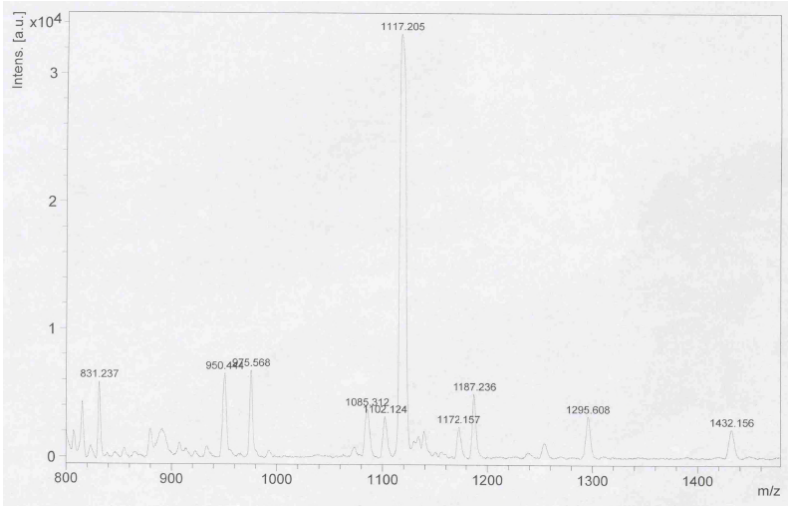

Mass found: 1117.205 $[M+H]^+$

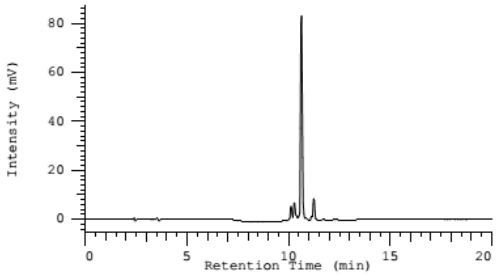

RP-HPLC chromatogram. (YMC Pack Pro C18 RS column, 5-100 % acetonitrile containing 0.1 % TFA in 15 min, detection at 214 nm).

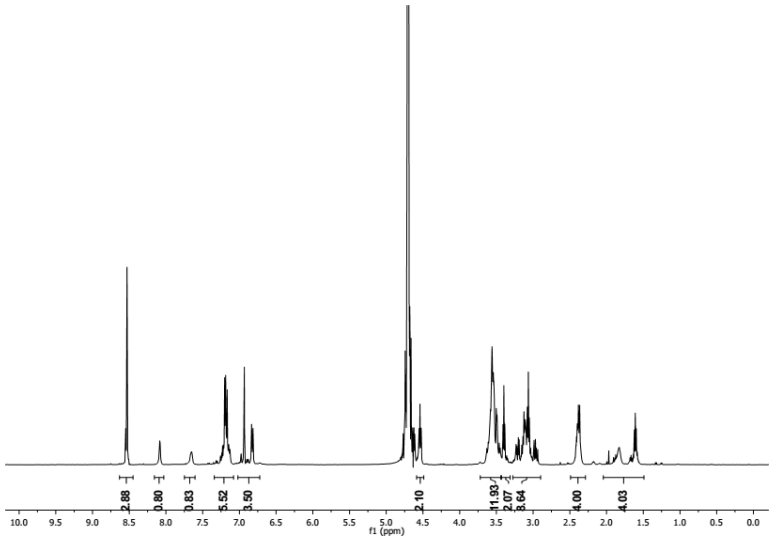

^{1}H-NMR (500 MHz, deuterium oxide) δ = 8.63 – 8.45 (m, 3H, Ar-H histidine), 8.16 – 8.03 (s, 1H, Ar-H FITC), 7.75 – 7.60 (s, 1H, Ar-H FITC), 7.34 – 7.08 (m, 6H, Ar-H histidine, Ar-H FITC), 7.02 – 6.72 (m, 4H, Ar-H FITC), 4.55 (t, 3H, αH histidine), 3.67 – 3.44 (m, 12H, -O-CH_2-CH_2-O- STOTDA, -CH_2-N-CS- STOTDA, -C-C-CH_2-O- STOTDA), 3.42 – 3.33 (m, 2H, -C-C-CH_2-O STOTDA), 3.29 – 2.90 (m, 8H, βH histidine, -CH_2-N-CO- STOTDA), 2.38 (m, 4H, -CO-CH_2-CH_2-CO- STOTDA), 2.04 – 1.49 (m, 4H, -C-CH_2-C- STOTDA, -C-CH_2-C- STOTDA).

H_6-FITC

Sequence: FITC-STOTDA-H_6

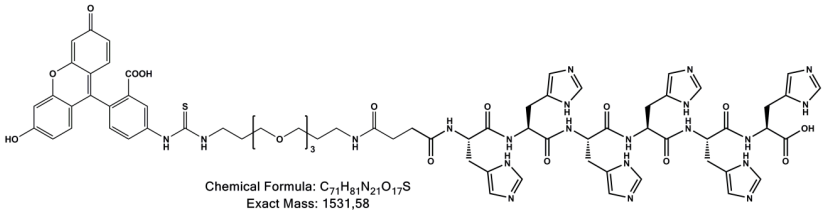

Chemical Formula: $C_{71}H_{81}N_{21}O_{17}S$
Exact Mass: 1531,58

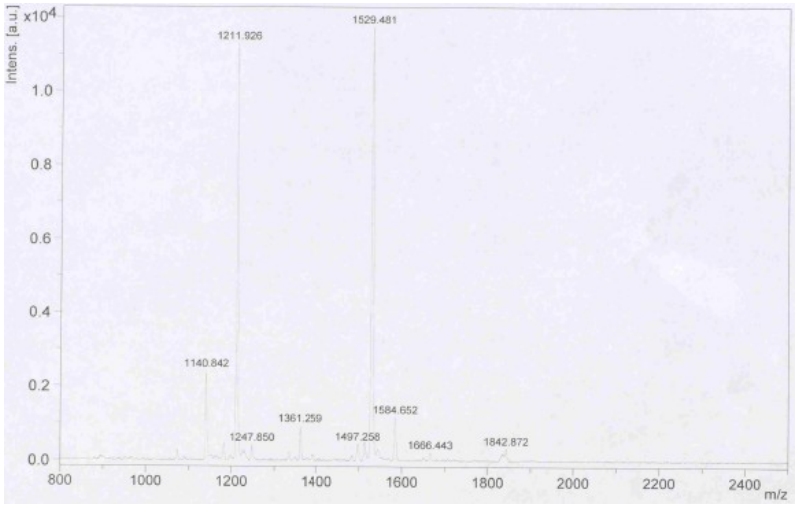

Mass found: 1529.481 $[M+H]^+$

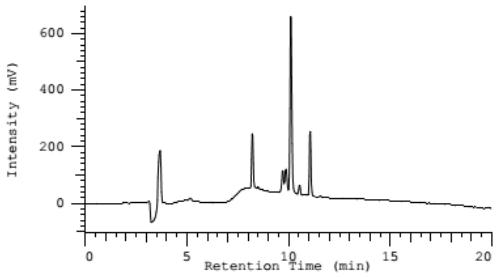

RP-HPLC chromatogram. (YMC Pack Pro C18 RS column, 5-100 % acetonitrile containing 0.1 % TFA in 15 min, detection at 214 nm).

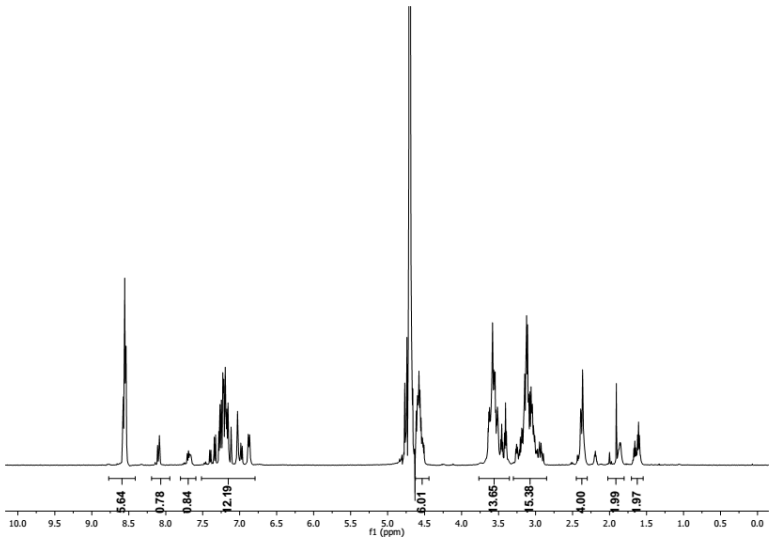

^{1}H-NMR (500 MHz, deuterium oxide) δ = 8.56 (m, 6H, Ar-H histidine), 8.10 (m, 1H, Ar-H FITC), 7.77 – 7.59 (m, 1H, Ar-H FITC), 7.52 – 6.79 (m, 13H, Ar-H histidine, Ar-H FITC), 4.62 – 4.44 (m, 6H, αH histidine), 3.77 – 3.35 (m, 14H, -O-CH_2-CH_2-O- STOTDA, -CH_2-N-CS- STOTDA, -C-C-CH_2-O- STOTDA), 3.30 – 2.85 (m, 14H, -CH_2-N-CO- STOTDA, βH histidine), 2.37 (m, 4H, -CO-CH_2-CH_2-CO- STOTDA), 1.88 (m, 2H, -C-CH_2-C- STOTDA), 1.63 (m, 2H, -C-CH_2-C- STOTDA).

H_6-PEG_{12}

Sequence: PEG_{12}-H_6-NH_2

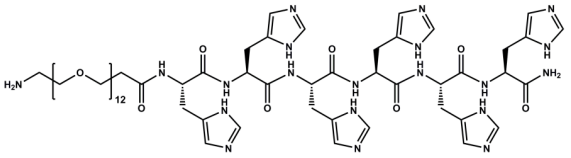

Chemical Formula: $C_{63}H_{98}N_{20}O_{19}$
Exact Mass: 1438,7317

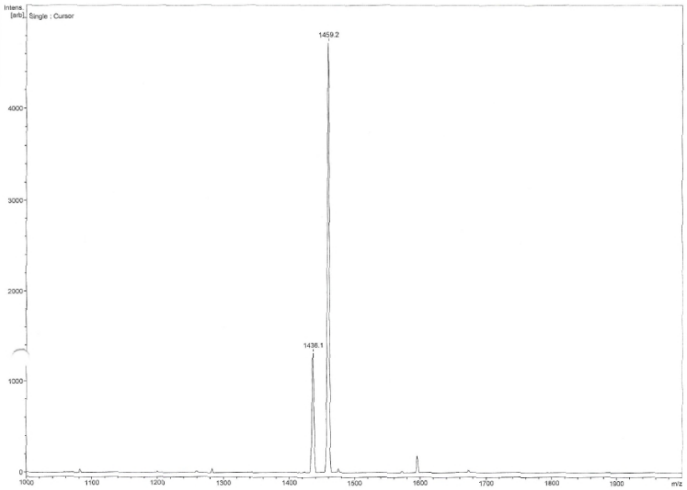

Mass found: 1436.1 $[M+H]^+$, 1459.2 $[M+Na]^+$

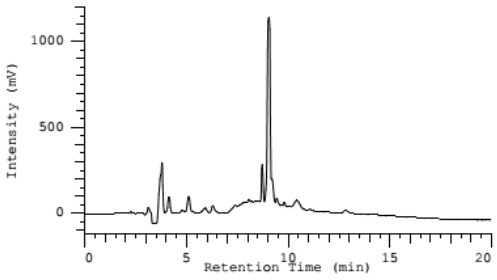

RP-HPLC chromatogram. (YMC Pack Pro C18 RS column, 5-100 % acetonitrile containing 0.1 % TFA in 15 min, detection at 214 nm).

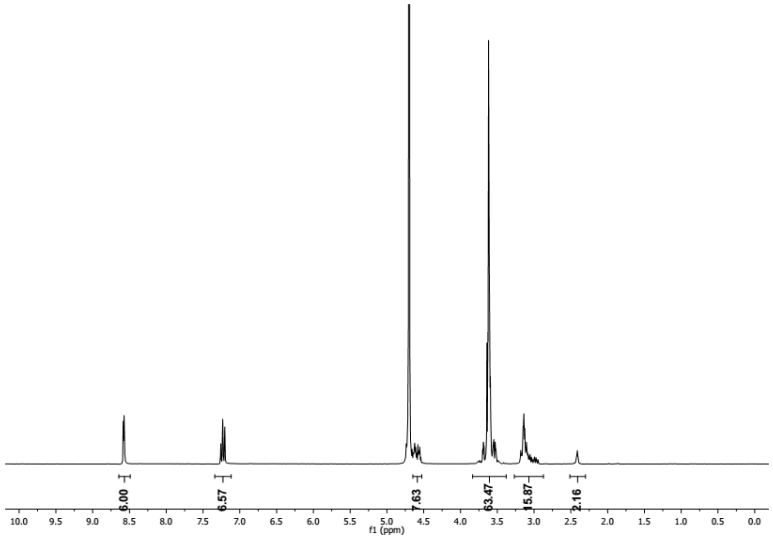

^{1}H-NMR (500 MHz, deuterium oxide) δ = 8.58 (m, 6H, Ar-H histidine), 7.23 (m, 6H, Ar-H histidine), 4.64 – 4.50 (m, 6H, αH histidine), 3.84 – 3.38 (m, 50H, -CH_2-O- $dPEG_{12}$,-CH_2-N-$dPEG_{12}$), 3.27 – 2.87 (m, 12H, βH histidine), 2.41 (t, 2H, -CH_2-COO- $dPEG_{12}$).

H_6-A647N

Sequence: ATTO647N-PEG_{12}-H_6-NH_2

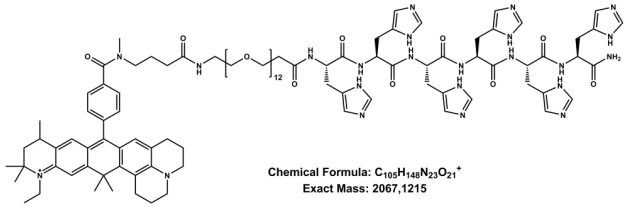

Chemical Formula: $C_{105}H_{148}N_{23}O_{21}^{+}$
Exact Mass: 2067,1215

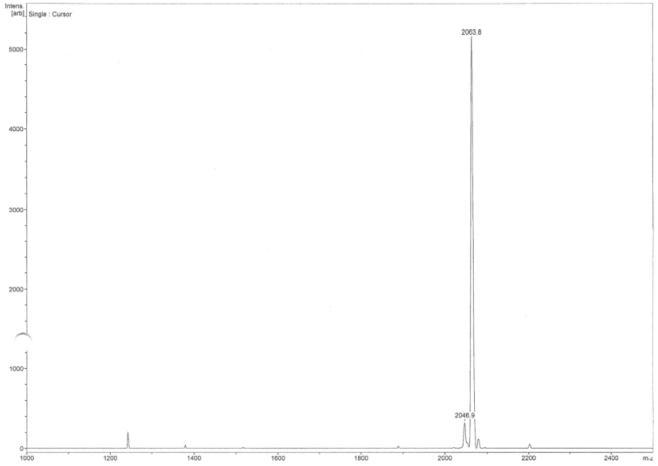

Mass found: 2063.8 $[M+H]^{+}$

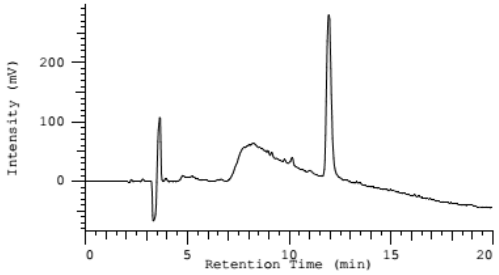

RP-HPLC chromatogram. (YMC Pack Pro C18 RS column, 5-100 % acetonitrile containing 0.1 % TFA in 15 min, detection at 214 nm).

H_6-CF

Sequence: Carboxyfluorescein-PEG_{12}-H_6-NH_2

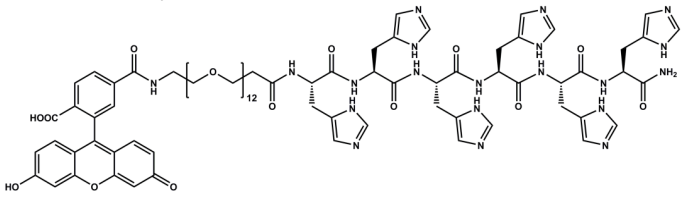

Chemical Formula: $C_{84}H_{108}N_{20}O_{25}$
Exact Mass: 1796,78

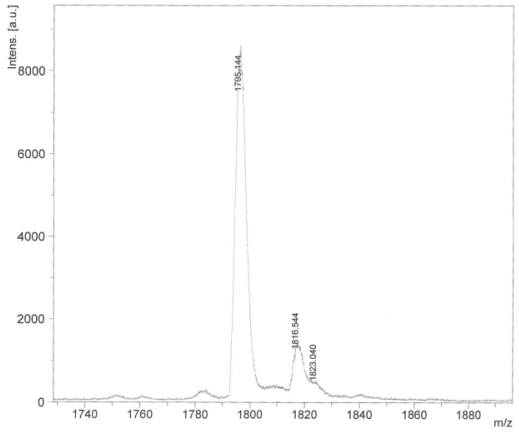

Mass found: 1795.144 $[M+H]^+$, 1816.544 $[M+Na]^+$

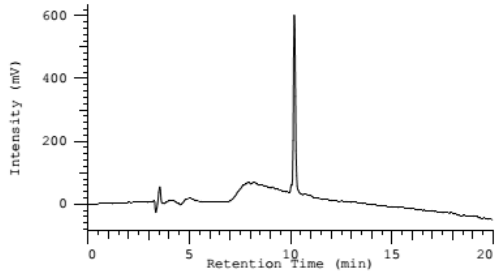

RP-HPLC chromatogram. (YMC Pack Pro C18 RS column, 5-100 % acetonitrile containing 0.1 % TFA in 15 min, detection at 214 nm).

H_6-PEG_{36}-5ANV

Sequence: 5-Azidonorvaline-PEG_{36}-H_6-NH_2

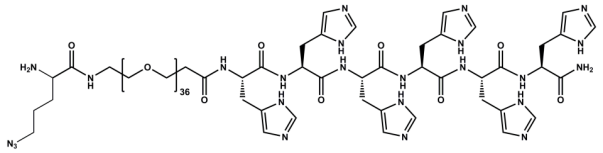

Chemical Formula: $C_{116}H_{202}N_{24}O_{44}$
Exact Mass: 2635,4307

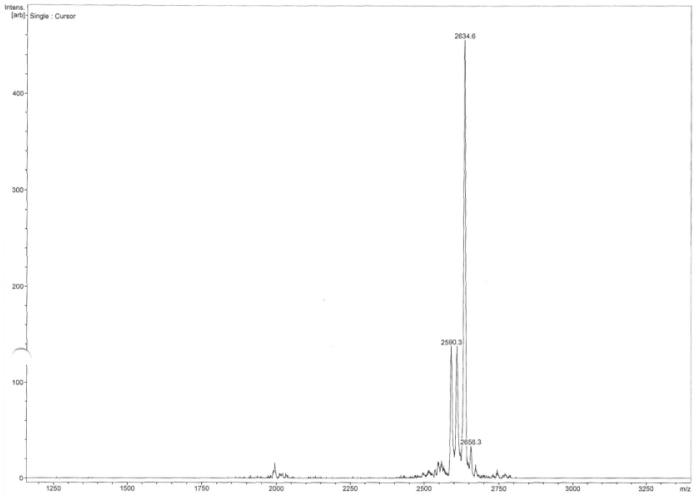

Mass found: 2634.6 $[M+H]^+$, 2656.3 $[M+Na]^+$

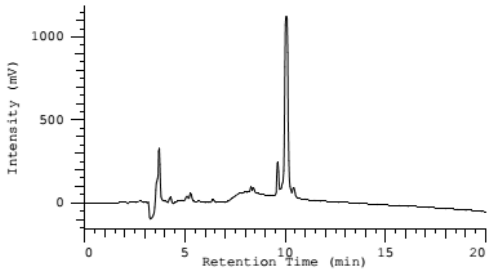

RP-HPLC chromatogram. (YMC Pack Pro C18 RS column, 5-100 % acetonitrile containing 0.1 % TFA in 15 min, detection at 214 nm).

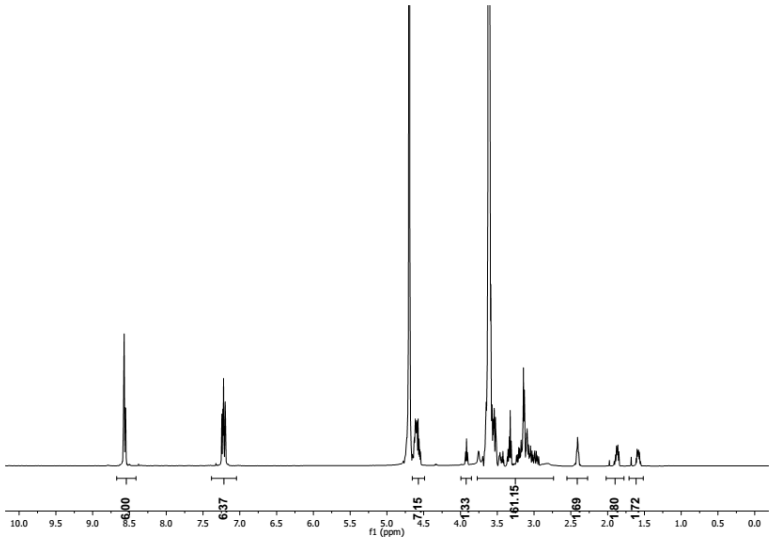

^{1}H-NMR (500 MHz, deuterium oxide) δ = 8.67 – 8.41 (m, 6H, Ar-H histidine), 7.39 – 7.05 (m, 6H, Ar-H histidine), 4.66 – 4.49 (m, 6H, αH histidine), 3.92 (t, 1H,αH 5-azidonorvaline), 3.77 – 2.74 (m, 158H, -CH_2-O- dPEG$_{36}$,-CH_2-N- dPEG$_{36}$, βH histidine, δH 5-azidonorvaline), 2.41 (t, 2H, -CH_2-COO- dPEG$_{36}$), 2.05 – 1.78 (m, 2H, γH 5-azidonorvaline), 1.64 – 1.46 (m, 2H, βH5-azidonorvaline).

H_6-Azide

Sequence: 6AHX-H_6-NH_2

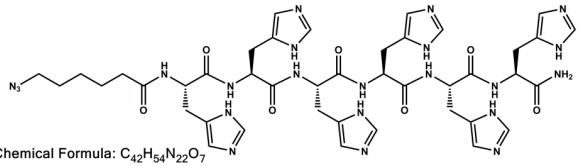

Chemical Formula: $C_{42}H_{54}N_{22}O_7$
Exact Mass: 978,45

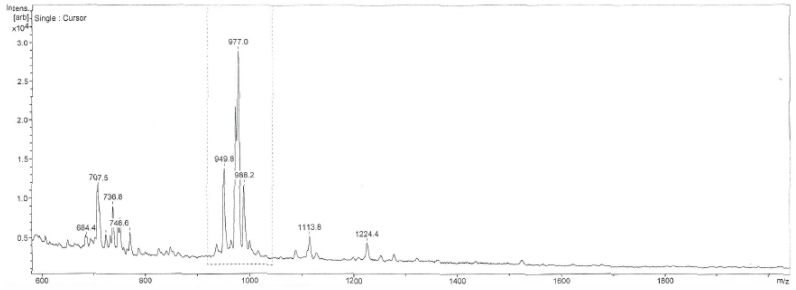

Mass found: 977.0 $[M+H]^+$

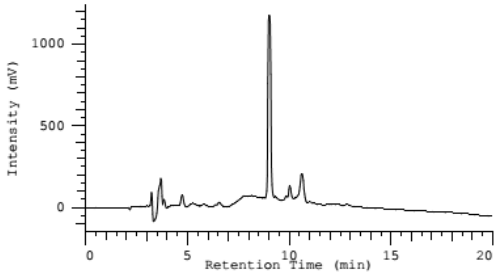

RP-HPLC chromatogram. (YMC Pack Pro C18 RS column, 5-100 % acetonitrile containing 0.1 % TFA in 15 min, detection at 214 nm).

H_6-Bak

Sequence: H_6-GGQVGRQLAIIGDDINR-NH_2

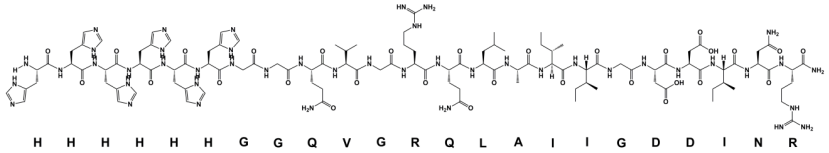

H H H H H H G G Q V G R Q L A I I G D D I N R

Chemical Formula: $C_{110}H_{171}N_{45}O_{30}$
Exact Mass: 2602,3238

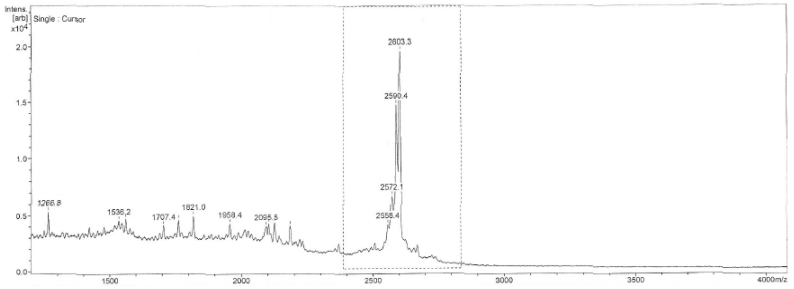

Mass found: 2603.3 $[M+H]^+$

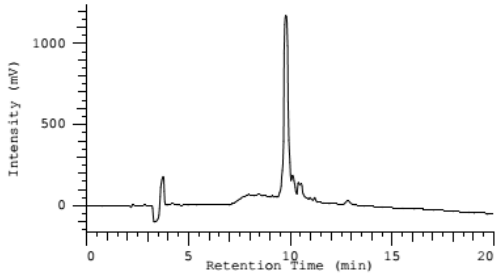

RP-HPLC chromatogram. (YMC Pack Pro C18 RS column, 5-100 % acetonitrile containing 0.1 % TFA in 15 min, detection at 214 nm).

H_6-Bad

Sequence: H_6-GNLWAAQRYGRELRRMSDEFVD-NH_2

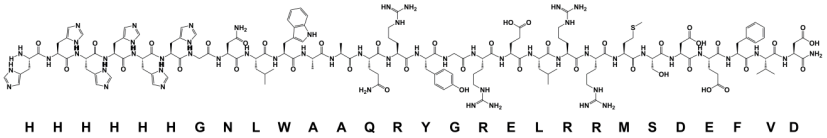

H H H H H H G N L W A A Q R Y G R E L R R M S D E F V D

Chemical Formula: $C_{151}H_{220}N_{56}O_{40}S$
Exact Mass: 3489,6623

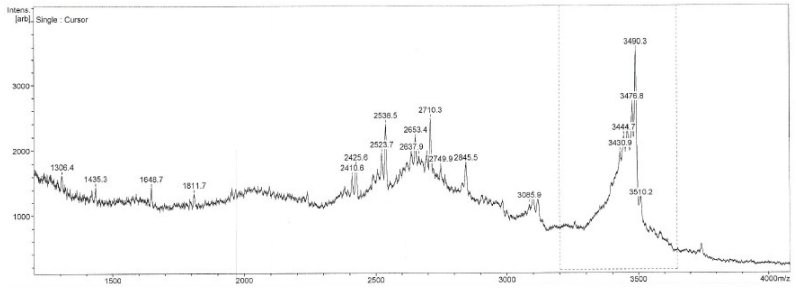

Mass found: 2490.3 $[M+H]^+$

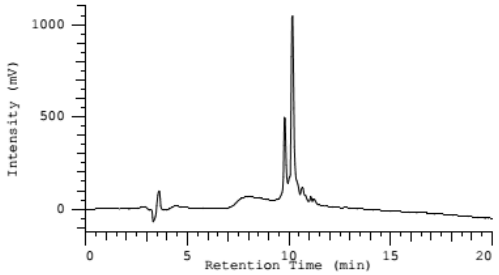

RP-HPLC chromatogram. (YMC Pack Pro C18 RS column, 5-100 % acetonitrile containing 0.1 % TFA in 15 min, detection at 214 nm).

H_6-KLK

Sequence: H_6-GGKLAKLAKKLAKLAK-NH_2

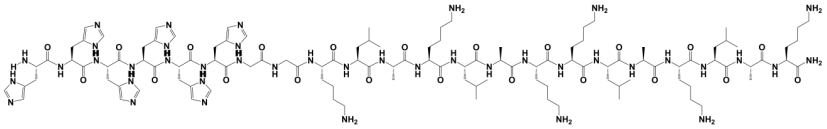

H H H H H H G G K L A K L A K K L A K L A K

Chemical Formula: $C_{112}H_{187}N_{41}O_{22}$
Exact Mass: 2458,4774

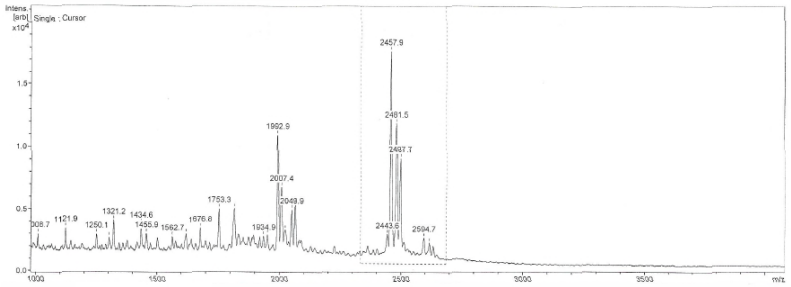

Mass found: 2457.9 $[M+H]^+$, 2481.5 $[M+Na]^+$, 2497.7 $[M+K]^+$

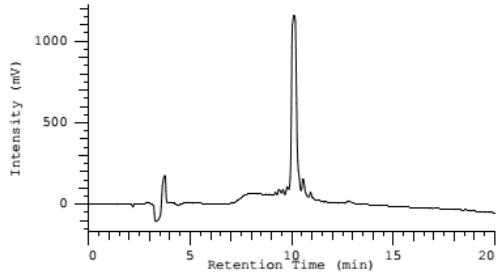

RP-HPLC chromatogram. (YMC Pack Pro C18 RS column, 5-100 % acetonitrile containing 0.1 % TFA in 15 min, detection at 214 nm).

2.4 Labeling of H_6-PEG_{12}-NH_2

For each labeling reaction 3 mg of H_6-PEG_{12} (HCl salt, 1.8 µmol) were dissolved in 100 µL acetonitrile, 100 µL DMSO and 3.3 µL DIPEA (18 µmol). 3 mg ATTO 647N NHS ester (3.6 µmol) or 1.7 mg of carboxyfluorescein NHS ester (3.6 µmol) were dissolved in 100 µL DMSO and added to the peptide solutions. The mixtures were incubated for 3 h at room temperature. The carboxyfluorescein labeled peptide was purified by SEC using an Äkta purifier system (GE Healthcare Bio-Sciences AB, Sweden), a Sephadex G10 size exclusion column and 10 mM HCl – acetonitrile 70 : 30 as mobile phase. The ATTO 647N labeled peptide was first subjected to immobilized metal ion chromatography (IMAC) using a HisTrap HP 1 mL column and a gradient of binding buffer (20 mM sodium phosphate, 0.5 M NaCl, pH 7.4) and elution buffer (20 mM sodium phosphate, 0.5 M NaCl, 0.5 M imidazole, pH 7.4) as mobile phase. The pooled fractions were desalted by SEC as described for the carboxyfluorescein labeled peptide. The solutions were lyophilized. The labeled peptides are called H_6-A647N and H_6-CF in the manuscript.

2.5 Modification of transferrin with H_6-tag and ATTO 647N dye

50 mg of transferrin from human plasma (0.67 µmol) were dissolved in 1 mL HEPES buffer (20 mM, pH 7.4). DBCO-PEG_4-NHS ester was dissolved in DMSO (20 mg/mL) and 43.5 µL (0.87 mg, 1.3 µmol) were added to the transferrin solution. The reaction mixture was incubated for 3 h at room temperature under shaking. A solution of H_6-PEG_{36}-5ANV (HCl salt) was prepared in water at 20 mg/mL. 190 µL (1.3 µmol) of the peptide solution were added to the protein solution and the mixture was incubated at room temperature overnight. Purification was carried out by a combination of immobilized metal ion chromatography (IMAC) and size exclusion chromatography (SEC). First, a HisTrapHP 1 mL column connected to an Äkta purifier system (GE Healthcare Bio-Sciences AB, Sweden) was used to isolate H_6-tagged protein. As mobile phase a gradient of binding buffer (20 mM sodium phosphate, 0.5 M NaCl, pH 7.4) and elution buffer (20 mM sodium phosphate, 0.5 M NaCl, 0.5 M imidazole, pH 7.4) was used. The protein containing fractions with highest affinity to the column were pooled and concentrated using Amicon Ultra centrifugal filter units (MWCO= 10.000; Millipore, USA). For desalting and removal of unconjugated H_6-PEG_{36}-5ANV, the solution was subjected to SEC using the Äkta purifier system, a Sephadex G25 super fine size exclusion column and HEPES buffer (20 mM, pH 7.4) as mobile phase. Protein containing fractions were pooled, concentrated using Amicon Ultra centrifugal filter units (MWCO=10.000; Millipore, USA) and concentration was determined photometrically at 280 nm. The H_6-PEG_{36} conjugated transferrin is called H_6-Tf in the manuscript. A solution containing 60 nmol H_6-Tf in 357 µL HEPES buffer (20 mM, pH 7.4) was

prepared. ATTO 647N NHS ester was dissolved in DMSO at a concentration of 8 mM and 15 µL (120 nmol) were added to the H_6-Tf solution. The mixture was incubated for 2 h at room temperature, subsequently SEC (Sephadex G25 super fine) was carried out as described before, protein containing fractions were pooled and the concentration was determined photometrically at 280 nm. ATTO 647N labeled H_6-Tf is called H_6-Tf* in the manuscript.

2.6 Modification of cytochrome C with H_6-tag

Cytochrome C (CytC) from equine heart was solubilized in PBS (pH 7.4, 20 mg/mL) and a DBCO-PEG_4-NHS ester was solubilized in DMSO (50 mg/mL). One molar equivalent of linker was added to the protein solution and incubated for 3 h at 37 °C with shaking. Non coupled linker was removed by size exclusion chromatography using an Äkta purifier system (GE Healthcare Bio-Sciences AB, Sweden), a Sephadex G25 super fine size exclusion column and PBS pH 7.4 as mobile phase.

Afterwards four molar equivalents of H_6-Azide were added to the DBCO modified CytC (3.56 mg/mL) and the mixture was incubated for 3 h at 37 °C with shaking. Non modified CytC was removed by nickel chromatography using an Äkta purifier system (GE Healthcare Bio-Sciences AB, Sweden), PBS (pH 7.4, 500 mM NaCl, 20 mM Imidazole) as binding buffer and PBS (pH 7.4, 500 mM NaCl, 500 mM Imidazole) as elution buffer, followed by size exclusion chromatography (Sephadex G25 super fine size exclusion column) using PBS pH 7.4 as mobile phase to remove non coupled H_6-Azide and for buffer exchange.

The purified protein was concentrated using Amicon Ultra centrifugal filter units (MWCO= 10.000; Millipore, USA). The modified CytC is called H_6-CytC in the manuscript.

2.7 Preparation of MOF suspensions in HBG

MOF suspensions in HBG were always freshly prepared prior to performing the experiment. The necessary amount of MOF material in ethanol was centrifuged (10 min, 10000 rpm), followed by carefully inverting the tubes and gently tapping them on a paper towel in order to get rid of the ethanol supernatant without damaging the MOF-pellet. The MOF pellet was then resuspended in HBG (pH 7.4) at a final concentration of 5 or 10 mg/mL by continuous pipetting, followed by 10 min sonication.

2.8 Investigation of peptide binding (A_6, H_6) by RP-HPLC

MOF suspensions in ethanol were centrifuged for 10 min at 13400 rpm, the supernatant was discarded and the pellet was resuspended in the appropriate volume of HBG (pH 7.4) resulting in a 5 mg/mL suspension. 3 µL of a solution containing equimolar amounts of H_6-Acr and A_6-Acr (5 mM) in HBG were added to 47 µL HBG (pH 7.4) in a 1.5 mL reaction tube. 100 µL of MOF suspension were added and vortexed briefly. As control, 100 µL HBG (pH 7.4) without MOF particles were added to an analogous sample. The mixtures were incubated at room temperature for 15 min under shaking and centrifuged for 10 min at 13400 rpm subsequently. 120 µL of the supernatant were transferred into HPLC sample vials. RP-HPLC analysis was carried out using a YMC Pack Pro C18 RS column (250 x 4.6 mm) connected to a VWR Hitachi Chromaster HPLC system (5160 pump module, 5260 auto sampler, 5310 column oven, 5430 diode array detector).100 µL of the samples were injected and a gradient from 5 % acetonitrile (0.1 % TFA) to 100 % acetonitrile (0.1 % TFA) over 15 min was used for the analysis. Acridine containing compounds were detected photometrically at 360 nm.

2.9 Zeta potential measurements of MOF nanoparticle functionalization

3 nmol H_6-Acr or A_6-Acr were diluted in HBG (pH 7.4). In case of pro-apoptotic peptides and CytC 5 nmol were used. 100 µg MOF NPs (5 mg/mL in HBG, pH 7.4) were added (final volume 30 µL) and samples were incubated at room temperature for 15 min with shaking. Shortly before the measurement in a folded capillary cell (DTS1070), samples were diluted to a final MOF concentration of 0.1 mg/mL. Zeta potential was measured by electrophoretic laser-light scattering using a Zetasizer Nano ZS (Malvern Instruments, Worcestershire, U.K.). Zeta potentials were calculated by the Smoluchowski equation, each sample was measured 3 times with 10 to 30 subruns at 25 °C.

2.10 Quantitative determination of bound H_0-, H_3-, H_6-FITC to Zr-*fum*

The data was acquired by conducting fluorescence-based measurements in a high-throughput method: The wells of a round-bottom 96-microwell plate were filled with 200 µL solutions of FITC labeled peptides in HBG buffer (pH 7.4). To each second column an ethanolic solution of Zr-*fum* (6.2 mg/mL, 4.14 µL) was added. The reaction was incubated for 15 min followed by the removal of the MOF nanoparticles via centrifugation (4000 rpm, 30 min) and transferring the supernatant (170 µL) into a flat-bottom microwell plate. Subsequent recording of the fluorescence signal of these flat-bottom wells was conducted using a microplate reader (Fluostar OPTIMA, BMG

Labtech). By calculating the difference of the mean fluorescence signal between the solutions incubated with MOF nanoparticles and the control samples each for three separate measurements, the average dye-uptake of the particles was determined. All experiments were performed at 30 °C. In the graph corresponding error bars are connected using the B-spline function of the program OriginPro v9.0.0**.** For competition experiments 500 mM imidazole was added to the loading solution prior to incubation with MOF NPs. Experiments were performed in triplicates.

2.11 Fluorescence Correlation Spectroscopy (FCS)

Theory

FCS is a fluorescence technique that is able to determine concentrations and diffusion coefficients of fluorescently labeled molecules or particles in nanomolar concentrated solutions. Magde *et al.*[6] described its principles in 1972 and Rigler *et al.*[7] improved its signal to noise by including a confocal design. The fluctuating fluorescence signal F(t) of fluorophores diffusing though the 3D Gaussian detection volume is used to calculate the autocorrelation function $G(\tau) = \frac{\langle F(t)F(t+\tau)\rangle}{\langle F\rangle^2}$. In case of one species that is diffusing in the sample it is possible to derive the hydrodynamic radius and the particle concentration from the correlation curve by a physical model that is represented by $G(\tau) = G(0)\frac{1}{1+\frac{\tau}{\tau_D}}\frac{1}{\sqrt{1+\frac{\tau}{S^2\tau_D}}}$, where $G(0)$ is the correlation's amplitude and represents the reciprocal of the mean number of fluorescing particles in the detection volume, S is the ratio between the lateral and the axial confocal volume radius, while τ_D is the mean time a particle needs to diffuse across the focal volume[8]. By calibration measurement with a sample of known diffusion coefficient, the width ω of the confocal volume could be determined. With that, the Boltzmann constant k_B, temperature $T = 295$K and viscosity $\eta = 0.96$ mPa·s of the measured aqueous suspension, the hydrodynamic radius is given by $R_H = \frac{2k_BT\tau_D}{3\pi\eta\omega^2}$.

Few agglomerates were omitted by using so called dust filter of the instrument's software (70%). By this the fluorescence fluctuations are analysed prior to correlation and spikes caused by agglomerated particles having a deviation of more than 70% from the average count rate within a binned count rate time are cut out and not used for the correlation analysis similar to the method described by Persson *et al.*[10].

An expansion of FCS is dual-color fluorescence cross-correlation (FCCS)[11], which gives access to binding properties of two differently labeled species of particles in the sample. Two lasers with different wavelengths are focused to the same confocal spot and excite two different types of fluorophore with different emission spectra. The two fluorescence signals get separated by a

dichroic mirror and are recorded individually. The fluctuations $F_1(t)$ and $F_2(t)$ are then correlated crosswise: $G(\tau) = \frac{\langle F_1(t)F_2(t+\tau)\rangle}{\langle F_1(t)\rangle\langle F_2(t)\rangle}$. The amplitude of the cross-correlation is proportional to the fraction of double-labeled particles. Due to physical and technical reasons, the alignment of the two exciting laser beams leads to slightly displaced laser foci[12]. In addition to other effects, this causes non-overlapping correlation curves even if a perfect coincidence of both labels is obtained.

Experimental Setup

The non-fluorescent MOF nanoparticles are not detectable by the FCS unless fluorescently labeled His-tags are attached to the nanoparticles. Thus a shift to higher diffusion times of correlation curve after addition of NPs to fluorescently labeled His-tags certifies the binding of His-tags to NPs surface. Normalization of autocorrelation curves helps to clearly visualize that the autocorrelation function of the MOF/His-tag is shifted towards higher correlation times with respect to the free His-tag molecules. Dual-color fluorescence Cross-Correlation Spectroscopy (FCCS) allows for a comparison between spectrally separated channels to extract codiffusion events that reflect interactions between differently labeled molecules[11,13].

For FCS and FCCS measurements, an Axiovert 200 microscope with a ConfoCor 2 unit (Carl Zeiss, Jena, Germany) equipped with a 40x (NA 1.2) water immersion apochromat objective (Carl Zeiss) was used. A helium neon laser (633 nm) and for FCCS additionally an argon laser (488 nm) was used for illumination. Samples were measured in eight-well LabTek chamber slides (Nunc, Rochester, NY). If nothing else mentioned, measurements were performed in HBG pH 7.4 at a temperature of 22.5 °C. Correlation was performed using ConfoCor 2 software.

Investigation of functionalization of MOFs with H_6-A647N by FCS

200 µL of H_6-A647N in HBG pH 7.4 were measured in a 8-well chamber slide (Nunc™ Lab-Tek™ II) prior to and after addition of 2 µL of MOF stock solution.

We found that the measured FCS autocorrelation function of MOF/H_6-A647N confirms binding of His-tags to MOF nanoparticles (Figure 4). The hydrodynamic radius of H_6-A647N was found to be $R_H^{H6A647N}$=2 nm ($D_{H6A647N}$=120 µm²/s). A two-component analysis (taking into account that part of His-tag molecules are not bound) resulted in an apparent diffusion time of 3.5 ms which corresponds to a hydrodynamic radius of Zr-*fum*/H_6-A647N of $R_H^{Zr\text{-}fum/H6A647N}$=56 nm and a diffusion constant $D_{Zr\text{-}fum/H6A647N}$=4.1 µm²/s (using finite size correction according to Wu et al.[14]).

Investigation of the acidic release of H_6-A647N from Zr-fum nanoparticles by FCS

The Zr-*fum*/H_6-A647N solution was prepared as described above and acidified by the addition of 3 µL of HCl (1 M) / 200 µL sample. The two-component analysis provides a fraction of the fast diffusing species (His-tag molecules) of 50%. As the curve is biased by agglomerates this value is just a rough estimation. But by comparison with the autocorrelation function in neutral environment the separation of His-tag in acidic environment is evident, providing an indication of pH-dependent detachment of His-tags from MOF nanoparticles.

Investigation of the influence of serum on Zr-fum/H_6-A647N stability by FCS

As described above, Zr-*fum* nanoparticles were functionalized with H_6-A647N in HBG at pH 7.4. Subsequently the coated NPs were diluted in Dulbecco's Modified Eagle's Medium (DMEM) containing 10% FBS. Also here the slow diffusion confirms the successful coating of Zr-*fum* with His-Tag (Figure 4, upper right). To confirm these results, the same experiment was repeated but replacing the NP suspension by pure HBG as a control. H_6-A647N in HBG at pH 7.4 was diluted with DMEM (10% FBS). The ensuing FCS measurements showed the same fast decay as before for H_6-A647N in HBG at pH 7.4, proving that H_6-A647N is not clustering/agglomerating in DMEM (10% FBS).

Fluorescence cross-correlation (FCCS) analysis

FCCS analysis was performed in order to confirm the co-localization of two proteins (H_6-GFP and H_6-Tf*) at the nanoparticles surface. 100 µL of a 60 nM H_6-GFP solution in HBG pH 7.4 and 100 µl of a 50 nM H_6-Tf* solution in HBG pH 7.4 were mixed in an 8-well chamber slide and measured prior to and after addition of 2 µL of MOF stock solution.

Figure 4 (lower right) shows autocorrelation and coss-correlation curves of mixed H_6-GFP and H_6-Tf* solutions before and after the addition of Zr-*fum* NPs. We find no coincidence of H_6-GFP and H_6-Tf* without NPs since the cross-correlation curve of protein mixture is close to baseline (not exactly baseline due to crosstalk of GFP into red channel). After addition of Zr-*fum* NPs the analysis of the cross-correlation shows a high ratio of co-localization of both proteins which is interpreted as simultaneous attachment of H_6-GFP and H_6-Tf* to NPs surface.

2.12 Cell culture

HeLa cells were grown in Dulbecco's Modified Eagle's Medium (DMEM) (1000 mg/mL glucose, L-glutamine and sodium bicarbonate) supplemented with 10 % FBS, 100/UmL penicillin, 100 µg/mL streptomycin at 37 °C and 5 % CO_2 in a humidified incubator.

2.13 Cell viability assay

Cells were seeded in 96-well plates (Corning ® Costar, Sigma-Aldrich, Germany) at a density of 4.000 cells/well. After 24 h medium was replaced with 80 µL fresh medium. The appropriate amount of compound to be tested was diluted in HBG (pH 7.4) and 20 µL of each sample/well were added. Cells were incubated for 48 h at 37 °C and 5 % CO_2 in a humified incubator. 10 µL MTT (3-(4,5-dimethylthiazol-2-yl)-2,5-diphenyltetrazolium bromide) (5 mg/mL) were added to each well reaching a final concentration of 0.5 mg/mL. After an incubation time of 2 h, unreacted dye and medium were removed and the 96-well plates were frozen at −80 °C for at least 30 min. To dissolve the purple formazan product 100 µL DMSO were added per well and the plate was incubated for 30 min at 37 °C with shaking. The wells were quantified by measuring absorbance at 590 nm with background correction at 630 nm using a microplate reader (TecanSpectrafluor Plus, Tecan, Switzerland). All studies were performed in triplicates. The relative cell viability (%) related to control wells treated only with 20 µL HBG (pH 7.4) was calculated as ([A] test/[A] control) × 100 %.

2.14 Cellular uptake experiments using flow cytometry analysis

Cells were seeded in 24-well plates (Corning ® Costar, Sigma-Aldrich, Germany) at a density of 20.000 cells/well. After 24 h, medium was replaced with 400 µL fresh medium. 0.5 nmol H_6-CF or H_6-GFP were diluted in HBG (pH 7.4), 50 µg MOF NPs (5 mg/mL in HBG, pH 7.4) were added (final volume 50 µL) and the solution was strongly mixed. For the co-delivery of H_6-GFP and H_6-Tf*, 0.25 nmol H_6-GFP and 0.25 nmol H_6-Tf* were pre-mixed in HBG (pH 7.4) before 50 µg Zr-*fum* MOF NPs (5 mg/mL in HBG, pH 7.4) were added (final volume 50 µL). The mixtures were incubated for 15 min at room temperature, diluted 1:1 with HBG (pH 7.4, final volume 100 µL) and added to the cells (100 µL MOF/His-tag solution per well). Controls were performed without the addition of MOF NPs. Cells were incubated for 24 h at 37 °C and 5 % CO_2 in a humified incubator. In case of HKUST-1 MOF NPs, medium was changed after 2 h and cells were incubated for further 22 h in fresh medium. Cells were washed with PBS (pH 7.4), detached with trypsin/ EDTA and diluted with fresh medium. Cells were centrifuged and resuspended in 500 µL PBS containing 10 % FBS at pH 4 to quench extracellular fluorescence. 1 ng/µL DAPI (4′,6-diamidino-2-phenylindole) was added shortly before the measurement. The cellular fluorescence was assayed by excitation of DAPI at 358 nm and detection of emission at 461 nm, fluorescein at 488 nm and detection of emission at 510 nm. For the co-delivery of H_6-GFP and H_6-Tf* the cellular fluorescence was also assayed by excitation of A647N at 635 nm and detection of emission at 665 nm. Cells were appropriately gated by forward/ sideward

scatter and pulse width for exclusion of doublets. DAPI was used to discriminate between viable and dead cells. Data were recorded by Cyan™ ADP flow cytometer (Dako, Hamburg, Germany) using Summit™ acquisition software (Summit, Jamesville, NY). Ten thousand gated cells per sample were collected. Analysis was done by FlowJo 7.6.5 flow cytometric analysis software. All experiments were performed in triplicates. MFI was calculated by FlowJo 7.6.5 flow cytometric analysis software and is depicted as normalization to HBG ± SD (n=3).

2.15 Cell fixation and staining

After incubation of cells with MOF mixtures according to the experimental description, medium was removed and cells were washed two times with PBS (pH 7.4). 4% (w/v) cold paraformaldehyde solution was added and cells were incubated for 30 min at room temperature with shaking. Cells were washed three times with PBS (pH 7.4). The nucleus was stained with DAPI (1 ng/µL), and Actin with rhodamine-phalloidin (2 µL/mL) for 15 min at room temperature. Staining solution was replaced with PBS (pH 7.4) and cells were stored at 4 °C.

2.16 Confocal laser scanning microscopy (CLSM)

Cells were seeded in 8-Well Nunc chamber slights (Thermo Scientific, Germany) at a density of 12.000 cells/well. Wells were coated with collagen A prior to seeding. After 24 h medium was replaced with 240 µL fresh medium. The various samples were prepared in the same way as has been described above but in a final volume of 60 µL HBG. 30 µg MOF NPs were functionalized with 0.3 nmol H_6-CF or H_6-GFP in 30 µL HBG (pH 7.4). In case of the co-delivery experiment, 0.15 nmol H_6-GFP were mixed with 0.15 nmol H_6-Tf* before the addition of 30 µg Zr-*fum* MOF NPs. After incubation of the mixtures for 15 min at room temperature, they were diluted 1:1 in HBG (pH 7.4, final volume 60 µL).The mixtures were added to the cells (60 µL MOF/His-tag solution per well) and incubated for 24 h. Controls were performed without the addition of MOF NPs. In case of HKUST-1 MOF NPs, the medium was changed after 2 h and cells were incubated for further 22 h in fresh medium. Prior to imaging nuclei were stained with Hoechst dye (1 ng/µL). Medium was replaced by DMEM without phenol red supplemented with 10 % FBS, 100 U/mL penicillin, 100 µg/mL streptomycin and cells were imaged using a Leica TCS SP8 confocal microscope with an 63x DIC oil immersion objective (Plan-APOCHROMAT).
For imaging of z-stacks, cells were fixated and Actin and the nucleus were stained prior to imaging (2.15). Images were recorded with a z-distance of 0.3 µm from basolateral (top) to

apical (bottom) pole of a representative cell. Pictures were taken at 405 nm (Hoechst dye or DAPI), 488 nm (H_6-GFP, H_6-CF), 514 nm (rhodamine-phalloidine), 633 nm (Atto647N).

2.17 Determination of transferrin receptor level

HeLa cells were washed with PBS (pH 7.4), detached with trypsin/ EDTA and diluted with fresh medium. Cells were counted and 100000 cells per sample were centrifuged and resuspended in 100 µL PBS (pH 7.4, 10 % FBS). 1 µL mouse anti-hCD71 (Dako) (1:100 dilution) for detection of the transferrin receptor or IgG1 (Dako) (1:100 dilution) as isotype control were added, cells were incubated for 1 h on ice and washed twice with PBS (pH 7.4, 10 % FBS). Cells were then stained with 0.5 µL Alexa Fluor 488 Goat Anti -Mouse IgG(H+L) (Life technologies) as secondary antibody (1:200 dilution) for 1 h on ice, washed twice with PBS (10 % FBS) and resuspended in 700 µL PBS (pH 7.4, 10 % FBS). 1 ng/µL DAPI (4′,6-diamidino-2-phenylindole) were added shortly before the measurement.
The cellular fluorescence was assayed by excitation of DAPI at 358 nm and detection of emission at 461 nm and fluorescein at 488 nm and detection of emission at 510 nm. Cells were appropriately gated by forward/sideward scatter and pulse width for exclusion of doublets. DAPI (4′,6-diamidino-2-phenylindole) was used to discriminate between viable and dead cells. Data were recorded by Cyan™ ADP flow cytometer (Dako, Hamburg, Germany) using Summit™ acquisition software (Summit, Jamesville, NY). Analysis was done by FlowJo 7.6.5 flow cytometric analysis software.

2.18 Statistical analysis

The statistical significance of experiments were analyzed using the t-test, *** $p \leq 0.001$, ** $p \leq 0.01$, * $p \leq 0.05$.

3 Supplementary Figures

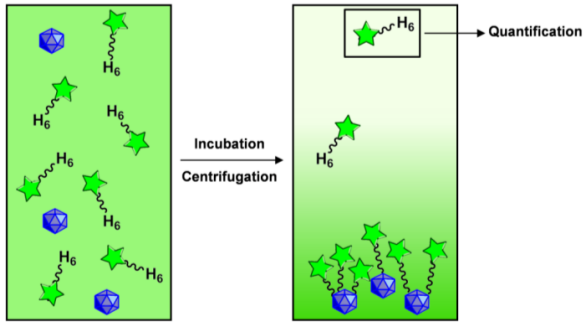

Scheme S1. **Investigation of His-tag binding to MOFs by detection of unbound peptides.** MOF NPs are added to an aqueous solution containing dye conjugated His-tags. The mixture is vortexted and incubated at room temperature. After centrifugation, residual free peptides are detected and quantified in the supernatant.

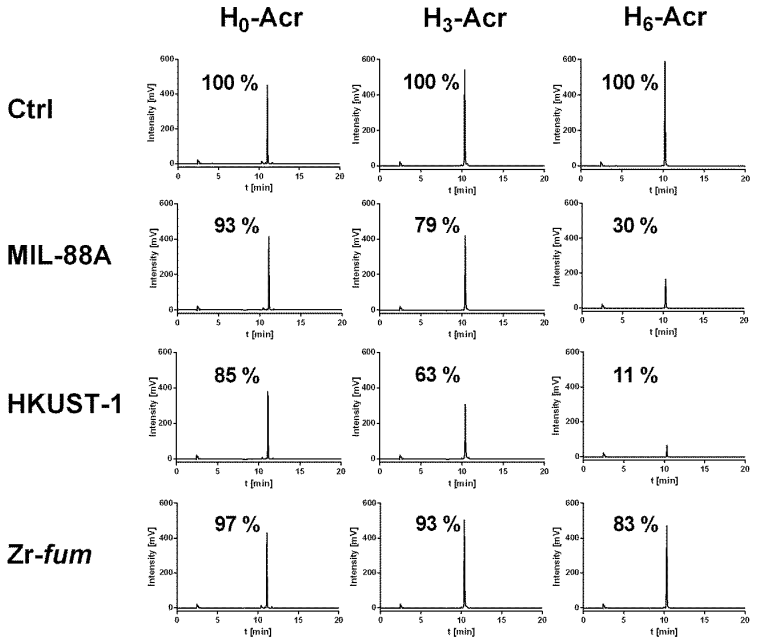

Figure S17. **Determination of free H_0-, H_3-, H_6-STOTDA-Acridine ($H_{0/3/6}$-Acr) in the supernatant after incubation with MOFs by RP-HPLC.** Sample preparation has been carried out analog to the assay illustrated in Scheme S1, Figure 1d and as described in the methods section 2.8 (Quantitative determination of H_0-, H_3-, H_6-Acr binding to MOF NPs). For the detection and quantification of free peptides a VWR Hitachi Chromaster HPLC system, a YMC Pack Pro C18 RS column (250 x 4.6 mm) and a gradient from 5 % acetonitrile (0.1 % TFA) to 100 % acetonitrile (0.1 % TFA) over 15 min was used for the analysis. Acridine containing compounds were detected at 360 nm. Peak areas were normalized to control samples without MOF incubation (Ctrl). 100 % values correspond to 130 nmol free peptide in the supernatant after incubation.

Table S6. **Quantitative determination of free and bound peptide $H_{0/3/6}$-Acr in the supernatant after incubation with MOFs based on RP-HPLC analysis Figure S17**

	Free peptide [nmol]			Bound peptide [nmol]		
	H_0-Acr	H_3-Acr	H_6-Acr	H_0-Acr	H_3-Acr	H_6-Acr
Ctrl	130	130	130	0	0	0
MIL-88A	120	103	39	10	27	91
HKUST	110	83	14	20	47	116
Zr-fum	126	121	108	4	9	22

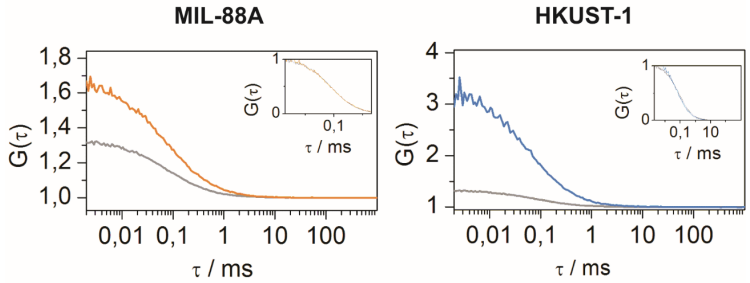

Figure S18. **Fluorescence correlation spectroscopy (FCS) measurements of H_6-A647N binding to MIL-88A (left) or HKUST-1 (right).** FCS measurements of H_6-A647N were performed before (grey) and after MOF addition (colored). Inserts show normalization of the same data.

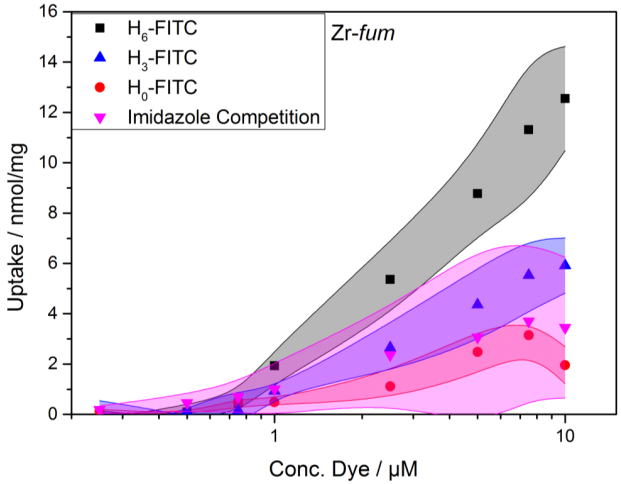

Figure S19. **Quantitative determination of bound H_0-, H_3-, H_6-FITC to Zr-*fum*.** After incubation of different amounts of dye with 25 µg Zr-*fum* in HBG buffer, MOF nanoparticles were removed by centrifugation, and the residual fluorescence signal of the supernatant was determined using a microplate reader (Fluostar OPTIMA, BMG Labtech). The average dye-uptake of the particles was calculated as the difference of the mean fluorescence signal between the solutions incubated with MOF nanoparticles and the control samples. For competition experiments 500 mM imidazole was added to the H_6-FITC solution prior to the incubation with Zr-*fum* MOF NPs. ± SD (*n*=3). The experiments resulted in a determined uptake of 13 nmol/mg H_6-FITC on the Zr-*fum* NP surface. The number of histidines in the H_n-sequence correlates with the uptake of the cargo-species on the MOF surface.

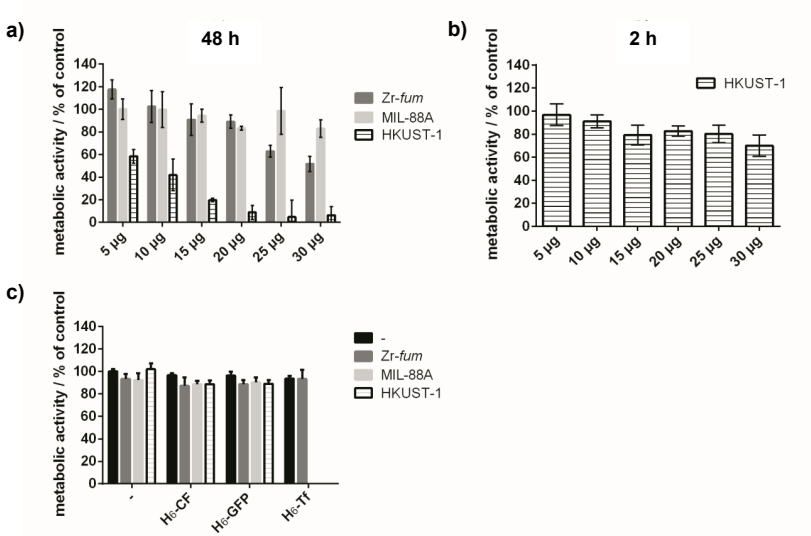

Figure S20. **Evaluation of cytotoxicity of different MOF nanoparticles and His-tags.** HeLa cells were incubated with different amounts of Zr-*fum* (dark grey), MIL-88A (light grey) and HKUST-1 (pattern) for 48 h **(a)** or 2 h **(b)**. **(c)** Incubation of HeLa cells with 10 µg MOFs modified with different His-tags or without His-tags (-). Data are presented as % metabolic activity of control cells ± SD (*n*=5) (MTT assay).

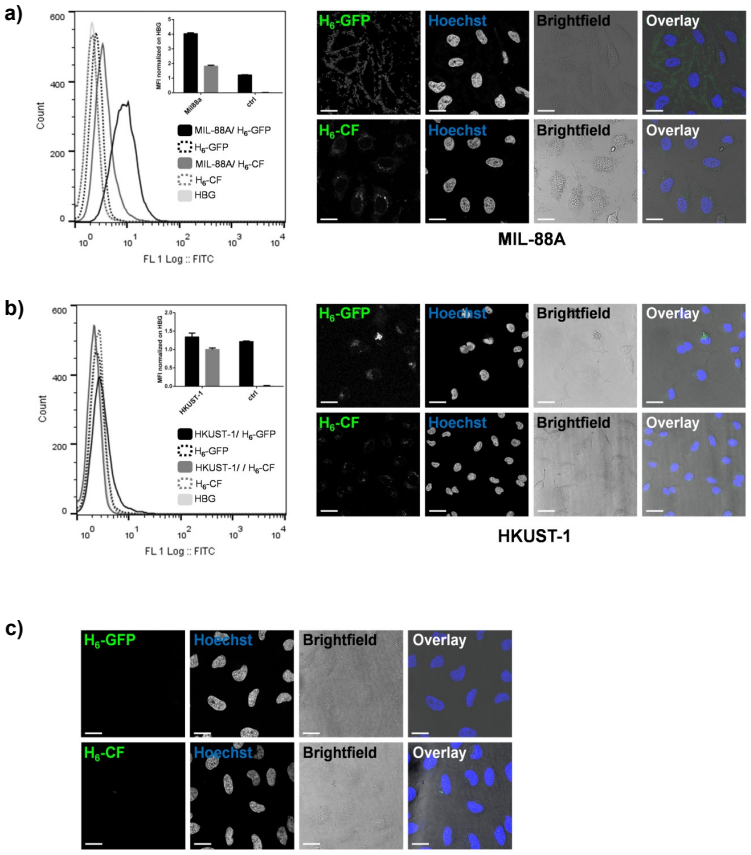

Figure S21. **Cellular uptake of H_6-GFP or H_6-CF functionalized MIL-88A or HKUST-1 MOF NPs.** H_6-GFP or H_6-CF were incubated with MOF NPs for 15 min at room temperature. Mixtures were put on HeLa cells at a concentration of 0.1 mg MOF NP/nmol His-tag per mL medium. MIL-88A MOF NPs were incubated on the cells for 24 h. HKUST-1 MOF NPs for 2 h.
Flow cytometric analysis: MOF NP/H_6-GFP (black), H_6-GFP (dotted black), MOF NP/H_6-CF (dark grey), H_6-CF (dotted dark grey), HBG (light grey). Inset shows mean fluorescence intensity (MFI) normalized to HBG. Ctrl indicates incubations without the addition of MOF NPs. Confocal laser scanning microscopy (CLSM) images from left to right: green fluoresence of H_6-GFP or H_6-CF, nuclear staining with Hoechst dye, brightfield picture, overlay of all three channels. Scale bar 25 µm.
a) Evaluation of cellular uptake using MIL-88A MOF NPs. Scale bar: 25 µm. **b)** Evaluation using HKUST-1 MOF NPs. Scale bar: 50 µm. **c)** Control incubations without the addition of MOF NPs H_6-GFP (upper row), H_6-CF (lower row). Scale bar: 25 µm.
Please note, that both MIL-88A and HKUST-1 MOF NPs have high quenching abilities, and especially the flow cytometric analysis might not be sensitive enough to detect the actual amount of internalized H_6-GFP, H_6-CF. The same might also be the case for CLSM.

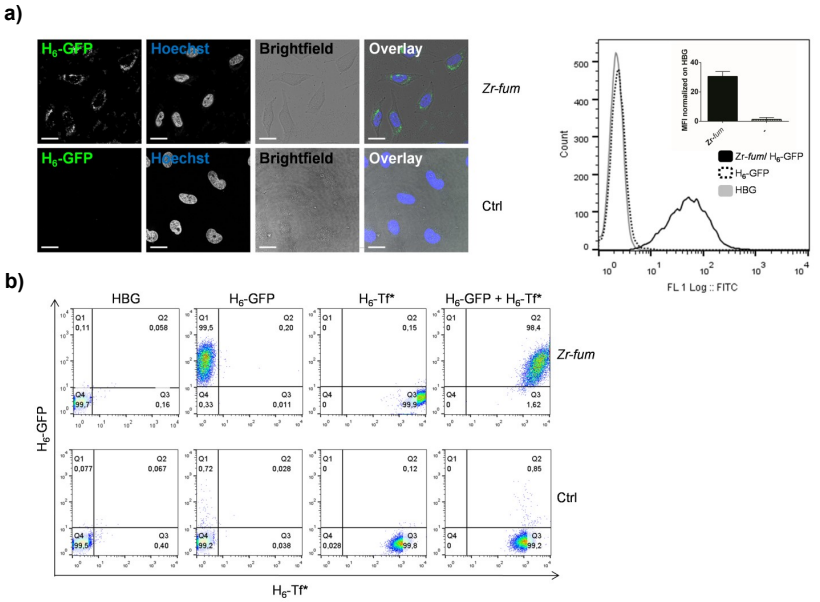

Figure S22. **Cellular uptake of H_6-GFP modified Zr-*fum* MOF NPs and co-delivery of H_6-GFP and H_6-Tf* into HeLa cells.** His-tags were incubated with Zr-*fum* MOF NPs for 15 min at room temperature. Different mixtures were incubated for 24 h on HeLa cells at a concentration of 0.1 mg Zr-*fum*MOF NP and 1 nmol His-tags per mL medium, followed by CLSM imaging or flow cytometric analysis. **a)** CLSM left to right: Green fluorescence of H_6-GFP, nuclear staining with hoechst dye, brightfield picture, overlay of all three channels. Ctrl: control without the addition of Zr-*fum* MOF NPs. Scale bar 25 µm. **b)** Evaluation of delivery of Zr-*fum*/H_6-GFP +H_6-Tf* (upper row) or control without the addition of Zr-*fum* MOF NPs (lower row). Left to right: HBG control. H_6-GFP, H_6-Tf*, H_6-GFP + H_6-Tf*. Scale bar: 25 µm.

Zr-fum/H_6-CF

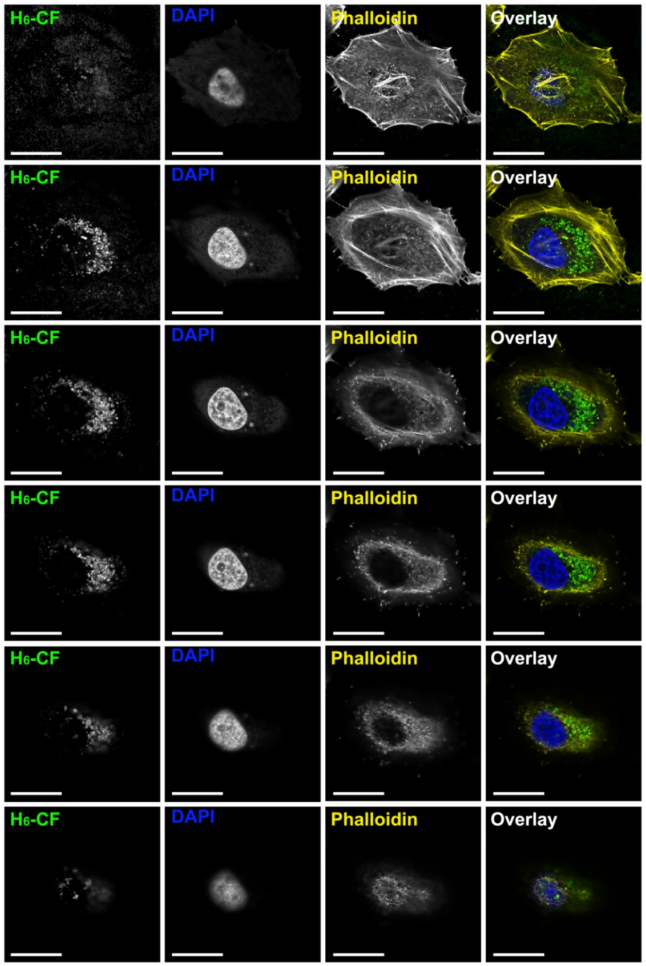

Figure S23. **Confocal laser scanning microscopy of cellular uptake of H_6-CF functionalized Zr-*fum* MOF NPs.** H_6-CF was incubated with MOF NPs for 15 min at room temperature. Mixtures were put on HeLa cells at a concentration of 0.1 mg MOF NP/nmol His-tag per mL medium and incubated on the cells for 24 h. Cells were fixated using 4% paraformaldehyde, and Actin was stained with rhodamine-phalloidin. 32 images with a z-distance of 0.3 µm were acquired from basolateral (top) to apical (bottom) pole of a representative cell. For illustration, planes with a distance of 0.9 µm were selected from the z-stack. Images from left to right: green: fluorescence of H_6-CF, nuclear staining with DAPI dye, yellow: Actin staining, overlay: overlay of all three channels. Scale bar: 25 µm.

H_6-CF

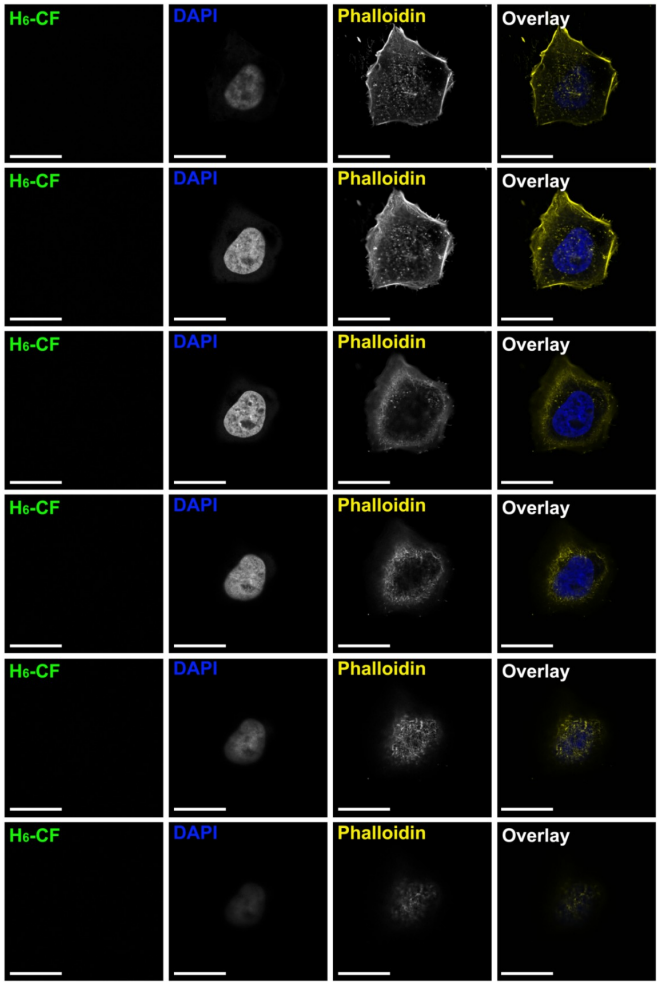

Figure S24. **Confocal laser scanning microscopy of cellular uptake of H_6-CF.** H_6-CF were put on HeLa cells at a concentration of 1 nmol His-tags per mL medium and incubated on the cells for 24 h. Cells were fixated using 4% paraformaldehyde, and Actin was stained with rhodamine-phalloidin. 24 images with a z-distance of 0.3 µm were acquired from basolateral (top) to apical (bottom) pole of a representative cell. For illustration, planes with a distance of 0.9 µm were selected from the z-stack. Images from left to right: green: fluorescence of H_6-CF, nuclear staining with DAPI dye, yellow: Actin staining, overlay: overlay of all three channels. Scale bar: 25 µm.

Zr-fum/H_6-GFP

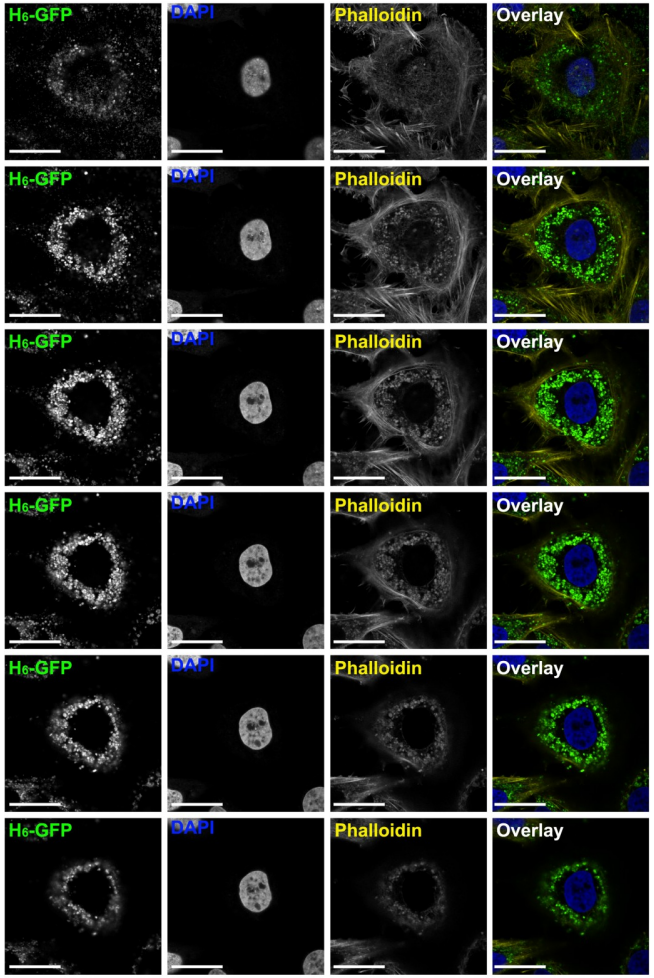

Figure S25. **Confocal laser scanning microscopy of cellular uptake of H_6-GFP functionalized Zr-*fum* MOF NPs.** H_6-GFP was incubated with MOF NPs for 15 min at room temperature. Mixtures were put on HeLa cells at a concentration of 0.1 mg MOF NP/nmol His-tag per mL medium and incubated on the cells for 24 h. Cells were fixated using 4% paraformaldehyde, and Actin was stained with rhodamine-phalloidin. 38 images with a z-distance of 0.3 µm were acquired from basolateral (top) to apical (bottom) pole of a representative cell. For illustration, planes with a distance of 0.9 µm were selected from the z-stack. Images from left to right: green: fluorescence of H_6-GFP, nuclear staining with DAPI dye, yellow: Actin staining, overlay: overlay of all three channels. Scale bar: 25 µm.

H_6-GFP

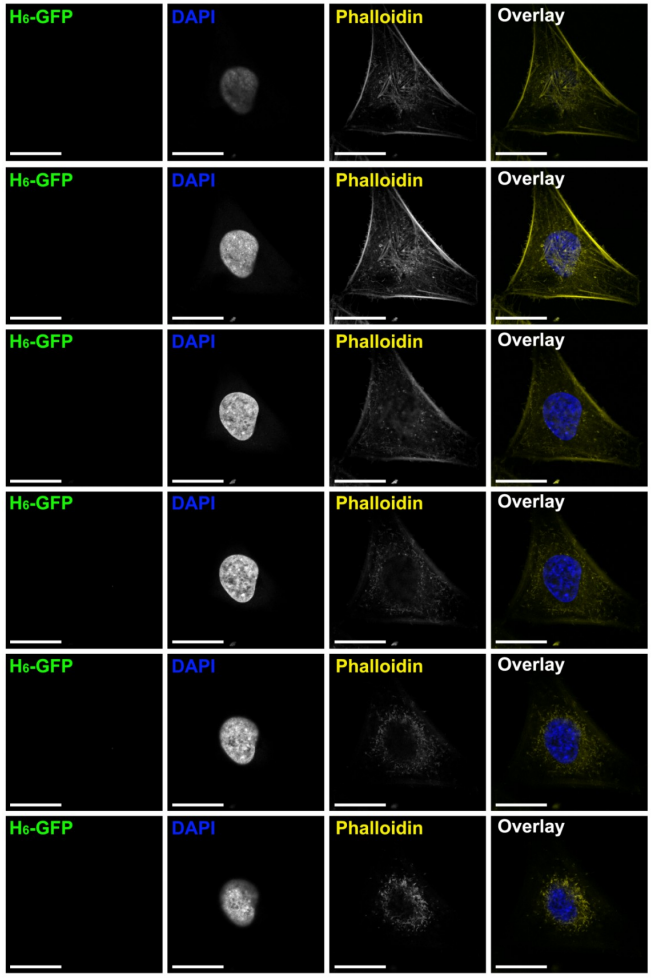

Figure S26. **Confocal laser scanning microscopy of cellular uptake of H_6-GFP.** H_6-GFP were put on HeLa cells at a concentration of 1 nmol His-tags per mL medium and incubated on the cells for 24 h. Cells were fixated using 4% paraformaldehyde, and Actin was stained with rhodamine-phalloidin. 38 images with a z-distance of 0.3 µm were acquired from basolateral (top) to apical (bottom) pole of a representative cell. For illustration, planes with a distance of 0.9 µm were selected from the z-stack. Images from left to right: green: fluorescence of H_6-GFP, nuclear staining with DAPI dye, yellow: Actin staining, overlay: overlay of all three channels. Scale bar: 25 µm.

Zr-fum/H_6-GFP – H_6-Tf*

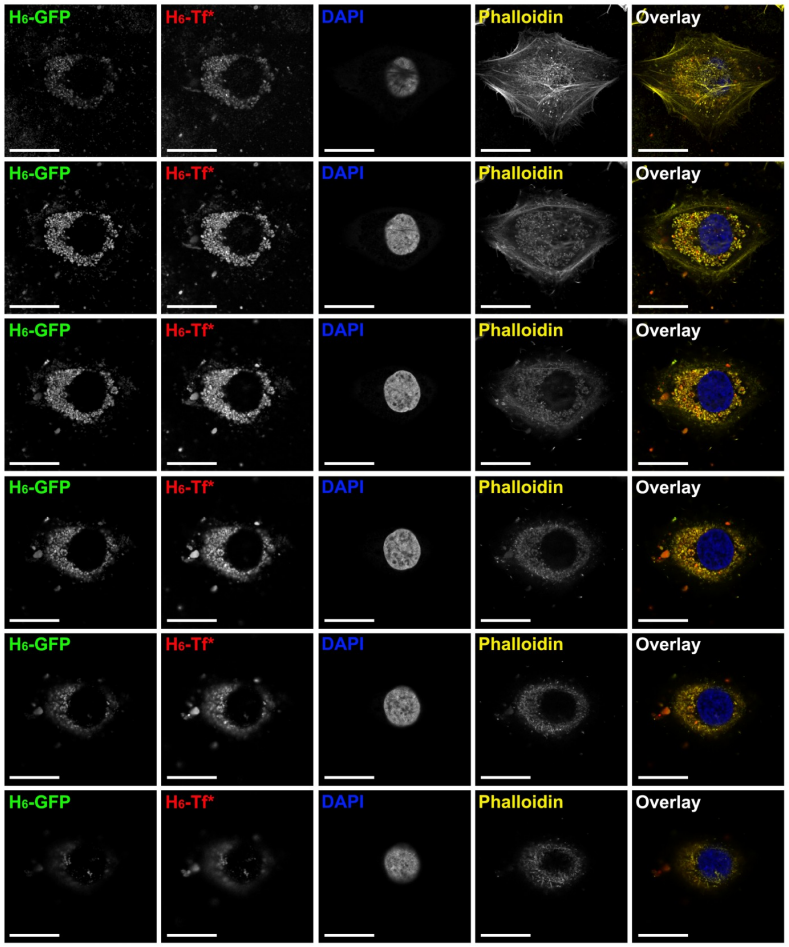

Figure S27. **Confocal laser scanning microscopy of cellular uptake of Zr-*fum* MOF NPs functionalized with H_6-GFP and H_6-Tf*.*** His-Tags were incubated with MOF NPs for 15 min at room temperature. Mixtures were put on HeLa cells at a concentration of 0.1 mg MOF NP/nmol His-tag per mL medium and incubated on the cells for 24 h. Cells were fixated using 4% paraformaldehyde, and Actin was stained with rhodamine-phalloidin. 29 images with a z-distance of 0.3 µm were acquired from basolateral (top) to apical (bottom) pole of a representative cell. For illustration, planes with a distance of 0.9 µm were selected from the z-stack. Images from left to right: green: fluorescence of H_6-GFP, red: fluorescence of H_6-Tf*, nuclear staining with DAPI dye, yellow: Actin staining, overlay: overlay of all three channels. Scale bar: 25 µm.

H_6-GFP – H_6-Tf*

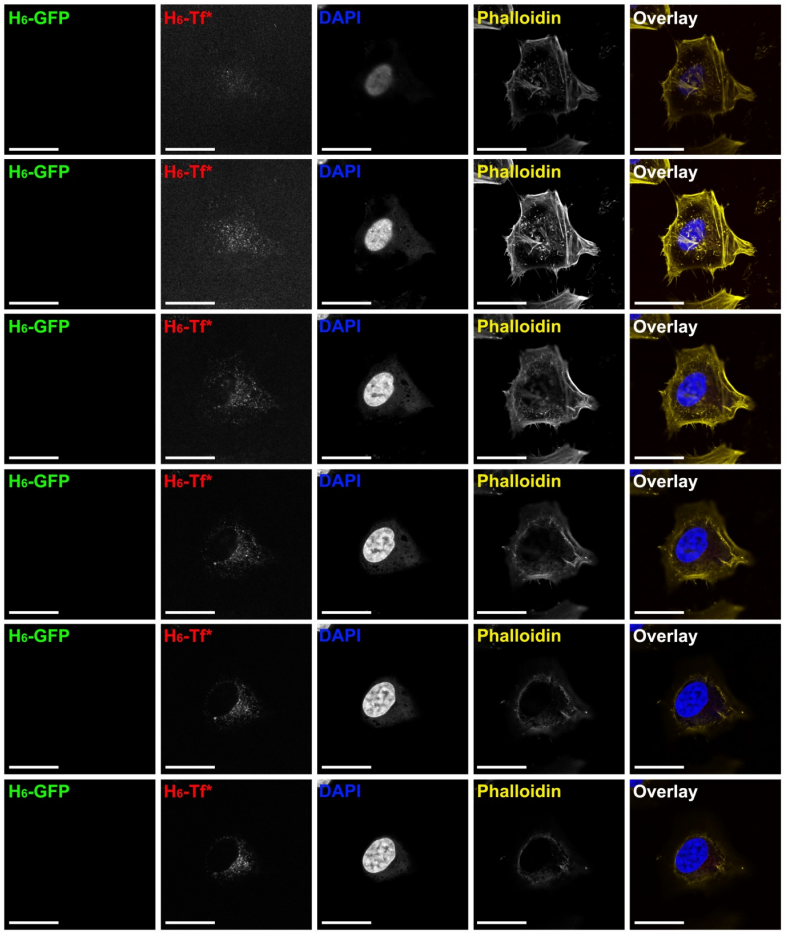

Figure S28. **Confocal laser scanning microscopy of cellular uptake of a mixture of H_6-GFP and H_6-Tf*.** A mixture of H_6-GFP and H_6-Tf* was put on HeLa cells at a concentration of 1 nmol His-tags per mL medium and incubated on the cells for 24 h. Cells were fixated using 4% paraformaldehyde, and Actin was stained with rhodamine-phalloidin. 29 images with a z-distance of 0.3 µm were acquired from basolateral (top) to apical (bottom) pole of a representative cell. For illustration, planes with a distance of 0.9 µm were selected from the z-stack. Images from left to right: green: fluorescence of H_6-GFP, red: fluorescence of H_6-Tf*, nuclear staining with DAPI dye, yellow: Actin staining, overlay: overlay of all three channels. Scale bar: 25 µm.

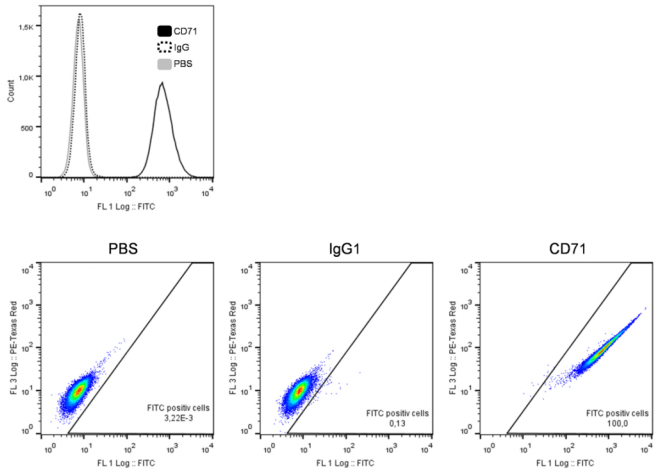

Figure S29. **Determination of surface expression level of transferrin receptor (TfR) in HeLa cells by flow cytometry.** Control cells (dotted black) were treated with mouse IgG1. Mouse anti-hCD71 antibody was used for the detection of the TfR (solid black). Alexa Fluor 488 Goat Anti -Mouse IgG(H+L) secondary antibody was used for the detection of receptor expression. Grey: PBS.

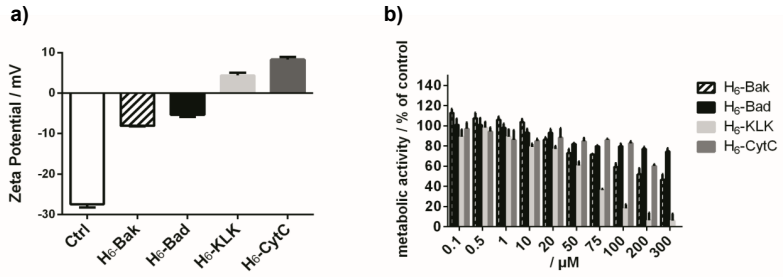

Figure S30. **Evaluation of toxicity and binding to Zr-*fum* MOF NPs of apoptosis inducing H_6- peptides and H_6-CytC. a)** H_6-Bak (pattern), H_6-Bad (black), H_6-KLK (light grey) or H_6-CytC (dark grey) were incubated with Zr-*fum* MOF NPs (Zr-*fum*/His-tag: 0.2 mg/nmol) for 15 min at room temperature. Samples were diluted to 0.1 mg Zr-*fum*/mL HBG and zeta potential was measured by electrophoretic laser-light scattering. Zeta potentials were calculated by the Smoluchowski equation, each sample was measured 3 times with 10 to 30 subruns at 25 °C. All samples differ significantly $p<0.0001$ from non-modified Zr-*fum* MOF NPs. White: unmodified Zr-*fum* MOF NPs, pattern: H_6-Bak, black: H_6-Bad, light grey: H_6-KLK, dark grey: H_6-CytC. **b)** After incubation of HeLa cells with different peptide concentrations for 48 h, metabolic activity was determined by MTT assay. H_6-Bak (pattern), H_6-Bad (black), H_6-KLK (light grey) or H_6-CytC (dark grey). Data are presented as % metabolic activity of control cells ± RSD (n=5). Please note that for H_6-CytC the highest concentration was 200 µM.

4 References

(1) Chalati, T.; Horcajada, P.; Gref, R.; Couvreur P.;Serre C.*J. Mat. Chem* **2011**, *21*, 2220.
(2) Huo J.; Brightwell M.; El Hankari S.; Ashesh, G.; Darren B. *J. Mat.Chem. A* **2013**, *1*, 15220
(3) Wißmann G.; Schaate A; Lilienthal S.; Bremer I.; Schneider A. M.; Behrens P. *Micropor. Mesopor. Mat.* **2012**, *152*, 64.
(4) Yakovenko, A.; Reibenspiels, J. H.; Bhuvanesh, N.; Zhour H.-C. *J. Appl. Crystallogr.* **2013**, 346.
(5) Maier, K.; Wagner, E. *J. Am.Chem. Soc.* **2012**, *134*, 10169.
(6) Magde D.; Elson E.; Webb W. W. *Phys. Rev. Lett.* **1972**, *29*.
(7) Rigler, R.; Mets, Ü.; Widengren, J.; Kask, P.*Eur. Biophys. J.* **1993**, *22*, 169.
(8) Haustein, E.; Schwille, P. *Annu.Rev. Biophys. Biomol. Struct.* **2007**, *36*, 151.
(9) Schwille, P.; Haustein, E. *Spectroscopy* **2009**, *94*, 1.
(10) Persson, G.; Thyberg, P.; Widengren, J. *Biophys. J.* **2008**, *94*, 977.
(11) Schwille, P.; Meyer-Almes, F. J.; Rigler, R. *Biophys. J.***1997**, *72*, 1878.
(12) Foo, Y. H.; Naredi-Rainer, N.; Lamb, D. C.; Ahmed, S.; Wohland, T. *Biophys.J.* **2012**, *102*, 1174.
(13) Rigler, R.; Foldes-Papp, Z.; Meyer-Almes, F. J.; Sammet, C.; Volcker, M.; Schnetz, A. *J. Biotechnol.* **1998**, *63*, 97.
(14) Wu, B.; Chen, Y.; Muller, J. D. *Biophys. J.* **2008**, *94*, 2800.

B.7 Originalpublikation P7

Tobias Preiß, Andreas Zimpel, Stefan Wuttke, Joachim O. Rädler.

Kinetic Analysis of the Uptake and Release of Fluorescein by Metal-Organic Framework Nanoparticles.

Materials 2017, 10 (2), 216.

materials

MDPI

Article

Kinetic Analysis of the Uptake and Release of Fluorescein by Metal-Organic Framework Nanoparticles

Tobias Preiß [1], Andreas Zimpel [2], Stefan Wuttke [2,*] and Joachim O. Rädler [1,*]

[1] Faculty of Physics and Center for NanoScience (CeNS), LMU Munich, Geschwister-Scholl-Platz 1, 80539 Munich, Germany; Tobias.Preiss@physik.lmu.de

[2] Department of Chemistry and Center for NanoScience (CeNS), LMU Munich, Butenandtstraße 11 (E), 81377 Munich, Germany; andreas.zimpel@cup.uni-muenchen.de

* Correspondence: stefan.wuttke@cup.uni-muenchen.de (S.W.); raedler@lmu.de (J.O.R.); Tel.: +49-89-218077626 (S.W.); +49-89-21802438 (J.O.R.)

Academic Editor: Claudio Pettinari

Received: 29 November 2016; Accepted: 9 February 2017; Published: 22 February 2017

Abstract: Metal-organic framework nanoparticles (MOF NPs) are promising guest-host materials with applications in separation, storage, catalysis, and drug delivery. However, on- and off-loading of guest molecules by porous MOF nanostructures are still poorly understood. Here we study uptake and release of fluorescein by two representative MOF NPs, MIL-100(Fe) and MIL-101(Cr). Suspensions of these MOF NPs exhibit well-defined size distributions and crystallinity, as verified by electron microscopy, dynamic light scattering, and X-ray diffraction. Using absorbance spectroscopy the equilibrium dissociation constants and maximum numbers of adsorbed fluorescein molecules per NP were determined. Time-resolved fluorescence studies reveal that rates of release and loading are pH dependent. The kinetics observed are compared to theoretical estimates that account for bulk diffusion into NPs, and retarded internal diffusion and adsorption rates. Our study shows that, rather than being simple volumetric carriers, MOF-NPs are dominated by internal surface properties. The findings will help to optimize payload levels and develop release strategies that exploit varying pH for drug delivery.

Keywords: metal organic framework; nanoparticle; loading and release

1. Introduction

The widespread use of porous materials in the field of separation, storage, and catalytic process technologies requires a thorough understanding of the adsorption and desorption of guest molecules within the porous structure. In this context, metal-organic frameworks (MOFs) are an interesting class of materials, as they are crystalline and, hence, possess a regular porous structure [1–4]. In MOFs, inorganic metal nodes connected by organic linkers create a diverse, but well-defined, chemical environment, which allows specific interactions with guest molecules. As a matter of fact, MOFs exhibit some of the highest porosities (1000 to 7000 m^2/g) of all known porous solids, with pore sizes in the range of 0.3 to 6 nm [5]. Their high porosities and, in particular, the combination of high surface area with tunable pore size render MOFs ideal for applications in gas storage and separation [6,7], catalysis [8–10], sensing [11,12], electronics [13], drug delivery [14–18], and X-ray analysis of the structures of guest molecules within the MOF scaffold [4,19].

Recently, several reports have pointed to the general applicability of MOF nanoparticles (MOF-NPs) for drug delivery, as they have high loading capacities and are functionalizable, and certain structures have been shown to be biocompatible (e.g., MIL-100(Fe); MIL stands for Materials of Institute Lavoisier) [11,15,16,18,20–25]. MOF-NPs have been loaded with various drugs, including cisplatin [26], 5-fluorouracil [27], ibuprofen [28], doxorubicin, and cidofovir [29]. Both MIL-100(Fe) and MIL-101(Cr) represent good model materials for drug delivery, due to their large pores (diameters of 25–29 Å for MIL-100 and 29–34 Å for MIL-101) and window sizes (diameters of 5–9 Å for MIL-100 and 12–17 Å for MIL-101) [24,30,31]. MIL-100 and 101 show high chemical stability and typically large BET surface areas of up to 6000 m^2/g for the bulk material (2000–4000 m^2/g as nanoparticles) [32–35]. Indeed, in many respects, MIL-100(Fe) NPs are the most promising MOF-based vehicles available for drug delivery [24,29,36].

The ability of NPs made of solid materials to load and then specifically release drug molecules within the human body has been at the forefront of biomedical nanotechnology for more than a decade [37–43]. Yet studies on the loading and release kinetics of drugs in porous nanocarriers are very rare, even for established systems based on polymer, silica, or liposome particles [38,44–46]. One basic question that remains open is how pore size affects uptake and offloading. It is known that, within porous materials, diffusion coefficients are reduced by a factor 10^4, as transport becomes an effectively 1D diffusion process [47]. Furthermore, the affinity of the cargo molecules for the internal surface of the porous material (host-guest interaction) is likely to play an important role in determining the kinetics of transport, as well as the loading capacity [48]. Within the diffusion-immobilization model it is conceived that molecules undergo repeated cycles of absorption, desorption, and brief spells of free diffusion before an equilibrium situation is reached [49,50]. In addition, the conditions will change during the course of in vivo delivery. Affinity is likely to depend on the pH value of the environment, owing to the influence of pH on the charge of both cargo and MOF. As the pH varies within the human body, release kinetics will vary with local acidity. With the use of MOF-NPs as reliable and tunable drug carrier systems in mind, characterization of host-guest interaction and release is essential for optimized dosing.

In this work, we study the loading and release kinetics of MIL-100(Fe) and MIL-101(Cr). Our goal is to elucidate—on the basis of these representative MOF-NPs—the mechanisms and limiting factors that drive and constrain, respectively, molecular transport in and out of porous NPs, and compare these results with theoretical estimates. To this end, we characterize the MOF-NPs using transmission electron microscopy (TEM), dynamic light scattering (DLS), and X-ray diffraction (XRD), and measure the uptake of fluorescein via fluorescence spectroscopy at various pH values. Fluorescein was used because its size is comparable to common drug molecules and it is possible to quantify it by fluorescence and absorption. We find that MIL-100(Fe) and MIL-101(Cr) NPs have well-defined size distributions and crystallinity, and remain crystalline in buffer. DLS and zeta-potential measurements show that NP agglomeration is strongly pH dependent. By performing titration studies we determined the dissociation constants for fluorescein (disodium salt) and find that the NPs have a high payload capacity, which is compatible with the internal area estimated from BET measurements. Kinetic fluorescence studies show fast loading kinetics with high affinity in (unbuffered) distilled water (at low pH) and slower loading kinetics (i.e., lower affinity) at high pH (7.4–8.4), while release shows the converse behavior: high affinity and slow release at low pH (and in water). We show that loading and release kinetics can be theoretically described by diffusion to target, followed by restricted internal diffusion and equilibrium binding to the internal surface (physisorption). These findings demonstrate that physicochemical studies of MOF-NP loading enable rational, predictive design of release scenarios, particularly with regard to varying pH conditions.

2. Results and Discussion

In all following experiments, we study MOF-NPs of types MIL-100(Fe) and MIL-101(Cr), which were synthesized as described in Wuttke et al. [51] Prior to the loading and release studies, we characterized the size distribution of the MOF-NPs using DLS, FCS, and TEM [52], their major structural features by XRD, and their porosities by measuring nitrogen adsorption and deriving sorption isotherms to confirm the expected regular porosity of MOF-NPs.

TEM images of MIL-100(Fe) and MIL-101(Cr) NPs reveal particles with an approximately spherical shape (Figure 1). Moreover, the TEM images indicate high crystallinity of the particles, as evidenced by the presence of electron diffraction fringes. We analyzed the size distribution based on different TEM images of MOF-NPs (see Supplementary material) [52]. Over 10,000 particles were examined for their projected size, assuming sphericity, and employing image analysis for the separation of closely adjacent particles (for details, see Supplementary material). The size histograms of both MOF-NPs reveal a slightly polydisperse ($\sigma > 5\%$ [53,54]) distribution (Figure 1d,e). MIL-100(Fe) NPs have a mean diameter of 52.4 nm ($\sigma = 32\%$, FWHM 30.9–69.5 nm), whereas MIL-101(Cr) NPs have a mean size of 18.9 nm ($\sigma = 35\%$, FWHM 10.3–25.7 nm). We utilized this information to estimate numbers of NPs per volume given an estimate of NP mass based on the crystallographic mass densities [30,31]. For MIL-100(Fe) NPs we used a mean radius of $r_{MIL-100} = 26.5$ nm and a mass density of $\rho_{MIL-100} = 0.98$ g/mL [30]. We obtained a mean mass per NP of $m_{MIL-100} = 76 \times 10^{-18}$ g and, thus, a number density of $N_{MIL-100} = 1.31 \times 10^{13}$ NPs per mg (for details, see SI). This corresponds to an NP number concentration of $n_{MIL-100} = 21.7$ pmol. Using the corresponding values $r_{MIL-101} = 9.45$ nm and $\rho_{MIL-101} = 0.62$ g/mL [31], we derived a mean particle mass of $m_{MIL-101} = 2.2 \times 10^{-18}$ g and thus $N_{MIL-101} = 4.56 \times 10^{14}$ particles per milligram ($n_{MIL-100} = 760$ pmol). These values were subsequently used to calculate molecular loading per NP.

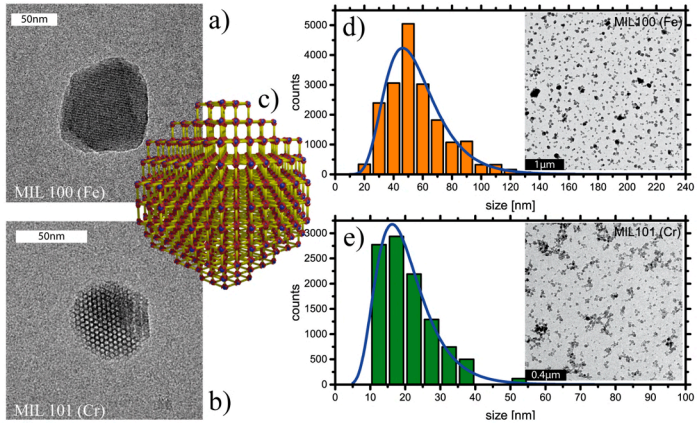

Figure 1. (**a**,**b**) TEM images of the two MOP-NP types used here show mesoporous structure and shape; (**c**) Simplified depiction of the crystalline structure with hollow pores taking up most of the volume; yellow rods with red ends: organic linker, blue dots: metal centers; (**d**,**e**) Size histogram of MOF-NPs based on particle analysis of electron micrographs yields a typical size for MIL-100(Fe) of 53 nm and for MIL-101(Cr) of 19 nm.

To complement the information derived from 2D projections of NPs imaged by TEM, DLS-based analysis of MOF-NPs in solution (see Supplementary material) provided information on their diffusive behavior and, hence, on the hydrodynamic radius of the NPs. In accordance with results reported in the literature [51], MIL-100(Fe), and MIL-101(Cr) NPs have hydrodynamic diameters of about 124 nm and 69 ($\pm$19) nm respectively. Comparison of these observations with the TEM size distribution results suggests that the NPs tend to form small agglomerations in unbuffered water. XRD measurements (see Supplementary material) confirm the crystallinity of the MOF-NPs observed in the TEM images [30,31].

In order to verify the stability of the particles over the time scales employed for loading and release, XRD measurements were performed on NPs that had been incubated in buffer for 1 h. The

results (see Supplementary material) show no significant change in the diffraction pattern, indicating that there is no structural change in the NPs.

On examining the size distributions of the NPs in the presence of various concentrations of fluorescein with DLS, we noted that the size of MIL-100(Fe) NPs increases slightly with increasing concentrations of fluorescein. This indicates that NPs tend to aggregate under varying fluorescein concentrations. One possible explanation is the alkalinity of fluorescein disodium salt, which will lead to concentration-dependent changes in pH. Electrostatic interactions between charged molecules or "crosslinking" of MOF NPs by fluorescein molecules, as has been found for, e.g., doxorubicin [55] might also contribute to this effect. In order to examine these possibilities more closely, we performed DLS and concurrent zeta-potential experiments on suspensions of MOF-NPs in water. The pH was increased incrementally in steps of 0.5 units (the initial suspension of MOFs in water has a pH of 2) by adding NaOH (see Supplementary material), allowing us to study the pH dependency of effective particle size in a well-defined system. DLS analysis yields an initial size of about 200 nm for MIL-100(Fe) and about 50 nm for MIL-101(Cr). With increasing alkalinity the zeta-potential drops, and below a value of about $\pm$25 mV particles tend to agglomerate. This finding is in agreement with the previous observation that a zeta-potential of greater than 25 mV (absolute value) is required for NPs to be stabilized by electrostatic repulsion [39,56]. In the case of MIL-100(Fe) NPs, the zeta-potential drops to negative values at pH values higher than 5.5. This leads to newly-emerging repulsion forces, so that agglomerates tend to separate again. The strong dependence of particle size and zeta-potential on the pH of the local environment is taken into account in our theoretical model (see below), but this could be avoided by appropriate coating of the MOF-NPs [36,51,57].

We then turned to the loading behavior, and determined the dissociation constants and the maximum capacities of MOF-NPs for uptake of fluorescein. For this purpose NP suspensions that had been incubated for a certain time (24 h) in fluorescein solutions of different concentrations were centrifuged, and the fluorescein remaining in the supernatant was quantified by UV-VIS absorption using a calibration curve based on a fluorescein dilution series (see Supplementary material). The difference in absorbance between the starting solutions and the supernatants recovered after centrifugal removal of both types of MOF-NPs is shown in Figure 2a,b (for details, see Supplementary material). We used initial fluorescein concentrations of between 20 µg/mL and 1500 µg/mL. Each data point represents the average of three independently prepared and measured samples. The data were fitted to a Langmuir-type sorption function:

$$P(c) = \frac{P_{\max} \cdot c}{c + K_D} \quad (1)$$

Here, c is the concentration of fluorescein, $P_{\max}$ is the saturation value of adsorbed fluorescein, and K_D is the dissociation constant (i.e., the concentration at which half of the maximal possible fluorescein is adsorbed). Both MIL-100(Fe) with $K_D^{MIL-100} = 4.4$ µg/mL = 11 µM and MIL-101(Cr) with $K_D^{MIL-101} = 11.7$ µg/mL =36 µM were found to have low dissociation constants, both compared to that of doxorubicin bound to MIL-100(Fe) as determined by Anand et al. (91 µM) and in light of its high maximal capacity for adsorbed fluorescein ($P_{\max}^{MIL-100} = 649.4$ µg =1.6 µmol and $P_{\max}^{MIL-101} = 413.5$ µg =1.0 µmol) [55]. We convert the adsorbed mass of fluorescein per mass unit of nanomaterial into a molar ratio (number of adsorbed fluorescein molecules per NP) using the molar mass of the NPs obtained from TEM analysis and $M_{FC} = 412.3$ g/mol for fluorescein disodium (see Supplementary material for further details). The calculated number of adsorbed fluorescein molecules per single NP is shown in Figure 2 (right axis). The large numbers (on the order of 10^3 to $>10^4$) indicate the high payload capacity of the MOF NPs. Note that these loading capacities correspond to a weight payload ratio (load weight/carrier weight) of 41% for MIL-101(Cr) and 65% for MIL-100(Fe). The latter is in good agreement with published data for other guest molecules [28,29,55]. We also constructed N_2 isotherms (Figure 2) for comparison of the amount of loaded fluorescein molecules with the accessible internal surface area of the MOF-NPs. The corresponding BET surface area is estimated to be $S_{BET} = 2004$ m^2/g

for MIL-100(Fe) and $S_{BET} = 3205\ m^2/g$ for MIL-101(Cr). By combining the maximum payload capacity per mg NPs with the BET surface results, we calculate the area occupied by one fluorescein molecule (A_{FC}) for both types of MOF-NPs: $A_{FC}^{MIL-100} = S_{BET}^{MIL-100} / p_{max}^{MIL-100} \cdot 1\ mg = 2\ nm^2$ and $A_{FC}^{MIL-101} = S_{BET}^{MIL-101} / p_{max}^{MIL-101} \cdot 1\ mg = 5\ nm^2$. For comparison, a single fluorescein molecule has an approximate projection area of about $1.1\ nm^2$ (see Supplementary material). Hence, we can assume that the internal surface of both MOF-NPs is densely packed with fluorescein molecules.

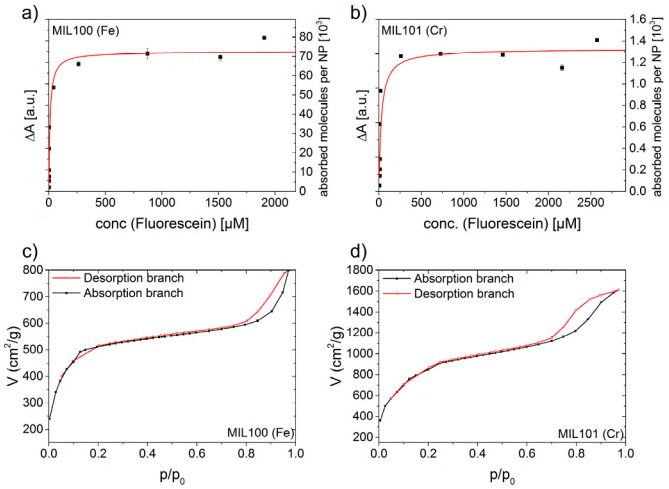

Figure 2. (**a**,**b**) Amounts of fluorescein loaded into MOF NP (obtained from the difference in absorption between the starting fluorescein solution and the supernatant recovered after loading) as a function of external fluorescein concentration fit to Langmuir-type curves. The calculated dissociation constants and maximum payload capacities per mg of NPs are: $K_D^{MIL100} = 11\ \mu M$, $K_D^{MIL101} = 136\ \mu M$, $P_{max}^{MIL100} = 649.4\ \mu g$, $P_{max}^{MIL101} = 413.5\ \mu g$ (**c**,**d**) Measurements of nitrogen gas absorption by the MOF-NPs. The BET surface area obtained for MIL-100(Fe) NPs is $2004\ m^2/g$ and for MIL-101(Cr) is $3205\ m^2/g$. Taking both into account yields a mean area occupied by one fluorescein molecule of $2\ nm^2$ for MIL-100(Fe) and $5\ nm^2$ for MIL-101(Cr).

We next addressed the questions of whether the entire payload can be released by reducing the external concentration of fluorescein, and whether this occurs on a reasonable timescale. To investigate offloading we measure the amounts of fluorescein molecules released by both types of MOF-NPs. To this end, MOF-NPs filled with fluorescein were resuspended in HBG buffer (20 mM HEPES + 5% glucose) at the physiologically relevant pH values of 5.1 (late endosome), 6.2 (early endosome) and 7.4 (blood) [58]. After 90 min, particles were removed by centrifugation and the absorbance of the supernatant was measured via UV-VIS (Figure 3). As future pharmaceutical applications will need cell culture experiments, we decided to use HBG as the environment for our experiments to have a cell culture approved buffer. As a reference for 100% release the absorbance of fluorescein solutions prepared in HBG at the same pH and concentration as the test solutions were used. In the case of MIL-101(Cr), almost no release (<3%) is observed within 90 min, while for MIL-100(Fe) the amount of released fluorescein increased with rising pH from below 3% at pH 5.1 to about 40% at pH 7.4. Thus, it appears that fluorescein binding to MIL-101(Cr) is essentially irreversible under our conditions, or at least exhibits very extremely long off-times.

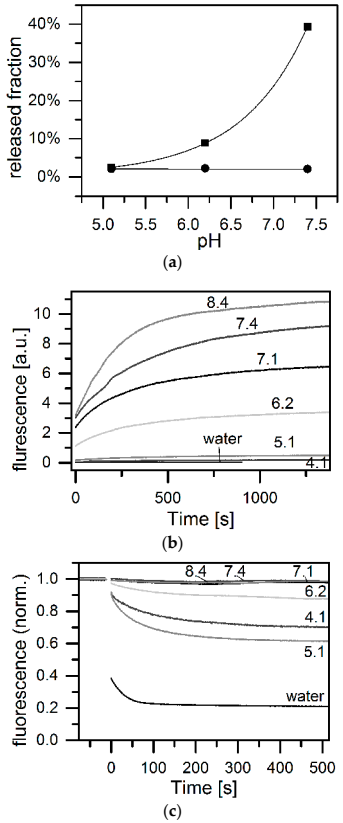

Figure 3. (**a**) Fraction of fluorescein released from prefilled MOF-NPs after 90 min in buffer (HBG) at different pH, determined by absorption measurements of supernatant containing free fluorescein. While MIL-101(Cr) (circles) shows almost no (<3%) release of fluorescein at any pH tested, for MIL-100(Fe) (squares) we observed a significant increase in release with rising pH (exponential fit to guide the eye); (**b**) Fluorescence quenching over the time course of release. MIL-100(Fe) nanoparticles filled with fluorescein were suspended in HBG buffered at different pHs. In water there is no increase in fluorescence intensity over time, indicating that there is no release; (**c**) Fluorescence quenching in the time course of loading. Fluorescein solution in HBG buffer at different pH and in water before and after addition of MIL-100(Fe) nanoparticles. In water the loading is the fastest and most efficient. In HBG at pH 4.1 to 6.2 it is slower and less efficient while at pH 7.1 to 8.4 no loading is observed at all.

The pH-dependent release from MIL-100(Fe) deserves further attention. We used time-resolved fluorescence measurements to determine the kinetics of MIL-100(Fe) loading and release, making use of the fluorescence quenching effect observed when fluorescein molecules bind to the porous scaffold of MIL-100(Fe) NPs. Since MIL-101(Cr) does not exhibit this quenching effect, this assay cannot be used on these NPs. Prefilled MIL-100(Fe) NPs were centrifuged and the remaining supernatant was

removed. Then the fluorescein-loaded MIL-100(Fe) NPs were re-suspended in HBG buffer at various pH values (pH = 4.1, 5.1, 6.2, 7.1, 7.4, and 8.4). Subsequently, the fluorescence signal originating from the fluorescein released from the MIL-100(Fe) NPs was recorded over time (see Figure 3b). The fluorescence signal at late time points increases with increasing pH, although the total amount of fluorescence released is more or less the same at all pHs tested, as can be seen when the fluorescence yield at the respective pH is taken into account. However, no rise in the fluorescence signal is seen in (unbuffered) water, indicating that no release occurs at all at the low pH of the suspension. When the fluorescence intensity after release into buffered medium was compared with that of the supernatant recovered after loading, it emerged that almost all of the fluorescein bound by the NPs is released again. When considering the release time traces in buffer with respect to the rates of fluorescein release, it is useful to normalize the data to the final fluorescence signal as shown in SI. Apart from the measurement at pH 8.4, all release curves end up stacked on top of each other, indicating that the temporal characteristics of cargo release are the same for all pH values.

These results require a detailed look at the on-loading kinetic. Loading was monitored by measuring the fluorescence of a 2 mL aliquot of dilute (0.1 µM) fluorescein solution from the moment a small amount (10 µg) of MIL-100(Fe) NPs was mixed into the solution. This was done for fluorescein dissolved in water and in HBG buffered at pH values of 4.1, 5.1, 6.2, 7.1, 7.4, and 8.4. The fluorescence of the solution was measured over time and normalized with respect to the fluorescence signal of the respective starting fluorescein solution without MOF-NPs (Figure 3c). This signal shows a significant decrease over time, which is interpreted as reflecting the decreasing amount of fluorescein remaining in solution due to uptake (and fluorescence quenching) by the MOF-NPs. Inspection of the normalized fluorescence signal after >400 s of loading time reveals a clear trend: In the case of distilled water (MilliQ), the fluorescence drops to ≈20% of the signal prior to NP addition. The drop is less obvious when loading is carried out in buffer (at all tested pHs from 4.1 to 8.4). In the latter case, however, a strong pH dependence is found: the initial level of fluorescence declines by about 35% at pH 4.1, the corresponding value at pH 6.1 is 14%, and no detectable change in fluorescence is observed at pH > 7. We, therefore, assume there is no uptake into the NPs under alkaline conditions, and no quenching of fluorescein. Thus, we find a clear dependence of the loading rate upon the pH, as revealed by the rate of decay of the fluorescence signal. To quantify this, we fitted an exponential decay to the data for the kinetics of loading (see Supplementary material). The resultant loading times are shown in Table 1. While loading takes place very rapidly in water, uptake rates in buffer fall with rising pH, and no loading can be quantified at pH 7.1 or higher.

Table 1. Results obtained from single exponential decay fitting of loading kinetics in water and HBG buffer at pH 4.1 to 8.4. While the loading process is very fast in water, in buffers with defined pH values rates of loading fall with rising pH, and no loading is detectable at pH 7.1 or higher.

pH	Rates of Decay (10^{-3}·s^{-1}) (from Exponential Fit)	Characteristic TIME Scales (s)
Water	13 ± 10	74.5 ±
4.1	10 ± 4	103.6 ±
5.1	10 ± 2	98.5 ±
6.2	6 ± 2	169.9 ±
7.1	-	-
7.4	-	-
8.4	-	-

Next we asked whether the observed loading kinetics can be understood as a reaction-limited diffusion process. To this end, we studied the time course of the change in the fluorescein signal during uptake by MIL-100(Fe) at various NP concentrations but constant fluorescein/NP ratio. In this way, the average distance a fluorescein molecule has to diffuse before reaching the NP surface is varied. Experiments were carried out at constant pH of 5.1. The fluorescence time courses decay exponentially

for all concentrations, as shown in Figure 4a. As before, we assume that fluorescein is quenched during adsorption to the internal MOF surface and, hence, that the fluorescence decay is a measure for the rate of loading. Data were fitted by single exponentials and the derived characteristic loading times were plotted as a function of NP concentration (Figure 4b). If the loading is dominated by diffusion of molecules from the bulk phase to the MOF surface, we can calculate the on-kinetics and compare the result to the data in Figure 4b. The expected time for diffusion to NP surfaces is estimated assuming that, for each NP, molecules are recruited from a spherical volume with a radius equal to half the average NP-NP distance. Diffusion of molecules in a spherical volume with radius R to a spherical absorber with radius r, in the center of that volume is described by the theory of Adam and Delbrück [59]. As further explicated in the SI we derive an estimate for the spherical radius R from the NP concentration. With this we obtain a typical diffusion-limited time for the capture of fluorescein (see Supplementary material):

$$\tau_{\mathrm{diff}}(c_{\mathrm{NP}}) \approx \frac{\pi\, r^2\, \rho}{18\, c_{\mathrm{NP}}\, D_{\mathrm{ex}}}$$

where D_{ex} is the external bulk diffusion coefficient of fluorescein, r the NP radius, ρ the NP mass density in mg/cm^3, and c_{NP} the NP concentration in mg/cm^3. Hence, the external diffusion time is predicted to decay in proportion to ${c_{\mathrm{NP}}}^{-1}$. The experimental loading times follow this prediction, as shown in Figure 4. The unbroken curve represents a fit to $A{\cdot}c_{NP}^{-1} + \tau_0$. The prefactor, A, is in good agreement with the time predicted assuming an effective density of ρ = 2 mg/cm^3 for the MOF-NPs (see also Supplementary material). However, there remains a finite loading time offset, τ_0 even at high NP concentrations, when diffusion time to the target becomes negligible. The latter offset time subsumes all internal processes that occur subsequently to diffusive transport to the NP, including internally hindered diffusion through the porous lattice, sorption to the internal surface and possibly surface rearrangements. A schematic representation of the molecular transport processes inside the mesoporous scaffold is depicted in Figure 5. If we consider a typical NP diameter to be of the order of 50 nm, then the corresponding internal diffusion constant ($D_{\mathrm{intra}} \approx r^2/t_0$) would be of the order of 10^{-17} m^2/s and, hence, 10^7 times smaller than the bulk diffusion constant (3.9×10^{-10} m^2/s) measured for fluorescein in water (see also supplementary information). Hence, the observed offset time, $\tau_0 \approx 60$ s, is surprisingly long. Possible explanations are the strong binding of fluorescein to the internal surface, slow relaxation processes take place in the adsorbed internal monolayer of fluorescein, or surface defects that lead to hindered diffusive entry) of fluorescein into the MOF NPs [60].

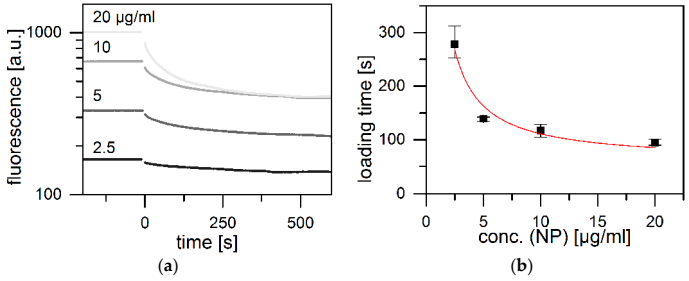

Figure 4. Fluorescence quenching in the time course of loading at various MIL-100(Fe) NP concentrations in HBG (pH 5.1) at fixed fluorescein to NP ratios. (**a**) Kinetics of the decay of fluorescein fluorescence after addition of NPs at time = 0. Time traces were fitted with single exponential decay; (**b**) The resulting loading times (in black) show a characteristic concentration dependency. This fits well with a model (red) involving a three-step process: free external diffusion, internal diffusion within the lattice and adsorption to the MOF network.

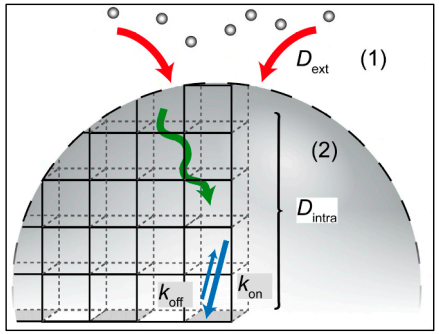

Figure 5. Illustration of the mass transport during loading: (1) external diffusion of fluorescein molecules towards the nanoparticles as described by the Adam and Delbrück model; (2) Concurrent intracrystalline diffusion and adsorption/desorption to/from the internal surface of the MOF NP (reaction-diffusion).

3. Materials and Methods

3.1. Equilibrium Measurements

Payload capacity was measured using a UV-VIS absorption spectrometer (NanoDrop 1000, Thermo Scientific, Waltham, UK). MOF-NPs (1 mg) in ethanol stock solution were centrifuged (45 min at 14,680 rpm, 20,238× *g*) to remove the supernatant ethanol. The pellet of MOF NPs was then dispersed in an aqueous dilution series of fluorescein sodium salt (Sigma-Aldrich, St. Louis, MO, USA) by vortexing and sonication (Bandelin Sonorex, Berlin, Germany), and incubated for 96 h under continuous agitation in a tube rotator. The suspensions were then centrifuged as before to obtain the supernatant fluorescein solution. The absorption spectra of the supernatant, as well as that of the original fluorescein solution, were measured and the area under the curve between 400 to 550 nm, hereinafter denoted as absorbance (see Supplementary material), was determined (OriginPro 9 64-bit, OriginLab, Wellesley Hills, MA, USA). This procedure was performed for a concentration series of fluorescein solutions ranging from 5 µg/mL to 1500 µg/mL. A straight line $A = m \cdot c + t$ was fitted to the integrated absorbance of the original fluorescein solution concentration series, where A is the measured absorbance and c the concentration of the original fluorescein solution (inset in Figure S2b).

To determine the amount of fluorescein released, 1 mg of MOF-NPs was first loaded with the compound by suspension in 1 mL of an aqueous solution (100 µg/mL) of fluorescein and incubated for 1 day on a rotary shaker at room temperature. Subsequently the nanoparticles were transferred into 1-mL aliquots of freshly-prepared HBG buffer at pH 5.1, 6.2, and 7.4 by centrifugation (15/45 min at 20,238× *g*), removal of the supernatant and resuspension in buffer. This was followed by 90-min incubation on the rotary shaker at room temperature. After final removal of the nanoparticles by centrifugation for 45 min as before, the absorption spectrum of the supernatant was measured. As a reference for 100% release, the absorption spectra of 100 µg/mL solutions of fluorescein in HBG buffered at pH 5.1, 6.2, and 7.4 were also obtained. The spectra were integrated over the range between 400 and 550 nm (OriginPro 9 64-bit) and the resulting absorbance of the released fluorescein solutions was compared with the reference absorbance at the same pH.

3.2. Kinetics of Loading/Release

Loading: For each measurement, a 2-mL aliquot of fluorescein solution (0.1 µg/mL ≈ 0.24 µmol), made up in water or HBG at pH 4.1, 5.1, 6.2, 7.1, 7.4, or 8.4, was filled into a polystyrene cuvette.

The fluorescence signal (divided by the instrument's lamp reference to correct for fluctuations in lamp brightness) emitted upon excitation at 492 nm (slit width, 3 nm) was recorded for at least 60 s in a Fluorolog 3 spectrometer (Horiba, Miyanohigashi, Japan) at 512 nm. Then 2 µL of MIL-100(Fe) suspension (=10 µg) in aqueous ethanol (5 mg/mL) was quickly pipetted into the cuvette and mixed, and the instrument cover was closed again (denoted as t = 0 s). The fluorescence signal was then monitored over the course of at least 500 s.

Release: For each measurement, 50-µg samples of NPs that had been incubated in 0.5 µg/mL fluorescein were recovered by centrifugation (for 15 min, as above), and the supernatant was discarded. The pellet was then re-suspended in 10 mL of water or HBG (buffered at one or another of the pH values mentioned above) by sonication (see above), and a 2-mL portion was rapidly transferred to a cuvette and the fluorescence signal was measured for at least 700 s as described above.

Sorption measurements (BET): Nitrogen sorption isotherms were measured at 77 K with a Quantachrome NOVA 4000e (Boynton Beach, FL, USA). Approximately 20 mg of nanoparticles was degassed at 150 °C in high vacuum for at least 12 h prior to measurement. Evaluation of the sorption data was carried out using ASiQwin™ software (Version 2.0, Quantachrome Instruments). BET surface areas were calculated with the linearized form of the BET equation. For all samples the correlation coefficient was higher than 0.999. Adsorption isotherms were used to calculate the pore size distribution by quenched-solid density functional theory (QSDFT, N_2 at 77 K on carbon, cylindrical/spherical pores adsorption branch).

Transmission Electron Microscopy (TEM): For TEM analysis 10 µL aliquots of ethanolic MOF-NP suspension were dried on 300 mesh Formvar/carbon copper grids (Ted Pella, Redding, CA, USA). Pictures of MOF NPs on grids were obtained on a JEM 1011 (JEOL, Tokyo, Japan) at an acceleration voltage of 80 kV.

X-ray diffraction (XRD): For XRD measurements, approx. 1 mg of the powdered material was distributed homogeneously between two acetate foils (ultraphan) with a thickness of 0.014 mm and fixed in the sample holder. The samples were the measured with the transmission diffractometer system Stadi MP (STOE, Darmstadt, Germany) with Cu Kα1 radiation (λ = 1.54060 Å) and a Ge(111) single-crystal monochromator. Diffraction patterns were recorded with a solid-state strip detector MYTHEN 1K (DECTRIS, Baden-Daettwil, Switzerland) in omega-2-theta scan mode using a step size of 4.71° and a counting time of 80 s per step.

Dynamic light scattering (DLS) and zeta-potential measurements: DLS and zeta-potential measurements of the particles in dispersion (approx. 0.1 mg/mL) were carried out using a Malvern Zetasizer (Nano Series, Nano-ZS, Herrenberg, Germany). For measurements of the pH dependence of the zeta-potential, the instrument was equipped with a Malvern Multi-Purpose Titrator (MPT-2, Herrenberg, Germany). A 10-mL aqueous suspension of nanoparticles (0.1 mg/mL) was set to the starting pH with HCl (0.1 M) and titrated in steps of 0.5 pH units with NaOH (0.01 or 0.1 M, respectively) up to the final pH value.

4. Conclusions

In summary, we have studied the loading (release) of a model guest molecule (fluorescein) into (from) porous MOF-NPs. We found for both studied NP types, MIL-100(Fe) and MIL-101(Cr), that significant amounts of fluorescein can be adsorbed at room temperature. The measured loading capacities, in the range of $>10^3$ molecules per NP, are compatible with the measured internal surface area available. The loading rate in the case of MIL-100(Fe) is found to be dependent on the pH and the solvent (water or HBG). Our studies show that optimal loading of fluorescein is achieved in MilliQ water, and no release from the NPs is detected in this case. Unlike loading, however, the pH dependence of payload release varies between the two types of NPs studied. Virtually no release from MIL-101(Cr) occurs at any of the pH values tested, whereas MIL-100(Fe) NPs release between 3% (at pH 5.1) and about 40% (at pH 7.4) of their adsorbed fluorescein. These findings suggest that electrostatic interactions possibly contribute to the confinement of the guest molecules inside the MOF

pores. Considering the versatile MOF chemistry, as well as the different ways how to functionalize a MOF scaffold encompass a controlling of the MOF host-guest interactions.

Thus, MOF nanocarriers are good candidates for drug delivery and other applications where a high payload is desirable. In addition, MIL-100(Fe) shows release characteristics that can be tuned via pH. The latter result demonstrates that controlled release from MOF-NPs can be detected when loading and offloading of payload molecules by these nanocarriers are characterized. This information is vital for clinical applications as a possible drug delivery system. However, only a small number of relevant drugs exhibit optical fluorescence or optical adsorption changes that can be exploited for time-resolved release studies. Thus, there remains a need for alternative characterization methods to assess loading and release behavior, and to optimize MOF nanocarriers for regulated drug delivery using refined chemical functionalization.

Supplementary Materials: The following are available online at www.mdpi.com/1996-1944/10/2/216/s1.

Acknowledgments: The authors are grateful for financial support from the Excellence Clusters NIM (Nanosystems Initiative Munich), CeNS (Center for Nanoscience Munich), FP7 EU grants NanoMILE and NanoTransKinetics. S.W. is grateful for financial support from the Deutsche Forschungsgemeinschaft (DFG) through DFG-project WU 622/4-1. We thank Susanne Kempter for her support with the TEM set-up, Ulrich Lächelt for HBG support and for fruitful discussions.

Author Contributions: T.P. performed loading and release experiments and evaluated the results in discussions with J.O.R. and S.W. on a physical background. MOF nanoparticles synthesis and characterization was done by A.Z. All authors contributed to writing of the paper and the revisions, while T.P. and S.W. did the main part of the manuscript.

Conflicts of Interest: The authors declare no conflict of interest.

References

1. Zhou, H.C.; Long, J.R.; Yaghi, O.M. Introduction to Metal-Organic Frameworks. *Chem. Rev.* **2012**, *112*, 673–674. [CrossRef] [PubMed]
2. Zhou, H.-C.; Kitagawa, S. Metal–organic Frameworks (MOFs). *Chem. Soc. Rev.* **2014**, *43*, 5415–5418. [CrossRef] [PubMed]
3. Férey, G. Hybrid Porous Solids: Past, Present, Future. *Chem. Soc. Rev.* **2008**, *37*, 191–214. [CrossRef] [PubMed]
4. Inokuma, Y.; Yoshioka, S.; Ariyoshi, J.; Arai, T.; Hitora, Y.; Takada, K.; Matsunaga, S.; Rissanen, K.; Fujita, M. X-Ray Analysis on the Nanogram to Microgram Scale Using Porous Complexes. *Nature* **2013**, *495*, 461–466. [CrossRef] [PubMed]
5. Furukawa, H.; Cordova, K.; O'Keeffe, M.; Yaghi, O.M. The Chemistry and Applications of Metal-Organic Frameworks. *Science* **2013**, *341*, 974–990. [CrossRef] [PubMed]
6. He, Y.; Zhou, W.; Qian, G.; Chen, B. Methane Storage in Metal–organic Frameworks. *Chem. Soc. Rev.* **2014**, *43*, 5657–5678. [CrossRef] [PubMed]
7. Van de Voorde, B.; Bueken, B.; Denayer, J.; de Vos, D. Adsorptive Separation on Metal-Organic Frameworks in the Liquid Phase. *Chem. Soc. Rev.* **2014**, *43*, 5766–5788. [CrossRef] [PubMed]
8. Corma, A.; García, H.; Llabrés i Xamena, F.X. Engineering Metal Organic Frameworks for Heterogeneous Catalysis. *Chem. Rev.* **2010**, *110*, 4606–4655. [CrossRef] [PubMed]
9. Dhakshinamoorthy, A.; Garcia, H. Metal–organic Frameworks as Solid Catalysts for the Synthesis of Nitrogen-Containing Heterocycles. *Chem. Soc. Rev.* **2014**, *5750*, 5750–5765. [CrossRef] [PubMed]
10. Lee, J.; Farha, O.K.; Roberts, J.; Scheidt, K.A.; Nguyen, S.T.; Hupp, J.T. Metal-Organic Framework Materials as Catalysts. *Chem. Soc. Rev.* **2009**, *38*, 1450–1459. [CrossRef] [PubMed]
11. Kreno, L.E.; Leong, K.; Farha, O.K.; Allendorf, M.; van Duyne, R.P.; Hupp, J.T. Metal–Organic Framework Materials as Chemical Sensors. *Chem. Rev.* **2012**, *112*, 1105–1125. [CrossRef] [PubMed]
12. Falcaro, P.; Ricco, R.; Doherty, C.M.; Liang, K.; Hill, A.J.; Styles, M.J. MOF Positioning Technology and Device Fabrication. *Chem. Soc. Rev.* **2014**, *43*, 5513–5560. [CrossRef] [PubMed]
13. Stavila, V.; Talin, A.A.; Allendorf, M.D. MOF-Based Electronic and Opto-Electronic Devices. *Chem. Soc. Rev.* **2014**, *43*, 5994–6010. [CrossRef] [PubMed]
14. Horcajada, P.; Gref, R.; Baati, T.; Allan, P.K.; Maurin, G.; Couvreur, P.; Férey, G.; Morris, R.E.; Serre, C. Metal–Organic Frameworks in Biomedicine. *Chem. Rev.* **2012**, *112*, 1232–1268. [CrossRef] [PubMed]

15. Giménez-Marqués, M.; Hidalgo, T.; Serre, C.; Horcajada, P. Nanostructured Metal-Organic Frameworks and Their Bio-Related Applications. *Coord. Chem. Rev.* **2015**, *307*, 342–360. [CrossRef]
16. He, C.; Liu, D.; Lin, W. Nanomedicine Applications of Hybrid Nanomaterials Built from Metal–Ligand Coordination Bonds: Nanoscale Metal–Organic Frameworks and Nanoscale Coordination Polymers. *Chem. Rev.* **2015**, *115*, 11079–11108. [CrossRef] [PubMed]
17. Lismont, M.; Dreesen, L. Wuttke, S Metal-Organic Framework Nanoparticles in Photodynamic Therapy: Current Status and Perspectives. *Adv. Funct. Mater.* **2017**. [CrossRef]
18. Wuttke, S.; Lismont, M.; Escudero, A.; Rungtaweevoranit, B.; Parak, W.J. Positioning Metal-Organic Framework Nanoparticles within the Context of Drug Delivery–A Comparison with Mesoporous Silica Nanoparticles and Dendrimers. *Biomaterials* **2017**. [CrossRef] [PubMed]
19. Lee, S.; Kapustin, E.A.; Yaghi, O.M. Coordinative Alignment of Molecules in Chiral Metal-Organic Frameworks. *Science* **2016**, *353*, 808–811. [CrossRef] [PubMed]
20. Rungtaweevoranit, B.; Zhao, Y.; Choi, K.M.; Yaghi, O.M. Cooperative Effects at the Interface of Nanocrystalline Metal–organic Frameworks. *Nano Res.* **2016**, *9*, 47–58. [CrossRef]
21. Furukawa, S.; Reboul, J.; Diring, S.; Sumida, K.; Kitagawa, S. Structuring of Metal-Organic Frameworks at the Mesoscopic/macroscopic Scale. *Chem. Soc. Rev.* **2014**, *43*, 5700–5734. [CrossRef] [PubMed]
22. McGuire, C.V.; Forgan, R.S. The Surface Chemistry of Metal-Organic Frameworks. *Chem. Commun.* **2015**, *51*, 5199–5217. [CrossRef] [PubMed]
23. Kundu, T.; Mitra, S.; Patra, P.; Goswami, A.; Díaz Díaz, D.; Banerjee, R. Mechanical Downsizing of a Gadolinium(III)-Based Metal-Organic Framework for Anticancer Drug Delivery. *Chem. A Eur. J.* **2014**, *20*, 10514–10518. [CrossRef] [PubMed]
24. Wuttke, S.; Zimpel, A.; Bein, T.; Braig, S.; Stoiber, K.; Vollmar, A.; Müller, D.; Haastert-Talini, K.; Schaeske, J.; Stiesch, M.; et al. Nanosafety: Validating Metal-Organic Framework Nanoparticles for Their Nanosafety in Diverse Biomedical Applications (Adv. Healthcare Mater. 2/2017). *Adv. Healthc. Mater.* **2017**, *6*, 1600818. [CrossRef] [PubMed]
25. Röder, R.; Preiß, T.; Hirschle, P.; Steinborn, B.; Zimpel, A.; Hoehn, M.; Rädler, J.O.; Bein, T.; Wagner, E.; Wuttke, S.; et al. Multifunctional Nanoparticles by Coordinative Self- Assembly of His-Tagged Units with Metal-Organic Frameworks. *J. Am. Chem. Soc.* **2017**. [CrossRef] [PubMed]
26. Huxford, R.C.; Della Rocca, J.; Lin, W. Metal-Organic Frameworks as Potential Drug Carriers. *Curr. Opin. Chem. Biol.* **2010**, *14*, 262–268. [CrossRef] [PubMed]
27. Wang, J.; Jin, J.; Li, F.; Li, B.; Liu, J.; Jin, J.; Wang, C.; Zeng, Y.; Wang, Y. Combined Experimental and Theoretical Insight into the Drug Delivery of Nanoporous Metal-Organic Frameworks. *RCS Adv.* **2015**, *5*, 85606–85612. [CrossRef]
28. Bernini, M.C.; Fairen-Jimenez, D.; Pasinetti, M.; Ramirez-Pastor, A.J.; Snurr, R.Q. Screening of Bio-Compatible Metal-Organic Frameworks as Potential Drug Carriers Using Monte Carlo Simulations. *J. Mater. Chem. B* **2014**, *2*, 766–774. [CrossRef]
29. Horcajada, P.; Chalati, T.; Serre, C.; Gillet, B.; Sebrie, C.; Baati, T.; Eubank, J.F.; Heurtaux, D.; Clayette, P.; Kreuz, C.; et al. Porous Metal-Organic-Framework Nanoscale Carriers as a Potential Platform for Drug Delivery and Imaging. *Nat. Mater.* **2010**, *9*, 172–178. [CrossRef] [PubMed]
30. Horcajada, P.; Surblé, S.; Serre, C.; Hong, D.-Y.; Seo, Y.-K.; Chang, J.-S.; Grenèche, J.-M.; Margiolaki, I.; Férey, G. Synthesis and Catalytic Properties of MIL-100(Fe), an iron(III) Carboxylate with Large Pores. *Chem. Commun.* **2007**, *100*, 2820–2822. [CrossRef] [PubMed]
31. Férey, G.; Mellot-Draznieks, C.; Serre, C.; Millange, F.; Dutour, J.; Surblé, S.; Margiolaki, I. A Chromium Terephthalate-Based Solid with Unusually Large Pore Volumes and Surface Area. *Science* **2005**, *309*, 2040–2042. [CrossRef] [PubMed]
32. Llewellyn, P.L.; Bourrelly, S.; Serre, C.; Vimont, A.; Daturi, M.; Hamon, L.; de Weireld, G.; Chang, J.S.; Hong, D.-Y.; Hwang, Y.K.; et al. High Uptakes of CO_2 and CH_4 in Mesoporous Metal-Organic Frameworks MIL-100 and MIL-101. *Langmuir* **2008**, *24*, 7245–7250. [CrossRef] [PubMed]
33. Walton, K.S.; Snurr, R.Q. Applicability of the BET Method for Determining Surface Areas of Microporous Metal-Organic Frameworks. *J. Am. Chem. Soc.* **2007**, *129*, 8552–8556. [CrossRef] [PubMed]
34. Jhung, S.H.; Lee, J.H.; Yoon, J.W.; Serre, C.; Férey, G.; Chang, J.S. Microwave Synthesis of Chromium Terephthalate MIL-101 and Its Benzene Sorption Ability. *Adv. Mater.* **2007**, *19*, 121–124. [CrossRef]

35. García Márquez, A.; Demessence, A.; Platero-Prats, A.E.; Heurtaux, D.; Horcajada, P.; Serre, C.; Chang, J.S.; Férey, G.; de La Peña-O'Shea, V.A.; Boissière, C.; et al. Green Microwave Synthesis of MIL-100(Al, Cr, Fe) Nanoparticles for Thin-Film Elaboration. *Eur. J. Inorg. Chem.* **2012**, *100*, 5165–5174. [CrossRef]
36. Zimpel, A.; Preiß, T.; Röder, R.; Engelke, H.; Ingrisch, M.; Peller, M.; Rädler, J.O.; Wagner, E.; Bein, T.; Lächelt, U.; et al. Imparting Functionality to MOF Nanoparticles by External Surface Selective Covalent Attachment of Polymers. *Chem. Mater.* **2016**, *28*, 3318–3326. [CrossRef]
37. Kim, B.; Han, G.; Toley, B.J.; Kim, C.; Rotello, V.M.; Forbes, N.S. Tuning Payload Delivery in Tumour Cylindroids Using Gold Nanoparticles. *Nat. Nanotechnol.* **2010**, *5*, 465–472. [CrossRef] [PubMed]
38. Andersson, J.; Rosenholm, J.; Areva, S.; Lindén, M. Influences of Material Characteristics on Ibuprofen Drug Loading and Release Profiles from Ordered Micro-and Mesoporous Silica Matrices. *Chem. Mater.* **2004**, *16*, 4160–4167. [CrossRef]
39. Goesmann, H.; Feldmann, C. Nanoparticulate Functional Materials. *Angew. Chem. Int. Ed.* **2010**, *49*, 1362–1395. [CrossRef] [PubMed]
40. Mura, S.; Nicolas, J.; Couvreur, P. Stimuli-Responsive Nanocarriers for Drug Delivery. *Nat. Mater.* **2013**, *12*, 991–1003. [CrossRef] [PubMed]
41. Farokhzad, O.C.; Langer, R. Impact of Nanotechnology on Drug Delivery. *ACS Nano* **2009**, *3*, 16–20. [CrossRef] [PubMed]
42. Li, Z.; Barnes, J.C.; Bosoy, A.; Stoddart, J.F.; Zink, J.I. Mesoporous Silica Nanoparticles in Biomedical Applications. *Chem. Soc. Rev.* **2012**, *41*, 2590–2605. [CrossRef] [PubMed]
43. Chou, L.Y.T.; Ming, K.; Chan, W.C.W.; Smith, A.M.; Nie, S.M.; Eustis, S.; El-Sayed, M.A.; Lu, A.H.; Salabas, E.L.; Schuth, F.; et al. Strategies for the Intracellular Delivery of Nanoparticles. *Chem. Soc. Rev.* **2011**, *40*, 233–245. [CrossRef] [PubMed]
44. Zhao, Y.; Ren, W.; Zhong, T.; Zhang, S.; Huang, D.; Guo, Y.; Yao, X.; Wang, C.; Zhang, W.-Q.; Zhang, X.; et al. Tumor-Specific pH-Responsive Peptide-Modified pH-Sensitive Liposomes Containing Doxorubicin for Enhancing Glioma Targeting and Anti-Tumor Activity. *J. Control. Release* **2016**, *222*, 56–66. [CrossRef] [PubMed]
45. Kamarudin, N.H.N.; Jalil, A.A.; Triwahyono, S.; Artika, V.; Salleh, N.F.M.; Karim, A.H.; Jaafar, N.F.; Sazegar, M.R.; Mukti, R.R.; Hameed, B.H.; et al. Variation of the Crystal Growth of Mesoporous Silica Nanoparticles and the Evaluation to Ibuprofen Loading and Release. *J. Colloid Interface Sci.* **2014**, *421*, 6–13. [CrossRef] [PubMed]
46. Xiao, X.; Liu, Y.; Guo, M.; Fei, W.; Zheng, H.; Zhang, R.; Zhang, Y.; Wei, Y.; Zheng, G.; Li, F. pH-Triggered Sustained Release of Arsenic Trioxide by Polyacrylic Acid Capped Mesoporous Silica Nanoparticles for Solid Tumor Treatment in Vitro and in Vivo. *J. Biomater. Appl.* **2016**, *31*, 23–25. [CrossRef] [PubMed]
47. Zürner, A.; Kirstein, J.; Döblinger, M.; Bräuchle, C.; Bein, T. Visualizing Single-Molecule Diffusion in Mesoporous Materials. *Nature* **2007**, *450*, 705–708. [CrossRef] [PubMed]
48. Medved, I.; Cerny, R. Surface Diffusion in Porous Media: A Critical Review. *Microporous Mesoporous Mater.* **2011**, *142*, 405–422. [CrossRef]
49. Han, S.; Hermans, T.M.; Fuller, P.E.; Wei, Y.; Grzybowski, B.A. Transport into Metal-Organic Frameworks from Solution Is Not Purely Diffusive. *Angew. Chem. Int. Ed.* **2012**, *51*, 2662–2666. [CrossRef] [PubMed]
50. Titze, T.; Lauerer, A.; Heinke, L.; Chmelik, C.; Zimmermann, N.E.R.; Keil, F.J.; Ruthven, D.M.; Kärger, J. Transport in Nanoporous Materials Including MOFs: The Applicability of Fick's Laws. *Angew. Chem. Int. Ed.* **2015**, *54*, 14580–14583. [CrossRef] [PubMed]
51. Wuttke, S.; Braig, S.; Preiß, T.; Zimpel, A.; Sicklinger, J.; Bellomo, C.; Rädler, J.O.; Vollmar, A.M.; Bein, T. MOF Nanoparticles Coated by Lipid Bilayers and Their Uptake by Cancer Cells. *Chem. Commun.* **2015**, *51*, 15752–15755. [CrossRef] [PubMed]
52. Hirschle, P.; Preiß, T.; Auras, F.; Pick, A.; Völkner, J.; Valdepérez, D.; Witte, G.; Parak, W.J.; Rädler, J.O.; Wuttke, S. Exploration of MOF Nanoparticle Sizes Using Various Physical Characterization Methods—Is What You Measure What You Get? *CrystEngComm* **2016**, *18*, 4359–4368. [CrossRef]
53. Sun, S. Monodisperse FePt Nanoparticles and Ferromagnetic FePt Nanocrystal Superlattices. *Science* **2000**, *287*, 1989–1992. [CrossRef] [PubMed]
54. Park, J.; Lee, E.; Hwang, N.-M.; Kang, M.; Kim, S.C.; Hwang, Y.; Park, J.-G.; Noh, H.-J.; Kim, J.-Y.; Park, J.-H.; et al. One-Nanometer-Scale Size-Controlled Synthesis of Monodisperse Magnetic Iron Oxide Nanoparticles. *Angew. Chem. Int. Ed.* **2005**, *44*, 2873–2877. [CrossRef] [PubMed]

55. Anand, R.; Borghi, F.; Manoli, F.; Manet, I.; Agostoni, V.; Reschiglian, P.; Gref, R.; Monti, S. Host-Guest Interactions in Fe(III)-Trimesate MOF Nanoparticles Loaded with Doxorubicin. *J. Phys. Chem. B* **2014**, *118*, 8532–8539. [CrossRef] [PubMed]
56. Tay, C.Y.; Setyawati, M.I.; Xie, J.; Parak, W.J.; Leong, D.T. Back to Basics: Exploiting the Innate Physico-Chemical Characteristics of Nanomaterials for Biomedical Applications. *Adv. Funct. Mater.* **2014**, *24*, 5936–5955. [CrossRef]
57. Agostoni, V.; Horcajada, P.; Noiray, M.; Malanga, M.; Aykaç, A.; Jicsinszky, L.; Vargas-Berenguel, A.; Semiramoth, N.; Daoud-Mahammed, S.; Nicolas, V.; et al. A "green" Strategy to Construct Non-Covalent, Stable and Bioactive Coatings on Porous MOF Nanoparticles. *Sci. Rep.* **2015**, *5*, 7925. [CrossRef] [PubMed]
58. Geisow, M.J.; Evans, W.H. pH in the Endosome. Measurements during Pinocytosis and Receptor-Mediated Endocytosis. *Exp. Cell Res.* **1984**, *150*, 36–46. [CrossRef]
59. Adam, G.; Delbrueck, M. Reduction of Dimensionality in Biological Diffusive Processes. In *Structural Chemistry and Molecular Biology*; Rich, A., Davidson, N., Eds.; Freeman: San Francisco, CA, USA, 1968; pp. 198–215.
60. Heinke, L.; Gu, Z.; Wöll, C. The Surface Barrier Phenomenon at the Loading of Metal-Organic Frameworks. *Nat. Commun.* **2014**, *5*, 4562. [CrossRef] [PubMed]

Supplementary Materials: Kinetic Analysis of the Uptake and Release of Fluorescein by Metal-Organic Framework Nanoparticles

Tobias Preiß, Andreas Zimpel, Stefan Wuttke and Joachim O. Rädler

Methods and Characterization

Powder X-ray diffraction (XRD) measurements were performed using a Bruker D8 diffractometer (Cu-$K_{\alpha1}$ = 1.5406 Å; Cu-$K_{\alpha2}$ = 1.5444 Å) in theta-theta geometry equipped with a Lynx-Eye detector. The powder samples were measured between 2° and 45° two theta, with a step-size of 0.05° two theta.

Nitrogen sorption measurements were performed on a Quantachrome Instruments Autosorb at 77 K. Sample outgassing was performed for 12 hours at 393 K. Pore size and pore volume were calculated by a NLDFT equilibrium model of N_2 on silica, based on the adsorption branch of the isotherms. BET surface area was calculated over the range of partial pressure between 0.05 – 0.20 p/p0. The pore volume was calculated based on the uptake (cm^3/g) at a relative pressure of 0.30 p/p0.

Dynamic light scattering (DLS) measurements were performed on a Malvern Zetasizer- Nano instrument equipped with a 4 mW He-Ne laser (633 nm) and an avalanche photodiode. The hydrodynamic radius of the particles was determined by dynamic light scattering in a diluted aqueous suspension.

Experimental section

Chemicals

Chromium(III) nitrate nonahydrate (99%, Aldrich, city, country), terephthalic acid (98%, Aldrich), ethanol (99%, Aldrich) Iron (III) chloride hexahydrate (Grüssing GmbH), trimesic acid (BTC, Aldrich).

Synthesis of MIL-101(Cr) Nanoparticles

The microwave synthesis of MIL-101(Cr) nanoparticles was based on a modified procedure reported in the literature. An amount of 20 mL (1.11 mol) of H_2O was added to 615 mg (3.70 mmol) terephthalic acid and 1.48 g $Cr(NO_3)_3 \cdot 9\ H_2O$ (3.70 mmol) [1]. This mixture was put into a Teflon tube, sealed and placed in the microwave reactor (Microwave, Synthos, Anton Paar). Four tubes were filled and inserted into the reactor: one tube contained the reaction mixtures described above; the remaining tubes including the reference tube with the pressure/temperature sensor (PT sensor) were filled with 20 mL H_2O. For the synthesis, a temperature programme was applied with a ramp of 4 min to 180 °C and a holding time of 2 min at 180 °C. After the sample had cooled down to room temperature, it was filtrated and washed with 50 ml EtOH to remove residual e.g., terephthalic acid. For purification, the filtrate was centrifuged and redispersed in 50 ml EtOH three times. The sample was centrifuged at 20000 rpm (47808 rcf) for 60 min.

Synthesis of MIL-100(Fe) Nanoparticles

For the microwave synthesis of MIL-100 (Fe) nanoparticles, iron(III) chloride hexahydrate (2.43 g, 9.00 mmol) and trimesic acid (0.84 g, 4.00 mmol) in 30 mL H_2O were put into a Teflon tube, sealed and placed in the microwave reactor (Microwave, Synthos, Anton Paar). The mixture was heated to 130 °C under solvothermal conditions (p = 2.5 bar) within 30 seconds, kept at 130 °C for 4 min and 30 s and the tube was cooled down to room temperature [1]. For the purification of the solid, the reaction mixture was centrifuged (20,000 rpm = 47,808 rcf, 20 min), the solvent was removed and the pellet was redispersed in 50 mL EtOH. This cycle was repeated two times and the dispersed solid was allowed to sediment overnight. The supernatant of the sedimented suspension was filtrated (filter discs grade: 391, Sartorius Stedim Biotech) three times, yielding MIL-100(Fe) nanoparticles.

Calculations

Particle Density

To calculate the number of particles per mg we assume spherical particles (Volume $V = \frac{4}{3}\,\pi\, r^3$, with NP Radius r) The mass of one NP m_{NP} is then $m_{NP} = V \times \varrho$ with the mass density ϱ of the NP material. The number of particles N in 1 mg is then $N = \frac{1\text{mg}}{m_{NP}}$. For MIL-100(Fe) nanoparticles we used a mean radius of $r_{MIL-100}$ =26.5 nm (obtained from TEM analysis) and a mass density of ρ_{MIL100} = 0.98 g/mL [2]. As a result we arrive at a mean mass per particle of m_{MIL100} = 0.076 fg and thus the number of N_{MIL100} = 1.31 × 10^{13} particles per milligramm of material. This corresponds to n_{MIL100} = 21.7 pmol. Respectively for MIL-101(Cr) nanoparticles with r_{MIL101} =9.45 nm and ρ_{MIL101} = 0.62 g/mL [3] we derived a mean particle mass of m_{MIL101} = 2.2 ag and thus N_{MIL101} =4.56 × 10^{14} particles per milligram (n_{MIL100} = 0.76 nmol).

On-Kinetics

To calculate the calculate the on-kinetics in a diffusion dominated process we adapt the theory of Adam and Delbrück [4]: The original formula for the mean time τ a molecule within a Volume with radius r needs to hit a sphere with radius R is $\tau = \frac{\left(1-\frac{r}{R}\right)^2}{3\,r\,D} R^3$ with D, the diffusion coefficient of the diffusing molecules. This function was adapted to the system at hand: for r we used the particles radius we derived from DLS measurements at used pH 5.1 of 400 nm, the diffusion coefficient for fluorescein was found to be 390 μm²/s (FCS measurement), the radius R of the volume was determined by calculating the mean solution volume per particle from the overall Volume V and the containing number of nanoparticles N: $R^3 = \frac{V}{N} = \frac{M}{c\,N_A}$. Where M is the molar mass of the nanoparticle, c the mass concentration and the Avogadro constant N_A. The molar Mass is derived by the volume of a sphere with the radius of one particle, its mass density ϱ and the Avogadro constant: $M = \frac{4}{3}\pi\, r^3\, \rho\, N_A$. This results in the following formula:

$$\tau(c_{NP}) = \frac{A \cdot 4\pi r^2 \rho}{72 c_{NP} D}\left(1 - \frac{2}{\sqrt[3]{\frac{4\pi\rho}{c_{NP}}}}\right)^2 + \tau_0 \approx \frac{A \cdot \pi r^2 \rho}{18\, c_{NP} D} + \tau_0$$

Whereas an offset τ_0 was added to compensate for the internal diffusion through the lattice and sorbtion that is represented in **Error! Reference source not found.** by the sum of τ_{intra} and τ_{on}. Here we used the mass density ϱ = 2 mg/cm³ that respects the filling of the nanoparticles with water (mass density of empty MOFs: 0.98mg/cm³ [2] + pore volume 1.030cm³/g [5] filled with water at 0.997mg/cm³ results in 2 mg/mL).

Supplementary Figure

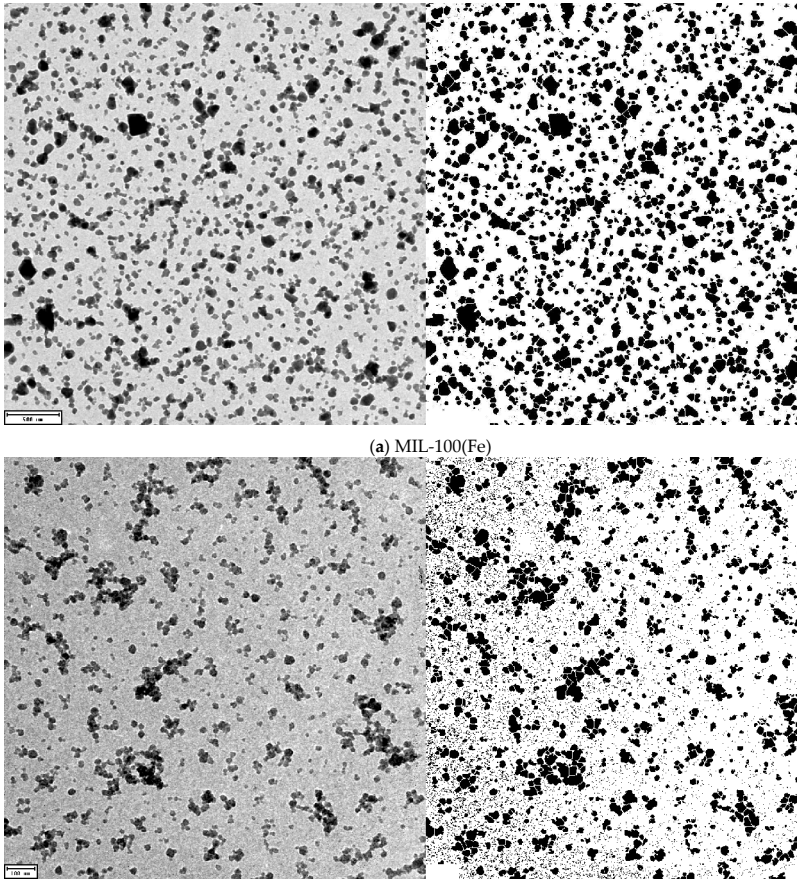

(**a**) MIL-100(Fe)

(**b**) MIL-101(Cr)

Figure S1. Juxtaposition of exemplary original TEM image (left) and processed image used for particle analysis (right) of (**a**) MIL-100(Fe) and (**b**) MIL-101(Cr). Original TEM image was converted to binary image. By applying watershed filter, NP that are close together are separated by a thin white line for the subsequent particle analysis. The "analyse particles" function of ImageJ was used to determine the area of all particles larger than 5 nm² (to get rid of background sparkles).

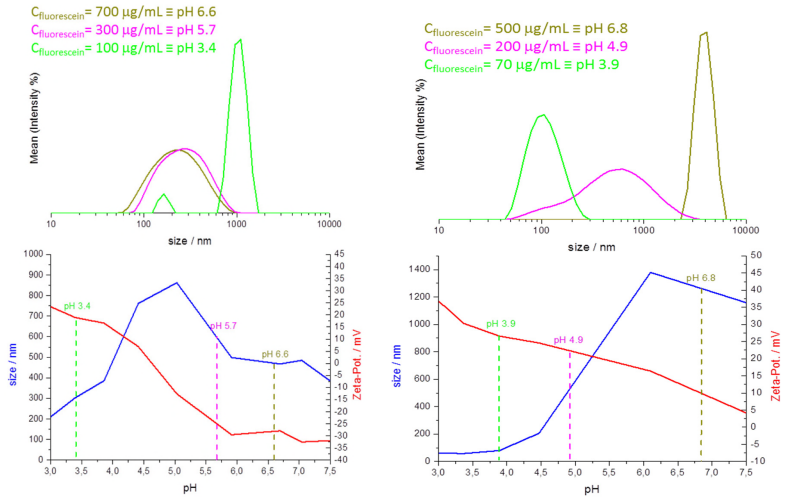

(**a**) MIL-101(Cr) (**b**) MIL-100(Fe)

Figure S2. DLS (blue) and Zeta-Potential (red) measurements of (**a**) MIL-100(Fe) (left) and (**b**) MIL-101(Cr) (right) at different pH in water.

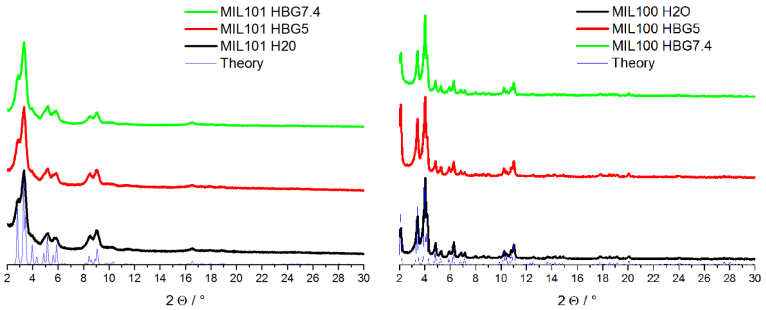

(**a**) (**b**)

Figure S3. XRD measurements of NPs before (black) and after incubation in buffer (red: in HBG pH = 5.0, green: in HBG pH = 7.4) certifies crystallinity and stability of MOF structure. Theoretical data is shown in blue.

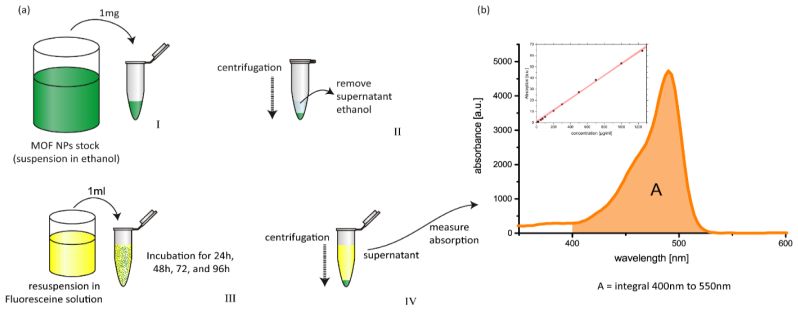

Figure S4. Assay for measuring the Payload capacity established, using UV/VIS absorption. Fluorescein solutions were used as calibration standard. (**a**) Preparation and loading process: 1 mg MOF NPs (I) were separated from ethanol (II), resuspended in fluorescein solutions of different concentrations and incubated for a certain time (III). For UV/VIS measurement the MOF NPs were separated from incubation solution (IV). (**b**) The absorption spectra of the supernatant solution as well as the original fluorescein solution were measured and integrated within the limits of 400 nm to 550 nm to determine the remaining amount of fluorescein in the supernatant. Inset: Fluorescein calibration curve with linear fit.

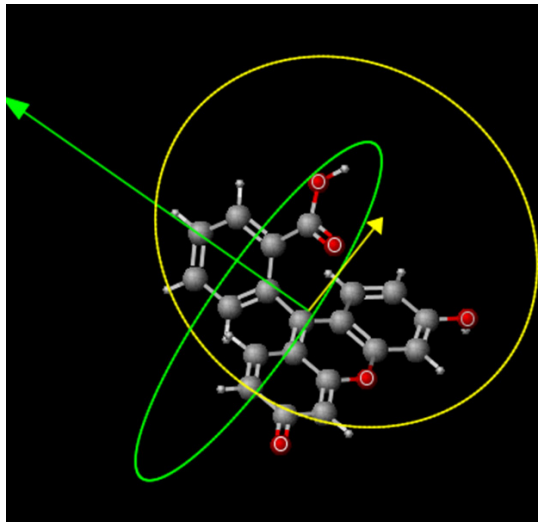

Figure S5. Structure of fluorescein molecule and its minimal and maximal projection area (MarvinSketch) max: radius = 6.27 Å; min: radius = 6.15 Å. Arrows indicate surface normal.

Release kinetics in HBG Buffer:

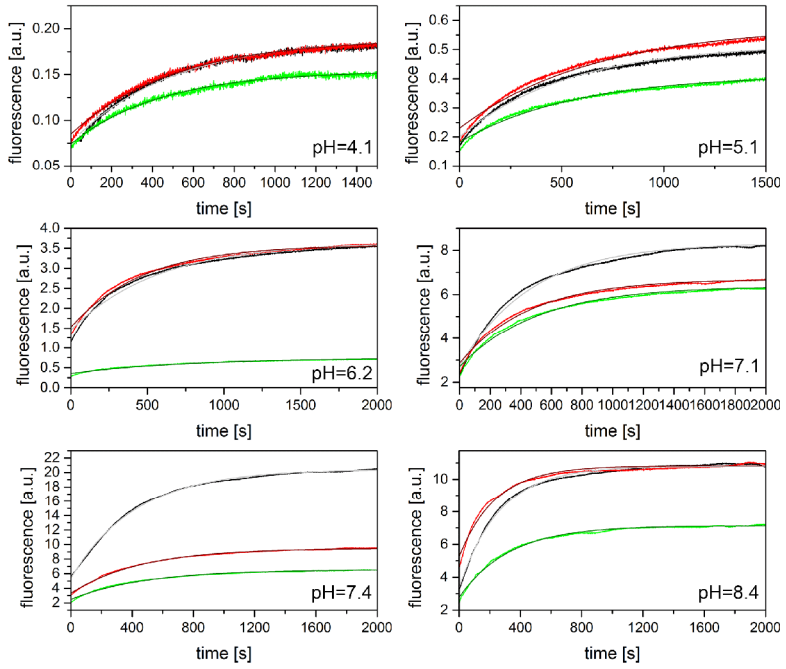

Figure S6. Release kinetics of fluorescein in MIL-100(Fe) NPs in HBG at depicted pH. Experiments were carried out in triplicate (black, red, green)

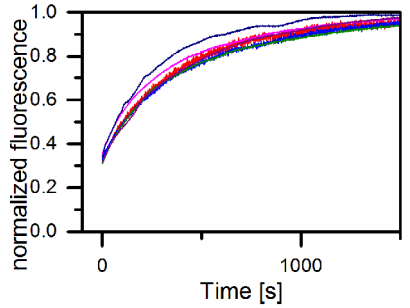

Figure S7. Release kinetic measurements at different pH values normalized to its final signal. pH = 4.1 (red); pH = 5.1 (blue); pH = 6.2 (green), pH = 7.1(pink) pH = 7.4 (violet), pH = 8.4 (dark blue)

Loading Kinetics

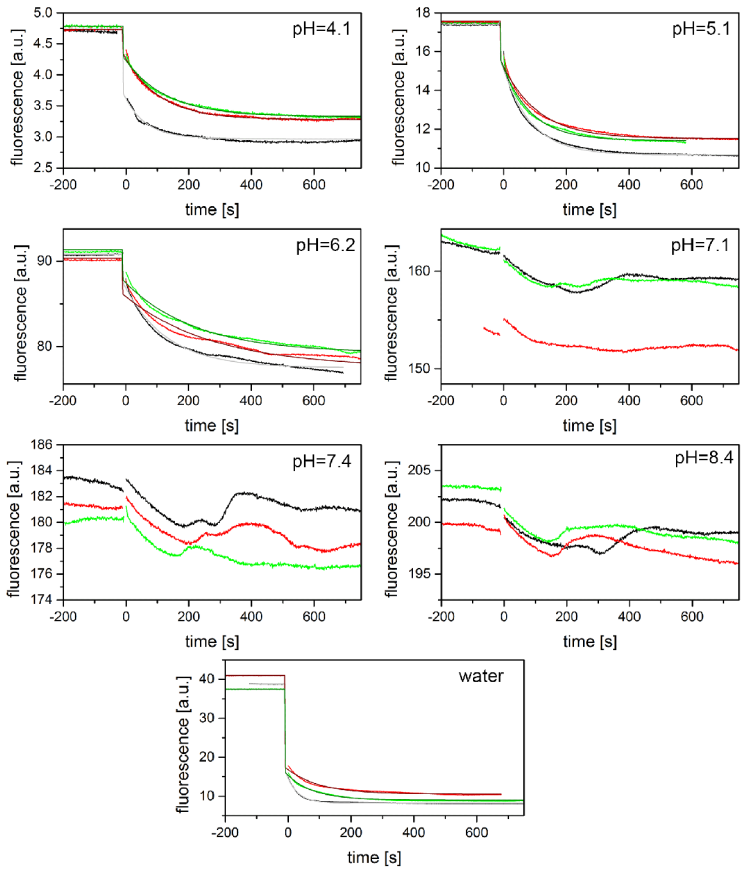

Figure S8. Loading kinetics of fluorescein into MIL-100(Fe) NPs in HBG at depicted pH and in water. Experiments were carried out in triplicate (black, red and green)

References

1. Wuttke, S.; Braig, S.; Preiß, T.; Zimpel, A.; Sicklinger, J.; Bellomo, C.; Rädler, J. O.; Vollmar, A. M.; Bein, T. MOF Nanoparticles Coated by Lipid Bilayers and Their Uptake by Cancer Cells. *Chem. Commun.* **2015**, *51*, 15752–15755.
2. Horcajada, P.; Surblé, S.; Serre, C.; Hong, D.-Y.; Seo, Y.-K.; Chang, J.-S.; Grenèche, J.-M.; Margiolaki, I.; Férey, G. Synthesis and Catalytic Properties of MIL-100(Fe), an iron(III) Carboxylate with Large Pores. *Chem. Commun.* **2007**, *100*, 2820–2822.
3. Férey, G.; Mellot-Draznieks, C.; Serre, C.; Millange, F.; Dutour, J.; Surblé, S.; Margiolaki, I. A Chromium Terephthalate-Based Solid with Unusually Large Pore Volumes and Surface Area. *Science* **2005**, *309*, 2040–2042.
4. Adam, G.; Delbrueck, M. Reduction of Dimensionality in Biological Diffusive Processes. In *Structural Chemistry and Molecular Biology*; Rich, A.; Davidson, N., Eds.; Freeman: San Francisco, CA, USA, 1968; pp. 198–215.
5. Bernini, M. C.; Fairen-Jimenez, D.; Pasinetti, M.; Ramirez-Pastor, A. J.; Snurr, R. Q. Screening of Bio-Compatible Metal-Organic Frameworks as Potential Drug Carriers Using Monte Carlo Simulations. *J. Mater. Chem. B* **2014**, *2*, 766–774.

Abkürzungsverzeichnis

AFM Rasterkraftmikroskop

CF CarboxyFluorescein

DLS Dynamische Lichtstreuung

DMEM Dulbecco's Modified Eagle Medium

FBS fötales Kälberserum

FCCS Fluoreszenz-Kreuzkorrelations-Spektroskopie

FCS Fluoreszenz-Korrelations-Spektroskopie

GFP grün fluoreszierendes Protein

HBG HEPES gepufferte Glucose

HEPES 2-(4-(2-Hydroxyethyl)-1-piperazinyl)-ethansulfonsäure

His-A647N H_6-PEG_{12}-*ATTO 647 N*

His-Tag Polyhistidin-Tag

MIL-100(Fe) Materials of Institute Lavoisier 100 (Fe)

MIL-101(Cr) Materials of Institute Lavoisier 101 (Cr)

MOF Metall-Organische Gerüstverbindung

NP Nanopartikel

PEG Polyethylenglycol

REM Rasterelektronenmikroskop

TEM Transmissionselektronenmikroskop

Zr-*fum* Zirkonium-Fumarat

Literaturverzeichnis

[1] DAVIS, M. E. ; CHEN, Z. G. ; SHIN, D. M.: Nanoparticle therapeutics: an emerging treatment modality for cancer. *Nature Reviews. Drug Discovery* 7 (2008), 771–782

[2] DYSON, P. J. ; SAVA, G.: Metal-based antitumour drugs in the post genomic era. *Dalton Transactions* 16 (2006), 1929–1933

[3] LÜHMANN, T. ; MEINEL, L.: Nanotransporters for drug delivery. *Current Opinion in Biotechnology* 39 (2016), 35–40

[4] TIWARI, G. ; TIWARI, R. ; SRIWASTAWA, B. ; BHATI, L. ; PANDEY, S. ; PANDEY, P. ; BANNERJEE, S. K.: Drug delivery systems: An updated review. *Journal of Pharmaceutical Investigation* 2 (2012), 2–11

[5] COUVREUR, P. ; VAUTHIER, C.: Nanotechnology: Intelligent design to treat complex disease. *Pharmaceutical Research* 23 (2006), 1417–1450

[6] KLIBANOV, A. L. ; MARUYAMA, K. ; TORCHILIN, V. P. ; HUANG, L.: Amphipathic polyethyleneglycols effectively prolong the circulation time of liposomes. *FEBS Letters* 268 (1990), 235–237

[7] TORCHILIN, V. P.: Micellar nanocarriers: Pharmaceutical perspectives. *Pharmaceutical Research* 24 (2007), 1–16

[8] HOSSANN, M. ; SYUNYAEVA, Z. ; SCHMIDT, R. ; ZENGERLE, A. ; EIBL, H. ; ISSELS, R. D. ; LINDNER, L. H.: Proteins and cholesterol lipid vesicles are mediators of drug release from thermosensitive liposomes. *Journal of Controlled Release* 162 (2012), 400–406

[9] PELLER, M. ; SCHWERDT, A. ; HOSSANN, M. ; REINL, H. M. ; WANG, T. ; SOURBRON, S. ; OGRIS, M. ; LINDNER, L. H.: MR characterization of mild hyperthermia-induced

gadodiamide release from thermosensitive liposomes in solid tumors. *Investigative Radiology* 43 (2008), 877–892

[10] HIRSCH, L. R. ; STAFFORD, R. J. ; BANKSON, J. A. ; SERSHEN, S. R. ; RIVERA, B. ; PRICE, R. E. ; HAZLE, J. D. ; HALAS, N. J. ; WEST, J. L.: Nanoshell-mediated near-infrared thermal therapy of tumors under magnetic resonance guidance. *Proceedings of the National Academy of Sciences of the United States of America* 100 (2003), 13549–13554

[11] HIRSCH, L. R. ; GOBIN, A. M. ; LOWERY, A. R. ; TAM, F. ; DREZEK, R. A. ; HALAS, N. J. ; WEST, J. L.: Metal nanoshells. *Annals of Biomedical Engineering* 34 (2006), 15–22

[12] BATRAKOVA, E. V. ; DORODNYCH, T. Y. ; KLINSKII, E. Y. ; KLIUSHNENKOVA, E. N. ; SHEMCHUKOVA, O. B. ; GONCHAROVA, O. N. ; ARJAKOV, S. A. ; ALAKHOV, V. Y. ; KABANOV, A. V.: Anthracycline antibiotics non-covalently incorporated into the block copolymer micelles: in vivo evaluation of anti-cancer activity. *British Journal of Cancer* 74 (1996), 1545–1552

[13] NAKANISHI, T. ; FUKUSHIMA, S. ; OKAMOTO, K. ; SUZUKI, M. ; MATSUMURA, Y. ; YOKOYAMA, M. ; OKANO, T. ; SAKURAI, Y. ; KATAOKA, K.: Development of the polymer micelle carrier system for doxorubicin. *Journal of Controlled Release* 74 (2001), 295–302

[14] GILLIES, E. R. ; FRÉCHET, J. M. J.: Dendrimers and dendritic polymers in drug delivery. *Drug Discovery Today* 10 (2005), 35–43

[15] KUKOWSKA-LATALLO, J. F. ; CANDIDO, K. A. ; CAO, Z. ; NIGAVEKAR, S. S. ; MAJOROS, I. J. ; THOMAS, T. P. ; BALOGH, L. P. ; KHAN, M. K. ; BAKER, J. R.: Nanoparticle targeting of anticancer drug improves therapeutic response in animal model of human epithelial cancer. *Cancer Research* 65 (2005), 5317–5324

[16] AHMED, F. ; PAKUNLU, R. I. ; SRINIVAS, G. ; BRANNAN, A. ; BATES, F. ; KLEIN, M. L. ; MINKO, T. ; DISCHER, D. E.: Shrinkage of a rapidly growing tumor by drug-loaded polymersomes: pH-triggered release through copolymer degradation. *Molecular Pharmaceutics* 3 (2006), 340–350

[17] DISCHER, D. E. ; AHMED, F.: Polymersomes. *Annual Review of Biomedical Engineering* 8 (2006), 323–341

[18] DANSON, S. ; FERRY, D. ; ALAKHOV, V. ; MARGISON, J. ; KERR, D. ; JOWLE, D. ; BRAMPTON, M. ; HALBERT, G. ; RANSON, M.: Phase I dose escalation and pharmacokinetic study of pluronic polymer-bound doxorubicin (SP1049C) in patients with advanced cancer. *British Journal of Cancer* 90 (2004), 2085–2091

[19] MOGHIMI, S. M.: Recent developments in polymeric nanoparticle engineering and their applications in experimental and clinical oncology. *Anti-Cancer Agents in Medicinal Chemistry* 6 (2006), 553–561

[20] HUXFORD, R. C. ; DELLA ROCCA, J. ; LIN, W.: Metal-organic frameworks as potential drug carriers. *Current Opinion in Chemical Biology* 14 (2010), 262–268

[21] ASHLEY, C. E. ; CARNES, E. E. C. ; PHILLIPS, G. G. K. ; PADILLA, D. ; DURFEE, P. N. P. ; BROWN, P. a. P. ; HANNA, T. T. N. ; LIU, J. ; PHILLIPS, B. ; CARTER, M. B. M. ; CARROLL, N. J. ; JIANG, X. ; DUNPHY, D. R. ; WILLMAN, C. L. ; PETSEV, D. N. ; EVANS, D. G. ; PARIKH, A. N. ; CHACKERIAN, B. ; WHARTON, W. ; PEABODY, D. S. ; BRINKER, C. J.: The targeted delivery of multicomponent cargos to cancer cells by nanoporous particle-supported lipid bilayers. *Nature Materials* 10 (2011), 1–54

[22] FURUKAWA, H. ; CORDOVA, K. ; O'KEEFFE, M. ; YAGHI, O. M. O.: The chemistry and applications of metal-organic frameworks. *Science* 341 (2013), 974–990

[23] ZHOU, H.-C. ; KITAGAWA, S.: Metal–organic frameworks (MOFs). *Chemical Society Reviews* 43 (2014), 5415–5418

[24] ZHOU, H. C. ; LONG, J. R. ; YAGHI, O. M.: Introduction to metal-organic frameworks. *Chemical Reviews* 112 (2012), 673–674

[25] MAGDE, D. ; ELSON, E. ; WEBB, W. W.: Thermodynamic fluctuations in a reacting system—measurement by fluorescence correlation spectroscopy. *Physical Review Letters* 29 (1972), 705–708

[26] MAGDE, D. ; ELSON, E. L. ; WEBB, W. W.: Fluorescence correlation spectroscopy. II. An experimental realization. *Biopolymers* 13 (1974), 29–61

[27] RIGLER, R. ; METS, Ü. ; WIDENGREN, J. ; KASK, P.: Fluorescence correlation spectroscopy with high count rate and low background: analysis of translational diffusion. *European Biophysics Journal* 22 (1993), 169–175

[28] PAL, N. ; DEV VERMA, S. ; SINGH, M. K. M. ; SEN, S.: Fluorescence correlation spectroscopy: An efficient tool for measuring size, size-distribution and polydispersity of microemulsion droplets in solution. *Analytical Chemistry* 83 (2011), 1–7

[29] SCHWILLE, P. ; HAUSTEIN, E.: Fluorescence correlation spectroscopy: An introduction to its concepts and applications. *Spectroscopy* 94 (2009), 1–33

[30] PETROV, E. P. ; SCHWILLE, P.: State of the art and novel trends in fluorescence correlation spectroscopy. Version: 2008. RESCH-GENGER, U. (Hrsg.): *Standardization and Quality Assurance in Fluorescence Measurements II: Bioanalytical and Biomedical Applications*. Springer Berlin Heidelberg, 2008, 145–197

[31] BONNET, G. ; KRICHEVSKY, O.: Fluorescence correlation spectroscopy: the technique and its applications. *Reports on Progress in Physics* 65 (2002), 251–297

[32] KOGA, K. ; IKESHOJI, T. ; SUGAWARA, K. I.: Size- and temperature-dependent structural transitions in gold nanoparticles. *Physical Review Letters* 92 (2004), 115507–1–4

[33] WITTSTOCK, A. ; ZIELASEK, V. ; BIENER, J. ; FRIEND, C. M. ; BÄUMER, M.: Nanoporous gold catalysts for selective methanol at low temperature. *Science* 327 (2010), 319–322

[34] BOND, G. C. ; THOMPSON, D. T.: Gold-catalysed oxidation of carbon monoxide. *Gold Bulletin* 33 (2000), 41–50

[35] PRATI, L. ; MARTRA, G.: New gold catalysts for liquid phase oxidation. *Gold Bulletin* 96 (1999), 96–101

[36] CHAE, H. K. ; SIBERIO-PÉREZ, D. Y. ; KIM, J. ; GO, Y. ; EDDAOUDI, M. ; MATZGER, A. J. ; O'KEEFFE, M. ; YAGHI, O. M.: A route to high surface area, porosity and inclusion of large molecules in crystals. *Nature* 427 (2004), 523–527

[37] ROCCA, J. D. ; LIN, W.: Nanoscale metal-organic frameworks: Magnetic resonance imaging contrast agents and beyond. *European Journal of Inorganic Chemistry* (2010), 3725–3734

[38] WANG, H. ; LIU, Y. ; LI, M. ; HUANG, H. ; XU, H. M. ; HONG, R. J. ; SHEN, H.: Multifunctional TiO2 nanowires-modified nanoparticles bilayer film for 3D dye-sensitized solar cells. *Optoelectronics and Advanced Materials, Rapid Communications* 4 (2010), 1166–1169

[39] HORCAJADA, P. ; SURBLÉ, S. ; SERRE, C. ; HONG, D.-Y. ; SEO, Y.-K. ; CHANG, J.-S. ; GRENÈCHE, J.-M. ; MARGIOLAKI, I. ; FÉREY, G.: Synthesis and catalytic properties of MIL-100(Fe), an iron(III) carboxylate with large pores. *Chemical Communications* 100 (2007), 2820–2822

[40] FÉREY, G. ; MELLOT-DRAZNIEKS, C. ; SERRE, C. ; MILLANGE, F. ; DUTOUR, J. ; SURBLÉ, S. ; MARGIOLAKI, I.: A chromium terephthalate-based solid with unusually large pore volumes and surface area. *Science* 309 (2005), 2040–2

[41] WISSMANN, G. ; SCHAATE, A. ; LILIENTHAL, S. ; BREMER, I. ; SCHNEIDER, A. M. ; BEHRENS, P.: Modulated synthesis of Zr-fumarate MOF. *Microporous and Mesoporous Materials* 152 (2012), 64–70

[42] HORCAJADA, P. ; CHALATI, T. ; SERRE, C. ; GILLET, B. ; SEBRIE, C. ; BAATI, T. ; EUBANK, J. F. ; HEURTAUX, D. ; CLAYETTE, P. ; KREUZ, C. ; CHANG, J.-S. ; HWANG, Y. K. ; MARSAUD, V. ; BORIES, P.-N. ; CYNOBER, L. ; GIL, S. ; FÉREY, G. ; COUVREUR, P. ; GREF, R.: Porous metal-organic-framework nanoscale carriers as a potential platform for drug delivery and imaging. *Nature Materials* 9 (2010), 172–178

[43] AGOSTONI, V. ; HORCAJADA, P. ; NOIRAY, M. ; MALANGA, M. ; AYKAÇ, A. ; JICSINSZKY, L. ; VARGAS-BERENGUEL, A. ; SEMIRAMOTH, N. ; DAOUD-MAHAMMED, S. ; NICOLAS, V. ; MARTINEAU, C. ; TAULELLE, F. ; VIGNERON, J. ; ETCHEBERRY, A. ; SERRE, C. ; GREF, R.: A "green" strategy to construct non-covalent, stable and bioactive coatings on porous MOF nanoparticles. *Scientific Reports* 5 (2015), 7925–1–5

[44] DEMESSENCE, A. ; HORCAJADA, P. ; SERRE, C. ; BOISSIÈRE, C. ; GROSSO, D. ; SANCHEZ, C. ; FÉREY, G.: Elaboration and properties of hierarchically structured optical thin films of MIL-101(Cr). *Chemical Communications* 101 (2009), 7149–7151

[45] PORATH, J.: Immobilized metal ion affinity chromatography. *Protein Expression and Purification* 3 (1992), 263–281

[46] SHAO, S. ; GENG, J. ; AH YI, H. ; GOGIA, S. ; NEELAMEGHAM, S. ; JACOBS, A. ; LOVELL, J. F.: Functionalization of cobalt porphyrin–phospholipid bilayers with his-tagged ligands and antigens. *Nature Chemistry* 7 (2015), 438–446

[47] KNECHT, S. ; RICKLIN, D. ; EBERLE, A. N. ; ERNST, B.: Oligohis-tags: mechanisms of binding to Ni2+-NTA surfaces. *Journal of Molecular Recognition* 22 (2009), 270–279

[48] KHAN, F. ; HE, M. ; TAUSSIG, M. J.: Double-hexahistidine tag with high-affinity binding for protein immobilization, purification, and detection on Ni-nitrilotriacetic acid surfaces. *Analytical Chemistry* 78 (2006), 3072–3079

[49] LAKOWICZ, J. R.: *Principles of Fluorescence Spectroscopy*. 3. Auflage. Springer, 2006

[50] THOMPSON, N. L.: Fluorescence Correlation Spectroscopy. J.R. LAKOWICZ (Hrsg.): *Topics in Fluorescence Spectroscopy*. Plenum Press, New York., 1991, 337–378

[51] CORDES, T. ; MAISER, A. ; STEINHAUER, C. ; SCHERMELLEH, L. ; TINNEFELD, P.: Mechanisms and advancement of antifading agents for fluorescence microscopy and single-molecule spectroscopy. *Physical Chemistry Chemical Physics* 13 (2011), 6699–6709

[52] WU, B. ; CHEN, Y. ; MÜLLER, J. D.: Fluorescence correlation spectroscopy of finite-sized particles. *Biophysical Journal* 94 (2008), 2800–2808

[53] MESETH, U. ; WOHLAND, T. ; RIGLER, R. ; VOGEL, H.: Resolution of fluorescence correlation measurements. *Biophysical Journal* 76 (1999), 1619–1631

[54] STARCHEV, K. ; BUFFLE, J. ; PÉREZ, E.: Applications of fluorescence correlation spectroscopy: Polydispersity measurements. *Journal of Colloid and Interface Science* 213 (1999), 479–487

[55] SCHWILLE, P. ; MEYER-ALMES, F. J. ; RIGLER, R.: Dual-color fluorescence cross-correlation spectroscopy for multicomponent diffusional analysis in solution. *Biophysical Journal* 72 (1997), 1878–1886

[56] WEIDEMANN, T. ; SCHWILLE, P.: Dual-color fluorescence cross-correlation spectroscopy with continuous laser excitation in a confocal setup. Version: 1, 2013. *Methods in Enzymology* Bd. 518. 1. Elsevier Inc., 2013, 43–70

[57] WOHLAND, T. ; RIGLER, R. ; VOGEL, H.: The standard deviation in fluorescence correlation spectroscopy. *Biophysical Journal* 80 (2001), 2987–2999

[58] SCHWILLE, P.: Fluorescence correlation spectroscopy and its potential for intracellular applications. *Cell Biochemistry and Biophysics* 34 (2001), 383–408

[59] HIRSCHLE, P. ; PREISS, T. ; AURAS, F. ; PICK, A. ; VÖLKNER, J. ; VALDEPÉREZ, D. ; WITTE, G. ; PARAK, W. J. ; RÄDLER, J. O. ; WUTTKE, S.: Exploration of MOF nanoparticle sizes using various physical characterization methods - is what you measure what you get? *CrystEngComm* 18 (2016), 4359–4368

[60] KULKARNI, S. A. ; FENG, S.-S.: Effects of particle size and surface modification on cellular uptake and biodistribution of polymeric nanoparticles for drug delivery. *Pharmaceutical Research* 30 (2013), 2512–2522

[61] WILSON, O. M. ; KNECHT, M. R. ; GARCIA-MARTINEZ, J. C. ; CROOKS, R. M.: Effect of Pd nanoparticle size on the catalytic hydrogenation of allyl alcohol. *Journal of the American Chemical Society* 128 (2006), 4510–4511

[62] WIN, K. Y. ; FENG, S.-S.: Effects of particle size and surface coating on cellular uptake of polymeric nanoparticles for oral delivery of anticancer drugs. *Biomaterials* 26 (2005), 2713–2722

[63] RESKE, R. ; MISTRY, H. ; BEHAFARID, F. ; ROLDAN CUENYA, B. ; STRASSER, P.: Particle size effects in the catalytic electroreduction of CO2 on Cu nanoparticles. *Journal of the American Chemical Society* 136 (2014), 6978–6986

[64] HE, C. ; HU, Y. ; YIN, L. ; TANG, C. ; YIN, C.: Effects of particle size and surface charge on cellular uptake and biodistribution of polymeric nanoparticles. *Biomaterials* 31 (2010), 3657–3666

[65] HUANG, J. ; BU, L. ; XIE, J. ; CHEN, K. ; CHENG, Z. ; LI, X. ; CHEN, X.: Effects of nanoparticle size on cellular uptake and liver MRI with PVP-coated iron oxide nanoparticles. *ACS Nano* 4 (2010), 7151–7160

[66] LU, F. ; WU, S. H. ; HUNG, Y. ; MOU, C. Y.: Size effect on cell uptake in well-suspended, uniform mesoporous silica nanoparticles. *Small* 5 (2009), 1408–1413

[67] CHITHRANI, B. D. ; GHAZANI, A. A. ; CHAN, W. C. W.: Determining the size and shape dependence of gold nanoparticle uptake into mammalian cells. *Nano Letters* 6 (2006), 662–668

[68] JIANG, W. ; KIM, B. Y. S. ; RUTKA, J. T. ; CHAN, W. C. W.: Nanoparticle-mediated cellular response is size-dependent. *Nature Nanotechnology* 3 (2008), 145–150

[69] JIANG, J. ; OBERDÖRSTER, G. ; BISWAS, P.: Characterization of size, surface charge, and agglomeration state of nanoparticle dispersions for toxicological studies. *Journal of Nanoparticle Research* 11 (2009), 77–89

[70] ZAHN, G. ; SCHULZE, H. A. ; LIPPKE, J. ; KÖNIG, S. ; SAZAMA, U. ; FRÖBA, M. ; BEHRENS, P.: A water-born Zr-based porous coordination polymer: Modulated synthesis of Zr-fumarate MOF. *Microporous and Mesoporous Materials* 203 (2015), 186–194

[71] PETRÁŠEK, Z. ; SCHWILLE, P.: Precise measurement of diffusion coefficients using scanning fluorescence correlation spectroscopy. *Biophysical Journal* 94 (2008), 1437–1448

[72] PERSSON, G. ; THYBERG, P. ; SANDÉN, T. ; WIDENGREN, J. ; SANDE, T. ; WIDENGREN, J.: Modulation filtering enables removal of spikes in fluorescence correlation spectroscopy measurements without affecting the temporal information. *Journal of Physical Chemistry B* 113 (2009), 8752–8757

[73] CHOI, K. M. ; JEONG, H. M. ; PARK, J. H. ; ZHANG, Y.-b. ; KANG, J. K.: Supercapacitors of nanocrystalline metal-organic frameworks. *ACS Nano* 8 (2014), 7451–7457

[74] ZHANG, F. ; LEES, E. ; AMIN, F. ; RIVERA-GIL, P. ; YANG, F. ; MULVANEY, P. ; PARAK, W. J.: Polymer-coated nanoparticles: A universal tool for biolabelling experiments. *Small* 7 (2011), 3113–3127

[75] GOESMANN, H. ; FELDMANN, C.: Nanoparticulate functional materials. *Angewandte Chemie* 49 (2010), 1362–1395

[76] TAY, C. Y. ; SETYAWATI, M. I. ; XIE, J. ; PARAK, W. J. ; LEONG, D. T.: Back to basics: Exploiting the innate physico-chemical characteristics of nanomaterials for biomedical applications. *Advanced Functional Materials* 24 (2014), 5936–5955

[77] NEL, A. E. ; MÄDLER, L. ; VELEGOL, D. ; XIA, T. ; V HOEK, E. M. ; SOMASUNDARAN, P. ; KLAESSIG, F. ; CASTRANOVA, V. ; THOMPSON, M. ; HOEK, E. M. V. ; SOMASUNDARAN, P. ; KLAESSIG, F. ; CASTRANOVA, V. ; THOMPSON, M.: Understanding biophysicochemical interactions at the nano-bio interface. *Nature Materials* 8 (2009), 543–557

[78] BOGART, L. K. ; POURROY, G. ; MURPHY, C. J. ; PUNTES, V. ; PELLEGRINO, T. ; ROSENBLUM, D. ; PEER, D. ; LÉVY, R.: Nanoparticles for imaging, sensing, and therapeutic intervention. *ACS Nano* 8 (2014), 3107–3122

[79] FALCARO, P. ; RICCO, R. ; DOHERTY, C. M. ; LIANG, K. ; HILL, A. J. ; STYLES, M. J.: MOF positioning technology and device fabrication. *Chemical Society Reviews* 43 (2014), 5513–5560

[80] WUTTKE, S. ; BRAIG, S. ; PREISS, T. ; ZIMPEL, A. ; SICKLINGER, J. ; BELLOMO, C. ; RÄDLER, J. O. ; VOLLMAR, A. M. ; BEIN, T.: MOF nanoparticles coated by lipid bilayers and their uptake by cancer cells. *Chemical Communications* 51 (2015), 15752–15755

[81] GORDON, A. ; FLEAGLE, J. ; GUTHRIE, D. ; PARKIN, D. ; GORE, M. ; LACAVE, A.: Recurrent epithelial ovarian carcinoma: a randomized phase III study of pegylated liposomal doxorubicin versus topotecan. *Journal of Clinical Oncology* 19 (2001), 3312–3322

[82] TARDI, P. G. ; BOMAN, N. L. ; CULLIS, P. R.: Liposomal doxorubicin. *Journal of Drug Targeting* 4 (1996), 129–140

[83] CAUDA, V. ; ENGELKE, H. ; SAUER, A. ; ARCIZET, D. ; BRÄUCHLE, C. ; RÄDLER, J. O. ; BEIN, T.: Colchicine-loaded lipid bilayer-coated 50 nm mesoporous nanoparticles efficiently induce microtubule depolymerization upon cell uptake. *Nano Letters* 10 (2010), 2484–2492

[84] HOHNER, A. O. ; DAVID, M. P. C. ; RÄDLER, J. O.: Controlled solvent-exchange deposition of phospholipid membranes onto solid surfaces. *Biointerphases* 5 (2010), 1–8

[85] UHRÍKOVÁ, D. ; KUČERKA, N. ; ISLAMOV, A. ; KUKLIN, A. ; GORDELIY, V. ; BALGAVÝ, P.: Small-angle neutron scattering study of the lipid bilayer thickness in

unilamellar dioleoylphosphatidylcholine vesicles prepared by the cholate dilution method: n-decane effect. *Biochimica et Biophysica Acta - Biomembranes* 1611 (2003), 31–34

[86] ZIMPEL, A. ; PREISS, T. ; RÖDER, R. ; ENGELKE, H. ; INGRISCH, M. ; PELLER, M. ; RÄDLER, J. O. ; WAGNER, E. ; BEIN, T. ; LÄCHELT, U. ; WUTTKE, S.: Imparting functionality to MOF nanoparticles by external surface selective covalent attachment of polymers. *Chemistry of Materials* 28 (2016), 3318–3326

[87] ROLLAND, J. P. ; MAYNOR, B. W. ; EULISS, L. E. ; EXNER, A. E. ; DENISON, G. M. ; DESIMONE, J. M.: Direct fabrication and harvesting of monodisperse, shape-specific nanobiomaterials. *Journal of the American Chemical Society* 127 (2005), 10096–10100

[88] GRUBBS, R. B.: Roles of polymer ligands in nanoparticle stabilization. *Polymer Reviews* 47 (2007), 197–215

[89] SALVATI, A. ; ÅBERG, C. ; DAWSON, K. A. ; MONOPOLI, M. P. ; ÅBERG, C. ; SALVATI, A. ; DAWSON, K. A. ; ABERG, C. ; SALVATI, A. ; DAWSON, K. A.: Biomolecular coronas provide the biological identity of nanosized materials. *Nature Nanotechnology* 7 (2012), 779–786

[90] ROWE, M. D. ; THAM, D. H. ; KRAFT, S. L. ; BOYES, S. G.: Polymer-modified gadolinium metal-organic framework nanoparticles used as multifunctional nanomedicines for the targeted imaging and treatment of cancer. *Biomacromolecules* 10 (2009), 983–993

[91] BELLIDO, E. ; HIDALGO, T. ; LOZANO, M. V. ; GUILLEVIC, M. ; SIMÓN-VÁZQUEZ, R. ; SANTANDER-ORTEGA, M. J. ; GONZÁLEZ-FERNÁNDEZ, Á. ; SERRE, C. ; ALONSO, M. J. ; HORCAJADA, P.: Heparin-engineered mesoporous iron metal-organic framework nanoparticles: Toward stealth drug nanocarriers. *Advanced Healthcare Materials* 4 (2015), 1246–1257

[92] WANG, S. ; MORRIS, W. ; LIU, Y. ; MCGUIRK, C. M. ; ZHOU, Y. ; HUPP, J. T. ; FARHA, O. K. ; MIRKIN, C. A.: Surface-specific functionalization of nanoscale metal-organic frameworks. *Angewandte Chemie - International Edition* 54 (2015), 14738–14742

[93] MCGUIRE, C. V. ; FORGAN, R. S.: The surface chemistry of metal-organic frameworks. *Chemical Communications* 51 (2015), 5199–5217

[94] COHEN, S. M.: Postsynthetic methods for the functionalization of metal-organic frameworks. *Chemical Reviews* 112 (2012), 970–1000

[95] BEZVERKHYY, I. ; WEBER, G. ; BELLAT, J.-P.: Degradation of fluoride-free MIL-100(Fe) and MIL-53(Fe) in water: Effect of temperature and pH. *Microporous and Mesoporous Materials* 219 (2016), 117–124

[96] BELLIDO, E. ; GUILLEVIC, M. ; HIDALGO, T. ; SANTANDER-ORTEGA, M. J. ; SERRE, C. ; HORCAJADA, P.: Understanding the colloidal stability of the mesoporous MIL-100(Fe) nanoparticles in physiological media. *Langmuir* 30 (2014), 5911–5920

[97] BAATI, T. ; NJIM, L. ; NEFFATI, F. ; KERKENI, A. ; BOUTTEMI, M. ; GREF, R. ; NAJJAR, M. F. ; ZAKHAMA, A. ; COUVREUR, P. ; SERRE, C. ; HORCAJADA, P.: In depth analysis of the in vivo toxicity of nanoparticles of porous iron(III) metal–organic frameworks. *Chemical Science* 4 (2013), 1597

[98] RÖDER, R. ; PREISS, T. ; HIRSCHLE, P. ; STEINBORN, B. ; ZIMPEL, A. ; HOEHN, M. ; RÄDLER, J. O. ; BEIN, T. ; WAGNER, E. ; WUTTKE, S. ; LÄCHELT, U.: Multifunctional nanoparticles by coordinative self- assembly of His-tagged units with metal-organic frameworks. *Journal of the American Chemical Society* (2017)

[99] GEISOW, M. J. ; EVANS, W. H.: pH in the endosome. Measurements during pinocytosis and receptor-mediated endocytosis. *Experimental Cell Research* 150 (1984), 36–46

[100] FUCHS, R. ; SCHMID, S. ; MELLMAN, I.: A possible role for Na+,K+-ATPase in regulating ATP-dependent endosome acidification. *Proceedings of the National Academy of Sciences of the United States of America* 86 (1989), 539–543

[101] CAIN, C. C. ; SIPE, D. M. ; MURPHY, R. F.: Regulation of endocytic pH by the Na+, K+ -ATPase in living cells. *Proceedings of the National Academy of Sciences of the United States of America* 86 (1989), 544–548

[102] STEIN, I. H. ; SCHÜLLER, V. ; BÖHM, P. ; TINNEFELD, P. ; LIEDL, T.: Single-molecule FRET ruler based on rigid DNA origami blocks. *ChemPhysChem* 12 (2011), 689–695

[103] BLEIL, J. D. ; BRETSCHER, M. S.: Transferrin receptor and its recycling in HeLa cells. *The EMBO Journal* 1 (1982), 351–355

[104] PREISS, T. ; ZIMPEL, A. ; WUTTKE, S. ; RÄDLER, J.: Kinetic Analysis of the Uptake and Release of Fluorescein by Metal-Organic Framework Nanoparticles. *Materials* 10 (2017), 216

[105] GRALL, R. ; HIDALGO, T. ; DELIC, J. ; GARCÍA MÁRQUEZ, A. ; CHEVILLARD, S. ; HORCAJADA, P.: In vitro biocompatibility of mesoporous metal (III; Fe, Al, Cr) trimesate MOF nanocarriers. *Journal of Materials Chemistry B* 3 (2015), 8279–8292

[106] CUNHA, D. ; YAHIA, M. B. ; HALL, S. ; MILLER, S. R. ; CHEVREAU, H. ; ELKA, E. ; MAURIN, G. ; HORCAJADA, P. ; SERRE, C.: Rationale of drug encapsulation and release from biocompatible porous metal-organic frameworks. *Chemistry of Materials* (2013), 2767–2776

[107] BERNINI, M. C. ; FAIREN-JIMENEZ, D. ; PASINETTI, M. ; RAMIREZ-PASTOR, A. J. ; SNURR, R. Q.: Screening of bio-compatible metal-organic frameworks as potential drug carriers using Monte Carlo simulations. *Journal of Materials Chemistry B* 2 (2014), 766–774

[108] ANAND, R. ; BORGHI, F. ; MANOLI, F. ; MANET, I. ; AGOSTONI, V. ; RESCHIGLIAN, P. ; GREF, R. ; MONTI, S.: Host-guest interactions in Fe(III)-trimesate MOF nanoparticles loaded with doxorubicin. *Journal of Physical Chemistry B* 118 (2014), 8532–8539

[109] ZÜRNER, A. ; KIRSTEIN, J. ; DÖBLINGER, M. ; BRÄUCHLE, C. ; BEIN, T.: Visualizing single-molecule diffusion in mesoporous materials. *Nature* 450 (2007), 705–708

[110] MEDVED, I. ; CERNY, R.: Surface diffusion in porous media: A critical review. *Microporous and Mesoporous Materials* 142 (2011), 405–422

[111] AGOSTONI, V. ; ANAND, R. ; MONTI, S. ; HALL, S. ; MAURIN, G. ; HORCAJADA, P. ; SERRE, C. ; BOUCHEMAL, K. ; GREF, R.: Impact of phosphorylation on the encapsulation of nucleoside analogues within porous iron(iii) metal–organic framework MIL-100(Fe) nanoparticles. *Journal of Materials Chemistry B* 1 (2013), 4231–4242

[112] GIARD, D. J. ; AARONSON, S. a. ; TODARO, G. J. ; ARNSTEIN, P. ; KERSEY, J. H. ; DOSIK, H. ; PARKS, W. P.: In vitro cultivation of human tumors: establishment of cell lines derived from a series of solid tumors. *Journal of the National Cancer Institute* 51 (1973), 1417–1423

[113] ADAM, G. ; DELBRUECK, M.: Reduction of dimensionality in biological diffusive processes. RICH, A. (Hrsg.) ; DAVIDSON, N. (Hrsg.): *Structural Chemistry and Molecular Biology*. Freeman, San Francisco, 1968, 198–215

[114] LEADER, B. ; BACA, Q. J. ; GOLAN, D. E.: Protein therapeutics: a summary and pharmacological classification. *Nature Reviews. Drug Discovery* 7 (2008), 21–39

[115] LIU, X. ; ZHANG, P. ; HE, D. ; RÖDL, W. ; PREISS, T. ; RÄDLER, J. O. ; WAGNER, E. ; LÄCHELT, U.: pH-reversible cationic RNase A conjugates for enhanced cellular delivery and tumor cell killing. *Biomacromolecules* 17 (2016), 173–182

[116] MAIER, K. ; WAGNER, E.: Acid-labile traceless click linker for protein transduction. *Journal of the American Chemical Society* 134 (2012), 10169–10173

[117] RÖDER, R. ; HELMA, J. ; PREISS, T. ; RÄDLER, J. O. ; LEONHARDT, H. ; WAGNER, E.: Intracellular Delivery of Nanobodies for Imaging of Target Proteins in Live Cells. *Pharmaceutical Research* 34 (2017), 161–174

[118] HAMERS-CASTERMAN, C. ; ATARHOUCH, T. ; MUYLDERMANS, S. ; ROBINSON, G. ; HAMERS, C. ; SONGA, E. B. ; BENDAHMAN, N. ; HAMERS, R.: Naturally occurring antibodies devoid of light chains. *Nature* 363 (1993), 446–448

[119] ROTHBAUER, U. ; ZOLGHADR, K. ; TILLIB, S. ; NOWAK, D. ; SCHERMELLEH, L. ; GAHL, A. ; BACKMANN, N. ; CONRATH, K. ; MUYLDERMANS, S. ; CARDOSO, M. C. ; LEONHARDT, H.: Targeting and tracing antigens in live cells with fluorescent nanobodies. *Nature Methods* 3 (2006), 887–889

[120] RAJAN, M. ; MORTUSEWICZ, O. ; ROTHBAUER, U. ; HASTERT, F. D. ; SCHMIDTHALS, K. ; RAPP, A. ; LEONHARDT, H. ; CARDOSO, M. C.: Generation of an alpaca-derived nanobody recognizing γ-H2AX. *FEBS Open Bio* 5 (2015), 779–788

[121] KIRCHHOFER, A. ; HELMA, J. ; SCHMIDTHALS, K. ; FRAUER, C. ; CUI, S. ; KARCHER, A. ; PELLIS, M. ; MUYLDERMANS, S. ; CASAS-DELUCCHI, C. S. ; CRISTINA CARDOSO, M. ; LEONHARDT, H. ; HOPFNER, K.-P. ; ROTHBAUER, U. ; CARDOSO, M. C. ; LEONHARDT, H. ; HOPFNER, K.-P. ; ROTHBAUER, U.: Modulation of protein properties in living cells using nanobodies. *Nature Structural & Molecular Biology* 17 (2010), 133–138

[122] ASHOUR, J. ; SCHMIDT, F. I. ; HANKE, L. ; CRAGNOLINI, J. ; CAVALLARI, M. ; ALTENBURG, A. ; BREWER, R. ; INGRAM, J. ; SHOEMAKER, C. ; PLOEGH, H. L.: Intracellular expression of camelid single-domain antibodies specific for influenza virus nucleoprotein uncovers distinct features of its nuclear localization. *Journal of Virology* 89 (2015), 2792–2800

[123] STIJLEMANS, B. ; CALJON, G. ; NATESAN, S. K. A. ; SAERENS, D. ; CONRATH, K. ; PÉREZ-MORGA, D. ; SKEPPER, J. N. ; NIKOLAOU, A. ; BRYS, L. ; PAYS, E. ; MAGEZ, S. ; FIELD, M. C. ; DE BAETSELIER, P. ; MUYLDERMANS, S.: High affinity nanobodies against the Trypanosome brucei VSG are potent trypanolytic agents that block endocytosis. *PLoS Pathogens* 7 (2011), 1–2

[124] BLECK, M. ; ITANO, M. S. ; JOHNSON, D. S. ; THOMAS, V. K. ; NORTH, A. J. ; BIENIASZ, P. D. ; SIMON, S. M.: Temporal and spatial organization of ESCRT protein recruitment during HIV-1 budding. *Proceedings of the National Academy of Sciences of the United States of America* 111 (2014), 12211–12216

[125] BROISAT, A. ; HERNOT, S. ; TOCZEK, J. ; DE VOS, J. ; RIOU, L. M. ; MARTIN, S. ; AHMADI, M. ; THIELENS, N. ; WERNERY, U. ; CAVELIERS, V. ; MUYLDERMANS, S. ; LAHOUTTE, T. ; FAGRET, D. ; GHEZZI, C. ; DEVOOGDT, N.: Nanobodies targeting mouse/human VCAM1 for the nuclear imaging of atherosclerotic lesions. *Circulation Research* 110 (2012), 927–937

[126] LIU, H. ; WANG, Y. ; DUAN, H. ; ZHANG, A. ; LIANG, C. ; GAO, J. ; ZHANG, C. ; HUANG, B. ; LI, Q. ; LI, N. ; XIAO, S. ; ZHOU, E.-M.: An intracellularly expressed Nsp9-specific nanobody in MARC-145 cells inhibits porcine reproductive and respiratory syndrome virus replication. *Veterinary Microbiology* 181 (2015), 252–260

[127] MAIER, K. ; MARTIN, I. ; WAGNER, E.: Sequence defined disulfide-linked shuttle for strongly enhanced intracellular protein delivery. *Molecular Pharmaceutics* 9 (2012), 3560–3568

[128] ZHANG, P. ; HE, D. ; KLEIN, P. M. ; LIU, X. ; RÖDER, R. ; DÖBLINGER, M. ; WAGNER, E.: Enhanced intracellular protein transduction by sequence defined tetra-oleoyl oligoaminoamides targeted for cancer therapy. *Advanced Functional Materials* 25 (2015), 6627–6636

[129] MÖLLER, K. ; MÜLLER, K. ; ENGELKE, H. ; BRÄUCHLE, C. ; WAGNER, E. ; BEIN, T.: Highly efficient siRNA delivery from core–shell mesoporous silica nanoparticles with multifunctional polymer caps. *Nanoscale* 8 (2016), 4007–4019

[130] DOUDNA, J. A. ; CHARPENTIER, E.: The new frontier of genome engineering with CRISPR-Cas9. *Science* 346 (2014), 1258096–1258096